School of Electrical Engineering, Computing and
Mathematical Sciences

Palaeontology with SKA precursors: observations of fossil radio plasmas in galaxy clusters

Stefan W. Duchesne

0000-0002-3846-0315

This thesis is presented for the Degree of
Doctor of Philosophy
of
Curtin University

October 2021

To the best of my knowledge and belief this thesis contains no material previously published by any other person except where due acknowledgement has been made. This thesis contains no material which has been accepted for the award of any other degree or diploma in any university.

Stefan W. Duchesne

17/10/2021

"*But you, you're supposed to change. You're never the same even moment to moment—you're allowed and expected to invent who you are. What an incredible power—the ability to 'grow up'.*"

— Rose Quartz, *Steven Universe*

Acknowledgements

Firstly, I would like to sincerely thank Melanie, for supporting me completely through this research over the last few years. She has not only been an excellent scientific mentor but has also taught me (perhaps more importantly?) how to navigate the sometimes frustrating bureaucratic and political complexities of academic life. I would also like to thank Randall, who has been a key component in making sure this Thesis has come together.

The work in this Thesis would also not be possible without the input, help, or otherwise general support of numerous people. Some are acknowledged in official capacities as Co-authors on papers with all the specific requirements that entails, but others have helped in more subtle, general ways. In that capacity I would like to thank Susie, Torrance, Kat, Ben, Jai, Jaiden, and Steve—friends with whom I have had excellent discussions about radio astronomy, hobbies, and life in general, providing a necessary social sustenance to break up the (what I like to think is) meticulous research performed here. I would also like to thank Natasha, Paul, and Tim for useful discussion on MWA-specific data processing.

I would like to thank Paula Tarrío Alonso for providing mass estimates for Abell 2680 and Abell 2693 and Tiziana Venturi for providing the calibrated GMRT dataset of Abell 141. I would also like to thank Andrea Botteon, Simona Giacintucci, and Surajit Paul for providing their published radio and X-ray images of clusters for use in the introduction to this Thesis. Additionally, I would like to acknowledge the anonymous referees of the various papers that comprise a large portion of this Thesis, and thank them for the comments and suggestions that have improved the quality of the papers.

Finally I have to thank my parents, Tracey and Guy, for endless support and excitement for and about my work and study.

Abstract

Non-thermal, diffuse radio emission within clusters of galaxies has been studied with increasing intensity since the 1970s after the large (∼ 1 Mpc) synchrotron radio source in the Coma Cluster was determined to be associated with the magnetised intra-cluster medium (ICM) itself rather than any active radio galaxies (Willson, 1970). Since then detections of these diffuse cluster sources have only increased as radio telescopes have improved in surface brightness sensitivity and angular resolution. These Mpc-scale radio sources are typically broken down into two categories: centrally-located, amorphous radio halos and peripherally-located, arc-like radio relics. Due to the large source sizes and finite lifetimes of particles in the ICM, energy must be provided to these particles *in situ*. As clusters form hierarchically through major merger events and accretion, shocks and turbulence permeate the ionised plasma that makes up the ICM, providing a mechanism to energise particles over vast intra-cluster distances. While these physical mechanisms are largely accepted to generate these sources, there is currently no consensus on what population of particles is responsible for the emission. The ICM is filled with low-energy thermal electrons but may also host a significant population of 'fossil' electrons: remnants from long-dead radio galaxies, past episodes of nuclear activity, or outflows from active galactic nuclei. These Mpc-scale sources are not the only diffuse radio sources in clusters—in addition to halos and relics smaller-scale mini-halos, and other fossil radio plasmas are observed, suggesting a significant population of fossil electrons may be present within the ICM to be re-accelerated by shocks and turbulence.

In this work the link between fossil radio plasma and Mpc-scale radio halos and relics is explored, by first improving population statistics and by using the previously under-utilised low-frequency spectral energy distribution (SED) to help in both classifying

sources and to compare the diffuse source populations. The low-frequency radio interferometer, the Murchison Widefield Array (MWA), as well as the Australian Square Kilometre Array Pathfinder (ASKAP) are used extensively to observe and characterise a sample of candidate diffuse radio sources in Southern clusters. As part of this work, a new data-processing pipeline for the MWA Phase II in its 'extended' configuration (MWA-2) is presented, and in particular updates to post-imaging stages are made to enable reliable flux density measurements and determination of low-frequency spectra. Low-frequency spectra are used to: i) confirm the remnant radio galaxy associated with NGC 1534, ii) report a new double relic system associated with the massive cluster SPT-CL J2032−5627, iii) report of a new radio halo in Abell 3404 and, iv) follow-up of the radio halo detected in Abell 141, and v) characterise numerous diffuse cluster sources with MWA-2 and the Rapid ASKAP Continuum Survey (RACS). The known scaling relations between diffuse source monochromatic power and cluster mass are updated for double relic systems at 1.4 GHz and radio halos at both 1.4 GHz and 150 MHz with the full literature sample of radio halos. This update finds that for radio halos the large samples are allowing convergence to a well-defined P_ν–M_{500} relation, with few differences between the 1.4 GHz and 150 MHz relations. The final sample of diffuse sources reported in this work is compared to literature samples of remnant AGN, halos, relics, mini-halos, and miscellaneous fossil sources via their low-frequency integrated spectra, finding an ultra-steep ($\alpha \lesssim -1.5$) spectrum tail of the α distributions hinting towards a common link in their underlying particle populations.

Future studies at higher angular resolution and surface brightness sensitivities with Square Kilometre Array (SKA) pathfinders and precursors as well as the SKA itself will continue to uncover the particle populations responsible.

Contents

List of Figures

Chapter 1.

Introduction

This section acts as an introduction to galaxy clusters, structure formation, relevant radiation mechanisms, cosmic magnetic fields, and the observed diffuse, non-thermal radio emission in galaxy clusters. The questions regarding diffuse, non-thermal radio emission in galaxy clusters are summarised, highlighting the purpose of this Thesis which is to explore the link between structure formation, diffuse emission, and underlying electron populations.

1.1. Structure formation at the largest scales in the Universe

The Universe at the largest scales is comprised of $>$ 1 Mpc filaments of matter, with clusters of galaxies forming nodes along what is known as the Cosmic Web (e.g. Peebles, 1980; Cen & Ostriker, 1999; Davé et al., 2001). The distribution of galaxy clusters is not uniform with chains of clusters connected together in so-called 'super clusters' and close pairs of clusters interacting with one another (e.g. Oort, 1983). Galaxy clusters are predominantly comprised of dark matter, with $\sim$ 15 per cent of the matter made up of the hot (10^7–10^8 K; Serlemitsos et al., 1977) ionised plasma of the intra-cluster medium (ICM; e.g. Mitchell et al., 1976; Jones & Forman, 1999), and only $\sim$ 5 per cent of the cluster matter is the traditionally observed optical light from galaxies (see e.g. Kravtsov & Borgani, 2012, and references therein).

In the Λ Cold Dark Matter (ΛCDM) cosmology, galaxy clusters are thought to form hierarchically; mergers between massive clusters or accretion of matter from the filamentary Cosmic Web connecting nearby clusters work together to form the clusters we see today (e.g. Blumenthal et al., 1984). Binary mergers between massive

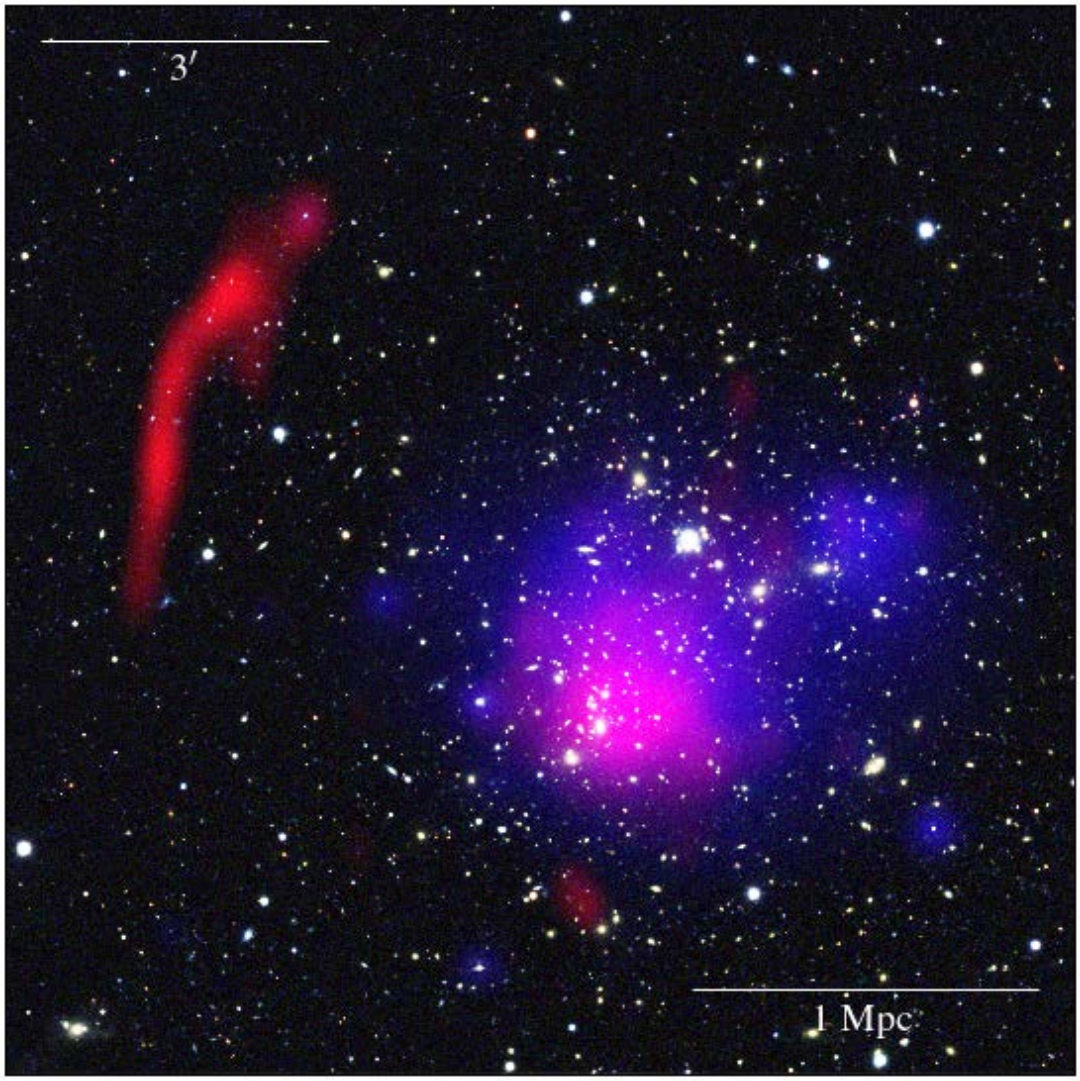

Figure 1.1. A multi-wavelength composite image of the massive, complex merging galaxy cluster Abell 2744 (see e.g. Giovannini et al., 1999; Orrú et al., 2007; Lotz et al., 2017; Pearce et al., 2017; Paul et al., 2019; George et al., 2017; Duchesne et al., 2021b; Rajpurohit et al., 2021a). The background optical data (RGB) are from the Dark Energy Survey (DES; Abbott et al., 2018; Morganson et al., 2018; Flaugher et al., 2015), the diffuse red overlay is at radio wavelengths (re-processed archival Karl G. Jansky Very Large Array (JVLA) data), and the diffuse blue overlay corresponds to X-ray wavelengths (re-processed archival XMM-*Newton* data). The radio data trace non-thermal (synchrotron) emission processes associated with the ICM (see Section 1.4) and the X-ray emission directly traces the ICM largely through Bremsstrahlung processes.

clusters of similar mass ($\sim 10^{15}$ $M_\odot$) can inject energy into the ICM on the order of $\sim 10^{64}$ ergs, resulting in large-scale shock waves and turbulence throughout the cluster (e.g. Markevitch et al., 1999; Markevitch & Vikhlinin, 2007). These merger events can induce substructure in the distribution of the optically visible constituent galaxies (e.g. Dahle et al., 2002; Shakouri et al., 2016a; Dehghan et al., 2017; Golovich et al., 2019) or in the morphology of the ICM as observed through X-ray thermal Bremsstrahlung emission (e.g. Mitchell et al., 1976). Indeed many clusters show some substructure and are in fact not relaxed (Jones & Forman, 1999).

Shock waves themselves can be observed as discontinuities in the X-ray surface brightness or cluster temperature profiles (e.g. Markevitch et al., 2002, 2005; Bourdin et al., 2013; Akamatsu et al., 2015; Eckert et al., 2016; Di Gennaro et al., 2019). The scale of the discontinuities can be directly related to the Mach number of the shock [1], assuming the Rankine–Hugoniot jump conditions across the shock boundary (e.g. Landau & Lifshitz, 1959), e.g. via

$$\mathcal{M} = \sqrt{\frac{2r}{\gamma + 1 - r\,(\gamma - 1)}}\,, \tag{1.1}$$

for $r = n_{\rm post}/n_{\rm pre}$, with the electron density, n in the post- and pre-shock regions, and $\gamma = 5/3$ the polytropic index, assuming a monatomic gas (e.g. Markevitch & Vikhlinin, 2007). As well as shocks, cold fronts are also observed as discontinuities in surface brightness, however, they differ observationally from shocks as the temperature in the region outside of the boundary is higher than inside (as opposed to shocks, where the temperature inside is higher) and there is little-to-no pressure change at the boundary. Cold fronts are interpreted as a discontinuity between an older core as it passes through a warmer cloud of ICM gas, e.g. during a merger (e.g. Markevitch & Vikhlinin, 2007; ZuHone & Roediger, 2016, and see the canonical example in Abell 3667; Vikhlinin, Markevitch & Murray 2001).

Merging clusters have a complex collection of processes including shocks as described above at various scales, interactions of active galactic nuclei (AGN) and other

[1] The Mach number is defined as $\mathcal{M} \equiv v/c_{\rm s}$, with $c_{\rm s}$ the sound speed in the post-shock region, and v to velocity of gas relative to the shock surface.

galaxies with the surrounding ICM, sloshing of the cluster core within the surrounding medium, and intra-cluster turbulence (see e.g. Brunetti & Jones, 2014). While these processes are often observed in X-rays, in a growing number of merging (and sometimes non-merging) clusters radio emission has been observed. This emission is unrelated to active galaxies (see the review by van Weeren et al., 2019, and Section 1.4). An example of a complex, merging cluster is shown in Fig. 1.1 at multiple wavelengths. Non-merging clusters also show evidence of turbulent motions especially via sloshing and AGN outflows, though this is usually restricted much more closely to the core (e.g. Ascasibar & Markevitch, 2006; ZuHone et al., 2013).

1.2. Radiation emission mechanisms

A number of mechanisms induce radiation from particles in Galactic and extra-galactic objects; both continuum and line emission processes are ubiquitous throughout the Universe. In this work, we focus on two continuum emission mechanisms: synchrotron radiation (non-thermal) in the radio regime and to a (much) lesser degree Bremsstrahlung (thermal) in the X-ray regime, and the implications of their observation on structure formation as discussed in Section 1.1. While synchrotron radiation is the main energy loss mechanism of most nearby radio sources and will be discussed in more detail in Section 1.2.1, other energy loss mechanisms exist that alter the shape of the observed emission spectrum: namely adiabatic losses and inverse-Compton losses.

The hot ICM plasma predominantly radiates at X-ray wavelengths, and while a number of emission mechanisms are thought to occur (e.g. Sarazin, 1988), thermal Bremsstrahlung is the most prominent. Bremsstrahlung in the ICM plasma, referred to also as 'free-free' emission, occurs as unbound electrons are deflected by mostly hydrogen ions (i.e. protons) while moving within the plasma (see e.g. Longair, 2011).

1.2.1. *Synchrotron radiation*

Synchrotron radiation is, in the simplest sense, radiation from charged relativistic particles (e.g. electrons) as they gyrate while travelling through a magnetic field, hence it is considered a 'non-thermal' radiation mechanism. In the following, I will briefly highlight the salient observable features of this type of emission (following Longair,

2011) [2].

The power radiated by a single relativistic electron gyrating in a magnetic field is obtained via the Larmor formula in the case of acceleration due to curvature along a magnetic field line, and can be represented as

$$-\left(\frac{\mathrm{d}E}{\mathrm{d}t}\right) = 2\sigma_{\mathrm{T}} c U_{\mathrm{mag}} \beta^2 \gamma^2 \sin^2\theta \,, \tag{1.2}$$

where σ_{T} is Thompson cross-section, U_{mag} is the magnetic field energy density, and θ is the pitch angle [3], i.e. the angle between the particle velocity and the magnetic field direction. Assuming an isotropic distribution of pitch angles, the average power emitted over the lifetime of the particle can be averaged over all pitch angles, resulting in

$$\left\langle -\left(\frac{\mathrm{d}E}{\mathrm{d}t}\right)\right\rangle = \frac{4}{3}\sigma_{\mathrm{T}} c U_{\mathrm{mag}} \beta^2 \gamma^2 \,, \tag{1.3}$$

at a frequency, $\nu \approx \gamma^2 \nu_{\mathrm{g}}$, where ν_g is the gyration frequency. For an ultra-relativistic particle $v \rightarrow c$, $\beta \approx 1$, and $\gamma \gg 1$; ν increases dramatically as a result of beaming of the dipole radiation ahead of the particle's trajectory and a Doppler shift of the wave. In the ultra-relativistic case, γ is large and the angle within which the particle emits radiation is $\sim 1/\gamma$ and thus very small.

While a single particle may not provide a continuous emission of electromagnetic waves, an ensemble with a range of energies will generate a spectrum of emission. For a distribution of charged particles, N, it is assumed that the particles are distributed with a power law distribution of energies with index $-\delta$, e.g. for a distribution with energies between E and $E + \mathrm{d}E$ this is

$$N(E)\,\mathrm{d}E \propto E^{-\delta}\mathrm{d}E \,, \tag{1.4}$$

[2] For a full theoretical framework of synchrotron processes, see also one of the many other textbooks on the subject of radiation mechanisms and high-energy astrophysics, e.g. Pacholczyk (1970); Jackson (1975); Rybicki & Lightman (2004).

[3] Often α is used, however α is used frequently for power law index in this work.

and the emissivity the distribution between ν and $\nu + \mathrm{d}\nu$ is then

$$j(\nu)\mathrm{d}\nu \propto -\left(\frac{\mathrm{d}E}{\mathrm{d}t}\right) N(E)\,\mathrm{d}E = -\left(\frac{\mathrm{d}E}{\mathrm{d}t}\right) E^{-\delta}\mathrm{d}E\,. \tag{1.5}$$

This can be re-written in terms of ν and B with appropriate substitutions [2], yielding

$$j(\nu) \propto B^{(1+\delta)/2}\nu^{(1-\delta)/2}\,, \tag{1.6}$$

from which can define the spectral index, $\alpha = (1-\delta)/2$, and we obtain the standard power law spectral energy distribution (SED) that we observe in many radio-emitting astronomical sources,

$$S(\nu) = S_0\left(\frac{\nu}{\nu_0}\right)^{\alpha} \quad [\mathrm{Jy}]\,, \tag{1.7}$$

for some reference flux density S_0 measured at ν_0 [4].

Most of the continuum [5] radio emission generated by extra-galactic astronomical objects is synchtrotron radiation (e.g. Scheuer & Williams, 1968). A key feature of the synchtrotron emission spectrum in many extra-galactic radio sources is a high-frequency 'break' where synchrotron energy loss dominates energy injection. This is a natural consequence of Eq. 1.3, where $-(\mathrm{d}E/\mathrm{d}t) \propto B^2E^2$, implying a situation wherein the highest energy electrons emitting synchrotron radiation at the highers frequency radiate their energy more quickly than their low-frequency counterparts, causing a break in the synchrotron spectrum beyond a critical frequency, ν_c, after some time. In the presence of inverse Compton losses this results in the ability to determine a characteristic 'age' of the synchrotron-emitting electrons of

$$t_\mathrm{age} = 1590\frac{B^{1/2}}{B^2 + {B_\mathrm{CMB}}^2}\left[(1+z)\,\nu_\mathrm{c}\right]^{1/2} \quad [\mathrm{Myr}]\,, \tag{1.8}$$

[4] Note I will use an alternate form of this equation in some places in this work, namely setting $A = S_0/{\nu_0}^{\alpha}$ as a more general power law function.

[5] Note radio emission from atomic or molecular transition lines, e.g. neutral hydrogen, are observed in some AGN and other galaxies (e.g. neutral hydrogen emission from the Magellanic Clouds; Kerr & Hindman, 1953).

for an isotropic distribution of pitch angles, where $B_{\rm CMB} = 3.25(1+z)^2$ μG and is the Cosmic Microwave Background (CMB) equivalent magnetic field, and $\nu_{\rm c}$ is in GHz (e.g. Feretti & Giovannini, 2008, and references therein). This is particularly prominent in radio sources that no longer have an injection mechanism fuelling them, as is the case for the so-called 'remnant' radio galaxies [6] (see e.g. Cordey, 1986; Parma et al., 2007; Murgia et al., 2011; Brienza et al., 2017; Quici et al., 2021, and Section 1.4.3 for further details).

In addition to the importance of the observed spectrum and loss rate for synchrotron radiation, the generally observed emission is linearly polarized. While the radiation mechanism technically results in elliptically polarized waves, when the particles are ultra-relativistic ($\gamma \approx 1000$) the opening angle, $\sim 1/\gamma$, of the radiation is small. In this regime the components of the elliptical polarization that are parallel to the projection of the magnetic field, **B** on the particle's velocity vector, **v** cancel which results in a linear polarization. It can be shown that for a uniform magnetic field the fractional (linear) polarization, $p_{\rm l}$, is then (e.g. Longair, 2011)

$$p_{\rm l} = \frac{\delta + 1}{\delta + \frac{7}{3}}, \tag{1.9}$$

where δ is as above.

1.3. Galaxy cluster magnetic fields

Galaxy clusters are permeated by magnetic fields on the order of 0.1–1 µG (Clarke et al., 2001; Johnston-Hollitt, 2003; Bonafede et al., 2010). The evidence for large-scale magnetic fields in clusters can be attributed to (1) the existence of large-scale synchrotron radio sources (i.e. diffuse cluster emission—see Section 1.4 for the full discussion of these sources) and (2) the observation of a rotation of the position angle of the linearly polarized emission from background and cluster sources via Faraday rotation (see e.g. Burn, 1966). As the rotation measure is proportional to the magnetic

[6] Also called remnant AGN or 'dead' radio galaxies. Some authors have used the term 'relic', which would be accurate, however, this would be confused Mpc-scale radio relics, which confusingly are perhaps not actually 'relic' emission.

field strength along the line of sight, i.e.

$$RM \propto \int_0^L n_{\rm e}(\mathbf{r})\mathbf{B} \cdot \mathrm{d}\mathbf{r}\,, \tag{1.10}$$

where $n_{\rm e}$ is the thermal electron density along the line of sight, with sufficient knowledge of the thermal electron density and structure of the magnetic field, the magnetic field strength within cluster can be estimated if sufficient radio sources are present (e.g. Kim et al., 1991; Johnston-Hollitt, 2003; Johnston-Hollitt & Ekers, 2004; Johnston-Hollitt, 2004; Murgia et al., 2004; Vacca et al., 2010; Bonafede et al., 2010; Pratley et al., 2013; Govoni et al., 2017; Stuardi et al., 2021) and if other Faraday rotating screens, like our Galaxy, can be removed or otherwise accounted for.

At present, the origin and evolution of cluster magnetic fields is not clear. It is thought that magnetic fields were seeded primordially (see e.g. Subramanian, 2016, and references therein), with limiting magnetic field strength $\leq 10^{-9}$ G (Ade et al., 2015; Planck Collaboration et al., 2016a), and are amplified by dynamo fluctuations caused by the various mechanical process involved in structure formation (see Donnert et al., 2018, for a review). Recent work with high-redshift radio halos (see Section 1.4.1) suggests a magnetic strength that has not evolved significantly since $z \approx 0.8$—0.9 and that amplification of the seed fields must be relatively fast (Di Gennaro et al., 2021).

Answering lingering questions regarding cosmic magnetism is a key science question for the upcoming Square Kilometre Array (SKA), where one of the main goals is to generate a dense grid of Faraday rotation measures for all sources across the sky, thereby providing a better understanding of not only the magnetic fields in clusters but also the foreground magnetic fields, e.g., from the Milky Way (see e.g. Johnston-Hollitt et al., 2015; Loi et al., 2019a,b; Heald et al., 2020), improving upon the recent rotation measure grids developed by Oppermann et al. (2015); Hutschenreuter et al. (2021) at $>$ 1 GHz radio frequencies and Van Eck et al. (2018); Riseley et al. (2018, 2020) at $\lesssim$ 200 MHz.

1.4. Diffuse, non-thermal radio emission

While most radio-emitting sources found in galaxy clusters are associated with active galaxies: e.g. star-forming galaxies, AGN, and otherwise lobed radio galaxies; a now rapidly growing number of galaxy clusters are found to host large-scale (up to ~ 2 Mpc [7]), diffuse radio emission both in the centre of the cluster and towards the periphery (see e.g. reviews by Feretti et al., 2012; Brunetti & Jones, 2014; van Weeren et al., 2019). These diffuse radio sources come in a range of flavours, but share a number of common properties: (1) an SED that can typically be modelled as a power law with a spectral index [8], $\alpha \lesssim -1$ (see Section 1.2.1); (2) low surface brightness (~ 1 μJy arcsec^{-2} at 1 GHz) punctuated in some cases by brighter filamentary components; and (3) no active host galaxy/AGN fuelling the source. From these observed properties it is inferred that the emission is non-thermal, synchrotron emission. These observed properties imply that the acceleration (or re-acceleration) of charged particles must occur *in situ* rather than directly from AGN. As described in Section 1.2.1 the synchrotron and inverse Compton losses provide a finite lifetime to the particle ($\lesssim 10^8$ yr) limiting their ability to diffuse over ~ 1 Mpc distances and still be detectable without additional energy input. Indeed, even if particles could diffuse over that timescale, due to energy loss rates steepening the observed spectrum one would observe spectral gradients originating at the particle injection site [9].

The following sections outline the various types of diffuse, non-thermal emission observed in galaxy clusters.

1.4.1. *Radio halos*

Radio halos are the prototypical Mpc-scale source detected in galaxy clusters, since the discovery of the Coma Cluster radio halo (Large et al., 1959; Willson, 1970). Radio halos are generally observed with a roughly circular morphology at the centre of the cluster. The radio emission is generally observed to correlate strongly with the X-ray–emitting ICM (e.g. Govoni et al., 2001), and there exist empirical scaling relationships

[7] Normally, with some extreme examples up to ~ 3.5 Mpc (e.g. Hoang et al., 2021).

[8] α is defined through $S_\nu \propto \nu^\alpha$, where S_ν is the flux density of the source at frequency ν.

[9] And indeed this is observed for relics but not from a single AGN, rather from the outer edge of the emission.

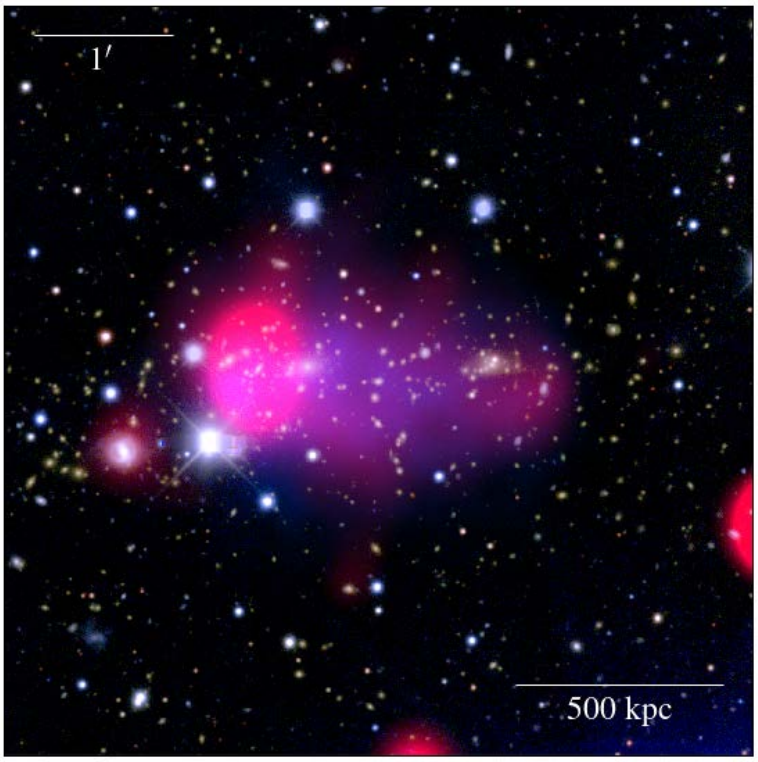

Figure 1.2. Composite image of the giant radio halo in MACS J0553.4−3342. Background optical (RGB) DES data, radio in red, and X-ray in blue (radio and X-ray data from Wilber et al., 2020, see their work for details). Note the correspondence of the radio and X-ray emission. The brighter component to the East is a blend of compact sources.

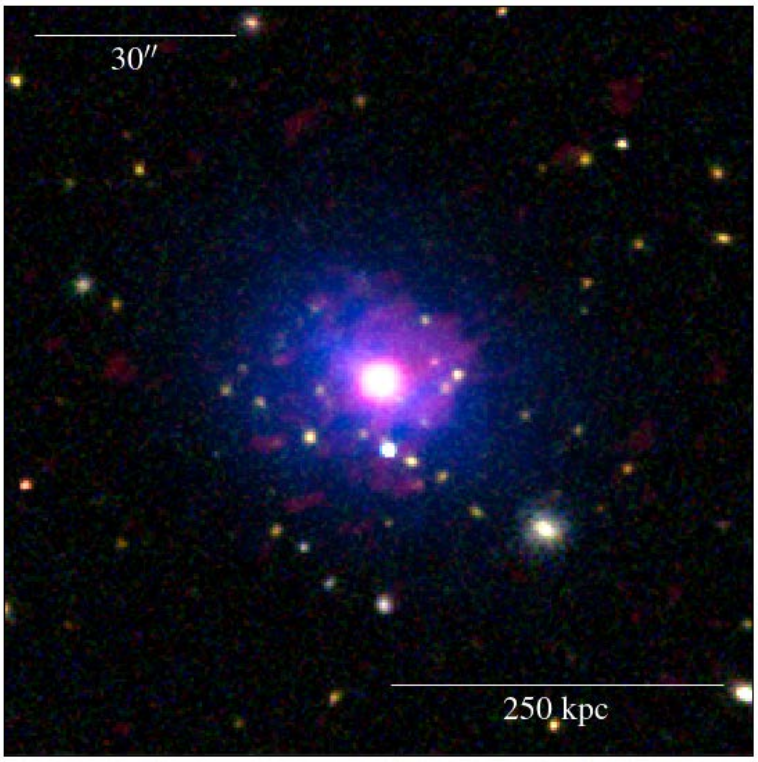

Figure 1.3. Composite image of the mini-halo in MACS J1532.8+3021. Background optical data are from the Sloan Digital Sky Survey (York et al., 2000; Eisenstein et al., 2011; Alam et al., 2015), radio in red, and X-ray in blue (radio and X-ray data from Giacintucci et al., 2014a, see their work for details). Note the bright compact source at the centre of the cluster, surrounded by diffuse radio emission.

between the radio power of the halo and the X-ray luminosity of the cluster (as well as other, closely linked cluster properties; e.g. Liang et al., 2000). Radio halos are broken down into two types: *(giant) radio halos* and smaller *mini-halos* ($\lesssim$ 500 kpc). While the objects have distinct differences as noted below, they share some similarities and there is suggestion that mini-halos may transition into their larger cousins as the radio-emitting electrons diffuse out to larger radii (Brunetti & Jones, 2014, furthermore, see Kale, Shende & Parekh 2019). For all types of radio halos, polarized emission is typically not detected beyond $\sim$ 10 per cent, though this may be partially due to beam de-polarization, i.e. smearing of polarization position angles within a large point-spread function (PSF; e.g. Govoni et al., 2013).

1.4.1.1. Giant radio halos

Giant radio halos [10] as their name would suggest are large ($\gtrsim$ 500 kpc) and are almost exclusively found in clusters that feature some morphological disturbance as evidenced from the X-ray emission (e.g. Cassano et al., 2010), implying a merger of some description (see an example in Fig. 1.2 and Fig. 1.1). X-ray morphological indicators such as the centroid shift, w, (e.g. Poole et al., 2006, furthermore, see Mohr, Fabricant & Geller 1993), which compares the surface brightness centroid for increasing apertures about the cluster centre, and the surface brightness concentration parameter c_{r_1/r_2}, defined via

$$c_{r_1/r_2} = \frac{I_{\rm X}\,(r < r_1\ {\rm kpc})}{I_{\rm X}\,(r < r_2\ {\rm kpc})}\,, \tag{1.11}$$

(Santos et al., 2008) with $I_{\rm X}$ the X-ray surface brightness, r the distance from the cluster centre, and $(r_1, r_2) = (40, 400)$ kpc or $(r_1, r_2) = (100, 500)$ kpc, provide indications of the substructure in the X-ray–emitting region. These, among other parameters, have been used by Cassano et al. (2010, 2013) to quantify the incidence of halos in un-relaxed (e.g. merging) clusters compared to otherwise relaxed clusters. A correlation between

[10] Note that 'giant' radio halos typically refer to halos with a size $\gtrsim$ 1 Mpc, however, here I will refer to halos that are not mini-halos as 'giant radio halos' or just 'radio halos' for brevity.

the X-ray surface brightness, $I_{\rm X}$, and the radio halo surface brightness, $I_{\rm R}$, with

$$I_R \propto {I_X}^k \,, \tag{1.12}$$

is generally seen, often with a linear or sub-linear slope (Govoni et al., 2001), with $k \gtrsim 0.6$ (e.g. Giacintucci et al., 2005; Botteon et al., 2020c; Rajpurohit et al., 2021c, though this is not always the case, with some radio halos ignoring this trend altogether; e.g. Shimwell et al. 2014; Cova et al. 2019).

The observed radio spectra of giant radio halos is typically power law within the range $\sim$ 100–1400 MHz (e.g. Rajpurohit et al., 2021c,a), though the prototypical example in the Coma Cluster (and the most well-sampled in frequency space) shows signs of curvature in this regime (e.g. Schlickeiser et al., 1987; Thierbach et al., 2003) and indeed is used as an example for the 'in situ re-acceleration' model for providing energy to the particles responsible for the synchrotron emission (Jaffe, 1977, cf. a solely power law energy distribution as described in Section 1.2.1). This re-acceleration model is based on energy being provided to the particles by turbulence in the region, and while the exact mechanism is not clear it is thought to be dominated by a Fermi-II–like process, where particles statistically gain energy proportional to β^2 as they cross between pockets of magnetised plasma of varying velocities as a result of cluster dynamics (e.g. Brunetti & Jones, 2014). The true process is likely a complex set of magneto-hydro dynamic (MHD)-driven turbulence-inducing processes triggered by mergers and other ICM dynamics (e.g. AGN outflow at smaller scales), as discussed by Brunetti & Lazarian (2007, 2011, 2016). It is not clear yet where (re-)accelerated electrons originate: the thermal pool of the ICM (i.e. those responsible for the X-ray emission) or from a population of fossil electrons left over from ancient radio galaxies or AGN outflows. There may be sufficient radio galaxy and AGN populations within clusters to seed such a population, however, the high-energy tail end of the thermal electron distribution may also provide sufficient particles for this purpose.

For giant radio halos, there exist scaling relationships between radio halo monochromatic power, P_ν, and (related) cluster properties such as temperature (Liang et al., 2000), X-ray luminosity (e.g. Brunetti et al., 2007), or the integrated Sunyaev–Zel'dovich (SZ)

signal (Sunyaev & Zel'dovich, 1970) and derived cluster mass (Basu, 2012), e.g. in the form

$$P_\nu \propto M^b \,, \tag{1.13}$$

where ν has historically been 1.4 GHz, and the cluster mass, M, is typically M_{500} [11]. Cassano et al. (2007) show that these relations can be predicted from turbulent re-acceleration mechanisms by comparison with MHD simulations and theory (see also Cassano et al., 2013), and scaling relations derived from cluster samples tend to roughly follow these expectations (e.g. Martinez Aviles et al., 2016; van Weeren et al., 2021; Cuciti et al., 2021b; Duchesne et al., 2021b). One limitation of the current sample of radio halos is a lack of low mass clusters—traditionally surveys intent on discovering new radio halos would observe either massive (e.g. Bernardi et al., 2016; Knowles et al., 2019, 2021; Cuciti et al., 2021a) or X-ray luminous (e.g. Giovannini et al., 1999; Venturi et al., 2007, 2008; Kale et al., 2013, 2015) clusters that are massive due to the cluster L_X–M scaling (e.g. Böhringer et al., 2007, furthermore, see Arnaud, Pointecouteau & Pratt 2005), and only recently have wide-field, deep radio surveys been able to perform 'blind' searches on cluster catalogues (though still with inherent limitations of the respective cluster catalogues, e.g. Duchesne et al., 2021b; van Weeren et al., 2021; Osinga et al., 2021), and specifically in high-redshift clusters (e.g. Di Gennaro et al., 2021; Raja et al., 2021). The low-mass cluster regime will result in low-energy cluster merger events, and re-acceleration models suggest low-energy mergers (or mergers in a later stage) are likely to host radio halos with lower powers (e.g. Botteon et al., 2021) and halos with the the steepest spectra (Brunetti et al., 2008)—the so-called ultra-steep–spectrum radio halos (USSRHs).

1.4.1.2. Mini-halos

As with giant radio halos, mini-halos are found in clusters with specific X-ray properties (see an example of a mini-halo in Fig. 1.3): they are almost exclusively found in cool-

[11] i.e., the mass enclosed in the radius within which the mean density of the cluster is 500 times the critical density of the Universe.

core (CC) clusters (e.g. Giacintucci et al., 2017, 2019) [12]. These CC clusters hosting mini-halos are typically relaxed at the largest scales, but usually feature sloshing and other signatures of accretion activity within the core (e.g. Fujita et al., 2004; Hlavacek-Larrondo et al., 2013; Giacintucci et al., 2014a,b). Additionally, mini-halos surround a central AGN associated with the brightest cluster galaxy (BCG) (e.g. the prototypical mini-halo in the Perseus Cluster: 3C 84; e.g. Burns et al., 1992; Gendron-Marsolais et al., 2017). Sloshing in the cluster core may turbulently re-accelerate fossil plasma outflows from the central BCG AGN (e.g. Gitti et al., 2002, 2004; ZuHone et al., 2013). Ignesti et al. (2020) showed that the radio–X-ray correlation for mini-halos (Eq. 1.12) tends towards a super-linear slope, implying a sharp decrease in radio power away from the BCG relative to the X-ray–emitting region. This highlights the potential link between the BCG and the mini-halos.

As with giant radio halos, mini-halos have their own scaling relations. While Giacintucci et al. (2014b, furthermore, see Giacintucci et al. 2019; Richard-Laferrière et al. 2020) find little correlation for P_ν–M, mini-halos show strong correlation for P_ν–L_X when X-ray luminosity is extracted within a radii $\lesssim R_{500}$ (e.g. 70 kpc: Giacintucci et al. 2019; and 600 kpc: Richard-Laferrière et al. 2020) which highlights the link between the core sloshing and the observed radio emission. Other authors have explored this correlation for X-ray luminosity within R_{500} (or even total L_X) as is done for giant radio halos, resulting in weaker correlation where a smaller sample size and significant scatter result in large uncertainty on fitted scaling relations (Cassano et al., 2008; Kale et al., 2013, 2015; Yuan et al., 2015; Gitti et al., 2018). Additionally, Richard-Laferrière et al. (2020) finds a correlation between the mini-halo power and the radio power of the central BCG AGN, further supporting a scenario wherein mini-halos are generated from AGN outflows (furthermore, see Bravi, Gitti & Brunetti, 2016).

Well-sampled mini-halo spectra are rare, which is generally an observational limit combining difficulty in measurement of diffuse, extended radio emission and the subtraction of comparatively strong compact sources embedded within the emission (i.e. the AGN). Giacintucci et al. (2014b) present the best-sampled mini-halo SED finding some evidence of a potential steepening beyond $\sim$ 5 GHz consistent with a re-

[12] Though note clear distinction between CC and non-CC clusters is not trivial (Hudson et al., 2010).

acceleration mechanism at work, though for most mini-halos only few measurements are available and generally a power law is seen (and assumed) in the measured regime.

1.4.2. *Radio relics*

As opposed to radio halos, radio relics [13] are found in the cluster outskirts, observed with elongated, often arc-like morphologies with linear sizes up to $\sim$ 2 Mpc (e.g. the main relic in Abell 2744 as shown in Fig. 1.1; Pearce et al. 2017, but see also Giovannini, Tordi & Feretti 1999 and the examples in Fig. 1.4) and are typically found to be polarized up to $\sim$ 60 per cent at 1.4 GHz (e.g. van Weeren et al., 2010). Multiple relics can be found in a single system (e.g. Rajpurohit et al., 2021a) and in some cases so-called 'double-relic' systems are observed wherein two relics lie on opposing sides ofthe cluster (e.g. Johnston-Hollitt, 2003; de Gasperin et al., 2014b, 2015, and see the example in Fig. 1.4). As with giant radio halos, radio relics are found in merging clusters, and in the case of double relics they are often found perpendicular to the axis of the merger (e.g. Johnston-Hollitt, 2003; Johnston-Hollitt et al., 2008, furthermore see the compilation and analysis of a sample of merging clusters by Golovich et al. 2019).

Radio relics are thought to form through a diffusive shock accceleration (DSA) process (i.e. a Fermi-I process, e.g. Drury 1983; Blandford & Eichler 1987) as weak shocks pass through the low-density cluster outskirts (see e.g. Enßlin et al., 1998; Roettiger et al., 1999). Observationally, DSA is consistent with the steep power law spectra relics are observed with, and observed spectral gradients steepening away from the outer-edges of relics is consistent with an injection of energy at a shock boundary (van Weeren et al., 2012). Indeed, some radio relics are also found to coincide with X-ray–detected shocks (e.g. Finoguenov et al., 2010; Akamatsu et al., 2015; Di Gennaro et al., 2019). In a pure DSA process with injection of particles at the shock boundary only, a normal power law model is expected, and indeed the Mach number of the shock

[13] Note 'radio relic' are also referred to as 'cluster radio shocks' (van Weeren et al., 2019) or 'radio gischt' (Kempner et al., 2004).. The 'radio shock' term will become clear shortly.

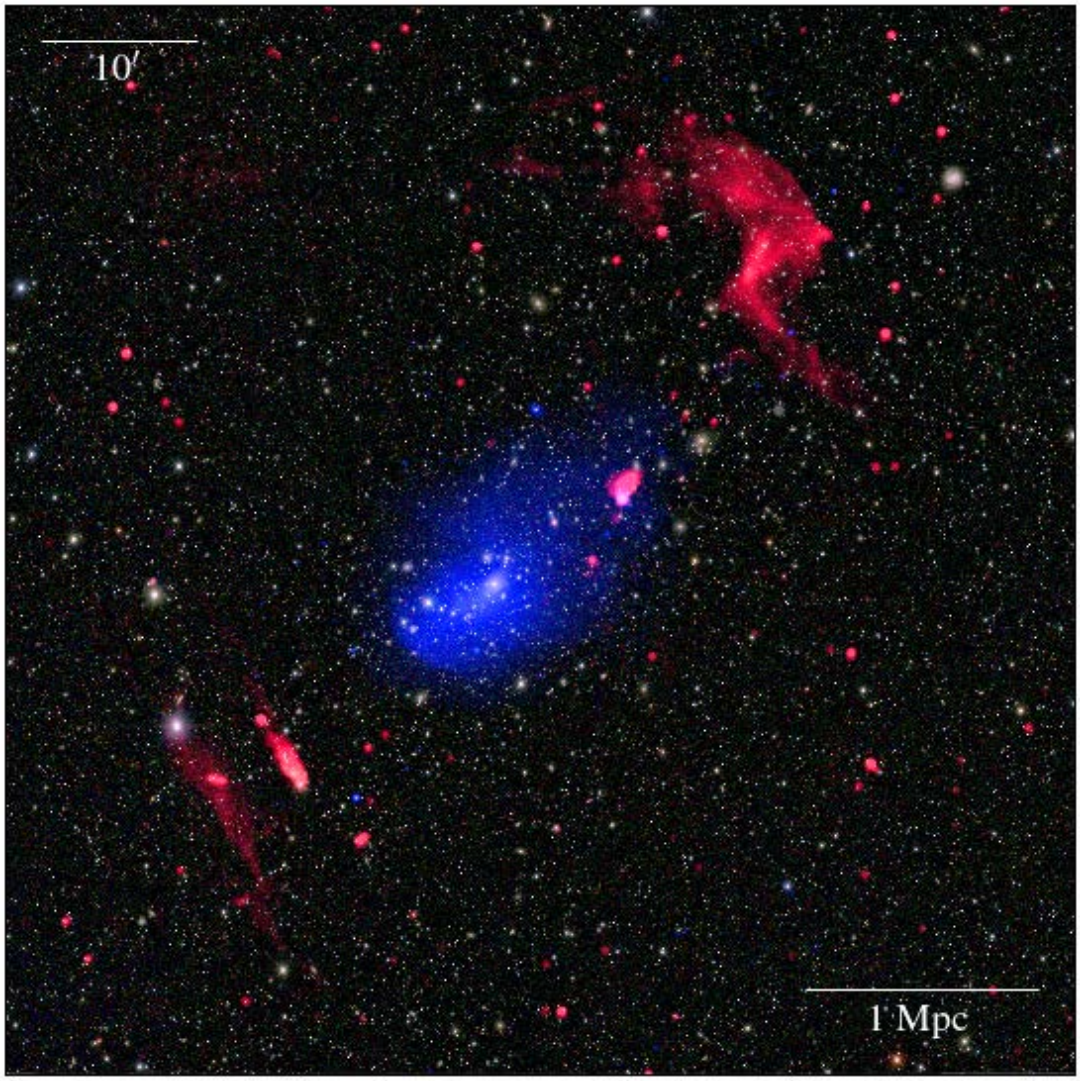

Figure 1.4. Composite image of the double relic system in Abell 3667 (see e.g. Johnston-Hollitt, 2003). Background optical data are from the DES, radio in red, and X-ray in blue. Radio data are re-imaged data from RACS [see Chapter 6, Duchesne, Johnston-Hollitt & Bartalucci (2021d)] and the X-ray data are archival *Chandra* data (see Chapter 5 for details on *Chandra* data processing). Note the relics are oriented roughly perpendicular to the elongation of the X-ray–emitting ICM and note the distance from the cluster centre.

can be related to the integrated spectral index, α, at the injection site, via

$$\mathcal{M} = \sqrt{\frac{2\alpha_{\rm inj} - 3}{2\alpha_{\rm inj} + 1}}, \tag{1.14}$$

(Blandford & Eichler, 1987), where $\alpha_{\rm inj} = \alpha + 0.5$ is the injection spectral index for normal synchrotron spectral breaks (Kardashev, 1962). For the most well-sampled relics, pure power law spectra have been observed (Loi et al., 2020; Rajpurohit et al., 2020b), however, some physical constraints limit this scenario. The observed brightness of some relics is not consistent with the acceleration efficiency expected from DSA if electrons are accelerated from the thermal pool (e.g. Botteon et al., 2016; Eckert et al., 2016; Botteon et al., 2020b, furthermore, see Hoeft & Brüggen 2007), and additionally one might question why relics are not ubiquitous in merging clusters given shocks are also detected in clusters *without* radio relics (e.g. Botteon et al., 2018), and sometimes in clusters with giant radio halos but no observed relic (e.g. Botteon et al., 2018; Wilber et al., 2020)—this may simply indicate a population of faint relics exist that are yet to be detected. It has been proposed that instead of particles being accelerated from the thermal pool, that there is a population of mildly-relativistic particles that are instead (re-)accelerated via DSA which can help remedy the acceleration efficiency problem (e.g. Markevitch et al., 2005; Kang et al., 2012; Pinzke et al., 2013; Kang, 2018). Additionally, Mach numbers derived from X-ray observations (e.g. Eq. 1.1) are not always consistent with those derived through Eq. 1.14 (e.g. Hindson et al., 2014; van Weeren et al., 2016) whereas assuming a pre-existing fossil electron population is responsible then $\alpha \sim \alpha_{\rm inj}$ may describe the energy injection and previously inconsistent Mach numbers may be explained (e.g. Hindson et al., 2014; van Weeren et al., 2016). Vazza et al. (2021) show via simulations that the particles from the radio lobes of an AGN may be distributed to the cluster outskirts where relics are located. These fossil electrons may be responsible for the observed relic emission, and some relics have been observed to be connected to active radio galaxies (e.g. Bonafede et al., 2014b; van Weeren et al., 2017, though note such sources perhaps begin to blend into the 'revived fossil plasmas' described in Section 1.4.3.2). Traditional DSA may also not be exactly the mechanism at work, and indeed other somewhat similar shock-

acceleration processes may be responsible (e.g. Kang, 2018). Finally, Mach numbers may also be inconsistent if a superposition of shocks are observed and X-ray and radio emission preferentially trace shocks of different Mach numbers (van Weeren et al., 2016; Rajpurohit et al., 2020a) and finally turbulence near the shock front may also affect the radio-estimated Mach number (Domínguez-Fernández et al., 2021).

Radio relic power also shows some scaling with their host cluster properties as with radio halos (van Weeren et al., 2009; Bonafede et al., 2012; de Gasperin et al., 2014b), however, in the case of the P_ν–LLS [14] relation only double relics are considered as a double relic implies a merger close to the plane of the sky and so projection effects are less likely to affect the measured LLS (Bonafede et al., 2012). The P_ν–M relation can be shown to fall out of energy budget considerations for mergers between massive clusters and simulations also result in such a relation which agrees somewhat with the measured data (de Gasperin et al., 2014b). At present there is a smaller number of double relic systems than giant radio halos or mini-halos, so results for these scaling relations are more uncertain.

1.4.3. *Fossil radio plasmas*

Beyond the Mpc-scale radio relics there are other relic-like sources that have been observed including remnant AGN (including the prototypical example associated with IC 2476; Cordey, 1987), *phoenices* (e.g. Slee et al., 2001), or otherwise revived fossil plasma (e.g. de Gasperin et al., 2017). Observationally these sources can begin to become difficult to distinguish from giant radio halos and mini-halos as their locations can be nearer the cluster centre than in the case of radio relics, however, they may also be further towards the cluster outskirts and can become observationally similar to radio relics as well. While linear size is usually a good characteristic in distinguishing between these sources and true relics and radio halos, other important features such as their locations within the cluster and their spectra may be useful for this purpose.

[14] Largest linear size.

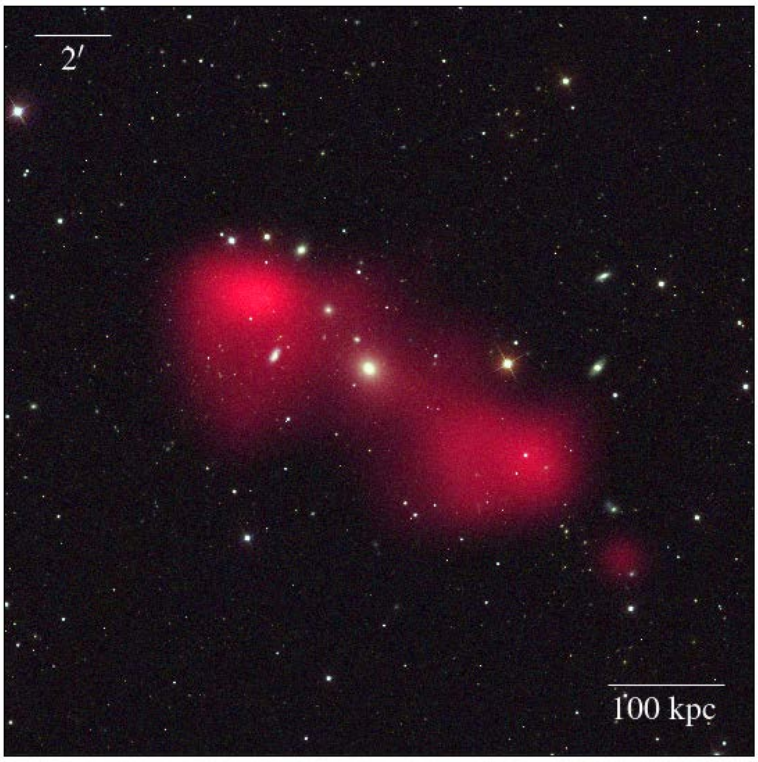

Figure 1.5. Composite image of the remnant AGN B2 0924+30 associated with IC 2476. Background optical (RGB) data are from the SDSS, and radio is in red (radio data from Shulevski et al., 2017, see their work for details). Note little-to-no compact radio emission seen from the host.

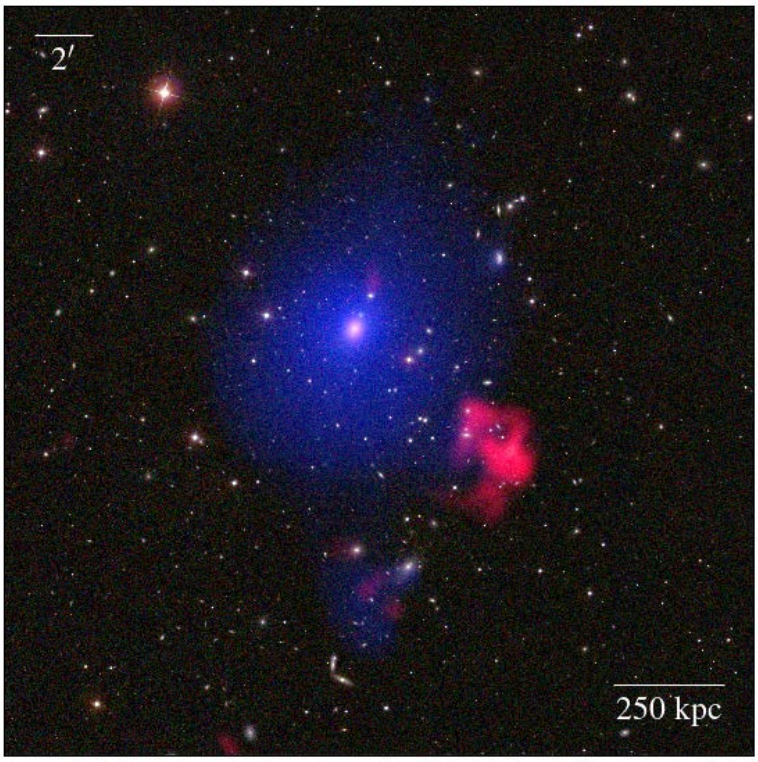

Figure 1.6. Composite image of phoenix in Abell 85 (see e.g. Slee et al., 2001). Background optical (RGB) data are from the SDSS, radio in red, and X-ray in blue. Radio data are from the TGSS (Intema et al., 2017, see Section 1.6.4) and the X-ray data are archival *Chandra* data (see Chapter 5 for details of *Chandra* data processing). Note the small size of the phoenix and the proximity to the cluster core.

1.4.3.1. Remnant AGN

Remnant AGN are characterised by a cocoon of radio plasma with a steepening radio spectrum due to synchrotron ageing (and inverse-Compton losses), after jets have switched off due to cessation of activity from a radio-loud AGN host (e.g. Komissarov & Gubanov, 1994, and see Fig. 1.5 for an example). Remnant AGN are found in some clusters (e.g. Cordey, 1987; Parma et al., 2007; Murgia et al., 2011; Quici et al., 2021), though a thorough survey of clusters for remnants has not yet been done, partially due to the complexity in confirming remnant AGN which typically requires a wide range of multi-wavelength data to confirm the spectral shape of the remnant lobes as well as identification of a host (e.g. Quici et al., 2021). To date, remnants have been predominantly found outside of clusters (e.g. de Gasperin et al., 2014a; Hurley-Walker et al., 2015; Brienza et al., 2016, 2017; Mahatma et al., 2018) and the effect of the cluster environment, on e.g. radio plasma/lobe confinement, is not yet clear (e.g. Murgia et al., 2011). While it is expected that every radio galaxy should eventually die, the limited lifetime of the remnant lobe component, combined with the fading of brightness of the radio plasma, precludes large fractions of remnants being observed, and indeed current estimates suggest the remnant fraction of radio galaxies of $\sim$ 4–10 per cent (Saripalli et al., 2012; Brienza et al., 2017; Mahatma et al., 2018; Jurlin et al., 2020; Quici et al., 2021).

Besides an often double-lobed morphology, one of the main characteristics of remnant AGN is an SED that begins to rapidly steepen beyond $\sim$ 1 GHz, though the exact break frequency is dependent on a number of factors, such as the lobe magnetic field and size (Komissarov & Gubanov, 1994). Spectral models exist for both active and remnant radio galaxies. Active sources are generally modelled as a continuous injection with losses (CI; Jaffe & Perola, 1973) and remnant sources are described by a CI model with an additional spectral feature representing energy loss after the AGN stops fuelling the radio lobes ($\mathrm{CI_{off}}$; Komissarov & Gubanov 1994). The extreme spectral curvature of remnants provides a mechanism to conduct searches for these sources (e.g. Parma et al., 2007; Murgia et al., 2011; Hurley-Walker et al., 2015), though use of only a steep-spectrum criterion ($\alpha \gtrsim -1.3$) may miss or misclassify some remnants (e.g. Brienza et al., 2017; Godfrey et al., 2017). One important characteristic of the remnant

spectrum is a power law in the $\sim$ 100–1000 MHz regime, often with $\alpha \lesssim -0.8$ (i.e., steeper than the lobes of a normal active radio galaxy [15]).

1.4.3.2. Revived fossil plasmas and phoenices

Perhaps closely related to remnant AGN are the various revived or re-accelerated fossil plasma sources [16] (see Fig. 1.6 for an example). These sources are considered remnant radio galaxy plasma (i.e. remnant lobes from AGN as discussed above) but at a later stage in their life after some shock(s) and/or turbulence has re-energised the radio plasma (e.g. Enßlin & Gopal-Krishna, 2001; Shimwell et al., 2015; van Weeren et al., 2017; de Gasperin et al., 2017). The exact mechanism for re-acceleration is not clear, and indeed it may be a combination of processes or different processes in different circumstances: e.g. Enßlin & Gopal-Krishna (2001) suggest an adiabatic compression of a radio plasma as a weak shock passes through the ICM and the radio plasma [17]. This mechanism is expected to generate the $\lesssim$ 400 kpc 'phoenices', and such a shock would generate spectra that deviate marginally from the $\mathrm{CI}_{\mathrm{off}}$ model mentioned in Section 1.4.3.1, though it has been used to accurately model the observed spectra of a number of revived fossil sources (e.g. Enßlin & Gopal-Krishna, 2001; Kale et al., 2012). For many fossil radio plasma sources, as with remnants, a power law can sufficiently model the $\sim$ 100–1000 GHz regime finding they are generally ultra-steep (e.g. Slee et al., 2001). Recently, a complex 'poly-phoenix' has been observed with the steepest synchrotron spectrum observed to date (Hodgson et al., 2021), which is thought to be a phoenix but with multiple distinct (but connected) re-accelerated components.

Other related mechanisms include a 'gentle' re-energisation of radio plasma (de Gasperin et al., 2017), which is perhaps a combination of small-scale effects such as adiabatic compression as described above combined with turbulence driven by instabilities along the radio plasma/lobe. Such a process is deemed 'gentle' as the

[15] I will note that normally the core of such a radio galaxy would have $\alpha \gtrsim -0.5$, with the lobe plasma representing a slowly fading population of particles.

[16] Note these have been considered 'roundish' relics or otherwise small-scale relics in the literature, though I will differentiate here if only to reinforce the point that these smaller scale sources are almost certainly remnants of radio galaxies, whereas in the Mpc-scale radio relic case the origin of the particles responsible is not yet clear. Of course, the term relic is then unfortunately confusing.

[17] For context, this process was intended to apply to Mpc-scale radio relics described in Section 1.4.2, however, most relics do not show the steepening expected by such a model.

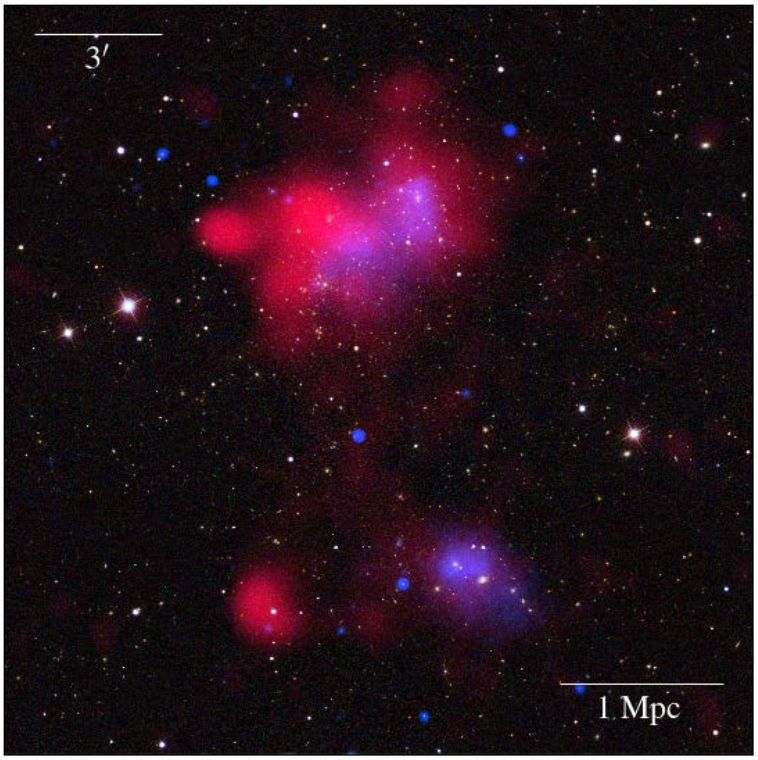

Figure 1.7. Composite image of the radio bridge between Abell 1758N and Abell 1758S. Background optical data are are from the SDSS, red is radio, and blue is X-ray (radio and X-ray data from Botteon et al., 2020a, see their work for details). Note each cluster also hosts a radio halo, and the bridge is particularly faint in comparison.

re-energisation is perhaps minimal, allowing an ancient plasma to shine and retain an ultra-steep spectral shape, e.g. $\alpha \gtrsim -4.5$ in the case of the emission in Abell 1033 (de Gasperin et al., 2017). Abell 1033 is an interesting example because it highlights the cases wherein faded radio lobes still connected to an active host may be re-accelerated. A similar scenario is seen in Abell 1314 where a giant head-tail radio galaxy is detected with evidence of re-acceleration along the tail (Wilber et al., 2019). The relics seen in PLCKG287.0+32.9 (Bonafede et al., 2014b) and Abell 3411–3412 (van Weeren et al., 2017) have similar features; an active radio galaxy is connected to steeper-spectrum emission with evidence of shocks having passed through a lobe. As hinted at in Section 1.4.2, this is where classification become difficult: are these sources examples of true relics, caught in the act? Or are these just examples of revived fossil plasmas, albeit at a larger scale than is usually observed?

1.4.4. *Radio bridges*

Finally, between two of close pairs of clusters or subclusters bridges of synchrotron emission have been observed (Govoni et al., 2019; Botteon et al., 2020a; Hoeft et al.,

2020; Bonafede et al., 2021). Note, though, that not all close cluster pairs have had bridges detected, despite deep radio observations and despite a bridge detected in X-ray (Reiprich et al., 2021; Brüggen et al., 2021). This emission has similarities with halos in that there may be some stochastic turbulent process re-accelerating particles between the clusters, and indeed there is scope for the interacting clusters to deposit the energy required in these inter-cluster regions (Brunetti & Vazza, 2020). Alternatively, the emission may also be generated via shock-related processes, and certainly the exact requirements for generation of a synchrotron-emitting bridge are an open topic. However, this is not the main topic of this work largely due to a difference in observational requirements [18]. An example synchrotron bridge is shown in Fig. 1.7.

1.5. Open questions and approaching answers

While the current taxonomy for these sources is largely separated by the underlying physical mechanism that is powering the source [19], exact mechanisms are, at present, not completely understood. Usually, the taxonomy used by Kempner et al. (2004) is still in use to some degree, and further clarified in the review by van Weeren et al. (2019), however, the requirements for certain classifications based on underlying physics typically requires enormous amounts of multi-wavelength data with very high fidelity [20]. Comparatively, a modest amount of data is required to measure the power law SED, hence spectral index, of such sources in the $\sim$ 100–1000 MHz regime (see e.g. George et al., 2017) and indeed we know that the general properties of these sources lend themselves to differences in spectral index (e.g. different spectral ageing characteristics combining with differences in injection of energy from possible re-acceleration processes, and a difference in particle population), even if all are classed as steep-spectrum [21]. With this in mind, answering the following question should benefit understanding of diffuse cluster emission:

[18] For example one would look outside of clusters rather than inside of them, as one would for the other cluster-based diffuse emission.

[19] Hence why relics are perhaps better referred to as 'radio shocks'.

[20] We may well be moving towards this for the entire sky with the next generation of telescopes, but for now there are still limitations in performing such studies over large samples—see Section 1.6.

[21] Ambiguous cases remain in the literature (e.g. the object in Abell 1213; Giovannini et al. 2009, or the the object in CL 0217+70; Brown, Duesterhoeft & Rudnick 2011).

Can the low-frequency SEDs of these sources, which are typically well-modelled as power laws, be used as a tool in distinguishing between radio halos, relics, remnants, and other revived fossil plasma sources?

Perhaps somewhat related, as the observed spectrum depends on particle population under acceleration, is the question of whether fossil electron populations can be invoked to explain the emission we observe as halos and relics. In the case of mini-halos, this is almost guaranteed due to the relationship with the cluster BCG, and in the case of fossil plasma these are by definition fossil electrons, but for radio halos and relics it is not yet clear if the thermal pool electrons commonly assumed to be responsible have sufficient energies to be accelerated up to relativistic energies (e.g. the known acceleration efficiency problem for for relics under a standard DSA assumption; Botteon et al., 2020b). Thus, this work aims to explore the following:

Is the (re-)accelerated electron population for halos and relics likely to originate in the thermal pool of electrons, from fossil electrons, or perhaps a combination thereof?

As an observed spectrum of a radio synchtrotron-emitting source will be shaped in some part by an underlying particle population, the observed spectrum should provide clues as to this unclear population. At present, two main populations exist in clusters: the thermal pool of the ICM, with comparatively low energies, and the fossil electron pool, e.g. relativistic remnants from radio galaxies and AGN. The thermal pool permeates the entire cluster, and indeed radio halo emission typically correlates with the X-ray–emitting ICM. However, lower energies require greater energy input or greater acceleration efficiency to obtain the relativistic speeds needed for synchrotron emission. The fossil electrons, however, are only confirmed with respect to e.g. remnant AGN, and whether a sufficient amount of the cluster volume could be seeded by such electrons is not yet clear, though simulations suggest a dying radio galaxy could have its lobe plasma disperse throughout the ICM to provide a seed population for halos and/or relics (Vazza et al., 2021).

1.6. Observations at radio wavelengths

For the purpose of obtaining radio images with sufficient resolution to disentangle sources we use the suite of radio interferometers available. A full review of radio synthesis imaging from interferometry is outside of the scope of this Thesis [22], however, I will give a brief overview and highlight features/aspects that will become important later. Additionally, I will discuss specific radio telescopes used in this work and highlight their properties and operation that make them able to tackle the questions posed in Section 1.5.

1.6.1. *Interferometry*

As the angular resolution, $\theta_{\rm res}$, of a normal telescope dish is a function of its diameter and observed wavelength (i.e. $\theta_{\rm res} \propto D/\lambda$), it becomes prohibitive to explore the radio sky with any great resolution with single dish telescopes, especially if wanting to observe below a few GHz. To overcome this, the technique of interferometry has been employed to exploit the diffractive nature of radio waves, allowing placement of sparse receiver elements (i.e. antennas) to synthesize an (incomplete) aperture.

Since Ryle & Vonberg (1946) detected radio emission from the Sun with a radio interferometer, observations of the sky with interferometers have only increased in sensitivity and resolution. With the advent of Earth-rotation synthesis to obtain a more complete knowledge of the observed sky brightness (Ryle, 1962) and better localised fringe patterns, positions of extra-Galactic radio sources were able to be measured to eventually $\lesssim$ arcec precision (e.g. Ryle et al., 1965; Hargrave & Ryle, 1974; Perley et al., 1984, for improvements upon the imaging and position of the radio galaxy Cygnus A; see Fig. 1.8).

Following Thompson et al. (2017), in the simplest case, an array of two elements is considered, without any rotation. In this example, it is assumed the incident waves detected by the array elements are in the far-field, such that the wave is planar at the receiver. The geometric delay in receiving a wave between two such elements is $\tau_{\rm g} = \mathbf{b} \cdot \mathbf{s}/c$, where $\mathbf{b}$ is the baseline vector between the elements, and $\mathbf{s}$ is the unit

[22] For an introduction to radio interferometry and synthesis, please see the excellent textbook by Thompson et al. (2017).

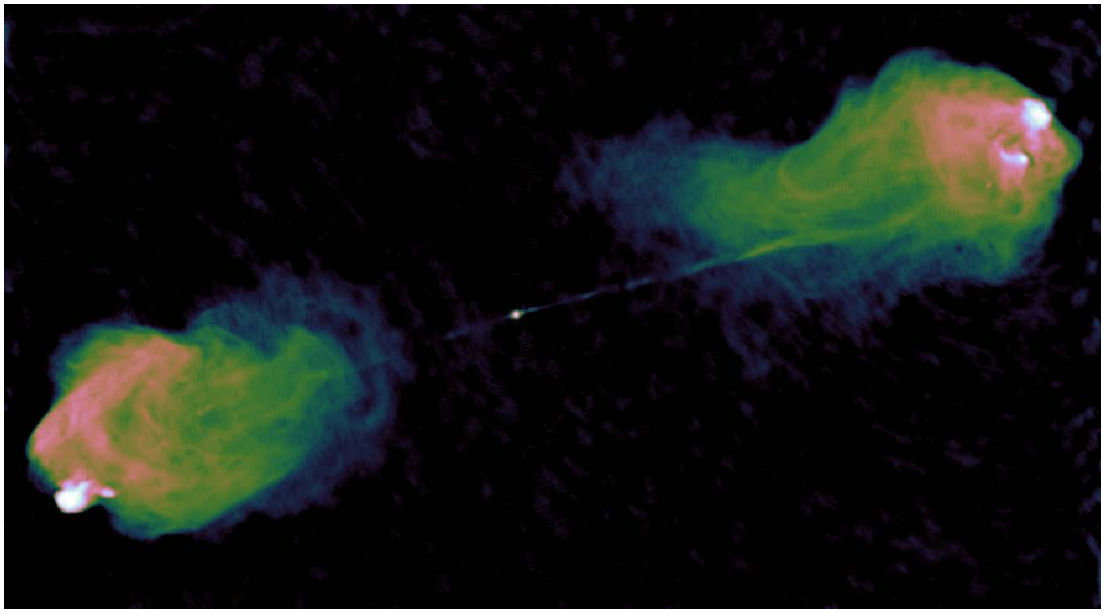

Figure 1.8. Radio image of Cygnus A (Perley, Dreher & Cowan, 1984), using the Very Large Array (VLA) at 4.5 GHz and exploiting Earth-rotation synthesis to image on multiple angular scales at 0.4 arcsec angular resolution. The colourscale is logarithmic, from 0.7 to 1900 mJy.

vector to the signal source. The phase difference between the two elements is then $\Theta = 2\pi \mathbf{b} \cdot \mathbf{s}/\lambda$, and the signal is multiplied by $e^{-2\pi i \nu \mathbf{b}\cdot\mathbf{s}/c}$ during complex correlation, which produces both sine and cosine fringes. The complex visibility is defined as the response of the interferometer to the sky brightness, which is then

$$V(\mathbf{b}) = \int_0^{4\pi} I_{\rm sky}(\boldsymbol{\sigma}) \exp\left(-2\pi i \nu \mathbf{b} \cdot \boldsymbol{\sigma}/c\right) \mathrm{d}\Omega\,, \qquad 1.15$$

for $\boldsymbol{\sigma} = \mathbf{s} - \mathbf{s}_0$, and $\mathbf{s}_0$ the phase centre of the array elements.

It is usual to consider coordinates as shown in Fig. 1.9 (e.g. Leshem, van der Veen & Boonstra, 2000), and the the full visibility function in this traditional Earth-rotation coordinate system is

$$V(u,v,w) = \int_{-\infty}^{\infty}\int_{-\infty}^{\infty} \frac{A(l,m)I(l,m)}{\sqrt{1-l^2-m^2}} \times \exp\left\{-2\pi i\left[ul + vm + w\left(\sqrt{1-l^2-m^2}-1\right)\right]\right\} \mathrm{d}l\mathrm{d}m\,, \qquad 1.16$$

where l, m are direction cosines on the sky, I is the sky brightness, A is the antenna

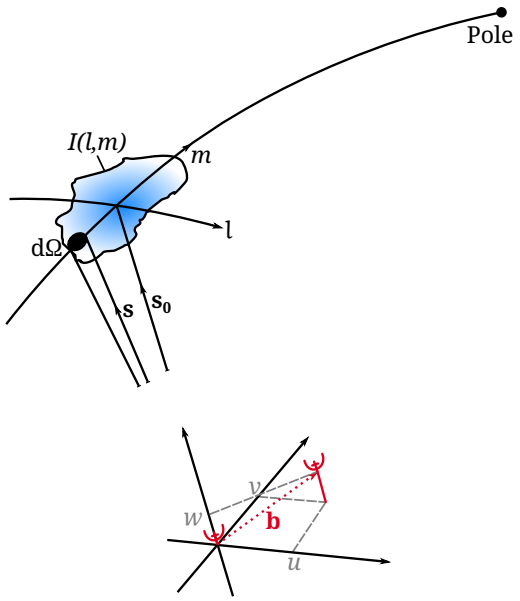

Figure 1.9. Coordinates used for the visibility equation, adapted from Thompson et al. (2017).

response pattern (and $I_{\rm sky} \sim AI$), and u, v, w are the baseline coordinates. For cases where $w \to 0$ or when $w\sqrt{1-l^2-m^2} - 1 \to 0$ (i.e. when l and m are small) then a simpler form of Eq. 1.16 can be considered, as

$$V(u,v) = \int_{-\infty}^{\infty}\int_{-\infty}^{\infty} \frac{A(l,m)I(l,m)}{\sqrt{1-l^2-m^2}} \exp[-2\pi i\,(ul+vm)]\;\mathrm{d}l\mathrm{d}m\,, \qquad 1.17$$

which is the traditionally considered form for small fields of view (e.g. when l, m small) or co-planar array ($w = 0$). To obtain the sky intensity (e.g. an image), the van Cittert–Zernike theorem states the inverse Fourier transform can be performed on Eq. 1.17 resulting in

$$I(l,m) = \frac{\sqrt{1-l^2-m^2}}{A(l,m)} \int_{-\infty}^{\infty}\int_{-\infty}^{\infty} V(u,v) \exp[2\pi i\,(ul+vm)]\;\mathrm{d}u\mathrm{d}v. \qquad 1.18$$

In the case where Eq. 1.16 is considered instead, this requires more care and indeed methods exist to perform this inverse Fourier transform, often on discrete ranges of w—this will be discussed further in Appendix A.4.

1.6.1.1. Polarization and the general measurement equation

Generally radio interferometers measure the polarization via feeds that measure the X, Y [23] components of the electric field of the incident radiation. In general, the radio emission is decomposed into the four Stokes parameters, I (total intensity), Q, U (linear polarization), and V (circular polarization), which are related to the correlations between the feeds. For example, in the case where instrumental feeds are orthogonal and linear as well as close to the boresight of the antenna, the correlations XX, YY, XY, YX (i.e. the instrumental polarization) are related to the Stokes parameters via

$$I_{\text{corr}}(l,m) = \begin{bmatrix} XX & XY \\ YX & YY \end{bmatrix} = \begin{bmatrix} I+Q & U+iV \\ U-iV & I-Q \end{bmatrix}, \tag{1.19}$$

where $I_{\text{corr}}(l,m)$ is the sky brightness correlation of X, Y linear feeds.

Visibilities obtained from telescopes are not completed represented by Eq. 1.16 or Eq. 1.17—usually additional operations should be applied to determine how other instrumental or propagation effects will be encapsulated in the measured visibilities. One such effect is the antenna response, $A(l,m)$, as seen above. These changes can be conveniently bundled into 2 by 2 Jones matrices, $\mathbf{J}$, that are applied to $I_{\text{corr}}(l,m)$. This results in a matrix form of Eq. 1.16 that separates sky intensity from other effects (e.g. Smirnov, 2011a,b) [24]

$$V_{ij}(u,v,w) = \int_{-\infty}^{\infty}\int_{-\infty}^{\infty} \frac{1}{n}\left(\mathbf{J}_i I_{\text{corr}}(l,m)\mathbf{J}_j^H\right) \exp\left[-2\pi i\left(ul+vm+w(n-1)\right)\right] \mathrm{d}l\mathrm{d}m\,, \tag{1.20}$$

for an antenna pair i, j, setting $n = \sqrt{1-l^2-m^2}$ for compactness, and noting that $A(l,m)$ has been incorporated into $\mathbf{J}$, with $\mathbf{J}^H$ the Hermitian conjugate. $\mathbf{J}$ in practice is a combination of effects, e.g. the complex receiver gains, $\mathbf{G}$, and forms a 'chain' wherein effects are applied in order. Many elements of visibility calibration are 'correcting' those effects with reference to a source with a known behaviour. Note that direction-independent effects can be pulled outside of the integral in Eq. 1.20 which allows for

[23] For a linear basis. Note a circular basis is also used.
[24] Though note other formulations exists.

e.g. self-calibration (e.g. Cornwell & Wilkinson, 1981).

1.6.1.2. Obtaining the sky brightness—imaging

Going back to 'Earth rotation synthesis', we typically do not want a single fringe pattern which would be observed with a single antenna pair/baseline for a single visibility measurement as that gives limited information about an astronomical source. Instead, we observe for some time, allowing the Earth to rotate while increasing 'u, v coverage', filling in the u, v plane. In real observations, the visibility function is not sampled fully, and a discrete sampling function, $S(u, v)$, is applied as

$$V_{\text{observed}}(u, v) = S(u, v)w(u, v)V(u, v)\,, \tag{1.21}$$

with the addition of a weighting function, w, and the equivalent Fourier inverse is

$$I_{\text{observed}}(l, m) = P(l, m) * I(l, m)\,, \tag{1.22}$$

where $*$ is the convolution and $P(l, m)$ is the PSF, which is the Fourier inversion of $S(u, v)w(u, v)$.

Weighting functions can vary from normal variance weighting (i.e. 'natural weighting', typically the best sensitivity, but with a degraded PSF shape) to inclusion of a factor to remove weight from high-density u, v points (i.e. 'uniform weighting', often with lower sensitivity, but a well-behaved PSF). Briggs (1995) proposed a method wherein weighting can be defined by a parameter, the 'robust' parameter, effective in the range $[-2, 2]$ that roughly goes between the extremes of uniform and natural weighting. This method is often used and is used extensively in this work. Some additional comparison of weighting effects on the PSF are shown in Fig. A.9. An important thing to note regarding u, v coverage is that a fringe pattern produced by a single u, v visibility is dependent on the baseline length, b. Therefore in a given summation of fringe patterns as used in an interferometric image, angular information is only available for scales $\geq \max(b)/\lambda$. Additionally, sensitivity for a particular angular scale is dependant on the number of samples for that scale (and how those u, v data are weighted). Hence, to

observe low surface-brightness, extended emission one requires many short baselines.

Finally, images are created via a direct fast Fourier transform of the visibilities, subject to Eq. 1.21. To return to the 'true' sky brightness $I(l,m)$, requires deconvolution of $P(l,m)$ (and removal of, e.g. $A(l,m)$), which is particularly important for incomplete u,v sampling as astronomical sources convolved with the PSF can spew sidelobes throughout an image, increasing noise, making characterisation almost impossible, and just generally being a nuisance. One such algorithm to reconstruct $I(l,m)$ is the CLEAN algorithm (Högbom, 1974), which effectively deconvolves the PSF on a source by source basis, finding a source, then Fourier transforming back to the visibilities to subtract some fraction of it (i.e. with the PSF), then moving back to the image and repeating until all sources (or some other stopping threshold) are reached. The subtracted sources are recorded as a collection of delta functions, which are then convolved with a 'CLEAN' beam (typically a Gaussian PSF fitted to the true PSF) and added to the residuals. This results in a 'CLEANed' image. We tend towards a modified version of the algorithm wherein a requisite number of sources are found prior to Fourier transforming back to the visibilities to save on computation (see Clark, 1980). Additionally, modifications have been made to also find extended sources (of some shape) as part of the deconvolution process—this is referred to as multi-scale CLEAN (e.g. Cornwell, 2008).

1.6.2. *The Murchison Widefield Array*

The Murchison Widefield Array (MWA) is an SKA precursor interferometer located in the remote Murchison Radio-astronomy Observatory in Western Australia. This remote location is necessary to avoid interference from human-made radio waves, i.e. radio-frequency interference (RFI). Between 2013–late 2017 the MWA operated with 128 antenna tiles (see Fig. 1.10) in its Phase I (Tingay et al., 2013). In this Phase I configuration, the MWA achieved an angular resolution $\sim$ 2 arcmin at 154 MHz (weighting-dependent) and offered excellent u,v coverage even in 2-min snapshot observations owing to a dense core of tiles and smooth distribution out to the maximum baseline of $\sim$ 2.8 km. The instrument in this configuration has naturally led to many advances in a range of fields in radio astronomy (Beardsley et al., 2019), including

Figure 1.10. Photograph of an MWA antenna, showcasing the cross-dipole design.

observations of diffuse clusters sources (Hindson et al., 2014; George et al., 2015, 2017; Zheng et al., 2018; Duchesne et al., 2021b).

In late 2017 the MWA was upgraded to its Phase II configuration (Wayth et al., 2018), consisting of 256 tiles split between a compact configuration including two close-packed hexagonal layouts for Epoch of Re-ionization science (and e.g. redundant baseline calibration) and an extended configuration consisting of a subset of the original Phase I array layout with the addition of 56 tiles spaced out to $\sim$ 5.3 km. In both configurations, due to limitations of the receivers and correlator only 128 tiles can be used at any one time, hence the split between a 'compact' and 'extended' configuration [25]. For this work, the 'compact' configuration is not used. The 'extended' configuration naturally boasts roughly a factor of two increase in resolution over the original Phase I, but suffers somewhat in its sensitivity to extended structures due to fewer short baselines (Hodgson et al., 2020).

Hereafter, the MWA Phase II 'extended' configuration will be referred to as the MWA-2. A full description of the MWA-2 data processing is included in Appendix A.

Figure 1.11. A photograph of a subset of ASKAP antennas.

1.6.3. *The Australian Square Kilometre Array Pathfinder*

Also at the Murchison Radio-astronomy Observatory is the Australian Square Kilometre Array Pathfinder (ASKAP; DeBoer et al., 2009; Hotan et al., 2021), which is an array comprised of 36 antennas of 12-m diameter (as pictured in Fig. 1.11). Antennas are placed with a dense core and maximum baseline $\sim$ 6 km. While the array with only a single primary beam of $\sim$ 1 deg at 1 GHz would still provide an instrument for deep radio astronomy imaging with excellent u, v coverage, one of the major technical achievements for ASKAP is the application of phased array feeds (PAFs; Chippendale et al., 2010; Hotan et al., 2014; McConnell et al., 2016), which allow 36 primary beams to be pointed simultaneously, increasing the effective field-of-view (FOV) of the instrument (dependent on pointing configuration, and within a $\sim$ 30 deg^2 region on the sky). This makes ASKAP an excellent surveying instrument, with 10-hr observations able to densely sample the u, v plane, resulting in not only a $\sim$ 20 μJy beam^{-1} noise at $\sim$ 900 MHz, but also excellent sensitivity to large-scale, low-surface brightness emission (and detections of new diffuse cluster sources and other low-sruface brightness objects have been reported in early science observations, e.g. HyeongHan et al., 2020; Wilber et al., 2020; Brüggen et al., 2021).

[25] As an aside, observing semesters have been split between these configurations due to the requirement to actually be on site to change which tiles are being used.

Figure 1.12. A photograph of two ATCA antennas.

The many beams of the PAFs do not share a common response, and the assumption of a simple 2-d Gaussian shape is often used but becomes questionable near the edges of the PAF tile (e.g. McConnell et al., 2020). Recent work by the observatory has been focused on better modelling of the PAF primary beams with holography (see e.g. Hotan et al., 2021, but see also Hotan 2016) though at the time of writing these upgraded beam models are not widely available. Careful quality assurance is generally done on resultant images to ensure the flux density scale after primary beam corrections is sensible, and brightness scaling is performed where necessary (e.g. McConnell et al., 2020).

Various ASKAP data products are used throughout this work, starting from Chapter 3, and will be introduced in the relevant chapters.

1.6.4. *Other instruments and all-sky surveys*

Other radio interferometers are also used in this work, including the Australia Telescope Compact Array (ATCA; Frater, Brooks & Whiteoak 1992, pictured in Fig. 1.12) with both its Compact Array Broadband Backend (CABB; Wilson et al., 2011) and in its 'pre-CABB' (i.e. smaller bandwidth) state. The ATCA is used extensively throughout this work, and has been active in observing and detecting diffuse cluster sources (e.g. Liang et al., 2000; Johnston-Hollitt, 2003; Shimwell et al., 2014, 2015; Martinez Aviles et al., 2016; Shakouri et al., 2016b; Zheng et al., 2018), but with only six antennas (five

movable) the array must be re-configured and observations generally require multiple configurations to obtain necessary u, v coverage for detection and characterisation of these sources.

A number of radio surveys are used in this work, including the GaLactic and Extra-galactic All-sky MWA (GLEAM) survey (Wayth et al., 2015) and its first data release the GLEAM Extra-Galactic Catalogue (GLEAM EGC; Hurley-Walker et al., 2017), which covers the Southern Sky and up to $\delta_{J2000} \approx +30°$, and features 20 narrowband ($\Delta\nu$ = 7.68 MHz) images from 72–231 MHz, three widebands ($\Delta\nu$ = 30.72 MHz) at 88, 118, and 154 MHz, and a single $\Delta\nu \approx 61$ MHz band centered on 200 MHz [26]. The noise in the GLEAM images varies by sky region and frequency, but can be as low as $\sim$ 7 mJy beam^{-1} in the 200-MHz images. The 'Briggs' robust -1 weighting used for the MWA Phase I data retains sensitivity to large-scale $\sim$ 1 deg emission while removing much of the diffuse Galactic foreground. As with the sensitivity, the PSF also varies across the bands, from $\sim$ 580 arcsec to $\sim$ 90 arcsec at the low and top end of the MWA band, respectively. The GLEAM survey provides both good spectral coverage and sampling, in principle allowing well-modelled spectra in the 72–231 MHz regime.

Other radio surveys used include the NRAO [27] VLA [28] Sky Survey (NVSS; Condon et al., 1998), the Sydney University Molonglo Sky Survey (SUMSS; Bock et al., 1999; Mauch et al., 2003; Murphy et al., 2007), and the TIFR [29] GMRT [30] Sky Survey, alternate data release 1 (TGSS; Intema et al., 2017).

1.7. Observations of clusters with the MWA-2

This section is largely included in Duchesne, Johnston-Hollitt & Bartalucci (2021d, Chapter 6).

Duchesne et al. (2021b, hereafter D21) report a number of candidate diffuse cluster sources detected in a large, deep 45°×45° MWA image created for foreground modelling of the Epoch of Re-ionization 0-h field (Offringa et al., 2016). Due to the low resolution

[26] This band is created by stacking the two 30-MHz widebands at 185 and 216 MHz, which were unfortunately not retained in the public release.
[27] National Radio Astronomy Observatory
[28] Very Large Array
[29] Tata Institute for Fundamental Research
[30] Giant Metrewave Radio Telescope

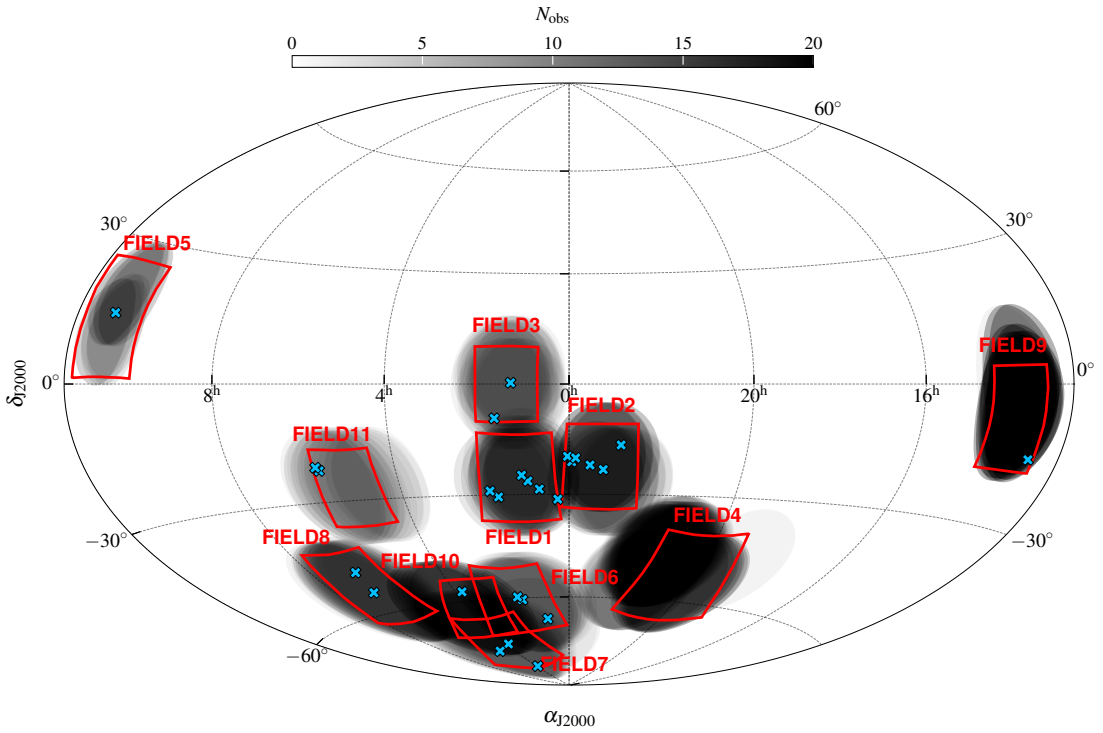

Figure 1.13. Survey coverage, with named fields labelled and cluster targets reported in this work noted as blue 'x' marks. Actual MWA-2 pointings at 154 MHz are show as transparent black circles, indicating relative sensitivity of fields. Note no sources from `FIELD4` are reported in the proceeding Chapters using MWA-2 data, as discussed in Appendix B.1.4. SPT-CL J2032−5627 (Chapter 3) is present in `FIELD4` but its angular size is too small and too confused for useful measurement. NGC 1534 (Chapter 2) is present in `FIELD10`, however, the source is sufficiently large and faint that it becomes barely detected above $\sim$ 154 MHz.

of the MWA, many of these sources had an uncertain nature. With the upgrade to the Phase 2 'extended' MWA (Wayth et al., 2018, hereafter MWA-2) and the allure of an increase in resolution by a factor of two, re-observation of a selection of these sources was carried out as part of MWA project G0045 with Director's Time observations of two additional fields and the addition of overlapping archival observations.

At the same time, a candidate list of diffuse cluster sources had been prepared based on visual searches of the GaLactic and Extragalactic MWA (GLEAM) survey (Wayth et al., 2015; Hurley-Walker et al., 2017). These searches focused on clusters from the Meta-Catalogue of X-ray detected Clusters (MCXC; Piffaretti et al., 2011), the Abell catalogues (Abell, 1958; Abell, Corwin & Olowin, 1989), *Planck* Sunyaev–Zel'dovich clusters (Planck Collaboration et al., 2015, 2016b), and a handful of miscellaneous clusters serendipitously found to host candidate diffuse emission that are nearby other

clusters from the aforementioned catalogues. While the full sample is not within the scope of this work (it would be prohibitive to perform targeted follow-up of close to 200 sources), in this work 35 sources [31] across 11 fields are reported. Due to the large field of view of the MWA (~ 20 deg at 216 MHz and ~ 60 deg at 88 MHz) we planned MWA-2 observations to cover a total 25 clusters (Table 1.1). While the 200-MHz wideband GLEAM image is usually sufficient to detect and measure flux density of these sources, the lower-frequency bands become prohibitively confused for use here. The fields observed (labelled `FIELD1–11`) are shown on Fig. 1.13. Generally we will not report non-detections (or more accurately, non-confirmations) from the non-public candidate list.

Chapter 2 and Chapter 3 detail non–MWA-2 work, focusing on ASKAP, ATCA, and MWA Phase I observations of the remnant radio galaxy associated with NGC 1534 near Abell 3229 and the detection of double relic system in SPT-CL J2032−5627. Details of the MWA-2 observation campaign are compiled in Appendix A (a detailed description of the data processing) and Appendix B (a detailed overview of the final images). Chapter 4 and Chapter 5 also highlight details of the observations and data processing, and Chapter 6 reports the bulk of the sample shown in Table 1.1.

[31] Note that for SPT-CL J2032−5627 MWA data are not used.

Table 1.1 Clusters discussed in Chapters 3 to 6, in order of appearance.

Cluster	FIELD	α_{J2000} [1] (J2000)	δ_{J2000} [1] (J2000)	z	M_{500} [2] (10^{14} $M_\odot$)	Type [3]	Ref. [4]
SPT-CL J2032−5627	4	20:32:19	−56:27:20	0.284	$5.74^{+0.56}_{-0.59}$	R, R	(a)/(a)/(i)/-
Abell 1127	5	10:54:08	+14:40:01	0.299	$6.64^{+0.49}_{-0.53}$	r/F	(b)/(c)/(z)/-
Abell 0141	1	01:05:34	−24:39:17	0.230	$5.67^{+36}_{-0.40}$	H	(b)/(e)/(z)/(g)
Abell 3404	8	06:45:29	−54:13:08	0.164	$7.96^{+0.23}_{-0.21}$	H	(b)/(z)/(z)/(d)
Abell 0122	1	00:57:24	−26:16:50	0.113	1.73	r/F	(b)/(h)/(f)/(g)
Abell 2751	1	00:16:20	−31:21:55	0.107	1.26	r/F	(b)/(e)/(f)/(g)
Abell 2811	1	00:42:09	−28:32:09	0.108	$3.67^{+0.35}_{-0.37}$	cH	(b)/(h)/(i)/(g)
Abell 2496	2	22:51:00	−16:24:24	0.123	$3.36^{+0.30}_{-0.32}$	r	(b)/(e)/(z)/(g)
Abell 2680	2	23:56:28	−21:02:18	0.190	$3.2^{+0.8}_{-1.0}$	cH	(b)/(k)/(l)/(g)
Abell 2693	2	00:02:10	−19:33:18	0.173	$2.1^{+0.5}_{-0.6}$	cH/p	(b)/(k)/-/(g)
Abell S1099	2	23:13:16	−23:08:40	0.110	-	r	(m)/(n)/-/(g)
AqrCC 087	2	23:31:30	−21:55:00	-	-	F	(n)/-/-/-
RXC J2351.0−1954	2	23:51:07	−19:58:52	0.248	$5.60^{+0.59}_{-0.62}$	p, r/F, U	(o)/(o)/(i)/(g)
Abell 0168	3	01:15:12	+00:19:48	0.045	$1.87^{+0.29}_{-0.31}$	R	(b)/(e)/(i)/(p)
RXC J0137.2−0912	3	01:37:15	−09:12:10	0.039	0.95	mH, RG	(q)/(q)/(f)/-
Abell S0112	6	00:57:48	−66:48:44	0.067	1.62	F	(m)/(r)/(f)/-
MCXC J0145.2−6033	6	01:45:12	−60:33:45	0.180	$3.55^{+0.42}_{-0.44}$	cmH	(s)/(s)/(i)/-
MCXC J0154.2−5937	6	01:54:15	−59:39:38	0.360	1.41	cGRG	(t)/(t)/(f)/-
Abell 3186	7	03:52:30	−74:01:51	0.127	$6.44^{+0.24}_{-0.24}$	R, R, cH	(m)/(e)/(i)/-
Abell S0405	7	03:51:09	−82:13:00	0.061	$2.51^{+0.20}_{-0.21}$	r	(m)/(u)/(i)/-
PSZ1 G287.95−32.98	7	04:59:38	−75:47:48	0.250	$5.88^{+0.40}_{-0.41}$	cH	(i)/(v)/(i)/-
Abell 3399	8	06:37:19	−48:28:42	0.203	$4.81^{+0.37}_{-0.39}$	cR, cH	(m)/(w)/(i)/-
MCXC J1253.2−1522	9	12:53:14	−15:22:48	0.046 [5]	0.98	F	(f)/(f)/(f)/-
Abell 3164	10	03:46:10	−57:03:00	0.059	$1.62^{+0.26}_{-0.28}$	F, F, F	(m)/(x)/(i)/-
Abell 3365	11	05:48:50	−21:54:43	0.093	1.66	R, U	(m)/(e)/(f)/(y)
Abell 0550	11	05:52:52	−21:03:25	0.099	$3.87^{+0.25}_{-0.27}$	r	(b)/(u)/(z)/-

[1] Coordinates are shown in units of hours, minutes, seconds, and degrees, arcminutes, arcseconds.

[2] Mass within R_{500}, the radius within which the mean density of the cluster is 500 times the critical density of the Universe.

[3] Source type (either as reported in the literature or as determined in this work): relic (R), halo (H), mini-halo (mH), remnant radio galaxy/AGN (r), miscellaneous fossil plasma/re-accelerated fossil plasma source (e.g. phoenix) (F), candidate (c), point source (p), normal radio galaxy (RG), giant radio galaxy (GRG), unclassified (U).

[4] References for position/z/M_{500}/previously detected diffuse emission: (a) Song et al. (2012). (b) Abell (1958). (c) Wen et al. (2012). (d) Brüggen et al. (2021). (e) Struble & Rood (1999). (f) ($M_{X,500}$) Piffaretti et al. (2011). (g) Duchesne et al. (2021b). (h) Zaritsky, Gonzalez & Zabludoff (2006). (i) ($M_{SZ,500}$) Planck Collaboration et al. (2015). (j) Cavagnolo et al. (2008). (k) Coziol et al. (2009). (l) Wen & Han (2015). (m) Abell et al. (1989). (n) Caretta et al. (2002). (o) Chon & Böhringer (2012). (p) Dwarakanath et al. (2018). (q) Cruddace et al. (2002). (r) Garilli, Maccagni & Tarenghi (1993). (s) Schwope et al. (2000). (t) Vikhlinin et al. (1998). (u) De Grandi et al. (1999). (v) Planck Collaboration et al. (2014). (w) Böhringer et al. (2004). (x) Fleenor et al. (2006). (y) van Weeren et al. (2011a). (z) ($M_{SZ,500}$) Planck Collaboration et al. (2016b).

[5] A second system (Abell 1631) is detected at $z = 0.014$ (Coziol et al., 2009)—see cluster entry in Chapter 6 (Duchesne et al., 2021d) for details.

Chapter 2.

The remnant radio galaxy associated with NGC 1534

The contents of this Chapter have been published as "The remnant radio galaxy associated with NGC 1534" (2019) in the Publications of the Astronomical Society of Australia, volume 36, E016, doi:10.1017/pasa.2018.26 (Duchesne & Johnston-Hollitt, 2019). The accepted manuscript is re-produced, with permission, in full at the end of this Thesis. The proceeding text is solely intended to provide context for the paper with respect to this work and to provide a summary of the paper.

2.1. Context

As the overarching goal of this work is in distinguishing between different types of diffuse, steep-spectrum radio sources within clusters, we begin by looking at a source that may provide the link between a normal radio galaxy and the large-scale cluster-based synchrotron emission of radio halos and relics: a remnant radio galaxy associated with the lenticular galaxy NGC 1534. While not in a cluster, this source was serendipitously detected by Hurley-Walker et al. (2015) in MWA Phase I calibrator scans, and is projected $\sim$ 2 Mpc from Abell 3229. Due to its location nearby Abell 3229, it was also added to the candidate list of diffuse cluster sources described in Section 1.7 and its observed properties made it a relic candidate. Its properties were also consistent with other sources, namely a remnant AGN. One of the key pieces of evidence for remnant radio sources are their integrated spectra that steepen significantly above $\sim$ 1 GHz, and Hurley-Walker et al. found a spectral index of $\alpha = -2.1 \pm 0.1$ based on measurements at 185 MHz, 408 MHz, and (partially) at 843 MHz—ultra-steep and certainly steeper than was traditionally seen in remnant AGN.

Additionally, its observed properties (i.e., steep spectrum, low-surface brightness, and generally extended) provided an excellent test of the MWA Phase I (GLEAM) data in characterising the integrated spectrum from an aged radio plasma, especially with the combination of other, higher-frequency data points to constrain any high frequency steepening of the spectrum. As an aside, the source is a combination of particularly rare objects: a giant radio galaxy (GRG) [1], a remnant AGN, and a dust-lane lenticular galaxy as a host. The combination of properties made it a particularly interesting source.

2.2. Summary

This work included combining the wideband GLEAM images with archival ATCA data, along with the available literature data, to constrain the integrated spectrum of the large-scale emission. Fig. 2.1 shows the galaxy and the surrounding 200-MHz emission, adapted from Duchesne & Johnston-Hollitt (2019). Additionally, the polarization properties of the large-scale radio lobes were investigated with the 16-cm ATCA data. The following summarises the key results of the paper:

- Integrated spectral fitting of the two lobes resulted in a $\mathrm{CI_{off}}$ model fitting the data well, providing key evidence for the remnant nature of the emission. A spectral age was estimated of $\sim$ 200 Myr, i.e. since the core AGN had switched off, with the active phase of the source only accounting for $\sim$ 40 Myr.

- Looking a the core of NGC 1534 with 17- and 19-GHz data from ATCA shows no evidence of compact emission suggestive of a currently active AGN. Some emission is seen, however, it is extended at sub-arcsec resolution at these frequencies suggesting this emission is not associated with the core.

- A comparison of the radio-estimated star-formation rate based on radio emission from NGC 1534 itself is consistent with that derived from mid-infrared measurements. This suggests little-to-no contribution from an AGN, consistent with the remnant AGN classification.

[1] Though note with the advent of LOw Frequency ARray (LOFAR) and recent searches (e.g. Dabhade et al., 2020), these numbers have certainly increased, and indeed recent work with MeerKAT (Delhaize et al., 2021) and ASKAP (Brüggen et al., 2021) have found higher densities of GRGs than was previously found, largely owing to the increase in sensitivity to the low-surface brightness lobes of these faint giants.

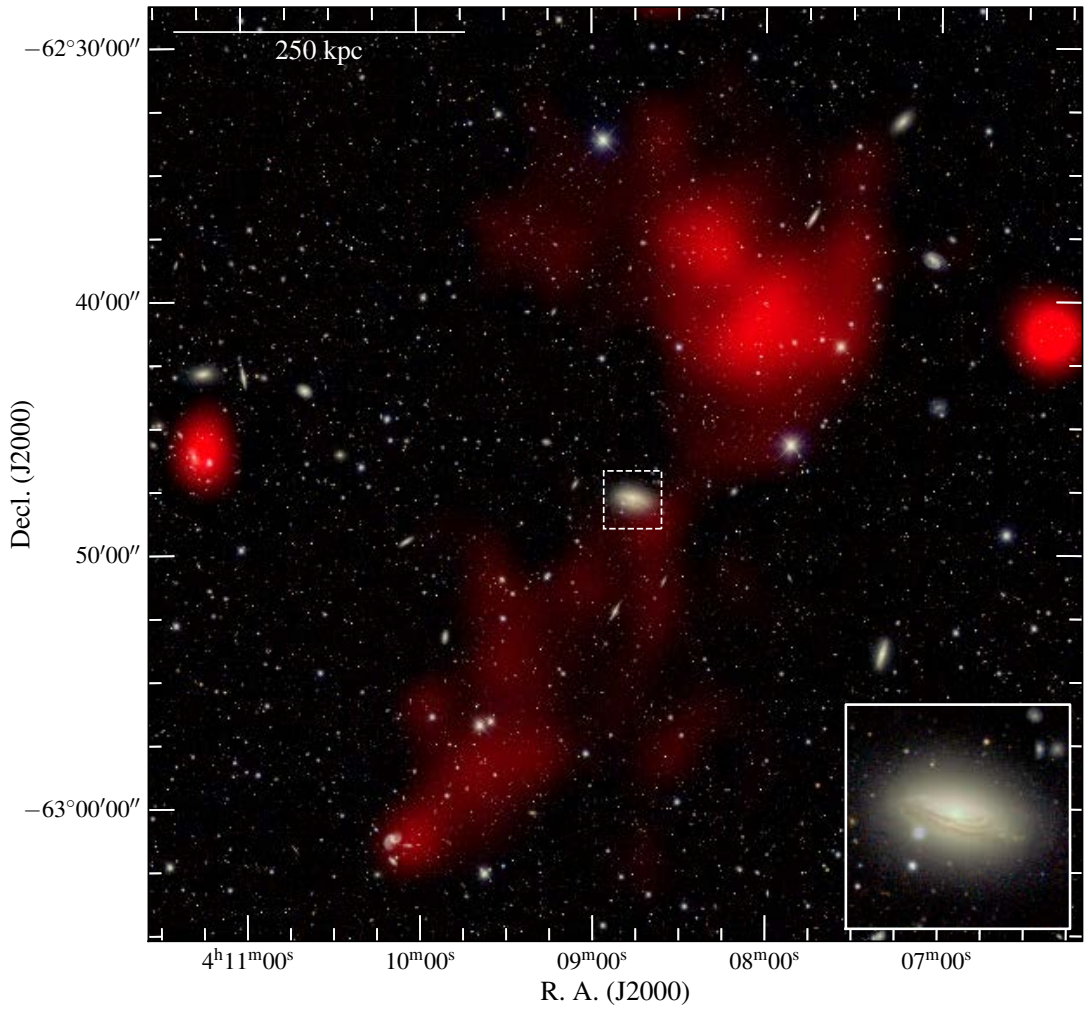

Figure 2.1. Image of NGC 1534 and associated radio emission, using DES (background optical, RGB) and GLEAM (diffuse red) data, adapted from Duchesne & Johnston-Hollitt (2019). The DES data were not available at the time of publication, however, the data show nothing more than the Digitized Sky Survey (DSS2) data used except in perhaps hinting more towards the spiral nature of NGC 1534 (as compared to the lenticular that has been previously suggested).

- The polarized nature of the lobes is curious, revealing an additional rotation-measure component not accounted for by known foreground screens suggesting polarized emission may be passing through a thin Faraday rotating skin surrounding the radio lobe, though this cannot be confirmed with present data.

The main result of the paper is the confirmation of the source as a true remnant, previously associated with NGC 1534, and indeed the integrated spectrum plays an important role in this classification, noting that the low-frequency integrated SED is actually reasonably flat (as compared to the estimate of $\alpha = -2.1 \pm 0.1$ by Hurley-Walker et al. (2015), which might point towards a useful tool in distinguishing between remnant AGN or relic emission.

Chapter 3.

SPT-CL J2032-5627: a double relic system

The contents of this Chapter have been published as "SPT-CL J2032−5627: a new Southern double relic cluster observed with ASKAP" (2021) in the Publications of the Astronomical Society of Australia, volume 38, E005, doi:10.1017/pasa.2020.51 (Duchesne et al., 2021a). The accepted manuscript is re-produced, with permission, at the end of this Thesis. The proceeding text is solely intended to provide context for the paper with respect to this work and to provide a summary of the paper.

3.1. Context

One of the issues in understanding diffuse cluster emission has always been the low numbers of these sources. The known sample of double relic systems still remains low despite some of the earliest work on diffuse cluster emission mechanisms focusing on the double relic system in Abell 3667 (e.g. Roettiger et al., 1999; Johnston-Hollitt, 2003; Hindson et al., 2014; Riseley et al., 2015). At the time of writing this Chapter/paper only 17 such systems were known. Low numbers preclude good statistical understanding of a population, and sources with extreme properties may be the earliest detections (e.g. detecting the brightest member of a population). Within this context, searches for diffuse cluster emission are underway with the current generation of radio telescopes, especially those with wide-field imaging capabilities, e.g. MWA, LOFAR,and ASKAP.

During the course of this work, ASKAP had released early pilot observations of a field used to test the processing strategy for the Evolutionary Map of the Universe (EMU) survey (Norris et al., 2011). This field aligned with a set of MWA-2 observations (Appendix B), and a cross-check was done for one of the observed fields. During

inspection of the data, a candidate double relic system associated with the cluster SPT-CL J2032-5627 was identified, making it the first double-relic detection with ASKAP and adding, even if only a single system, to the small sample of such systems.

3.2. Summary

The extended emission detected in the ASKAP data was confirmed to be a double relic system. Fig. 3.1 shows a composite image of the cluster system, showing the locations of the relics (red) with respect to the X-ray–emitting ICM (blue), with the relics aligned somewhat perpendicular to the elongation of the ICM, as expected from major mergers close to the plane of the sky. The paper is summarised as follows:

- The relic system was also detected in archival 5.5-GHz ATCA data, though at low resolution because of the compact H75 ATCA configuration used.
- Both relics could be modelled with a normal power law in the range $\sim$ 800–5500 MHz, finding $\alpha_{\rm SE} = -1.52 \pm 0.10$ and $\alpha_{\rm NW,full} = -1.18 \pm 0.10$ (or $\alpha_{\rm NW,west} = -1.54 \pm 0.45$ for the western component only, which could not be measured in the ATCA data due to blending with the eastern component).
- An investigation into the X-ray properties of the cluster with XMM-*Newton* data revealed no shocks detected at the locations of the relics, however, a candidate cold front was observed to align with the location of the SE relic. The interpretation of this is not clear. A lack of shocks detected could result from a number of things: not enough sensitivity in the X-ray observations, multiple shocks along the line of sight, or the merger being off the plane of the sky could limit shock detectability in the projected X-ray data (e.g. van Weeren et al., 2010).
- The double radio relic $P_{1.4}$–M_{500} scaling relations were updated with the inclusion of SPT-CL J2032−5627 and other recent detections, showing consistent results with relations fit by de Gasperin et al. (2014b). The relations were fit assuming the two relics per system were independent, and then assuming they could be summed and count as a single measurement for the cluster. The independent case naturally has a larger sample as well as a tighter relation, though when considering scaling relations

naturally fall out of energy considerations it may be more appropriate to consider double relics as a single system.

- As it was not expected to detect the relics at 5.5 GHz, a comparison of the ASKAP and ATCA surface brightness sensitivities was performed, showing that the ATCA H75 configuration with the removal of the sixth antenna (resulting in a compact, fairly well-sampled u, v plane) was most sensitive to angular scales equal to the angular scale of the SE relic.

- Finally, a comparison is made between ASKAP and MeerKAT within the context of performing an all-sky survey for diffuse radio emission as presented here. For an equivalent survey rate [1], MeerKAT, owing to larger bandwidth and almost two times the number of antennas would exceed ASKAP in point source sensitivity but is less sensitive to large-scale emission. Naturally, this paints ASKAP as a strong survey instrument with MeerKAT then able to perform deep follow-up analysis of detected systems.

[1] $\sim$ 16.7 min integration per pointing for MeerKAT cf. 10-hr integration times per pointing for ASKAP to match sky coverage within a given time.

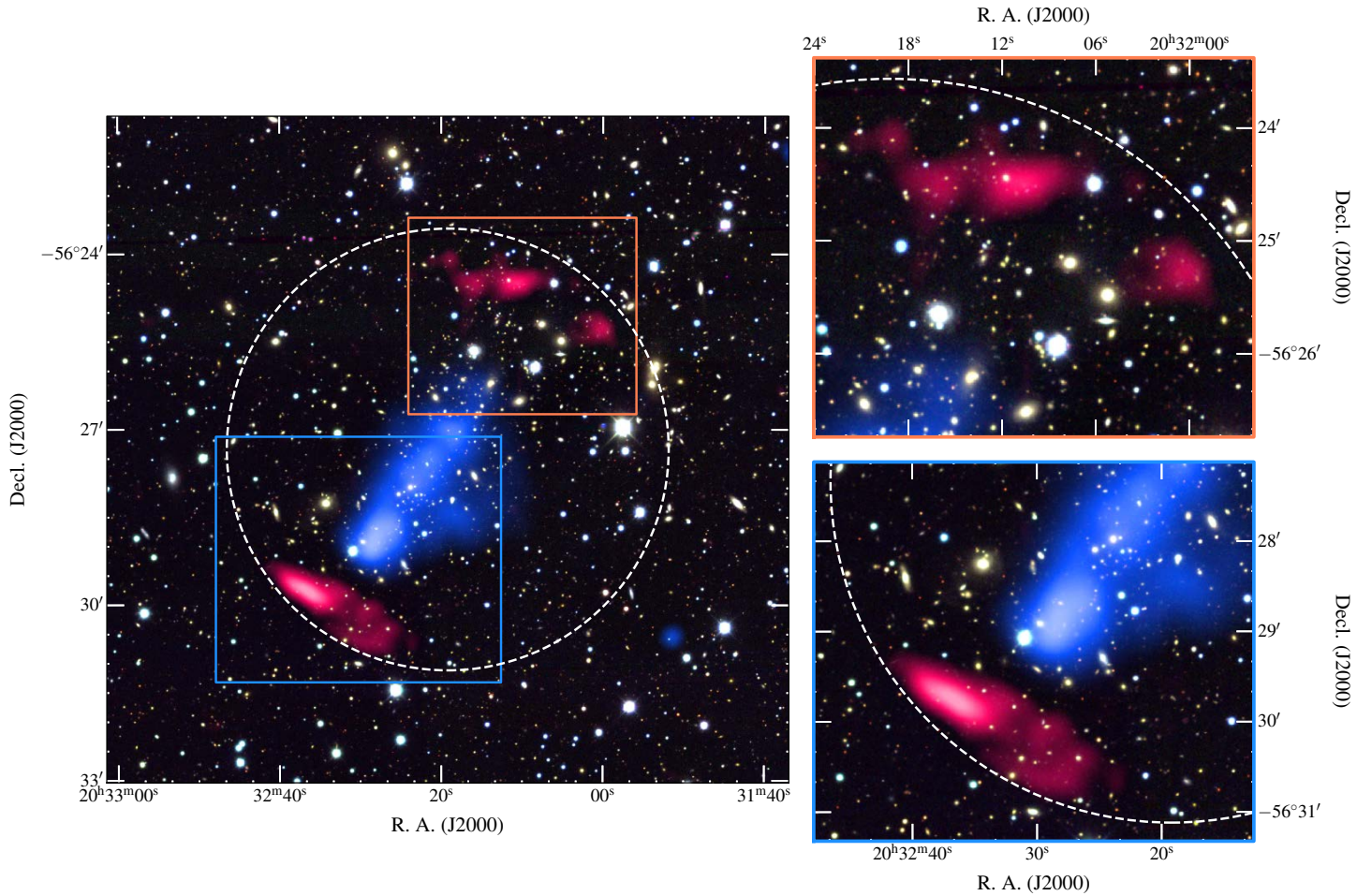

Figure 3.1. The SPT-CL J2032−5627 system. The background is the optical DES data. The blue overlay is the XMM-*Newton* data, processed by I. Bartalucci and the red overlay is the re-processed ASKAP data. The dashed, white circle is centered on the cluster with a 1 Mpc radius, and the insets are indicated on the main image with blue and orange rectangles. Image adapted from Duchesne et al. (2021a).

Chapter 4.

Testing the MWA-2 observations: Abell 1127

The contents of this Chapter have been published as "Murchison Widefield Array detection of steep-spectrum, diffuse, non-thermal radio emission within Abell 1127" (2020) in the Publications of the Astronomical Society of Australia, volume 37, E037, doi:10.1017/pasa.2020.29 *(Duchesne et al., 2020). The accepted manuscript is re-produced in full, with permission, at the end of this Thesis. The proceeding text is solely intended to provide context for the paper with respect to this work and to provide a summary of the paper. Elements of Appendix A are included in the paper, albeit significantly reduced in scope, as a means to describe the MWA-2 data processing in sufficient enough detail as appropriate when describing data from what was at the time a new instrument (i.e. the MWA-2).*

4.1. Context

With completion of the Phase II Pipeline (`piip` [1]) for imaging of MWA-2 data and having observed a number of target fields containing clusters with candidate diffuse radio emission (described in Section 1.7), we opted to showcase the MWA-2 imaging capabilities for a source that was detected in the original GLEAM data. The source in Abell 1127 was chosen because the original GLEAM image resolution at the lower frequencies confused the source with a nearby, bright double radio galaxy, limiting the ability to measure the flux density of the source accurately. Additionally, the source exhibited an ultra-steep–spectrum as evidenced by its brightness in the GLEAM data without any detection in the 1.4-GHz NVSS data, and its co-location with a disturbed,

[1] https://gitlab.com/Sunmish/piip

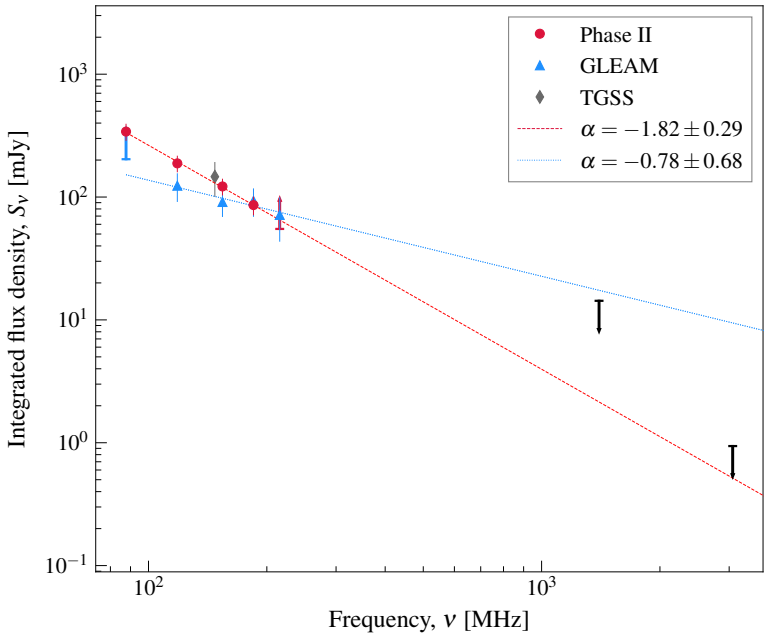

Figure 4.1. SED of the source in Abell 1127, adapted from Duchesne et al. (2020) but with the addition of the equivalent GLEAM measurements.

X-ray–emitting ICM hinted at a possible ultra-steep–spectrum radio halo (USSRH, with $\alpha \leq -1.5$; e.g. Brunetti et al., 2008). These features proved a good test case for the MWA-2 data.

4.2. MWA-2 compared to GLEAM

In Fig. 4.1, the SED of the source as shown in Figure 8 from Duchesne et al. (2020) is reproduced with the addition of equivalent measurements made in GLEAM survey images. For the purpose of this comparison, 185- and 216-MHz GLEAM images are made by stacking the relevant narrowband images in this range, as the GLEAM survey does not provide these 30-MHz wideband images [2]. The stacking is performed in the usual way and similarly to the stacking as described in Appendix A.6, thus the 185- and 216-MHz GLEAM images are at the resolution of the lower end of the four constituent narrowbands, rather than the equivalent resolution for the centre of the band (as is the case for the MWA-2 wideband images used here).

One thing to note is that, as evidenced in Fig. 4.2 the 88-MHz GLEAM image

[2]A choice was made to keep only the 60-MHz wideband image centered on 200 MHz as the main output from the survey was expected to be the 7-MHz narrowband images/data.

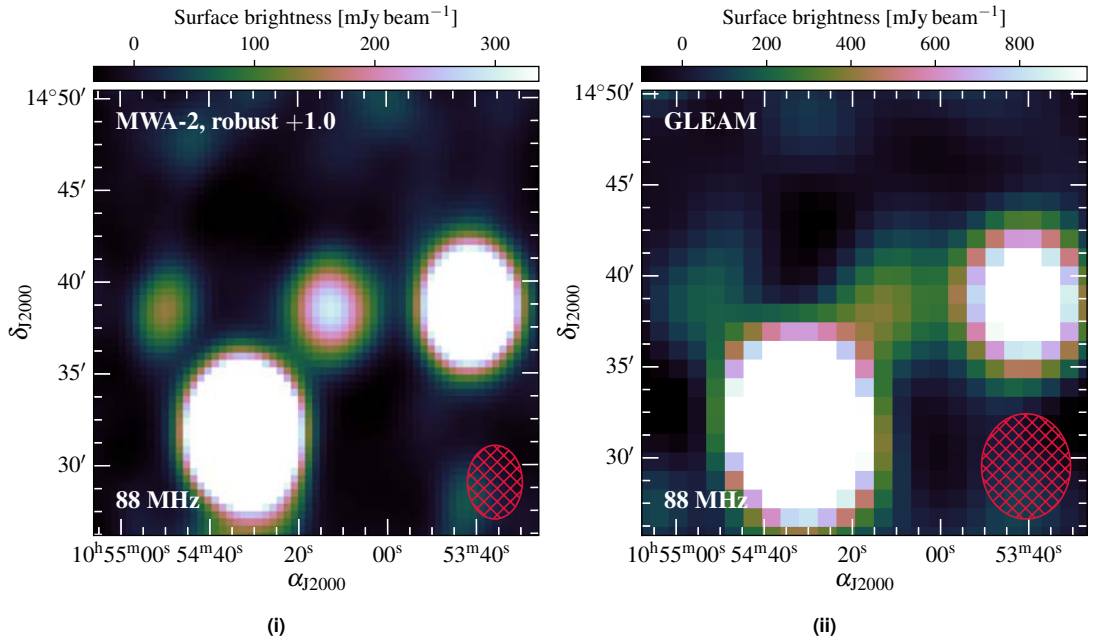

Figure 4.2. A comparison between the (i) 88-MHz MWA-2, robust +1.0 image and the (ii) 88-MHz GLEAM image. Note the blending with the SE radio galaxy, which at the resolution of the TGSS or VLA data becomes a classic double radio galaxy.

becomes confused with the SE double radio galaxy, precluding good measurement of the integrated flux density. For the GLEAM data, only a lower limit is obtained at 88-MHz based on the peak flux density. The MWA-2 do not suffer this problem. Conversely, the 216-MHz MWA-2 data become less sensitive to the emission, and only an *upper* limit is provided. This illustrates where the MWA-2 data are most useful: at the lower end of the MWA band, with MWA Phase I data being—in some cases—more useful at the higher end of the band for characterisation of these diffuse radio sources.

4.3. Summary

As mentioned, the full work is described in detail in Duchesne et al. (2020) and the key conclusions are summarised as follows:

- The first results from the follow-up survey of candidate diffuse cluster sources was reported, describing both the new `piip` for MWA-2 data reduction, as well as the diffuse radio source in Abell 1127.

- High-resolution VLA S-band (2–4 GHz) data are used in conjunction with various

survey data to constrain the contribution of discrete point sources to the extended diffuse emission as seen by the MWA. This set a precedent for discrete-source subtraction in later work/Chapters.

- The integrated spectrum of the source is modelled with a simple power law, resulting in a spectral index of $\alpha = -1.83 \pm 0.29$, classing the spectrum as ultra-steep.
- The morphology of the emission as detected at 150 MHz by the TGSS precluded classification of a radio halo. Instead, the source is likely to be a cluster-based remnant radio galaxy, radio phoenix, or otherwise fossil plasma.
- The X-ray properties of the cluster were investigated: the cluster is confirmed to be morphologically disturbed, and the ultra-steep–spectrum radio sources is projected onto a gap between two X-ray subclumps. Such a location in a dynamic cluster may experience turbulence and/or shocks perhaps providing a re-acceleration mechanism for a fossil plasma, forming e.g. a radio phoenix.
- Based of the shape of the spectrum and the limits provided by the VLA data, a distinction between revived fossil plasma (e.g. radio phoenix) or fossil plasma (e.g. remnant radio plasma) cannot be made, however, the spectrum is used in aiding the classification of fossil plasma as opposed to a true relic source.

The remaining MWA cluster sample form Chapter 5 and Chapter 6.

Chapter 5.

Radio halos in clusters with atypical morphologies

The contents of this Chapter have been published as "MWA and ASKAP observations of atypical radio-halo–hosting galaxy clusters: Abell 141 and Abell 3404" in the Publications of the Astronomical Society of Australia, volume 38, E031, doi:10.1017/pasa.2021.24 (Duchesne, Johnston-Hollitt & Wilber, 2021c). The accepted manuscript is re-produced in full, with permission, at the end of this Thesis. The proceeding text is solely intended to provide context for the paper with respect to this work and to provide a summary of the paper. Elements of Appendix A.9 and Appendix B.2 have been included.

5.1. Context

Radio halos are typically found in massive, merging clusters where the morphological state of the cluster is disturbed, as evidenced by its X-ray–emitting ICM (e.g. Cassano et al., 2013)—halos are therefore thought to form during mergers. However, a handful of halos have been found in clusters with little-to-no evidence of merger activity. For example, a giant radio halo is detected in CL1821+643, which is a CC cluster (Bonafede et al., 2014a), and such systems might provide a link between mini-halos and giant radio halos. In some cases, pre-merging clusters have been found to host radio halos (e.g. the cluster pair Abell 1758N-S; Botteon et al., 2018), however, in these cases the individual clusters have complex morphologies and the halos are perhaps associated with formation of the individual clusters. Halos in clusters with atypical merger-states (and atypical morphologies) can therefore highlight either transition systems (perhaps with CL1821+643) or highlight limits of current (re-)acceleration models for

generation.

5.2. Summary

The radio halos in Abell 0141 and Abell 3404 were analysed within the context of atypical halo-hosting clusters. These clusters are shown in Fig. 5.1 and Fig. 5.2 as composite multi-wavelength images. The paper presents the first joint MWA-2–ASKAP work on galaxy clusters in this Thesis, and highlights the utility of the spectral range and coverage between the instruments. The paper can be summarised as follows:

- The diffuse sources in each cluster are confirmed to be giant radio halos.
- The radio halo in Abell 0141 is well-fit by a power law in the range $\sim$ 100–1000 MHz with a spectral index $\alpha = -1.06 \pm 0.09$, flatter than reported in Duchesne et al. (2021b), though this partly due to compact source subtraction and a likely under-estimated 610-MHz limit from Venturi et al. (2007, 2008).
- For Abell 3404, the radio halo is also modelled by a power law with $\alpha = -1.66 \pm 0.07$, classing it as a USSRH, which is the first reported detection of a USSRH by ASKAP.
- Using *Chandra* data, Abell 3404 is found to be only 'weakly dynamic' as evidenced in only a minor disturbance to its morphology—which may suggest either a weak merger or a merger at an early or late stage. Such situations are suggested to generate USSRH (e.g. Brunetti et al., 2008). A merger along the line of sight may also show little morphological disturbance via X-rays.
- Using *Chandra* data, a point-to-point comparison is performed with the ASKAP data. This comparison finds a correlation between X-ray and radio surface brightnesses for Abell 3404, consistent with many other radio halos, however, for Abell 0141 no correlation is seen, similar to the case of the radio halo in the Bullet Cluster (Shimwell et al., 2014), perhaps due to a complex merger history.
- Additional diffuse peripheral sources are found in each cluster—one such source is likely a component of the radio halo in Abell 3404 as it follows the radio–X-ray

[1]Panoramic Survey Telescope And Rapid Response System.

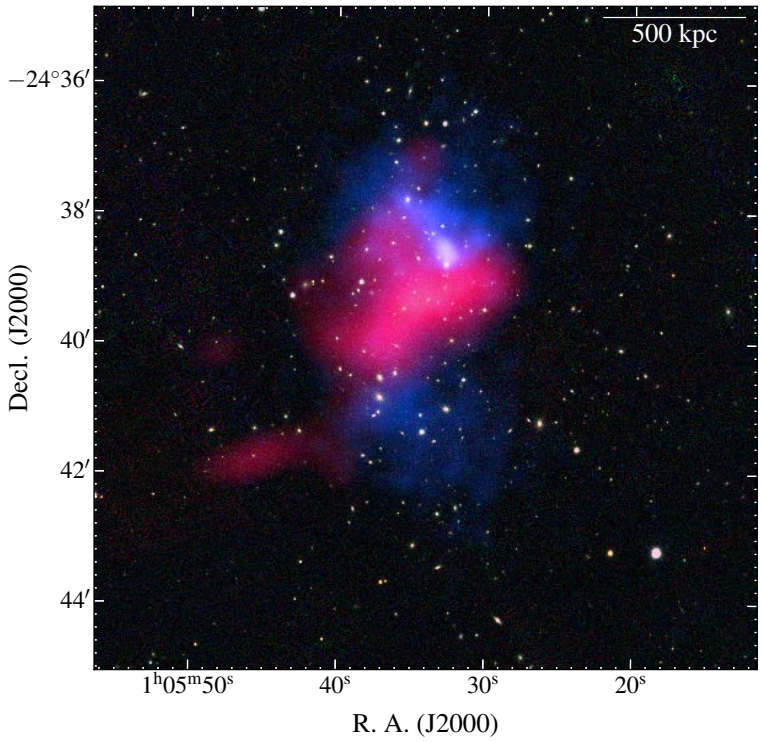

Figure 5.1. Composite image of Abell 0141. The background map is from the Pan-STARRS [1] survey (PS1; Tonry et al., 2012; Chambers et al., 2016, RGB corresponding to the i, r, and g bands, respectively), the blue overlay is the *Chandra* X-ray data, and the red overlay is the source-subtracted ASKAP data (see Duchesne et al., 2021c, for details). The linear scale in the top right is at the redshift of the cluster, $z = 0.23$.

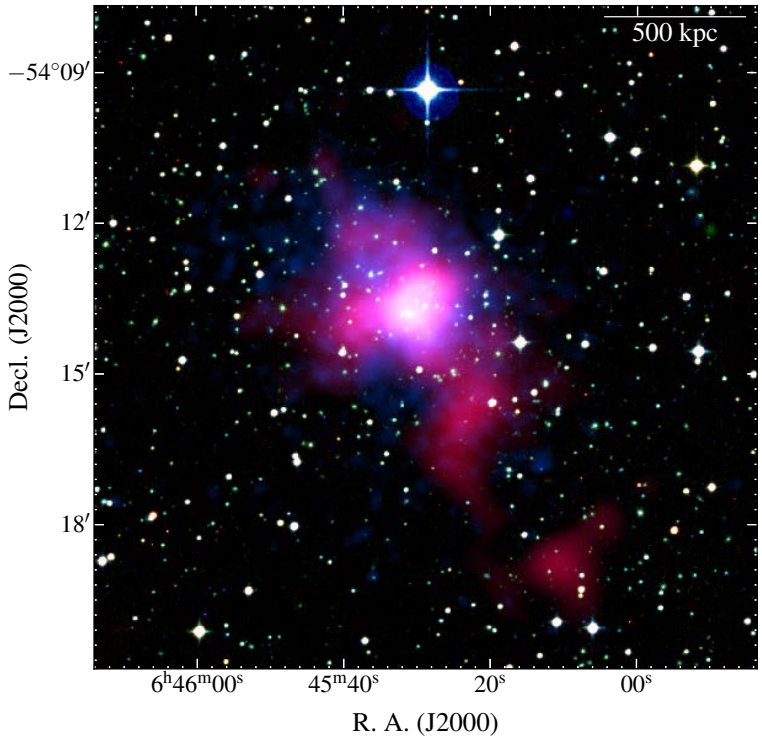

Figure 5.2. Composite image of Abell 3404. The background map is from the DSS2 (RGB corresponding to infrared, red, and blue bands, respectively), the blue overlay is the *Chandra* X-ray data, and the red overlay is the source-subtracted ASKAP data (see Duchesne et al., 2021c, for details). The linear scale in the top right is at the redshift of the cluster, $z = 0.167$.

surface brightness correlation, however, for the other peripheral components the picture is less clear. Additionally, no shocks are detected in the Abell 3404 *Chandra* data, limiting a relic classification.

- The 1.4-GHz and 150 MHz P_ν–M_{500} scaling relations for radio halos are updated with Abell 0141 and Abell 3404, and with the full sample of radio halos from the literature where flux density measurements and SZ-derived masses exists. Abell 0141 and Abell 3404 appear in expected places on the relations, and the updates at both frequencies.

- Finally, we find that the P_ν–M_{500} scaling relations are converging on a tight set of parameters with the increase in sample size to 86. We also find agreement with recent work with smaller samples at 0.15 GHz (van Weeren et al., 2021) and 1.4 GHz (Cuciti et al., 2021b).

Chapter 6.

Palaeontology with the MWA and ASKAP

The contents of this Chapter have been published as "Low-frequency integrated radio spectra of diffuse, steep-spectrum sources in galaxy clusters: palaeontology with the MWA and ASKAP" in the Publications of the Astronomical Society of Australia, volume 38, E053, doi.org/10.1017/pasa.2021.45 (Duchesne, Johnston-Hollitt & Bartalucci, 2021d). The accepted manuscript is re-produced in full, with permission, at the end of this Thesis. The proceeding text is solely intended to provide context for the paper with respect to this work and to provide a summary of the paper. Elements of Appendix A.9, Appendix B.2, and Section 1.7 have been included explicitly.

6.1. Context

As the observed radio spectrum of diffuse cluster sources is linked to the underlying electron population, this paper and Chapter seeks to leverage that information to find a link, if it exists, between remnant AGN, dead radio galaxies, and other fossil sources with radio halos and radio relics. Indeed, for radio halos there may already be a link with respect to mini-halos, and as discussed in Section 1.4.3.2 some examples exist of relic-like sources connected to AGN (e.g. de Gasperin et al., 2017). A larger population of unambiguously classified halos, relics, and other diffuse sources is needed to confirm if a common electron population is required, or if perhaps a combined thermal and fossil pool could be at play (e.g. the recent results by Jones et al., 2021). As discussed in Section 1.5, one method in which to tackle this problem is in (1) obtaining a large-enough sample of unambiguously-classified sources and (2) comparison of source spectral properties in a regime where curvature is less likely to be significant ($\sim$ 100–

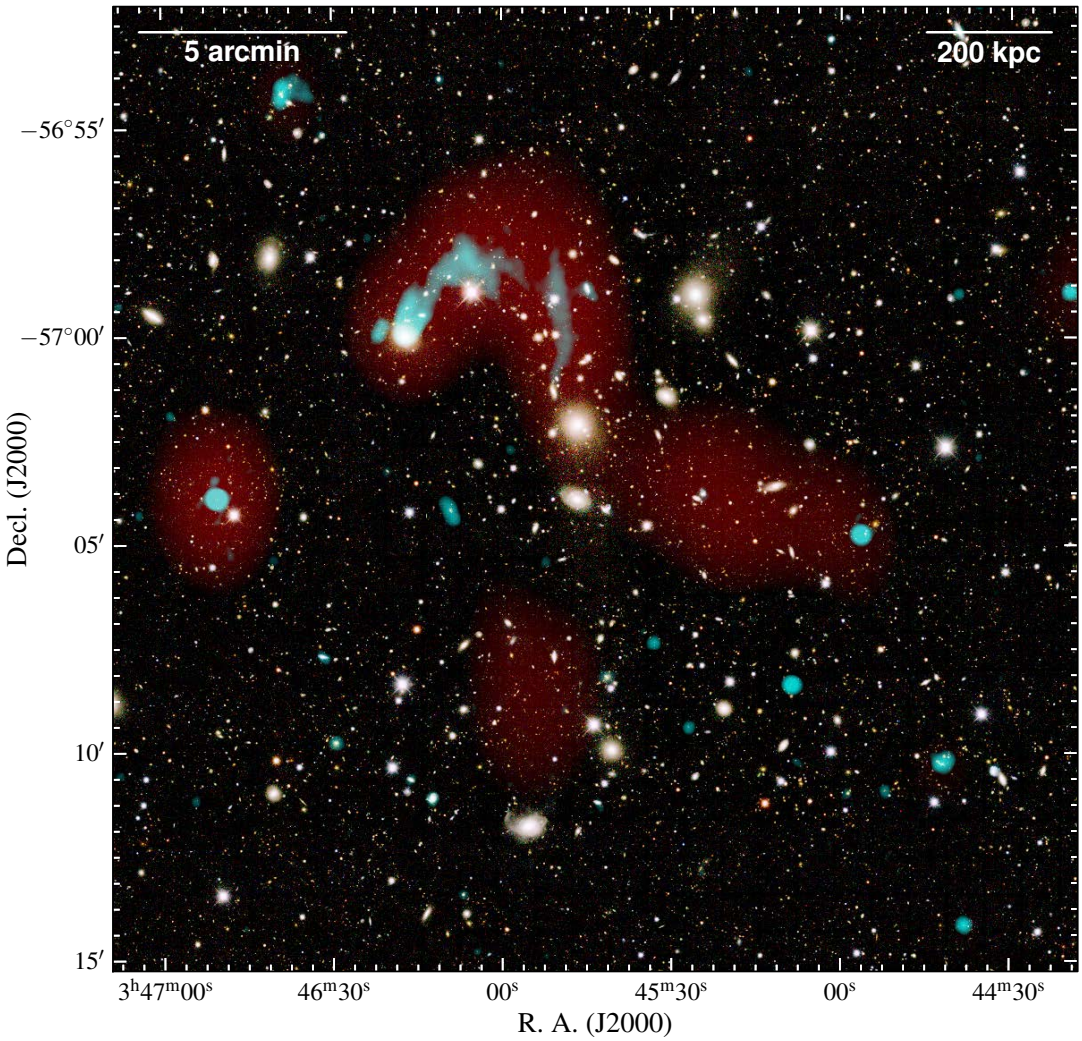

Figure 6.1. Radio (red, MWA-2, and cyan, ASKAP) and optical (DES) composite image of Abell 3164 featuring ultra-steep–spectrum radio emission. See Section 3.1.8 in Duchesne et al. (2021d) for further details on this cluster.

1000 MHz). To this end, this paper and Chapter concerns itself with the remainder of the MWA-2 follow-up of MWA-detected cluster emission, attempting to leverage the large spectral coverage to understand these sources better at a survey level.

6.2. Summary

In the paper 31 individual sources were examined [1], using the MWA-2 observations described in Section 1.6.2 and Appendix B along with additional, re-imaged archival ASKAP data including data from the Rapid ASKAP Continuum Survey (RACS; McConnell et al., 2020), a search for Variability And Slow Transients (VAST; Murphy et al., 2021), and additional miscellaneous observations of unrelated sources. The examined sources were then compared to the literature selection of radio halos, relics, miscellaneous fossil sources, and remnant AGN to attempt to understand links between these diffuse cluster sources. The paper is summarised by the following:

- The detections of new diffuse cluster sources with the MWA are reported, including a candidate double relic system in Abell 3186, a mini-halo in RXC J0137.2−0912, a candidate halo and relic in Abell 3399, and a complex head-tail radio galaxy in Abell 3164 (see Fig. 6.1) that shows episodic activity and some evidence of re-acceleration for at least one of its components. In total, 1 new relic (2 candidates), 1 new halo (3 candidates), 1 new mini-halo, 2 remnants, and 6 ambiguous fossil sources are reported for the first time.

- A number of (candidate) diffuse cluster sources previously reported by van Weeren et al. (2011b); Duchesne et al. (2021b); Dwarakanath et al. (2018) are also observed with the multi-frequency MWA and ASKAP data. Some classifications are updated, e.g. the source in Abell 2751 reported by Duchesne et al. (2021b) is likely to be a remnant/fossil/revived plasma rather than a relic.

- Additionally, observations of the double relic system in Abell 3365 reported by van Weeren et al. (2011b) yield spectral indices for each relic with reasonably flat spectra—$\alpha_{\rm NE} = -0.85 \pm 0.03$ and $\alpha_{\rm W} = -0.76 \pm 0.06$. Estimating Mach numbers from these spectral indices following Eq. 1.14 are somewhat consistent with Mach

[1] While many more candidates exist within the observed fields, as observed in GLEAM data, we have opted to only report on sources where the combination of MWA-2 and ASKAP data can actually measure a spectral index. As the sample would not represent a complete sample, reporting on sources that are too ambiguous and with no measured properties would not be useful at this stage. The low-resolution nature of the MWA observations make completeness studies of sources within clusters difficult due to confusion and the inability to unambiguously claim a "non-detection".

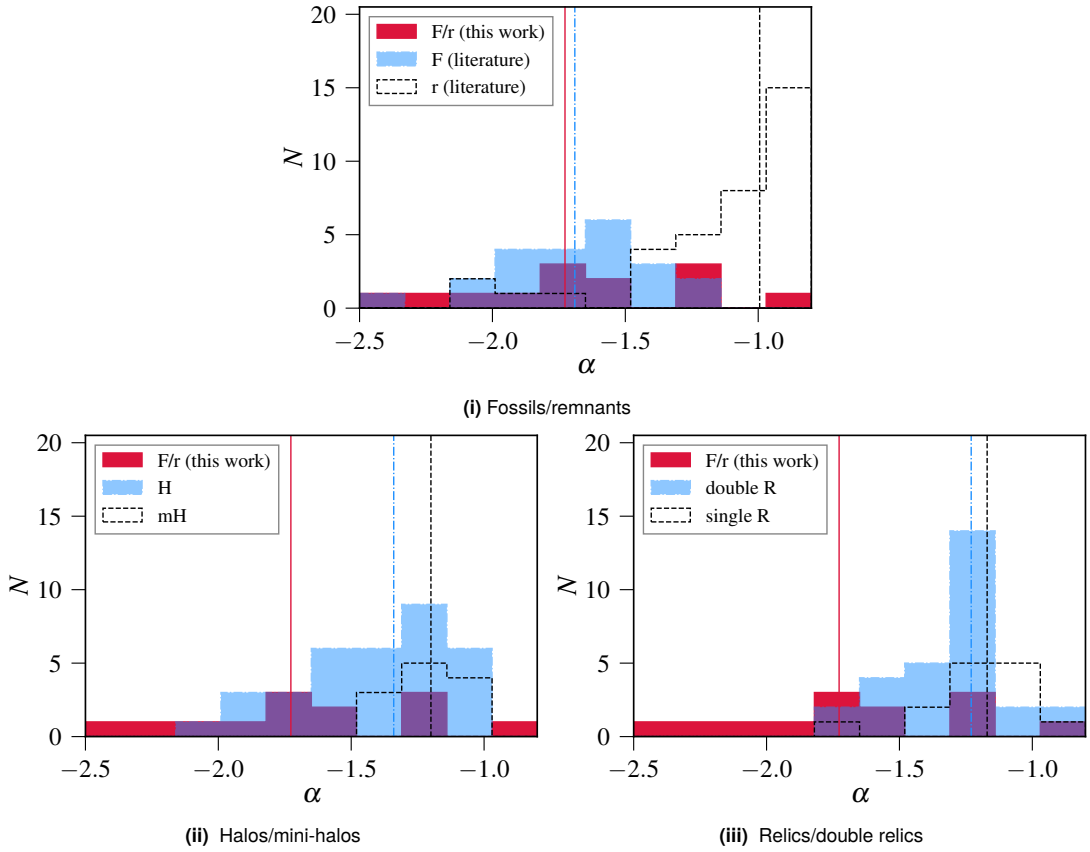

Figure 6.2. Spectral index distributions for (i) remnant radio galaxies and fossil radio plasma sources, (ii) radio halos/mini-halos, and (iii) relics (double and single), compared to the largely miscellaneous collection of fossils plasma sources reported in this work. See Duchesne et al. (2021d) for further detail. Reproduced from Duchesne et al. (2021d).

numbers derived from X-ray observations by Urdampilleta et al. (2021) if $\alpha = \alpha_{\rm inj}$ as might be the case if re-acceleration occurs from the fossil electron pool.

- Spectral index estimates are obtained for all cluster sources in the sample within the MWA data alone (i.e. between $\sim$ 88–231 MHz) and in some cases including higher frequency measurements near 1 GHz (e.g. from RACS, other ASKAP data, or the NVSS). Most diffuse sources in the sample are well-modelled by a normal power law (Eq. 1.7), however, in some cases curvature is seen and a generic curved power law model is additionally fit (Eq. A.2), suggesting these sources are remnant or otherwise (revived) fossil sources with synchrotron ageing playing an important role in the shape of the spectra.

- The halo and relics (and candidates) reported in this work are compared to the

expected P_ν–M_{500} scaling relation for $\nu \in \{0.15, 1.4\}$ GHz (as reported by Duchesne et al. 2021a, Chapter 3 for double relics, and Duchesne et al. 2021c, Chapter 5 for radio halos). The radio halo candidate in Abell 2693 sits far off the relation, though the uncertainty on the estimate on the X-ray–derived mass may limit the interpretation of this. Additionally, Abell 2693 is one of the least massive clusters to host a radio halo (surpassed by the 'Ant' cluster; Botteon et al. 2021), and the relation for low-mass cluster is not well-understood. Sources are otherwise located in reasonable locations, with steeper-spectrum sources moving closer to relations at 0.15 GHz as expected.

- The populations of diffuse cluster source types are compared via the distribution of their spectral indices, preferentially determined in the range $\sim$ 100—1000 MHz (see Fig. 6.2). A straight-forward comparison of these distributions suggests the possibility that the radio halos and relics may be linked to the fossil source distribution. Both relics and halos feature an ultra-steep–spectrum tail to the distributions, related to the lower-energy events (e.g. in weak mergers) and a distribution of these 'weak' halos and relics should approach a fossil distribution if halos and relics evolve from that population (after undergoing re-acceleration processes assuming these processes affect the spectra similarly). Additionally, we see remnant AGN in clusters are generally steeper in spectrum than field remnants.

Finally, a table is provided online with all flux density measurements at each frequency for all reported sources. This table is hosted at `https://dx.doi.org/10.26185/611f33b774e96` along with radio images used in the paper.

Conclusion

This Chapter acts as a summary for the Thesis, and outlines some limitations of the current research, finally discussing future work to be done within the context of the current research. Individual Chapters have also been specifically summarised in the preceding text, but a full summary is also presented here for completeness.

Summary

To begin with, Duchesne & Johnston-Hollitt (2019, Chapter 2) explored a known GRG to (1) confirm its nature as a remnant AGN rather than a cluster relic, given its angular proximity to Abell 3229 and (2) test the utility of the MWA in its Phase I configuration via the GLEAM data for characterising such a large-scale object. Other results from the paper helped to confirm the nature of the source as a remnant, and indeed the integrated spectrum between the MWA and ATCA observations was used to show a $\mathrm{CI}_{\mathrm{off}}$ model fit the emission well, under sensible assumptions about the magnetic field strength of the magnetised radio lobe plasma. Additional data were used to help in this classification, including higher-frequency ATCA data looking at the host NGC 1534 itself, as well as comparison to mid-infrared data for estimation of a star-formation rate. This work highlighted the utility of the low-frequency SED in classifying these diffuse radio sources, and indeed even the low-frequency spectral properties are generally consistent with field remnants we compile in Chapter 6.

Following the analysis of NGC 1534, Duchesne et al. (2021a, Chapter 3) reported on the serendipitous discovery of a double relic system with ASKAP. This double relic system was identified in ASKAP observations for the EMU survey (Norris et al., 2011), after a cross-match against known cluster diffuse sources is the region, as it lies fairly close to both SPT-CL J2023−5535 and Abell 3667. The cluster, SPT-CL J2032−5627

had also been observed with the ATCA at 5.5 and 9 GHz in a single compact array configuration. A detection of the relic is made at 5.5 GHz, which is a result of the sensitivity of the array configuration peaking at the angular scale of the relic. Both relics are observed to have power law spectra, and updating the known scaling relations for double relic systems from de Gasperin et al. (2014b) with SPT-CL J2032−5627 and other double relics detected since shows consistency with the results from de Gasperin et al., though significant scatter remains. No shocks are detected at the locations of the relics in the XMM-*Newton* data, though a candidate cold front is found at the location of the SE relic. This work highlighted the excellent observational quality and surveying capability of ASKAP with respect to finding more of these low surface-brightness sources, hinting that the full EMU survey should uncover a significant population.

The full scope of this project has been focused on larger numbers of sources, but a few more interesting sources prompted individual studies. Abell 1127 was one such source and was presented in Duchesne et al. (2020, Chapter 4), originally found in GLEAM images and presenting with a particularly steep spectrum based on non-detection in higher-frequency surveys. Its location was coincident with the X-ray–emitting ICM, as observed with radio halos. Further analysis was needed, motivating its inclusion in the MWA-2 cluster diffuse source follow-up survey. This paper described the full pipeline used for the MWA-2 data processing developed for this work, and this is also significantly expanded in Appendix A for completeness [2], introducing a number of enhances and fixes for MWA data processing procedures. The source itself proved to not be a halo as originally thought, instead based on its morphology and utra-steep spectrum it is likely a cluster-based remnant AGN/fossil source or revived fossil source—the location between X-ray sub-clumps hints at the possibility for re-acceleration mechanisms at work (hence a phoenix), though further confirmation is not possible with the data at hand. This work highlights the utility of the MWA-2 data, in conjunction with higher-resolution data for, e.g., compact source-subtraction to characterise these sources. At the same time, the MWA-2 limitations are still made clear especially in regards to the limiting angular resolution.

Chapter 5 (Duchesne, Johnston-Hollitt & Wilber, 2021c) is focused on two radio

[2]Though in principle a careful reading of the code available at `https://gitlab.com/Sunmish/piip` would allow one to get almost the same amount of information.

halos in galaxy clusters with somewhat atypical morphologies as evidenced by their X-ray emission. Typically, radio halos are found in clusters undergoing a major merger, however, in this work the radio halo in Abell 0141 is confirmed (originally reported by Duchesne et al. 2021b) and is found in a pre-merging cluster, but not associated with either of the subclusters. Additionally, Abell 3404, which has only minor disturbance to its morphology, is reported to host a USSRH. In the case of Abell 0141, the radio halo permeates to northern subcluster, the inter-cluster volume, and moves in some small part into the southern sub-cluster as well. Normally, if pre-merging clusters host radio halos the pre-merging sub-clusters are individually hosting a radio halo (e.g Botteon et al., 2018), which is not the case here. For Abell 3404, an almost relaxed cluster is perhaps indicative of a weak merger, or a cluster at the later stage of a merger, wherein less energy is available to turbulent processes for re-acceleration of particles. Such scenarios are suggested to form USSRH (Brunetti et al., 2008). This work also looked at the radio halo scaling relations (P_ν–M_{500}) at 1.4 GHz and 150 MHz (as had recently been done by van Weeren et al. 2021). For this purpose, the full sample of radio halos in the literature were considered if they had a flux density measurement and if the cluster had a mass estimate via the SZ-effect. This resulted in the largest sample used for the scaling relations to date, and it was found that the relations are consistent at either frequency, and consistent with the literature, within the respective uncertainties. While work needs to be done to reduce the scatter (though there is a limit to this based on intrinsic scatter in e.g. mass), these results paint the picture of a quickly converging set of relations.

Finally, Chapter 6 (Duchesne, Johnston-Hollitt & Bartalucci, 2021d) is a report on the remainder of the MWA-2 sample. This contains 31 sources, which are a mixture of candidate sources and known sources, as well as sources reported for the first time. This sample was selected from a larger list of MWA-detected candidates, which are not reported here, with the intention of leveraging the increase in resolution of the MWA-2 over the GLEAM survey to determine the nature of candidate sources. This resulted in a large-area survey comprised of 11 individual fields of observation, each covering ~ 20 by ~ 20 degrees at 216 MHz (increasing to ~ 60 by ~ 60 degrees at 88 MHz)—the details of the observed fields are reported in Appendix B. These sources are analysed

with the MWA-2 data, adding GLEAM, other MWA Phase I data, ASKAP data, and other literature data where appropriate. Most sources are well-modelled by a normal power law in the range $\sim$ 100–1000 GHz, though some show evidence of curvature in this range and are generally considered radio galaxies, remnants, or otherwise some type of miscellaneous fossil plasma source. The sample is compared to the established scaling relations for double relics and radio halos (see Chapter 3 and Chapter 5), finding generally consistent results, though in one case a candidate halo is found far off the relation and may indeed be an ultra-steep–spectrum point source.

The distributions of α generally derived in the range $\sim$ 100–1000 GHz for diffuse cluster sources are compared to each other and the presented sample of miscellaneous fossil sources. These show a number of things: (1) remnant radio galaxies in clusters are generally much steeper in spectrum than their field counterparts, (2) miscellaneous fossil sources match closely with the distribution of cluster remnants as expected as they are effectively the same sources, though re-acceleration mechanisms in the case of phoenices or gentle re-energisation are not distinguishable, (3) USSRH do not appear as a separate population from giant radio halos, and indeed the α distribution for radio halos trails off smoothly to steeper spectra, and (4) both radio halos and relics have an ultra-steep–spectrum tail in the α distributions, though the relic distribution is much more peaked around the median value. This is consistent with a population of 'low-energy' events that would only marginally re-accelerate a fossil electron population but does not rule out thermal pool electron involvement. Recent observations of the double relic system PSZ2 G096.88+24.18 suggest the possibility of both fossil and thermal electrons responsible in that particular system (Jones et al., 2021).

Conclusion and outlook

As discussed in Section 1.5, the origins of radio halos and relics is still unclear. Despite the successes of turbulent (re-)acceleration mechanisms for radio halos and DSA (or DSA-like processes) for relics as explanations for *how* a particle gains energy, there is no consensus on the the exact particle population under acceleration. In order to understand the underlying particle population, there is a need to increase the sample size of known diffuse cluster sources observed with wide—and well-sampled—spectral

coverage. This work has begun this process, by first increasing the known populations of halos, relics, and other diffuse cluster sources, and then using their generally well-sampled low-frequency spectra to not only find differences in those populations for classification purposes, but to also find the similarities that might hint towards a common (or uncommon) particle population under acceleration.

Knowledge of the spectral properties at multiple frequencies is fundamental information for understanding the origin of the emission. The SED (resolved or integrated) is a function of the (re-)acceleration mechanism (i.e. how much energy is provided to the emitting particles and how it is provided) and the original energy distribution of the particle population in question. Detailed work on single systems, e.g. Thierbach et al. (2003); Giacintucci et al. (2014b); Rajpurohit et al. (2021c,b,a), highlights the importance of full multi-wavelength studies of halos and relics, where (re-)acceleration mechanisms can be more completely tested for those particular sources. Fossil plasma sources, including remnant AGN and re-accelerated sources such as phoenices, also have multi-frequency studies performed for the brighter, well-known sources (e.g. Slee et al., 2001; Shulevski et al., 2017; Kale et al., 2018). These typically focus on the higher-frequency end of the SED. The spectral curvature present in such sources typically presents at $\nu \gtrsim 1$ GHz and provides information about the age of the source. For larger samples, such multi-wavelength studies are prohibitive technically due to the long integration times over multiple frequencies required with narrow FOV telescopes such as the JVLA and upgraded GMRT (uGMRT). Additionally, higher-frequency observations are typically less sensitive to large-scale structure due to limited sampling of the inner u, v plane. Present studies with LOFAR, while clearly an excellent machine for detecting diffuse emission in clusters both in its sensitivity and wide-field ability, are typically limited in information on the spectral properties of these sources (e.g. Di Gennaro et al., 2021; van Weeren et al., 2021; Botteon et al., 2021). With very little knowledge of the SED, understanding the nature of the sources is difficult and will require a follow-up with other instruments (or the LOFAR low-band array, see de Gasperin et al. 2021). Specifically, with radio halos the USSRH population provides a tantalizing glimpse into the radio halo formation process, and while there might be an expectation that halos detected in recent LOFAR surveys will have pre-

dominantly ultra-steep spectra by virtue of their low-frequency detection, this cannot be confirmed without multi-frequency follow-up. This limits the investigation into particle populations and mechanisms with these monochromatic studies.

The work presented in this Thesis highlights the potential for the low-frequency portion of the SED to classify these sources and understand their underlying physical mechanisms. This regime complements the current generation of sensitive wide-field radio interferometers (e.g. MWA, ASKAP, as well as the uGMRT and LOFAR). This work has also shown that a survey with the MWA and ASKAP to detect a sample of diffuse cluster sources and characterise their spectra is viable over the whole accessible sky in a relatively short period of time. The integrated spectral index is also shown to be useful in a statistical sense in linking the underlying particle populations. Future all-sky surveys will be required to not only increase population statistics (especially in regards to fossil sources) but to also provide a more homogeneous set of integrated spectral indices. Presently, measurements for all sources investigated are made roughly in the range 100–1000 MHz, but this includes two-point spectral indices, sources with many measurements, and sources at only the low or high end of that range.

This work highlights the complementary nature of the MWA(-2) and ASKAP, where the MWA works as a rapid [3], wide-field survey instrument, allowing easy detection of a large numbers of diffuse, steep-spectrum cluster sources, as well as providing multi-frequency coverage. ASKAP can follow up detections, providing both an additional frequency point of the diffuse source as well as knowledge of embedded discrete source populations. Despite the success of the present cluster diffuse source survey, some limitations (aside from the obvious resolution) remain. Indeed, situations are noted where falling back on GLEAM data has been required at the higher end of the MWA band when using MWA-2 data. This is largely due to the limitation of the shorter baselines at the higher frequencies (see also Hodgson et al., 2020), combined with adding snapshots in the manner we do. Upcoming upgrades to the MWA, including a correlator that can handle more than 128 tiles, will allow for additional short baselines to be incorporated into the 'extended' configuration. Alternatively, progress may be made in joint-deconvolution of e.g. MWA Phase I/MWA Phase II 'compact' configuration

[3]Once a processing pipeline has been created.

data and MWA-2 data. At this stage joint-deconvolution methods (e.g. Image Domain Gridding, IDG; van der Tol et al. 2018) are limited to only a handful of snapshots, and ionospheric effects become much more problematic without a consistent method to employ accurate phase screens during image gridding.

While these studies performed with the MWA and ASKAP complement studies performed by LOFAR (with appropriate multi-frequency follow-up), higher-resolution follow-up observations will be eventually required to unambiguously classify these sources. A natural progression from this project is to follow-up the remaining candidate sources detected in GLEAM data as in Duchesne et al. (2021d, Chapter 6), but with upcoming wide-field surveys. For example, the upcoming GLEAM eXtended (GLEAM-X) survey will allow follow-up of the candidate sources with a factor of ~ 4 increase in sensitivity and a factor of ~ 2 increase in resolution. This will also allow an additional, deeper Southern Sky survey for diffuse cluster sources to be completed with a focus on lower-mass and higher-redshift systems with fainter emission, steeper spectra, and smaller angular sizes. Such a survey will lead to a larger sample of fossil plasmas, helping to confirm the possible link between fossils and relics and halos found in this work. Further on, over the next few years, the EMU survey will begin providing images of the whole Southern Sky at 887 MHz with a sensitivity of ~ 20 μJy beam^{-1} and excellent u, v coverage offered by long ASKAP integrations. As seen in this work (notably Chapters 3, 5 and 6) 10-hr (or even less) ASKAP observations provide excellent sensitivity to extended, low-surface brightness sources such as relics, halos, and remnants (see also Quici et al., 2021). Additionally, as described in Duchesne et al. (2021a, Chapter 3) MeerKAT will also be able to provide deep, sensitive follow-up observations of diffuse cluster sources detected in surveys.

Based on predictions from a recent survey for radio halos in PSZ2 (Planck Collaboration et al., 2016b) clusters using recent LoTSS [4] (Shimwell et al., 2017) data (van Weeren et al., 2021), it is expected that LoTSS will uncover of the order 200 radio halos and 100 Mpc-scale relics across all PSZ2 clusters. Comparatively, EMU would be expected to find only half this number assuming spectral indices of -1.3. LoTSS and EMU share a common resolution and but with a factor of five difference in

[4]LOFAR Two-metre Sky Survey

point source sensitivity, though both surveys boast excellent and similar sensitivity to large-scale emission. GLEAM-X on the other hand is more restricted due to resolution but can still follow-up EMU-detected clusters with appropriate source subtraction, and has a similar surface brightness sensitivity at 154 MHz as LoTSS (assuming an rms noise of 3 mJy beam^{-1} with a 90 arcsec PSF). While halos and relics are only (typically) detected in merging clusters, determining exact source counts is difficult as the expected population statistics relies on knowledge of cluster dynamics—eROSITA (Predehl et al., 2021) surveys currently underway will help to provide this information over the sky to the necessary depth to match PSZ2 (see e.g. Reiprich et al., 2021; Ghirardini et al., 2021, for recent eROSITA results highlighting cluster dynamics). This will also somewhat mitigate selection biases from ROSAT cluster surveys wherein relaxed clusters are more likely to be selected (Eckert, Molendi & Paltani, 2011).

Assuming the expected detection statistics suggested by van Weeren et al. (2021), for SKA and MeerKAT surveys we can expect an increase to the halo and relics numbers in excess of 1000 sources. This increase will be due to a factor of ~ 3 increase in surface brightness sensitivity with ~ 10 times fainter sources detected (Prandoni & Seymour, 2015) over LoTSS. Fossil plasma sources should increase in a similar fashion, noting that source sizes with fossil plasmas are typically much smaller, and that multiple fossil plasmas may be found in a single cluster. Additionally, fossil sources that are simply remnants are expected to have shorter 'lifespans' than halos, relics, or other re-accelerated sources as the radio plasma fades quickly ($\lesssim 100$ Myr) without energy input. As noted, the numbers alone are not all that is required—detailed knowledge of their spectra is important in understanding the underlying physics, and these detections need to have the multi-wavelength follow-up (either dedicated or surveys at different frequencies) to provide this information. With a factor of 10 or more increase to source numbers, we should be able to interpret more clearly the distributions of the integrated spectral indices with more statistical certainty. Further resolved spectral index studies will further help uncover examples of re-accelerated plasmas connected to active galaxies.

This work has just gently brushed the dust off of a small collection of old fossils. Large-scale, deep, high-resolution surveys with the SKA pathfinders and precursors,

particularly ASKAP and MeerKAT with their $\sim$ 5–15 arcsec resolution over the Southern Sky, and LOFAR and uGMRT over the Northern Sky, will enable high-fidelity follow-up of these types of sources placing constraints on the $\lesssim$ 1 GHz spectrum. The SKA-Low instrument in the future will dig deeper, revealing myriad new ultra-steep spectrum radio fossils, providing key observational evidence to understand the physics involved including the (re-)acceleration mechanisms and their underlying particle populations.

Bibliography

Abbott T. M. C., et al., 2018, ApJS, 239, 18

Abell G. O., 1958, ApJS, 3, 211

Abell G. O., Corwin Jr. H. G., Olowin R. P., 1989, ApJS, 70, 1

Ade P. A. R., et al., 2015, Phys. Rev. D, 92, 123509

Akamatsu H., et al., 2015, A&A, 582, A87

Alam S., et al., 2015, ApJS, 219, 12

Arnaud M., Pointecouteau E., Pratt G. W., 2005, A&A, 441, 893

Arras P., Reinecke M., Westermann R., Enßin T. A., 2021, A&A, 646, A58

Ascasibar Y., Markevitch M., 2006, ApJ, 650, 102

Astropy Collaboration et al., 2013, A&A, 558, A33

Basu K., 2012, MNRAS, 421, L112

Beardsley A. P., et al., 2019, PASA, 36, e050

Becker R. H., White R. L., Helfand D. J., 1995, ApJ, 450, 559

Bernardi G., et al., 2016, MNRAS, 456, 1259

Blandford R., Eichler D., 1987, Phys. Rep., 154, 1

Blumenthal G. R., Faber S. M., Primack J. R., Rees M. J., 1984, Nature, 311, 517

Bock D. C.-J., Large M. I., Sadler E. M., 1999, AJ, 117, 1578

Böhringer H., et al., 2004, A&A, 425, 367

Böhringer H., et al., 2007, A&A, 469, 363

Bonafede A., Feretti L., Murgia M., Govoni F., Giovannini G., Dallacasa D., Dolag K., Taylor G. B., 2010, A&A, 513, A30

Bonafede A., et al., 2012, MNRAS, 426, 40

Bonafede A., et al., 2014a, MNRAS, 444, L44

Bonafede A., Intema H. T., Brüggen M., Girardi M., Nonino M., Kantharia N., van

Weeren R. J., Röttgering H. J. A., 2014b, ApJ, 785, 1

Bonafede A., et al., 2021, ApJ, 907, 32

Botteon A., Gastaldello F., Brunetti G., Dallacasa D., 2016, MNRAS, 460, L84

Botteon A., et al., 2018, MNRAS, 478, 885

Botteon A., et al., 2020a, MNRAS, 499, L11

Botteon A., Brunetti G., Ryu D., Roh S., 2020b, A&A, 634, A64

Botteon A., et al., 2020c, ApJ, 897, 93

Botteon A., et al., 2021, ApJ, 914, L29

Bourdin H., Mazzotta P., Markevitch M., Giacintucci S., Brunetti G., 2013, ApJ, 764, 82

Bravi L., Gitti M., Brunetti G., 2016, MNRAS, 455, L41

Brienza M., et al., 2016, A&A, 585, A29

Brienza M., et al., 2017, A&A, 606, A98

Briggs D. S., 1995, PhD thesis, The New Mexico Institute of Mining and Technology, Socorro, New Mexico, http://www.aoc.nrao.edu/dissertations/dbriggs/

Brown S., Duesterhoeft J., Rudnick L., 2011, ApJ, 727, L25

Brüggen M., et al., 2021, A&A, 647, A3

Brunetti G., Jones T. W., 2014, International Journal of Modern Physics D, 23, 1430007

Brunetti G., Lazarian A., 2007, MNRAS, 378, 245

Brunetti G., Lazarian A., 2011, MNRAS, 412, 817

Brunetti G., Lazarian A., 2016, MNRAS, 458, 2584

Brunetti G., Vazza F., 2020, Phys. Rev. Lett., 124, 051101

Brunetti G., Venturi T., Dallacasa D., Cassano R., Dolag K., Giacintucci S., Setti G., 2007, ApJ, 670, L5

Brunetti G., et al., 2008, Nature, 455, 944

Burn B. J., 1966, MNRAS, 133, 67

Burns J. O., Sulkanen M. E., Gisler G. R., Perley R. A., 1992, ApJ, 388, L49

Caretta C. A., Maia M. A. G., Kawasaki W., Willmer C. N. A., 2002, AJ, 123, 1200

Cassano R., Brunetti G., Setti G., Govoni F., Dolag K., 2007, MNRAS, 378, 1565

Cassano R., Gitti M., Brunetti G., 2008, A&A, 486, L31

Cassano R., Ettori S., Giacintucci S., Brunetti G., Markevitch M., Venturi T., Gitti M., 2010, ApJ, 721, L82

Cassano R., et al., 2013, ApJ, 777, 141

Cavagnolo K. W., Donahue M., Voit G. M., Sun M., 2008, ApJ, 682, 821

Cen R., Ostriker J. P., 1999, ApJ, 514, 1

Chambers K. C., et al., 2016, preprint, (arXiv:1612.05560)

Chippendale A. P., O'Sullivan J., Reynolds J., Gough R., Hayman D., Hay S., 2010, in Phased Array Systems and Technology (ARRAY. pp 648–652, doi:10.1109/ARRAY.2010.5613298

Chon G., Böhringer H., 2012, A&A, 538, A35

Clark B. G., 1980, A&A, 89, 377

Clarke T. E., Kronberg P. P., Böhringer H., 2001, ApJ, 547, L111

Condon J. J., Cotton W. D., Greisen E. W., Yin Q. F., Perley R. A., Taylor G. B., Broderick J. J., 1998, AJ, 115, 1693

Cordey R. A., 1986, MNRAS, 219, 575

Cordey R. A., 1987, MNRAS, 227, 695

Cornwell T. J., 2008, IEEE Journal of Selected Topics in Signal Processing, 2, 793

Cornwell T. J., Wilkinson P. N., 1981, MNRAS, 196, 1067

Cova F., et al., 2019, A&A, 628, A83

Coziol R., Andernach H., Caretta C. A., Alamo-Martínez K. A., Tago E., 2009, AJ, 137, 4795

Cruddace R., et al., 2002, ApJS, 140, 239

Cuciti V., et al., 2021a, A&A, 647, A50

Cuciti V., et al., 2021b, A&A, 647, A51

Dabhade P., et al., 2020, A&A, 635, A5

Dahle H., Kaiser N., Irgens R. J., Lilje P. B., Maddox S. J., 2002, ApJS, 139, 313

Davé R., et al., 2001, ApJ, 552, 473

De Grandi S., et al., 1999, ApJ, 514, 148

DeBoer D. R., et al., 2009, IEEE Proceedings, 97, 1507

Dehghan S., Johnston-Hollitt M., Colless M., Miller R., 2017, MNRAS, 468, 2645

Delhaize J., et al., 2021, MNRAS, 501, 3833

Di Gennaro G., et al., 2019, ApJ, 873, 64

Di Gennaro G., et al., 2021, Nature Astronomy, 5, 268

Domínguez-Fernández P., Bruggen M., Vazza F., Banda-Barragan W. E., Rajpurohit K., Mignone A., Mukherjee D., Vaidya B., 2021, MNRAS, 500, 795

Donnert J., Vazza F., Brüggen M., ZuHone J., 2018, Space Sci. Rev., 214, 122

Drury L., 1983, Space Sci. Rev., 36, 57

Duchesne S. W., Johnston-Hollitt M., 2019, PASA, 36, e016

Duchesne S. W., Johnston-Hollitt M., Zhu Z., Wayth R. B., Line J. L. B., 2020, PASA, 37, e037

Duchesne S. W., Johnston-Hollitt M., Bartalucci I., Hodgson T., Pratt G. W., 2021a, PASA, 38, e005

Duchesne S. W., Johnston-Hollitt M., Offringa A. R., Pratt G. W., Zheng Q., Dehghan S., 2021b, PASA, 38, e010

Duchesne S. W., Johnston-Hollitt M., Wilber A. G., 2021c, PASA, 38, e031

Duchesne S. W., Johnston-Hollitt M., Bartalucci I., 2021d, PASA, 38, e053

Duffy P., Blundell K. M., 2012, MNRAS, 421, 108

Dwarakanath K. S., Parekh V., Kale R., George L. T., 2018, MNRAS, 477, 957

Eckert D., Molendi S., Paltani S., 2011, A&A, 526, A79

Eckert D., Jauzac M., Vazza F., Owers M. S., Kneib J. P., Tchernin C., Intema H., Knowles K., 2016, MNRAS, 461, 1302

Eisenstein D. J., et al., 2011, AJ, 142, 72

Enßlin T. A., Gopal-Krishna 2001, A&A, 366, 26

Enßlin T. A., Biermann P. L., Klein U., Kohle S., 1998, A&A, 332, 395

Feretti L., Giovannini G., 2008, Clusters of Galaxies in the Radio: Relativistic Plasma and ICM/Radio Galaxy Interaction Processes. p. 24, doi:10.1007/978-1-4020-6941-3_5

Feretti L., Giovannini G., Govoni F., Murgia M., 2012, A&A Rev., 20, 54

Finoguenov A., Sarazin C. L., Nakazawa K., Wik D. R., Clarke T. E., 2010, ApJ, 715, 1143

Flaugher B., et al., 2015, AJ, 150, 150

Fleenor M. C., Rose J. A., Christiansen W. A., Johnston-Hollitt M., Hunstead R. W.,

Drinkwater M. J., Saunders W., 2006, AJ, 131, 1280

Frater R. H., Brooks J. W., Whiteoak J. B., 1992, Journal of Electrical and Electronics Engineering Australia, 12, 103

Fujita Y., Matsumoto T., Wada K., 2004, ApJ, 612, L9

Garilli B., Maccagni D., Tarenghi M., 1993, A&AS, 100, 33

Gendron-Marsolais M., et al., 2017, MNRAS, 469, 3872

George L. T., et al., 2015, MNRAS, 451, 4207

George L. T., et al., 2017, MNRAS, 467, 936

Ghirardini V., et al., 2021, A&A, 647, A4

Giacintucci S., et al., 2005, A&A, 440, 867

Giacintucci S., Markevitch M., Venturi T., Clarke T. E., Cassano R., Mazzotta P., 2014a, ApJ, 781, 9

Giacintucci S., Markevitch M., Brunetti G., ZuHone J. A., Venturi T., Mazzotta P., Bourdin H., 2014b, ApJ, 795, 73

Giacintucci S., Markevitch M., Cassano R., Venturi T., Clarke T. E., Brunetti G., 2017, ApJ, 841, 71

Giacintucci S., Markevitch M., Cassano R., Venturi T., Clarke T. E., Kale R., Cuciti V., 2019, ApJ, 880, 70

Giovannini G., Tordi M., Feretti L., 1999, New~Astron., 4, 141

Giovannini G., Bonafede A., Feretti L., Govoni F., Murgia M., Ferrari F., Monti G., 2009, A&A, 507, 1257

Gitti M., Brunetti G., Setti G., 2002, A&A, 386, 456

Gitti M., Brunetti G., Feretti L., Setti G., 2004, A&A, 417, 1

Gitti M., Brunetti G., Cassano R., Ettori S., 2018, A&A, 617, A11

Godfrey L. E. H., Morganti R., Brienza M., 2017, MNRAS, 471, 891

Golovich N., et al., 2019, ApJ, 882, 69

Govoni F., Enßlin T. A., Feretti L., Giovannini G., 2001, A&A, 369, 441

Govoni F., Murgia M., Xu H., Li H., Norman M. L., Feretti L., Giovannini G., Vacca V., 2013, A&A, 554, A102

Govoni F., et al., 2017, A&A, 603, A122

Govoni F., et al., 2019, Science, 364, 981

Green D. A., 2011, Bulletin of the Astronomical Society of India, 39, 289

Hancock P. J., Murphy T., Gaensler B. M., Hopkins A., Curran J. R., 2012, MNRAS, 422, 1812

Hancock P. J., Trott C. M., Hurley-Walker N., 2018, PASA, 35, e011

Hargrave P. J., Ryle M., 1974, MNRAS, 166, 305

Heald G., et al., 2020, Galaxies, 8, 53

Hindson L., et al., 2014, MNRAS, 445, 330

Hlavacek-Larrondo J., et al., 2013, ApJ, 777, 163

Hoang D. N., et al., 2021, arXiv e-prints, p. arXiv:2106.00679

Hodgson T., Johnston-Hollitt M., McKinley B., Vernstrom T., Vacca V., 2020, PASA, 37, e032

Hodgson T., Bartalucci I., Johnston-Hollitt M., McKinley B., Vazza F., Wittor D., 2021, ApJ, 909, 198

Hoeft M., Brüggen M., 2007, MNRAS, 375, 77

Hoeft M., et al., 2020, arXiv e-prints, p. arXiv:2010.10331

Högbom J. A., 1974, A&AS, 15, 417

Hotan A., 2016, ASKAP Commissioning and Early Science Memo 011, Holographic Measurement of ASKAP Primary Beams, https://www.atnf.csiro.au/projects/askap/ACES-memos. CSIRO Astronomy and Space Science, https://www.atnf.csiro.au/projects/askap/ACES-memos

Hotan A. W., et al., 2014, PASA, 31, e041

Hotan A. W., et al., 2021, PASA, 38, e009

Hudson D. S., Mittal R., Reiprich T. H., Nulsen P. E. J., Andernach H., Sarazin C. L., 2010, A&A, 513, A37

Hunter J. D., 2007, Computing in Science and Engineering, 9, 90

Hurley-Walker N., Hancock P. J., 2018, Astronomy and Computing, 25, 94

Hurley-Walker N., et al., 2015, MNRAS, 447, 2468

Hurley-Walker N., et al., 2017, MNRAS, 464, 1146

Hutschenreuter S., et al., 2021, arXiv e-prints, p. arXiv:2102.01709

HyeongHan K., et al., 2020, ApJ, 900, 127

Ignesti A., Brunetti G., Gitti M., Giacintucci S., 2020, A&A, 640, A37

Intema H. T., van der Tol S., Cotton W. D., Cohen A. S., van Bemmel I. M., Röttgering H. J. A., 2009, A&A, 501, 1185

Intema H. T., Jagannathan P., Mooley K. P., Frail D. A., 2017, A&A, 598, A78

Jackson J. D., 1975, Classical electrodynamics. New York: Wiley, 1975, 2nd ed.

Jaffe W. J., 1977, ApJ, 212, 1

Jaffe W. J., Perola G. C., 1973, A&A, 26, 423

Johnston-Hollitt M., 2003, PhD thesis, University of Adelaide, http://hdl.handle.net/2440/21954

Johnston-Hollitt M., 2004, in Reiprich T., Kempner J., Soker N., eds, The Riddle of Cooling Flows in Galaxies and Clusters of galaxies. p. 51

Johnston-Hollitt M., Ekers R. D., 2004, arXiv e-prints, pp astro–ph/0411045

Johnston-Hollitt M., Hunstead R. W., Corbett E., 2008, A&A, 479, 1

Johnston-Hollitt M., et al., 2015, in Advancing Astrophysics with the Square Kilometre Array (AASKA14). p. 92 (arXiv:1506.00808)

Jones C., Forman W., 1999, ApJ, 511, 65

Jones E., Oliphant T., Peterson P., et al., 2001, SciPy: Open source scientific tools for Python, http://www.scipy.org/

Jones A., et al., 2021, MNRAS, 505, 4762

Jurlin N., et al., 2020, A&A, 638, A34

Kale R., Dwarakanath K. S., Bagchi J., Paul S., 2012, MNRAS, 426, 1204

Kale R., Venturi T., Giacintucci S., Dallacasa D., Cassano R., Brunetti G., Macario G., Athreya R., 2013, A&A, 557, A99

Kale R., et al., 2015, A&A, 579, A92

Kale R., Parekh V., Dwarakanath K. S., 2018, MNRAS, 480, 5352

Kale R., Shende K. M., Parekh V., 2019, MNRAS, 486, L80

Kang H., 2018, Journal of Korean Astronomical Society, 51, 185

Kang H., Ryu D., Jones T. W., 2012, ApJ, 756, 97

Kardashev N. S., 1962, Soviet Ast., 6, 317

Kempner J. C., Blanton E. L., Clarke T. E., Enßlin T. A., Johnston-Hollitt M., Rudnick L., 2004, in Reiprich T., Kempner J., Soker N., eds, The Riddle of Cooling Flows in Galaxies and Clusters of galaxies. (arXiv:astro-ph/0310263)

Kerr F. J., Hindman J. V., 1953, AJ, 58, 218

Kim K. T., Tribble P. C., Kronberg P. P., 1991, ApJ, 379, 80

Knowles K., et al., 2019, MNRAS, 486, 1332

Knowles K., et al., 2021, MNRAS, 504, 1749

Komissarov S. S., Gubanov A. G., 1994, A&A, 285

Kravtsov A. V., Borgani S., 2012, ARA&A, 50, 353

Landau L. D., Lifshitz E. M., 1959, Fluid Mechanics. A-W series in advanced physics Vol. 6, Elsevier Science

Large M. I., Mathewson D. S., Haslam C. G. T., 1959, Nature, 183, 1663

Leshem A., van der Veen A.-J., Boonstra A.-J., 2000, ApJS, 131, 355

Liang H., Hunstead R. W., Birkinshaw M., Andreani P., 2000, ApJ, 544, 686

Line J. L. B., Webster R. L., Pindor B., Mitchell D. A., Trott C. M., 2017, PASA, 34, e003

Line J. L. B., et al., 2018, PASA, 35, 45

Loi S. T., et al., 2015, MNRAS, 453, 2731

Loi S. T., et al., 2016, Journal of Geophysical Research (Space Physics), 121, 1569

Loi F., Murgia M., Govoni F., Vacca V., Prandoni I., Bonafede A., Feretti L., 2019a, MNRAS, 485, 5285

Loi F., et al., 2019b, MNRAS, 490, 4841

Loi F., et al., 2020, MNRAS, 498, 1628

Longair M., 2011, High Energy Astrophysics. Cambridge University Press

Lotz J. M., et al., 2017, ApJ, 837, 97

Mahatma V. H., et al., 2018, MNRAS, 475, 4557

Markevitch M., Vikhlinin A., 2007, Phys. Rep., 443, 1

Markevitch M., Sarazin C. L., Vikhlinin A., 1999, ApJ, 521, 526

Markevitch M., Gonzalez A. H., David L., Vikhlinin A., Murray S., Forman W., Jones C., Tucker W., 2002, ApJ, 567, L27

Markevitch M., Govoni F., Brunetti G., Jerius D., 2005, ApJ, 627, 733

Martinez Aviles G., et al., 2016, A&A, 595, A116

Mauch T., Murphy T., Buttery H. J., Curran J., Hunstead R. W., Piestrzynski B., Robertson J. G., Sadler E. M., 2003, MNRAS, 342, 1117

McConnell D., et al., 2016, PASA, 33, e042

McConnell D., et al., 2020, PASA, 37, e048

McKean J. P., et al., 2016, MNRAS, 463, 3143

Mitchell R. J., Culhane J. L., Davison P. J. N., Ives J. C., 1976, MNRAS, 175, 29P

Mohan N., Rafferty D., 2015, PyBDSF: Python Blob Detection and Source Finder (ascl:1502.007)

Mohr J. J., Fabricant D. G., Geller M. J., 1993, ApJ, 413, 492

Morganson E., et al., 2018, PASP, 130, 074501

Murgia M., Govoni F., Feretti L., Giovannini G., Dallacasa D., Fanti R., Taylor G. B., Dolag K., 2004, A&A, 424, 429

Murgia M., et al., 2011, A&A, 526, A148

Murphy T., Mauch T., Green A., Hunstead R. W., Piestrzynska B., Kels A. P., Sztajer P., 2007, MNRAS, 382, 382

Murphy T., et al., 2021, arXiv e-prints, p. arXiv:2108.06039

Norris R. P., et al., 2011, PASA, 28, 215

Ochsenbein F., Bauer P., Marcout J., 2000, A&AS, 143, 23

Offringa A. R., Smirnov O., 2017, MNRAS, 471, 301

Offringa A. R., van de Gronde J. J., Roerdink J. B. T. M., 2012, A&A, 539, A95

Offringa A. R., et al., 2014, MNRAS, 444, 606

Offringa A. R., et al., 2016, MNRAS, 458, 1057

Oort J. H., 1983, ARA&A, 21, 373

Oppermann N., et al., 2015, A&A, 575, A118

Orrú E., Murgia M., Feretti L., Govoni F., Brunetti G., Giovannini G., Girardi M., Setti G., 2007, A&A, 467, 943

Osinga E., et al., 2021, A&A, 648, A11

Pacholczyk A. G., 1970, Radio astrophysics. Nonthermal processes in galactic and extragalactic sources. Series of Books in Astronomy and Astrophysics, San Francisco: Freeman, 1970

Parma P., Murgia M., de Ruiter H. R., Fanti R., Mack K. H., Govoni F., 2007, A&A, 470, 875

Paul S., Salunkhe S., Datta A., Intema H. T., 2019, MNRAS, 489, 446

Pearce C. J. J., et al., 2017, ApJ, 845, 81

Peebles P. J. E., 1980, The large-scale structure of the universe. Princeton Univ. Press, Princeton, N. J.

Perley R. A., Dreher J. W., Cowan J. J., 1984, ApJ, 285, L35

Piffaretti R., Arnaud M., Pratt G. W., Pointecouteau E., Melin J.-B., 2011, A&A, 534, A109

Pinzke A., Oh S. P., Pfrommer C., 2013, MNRAS, 435, 1061

Planck Collaboration et al., 2014, A&A, 571, A29

Planck Collaboration et al., 2015, A&A, 581, A14

Planck Collaboration et al., 2016a, A&A, 594, A19

Planck Collaboration et al., 2016b, A&A, 594, A27

Poole G. B., Fardal M. A., Babul A., McCarthy I. G., Quinn T., Wadsley J., 2006, MNRAS, 373, 881

Prandoni I., Seymour N., 2015, in Proceedings of Advancing Astrophysics with the Square Kilometre Array — PoS(AASKA14). p. 067, doi:10.22323/1.215.0067

Pratley L., Johnston-Hollitt M., Dehghan S., Sun M., 2013, MNRAS, 432, 243

Predehl P., et al., 2021, A&A, 647, A1

Price-Whelan A. M., et al., 2018, AJ, 156, 123

Quici B., et al., 2021, PASA, 38, e008

Raja R., Rahaman M., Datta A., van Weeren R. J., Intema H. T., Paul S., 2021, MNRAS, 500, 2236

Rajpurohit K., et al., 2020a, A&A, 636, A30

Rajpurohit K., et al., 2020b, A&A, 642, L13

Rajpurohit K., et al., 2021a, arXiv e-prints, p. arXiv:2104.05690

Rajpurohit K., et al., 2021b, A&A, 646, A56

Rajpurohit K., et al., 2021c, A&A, 646, A135

Reiprich T. H., et al., 2021, A&A, 647, A2

Richard-Laferrière A., et al., 2020, MNRAS, 499, 2934

Riseley C. J., Scaife A. M. M., Oozeer N., Magnus L., Wise M. W., 2015, MNRAS, 447, 1895

Riseley C. J., et al., 2018, PASA, 35, 43

Riseley C. J., et al., 2020, PASA, 37, e029

Robitaille T., Bressert E., 2012, APLpy: Astronomical Plotting Library in Python, Astrophysics Source Code Library (ascl:1208.017)

Roettiger K., Burns J. O., Stone J. M., 1999, ApJ, 518, 603

Rybicki G. B., Lightman A. L., 2004, Radiative processes in astrophysics. WILEY-VCH Verlag GmbH & Co. KGaA, Weinheim

Ryle M., 1962, Nature, 194, 517

Ryle M., Vonberg D. D., 1946, Nature, 158, 339

Ryle M., Elsmore B., Neville A. C., 1965, Nature, 207, 1024

Santos J. S., Rosati P., Tozzi P., Böhringer H., Ettori S., Bignamini A., 2008, A&A, 483, 35

Sarazin C. L., 1988, X-ray emission from clusters of galaxies. http://ned.ipac.caltech.edu/level5/March02/Sarazin/frames.html

Saripalli L., Subrahmanyan R., Thorat K., Ekers R. D., Hunstead R. W., Johnston H. M., Sadler E. M., 2012, ApJS, 199, 27

Sault R. J., Teuben P. J., Wright M. C. H., 1995, in Shaw R. A., Payne H. E., Hayes J. J. E., eds, Astronomical Society of the Pacific Conference Series Vol. 77, Astronomical Data Analysis Software and Systems IV. p. 433 (arXiv:astro-ph/0612759)

Scheuer P. A. G., Williams P. J. S., 1968, ARA&A, 6, 321

Schlickeiser R., Sievers A., Thiemann H., 1987, A&A, 182, 21

Schwope A., et al., 2000, Astronomische Nachrichten, 321, 1

Serlemitsos P. J., Smith B. W., Boldt E. A., Holt S. S., Swank J. H., 1977, ApJ, 211, L63

Shakouri S., Johnston-Hollitt M., Dehghan S., 2016a, MNRAS, 458, 3083

Shakouri S., Johnston-Hollitt M., Pratt G. W., 2016b, MNRAS, 459, 2525

Shimwell T. W., Brown S., Feain I. J., Feretti L., Gaensler B. M., Lage C., 2014, MNRAS, 440, 2901

Shimwell T. W., Markevitch M., Brown S., Feretti L., Gaensler B. M., Johnston-Hollitt M., Lage C., Srinivasan R., 2015, MNRAS, 449, 1486

Shimwell T. W., et al., 2017, A&A, 598, A104

Shulevski A., et al., 2017, A&A, 600, A65

Slee O. B., Roy A. L., Murgia M., Andernach H., Ehle M., 2001, AJ, 122, 1172

Smirnov O. M., 2011a, A&A, 527, A106

Smirnov O. M., 2011b, A&A, 527, A107

Sokolowski M., et al., 2017, PASA, 34, e062

Song J., et al., 2012, ApJ, 761, 22

Struble M. F., Rood H. J., 1999, ApJS, 125, 35

Stuardi C., Bonafede A., Lovisari L., Domínguez-Fernández P., Vazza F., Brüggen M., van Weeren R. J., de Gasperin F., 2021, MNRAS, 502, 2518

Subramanian K., 2016, Reports on Progress in Physics, 79, 076901

Sunyaev R. A., Zel'dovich Y. B., 1970, Ap&SS, 7, 3

Thierbach M., Klein U., Wielebinski R., 2003, A&A, 397, 53

Thompson A. R., Moran J. M., Swenson Jr. G. W., 2017, Interferometry and Synthesis in Radio Astronomy. Springer, Cham, doi:10.1007/978-3-319-44431-4

Tingay S. J., et al., 2013, PASA, 30, 7

Tonry J. L., et al., 2012, ApJ, 750, 99

Urdampilleta I., Simionescu A., Kaastra J. S., Zhang X., Di Gennaro G., Mernier F., de Plaa J., Brunetti G., 2021, A&A, 646, A95

Vacca V., Murgia M., Govoni F., Feretti L., Giovannini G., Orrù E., Bonafede A., 2010, A&A, 514, A71

Van Eck C. L., et al., 2018, A&A, 613, A58

Vazza F., Wittor D., Brunetti G., Brüggen M., 2021, A&A, 653, A23

Venturi T., Giacintucci S., Brunetti G., Cassano R., Bardelli S., Dallacasa D., Setti G., 2007, A&A, 463, 937

Venturi T., Giacintucci S., Dallacasa D., Cassano R., Brunetti G., Bardelli S., Setti G., 2008, A&A, 484, 327

Vikhlinin A., McNamara B. R., Forman W., Jones C., Quintana H., Hornstrup A., 1998, ApJ, 502, 558

Vikhlinin A., Markevitch M., Murray S. S., 2001, ApJ, 551, 160

Wayth R. B., et al., 2015, PASA, 32, 25

Wayth R. B., et al., 2018, PASA, 35

Wen Z. L., Han J. L., 2015, ApJ, 807, 178

Wen Z. L., Han J. L., Liu F. S., 2012, ApJS, 199, 34

White R. L., Becker R. H., Helfand D. J., Gregg M. D., 1997, ApJ, 475, 479

Wilber A., et al., 2019, A&A, 622, A25

Wilber A. G., Johnston-Hollitt M., Duchesne S. W., Tasse C., Akamatsu H., Intema H., Hodgson T., 2020, PASA, 37, e040

Willson M. A. G., 1970, MNRAS, 151, 1

Wilson W. E., et al., 2011, MNRAS, 416, 832

Ye H., Gull S. F., Tan S. M., Nikolic B., 2021, arXiv e-prints, p. arXiv:2101.11172

York D. G., et al., 2000, AJ, 120, 1579

Yuan Z. S., Han J. L., Wen Z. L., 2015, ApJ, 813, 77

Zaritsky D., Gonzalez A. H., Zabludoff A. I., 2006, ApJ, 638, 725

Zheng Q., Johnston-Hollitt M., Duchesne S. W., Li W. T., 2018, MNRAS, 479, 730

ZuHone J. A., Roediger E., 2016, Journal of Plasma Physics, 82, 535820301

ZuHone J. A., Markevitch M., Brunetti G., Giacintucci S., 2013, ApJ, 762, 78

de Gasperin F., Intema H. T., Williams W., Brüggen M., Murgia M., Beck R., Bonafede A., 2014a, MNRAS, 440, 1542

de Gasperin F., van Weeren R. J., Brüggen M., Vazza F., Bonafede A., Intema H. T., 2014b, MNRAS, 444, 3130

de Gasperin F., Intema H. T., van Weeren R. J., Dawson W. A., Golovich N., Wittman D., Bonafede A., Brüggen M., 2015, MNRAS, 453, 3483

de Gasperin F., et al., 2017, Science Advances, 3, e1701634

de Gasperin F., et al., 2020, A&A, 635, A150

de Gasperin F., et al., 2021, A&A, 648, A104

van Weeren R. J., et al., 2009, A&A, 506, 1083

van Weeren R. J., Röttgering H. J. A., Brüggen M., Hoeft M., 2010, Science, 330, 347

van Weeren R. J., Brüggen M., Röttgering H. J. A., Hoeft M., Nuza S. E., Intema H. T., 2011a, A&A, 533, A35

van Weeren R. J., Brüggen M., Röttgering H. J. A., Hoeft M., Nuza S. E., Intema H. T., 2011b, A&A, 533, A35

van Weeren R. J., Röttgering H. J. A., Intema H. T., Rudnick L., Brüggen M., Hoeft

M., Oonk J. B. R., 2012, A&A, 546, A124
van Weeren R. J., et al., 2016, ApJ, 818, 204
van Weeren R. J., et al., 2017, Nature Astronomy, 1, 0005
van Weeren R. J., de Gasperin F., Akamatsu H., Brüggen M., Feretti L., Kang H., Stroe A., Zandanel F., 2019, Space Sci. Rev., 215, 16
van Weeren R. J., et al., 2021, A&A, 651, A115
van der Tol S., Veenboer B., Offringa A. R., 2018, A&A, 616, A27
van der Velden E., 2020, The Journal of Open Source Software, 5, 2004
van der Walt S., Colbert S. C., Varoquaux G., 2011, Computing in Science Engineering, 13, 22

Appendices

Appendix A.

Creating an MWA data processing pipeline

At the commencement of this work, no data processing pipeline existed that could produce MWA Phase II 'extended' configuration images without modification. This motivated development of a pipeline that took inspiration from existing Phase I pipelines [1]. The Phase II Pipeline (`piip`) is a combination of a number of individual pieces of software used for calibration, imaging, and other tasks. Fig. A.1 is a flow-diagram displaying the end-to-end pipeline for individual observations, from data staging and download to post-imaging corrections. Some of the software used is labelled on the diagram, and in the following sections, each part of the pipeline is fleshed out further.

A.1. Data-staging and pre-processing

Data are initially staged using the MWA All-Sky Virtual Observatory (ASVO) [2] system. This allows not only the retrieval of raw data products from the Pawsey archive, but also utilises `cotter` (Offringa, van de Gronde & Roerdink, 2012) to pre-process the data—taking in the individual observatory-generated `gpubox` FITS files and converting them to a more standard and compact `MeasurementSet` format. The `MeasurementSet` format is widely used in radio astronomy software for storing and manipulating interferometer visilibities. For this work, data are originally recorded at a time and frequency resolution of 0.5 s and 10 kHz, though due to processing constraints we average further to 4 s and 40 kHz, which will result in only $< 3\%$ reducted in peak flux density for

[1] I had discussions with both Paul Hancock and Thomas Franzen about how their respective Phase I pipelines worked and which pieces of software were used at each stage, and indeed a lot of MWA data processing for normal continuum imaging work uses similar pieces of software for e.g. calibration and imaging.

[2] `asvo.mwatelescope.org`

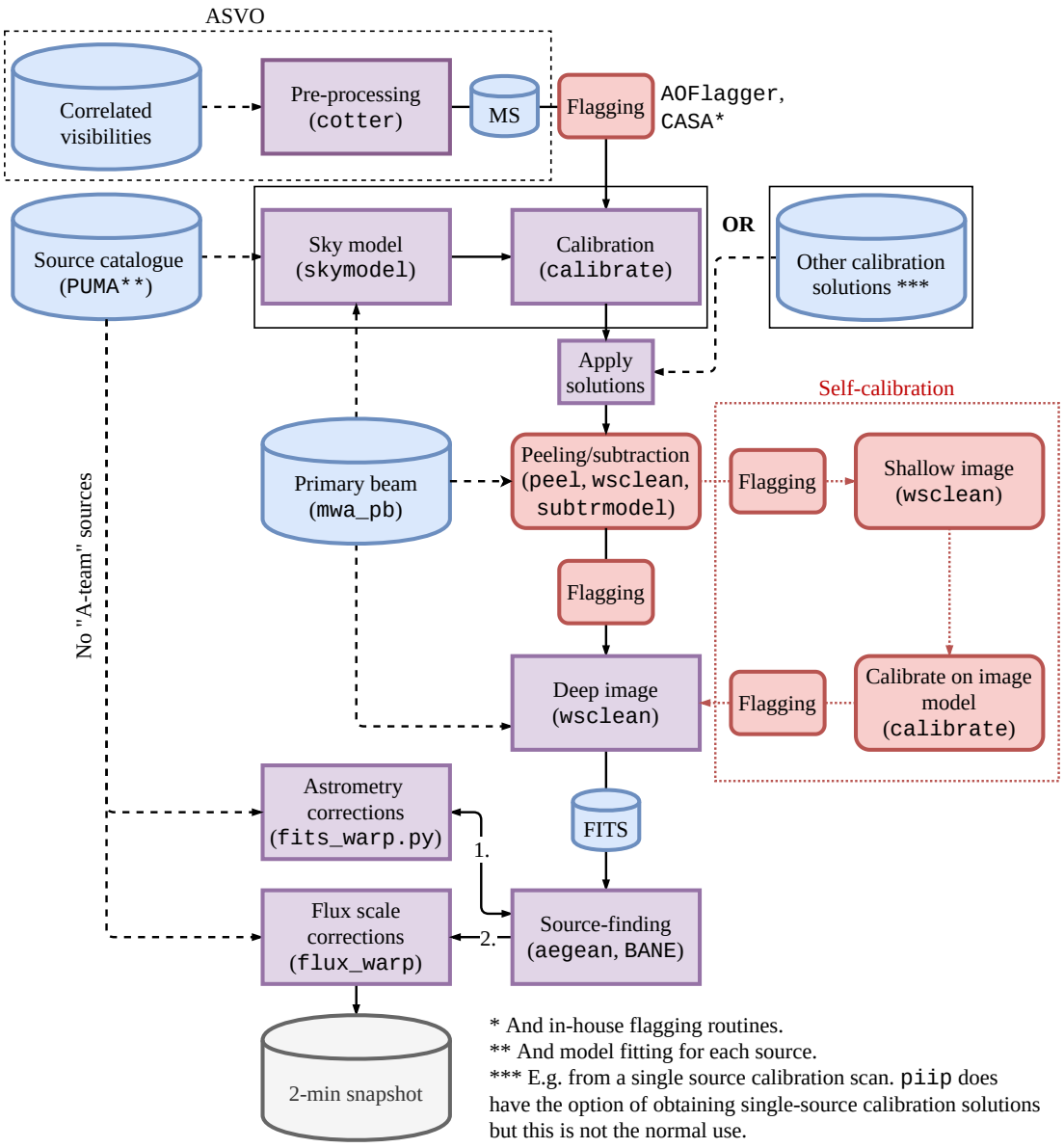

Figure A.1. The Phase II pipeline, `piip`. Nodes are indicated as follows: blue cylinders indicate input files, grey cylinders indicate output files, purple rectangles indicate required processing steps, and rounded red rectangles indicate optional processes.

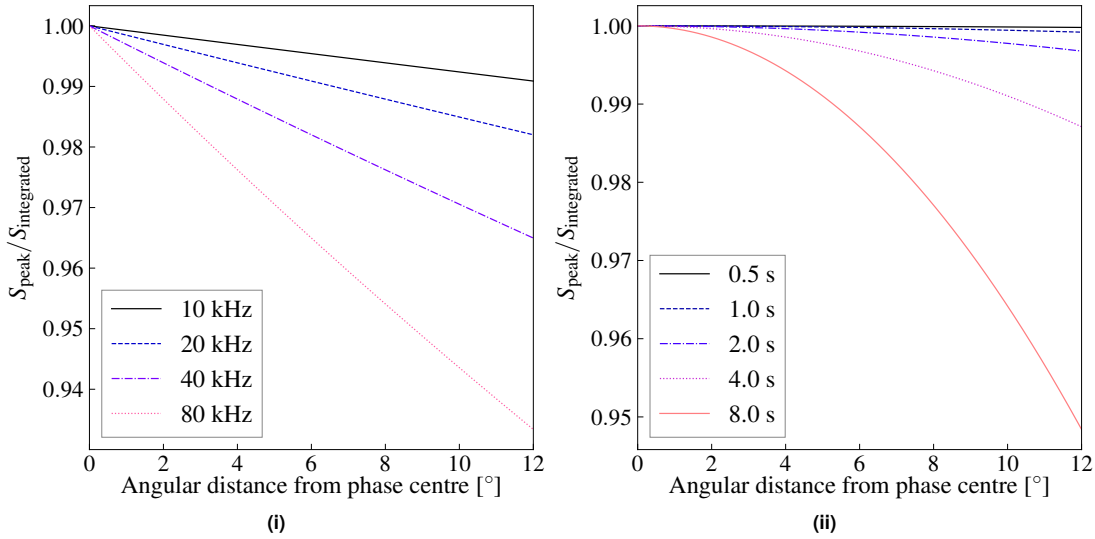

Figure A.2. (i) bandwidth smearing at 216 MHz for a selection of channel averaging values. (ii) temporal smearing for 50″ resolution (typical at 216 MHz) for a selection of time averaging values. The largest effect is that of channel averaging.

sources at the very edges of the FOV (see Fig. A.2 for a comparison for different time and frequency resolutions). Two types of flagging are performed during the `cotter` process: (1) the edges of the MWA coarse channels are flagged as bandpass roll-off results in poor sensitivity in the corresponding fine channels, and (2) general RFI flagging. General RFI flagging is performed by `AOFlagger` (Offringa et al., 2012), which uses the `SumThreshold` method on a per-baseline fashion to remove correlated RFI. Additionally, manually selected MWA tiles that were performing poorly (likely due to individual dipoles being offline or behaving strangely) are flagged at this stage.

A.2. Calibration

Calibration of MWA data can be done in a number of ways, with each method having pros and cons. The specific method of calibration will depend on what data are available and what the apparent brightness of the sky for a given pointing and frequency.

A.2.1. *Single-source calibration*

In the simplest case, calibration can be performed in the traditional way: using an observation of a single bright source with known properties. For this, a short scan of the calibrator source is performed at the beginning (or end, or at most 12 hours after the

science observation) of the observing run. The calibrators typical used are the so-called 'A-team' sources such as Pictor A, Hercules A, or Hydra A. These sources have fairly well-known integrated spectra at MWA frequencies, though their resolved models are less-well known.

This method of calibration uses the bright-source model to get gain correction factors for each MWA tile, calculating static phase offsets. Using a modified version of the `mitchcal` algorithm, the C++ tool `calibrate` (see Offringa et al., 2016) will determine these gain factors via least-squares optimization, predicting the visibilities of the input model (made up of either point sources of Gaussian model components). Primary beam attenuation is also included as part of this process. Once gain corrections are determined for the calibrator observation, these can be applied directly to the science observations provided they are at the same frequency (and time/frequency resolution).

A.2.2. *In-field calibration with a sky model*

Alternatively, due to the large FOV and the propensity for a significant number of bright sources to exist in the primary beam main and side lobes, we create sky models for given observations for calibration—this allows an in-field calibration to be done. To create a sky model, we start with a master cross-matched catalogue, using the Positional Update and Matching Algorithm (`PUMA`; Line et al. 2017) using the GLEAM EGC as a reference. The GLEAM EGC is cross-matched to the NVSS, SUMSS, and TGSS catalogues to provide additional frequency points which helps in constraining the SEDs of the sources (see Fig. A.3 for examples of spectral shapes).

This catalogue is generated by Jack B. L. Line for use in MWA sky model-based calibration, and the final output catalogue includes the Bayesian-determined positions of each source, the various matched flux density measurements and errors, and a classification indicating if the source is `isolated`, `dominant`, or `multiple` (see Section 3.3 of Line et al., 2017, for details on these descriptors). For the purpose of flux scale calibration, we utilise sources classified as `isolated` and `multiple`, where `multiple` means that sources in higher-resolution catalogues are grouped with the flux densities summed to match sources in lower-resolution catalogues.

With the `PUMA`-generated catalogue, power law and generic curved power law

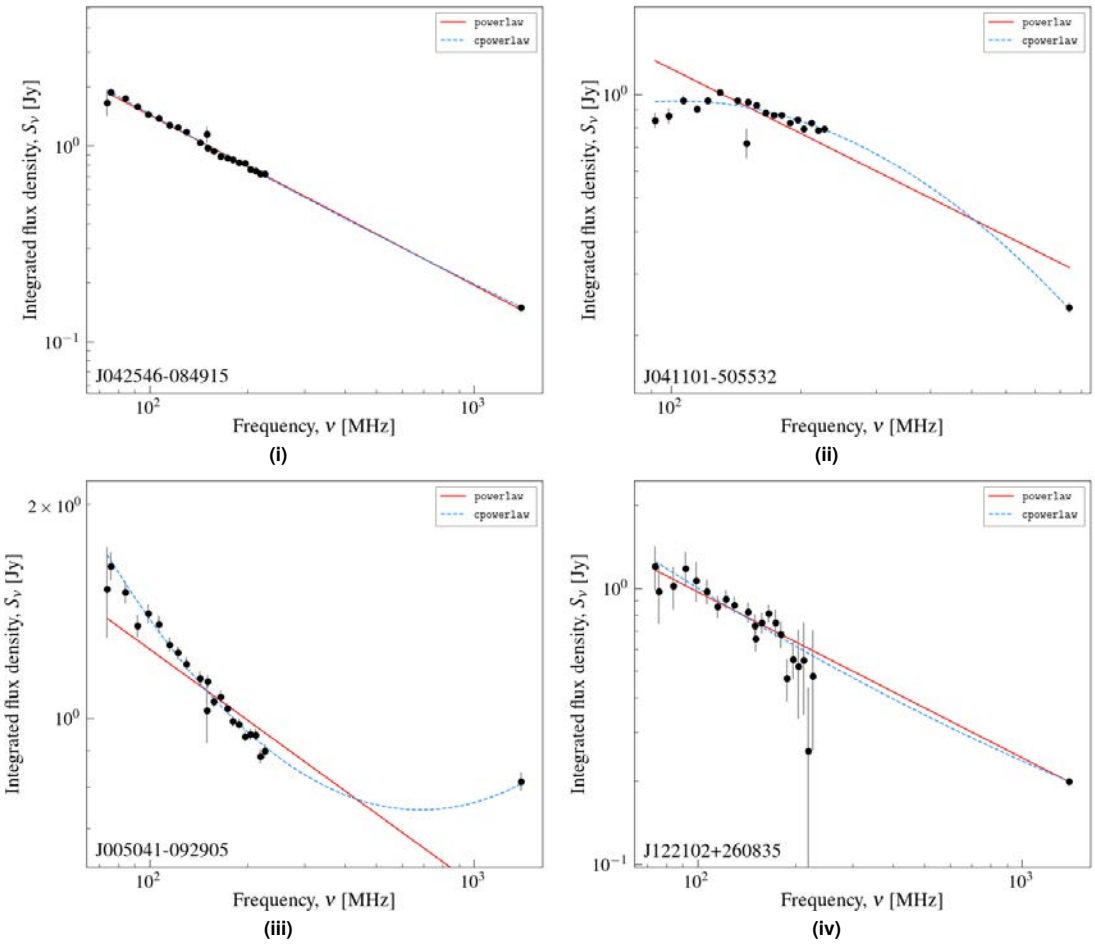

Figure A.3. Examples of sources after model fitting with the power law and curved power law models. (i): A source well-fit by a single power law. (ii): A source showing a turnover in at MWA frequencies, well-characterised by the curved power law model. (iii): A source showing a *turnunder* at MWA frequencies, again well-characterised by the generic curved power law model. (iv): A source with poor measurements at the top of the MWA band. This source is far north ($\delta_{J2000} \sim +26^\circ$) where the GLEAM survey becomes less reliable, which is compounded at the top of the MWA band where the primary beam is narrower and has sharper spectral dependence. The flux density measurement from NVSS at 1.4 GHz allows us to constrain the shape of the spectrum despite the poorer measurements at the top of the MWA band.

models are fit to every source with at least 10 measurements available. This ensures only sources within the GLEAM catalogue are used. The power law model is described by

$$S_\nu = A\nu^\alpha \,, \tag{A.1}$$

where S_ν is the integrated flux density at frequency ν, α is the usual radio spectral

index, and A is the power law normalisation (see also Eq. 1.7). The generic curved power law model is used to account for sources with curvature in the frequency range 72–1400 MHz, and is described by

$$S_\nu = A\nu^\alpha \exp\left[q\,(\ln \nu)^2\right] , \tag{A.2}$$

where S_ν, α, and A are as in the power law case, and q is the curvature term (e.g. Duffy & Blundell, 2012). When $q \to 0$, the power law model is recovered. In generating the model fits, we only consider flux density measurements that satisfy

$$S_\nu > 1\,\mathrm{Jy}\left(\frac{\nu}{72\,\mathrm{MHz}}\right)^{-1.3} , \tag{A.3}$$

to ensure good fits to what will be calibrator sources. $\alpha = -1.3$ is chosen as the higher-frequency data is typically more sensitive proportional to a normal radio galaxy spectral index (e.g. -0.8). This will rule out some inverted spectrum sources, though we would expect these to have less impact at low the MWA frequencies anyway.

A number of Parkes Catalog (PKS) sources are not well-modelled in the GLEAM EGC, with flux densities and morphologies being poorly fit and/or calibrated. Using the literature (i.e. The NASA/IPAC Extragalactic Database [NED]) point-source models are created with flux densities at MWA frequencies extrapolated from a generic curved power law model as in Eq. A.2. Each source is fitted with Eq. A.2 assuming they are compact sources. Other PKS sources would benefit from a similar treatment (e.g. PKS 2356−61) though in some cases the non-compact nature precludes use of literature data in the same way. For these sources, a self-calibration approach with MWA data would be more useful, though this relies on an initial calibrate-able observation that is not always present. Results of the fitted Parkes sources are shown in Fig. A.4.

For other bright, double-lobed galaxies such as Fornax A and Cygnus A a simple two-component Gaussian model is sufficient, and indeed comparison of the two-component model of Fornax A with its 2000-component CLEAN component model used elsewhere does not show appreciable difference at the cost of $\sim$ 1 hr of additional processing time in predicting the model to visibilities. Similarly, a simple two-Gaussian

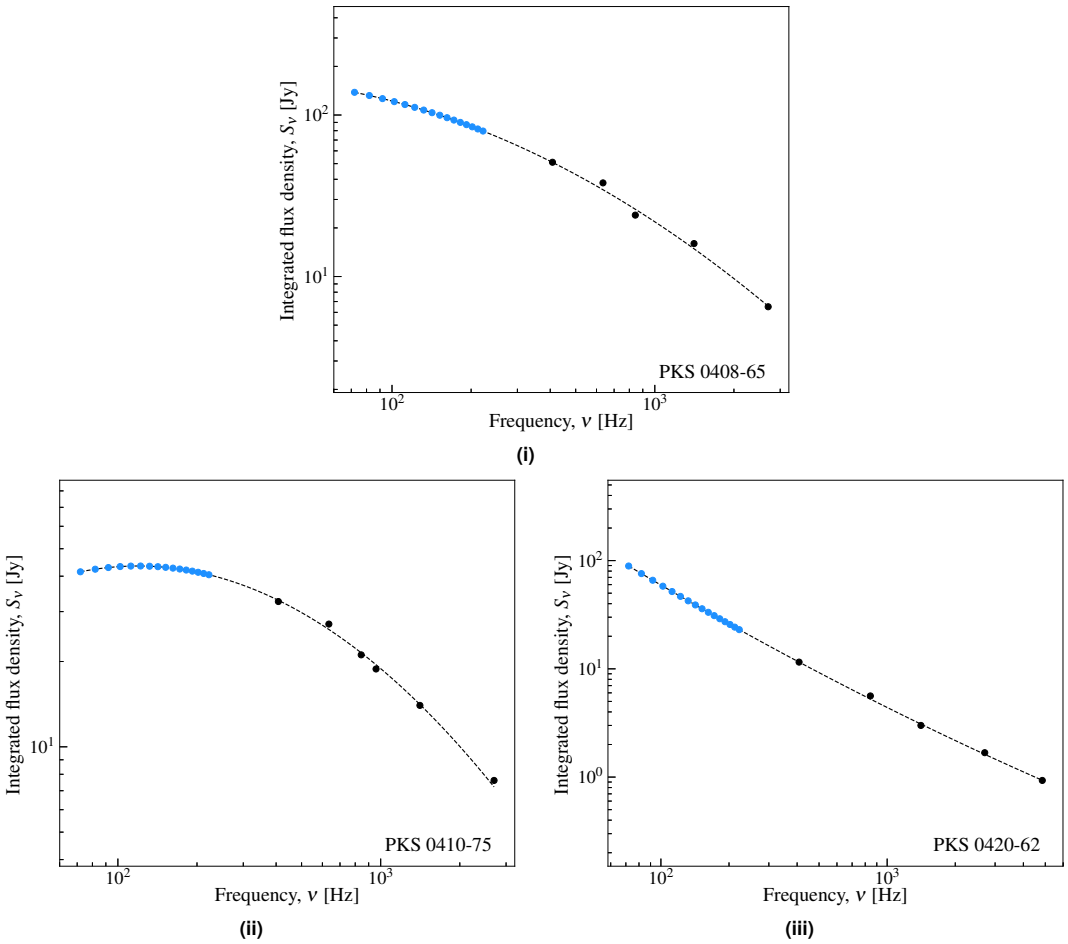

Figure A.4. The SED of the selected PKS sources. Black points are data from the literature, the black, dashed line is the model fit, and the blue points are the extrapolated data at MWA frequencies.

component model of Cygnus A shows the same results as the older many-component model. Enhancements could potentially be made with some of the recent LOFAR observations of Cygnus A (McKean et al., 2016; de Gasperin et al., 2020), however the intrinsic spectral properties of Cygnus A are not the limiting factor, rather its position near the horizon for the MWA limits its general use in calibration.

For each snapshot, we effectively create a cutout from this model-fit merged catalogue. This cutout is created by `skymodel` [3] and utilises the MWA primary beam code `mwa_pb` [4] (Sokolowski et al., 2017) to calculate the apparent brightness of sources within the merged model catalogue. Sources are then selected based on the user-selected radius, maximum number of sources, and apparent brightness threshold. With

[3] https://github.com/Sunmish/skymodel
[4] https://github.com/MWATelescope/mwa_pb

this snapshot-specific model in hand, we add a few bespoke bright, complex source models (if any are above the same apparent brightness threshold) and use `calibrate` as in the single-calibrator case, except that solutions are derived from the science-target snapshot observation itself.

A.2.3. *Direct bright source subtraction*

For zenith-pointed observations, the primary beam response is fairly well-behaved, with the main lobe corresponding to the brightest lobe, and a (mostly) symmetric beam response is seen. In this case, the sidelobes of the primary beam typically have a low-enough response that direct source subtraction is straight forward for sources outside of the imaged FOV. For sources in well-behaved locations within the primary beam (e.g., not near the horizon), we use a direct subtraction method, but do so as a function of frequency to account for the physical spectral properties of the source. To determine which sources require subtracting, we process a model file with known bright, complex sources, determine apparent brightness and distance from imaging centre, then if the source is above the threshold

$$S_{\text{subtract}} > S_0\,\text{Jy}\left(\frac{\nu}{215\,\text{MHz}}\right)^{-0.7}, \tag{A.4}$$

where S_0 is user-defined (and typically this is set as low as $\sim$ 5 Jy [5]) and outside of the imaging region then we order by apparent brightness and subtract. The number of channels to model is a function of the apparent brightness of the source,

$$N_{\text{chans}} = \begin{cases} 32 & \text{if } S_{\text{apparent}} > 500 \quad \text{Jy}, \\ 24 & \text{if } 200 < S_{\text{apparent}} \leq 500 \quad \text{Jy}, \\ 16 & \text{if } 100 < S_{\text{apparent}} \leq 200 \quad \text{Jy}, \\ 12 & \text{if } 50 < S_{\text{apparent}} \leq 100 \quad \text{Jy}, \\ 8 & \text{otherwise.} \end{cases} \tag{A.5}$$

[5]Note that this is variable as the primary beam response becomes a little less certain in the sidelobes and attenuating a model by the primary beam model to see if the apparent brightness is above a threshold is not always consistent.

Subtraction per source proceeds as follows.

(1) Phase rotate to the bright source (`chgcentre`).

(2) Image region around the bright source with N_{chans} channels out with `wsclean`.

(3) Directly subtract predicted CLEAN component model from visibilites with `subtrmodel`.

(4) Set `MODEL_DATA` column in `MeasurementSet` to zero, and repeat from (1).

(5) Phase rotate back to original phase centre.

As we are directly subtracting apparent brightness, we do not need to worry about primary beam effects, and indeed near the edges of sidelobes this is particularly useful so implicitly take care of more extreme primary beam spectral dependence when generating the model across multiple imaged channels. However, this method does not take into account temporal effects.

When the primary beam sidelobe is poorly behaved (e.g. near the horizon), direct subtraction can still produce good results, however, it would be beneficial to have some time dependence to account for a quickly changing primary beam with respect to the source. Fig. A.5 shows the sky above the MWA along with the pseudo-Stokes I response on the sky for a set of off-zenith pointings (with $ZA = 22°$ and $ZA = 29.3°$, from left to right). Note the main lobes, corresponding to the pointing direction, are still the strongest response, but also we have the addition of side lobes towards the horizon with peaks above the 10% level. These side lobes in extreme cases can rise above the sensitivity of the main lobe at which point one must wonder whether these 'side' lobes are in fact the 'main' lobes.

In the example of Fig. A.5, the right panel shows a pointing towards one of the science fields, `FIELD4` (described in Appendix B), which contains a number of exciting clusters such as Abell 3667 (see Hindson et al., 2014, for MWA Phase I data of the cluster), SPT-CL J2023−5535 (HyeongHan et al., 2020, , Zheng et al., in prep.), and generally covers the pilot observations for the Evolutionary Map of the Universe conducted by ASKAP (Norris et al., 2011). This pointing suffers from a reasonably bright side lobe ($\sim$ 50% attenuation). In this example, Cygnus A sits within the brightest sidelobe of the primary beam at the two highest frequency bands (and appears, albeit weaker, in the middle frequency band). Its location right at the edge of the sidelobe is

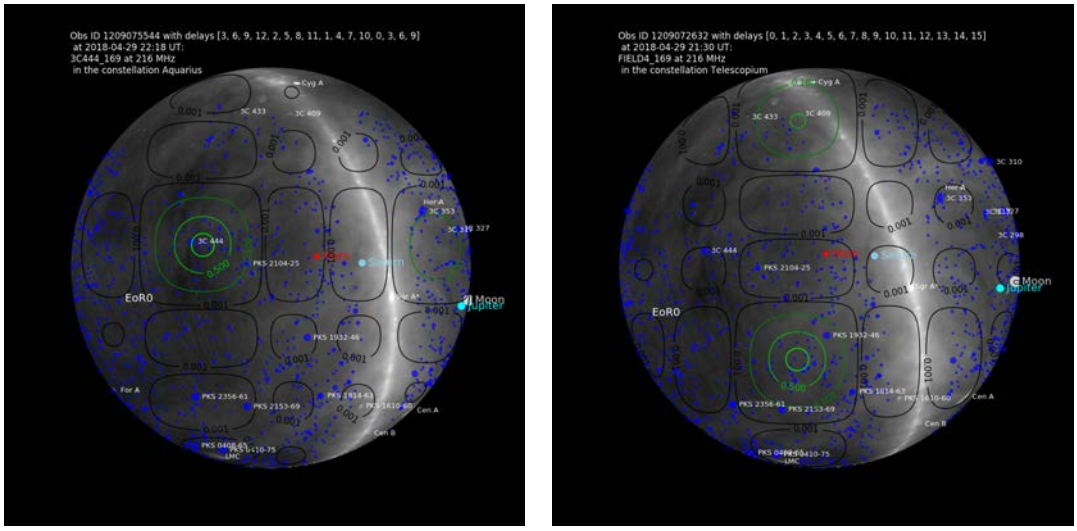

(i) (ii)

Figure A.5. (i) Calibrator pointing towards 3C444. (ii) science pointing towards FIELD4. In both panels the contours are the Stokes *I* primary beam response of the pointing. Note that for the very off-zenith pointing towards FIELD4 the sidelobe of the primary beam contains Cygnus A, Figures retrieved from http://mro.mwa128t.org/observation/obs/?obs_id=1209072632 and http://mro.mwa128t.org/observation/obs/?obs_id=1209075544.

particularly problematic; the spectral behaviour over the 30-MHz bandwidth becomes difficult to deal with because the source's intrinsic spectral properties combine with the spectral dependence of the primary beam attenuation and change as a function of time over the 2-min snapshot. Because of Cygnus A in particular, we perform a check prior to calibration (hence prior to direct source subtraction) to see whether Cygnus A is in a sidelobe with apparent flux density above

$$S_{\mathrm{peel,CygA}} > 50\,\mathrm{Jy}\left(\frac{\nu}{88\,\mathrm{MHz}}\right)^{-1.0}, \tag{A.6}$$

where the spectral index here is chosen as it is roughly the spectral index of Cygnus A at these frequencies. If Cygnus A falls below this threshold, it will be considered for subtraction after calibration, but if it is above this threshold then we use André Offringa's `peel` tool, which phase rotates to the source, calibrates with the supplied model, then subtracts from the visibilities before rotating back and removing the applied calibration solutions. This can be done on short time intervals, and in fact we select

solution intervals based on the apparent brightness of Cygnus A,

$$t_{\text{solution}} = \begin{cases} 4\ s & \text{if } S_{\text{peel,CygA}} > 400 \quad \text{Jy beam}^{-1}\,, \\ 40\ s & \text{if } 100 < S_{\text{peel,CygA}} \leq 400 \quad \text{Jy beam}^{-1}\,, \\ 112\ s & \text{otherwise.} \end{cases} \tag{A.7}$$

We have found that this approach does *not* provide as good results as directly subtracting the CLEAN component model when calibration can be performed, however, it is required when Cygnus A precludes good calibration. In cases where the apparent brightness of Cygnus A is $\gtrsim 400$ Jy beam^{-1} significant residual artefacts are still seen across the image [6].

A.3. Flagging

Many flagging routines are used in this pipeline at various stages, including `AOFlagger` (Offringa et al., 2012) (both during the pre-processing and between calibration and imaging) and the `CASA` task `flagdata` for quack interval flagging (i.e. the beginning and end 4 s). Despite these routines, we found that additional spikes in amplitude were present on some baselines which were on the order of a few times the mean amplitude across all baselines. This can cause some subtle striping in images and is missed in other routines like `AOFlagger`.

To remove this RFI (perhaps caused by the calibration), `ms_flag_by_uvdist.py` [7] was created, which orders a `MeasurementSet` by baseline length (a proxy for u, v distance, though with no frequency dependence) and calculates averaged visibilities for a given baseline. This code employs a sliding window approach to flag baselines with an amplitude greater than 3σ for the user-defined window. Fig. A.6 shows the resultant visibility amplitudes of an example observation, 1201782504, after two runs of the code: both with 3σ clipping. Normally this is only run once. In each round ~ 2 per cent of the data are flagged. Note that given the large number of baselines available to the MWA (≤ 8128) we can employ harsh flagging methods here. Also note that this

[6] The best solution is to simply point the telescope somewhere else on the sky.
[7] https://gitlab.com/Sunmish/piip/-/blob/master/ms_flag_by_uvdist.py

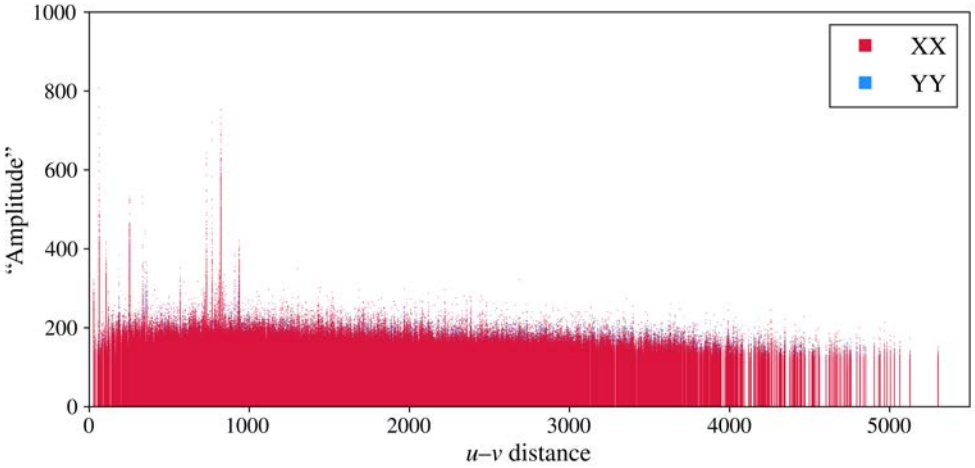

(i) Before flagging.

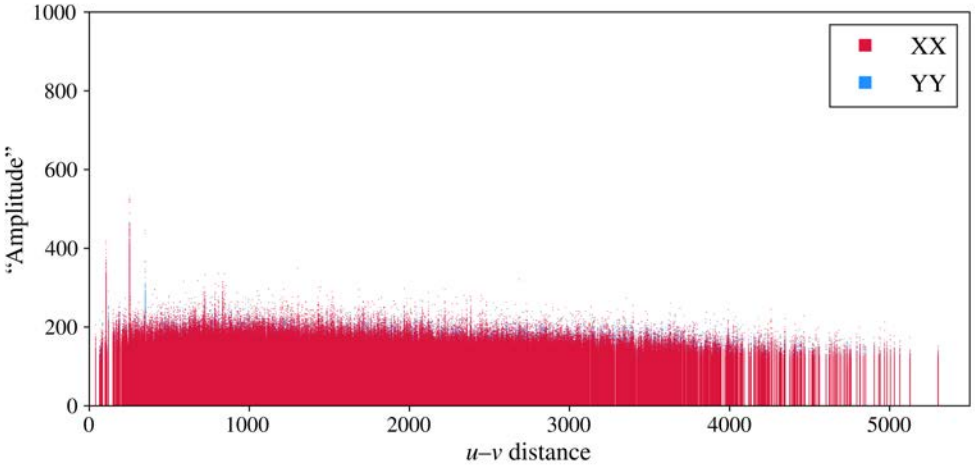

(ii) After flagging at 3σ. 2 per cent of data are flagged at this stage.

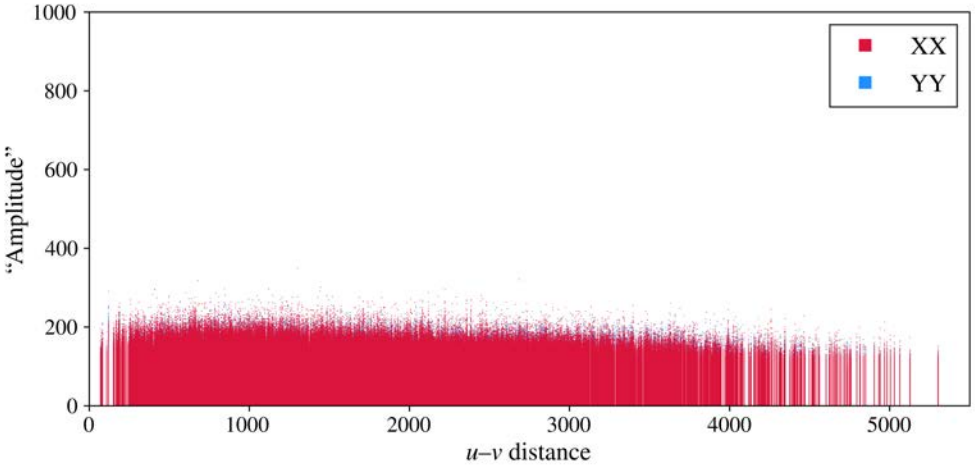

(iii) After flagging again at 3σ. A further 2 per cent of dat are flagged at this stage.

Figure A.6. Example of baseline-dependent u, v flagging employing on observation 1201782504.

task is employed on the calibrated visibilities. This code is *not* intended for use with data from other interferometers with fewer baselines.

The code is employed as part of `piip` and is now running as part of the GLEAM-X processing pipeline. An additional flagging routine was specifically creating to perform simple channel-dependent flagging in the same manner, though has a minimal effect on the data except in some specific bands/observations.

A.4. Imaging

A.4.1. *w-stacking*

Imaging of each snapshot is done using the image gridding and deconvolving software `WSClean` [8] (Offringa et al., 2014; Offringa & Smirnov, 2017). Due to the large FOV and the non–co-planar nature of the MWA, software such as `WSClean` are required to properly reconstruct images from MWA visibilities. The full visibility function is shown in Section 1.6.1 as Eq. 1.16. In the co-planar case, the w-terms are zero, and in the small field-of-view case the w-term is small enough to not introduce significant error, so traditionally many gridders would invert the visibility function assuming $w \approx 0$ requiring only a 2-d Fourier transform (i.e. an application of the inverse of Eq. 1.17).

To circumvent this issue, `WSClean` employs a w-stacking algorithm that grids cells of similar w values on a uniform grid, calculates the inverse Fourier transform for that grid, performs a direction-dependent phase shift, and finally *stacks* the result of each w-layer. Mathematically, each w-layer takes the form:

$$I_{\text{sky}}(l,m)(w_{\text{max}} - w_{\text{min}}) = \int_{w_{\text{min}}}^{w_{\text{max}}} \exp\left[2\pi i w \left(\sqrt{1-l^2-m^2}-1\right)\right] \times \int\int V(u,v,w) \exp\left[2\pi i \left(ul+vm\right)\right] \, \mathrm{d}u\mathrm{d}v\mathrm{d}w \,. \quad \text{A.8}$$

Further details of this algorithm are provided by Offringa et al. (2014). In practice, the choice of the number of w-layers to use depends on computational requirements, (where more layers results in slower gridding and de-gridding) and will be larger as the telescope points towards lower elevation. The default number (based on elevation

[8] https://gitlab.com/aroffringa/wsclean

and number of processing cores available) is often set too low, which introduces subtle positive and negative artefacts in the images. Increasing the number of layers manually will avoid this issue.

In an attempt to reduce the number of required w-layers, André Offringa implemented a method to phase rotate the visibilities to a location of the sky that would require the minimum number of w-layers (usually close to zenith) using the software `chgcentre` [9]. A keyword is added to the `MeasurementSet` metadata to inform `WSClean` that the image should be gridded at the original phase centre so that the sky area of interest is still imaged, but the phase centre for the image is not (necessarily) at the image centre. This process results in a significant speed-up for processing off-zenith data [10], though introduces additional issues when stacking images with varying pointings which will be discussed in Appendix A.6 while describing the mosaicking process.

Newer versions of `WSClean` (> 2.9) include an additional gridding algorithm, `wgridder` (described by Ye et al., 2021; Arras et al., 2021), which avoids the use of single w-layers and instead grids to small w-cells in the same way the u and v coordinates are gridded. The results are consistent with the w-snapshot algorithm and memory usage is typically much lower allowing better performance on local machines for large images. This method is not used for the MWA data in this work as its introduction did not occur early enough in the data processing, however, this has been used for data reduction from other instruments (e.g. ATCA and ASKAP, Chapter 5 and Chapter 6).

A.4.2. *Imaging parameters*

Exact imaging parameters vary slightly between the fields and frequency bands as needed, however, general imaging parameters are provided in Table A.1. The image size is chosen such that we are imaging out to a small fraction of the primary beam attenuation ($\lesssim$ 5 per cent), which ensures most sources with substantial sidelobes are

[9] Packaged as part of `WSClean`, and since version 2.11 the `-shiftback` parameter of `chgcentre` is implemented directly into `WSClean`.

[10] In that without it processing would not have been possible on the Pawsey Supercomputer Centre systems with 24-hr job time limits.

Table A.1 Basic imaging parameters for MWA-2 imaging.

Image size	8 000–10 000 px
Pixel size	$0.45/C$ degrees [a]
'Briggs' robustness	0.0, +1.0, +0.5, +2.0
Max. angular scale	1–2 degrees
Minor `CLEAN` iterations	250 000–500 000
`CLEAN` threshold	$3\sigma_{\rm rms}$
Major iteration gain	0.6/0.8 [b]
Minor iteration gain	0.1
Multi-scale	On

[a] The central channel of the observation, where $C = \nu_{C,\rm MHz}/1.28$, from 23.5–9.6 arcsec.
[b] robust $\geq +1.0$ / robust $< +1.0$.

deconvolved. Nominally, this would require images of $\sim$ 9000 pixels, though in some cases we are required to make the image slightly smaller (to avoid primary beam horizon effects) or slightly larger (e.g to include complex bright sources like the Galactic Plane which is not subtracted as described in Appendix A.2.3).

A range of image weightings are created using 'Briggs' weighting (Briggs, 1995), ranging from robust 0.0 to +2.0. Examples for the used weightings are shown in Fig. A.8 for a miscellaneous radio galaxy with a compact core and some extended diffuse emission comprising the lobes. Additionally, the PSFs for the example images are shown in Fig. A.9. We find that sensitivity to point sources is optimal around 0.0 but we begin to become insensitive to extended, diffuse emission at that image weighting. Fig. A.7 shows an example test of image weighting on flux recovery of simulated 1 Jy Gaussian sources with varying FWHM. The MWA in its Phase I compact configuration had a sufficiently large number of short baselines that most imaging weightings recovered extended source flux relatively well. The MWA-2 'extended' configuration, however, has lost some sensitivity with its fewer short spacings—this is clearly observed in Fig. A.7 where approaching uniform weighting loses significant flux density. Conversely, the MWA Phase I was traditionally imaged at uniform or robust -1.0, recovering significant flux density (e.g. Hurley-Walker et al., 2017; Offringa et al., 2016, and see Chapter 2). While we see from Fig. A.7 that robust +2.0 recovers flux density best, the resolution is only $\sim$ 1.5 times better than the MWA Phase I images, thus, images at robust 0.0 and robust +0.5 are still made to provide higher-resolution

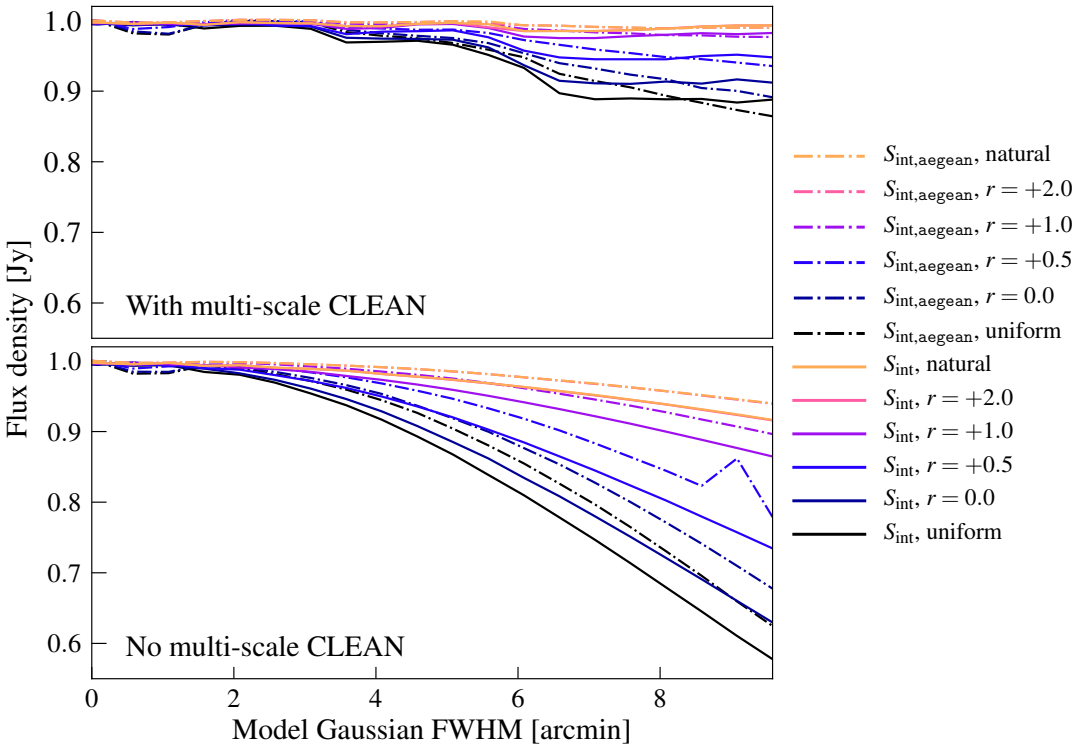

Figure A.7. A test of flux recovery for varying image weightings, measuring sources by fitting Gaussian models to them (i.e. with the `aegean` source-finder; Hancock et al., 2012, 2018) and by direct integration of the pixel brightness. The top panel includes multi-scale CLEANing while the bottom panel does not. Measurements are made assuming a 10σ source (i.e., the Gaussian peak is detected at 10σ). Note the steps in the multi-scale $S_{\rm int}$ measurements are likely due to the discrete choice of multi-scale scales.

information, especially in regards to determining if extended structures are blended point sources or otherwise confused with nearby sources. Additionally, Fig. A.7 highlights the effect of multi-scale CLEAN on extended Gaussian sources.

A.5. Post-processing

After imaging of individual snapshots, there are a two major post-processing steps required to create more uniformity to the snapshots prior to co-addition/stacking: (1) astrometry corrections and (2) flux scale corrections.

A.5.1. *Making astrometry corrections*

Astrometry corrections are generally necessary with MWA data due to the significant effect of the ionosphere—ionospheric effects typically scale with λ^2, hence low-frequency

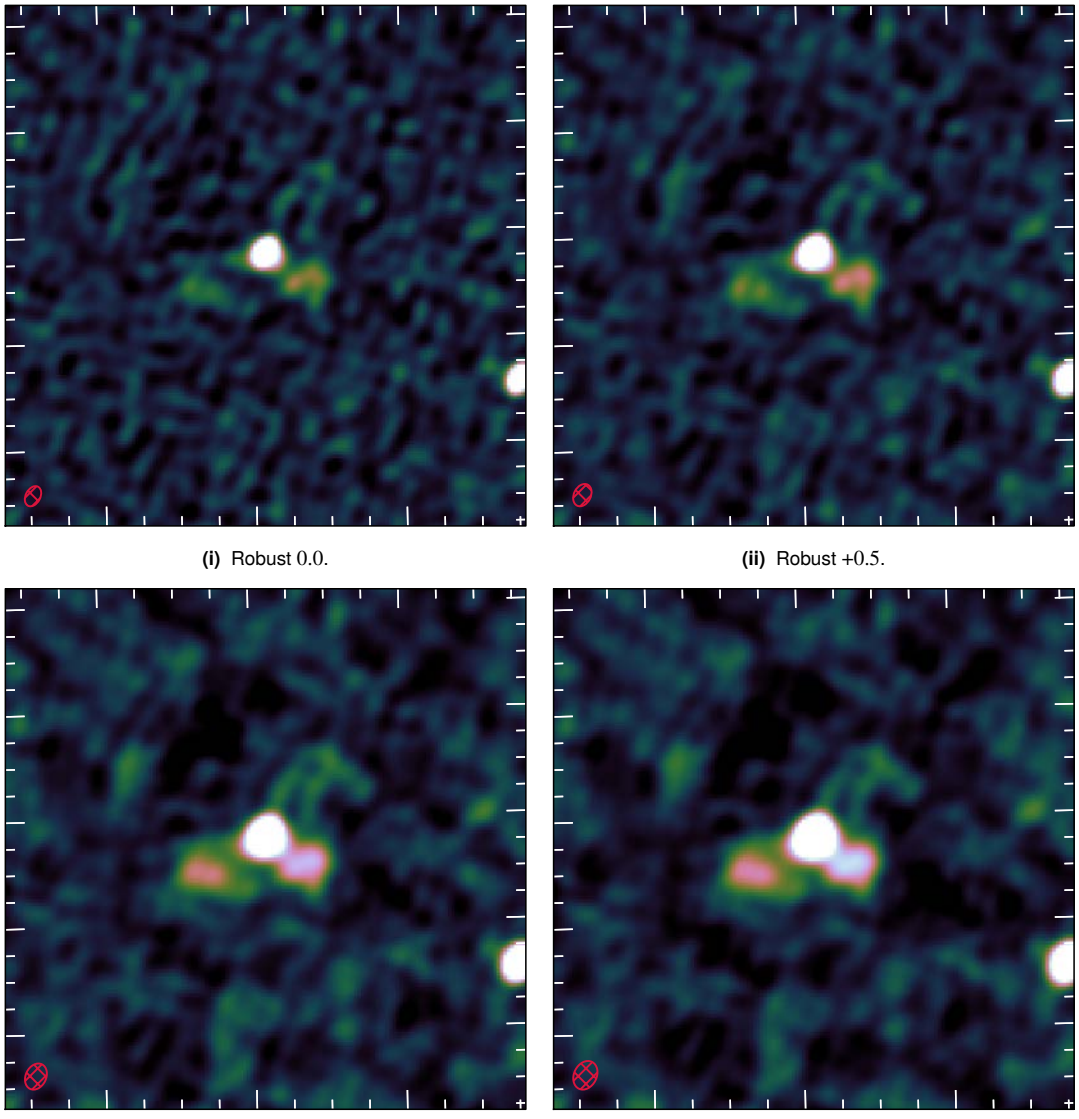

(i) Robust 0.0.

(ii) Robust $+0.5$.

(iii) Robust $+1.0$.

(iv) Robust $+2.0$.

Figure A.8. Example 216-MHz 2-min snapshot centered on a miscellaneous radio galaxy with diffuse lobes comparing the various image weightings used. Note the image is not primary beam corrected. This example illustrates how diffuse, low-surface brightness emission is affected by the image weighting, however, the individual snapshots are limited in how much flux density is recovered simply by virtue of lower integration time. The colour-scale is linear from -10 mJy beam^{-1} to 70 mJy beam^{-1}, and the red, hatched ellipses in the lower left corners are the fitted Gaussian PSF (i.e. the restoring beam).

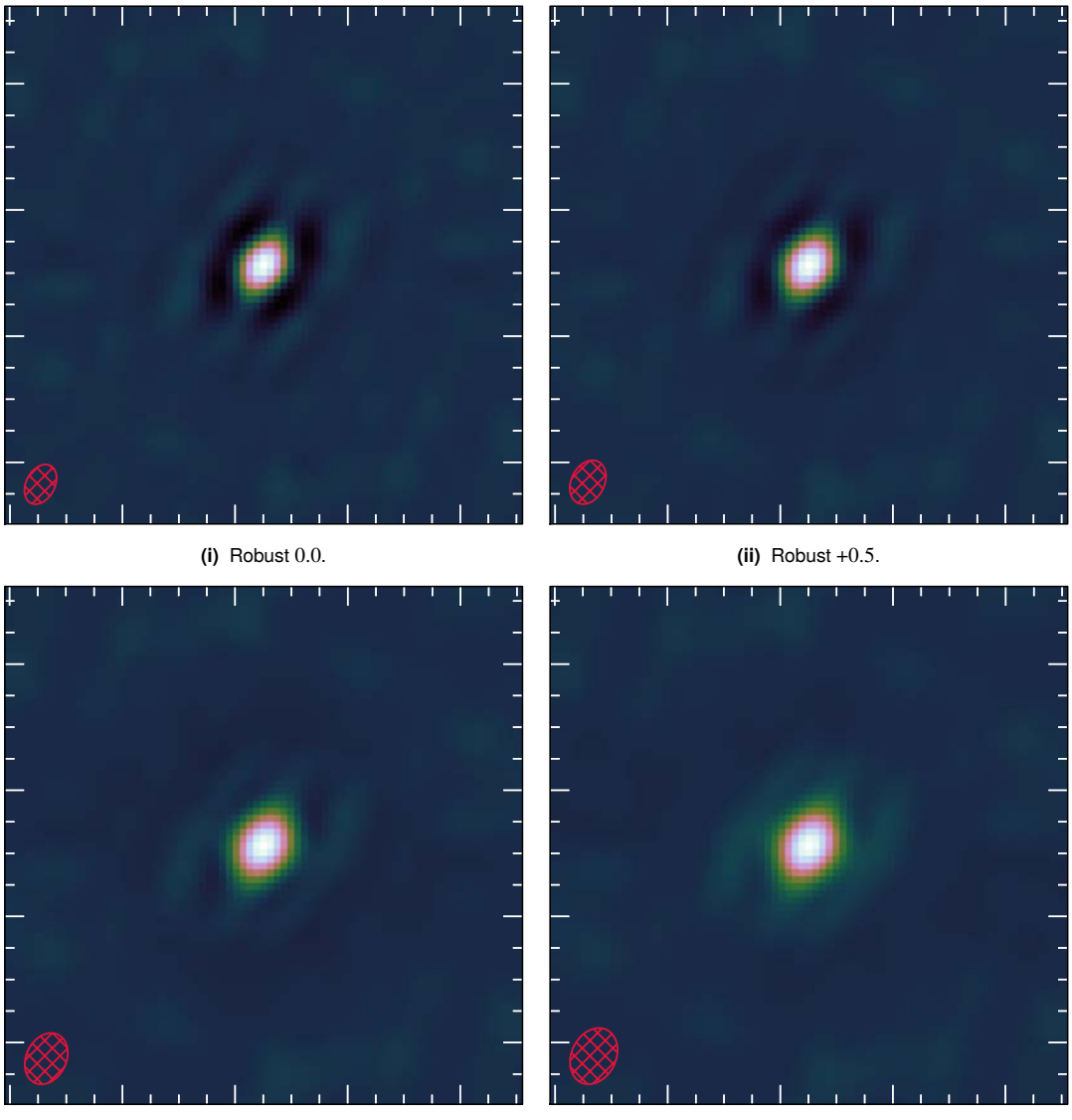

(i) Robust 0.0.

(ii) Robust $+0.5$.

(iii) Robust $+1.0$.

(iv) Robust $+2.0$.

Figure A.9. PSFs for the example 216-MHz 2-min snapshot shown in Fig. A.8. The colour scale is linear and runs from -0.2 to 1. Note the negative sidelobes around the robust 0.0 and $+0.5$ PSFs and the positive sidelobes around the robust $+1.0$ and $+2.0$ PSFs. The red ellipses are as in Fig. A.8.

inteferometers like the MWA suffer significantly. Historically, up to 50 per cent of data at 88 MHz is lost to ionospheric issues (e.g. significant blurring or change in angular position of sources, and in extreme cases complete de-correlation; see e.g. Intema et al., 2009; Loi et al., 2015, and references therin). In many cases, however, the effect of the ionosphere is small and results in only small shifts in source position ($\sim$ a few pixels usually, but up to a beam width can be observed). These shifts can be uniform over the imaged FOV or they may be position-dependent following e.g. 10–100 km travelling ionospheric disturbances (Loi et al., 2016). These angular shifts are corrected using `fits_warp.py` (Hurley-Walker & Hancock, 2018). This cross-matches an image catalogue with a model position catalogue to calculate positional offsets, interpolating between measured sources and creating an x,y offset screen which is used to shift pixels in an image. This generally works well to align images prior to co-addition to avoid significant blurring of sources. Note that source blurring typically only affects peak flux density, and integrated flux density remains largely unchanged.

A.5.2. *Making brightness/flux scale corrections*

As described in Appendix A.2, a number different calibration methods have been employed for the various fields observed as part of the G0045 project (and associated miscellaneous observations). The choice of initial calibration method (and in particular sky model) will set the overall flux scale for the final images. Additionally, use of amplitude self-calibration and CLEANing during the process may affect the final flux scale, with CLEAN-bias resulting in *less* flux in the final images (e.g. as described by Becker et al., 1995; White et al., 1997; Condon et al., 1998, though note this is not a brightness scaling effect, rather it will be an offset of a few mJy and is more prominent for poorly behaved PSFs) and amplitude self-calibration typically also resulting in *less* flux as well (as the model will usually have less flux than the data). An additional source of error on the final flux density scale after imaging is residual, un(over)-corrected leakage from the primary beam response. This introduces a nearly elevation-dependent flux scale gradient across the image, most noticeable for low-elevation (therefore low- and high-declination) pointings. Finally, additional primary errors may result in cases where a significant enough number of dipoles are faulty and unavailable to a tile during

an observation (Line et al., 2018).

To try to correct for the primary beam-related issues (and to re-enforce overall amplitude calibration), I have written the `python flux_warp` [11] package [12].

`flux_warp` has three main stages,

(1) cross-match image catalogue to model catalogue,

(2) determine ratio of measured to predicted flux densities ($S_{\text{measured}}/S_{\text{predicted}}$),

(3) create map of "correction factors" based on $S_{\text{measured}}/S_{\text{predicted}}$.

The first stage requires simple (but reasonably harsh) cross-matching. Using the model catalogue described in Appendix A.2.2, we perform a simple cross-match to the image catalogue output by `aegean`. This step has a number of options to restrict the cross-matching: based on source compactness, flux density threshold, within a certain radius of some input coordinates, and based on a maximum number of sources allowed, where a dynamic flux density threshold ensures no more than N_{src} can be returned in the cross-matched catalogue. By default, `flux_warp` comes packaged with a simpler model catalogue, with model power law and curved power law parameters determined as in Appendix A.2.2 but for only the GLEAM EGC as published (Hurley-Walker et al., 2017). This simpler catalogue gives very similar results, as the 20 narrow band GLEAM measurements tend to dominate any model fitting if adding measurements from, e.g., NVSS or SUMSS, though as discussed in Appendix A.2.2 some sources may be better represented with the additional high-frequency data point.

The second stage is a simple evaluation of model parameters that are present in the cross-matched catalogue (i.e., model parameters from the original model catalogue). The flux densities of sources are predicted via a number of methods, in the following priority order:

(1) Eq. A.2, optionally with a reference measurement,

(2) Eq. A.1, optionally with a reference measurement,

(3) Eq. A.1 with an assumed α.

By default, the curved power law model is preferred, followed by a power law model, and then a simple extrapolation from a reference frequency/measurement and assumed

[11] The name was chosen to match with `fits_warp.py`, though a more appropriate name may be "brightness rescale".

[12] https://gitlab.com/Sunmish/flux_warp

spectral index. The choice of which method to use is dependent on supplied parameters, whether columns exist in the supplied catalogue, and whether a particular model parameter is available for a particular source. The model file supplied with the software based on the GLEAM EGC contains the following columns: S_0 = `S154`, with ν_0 = 154 MHz; A = `alpha_c`; α = `beta_c`; q = `gamma_c` [13]. A source in the catalogue must satisfy at least one of the aforementioned prediction options for it to be used as a calibrator source.

At the third stage, we have a list of calibrator sources with associated $S_{\text{measured}}/S_{\text{predicted}}$ ratios. From here, various methods can be employed to recover a "true" brightness scale of the image—which method to use depends on the image in question and how it was generated. For MWA data, a simple average of these ratios is generally only valid for observations that are at or near zenith. For pointings off-zenith (low elevation), a gradient or structure is typically observed in the brightness scale after primary beam correction which requires some form of interpolation or position-dependent fitting between the calibrator sources to recover the "true" flux density of sources in the image (though note some other peculiar effects that might present as positional flux scale errors, as discussed in Appendix A.6.1 and Appendix A.7).

[13]The naming convention is for legacy reasons.

Table A.2 Brightness scaling methods.

Method	Pros	Cons	Used? [a]
(SNR-weighted) mean	Fast, ignores spatial errors in model	Cannot recover spatially varying errors	✓
Median	As with mean, but not affected by outliers	As with mean	✓
Polynomial (Decl.)	Fast	Errors not dependent on Decl.	×
Polynomial (Elev.)	Fast, recovers beam-related errors	Does not work for all snapshots	×
Nearest neighbour	Fast, recovers calibrator fluxes perfectly	Hard edges/facets/sensitive to edge cases	×
2-d linear interpolation	Recovers calibrator fluxes perfectly	Edges with gradients across them	×
2-d RBF linear	Can be smoothed, recovers most source flux	Slowest, sensitive to edge cases	✓

[a] Used in this work. Other methods may be appropriate for other observations.

We employ a number of methods to generate a correction-factor map to apply to the image. (1) We calculate the median correction-factor of the calibrator sources and apply this constant value to the entire map. This method is useful if there are outlier measurements and if there is no large-scale structure to the flux scale ratios. (2) We calculate a mean correction-factor (optionally) weighted by the signal-to-noise ratio (SNR) of the calibrator sources measured in the image. With σ-clipping, this is generally more effective than calculating the median though again relies on a lack of large-scale structure to the correction-factors. Both the median and weighted mean methods are valid particularly for zenith observations. In the case of off-zenith observations where uncorrected leakage plagues the final images, we can either (3) fit a 1-d n-degree polynomial screen of the form

$$f(x) = \sum_{k=0}^{n} c_k x^k \,, \tag{A.9}$$

for coordinate $x \in \{\delta_{\mathrm{J2000}}, ZA\}$. Fitting as a function of ZA is typically more useful than δ_{J2000}, though for certain observation set-ups δ_{J2000} may be more appropriate, as was the case for the GLEAM survey (Hurley-Walker et al., 2017). (4) A 2-d n-degree polynomial screen may be fit, of the form

$$f(x, y) = \sum_{i=0}^{n} \sum_{j=0}^{n} c_{i,j} x^i y^j \,, \tag{A.10}$$

where x and y are pixel coordinates. This 2-d screen is useful in cases where the off-zenith pointings introduce offsets that vary similarly to the primary beam response. Additionally, α_{J2000} and δ_{J2000} coordinates can be fit directly. Finally, (5) we can take our calibrator sources and interpolate correction-factors between them. An interpolation method was employed by Hindson et al. (2014) for early MWA observations, though only a handful of calibrators were used. A number of different direct interpolation methods can, in principle, be utilised, and Table A.2 briefly summarises the tested cases, where a test is incorporated for a MWA Phase I image as part of the software. Example output from a selection of methods for this Phase I dataset are shown in

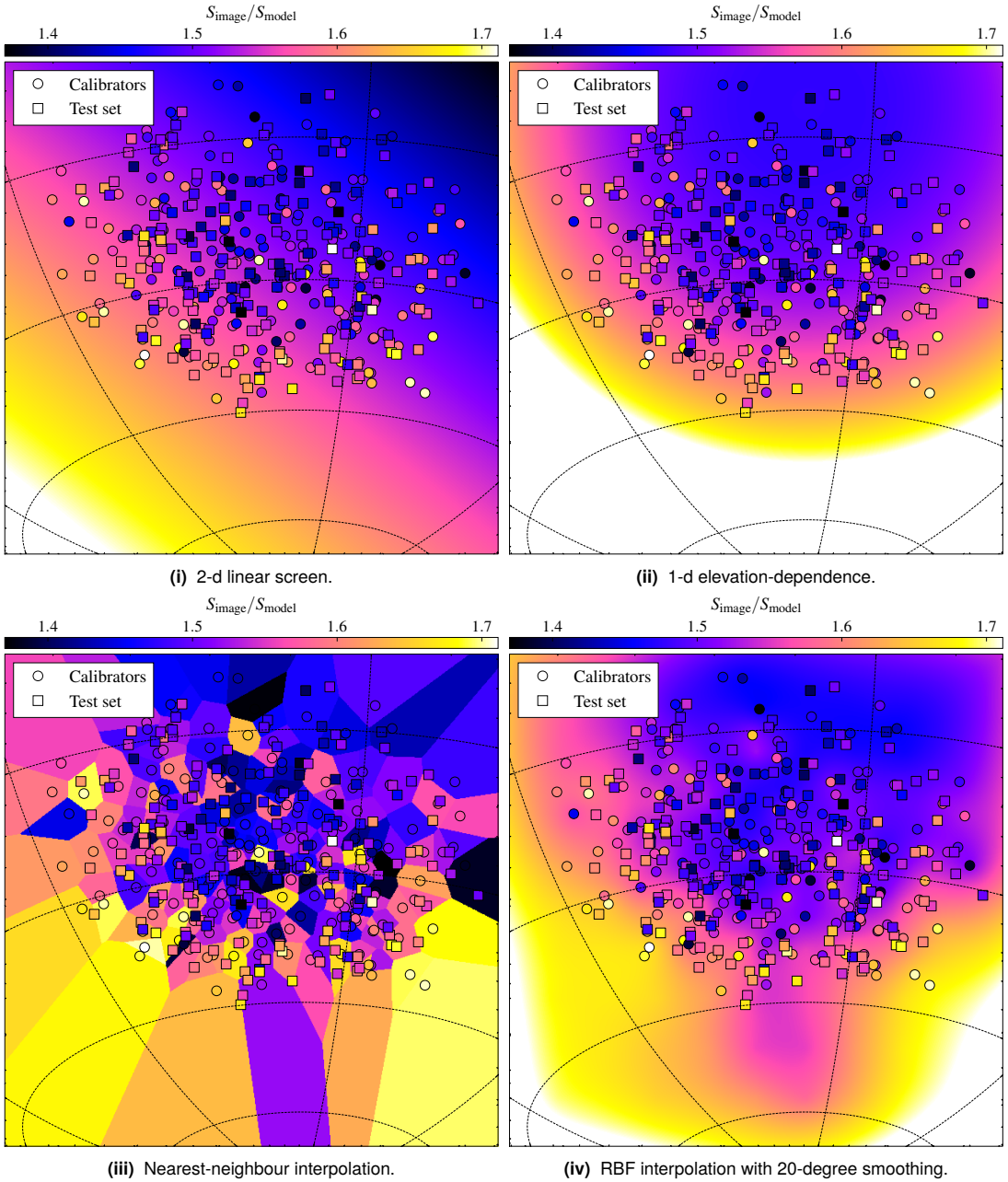

(i) 2-d linear screen.

(ii) 1-d elevation-dependence.

(iii) Nearest-neighbour interpolation.

(iv) RBF interpolation with 20-degree smoothing.

Figure A.10. Example `flux_warp` methods applied to an MWA Phase I snapshot at 88 MHz. The Phase I data are chosen due to the smaller image size in pixels. Note due to the primary beam response, the maximum sensitivity is not actually at the pointing centre. During the course of the pipeline the data are re-centered to the location of maximum primary beam sensitivity, though for this example this was not done.

Fig. A.10.

In practice, for this work a 2-d linear radial basis function (RBF) interpolation

method is used. The `scipy` implementation, `scipy.interpolate.Rbf` [14] is used. The linear RBF is similar to direct linear interpolation in the case of no additional smoothing, however, a smoothing scale of $\gtrsim 5$ degrees tends to provide a smooth model that begins to trace the primary beam response. This may be changed to reflect any position-dependence seen in the output images. This, in some cases, becomes close to 2-d/1-d polynomial models but is more consistent across frequencies and pointings. An example output from `flux_warp` is shown in Fig. A.11 and Fig. A.12 for MWA-2 88-MHz, off-zenith snapshot, displaying an almost elevation-dependent trend in the brightness scaling that is well-recovered by a smoothed RBF.

As part of this evaluation of image brightness, `flux_warp` has a built-in option to select a subset of the calibrator sources to reserve for testing the flux-scale correction model. This is chosen as a fraction of the selected calibrator sources (typically this would be 25 per cent, unless a particularly large number of sources are present in which case 50 per cent might be more appropriate). These test sources can either be selected from the faint end of the selected calibrators (i.e. the faintest 25 per cent) or selected in intervals to sample the full range of brightnesses (i.e. taking a test source every N calibrator sources, ordered by flux density).

Finally, `flux_warp` is used to compute simple statistics for the brightness calibration, including mean, median, and standard deviation which are used as an assessment of flux scale uncertainty (with respect to the input model catalogue). Additionally, the software may be used for an internal match between integrated flux densities and peak fluxes measured from the image—this provides a quick test to inspect whether the point-spread function (PSF) is appropriately defined for the image. This is discussed more in later sections.

A.6. Stacking the 2-min snapshots and making mosaics

Once all snapshots are astrometrically corrected and brightness scaled they are stacked to create mosaics. The pipeline for making mosaics is summarised in Fig. A.13, incor-

[14] https://docs.scipy.org/doc/scipy/reference/generated/scipy.interpolate.Rbf.html

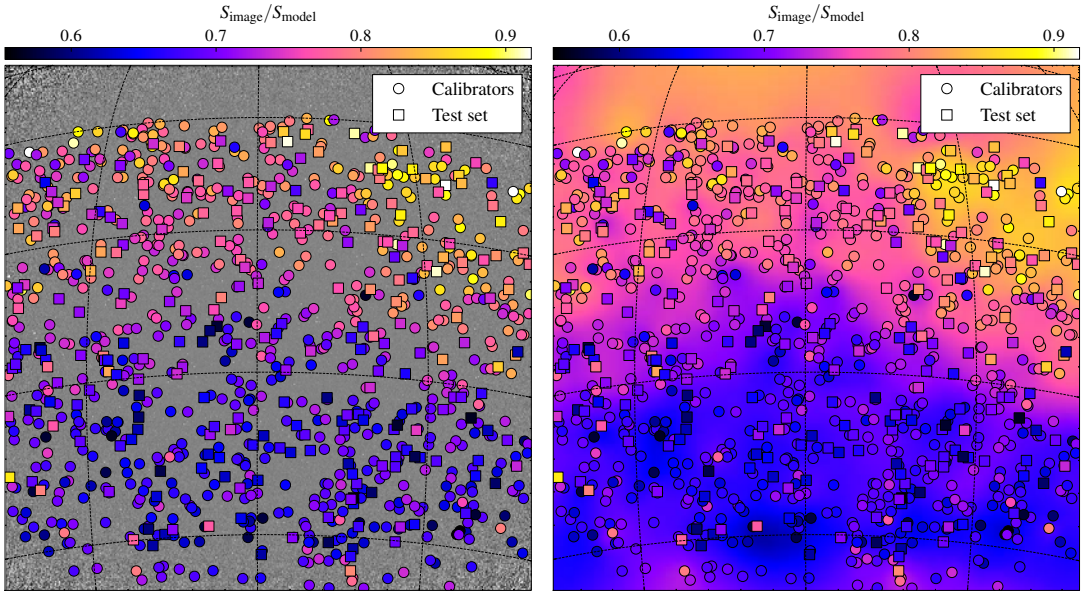

(i) Stokes *I* image. **(ii)** Correction factor map derived from $S_{\mathrm{image}}/S_{\mathrm{model}}$.

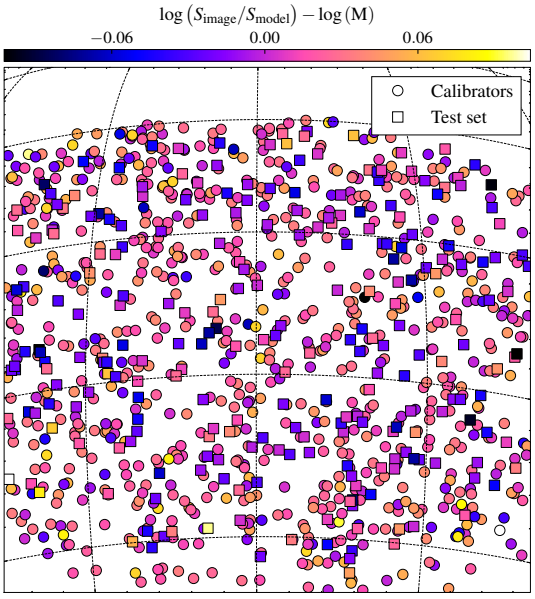

(iii) Residuals.

Figure A.11. Output run of `flux_warp` using the linear RBF method. (i) The image to be corrected with calibrator and (optionally) test sources plotted with their measured $S_{\mathrm{image}}/S_{\mathrm{model}}$ ratios. (ii) The derived correction factor map that is applied to the original image (i.e. image divided by correction factor map) with the same markers as in (i). The colourscale in this image is the same for the markers and background map. (iii) The residuals for the calibrator and (optionally) test sources from the derived correction factor map.

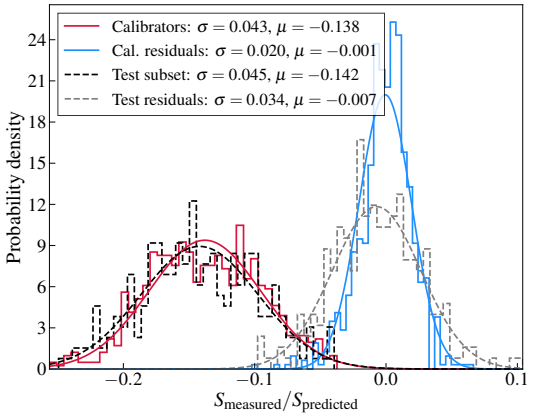

(i) Histogram of natural logarithm of the ratios and residuals.

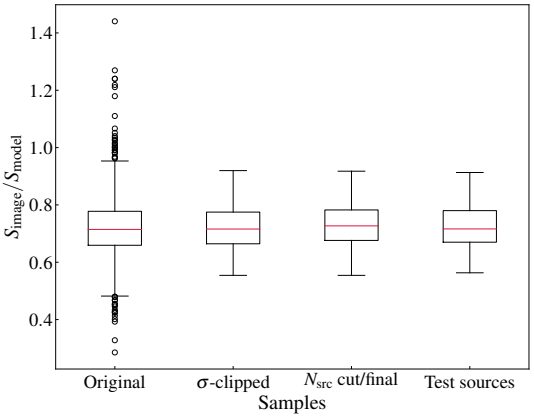

(ii) The sample clipping/selection process.

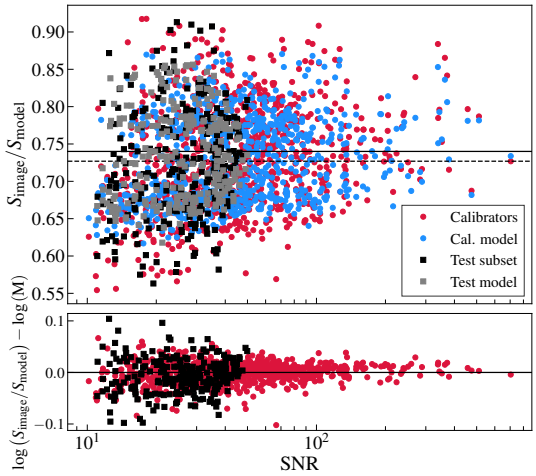

(iii) Ratios and residuals as per (i), but as a function of SNR for each source.

Figure A.12. Further output from a run of `flux_warp` using the linear RBF method. (i) The histogram of the natural logarithm of the derived $S_{\mathrm{image}}/S_{\mathrm{model}}$ ratios, along with the (optional) test sources and corresponding residuals. (ii) The sample clipping process showing removal of outlier sources. These outliers may be poorly fit sources, poorly modelled sources, or poorly cross-matched sources, or more unlikely transients so are unlikely to be the effect of some local flux-scaling issue. (iii) The ratios and residuals as a function of SNR with the (optional) test subset included, which in this case is selected from the faint end.

porated into the code `stackshots2.py` [15]. Making the mosaics (or *stacking*) makes heavy use of the `miriad` software suite (Sault et al., 1995). Prior to regridding, we convolve each snapshot to the lowest resolution of the snapshot list, which is typically a $\sim$ 5 per cent difference in major axis at most. This difference in synthesized beam between snapshots is due to the slight difference in pointing as well as the effect of different flagged tiles between observations introducing variation to the sampling

[15] https://gitlab.com/Sunmish/piip/-/blob/master/stackshots2.py; note the name is used for legacy reasons.

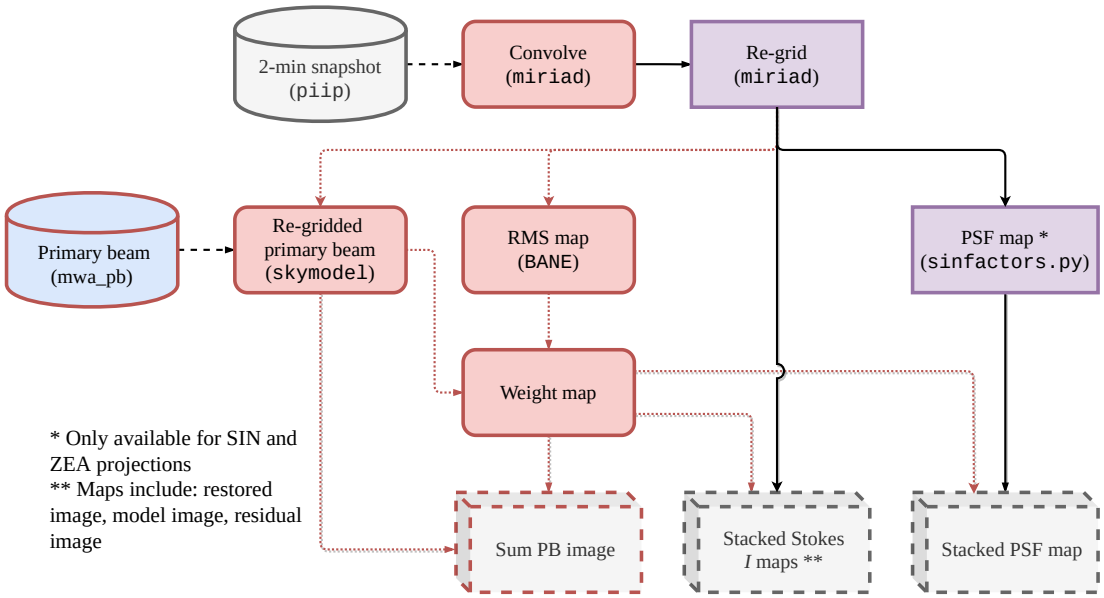

Figure A.13. The process of stacking the 2-min snapshot images. Note cylinders indicate input files, rectangles indicate processing steps, and boxes indicate output images. Grey colouring indicates files created as part of this work, purple indicates a required processing step, red an optional processing step, and blue input files not created as part of this work.

function/point-spread function from which the synthesized beam is found. We determine a common grid by using the minimum pixel size across all images (which in our processing case is the same for all images), and choose an output image size with central/reference coordinates. With this, each snapshot is regridded to the grid defined by these parameters using the `miriad` task `regrid`.

A.6.1. *Preserving total flux after regridding*

In its current implementation, `regrid` [16] does not preserve total flux when changing the image reference point, but does preserve the surface brightness (hence, peak flux). During imaging with `WSClean`, we have used the phase rotation method mentioned in Appendix A.4 with `chgcentre` and `WSClean` that, in essence, results in the image reference point (`CRPIXn` and `CRVALn`), for many of our observed fields occurring tens of degrees away from the actual centre of the image array. As we are only regridding between SIN (slant orthographic) projections (and perhaps ZEA), we can account for this change in total flux by considering the change in solid angle, $d\Omega$, as a function

[16] As well as other software such as `SWarp`: https://www.astromatic.net/software/swarp.

of l and m across the original and regridded image. The transformation from RA and declination (α and δ) to l and m direction cosines is (e.g. Thompson et al., 2017)

$$l = \cos\delta \sin(\alpha - \alpha_0) \text{ , and} \tag{A.11}$$

$$m = \sin\delta \cos\delta_0 - \cos\delta \sin\delta_0 \cos(\alpha - \alpha_0) \text{ ,} \tag{A.12}$$

where α_0 and δ_0 are the reference coordinates of the SIN-projected image. The solid angle across the projection then changes as (e.g. Thompson et al., 2017)

$$\mathrm{d}\Omega = \frac{\mathrm{d}l\mathrm{d}m}{n} \text{ ,} \tag{A.13}$$

where $n = \sqrt{1 - l^2 - m^2}$. With n defined by the original image reference coordinates and n' defined by the regridded image reference coordinates, the factor

$$f_{\mathrm{regrid}} = n/n' \text{ ,} \tag{A.14}$$

is used when measuring total or integrated flux density in the regridded image.

Some software such as `aegean` and our in-house `python` code, `fluxtools.py` [17] are built to accept a position-dependent point-spread function (PSF) that is used when measuring integrated flux densities. This position-dependent PSF can have the major axis multiplied by f_{regrid} to create an 'effective `BMAJ`' so that the factor can be incorporated into the integrated flux density measurements without impacting measurements of peak flux or noise. Note that this non-preserving of total flux has a relatively small (< 5 per cent) effect if the image has not been rotated by more than a few degrees. Because of the use of `chgcentre` to phase rotate the `MeasurementSet` prior to imaging (as discussed in Appendix A.4), regridding the image prior to stacking can be tens of degrees of more of rotation resulting in extreme variations to the effective PSF.

[17] https://gist.github.com/Sunmish/198ef88e1815d9ba66c0f3ef3b18f74c

A.6.2. *Stacking*

At this point, images can be averaged to form a simple stack, however better results occur when weighting images by their sensitivity or root mean square (rms) noise, since these properties vary greatly over the > 20 degree images. For rms noise calculations we use the Background And Noise Estimation tool (`BANE` [18]; Hancock et al. 2012, 2018), which generates a map of the rms noise across an image using a sparse grid, calculating the rms noise within a box centred on each grid point and interpolating between grid points. The grid spacing and box size are set using software-defaults which are set at $\sim 4 \times B_{\rm maj}$ and $\sim 20 \times B_{\rm maj}$, respectively. Additionally, we can weight by the pseudo-Stokes I primary beam response, which gives the sensitivity across an image. This is generally useful for stacks that have a number of different pointing centres, and is less sensitive to changes in flux scale between the individual snapshots as compared to rms noise maps [19]. The final stacks are a simple weighted average,

$$\bar{I}_w(x,y) = \frac{\sum_{i=0}^{N} I_i(x,y) w_i(x,y)}{\sum_{i=0}^{N} w_i(x,y)}\,, \tag{A.15}$$

where $w_i(x,y) = 1/\left(\sigma_{i,\rm rms}\right)^2$ for rms noise weighting, $w_i(x,y) = A_i(x,y)^2$ for primary beam weighting, where $A_i(x,y)$ is the Stokes I primary beam response, or $w_i(x,y) = A_i(x,y)^2/\left(\sigma_{i,\rm rms}\right)^2$ if using both. This stacking procedure is performed using `python` and `numpy` (van der Walt et al., 2011), but due to memory constraints the weighted average stack is created one layer at a time. When the snapshots are stacked, the reprojected PSF maps are stacked using the same weights to form a stacked PSF map. Examples of the resultant stacked PSF major axis are shown in Fig. A.14 for a selection of mosaics, highlighting the effect of projection away from zenith on the PSF major axis. Note that the $f_{\rm regrid}$ factor defined in Appendix A.6.1 corresponds to the beam solid angle rather than a particular axis, but for ease of use in applying the factor to flux

[18] https://github.com/PaulHancock/Aegean/wiki/BANE

[19] Though if the flux scale is consistent this should not be the case.

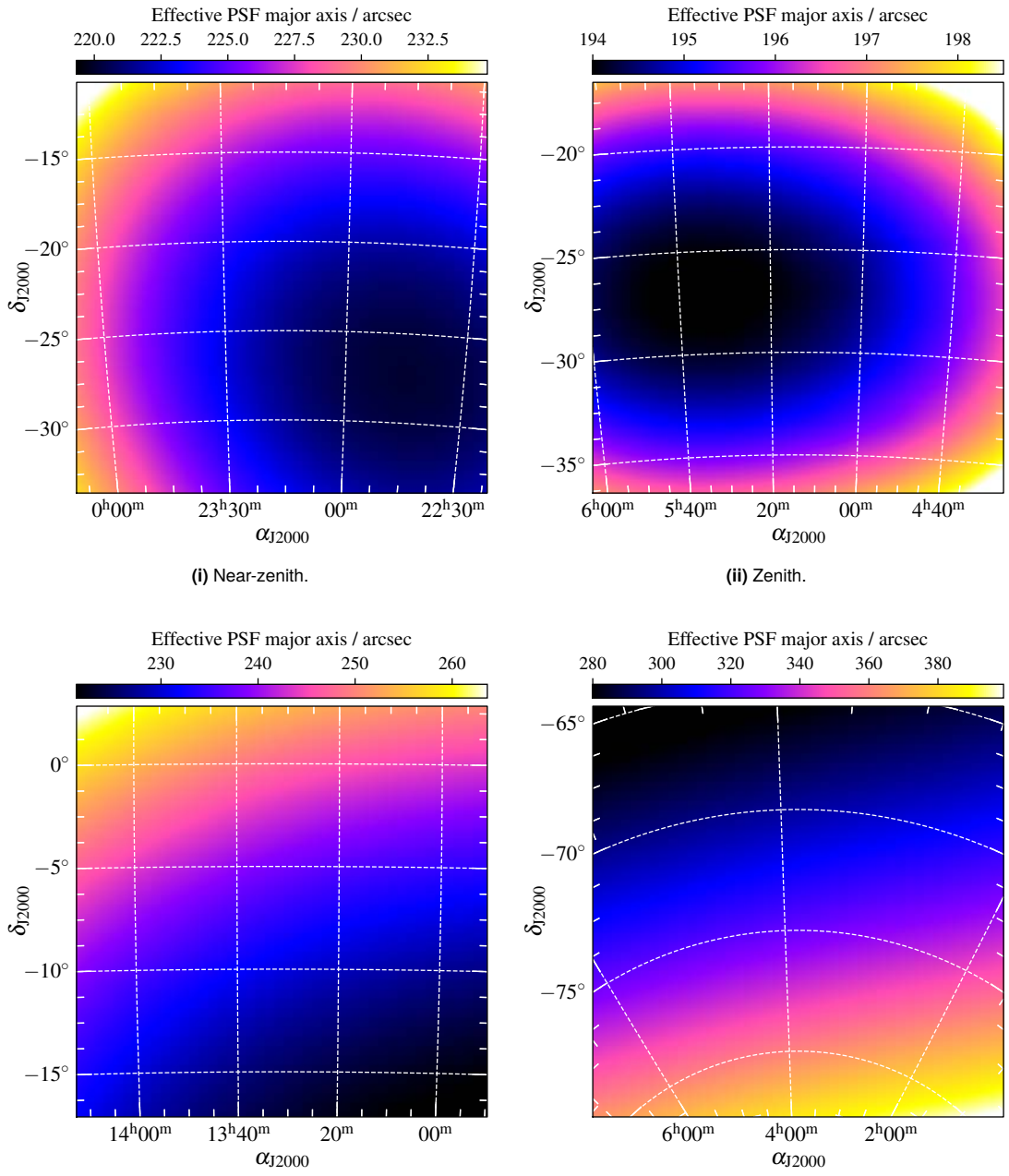

(i) Near-zenith.

(ii) Zenith.

(iii) Sub-equatorial.

(iv) Off-zenith, low-declination with many different pointings.

Figure A.14. Example weighted average PSF major axis stacked images. The major axis increases away from the phase centre (in this case, near zenith). Note the different colour-scale of each image.

density measurements, it is directly applied to the PSF major axis [20].

A.6.3. *Mosaic flux scale*

There is a final flux scale correction that is applied to the stacked mosaics. We use the `flux_warp` software again but this time we take a simple SNR-weighted mean, as the distribution of $S_{\text{measured}}/S_{\text{predicted}}$ is expected to follow a log-normal, position-independent distribution at this stage [21]. Typically the additional correction factor applied at this stage is 0.95–1.05. After applying the mean factor, we run `flux_warp` again and measure the standard error on the $S_{\text{measured}}/S_{\text{predicted}}$ values to estimate the uncertainty relative to the GLEAM survey. These values typically range from 2–10 per cent. The final flux scale uncertainty is then taken as the quadrature sum of this standard error and the declination-dependent flux scale error from GLEAM when measuring flux density from the maps. Thus, the error is

$$\sigma_{\text{flux scale}} = \begin{cases} \sqrt{0.08^2 + \sigma^2}, & \text{if } -72^\circ \leq \delta_{\text{J2000}} < +18.5^\circ \\ \sqrt{0.13^2 + \sigma^2}, & \text{otherwise.} \end{cases} \tag{A.16}$$

Note that for $\delta_{\text{J2000}} < -83.5^\circ$ the GLEAM catalogue has an 80 per cent external uncertainty, though we do not use this small region of the sky in calibration.

A.7. Additional integrated flux density challenges

A.8. Source-finding with aegean

As part of this work an issue with the `aegean` source-finding software [22] (Hancock et al., 2012, 2018) was uncovered regarding measurement of integrated flux densities. This issue has two facets: incorrect island flux density measurements and incorrect fitted-component flux density measurements, both for different reasons. *Islands.* For a source described as an 'island' of pixels (i.e. found via flood-fill prior to Gaussian fitting),

[20] Visual inspection of images with extreme PSF distortion tend to show point sources with a major axis size corresponding to the PSF major axis multiplied with f_{regrid}—this suggests only the PSF major axis is actually affected.

[21] If not, we have done something wrong.

[22] https://github.com/PaulHancock/Aegean

integrated flux density measurements are made via summation of pixel Jy beam^{-1} values. For a Gaussian beam, this is simply

$$S_{\text{island}} = \frac{4\ln(2)\,\|\Delta\alpha\Delta\delta\|}{\pi\theta_{\text{major}}\theta_{\text{minor}}}\sum_{i=0}^{N\text{pix}} S_i \quad [\text{Jy}]\,, \tag{A.17}$$

where $\Delta\alpha$ and $\Delta\delta$ are the RA and declination axis pixel sizes (`CDELT1/CD1_1` and `CDELT2/CD2_2` in the FITS header), θ_{major} and θ_{minor} are the synthesized beam major and minor axes, and S_i is the Jy beam^{-1} flux density of a single pixel with the sum over the pixels comprising the source. Previous versions of `aegean` ($\leq$ 2.0.2) simply divided the S_i sum by the angular beam area. This has been fixed post version 2.0.2.

Gaussian components. For the fitted Gaussian components, integrated flux density is calculated as

$$S_{\text{component}} = A\frac{\Theta_{\text{major}}\Theta_{\text{minor}}}{\theta_{\text{major}}\theta_{\text{minor}}} \quad [\text{Jy}]\,, \tag{A.18}$$

where A is the Gaussian-fit peak flux density for the source and Θ_{minor}, Θ_{major} are the source FWHM major and minor axes, respectively. This is how `aegean` has been calculating the integrated flux density for version 2.0.2 and prior, however the estimate of the projected beam size was less than it actually is due to a conversion between beam size at the phase center and beam size in pixels at the source position. This resulted in an over-estimate of the source integrated flux density. For SIN-projected (and ZEA-projected) images, a beam as defined at the image centre is sufficient for measurement (except if regridded, see Appendix A.6.1). Using a fixed beam size (or using a user-supplied PSF map) fixes this issue and returns a consistent set of flux density measurements. [23].

Testing. Testing for the above effect is performed on a simulated dataset. This simulated dataset uses an MWA Phase I u, v dataset as a template, sets all visibility data to zero, then predicts the visibilities of concentric rings of 1 Jy point sources out to 20 degrees from the nominal phase centre. From there, we image in two ways:

[23]Perhaps projections other than SIN and ZEA will also work in this way, however, SIN and ZEA are the only ones considered here.

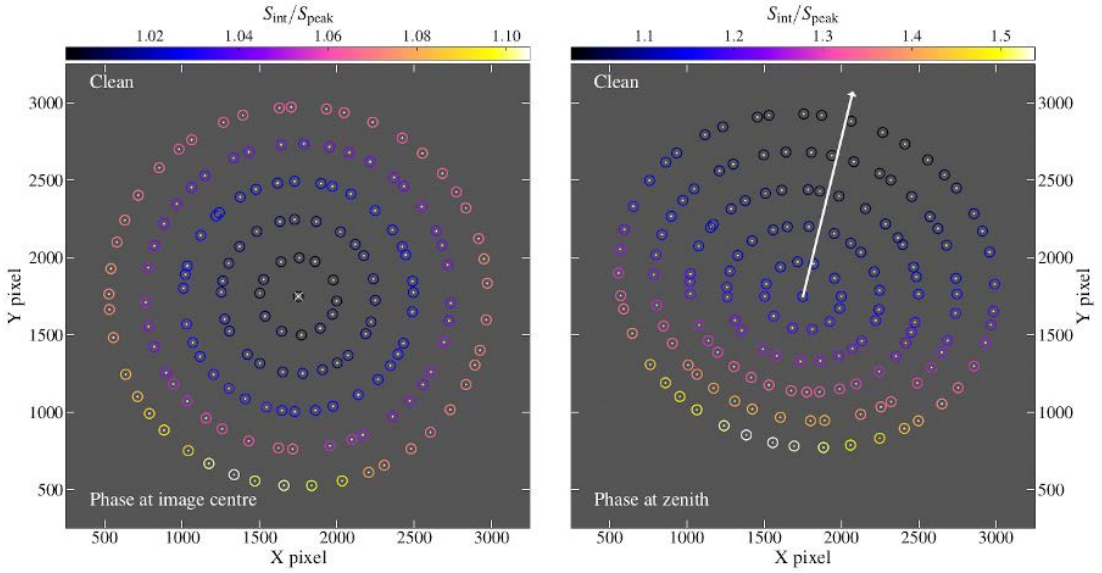

(i) Prior to fix.

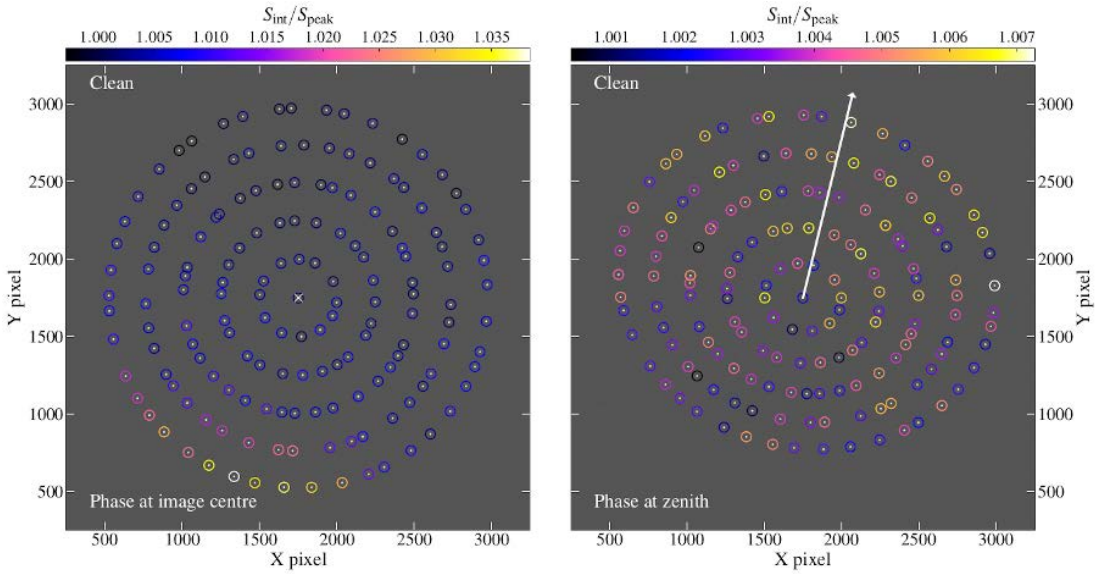

(ii) After fix.

Figure A.15. Testing the integrated flux density measurements of aegean on simulated data for a MWA Phase I observation with elevation $\sim 60^{\circ}$. (i) Measurements prior to employing fix. The cross at the centre indicates the image reference position/phase centre. (ii) Measurements after employing fix. The directional arrow indicates the direction towards the image reference position/phase centre as it falls outside of the actual image. Note the different colourscales between the images. Note also that the images are plotted in pixel coordinates as they are near the South Celestial Pole where the SIN projection in the zenith-centred case becomes extreme.

first, imaging with the phase centre unchanged; second, imaging with the phase centre rotated to the location on the sky that minimises the number of w-terms required for imaging, which results in images that are gridded at the nominal phase centre, but have a image reference coordinate defined at this minimum w-term coordinate (which is $\delta_{\mathrm{J2000}} \sim -26.7°$)—see Appendix A.4.

Fig. A.15 shows the output of source-finding on the simulated ring data. Fig. A.15(i) shows the measured ratio of $S_{\mathrm{int}}/S_{\mathrm{peak}}$ prior to applying the fix for measuring the integrated flux densities. In the case where the phase centre is the same as the image data array centre (i.e., the image reference coordinate is the centre of the image), S_{int} increases radially from the image centre whereas in the case where the phase centre is near zenith S_{int} increases from this new near-zenith position and increase up to $1.5 \times S_{\mathrm{peak}}$. Fig. A.15(ii) shows the results of applying the integrated flux density measurement fix. At this stage we have revealing another issue, where we have 'fixed' the integrated flux density measurements (in that they are now consistent), except we now have a ~ 3 per cent error on the integrated flux densities *away* from zenith for the case where the phase centre is the centre of the image!

The new issue revealed in the left panel of Fig. A.15(ii) is reasonably small but clearly systematic. As the issue again seems to be some elevation-dependent problem we find a different template observation with elevation $\sim 40°$. We simulate a similar set of 1 Jy point sources and image as before. Fig. A.16 shows the results of this, with A.16(i) showing source-finding on the dirty (i.e. un-CLEANed) images and A.16(ii) showing source-finding on the restored/CLEAN images. Fig. A.17 shows the same as Fig. A.16 but for peak flux density alone, showing clearly peak flux density is the culprit and the PSF as used for integrated flux densities is as expected. As the effect is for peak flux density only and reasonably small, we do not consider this further.

A.9. Stacking dirty signal

On the topic of dirty versus CLEAN flux densities, another issue is raised. As we only CLEAN images to the noise level of individual snapshots, when stacking residual 'dirty' emission becomes significant in the stacked mosaics. The resultant residual source signal is not deconvolved and its integrated flux density, when measured in the

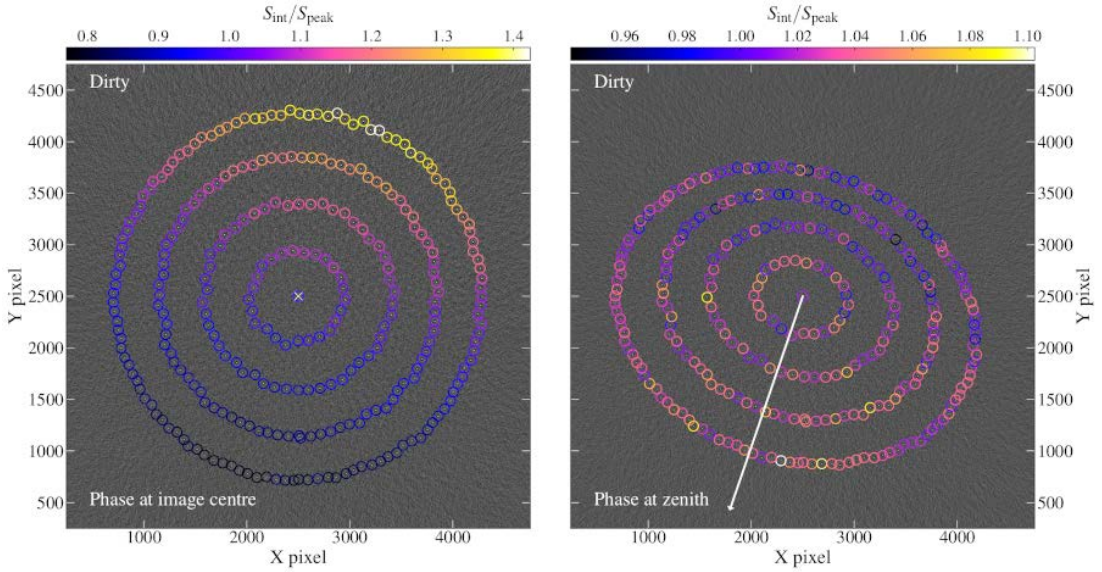

(i) Dirty images.

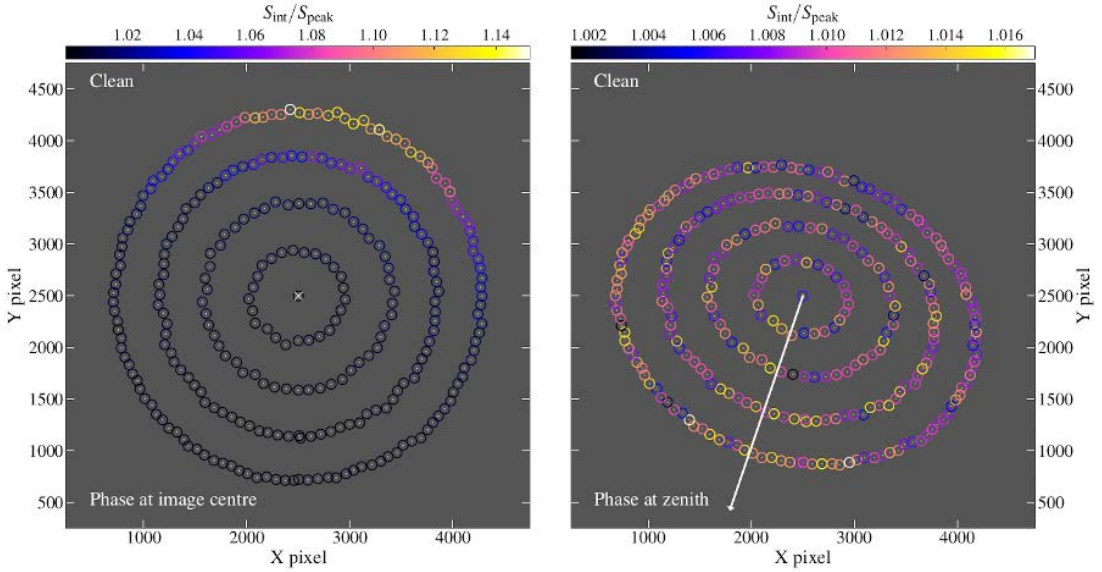

(ii) Restored images.

Figure A.16. Testing the integrated flux density measurements of sources when generating images using `WSClean`. A.16(i) The dirty images with the measured $S_{\rm int}/S_{\rm peak}$ ratios plotted. A.16(ii) The restored images after standard "deep" CLEAN with source $S_{\rm int}/S_{\rm peak}$ plotted. The directional arrow indicates the direction towards the image reference position/phase centre as it falls outside of the actual image. Note the different colourscales between the images. Note also that the images are plotted in pixel coordinates as they are near the horizon where the SIN projection in the zenith-centred case becomes extreme. Note that this template observation is at a higher declination than that used in Fig. A.15 hence the zenith location is below the image.

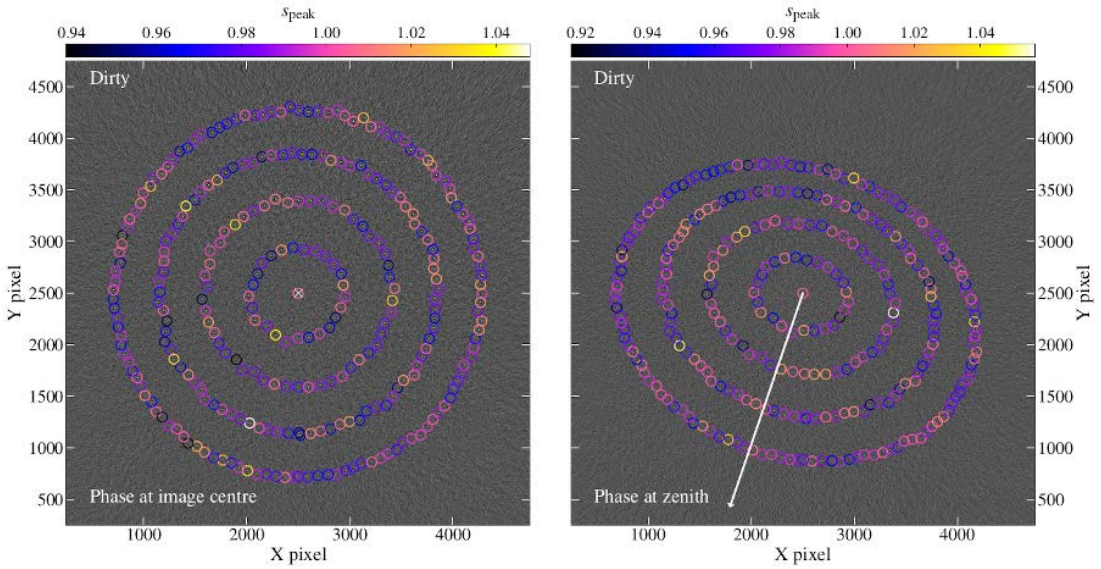

(i) Dirty images.

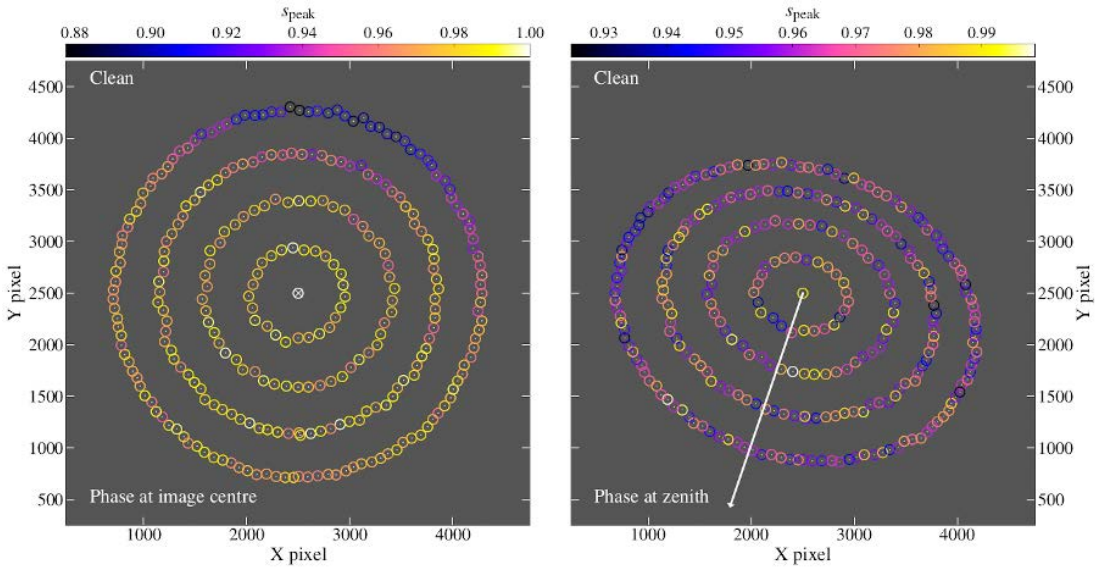

(ii) Restored images.

Figure A.17. Testing the peak flux measurement from sources after using `WSClean`. A.17(i) The dirty images with the measured S_{peak} plotted. A.17(ii) The restored images after standard "deep" CLEAN with source S_{peak} plotted. See Fig. A.16 for additional notes.

usual way, may be different than in the CLEANed image. Without joint-deconvolution with, e.g., the Image Domain Gridder (IDG; van der Tol, Veenboer & Offringa, 2018), the snapshot residuals will always be dirty. There are two effects at play here: (1) the restoring beam/PSF used for integrated flux density calculations is only an estimate of the true PSF, so residuals, which have units defined by the true PSF will be wrong by this difference, and (2) dirty flux, especially for extended sources, is spread through the image as sidelobes and interacts with other sources and their sidelobes (removing these sidelobes is part of the point of CLEAN).

To attempt to estimate the 'true' integrated flux density, we create additional mosaics of the residuals and CLEAN component models separately. These maps can then be measured separately. The CLEAN component map is simple in that the units are Jy pixel^{-1} so the integrated model flux density (S_{model}) is simply the pixel sum, however, the residuals still require usual integration over a Gaussian volume (which, given problem (1) above is only approximate but is our best possible guess). The integrated residual flux density (S_{dirty}) can then be corrected by some factor (f_{dirty}) that would be recovered in the CLEAN process. The integrated flux is then

$$S = S_{\text{model}} + f_{\text{dirty}} \times S_{\text{dirty}} \tag{A.19}$$

where S is the total integrated flux density. For this purpose, additional stacked model and residual images are created and used when measuring integrated flux densities via direct integration over pixels.

A.10. Concluding remarks

With `piip` able to produce flux-measuring–ready mosaics, it is useful to compare the MWA-2 imaging with equivalent MWA Phase I images: for this purpose we show Fig. A.18 as a comparison between MWA-2 and GLEAM images at 88 and 154 MHz. Fig. A.18 shows the double relic system Abell 3667, observed with the MWA prior to GLEAM by Hindson et al. (2014, see also Roettiger et al. 1999; Johnston-Hollitt 2003), highlighting the increase in resolution afforded by the robust 0.0 MWA-2 images. While image depth in this work is not sufficient to break any issues regarding confusion limits,

generally imaging is deeper than the GLEAM survey simply due to the combination of increased resolution (improving point source sensitivity) and longer integration for particular pointings.

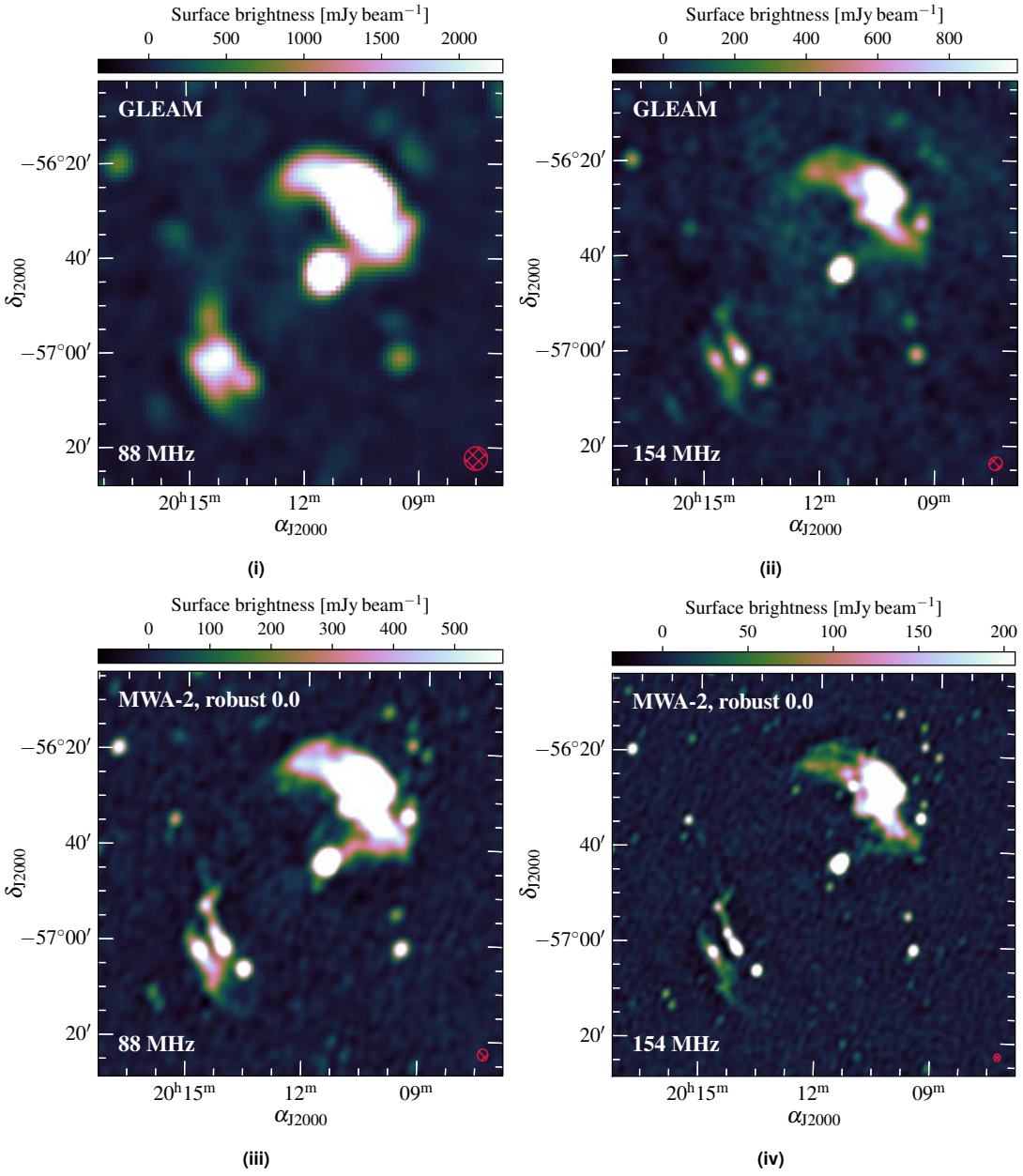

Figure A.18. Comparison between the GLEAM wideband images (robust -1.0 weighting) with the equivalent-frequency MWA-2 robust 0.0 images for 88 and 154 MHz. Note the negative bowls beginning to appear around the MWA-2 robust 0.0 data as seen in the PSF in Fig. A.9. The red ellipses in the lower right of each image represent the PSF at this location. The colour-scale for all images is set corresponding to a linear range between $-7\sigma_{\text{rms}}$ and $49\sigma_{\text{rms}}$.

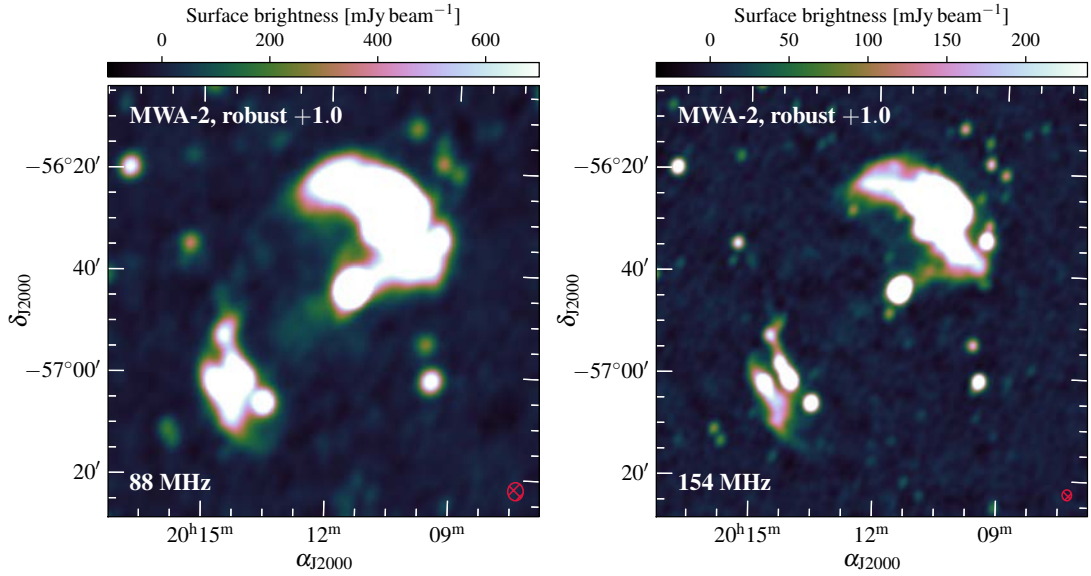

Figure A.18. *continued*, for robust +1.0 images.

Appendix B.

The MWA-2 observations

B.1. Reviewing the observed fields

In this section all of the created mosaics will be shown with some accumulated statistics and comparison with the GLEAM EGC. A code, `field_qa.py`, is written for the purpose of generating the following plots and basic summary statistics, including cross-matching and spectral fitting for comparison to the GLEAM EGC spectral properties. For the purpose of source-finding, `PyBDSF` (Mohan & Rafferty, 2015) [1] is used in some instances, though the results are identically for flux density measurements which is the only quantity compared [2]. A 10σ threshold is used, and for the purpose of fitting the power law models to obtain spectral indices, all five MWA-2 bands must have a detection above 10σ and 18/20 GLEAM narrows bands must have a detection above 5σ. Note the difference in threshold is due to a difference in sensitivity between the MWA-2 and GLEAM data. Additionally, we clip the distributions of α ensuring values satisfy $-3\sigma_\alpha \leq \alpha \leq 3\sigma_\alpha$ to avoid poor cross-matches and other potential artefacts from the source-finding process. Generally, this results in > 500 sources, though this exact number is incredibly variable due to the large range of image sensitivities across the fields and individual frequencies.

These data are used in Duchesne et al. (2020, Chapter 4), Duchesne et al. (Chapter 5 2021c), and Chapter 6. While I was involved in work by Brüggen et al. (2021) and

[1] https://github.com/lofar-astron/PyBDSF

[2] Note the choice to use `PyBDSF` is purely due to its speed over `aegean` for the final mosaics. Why their execution speeds differ by large factors is not entirely clear. While `PyBDSF` does not allow an input PSF map, the output catalogue integrated flux densities are multiplied by f_{regrid} for their particular location to obtain the PSF-correct flux densities consistent with `aegean`.

supplied FIELD8 images for that purpose, the FIELD8 images that appear in Duchesne et al. (2021c) and Chapter 6 were re-processed, allowing inclusion of a handful of extra snapshot observations.

Note that each observed field is shown with two sets of mosaics per frequency: a robust 0.0 or +0.5 and a robust +1.0 or +2.0 which we utilise as the high and low resolution mosaic, respectively. The low resolution mosaic is typically used for flux density measurements, unless otherwise stated, whereas the high resolution mosaic is for morphology analysis, source de-blending, and general point source measurements.

B.1.1. *FIELD1*

FIELD1 (along with FIELD2) was selected to cover a large section of the Epoch of Reionization (EoR) 0-hour field (EoR0; Offringa et al., 2016), giving a higher resolution follow-up to diffuse cluster emission detected in the EoR0 field image (Duchesne et al., 2021b). Observation details for this field are presented in Table B.1. As this field had been chosen for EoR experiments, it is generally a quiet field at most frequencies, with the exception of Fornax A to the SE, which is largely only a concern at 88 MHz. The field was observed over two nights, and both nights had reasonable ionospheric conditions such that only a few snapshots over the five frequencies were thrown away. Despite this, we have included additional snapshots from the GLEAM-X survey for added sensitivity.

Fig. B.1 shows the mosaic images and basic noise properties. For FIELD1 robust 0.0 is chosen for the higher resolution image, with robust +2.0 chosen for the low-resolution image. Some additional mosaics are created with tapering for the purpose of characterising Abell 141 specifically, which are described in more detail in Duchesne et al. (2021c, as described in Chapter 5re-). Fig. B.2 shows the diagnostic output of `field_qa.py` for the spectral properties of sources in the field and with comparison to the GLEAM EGC. Generally spectral properties are consistent with the GLEAM EGC, with $\mu_{\alpha,0.0} = -0.81 \pm 0.27$, $\mu_{\alpha,+2.0} = -0.86 \pm 0.22$ for the robust 0.0 and +2.0 images, cf. $\mu_{\alpha,\mathrm{GLEAM}} = -0.81 \pm 0.20$ for the cross-matched GLEAM sources.

Table B.1 Observational details for all fields.

Date	N_{88} [a]	N_{118}	N_{154}	N_{185}	N_{216}	Project [b]	Comments
(UTC)							
			FIELD1				
2017-10-23	0	0	0	0	0	G0008	> 50% antennas missing.
2017-11-03	5	5	5	6	6	G0008	Good.
2017-11-04	5	5	5	6	6	G0008	Good.
2017-12-22	12	12	12	11	11	G0045	Good.
2018-01-06	12	12	12	11	11	G0045	Good.
Totals [c]	34	34	34	34	34	...	...
			FIELD2				
2017-11-03	0/4	0/4	0/4	3/4	3/3	G0008	Poor ionosphere.
2017-11-04	3/4	4/4	4/4	4/4	4/4	G0008	Mostly good.
2018-06-03	3/3	2/2	2/2	2/2	2/2	G0008	Good.
2018-06-06	0/3	3/3	3/3	3/3	3/3	G0008	Poor ionosphere.
2018-06-10	0/10	3/10	0/8	1/9	0/9	G0045	Poor ionosphere.
2018-06-13	6/10	7/10	7/10	7/10	7/9	G0045	Variable ionosphere.
2018-06-15	0/11	0/10	2/11	0/11	3/11	G0045	Poor ionosphere.
2018-06-16	11/11	11/11	11/11	11/11	10/11	G0045	Good.
2018-06-18	8/8	5/8	8/8	9/9	7/9	G0045	Variable quality.
2018-06-22	0/8	1/8	2/8	4/9	0/9	G0045	Poor ionosphere.
2018-06-26	0/14	0/14	0/14	0/14	0/14	G0045	Poor ionosphere.
Totals	31/86	36/84	39/83	44/86	39/84	...	...
			FIELD3				
2017-11-20	1/1	1/1	-	1/1	1/1	G0008	Many missing tiles.
2017-11-21	1/1	1/1	-	1/1	1/1	G0008	Many missing tiles.
2017-11-30	1/1	1/1	-	1/1	1/1	G0008	Many missing tiles.
2017-12-03	1/1	1/1	-	1/1	1/1	G0008	Many missing tiles.
2017-12-06	1/1	3/3	-	1/1	1/1	G0008	Good.
2017-12-14	1/1	2/2	-	1/1	1/1	G0008	Good.
2017-12-16	1/1	2/2	-	1/1	1/1	G0008	Good.
2017-12-18	1/1	1/1	-	1/1	1/1	G0008	Good.
2017-12-23	11/11	11/11	12/12	11/11	11/11	G0045	Good.
2018-01-07	12/12	11/11	11/11	9/11	4/11	G0045	RFI in high band.
Totals	31/31	35/35	23/23	27/29	22/29	...	...

[a] Number of snapshot observations taken at the given frequency, with each snapshot 112–120s of data.

[b] G0008 is GLEAM-X, and G0045 is the dedicated cluster project.

[c] Total snapshots used after discarding snapshots with poor ionospheric conditions, too few tiles, particularly bad RFI.

Table B.1 *continued.* Observational details for all fields.

Date	N_{88}	N_{118}	N_{154}	N_{185}	N_{216}	Project	Comments
(UTC)							
				FIELD4			
2018-04-28	7/7	6/7	7/7	3/7	2/6	G0045	Cygnus A in sidelobe.
2018-04-29	8/8	8/8	7/7	7/7	7/7	G0045	Cygnus A in sidelobe.
2018-04-30	8/8	8/8	8/8	4/8	7/7	G0045	Cygnus A in sidelobe.
2018-05-01	9/9	8/8	8/8	6/8	4/4	G0045	Cygnus A in sidelobe.
2018-05-08	0/4	4/4	4/4	4/4	4/4	G0045	Cygnus A in sidelobe
2018-05-15	0/4	4/4	4/4	3/4	4/4	G0045	and poor ionosphere.
2018-05-22	3/4	4/4	4/4	3/4	4/4	G0045	Cygnus A in sidelobe.
2018-05-30	4/4	2/4	4/4	3/4	4/4	G0045	Cygnus A in sidelobe.
2018-07-25	0/12	-	-	-	-	G0045	
2018-07-26	0/80	-	-	-	-	G0045	Cygnus A in sidelobe
2018-07-27	-	10/59	-	-	-	G0045	and poor ionosphere.
2018-07-27	-	-	59/79	-	-	G0045	
2018-07-31	-	39/65	-	-	-	G0045	
Totals	39/140	93/171	105/125	33/46 [a]	36/40 [a]	...	...
				FIELD5			
2018-01-17	13/13	14/14	14/14	12/14	14/14	G0045	Good.
2018-01-18	0/14	11/14	9/14	8/14	13/14	G0045	Poor ionosphere.
2018-01-26	0/6	6/6	5/5	2/5	4/5	G0008	Variable ionosphere.
2018-02-01	0/6	0/6	2/5	2/5	4/5	G0008	Poor ionosphere.
2018-03-03	1/6	6/6	5/5	4/4	5/5	G0008	Poor ionosphere.
2018-05-07	5/5	5/5	4/4	4/4	4/4	G0008	Good.
2018-05-26	5/5	5/5	4/4	4/4	2/4	G0008	Good.
Totals	24/55	47/56	43/51	36/50	46/51	...	...
				FIELD6			
2017-12-24	9/11	9/11	11/11	9/10	9/9	G0045	Generally good.
2018-01-08	7/11	9/11	10/11	10/11	9/10	G0045	Variable ionosphere.
Totals	16/22	18/22	21/22	19/21	18/19	...	...
				FIELD8			
2018-01-10	16/17	7/17	12/17	11/17	10/19	G0045	Variable ionosphere.
2018-02-18	6/6	5/6	6/7	6/7	7/7	G0045	Good.
2018-02-21	2/2	0/1	0/1	2/2	2/2	G0045	Poor ionosphere.
2018-03-04	4/8	4/8	2/8	0/8	0/8	G0045	Poor ionosphere.
2018-03-13	1/3	0/4	1/4	4/4	4/4	G0045	Poor ionosphere.
Totals	29/36	16/36	21/37	23/38	23/40	...	...

Table B.1 *continued.* Observational details for all fields.

Date	N_{88}	N_{118}	N_{154}	N_{185}	N_{216}	Project	Comments
(UTC)							
			FIELD7 [d]				
2018-01-10	13/16	10/16	10/16	7/16	11/16	G0045	Calibration trouble.
2018-02-07	0/3	3/3	4/4	3/3	3/3	G0008	Variable ionosphere.
2018-02-19	7/8	9/9	6/8	4/8	4/7	G0008	Calibration trouble.
			FIELD10 [d]				
2018-02-08	7/7	7/7	7/7	5/7	5/7	G0008	Calibration trouble.
2018-02-11	7/7	7/7	7/7	5/7	5/7	G0008	Calibration trouble.
2018-02-12	1/6	7/7	6/7	5/7	3/7	G0008	Calibration trouble.
2018-02-13	5/6	6/6	5/6	4/7	5/7	G0008	Calibration trouble.
2018-02-14	5/6	6/6	5/6	5/6	5/7	G0008	Calibration trouble.
Totals	45/53	55/61	50/61	38/61	41/61	...	...
			FIELD9				
2018-06-05	16/16	18/18	16/16	15/16	14/15	G0045	Variable ionosphere.
2018-06-07	13/13	12/13	12/12	10/13	13/13	G0045	Good.
2018-06-08	13/13	12/13	13/13	12/13	12/13	G0045	Good.
2018-06-09	12/12	13/13	12/13	12/13	10/13	G0045	Good.
2018-06-10	13/13	13/13	12/13	13/13	11/13	G0045	Good.
2018-06-11	13/13	13/13	13/13	11/13	12/13	G0045	Good.
2018-06-13	13/13	10/13	10/13	10/13	9/13	G0045	Good.
2018-06-15	12/12	0/13	0/13	13/13	9/13	G0045	Good.
Totals	105/105	91/109	88/106	96/107	90/106	...	...
			FIELD11				
2018-02-04	8/8	8/8	8/8	8/8	8/8	G0008	Good.
2018-02-09	6/6	6/7	7/7	6/6	6/6	G0008	Good.
2018-02-20	4/4	4/4	4/4	5/5	5/5	G0008	Good.
Totals	18/18	18/19	19/19	19/19	19/19	...	...

[d] FIELD7 and FIELD10 are combined so share a snapshot total.

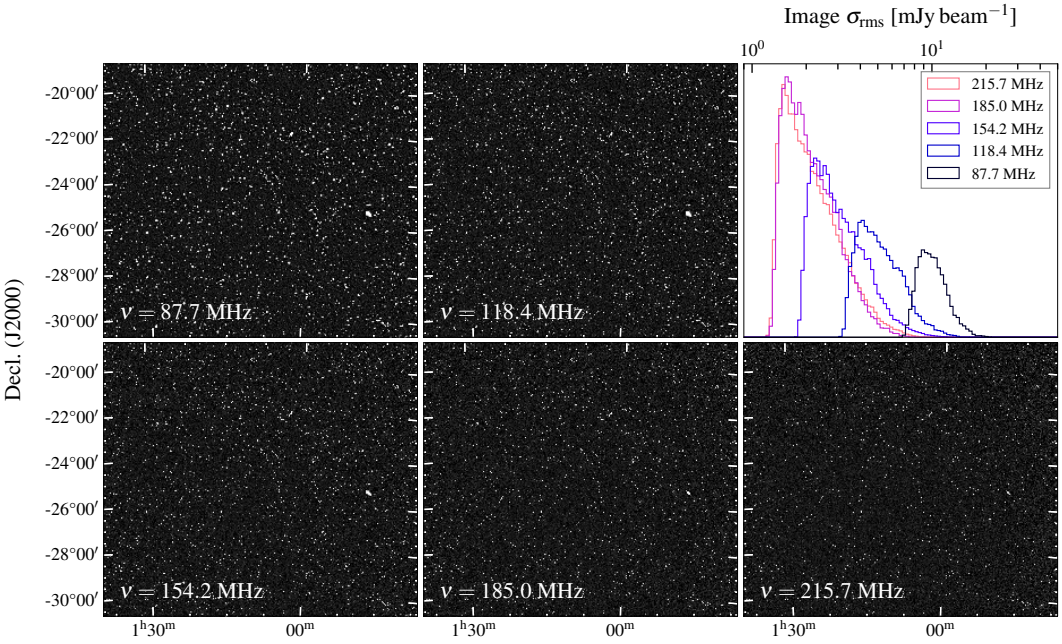

(i) Robust 0.0.

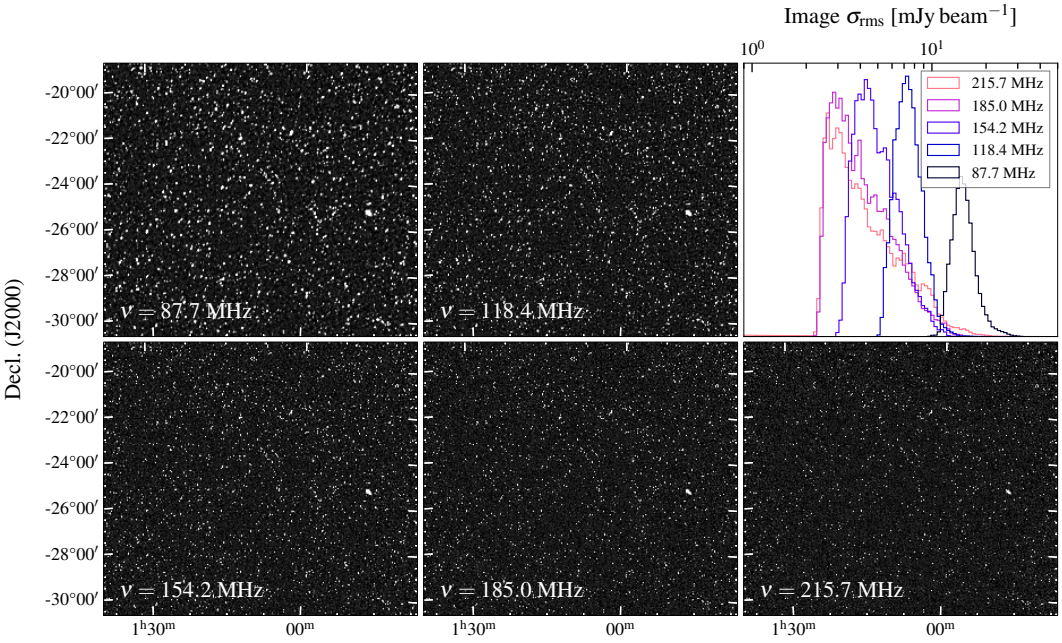

(ii) Robust +2.0.

Figure B.1. `FIELD1` robust 0.0 and +2.0 mosaics.

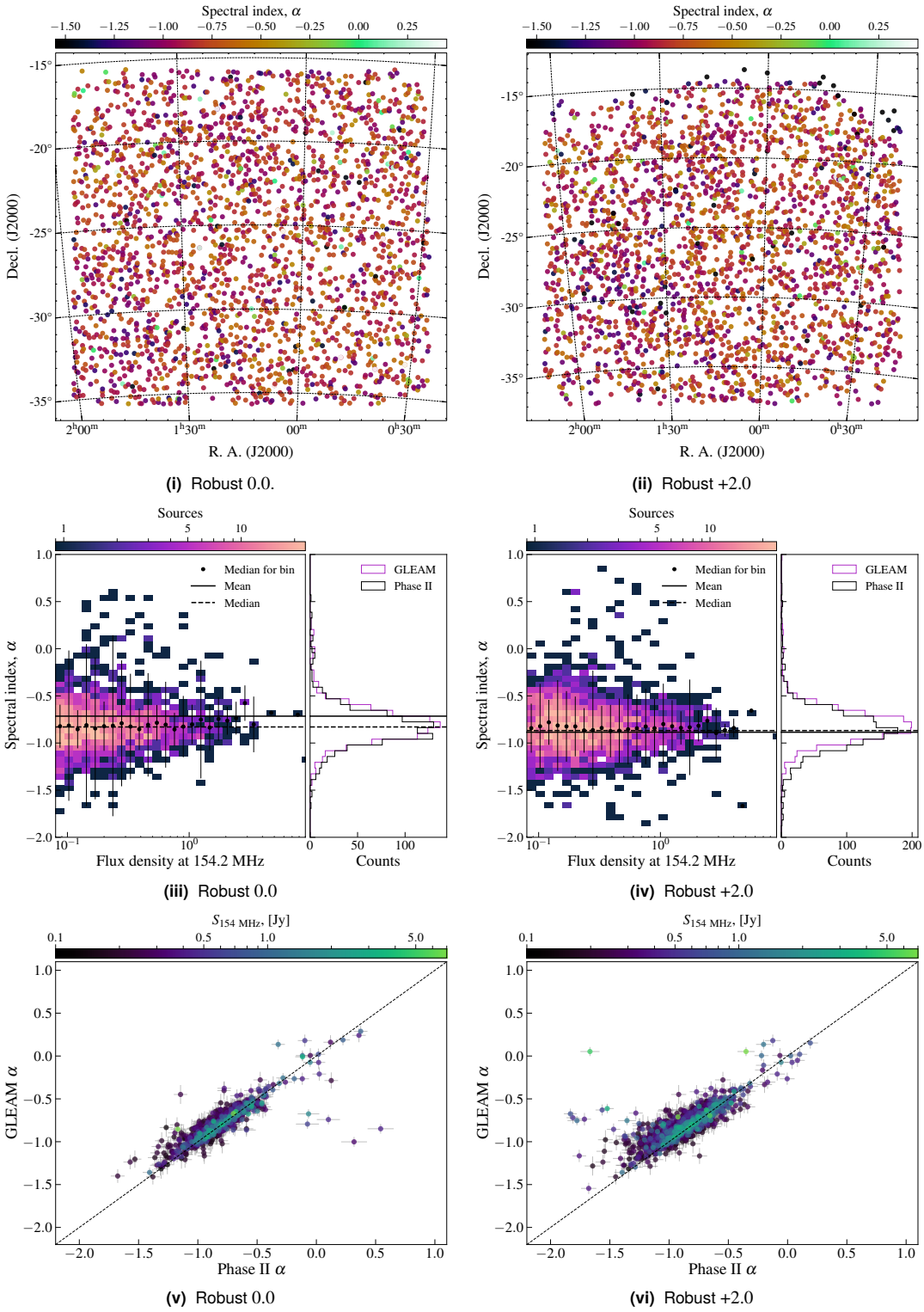

Figure B.2. `FIELD1`: output from `field_qa.py` showing the general spectral properties of sources across the robust 0.0 and +2.0 mosaics.

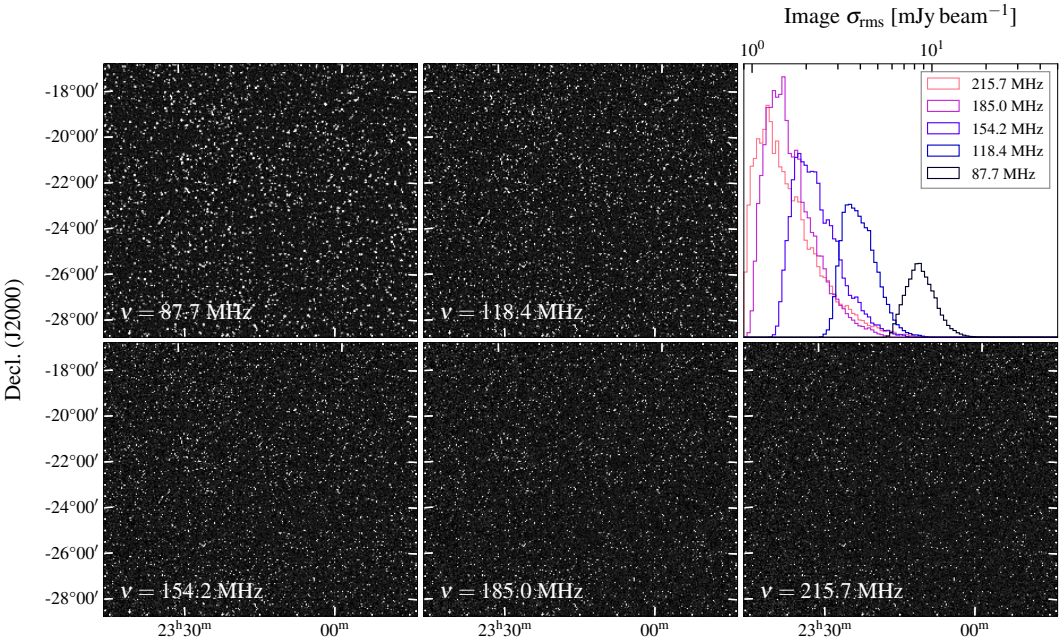

(i) Robust +0.5.

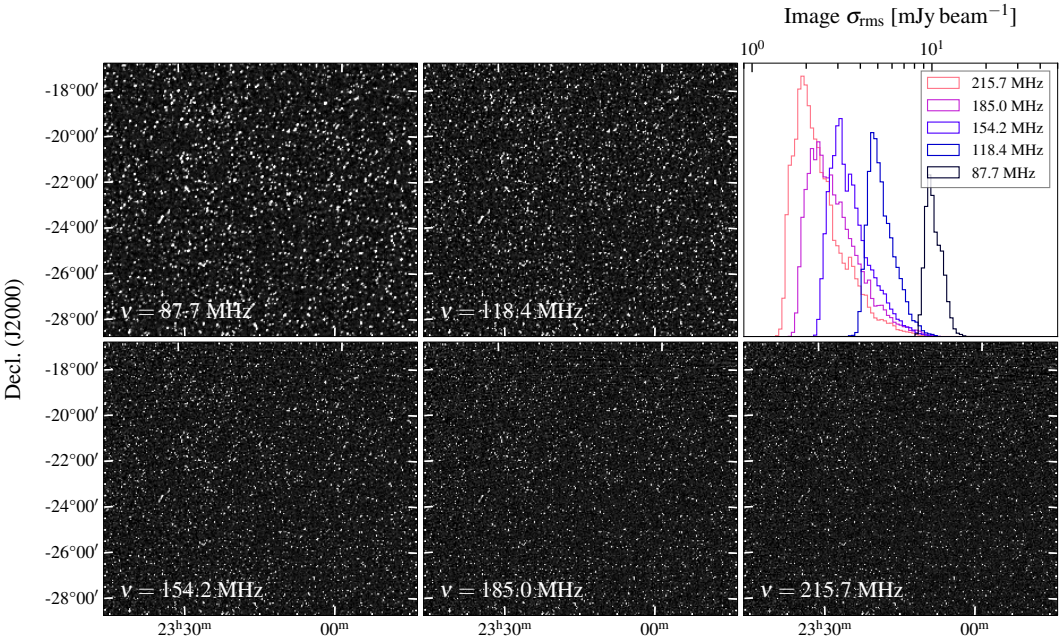

(ii) Robust +2.0.

Figure B.3. FIELD2 robust +0.5 and +2.0 mosaics.

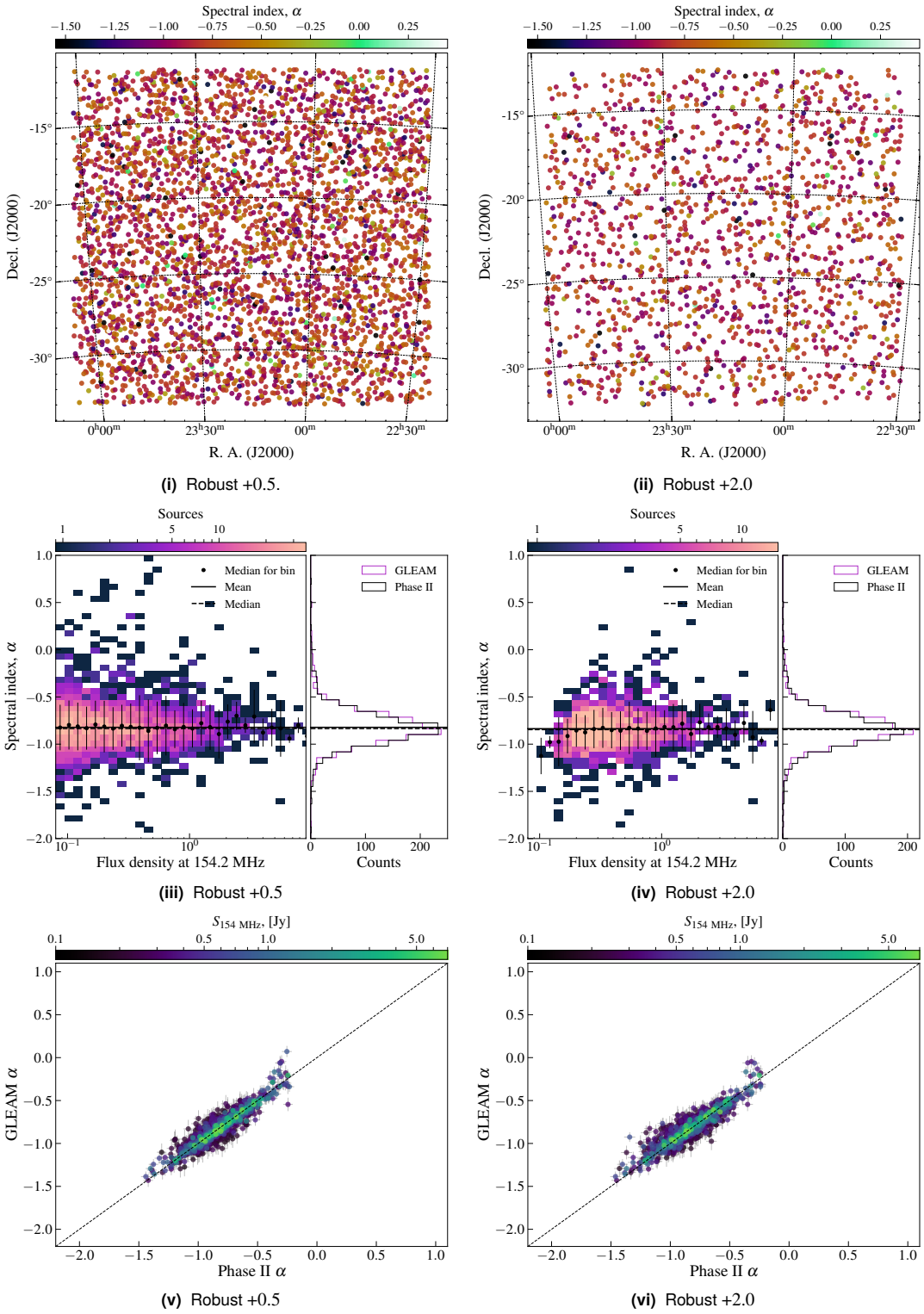

Figure B.4. `FIELD2`: output from `field_qa.py` showing the general spectral properties of sources across the robust +0.5 and +2.0 mosaics.

B.1.2. *FIELD2*

FIELD2 shares a quiet portion of the sky with FIELD1 to the West and has a similarly easy data-reduction compared to some of the later fields. Observation details are shown in Table B.1. Despite the quiet location and the near-zenith pointings, over half of the data taken for this field were rendered unusable due to poor ionospheric conditions. This was mitigated somewhat by having more nights of observing, hence more observations could be thrown away without worry of losing too much sensitivity. No bands required any complex source subtraction, and final images/mosaics are mostly free of bad bright source artefacts. For FIELD2 robust +0.5 is chosen for the higher resolution image, with robust +2.0 chosen for the low-resolution image (shown in Fig. B.3). There is a substantial difference in sensitivity between the two image weightings ($\sim$ a factor of two or more). The distribution of α for mosaics has $\mu_{\alpha,+0.5} = -0.82 \pm 0.18$ and $\mu_{\alpha,+2.0} = -0.84 \pm 0.18$ cf. $\mu_{\alpha,\mathrm{GLEAM}} = -0.82 \pm 0.17$, with the output from `field_qa.py` shown in Fig. B.4.

B.1.3. *FIELD3*

FIELD3 is situated NE of FIELD1 and overlaps slightly at the lower frequencies (hence, larger FOVs). The main target in this field is Abell 0168 which was followed up with the GMRT after initial detection in a parallel search for diffuse emission in GLEAM postage stamps by Dwarakanath et al. (2018). Some large-scale rippling is visible in most images, which is likely sidelobes from bright off-axis sources, though direct subtraction minimises this somewhat, no sources with known models were identified causing the ripples. Alternatively, the ripples may be an aliasing effect which is often fixed by increasing/decreasing image size or including sufficient padding though this was not successful in removing the ripples. No RFI could be identified to cause this effect. The ripples, while visible, do not significantly effect the science given the depth of the final mosaics and are not noticeable in cutout images or indeed in Fig. B.5. Table B.1 shows the observation details for FIELD3 and Fig. B.6 shows the `field_qa.py` output for the mosaics. The distribution of α for FIELD3 mosaics has $\mu_{\alpha,0.0} = -0.84 \pm 0.18$ and $\mu_{\alpha,+2.0} = -0.84 \pm 0.22$ cf. $\mu_{\alpha,\mathrm{GLEAM}} = -0.79 \pm 0.18$.

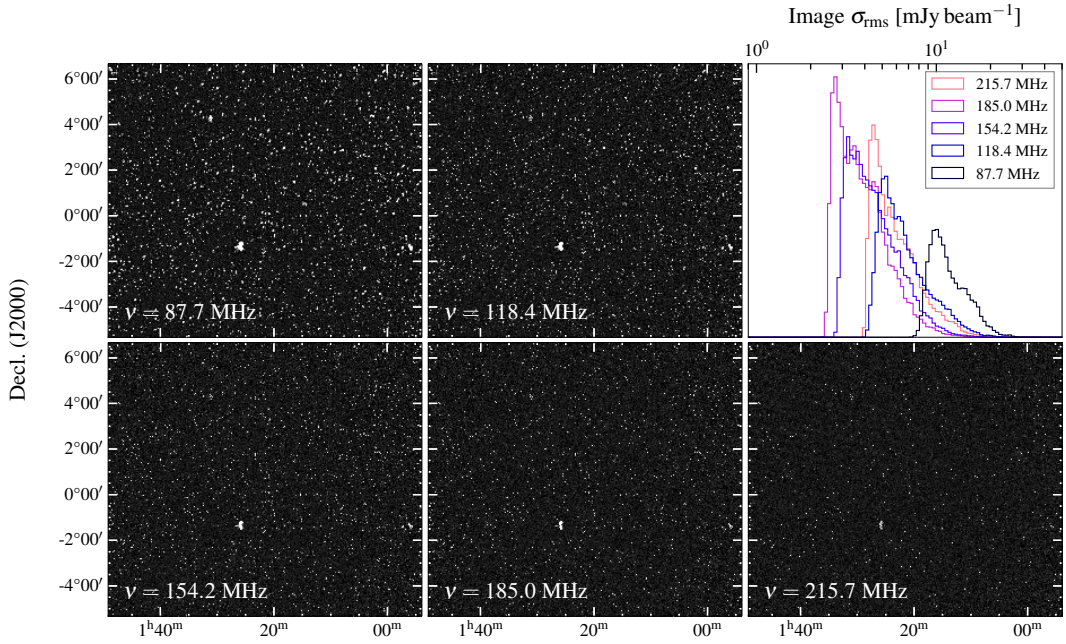

(i) Robust 0.0.

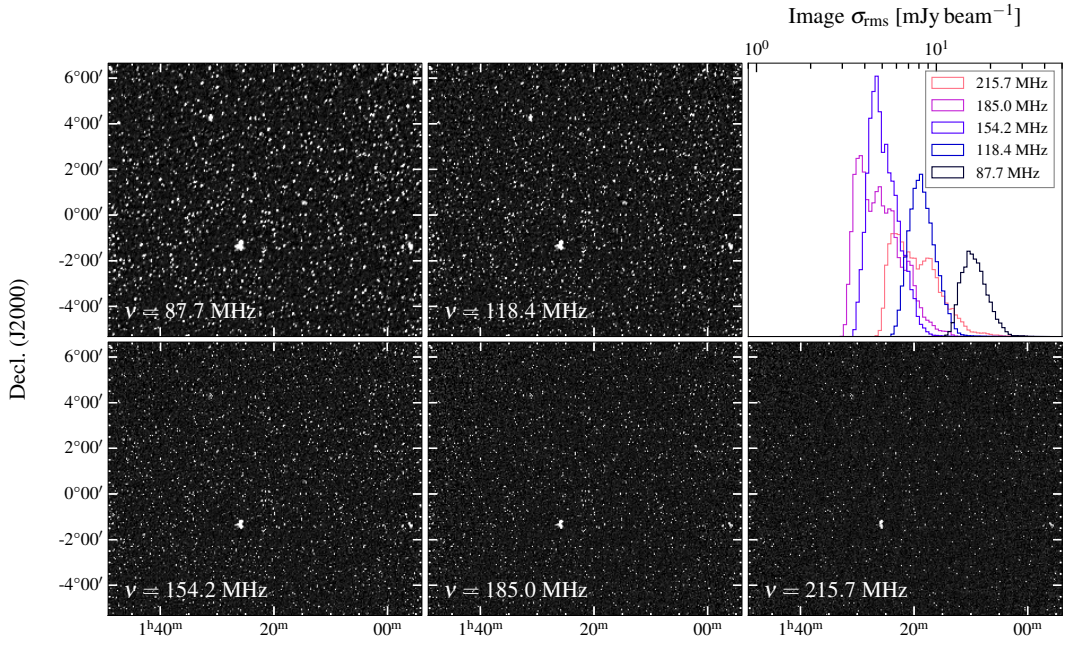

(ii) Robust +2.0.

Figure B.5. FIELD3 robust 0.0 and +2.0 mosaics.

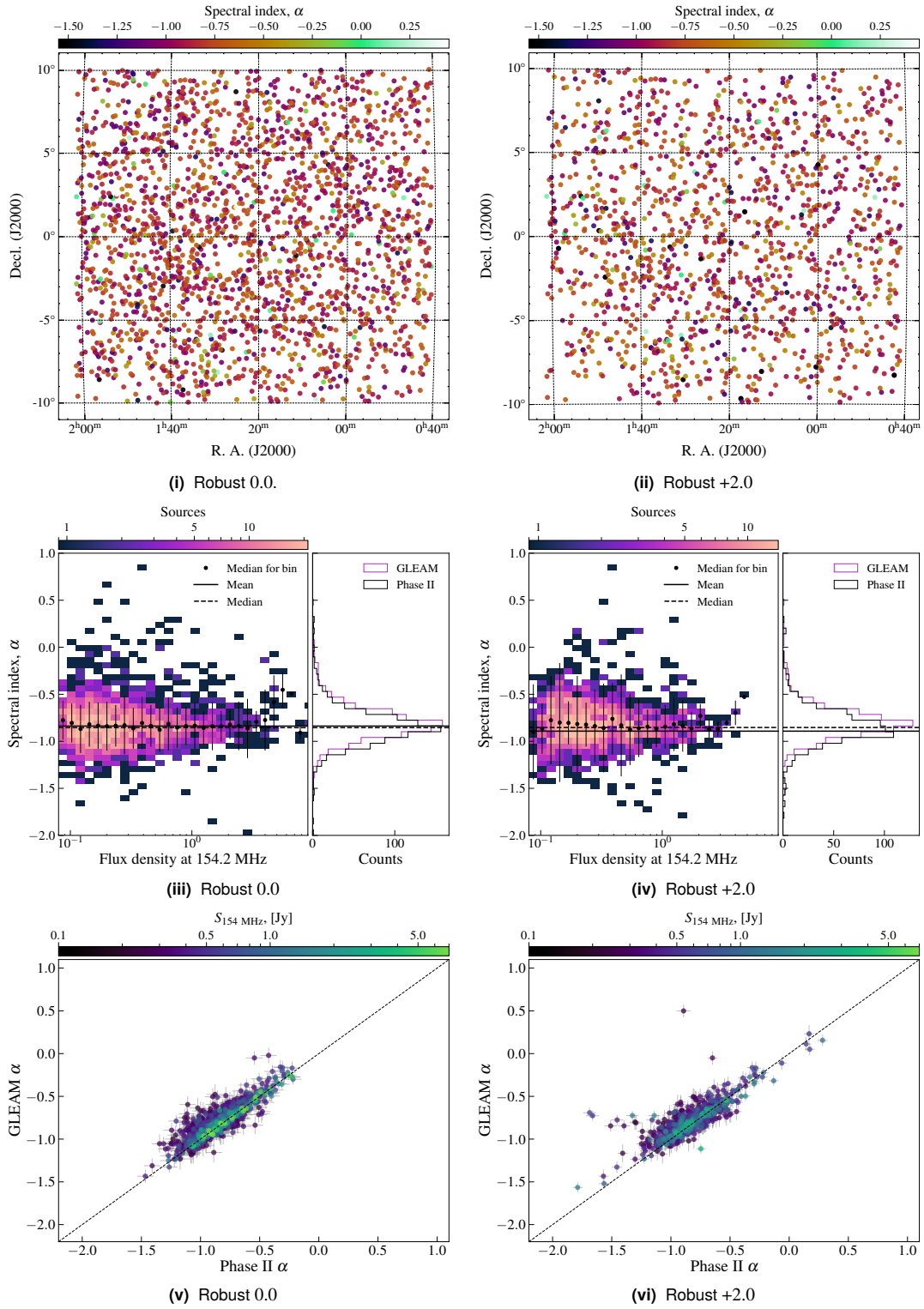

Figure B.6. `FIELD3`: output from `field_qa.py` showing the general spectral properties of sources across the robust 0.0 and +2.0 mosaics.

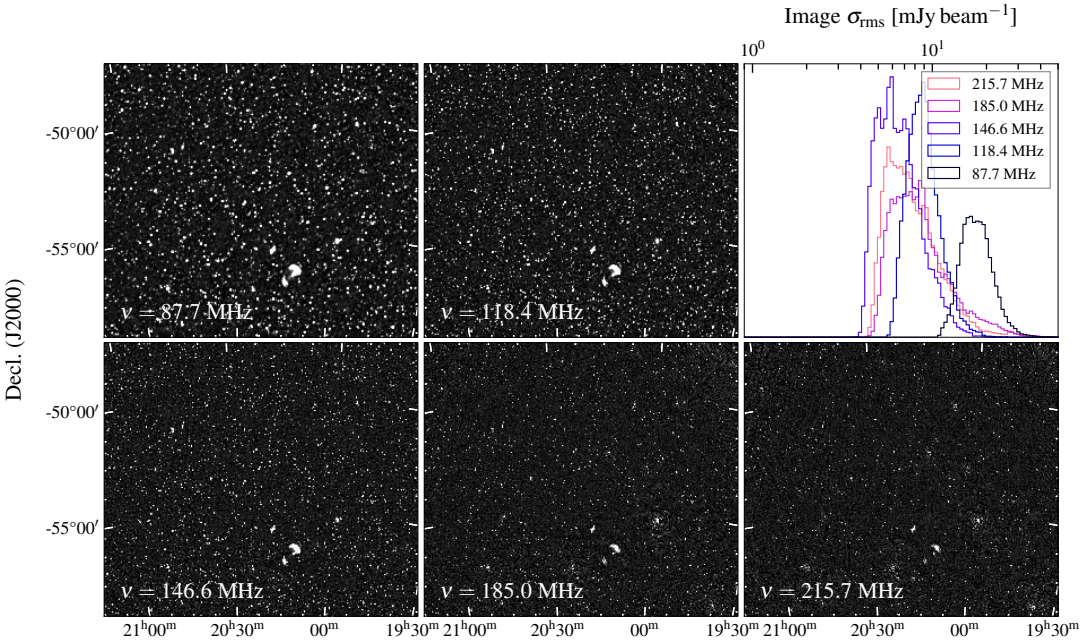

(i) Robust 0.0.

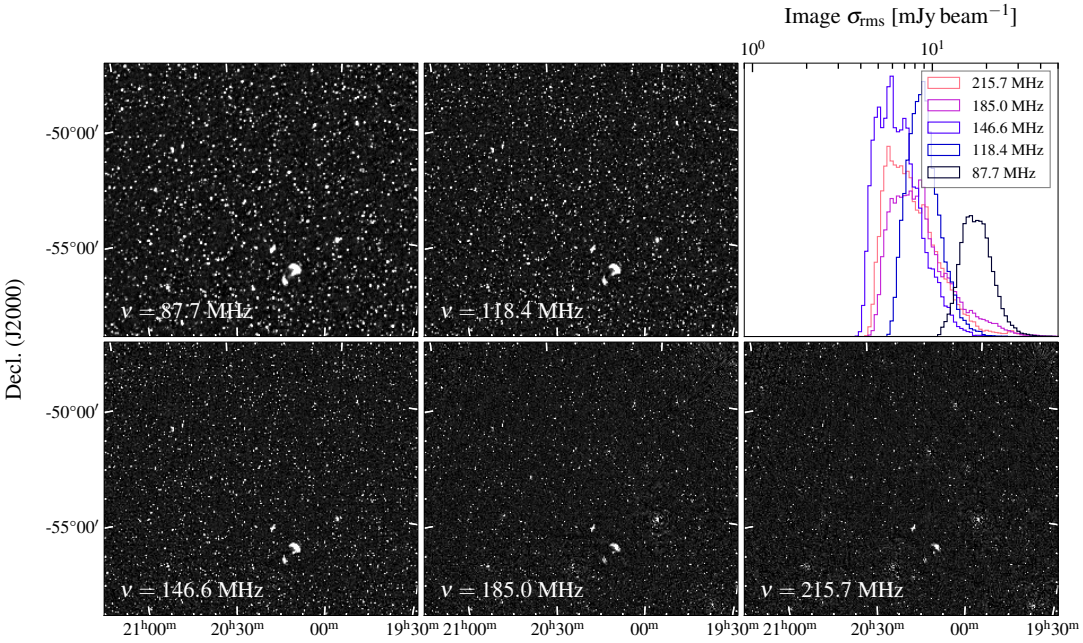

(ii) Robust +1.0.

Figure B.7. FIELD4 robust 0.0 and +1.0 mosaics.

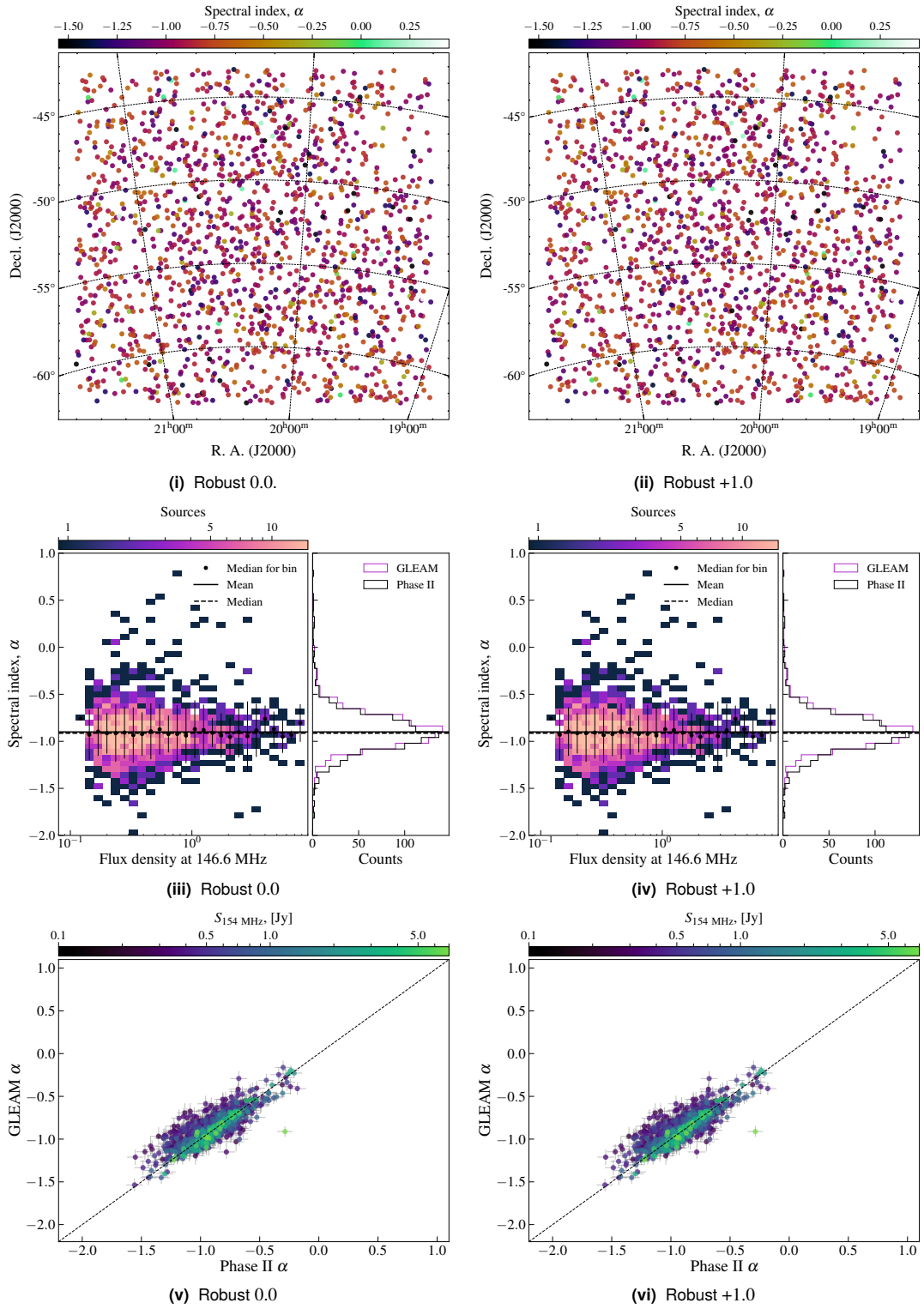

Figure B.8. `FIELD4`: output from `field_qa.py` showing the general spectral properties of sources across the robust 0.0 and +1.0 mosaics.

B.1.4. *FIELD4*

FIELD4 contains one of the brightest examples of diffuse cluster emission—the double relic system hosted by Abell 3667. Observations for this field unfortunately suffered quite strongly from the sidelobes of Cygnus A, some ~100 degrees to the north (with up to ~ 1000 Jy beam^{-1} apparent brightness at 185 MHz). While the subtraction procedure as described in Appendix A.2.3 mitigated this to allow images to be produced, the quality of the > 154 MHz images becomes questionable as sources begin to suffer significant phase errors resulting from calibration including Cygnus A—the 154-, 185-, and 216-MHz data were not able to be calibrated without using Cygnus A as a calibrator due to its relative brightness. True peeling in this case did not produce good results, likely due to the complexity of the primary beam response so far off zenith and close to the horizon, where the spectral dependence becomes extreme. In future observations of this field should be scheduled in a manner that places the sidelobes away from Cygnus A. Observation details are shown in Table B.1. Fig. B.7 shows the mosaics for the field, and Fig. B.8 shows the `field_qa.py` output. The distribution of α for the FIELD4 mosaics has $\mu_{\alpha,0.0} = -0.91 \pm 0.20$ and $\mu_{\alpha,+2.0} = -0.91 \pm 0.20$ cf. $\mu_{\alpha,\mathrm{GLEAM}} = -0.88 \pm 0.18$. Despite the errors visible in the images, the QA work suggests science with bright sources would be unaffected. The main result from errors is a limit on dynamic range which is especially problematic for low surface brightness, diffuse cluster emission.

B.1.5. *FIELD5*

FIELD5 was observed to cover a single cluster, Abell 1127, and is described in more detail in Duchesne et al. (2020, see Chapter 5). Due to ionospheric conditions and RFI in the 185 MHz band on one of the observing nights, this field has been supplemented with GLEAM-X data covering the same region, which roughly doubles the observing time for Abell 1127. As FIELD5 and the GLEAM-X observations are at high declination (centred $\delta_{\mathrm{J2000}} > +10°$), all observations are off-zenith, with elevation ranging from 40° to 55°. This low elevation exacerbates the ionospheric issues. Table B.1 shows the observation information, Fig. B.9 shows the FIELD5 mosaics, and Fig. B.10 shows the `field_qa.py` output. The distribution of α for the FIELD5 mosaics has $\mu_{\alpha,0.0} =$

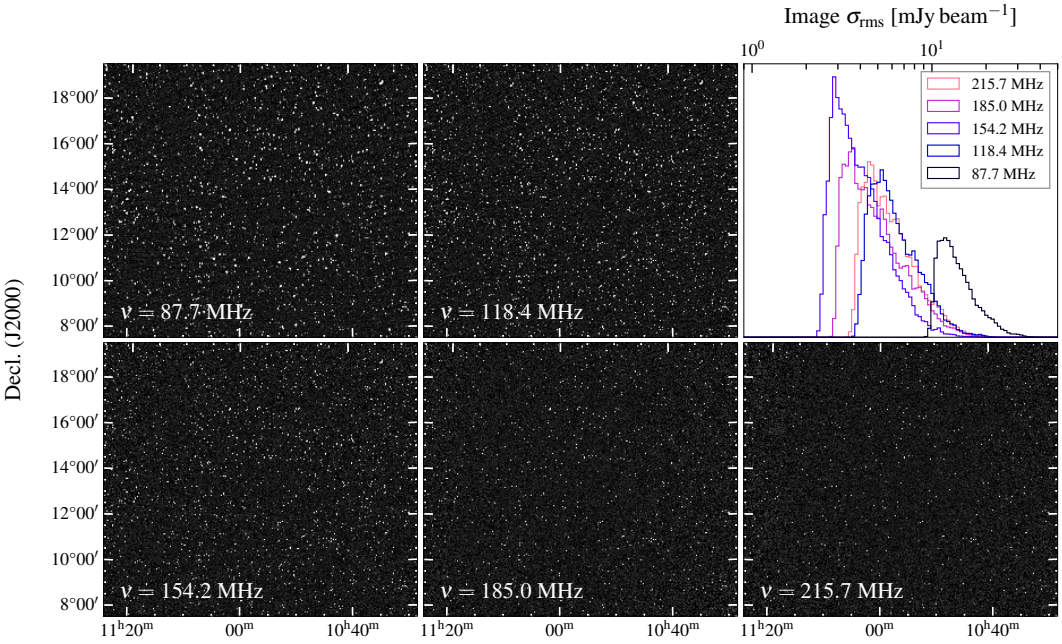

(i) Robust 0.0.

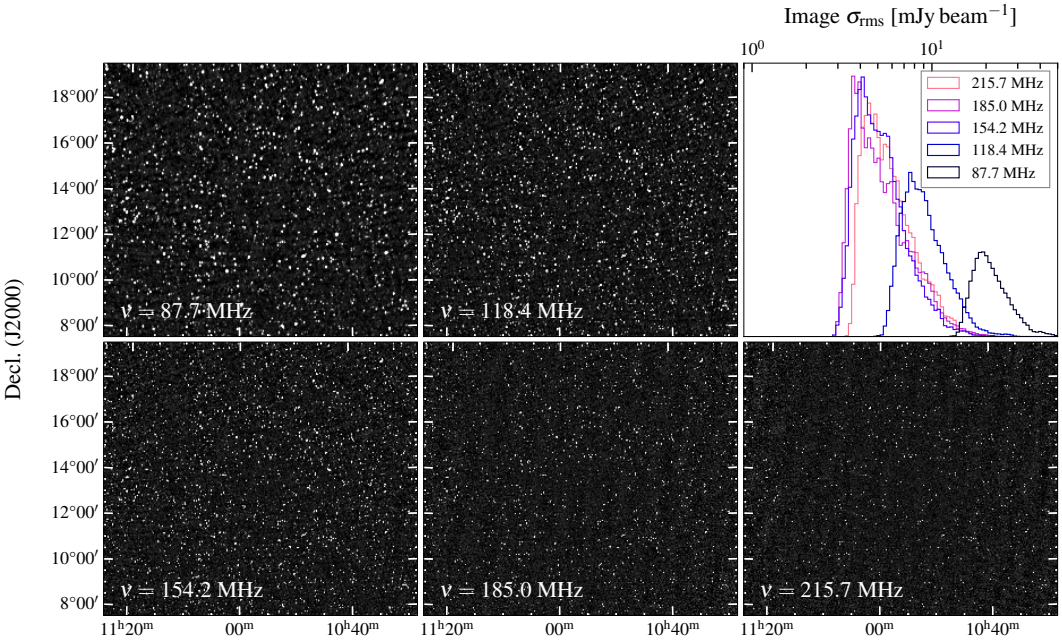

(ii) Robust +1.0.

Figure B.9. FIELD5 robust 0.0 and +1.0 mosaics.

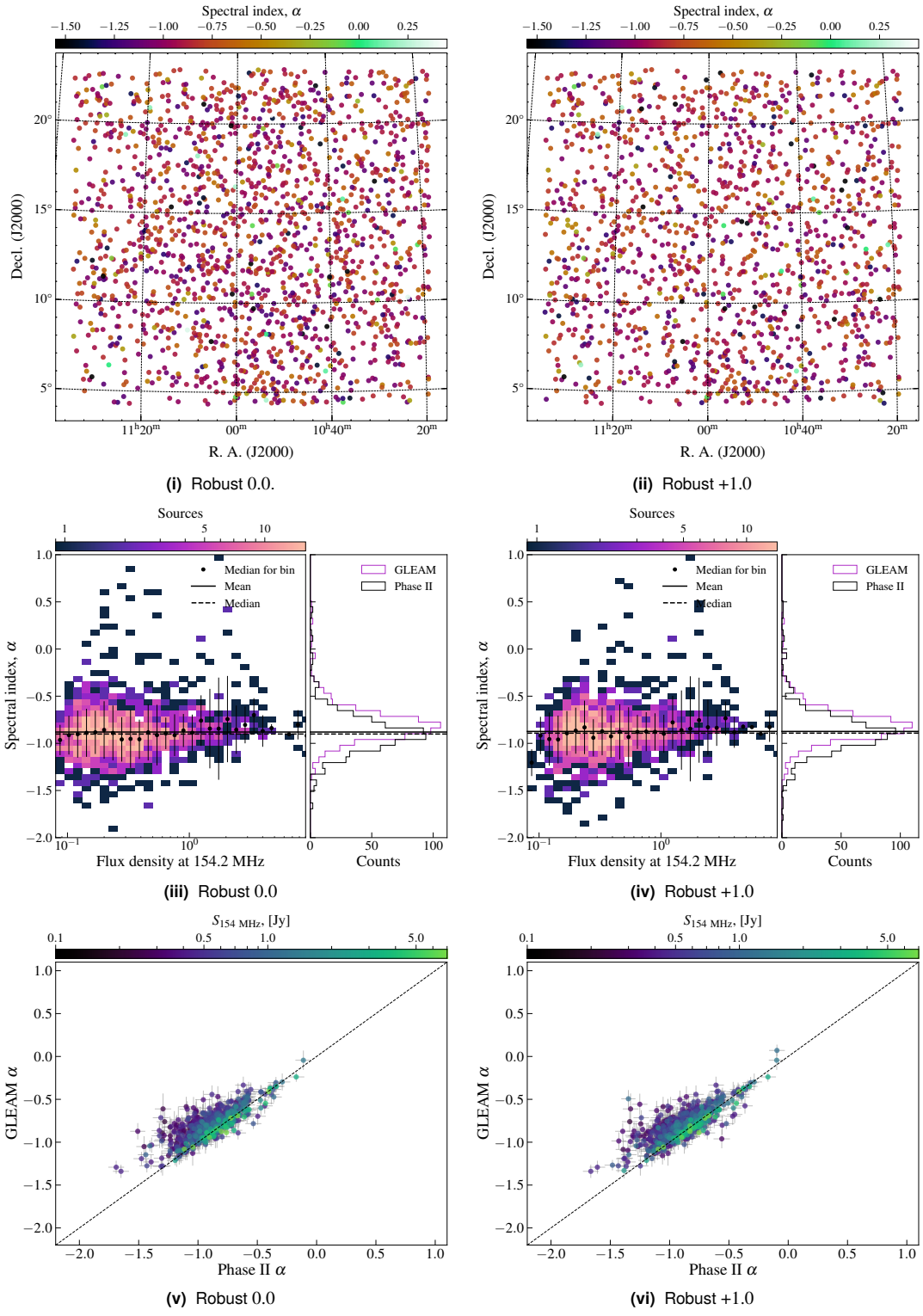

Figure B.10. `FIELD5`: output from `field_qa.py` showing the general spectral properties of sources across the robust 0.0 and +1.0 mosaics.

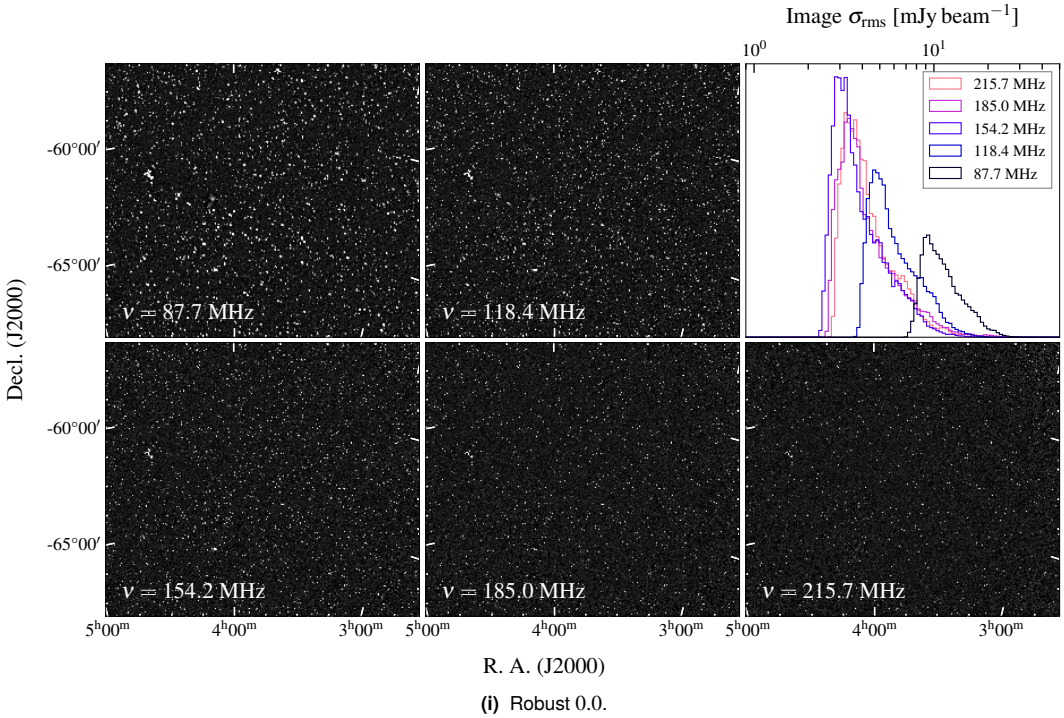

(i) Robust 0.0.

Figure B.11. FIELD10 robust 0.0 mosaics. As noted in Fig. B.15, FIELD10 shares snapshots from FIELD7 due to the significant overlap between the fields, and the robust +2.0 image is a single large image for both fields.

-0.90 ± 0.20 and $\mu_{\alpha,+2.0} = -0.89 \pm 0.21$ cf. $\mu_{\alpha,\rm GLEAM} = -0.80 \pm 0.17$.

B.1.6. *FIELD6*

FIELD6 is a region that sits between Pictor A, Fornax A, and the Small Magellanic Cloud. Despite these bright radio sources, the field itself is generally quiet, and the aforementioned "A-team" sources were subtracted without trouble where appropriate. The largest cause of issue for these observations was the variable ionosphere. Table B.1 lists some observation details for the two observing nights. Fig. B.14 shows the QA output from `field_qa.py` and Fig. B.13(i) shows the robust +0.0 mosaics and Fig. B.13(ii) shows the robust +2.0 mosaics, both with basic noise properties. The distribution of α for the FIELD5 mosaics has $\mu_{\alpha,0.0} = -0.86 \pm 0.21$ and $\mu_{\alpha,+2.0} = -0.83 \pm 0.26$ cf. $\mu_{\alpha,\rm GLEAM} = -0.80 \pm 0.18$.

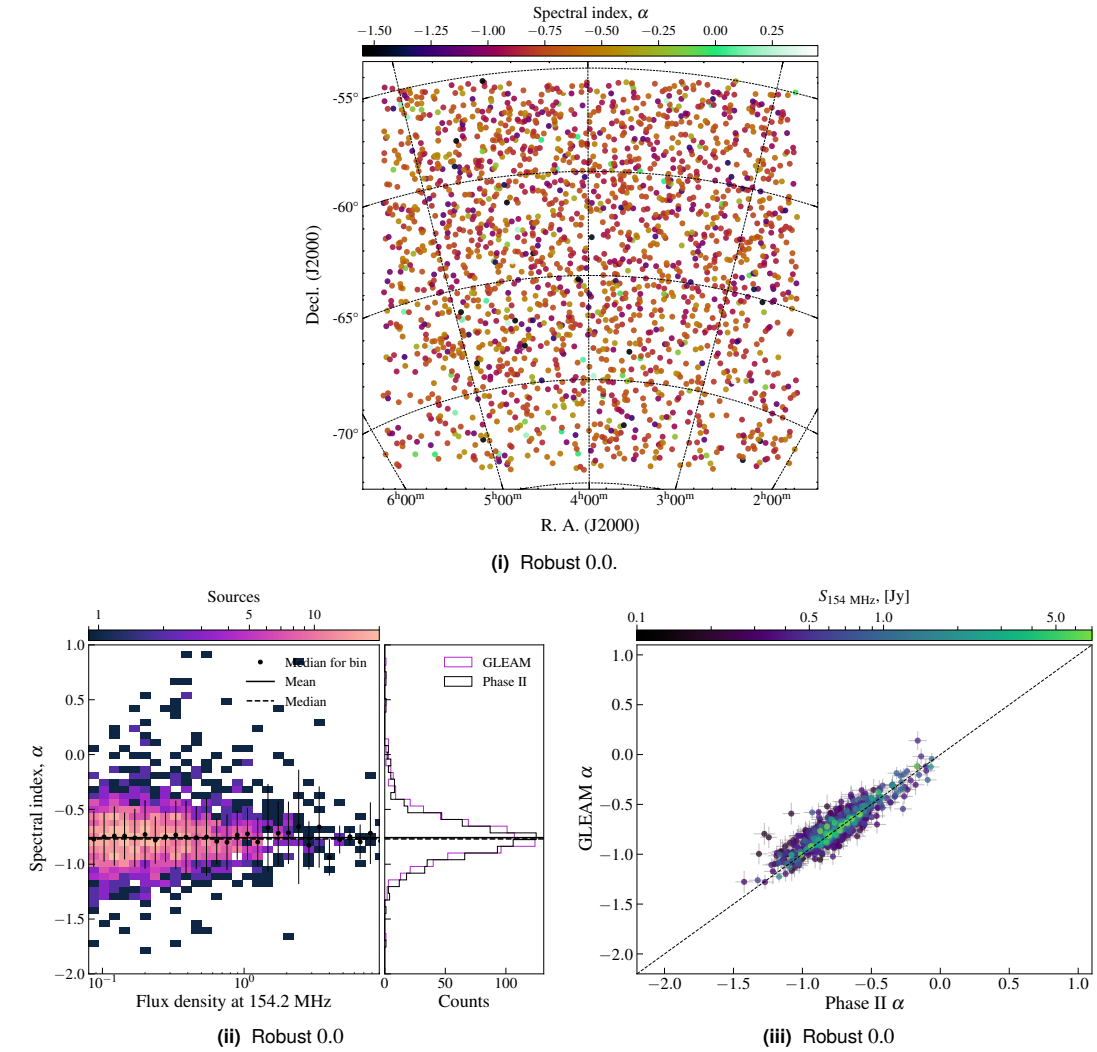

(i) Robust 0.0.

(ii) Robust 0.0

(iii) Robust 0.0

Figure B.12. `FIELD10`: output from `field_qa.py` showing the general spectral properties of sources across the robust 0.0 mosaics.

B.1.7. *FIELD7 and FIELD10*

`FIELD7` and `FIELD10` are complementary in that they cover a very similar region of the sky, offset by only ∼ 10 degrees. Additionally, these are somewhat nearby `FIELD6`. Originally, only `FIELD7` was planned to be observed but with Director's Discretionary Time (DDT) we were able to further observe this region, though with a pointing more closely centered on the cluster Abell 3266 and the large-scale remnant radio emission associated with NGC 1534 [3]. This field is particularly complex for

[3]Though note this source is sufficiently large with sufficiently low surface brightness that the emission begins to completely disappear beyond ∼ 154 MHz.

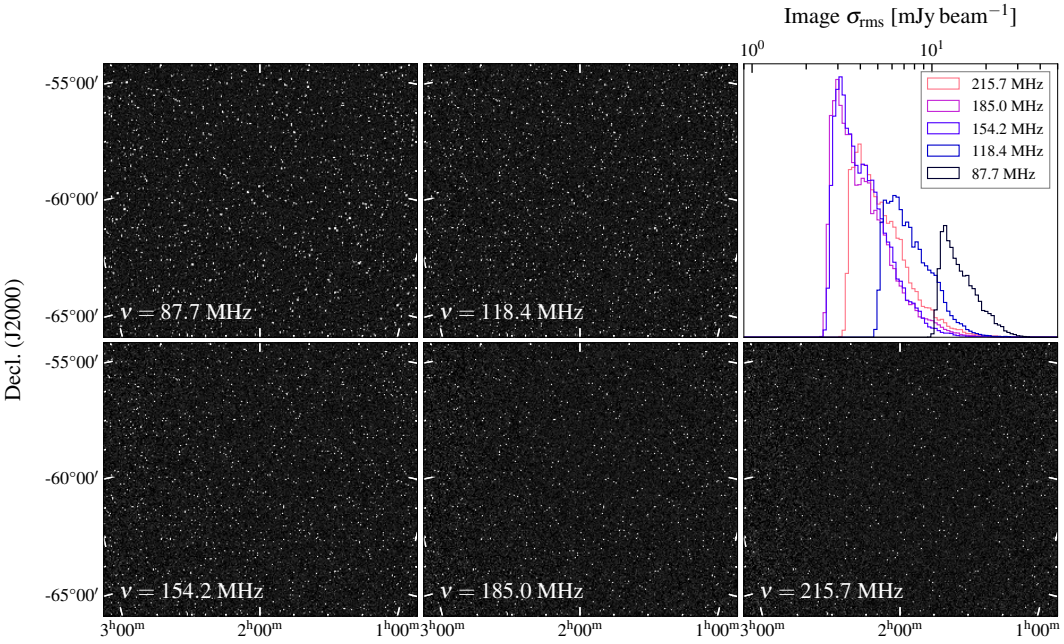

(i) Robust 0.0.

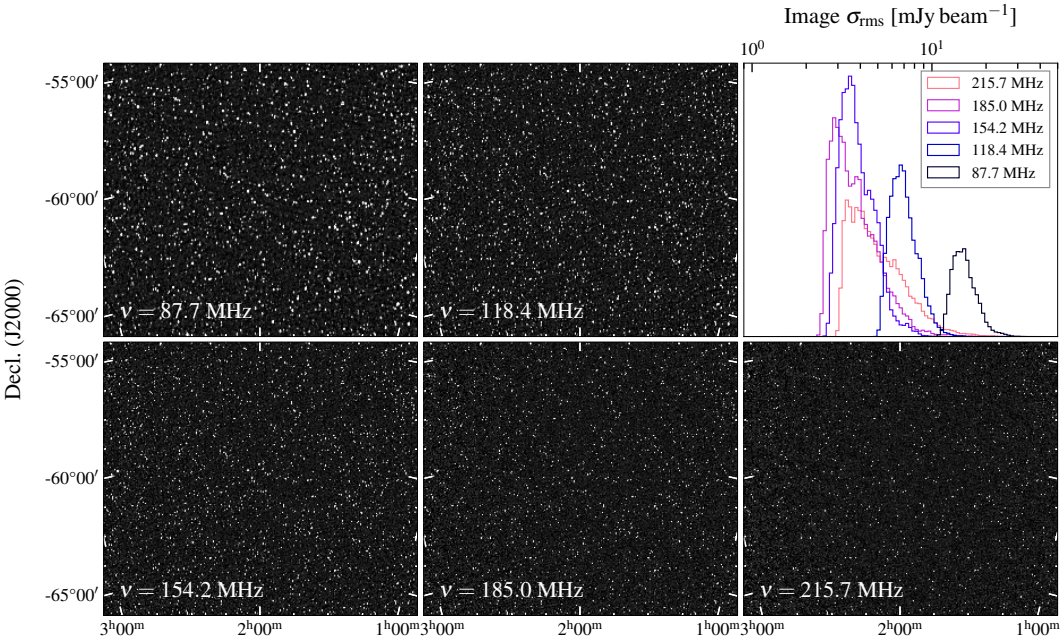

(ii) Robust +2.0.

Figure B.13. FIELD6 robust 0.0 and +2.0 mosaics.

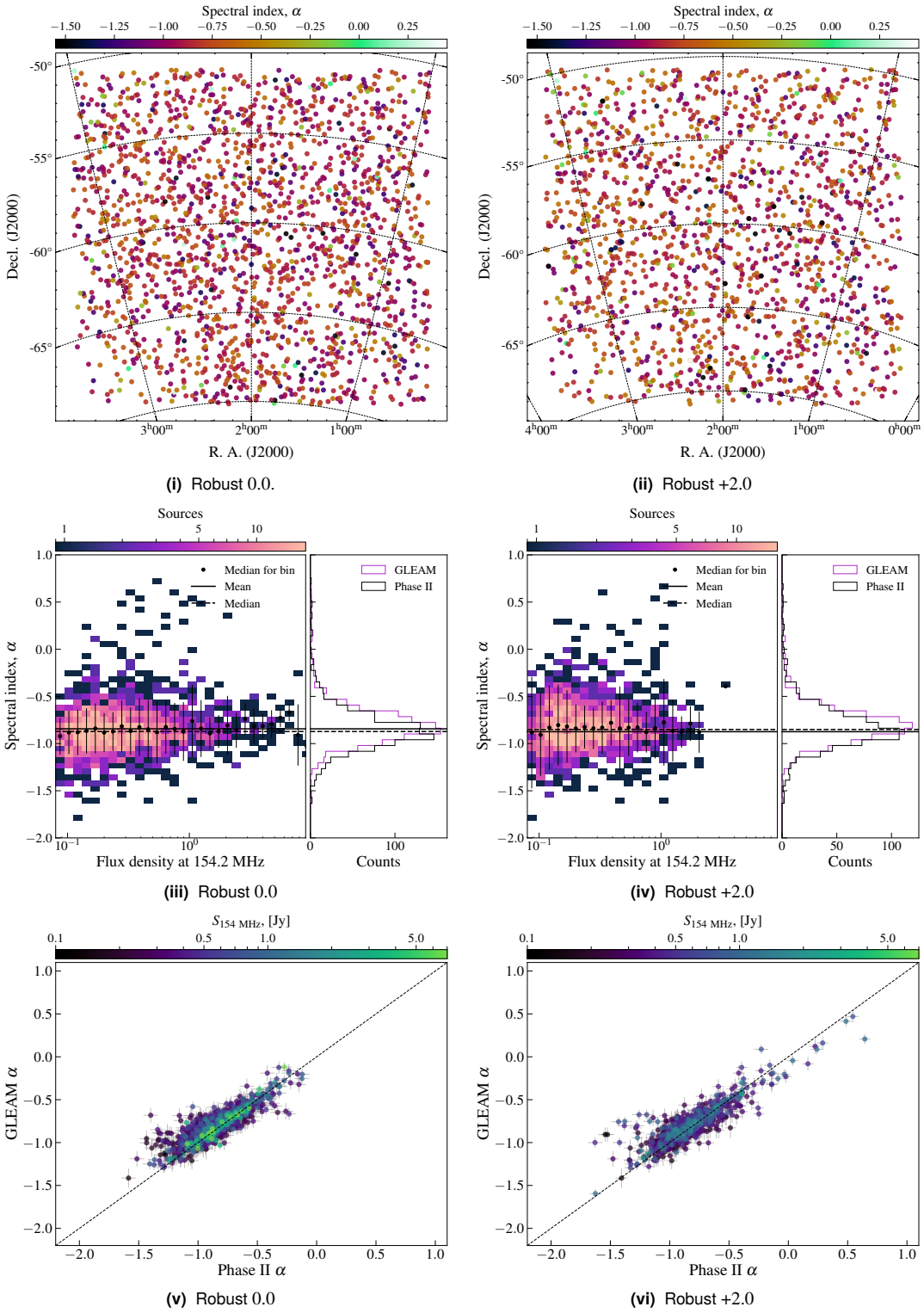

Figure B.14. `FIELD6`: output from `field_qa.py` showing the general spectral properties of sources across the robust 0.0 and +2.0 mosaics.

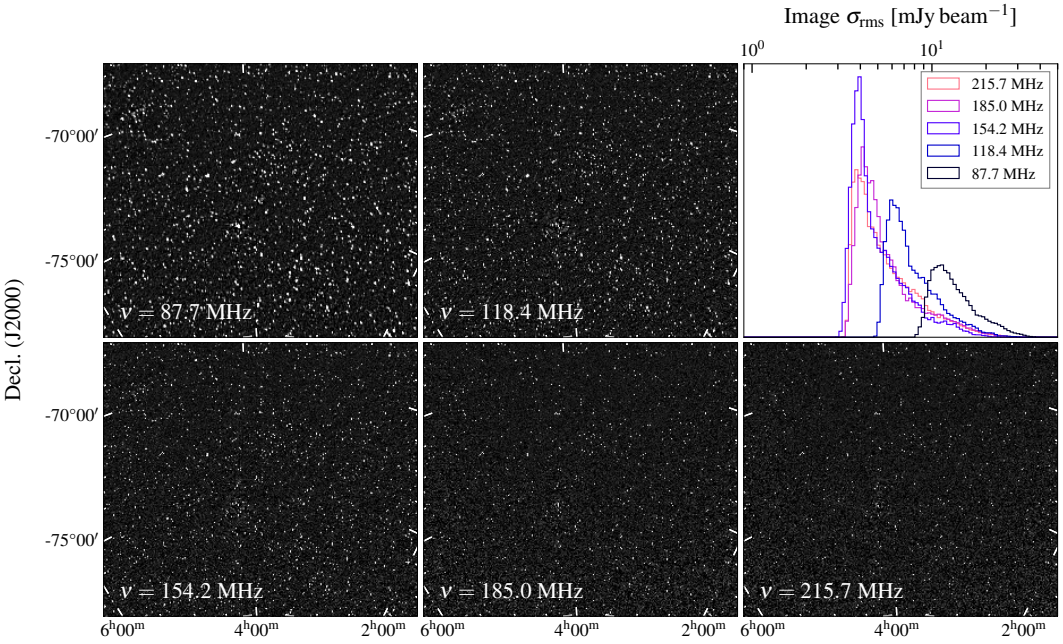

(i) Robust +0.5.

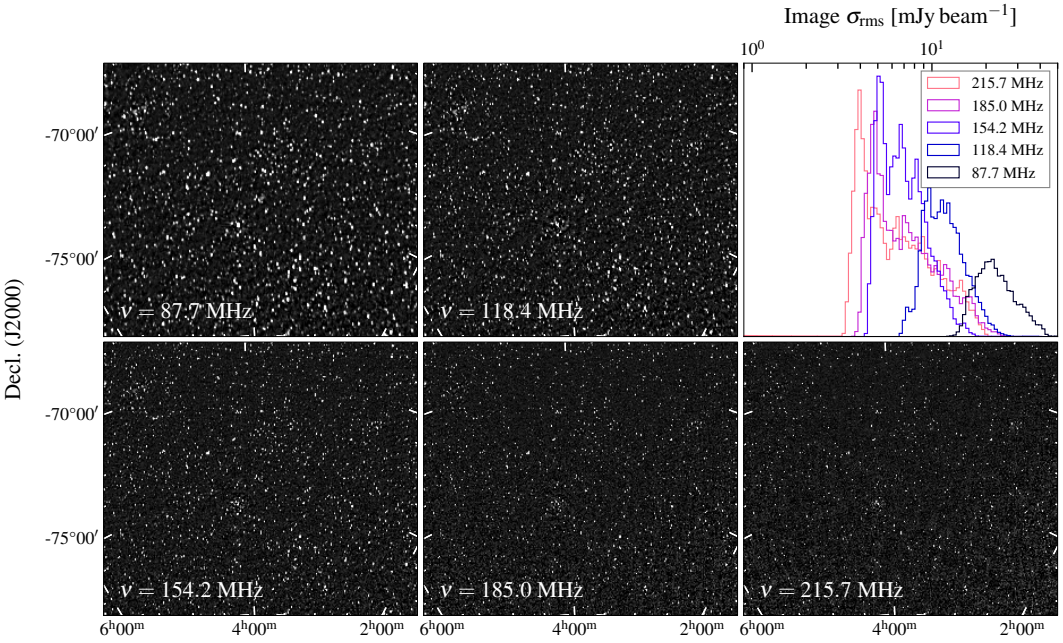

(ii) Robust +2.0.

Figure B.15. `FIELD7` robust +0.5 and +2.0 mosaics. Note that `FIELD7` and `FIELD10` have significant overlap so snapshots from each field are included in the mosaicking/stacking process.

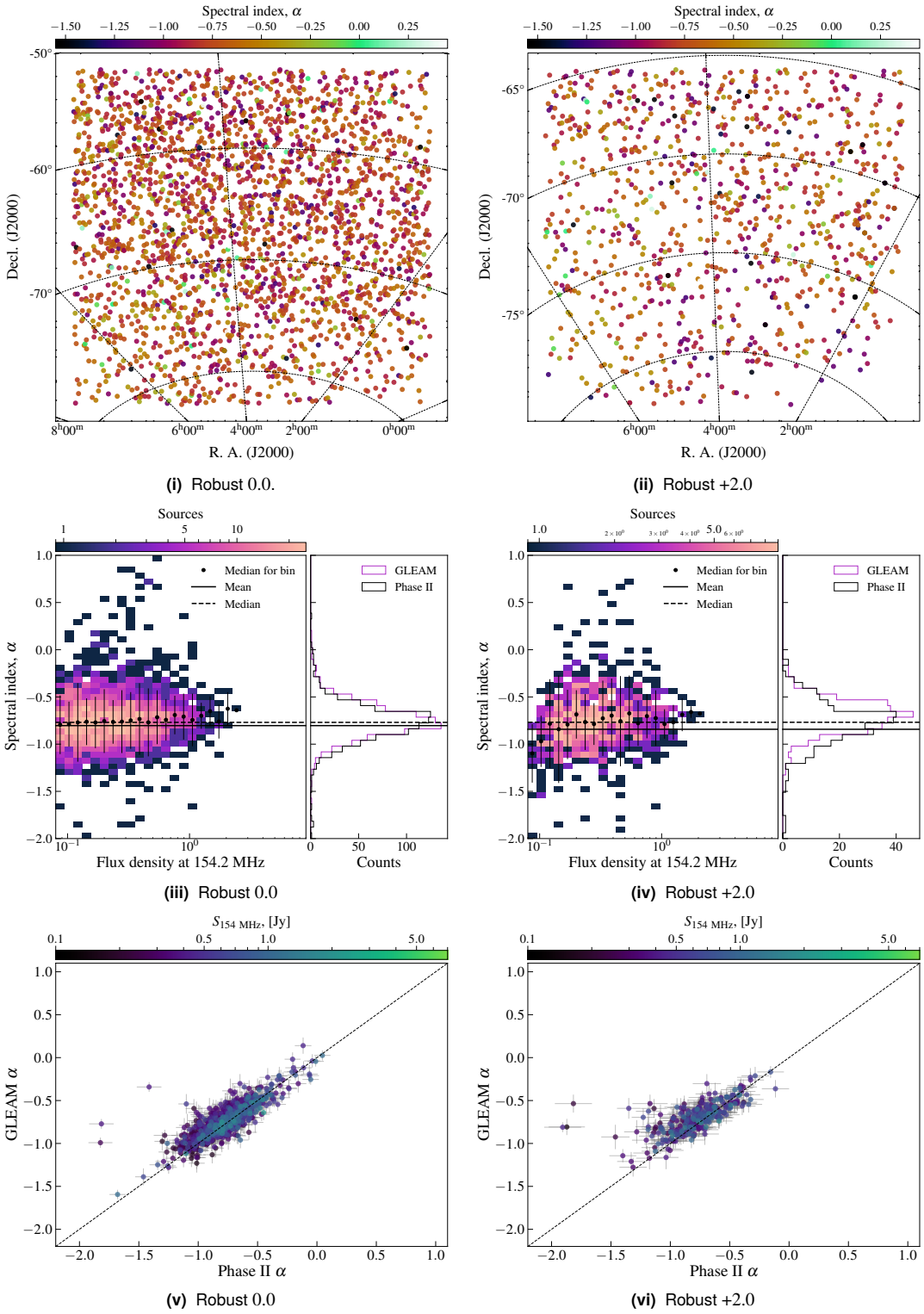

Figure B.16. `FIELD7`: output from `field_qa.py` showing the general spectral properties of sources across the robust +0.5 and +2.0 mosaics.

a number of reasons: (1) a number of large extended emission sources are present, including the Large and Small Magellanic Clouds, and Fornax A, Pictor A, and some PKS sources (e.g. those modelled in Appendix A.2.2) (2) low-elevation pointings, and (3) the south celestial pole, where the GLEAM EGC has a large flux density uncertainty. When generating mosaics, all snapshots are included for `FIELD10` and `FIELD7`, though individual mosaics are made centered on each field. Individual observation details are shown in Table B.1.

Fig. B.15(ii) shows the robust +2.0 mosaics for `FIELD7` and `FIELD10`, respectively, Fig. B.15(i) shows the robust +0.5 mosaics for `FIELD7` and Fig. B.11(i) shows the robust 0.0 mosaics for `FIELD10`. Fig. B.16 and Fig. B.12 show the spectral QA plots for each weighting of the two fields.

B.1.8. *FIELD8*

`FIELD8` presented a number of challenges: (1) Galactic Plane in the primary beam sidelobe for the higher frequencies (which was directly subtracted in a similar manner as described in Appendix A.2.3), (2) specific bright off-axis sources, e.g. Pictor A, and (3) difficulty in of calibration certain snapshots, likely due to the aforementioned bright sources combined with additional RFI. Observation details are shown in Table B.1. Fig. B.17 shows the resultant mosaics. The primary target for this field is Abell 3404, which forms part of Chapter 4 (Duchesne et al., 2021c), and Abell 3399, but these data have also been used for the project to observe the cluster pair, Abell 3391-95 (Brüggen et al., 2021) in an attempt to directly observe a radio synchrotron bridge between the clusters. No bridge is seen in the MWA-2 data or the deep ASKAP data, though limits are placed on the emission. Fig. B.17 shows the robust 0.0 and +2.0 mosaics for `FIELD8` and Fig. B.18 shows the `field_qa.py` output. The distribution of α for the `FIELD8` mosaics has $\mu_{\alpha,0.0} = -0.90 \pm 0.19$ and $\mu_{\alpha,+2.0} = -0.89 \pm 0.22$ cf. $\mu_{\alpha,\mathrm{GLEAM}} = -0.87 \pm 0.19$.

B.1.9. *FIELD9*

`FIELD9` was observed as part of a DDT request and all nights of observation showed fairly minimal ionospheric activity. This, in combination with a strong sky model at all

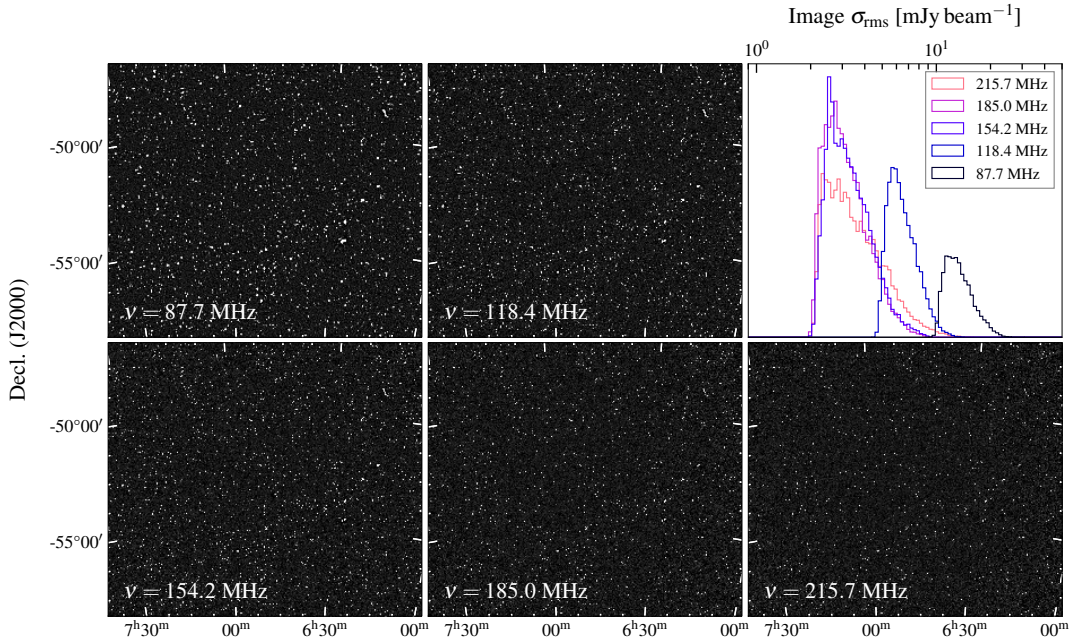

(i) Robust 0.0.

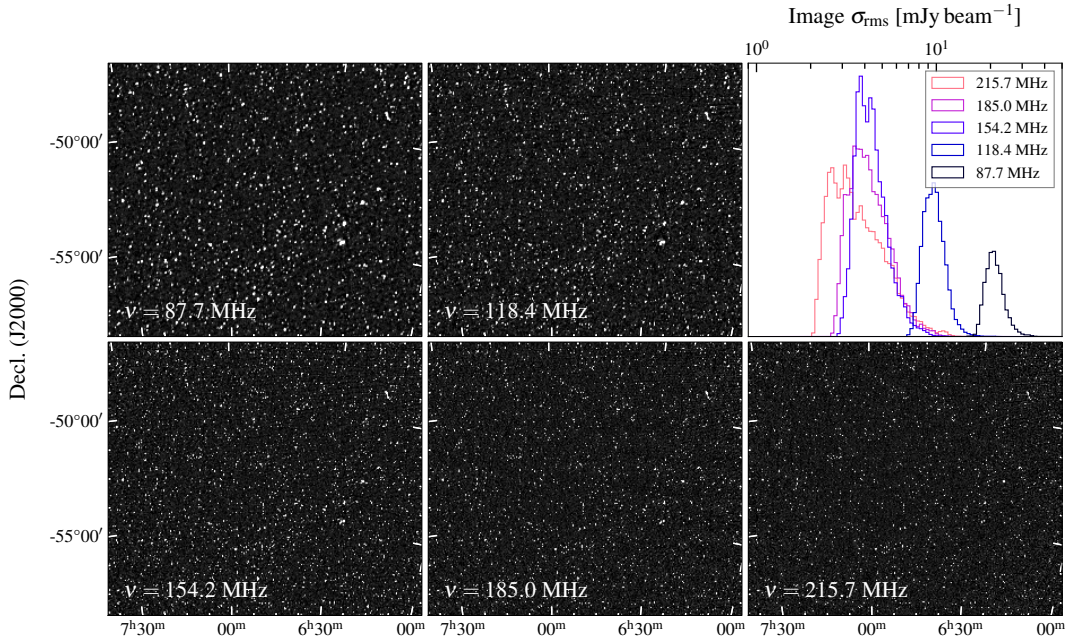

(ii) Robust +2.0.

Figure B.17. FIELD8 robust 0.0 and +2.0 mosaics.

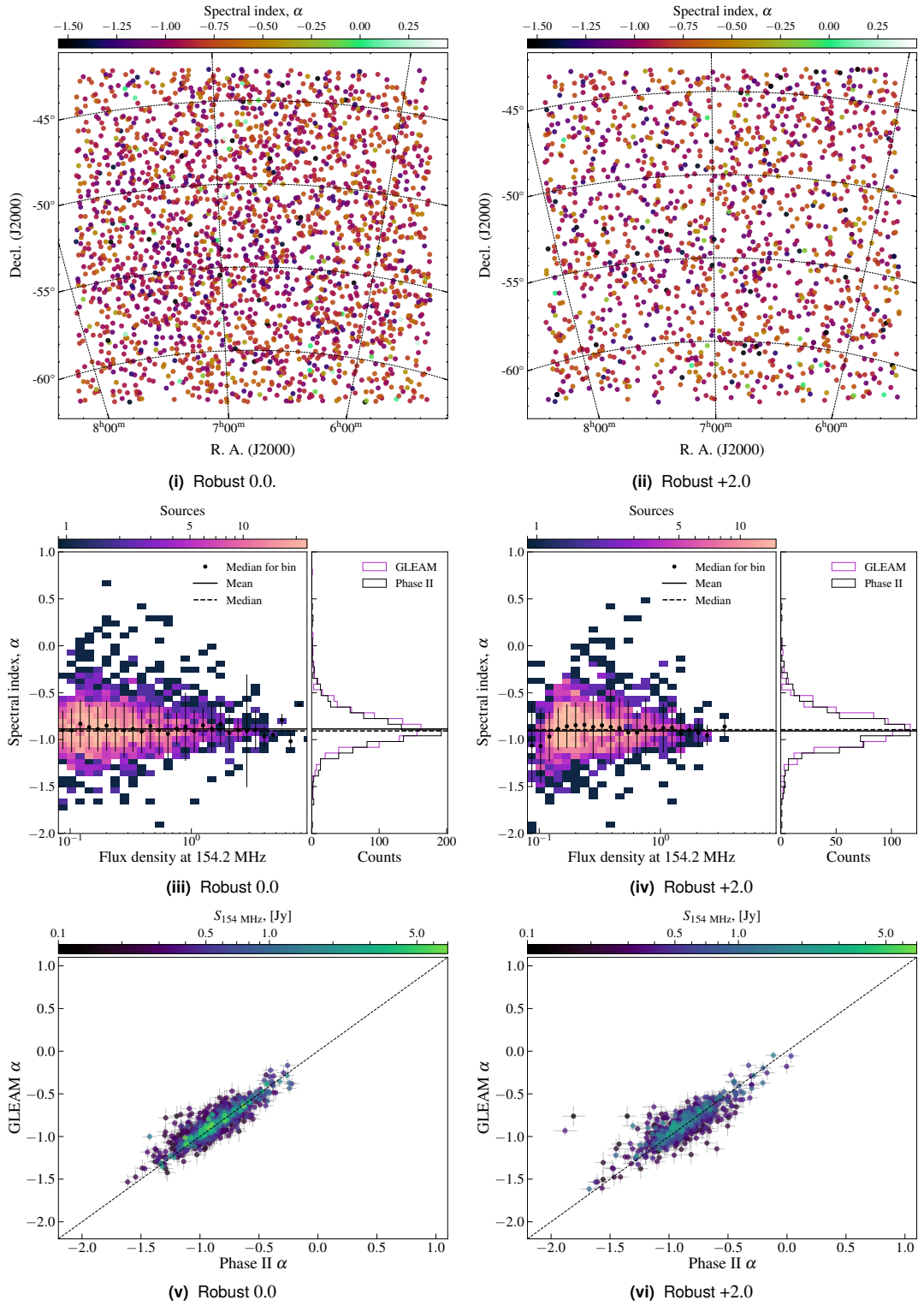

Figure B.18. `FIELD8`: output from `field_qa.py` showing the general spectral properties of sources across the robust 0.0 and +2.0 mosaics.

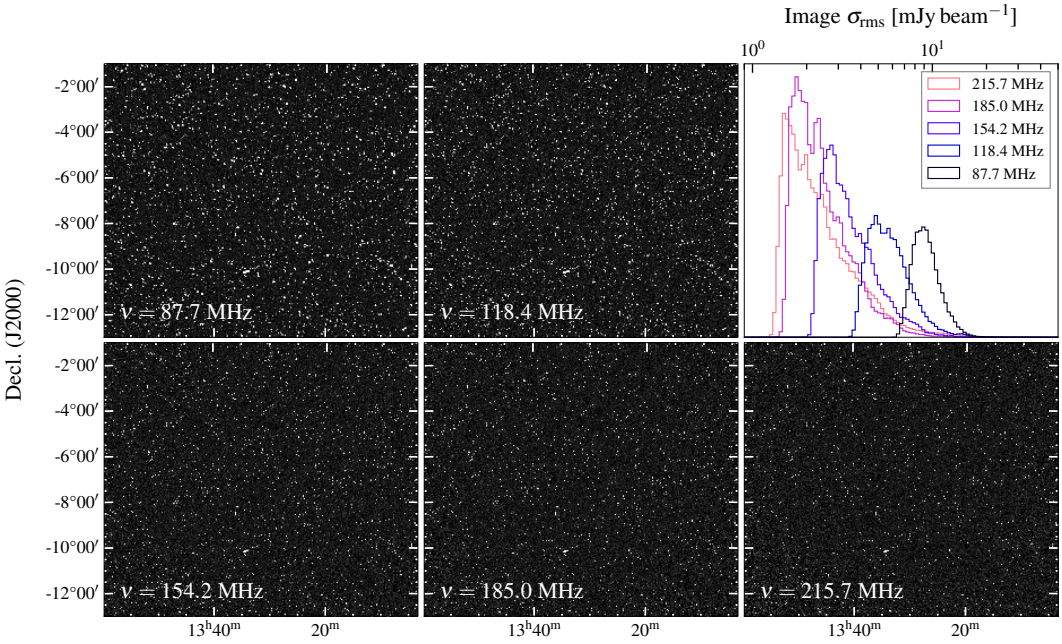

(i) Robust 0.0.

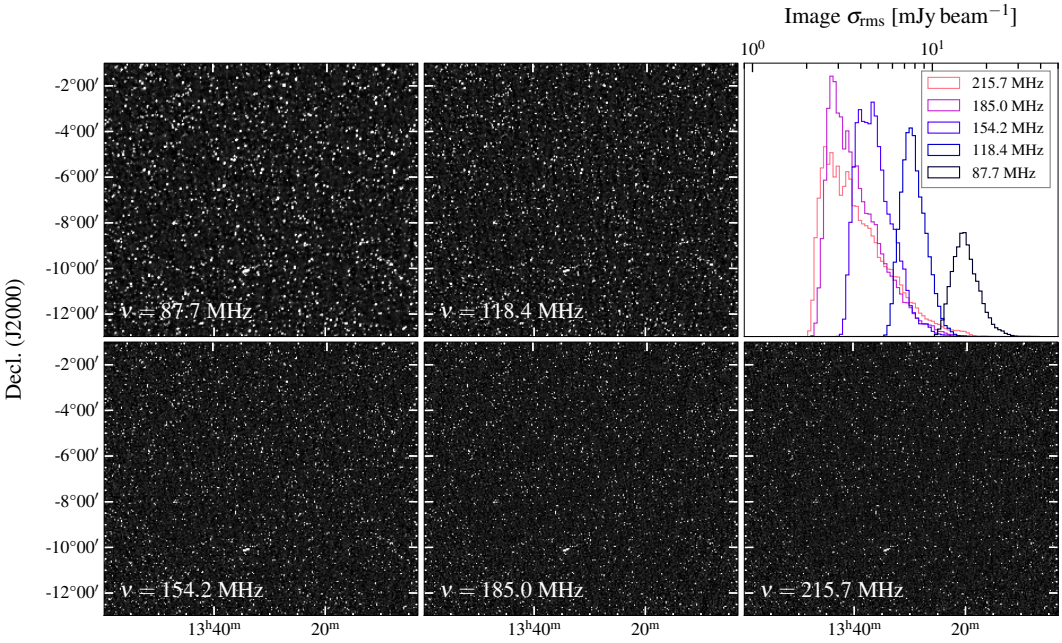

(ii) Robust +2.0.

Figure B.19. FIELD9 robust 0.0 and +2.0 mosaics.

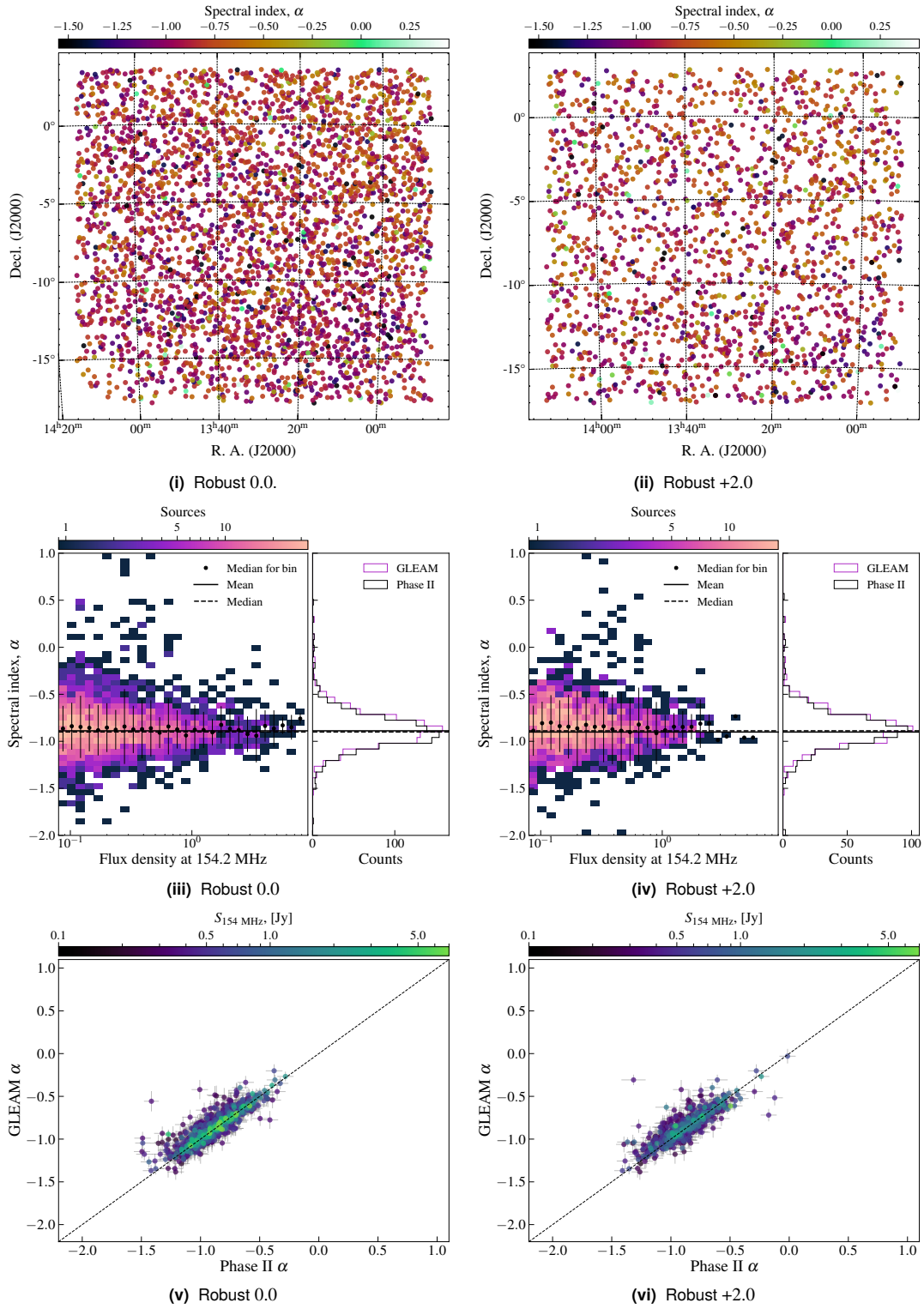

Figure B.20. `FIELD9`: output from `field_qa.py` showing the general spectral properties of sources across the robust 0.0 and +2.0 mosaics.

frequencies resulted in most data being able to be calibrated and imaged. Virgo A features towards the NW of this field (present within the images at the lower frequencies). While the model of Virgo A is sufficient for a snapshot, the combination of complex source structure, multiple intrinsic spectral components, and its location at the edge of the beam (especially in the higher frequency data), the residual errors limited the dynamic range of these mosaics. Source subtraction naturally helped where Virgo A was not within the image. Observation details are shown in Table B.1. Fig. B.19 shows the robust 0.0 and +2.0 mosaics for `FIELD9` and Fig. B.20 shows the `field_qa.py` output. The distribution of α for the `FIELD9` mosaics has $\mu_{\alpha,0.0} = -0.90 \pm 0.17$ and $\mu_{\alpha,+2.0} = -0.88 \pm 0.19$ cf. $\mu_{\alpha,\mathrm{GLEAM}} = -0.86 \pm 0.17$.

B.1.10. *FIELD11*

`FIELD11` is not part of the MWA project G0045, but is a collection of snapshot images taken from the GLEAM-X survey. The main target in this field is the GRG ESO 422−G028, which is not part of this work. Additionally, a number of clusters with diffuse cluster sources are within the field, including Abell 548b (see the MWA Phase I follow-up of this cluster by George et al., 2017), Abell 3365 (a double-relic system reported by van Weeren et al., 2011b), among other sources along with some newly detected sources. Fig. B.21 shows the robust 0.0 and +1.0 mosaics for `FIELD11` and Fig. B.22 shows the `field_qa.py` output. The distribution of α for the `FIELD11` mosaics has $\mu_{\alpha,0.0} = -0.84 \pm 0.18$ and $\mu_{\alpha,+1.0} = -0.84 \pm 0.21$ cf. $\mu_{\alpha,\mathrm{GLEAM}} = -0.82 \pm 0.17$.

B.2. Ratios of CLEAN and 'dirty' flux densities

As per Appendix A.9, we obtain ratios of $S_{\mathrm{CLEAN}}/S_{\mathrm{dirty}}$ for all mosaics where extended flux density measurements are required [4]. The measured ratios of $S_{\mathrm{CLEAN}}/S_{\mathrm{dirty}}$ are shown in Fig. 6.23(i)–(x) for the mosaics where integrated flux densities are measured via pixel sum. Note these factors are chosen based on the deconvolved largest-angular scale of a particular source, and the factor is only applied to the 'dirty' component of the

[4]Note this is not done for `FIELD5` as at the time a simple offset was calculated to correct, in part, for this effect.

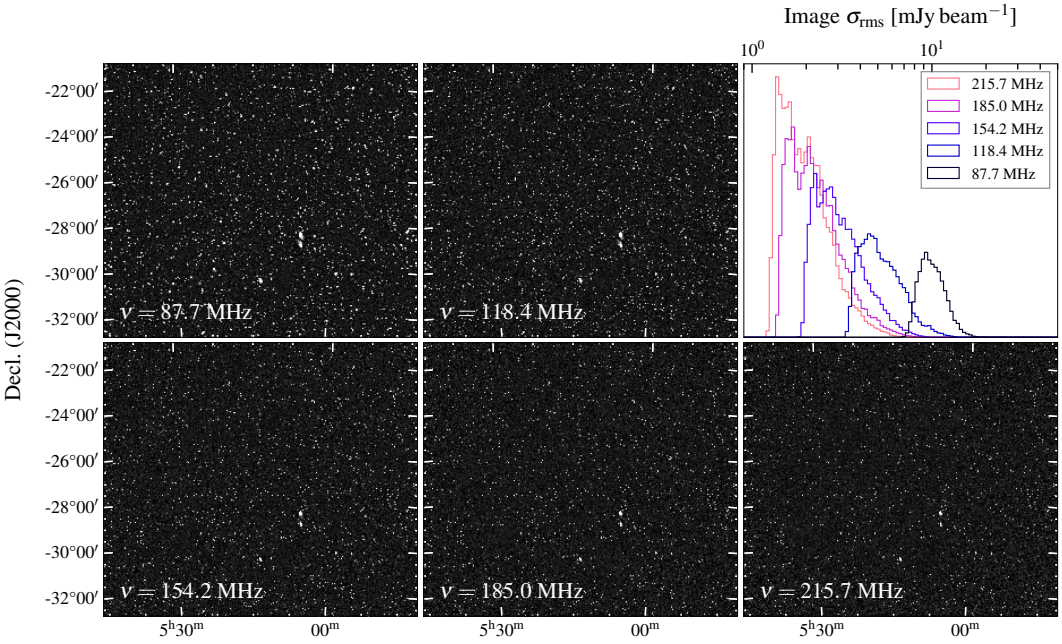

(i) Robust 0.0.

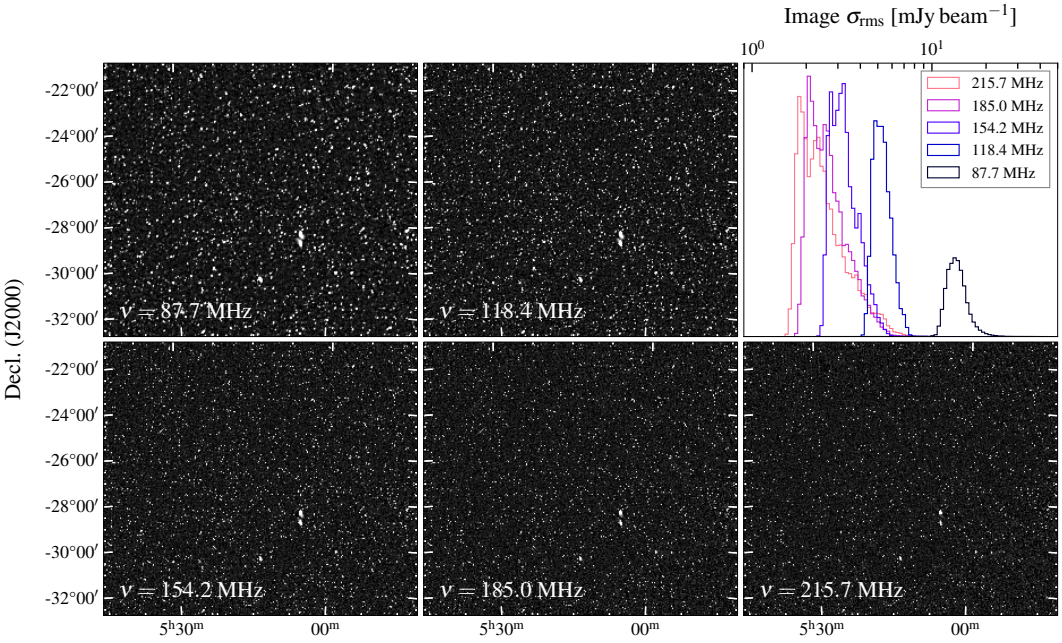

(ii) Robust +1.0.

Figure B.21. `FIELD11` robust 0.0 and +1.0 mosaics.

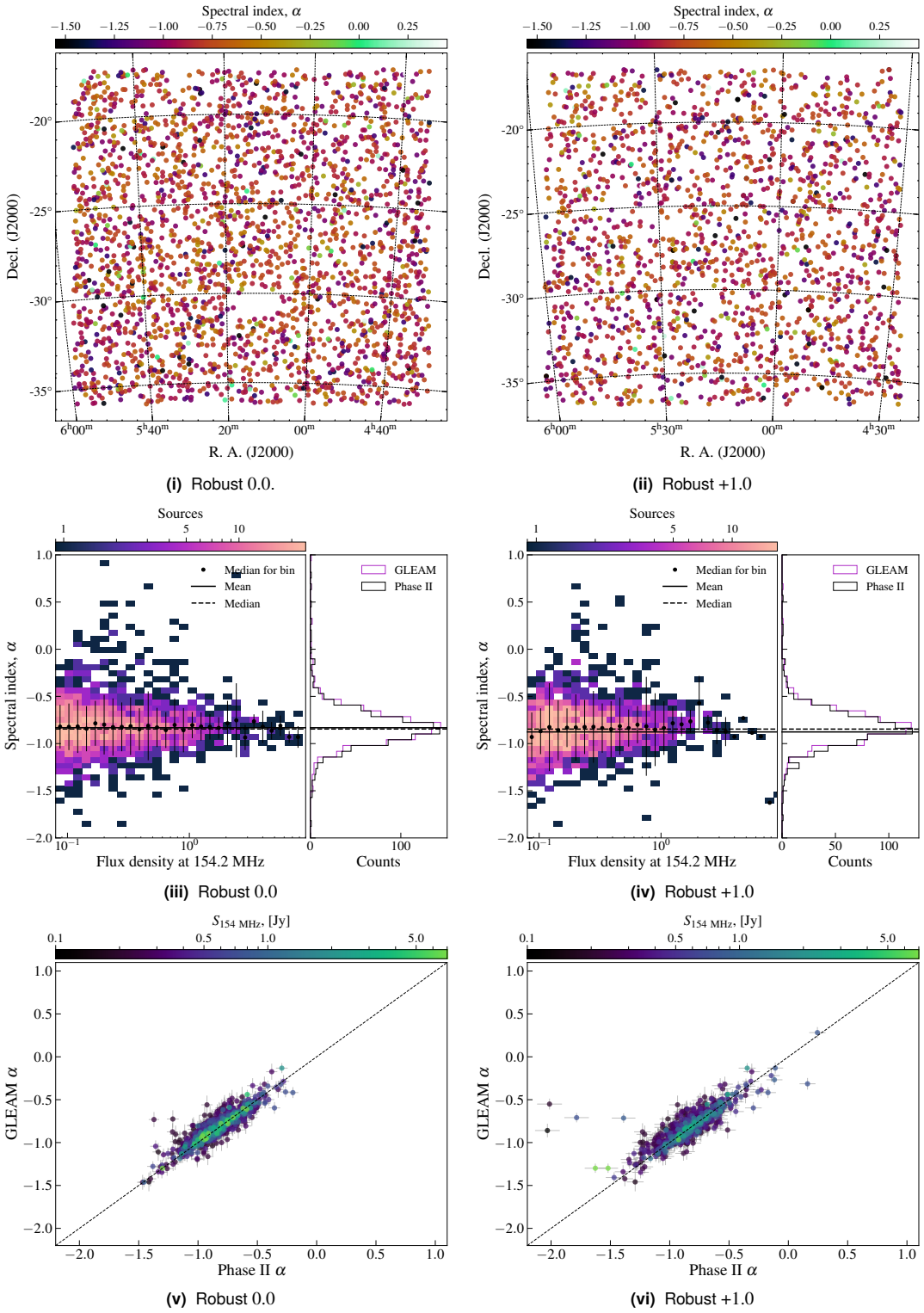

Figure B.22. `FIELD11`: output from `field_qa.py` showing the general spectral properties of sources across the robust 0.0 and +1.0 mosaics.

measurement. For most sources this is minimal, but for low-SNR sources this becomes significant (up to an additional $\sim$ 30 per cent). Of note from the presented mosaics is that in some mosaics 'dirty' flux density will be *higher*, counter to expectations from CLEANing—this suggests the Gaussian model PSF is perhaps significantly different from the true PSF for a given image. Additionally, given the combination of G0045 project observations with the drift-scan (i.e. fixed primary beam pointing) [5] observations used by the G0008 project, some mosaics have large variation in the $S_{\mathrm{dirty}}/S_{\mathrm{CLEAN}}$ factors. For this reason, we take an average over all snapshots, and use the standard deviation between snapshots to inform additional uncertainty on the measured 'dirty' signal.

[5] cf. a 'drift and shift' approach for observations as part of G0045. There is otherwise fundamentally nothing different about the G0008 observations.

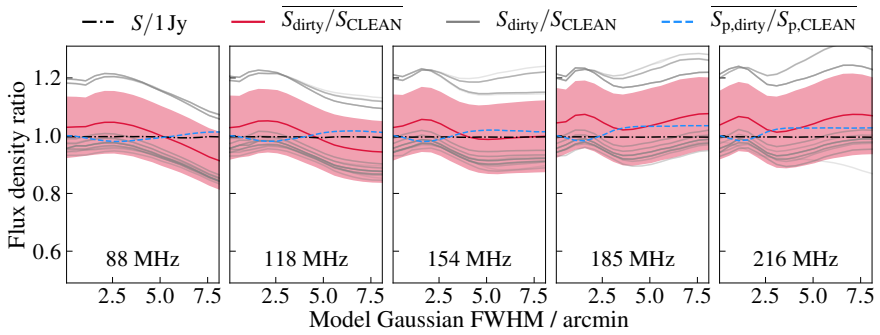

(i) `FIELD1` robust +2.0.

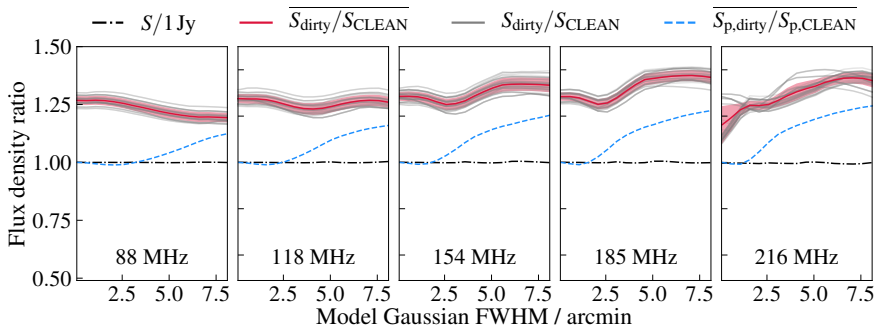

(ii) `FIELD2` robust +2.0.

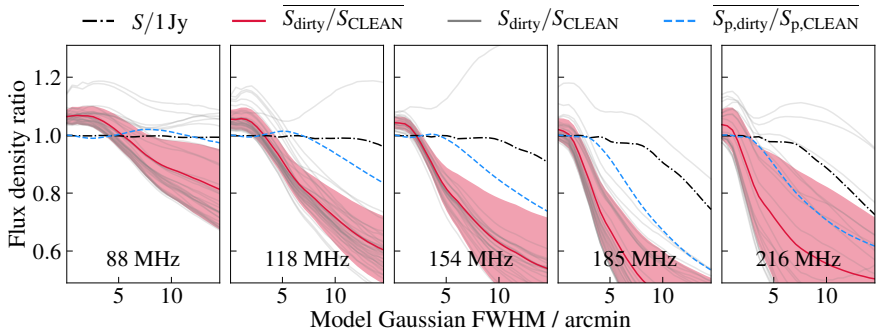

(iii) `FIELD3` robust +2.0.

Figure 6.23. Flux recovery and ratio of deconvolved ('CLEAN') to un-deconvolved ('dirty') integrated flux density for individual snapshots (grey lines). The angular scale on the abscissa corresponds to the FWHM of the simulated Gaussian sources (sampled every 30 arcsec). The mean profile, $\overline{S_{\mathrm{dirty}}/S_{\mathrm{CLEAN}}}$, is plotted with the standard deviation plotted as a red shaded region. The mean peak flux profile, $\overline{S_{\mathrm{p,dirty}}/S_{\mathrm{p,CLEAN}}}$, is also shown. Figures are adapted from Duchesne et al. (2021c,d).

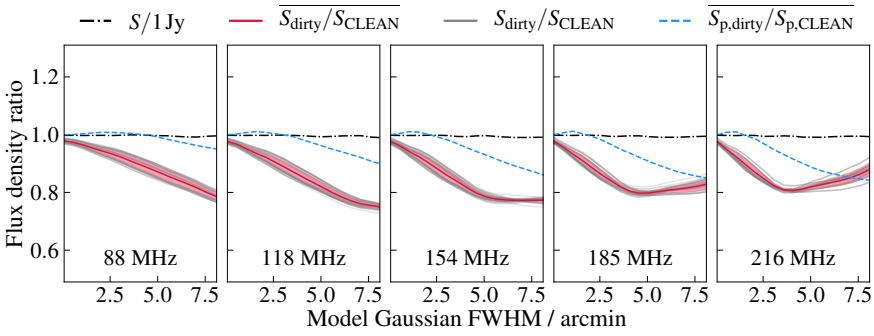

(iv) `FIELD5` robust +1.0.

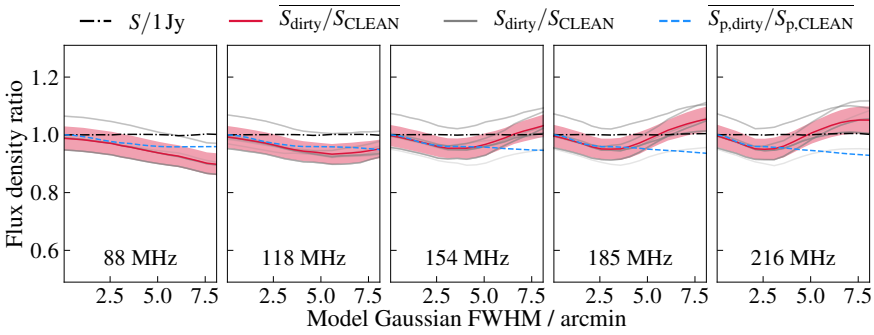

(v) `FIELD6` robust +2.0.

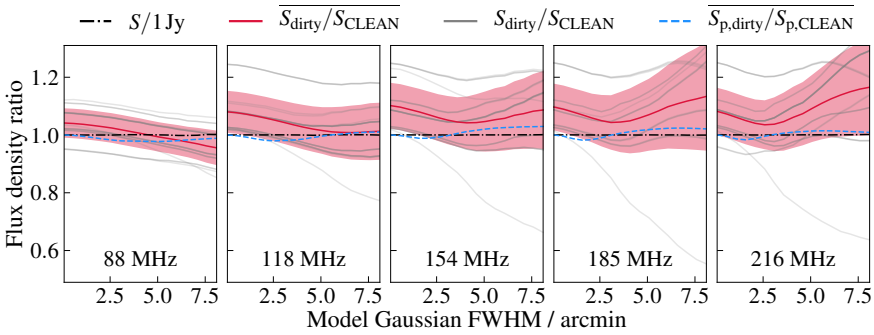

(vi) `FIELD7` robust +2.0.

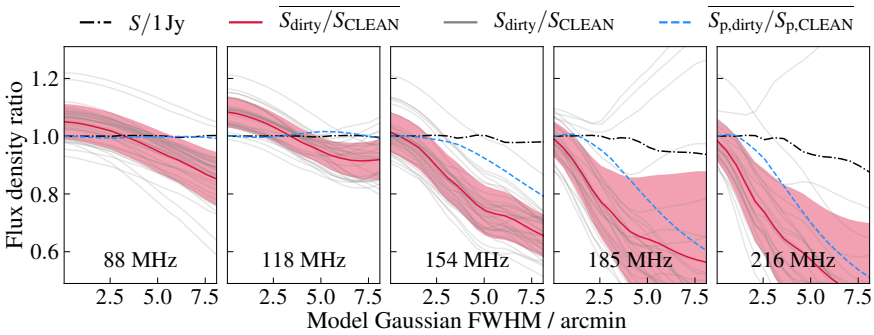

(vii) `FIELD8` robust +2.0.

Figure 6.23. *continued.*

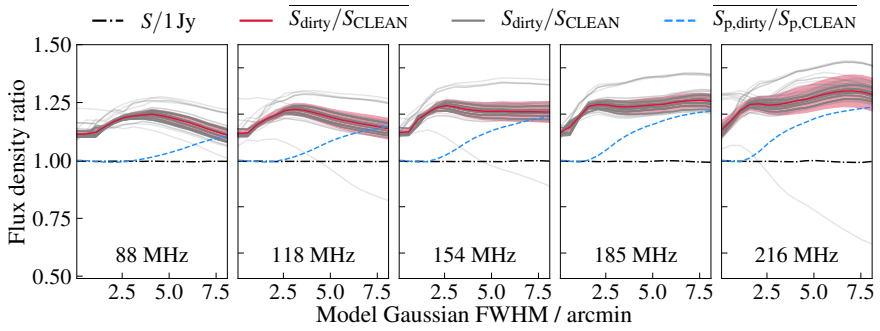

(viii) `FIELD9` robust +2.0.

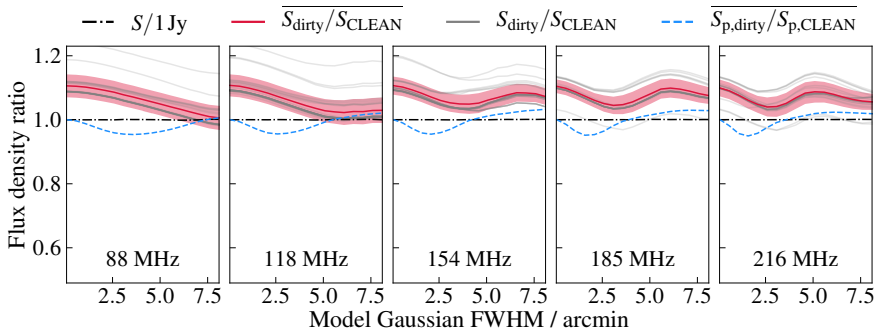

(ix) `FIELD10` robust +2.0.

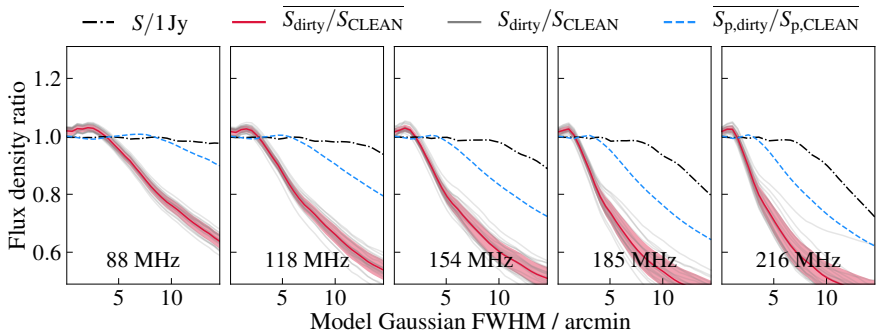

(x) `FIELD11` robust +1.0.

Figure 6.23. *continued.*

Funding, facility, and software acknowledgements

This research is supported by an Australian Government Research Training Program scholarship administered through Curtin University.

The Australia Telescope Compact Array is part of the Australia Telescope National Facility which is funded by the Australian Government for operation as a National Facility managed by CSIRO. This work includes archived data obtained through the Australia Telescope Online Archive (http://atoa.atnf.csiro.au/). The Australian SKA Pathfinder is part of the Australia Telescope National Facility which is managed by CSIRO. Operation of ASKAP is funded by the Australian Government with support from the National Collaborative Research Infrastructure Strategy. ASKAP uses the resources of the Pawsey Supercomputing Centre. Establishment of ASKAP, the Murchison Radio-astronomy Observatory and the Pawsey Supercomputing Centre are initiatives of the Australian Government, with support from the Government of Western Australia and the Science and Industry Endowment Fund. We acknowledge the Wajarri Yamatji people as the traditional owners of the Observatory site. Support for the operation of the MWA is provided by the Australian Government (NCRIS), under a contract to Curtin University administered by Astronomy Australia Limited. We acknowledge the Pawsey Supercomputing Centre which is supported by the Western Australian and Australian Governments. This research has made use of data obtained from the *Chandra* Data Archive and the *Chandra* Source Catalog, and software provided by the *Chandra* X-ray Center (CXC) in the application package CIAO. The National Radio Astronomy Observatory is a facility of the National Science Foundation operated under cooperative agreement by Associated Universities, Inc.

Funding for SDSS-III has been provided by the Alfred P. Sloan Foundation, the Participating Institutions, the National Science Foundation, and the U.S. Department

of Energy Office of Science. The SDSS-III web site is http://www.sdss3.org/. SDSS-III is managed by the Astrophysical Research Consortium for the Participating Institutions of the SDSS-III Collaboration including the University of Arizona, the Brazilian Participation Group, Brookhaven National Laboratory, Carnegie Mellon University, University of Florida, the French Participation Group, the German Participation Group, Harvard University, the Instituto de Astrofisica de Canarias, the Michigan State/Notre Dame/JINA Participation Group, Johns Hopkins University, Lawrence Berkeley National Laboratory, Max Planck Institute for Astrophysics, Max Planck Institute for Extraterrestrial Physics, New Mexico State University, New York University, Ohio State University, Pennsylvania State University, University of Portsmouth, Princeton University, the Spanish Participation Group, University of Tokyo, University of Utah, Vanderbilt University, University of Virginia, University of Washington, and Yale University.

This research has made use of the VizieR catalogue access tool, CDS, Strasbourg, France. The original description of the VizieR service was described in Ochsenbein et al. (2000). This research also made use of the NASA/IPAC Extragalactic Database (NED) which is operated by the Jet Propulsion Laboratory, California Institute of Technology, under contract with the National Aeronautics and Space Administration. The Digitized Sky Surveys were produced at the Space Telescope Science Institute under U.S. Government grant NAG W-2166. The images of these surveys are based on photographic data obtained using the Oschin Schmidt Telescope on Palomar Mountain and the UK Schmidt Telescope. The plates were processed into the present compressed digital form with the permission of these institutions.

This research made use of a number of `python` packages: `aplpy` (Robitaille & Bressert, 2012), `astropy` (Astropy Collaboration et al., 2013; Price-Whelan et al., 2018), `matplotlib` (Hunter, 2007), `numpy` (van der Walt et al., 2011), `scipy` (Jones et al., 2001), and `cmasher` (van der Velden, 2020). This work makes use of the `cubehelix` family of colourmaps (Green, 2011).

This project used public archival data from the Dark Energy Survey (DES). Funding for the DES Projects has been provided by the U.S. Department of Energy, the U.S. National Science Foundation, the Ministry of Science and Education of Spain, the Science

and Technology FacilitiesCouncil of the United Kingdom, the Higher Education Funding Council for England, the National Center for Supercomputing Applications at the University of Illinois at Urbana-Champaign, the Kavli Institute of Cosmological Physics at the University of Chicago, the Center for Cosmology and Astro-Particle Physics at the Ohio State University, the Mitchell Institute for Fundamental Physics and Astronomy at Texas A&M University, Financiadora de Estudos e Projetos, Fundação Carlos Chagas Filho de Amparo à Pesquisa do Estado do Rio de Janeiro, Conselho Nacional de Desenvolvimento Científico e Tecnológico and the Ministério da Ciência, Tecnologia e Inovação, the Deutsche Forschungsgemeinschaft, and the Collaborating Institutions in the Dark Energy Survey. The Collaborating Institutions are Argonne National Laboratory, the University of California at Santa Cruz, the University of Cambridge, Centro de Investigaciones Energéticas, Medioambientales y Tecnológicas-Madrid, the University of Chicago, University College London, the DES-Brazil Consortium, the University of Edinburgh, the Eidgenössische Technische Hochschule (ETH) Zürich, Fermi National Accelerator Laboratory, the University of Illinois at Urbana-Champaign, the Institut de Ciències de l'Espai (IEEC/CSIC), the Institut de Física d'Altes Energies, Lawrence Berkeley National Laboratory, the Ludwig-Maximilians Universität München and the associated Excellence Cluster Universe, the University of Michigan, the National Optical Astronomy Observatory, the University of Nottingham, The Ohio State University, the OzDES Membership Consortium, the University of Pennsylvania, the University of Portsmouth, SLAC National Accelerator Laboratory, Stanford University, the University of Sussex, and Texas A&M University. Based in part on observations at Cerro Tololo Inter-American Observatory, National Optical Astronomy Observatory, which is operated by the Association of Universities for Research in Astronomy (AURA) under a cooperative agreement with the National Science Foundation.

Statement of contribution by Co-authors

The published paper titled "*The remnant radio galaxy associated with NGC 1534*" (Duchesne & Johnston-Hollitt, 2019) is my own work except for additional contribution from my Supervisor, M. Johnston-Hollitt, including data processing and interpretation of and discussion surrounding the resultant images, along with feedback during preparation of the manuscript.

The published paper titled "*SPT-CL J2032−5627: a new Southern double relic cluster observed with ASKAP*" (Duchesne et al., 2021b) is my own work except for the following contributions: discussion and interpretation of general results, M. Johnston-Hollitt; processing and interpretation of *XMM*-Newton X-ray data, I Bartalucci & G. W. Pratt; generation of simulated radio images for Section 4.4, T. Hodgson. All Co-authors provided feedback during preparation of the manuscript.

The published paper titled "*Murchison Widefield Array detection of steep-spectrum, diffuse, non-thermal radio emission within Abell 1127*" (Duchesne et al., 2020) and Appendix A are my own work except for the following contributions: discussion and interpretation of results, M. Johnston-Hollitt; pipeline development, especially debugging and error analysis, R. B. Wayth & M. Johnston-Hollitt; cross-matching for the calibration sky model, J. L. B. Line; processing of *Chandra* data, Z. Zhenghao. All Co-authors provided feedback during preparation of the manuscript.

The published paper titled "*MWA and ASKAP observations of atypical radio-halo–hosting galaxy clusters: Abell 141 and Abell 3404*" (Duchesne et al., 2021a) is my own work except for the following contributions: discussion and interpretation of results, M. Johnston-Hollitt & A. G. Wilber; production of an early ASKAP image used in initial analysis for Abell 141, A. G. Wilber. Both Co-authors provided feedback during preparation of the manuscript.

For Chapter 6, titled "*Palaeontology with the MWA and ASKAP*", all work is my own except for: discussion and interpretation of results, M. Johnston-Hollitt; *Chandra* and *XMM*-Newton X-ray data processing, I. Bartalucci. Both Co-authors have provided feedback during preparation of the Chapter.

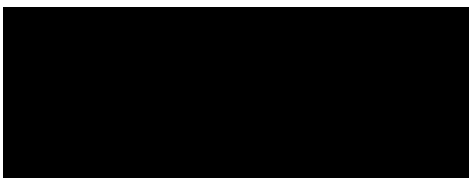

(Signature of Candidate)

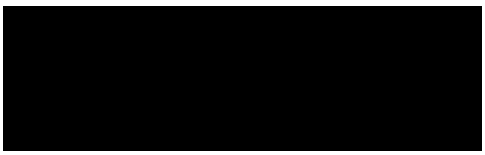

To Whom It May Concern

I, Stefan W. Duchesne have outlined my contributions and the contributions of Co-authors to the chapters in this Thesis that have been published as "*The remnant radio galaxy associated with NGC 1534*", "*SPT-CL J2032−5627: a new Southern double relic cluster observed with ASKAP*", "*Murchison Widefield Array detection of steep-spectrum, diffuse, non-thermal radio emission within Abell 1127*", and "*MWA and ASKAP observations of atypical radio-halo–hosting galaxy clusters: Abell 141 and Abell 3404*", as well as some contribution to Chapter 6, "*Palaeontology with the MWA and ASKAP*" as described.

[redacted]

(Signature of Candidate)

I, as a Co-Author, endorse that the level of contribution indicated by the candidate as in the 'Statement of contribution by Co-authors' is appropriate.

Professor Melanie Johnston-Hollitt

(Full name of Co-Author)

[redacted]

(Signature of Co-Author)

To Whom It May Concern

I, Stefan W. Duchesne have outlined my contributions and the contributions of Co-authors to the chapters in this Thesis that have been published as "*The remnant radio galaxy associated with NGC 1534*", "*SPT-CL J2032−5627: a new Southern double relic cluster observed with ASKAP*", "*Murchison Widefield Array detection of steep-spectrum, diffuse, non-thermal radio emission within Abell 1127*", and "*MWA and ASKAP observations of atypical radio-halo–hosting galaxy clusters: Abell 141 and Abell 3404*", as well as some contribution to Chapter 6, "*Palaeontology with the MWA and ASKAP*" as described.

[redacted]

(Signature of Candidate)

I, as a Co-Author, endorse that the level of contribution indicated by the candidate as in the 'Statement of contribution by Co-authors' is appropriate.

Randall Wayth

(Full name of Co-Author)

[redacted]

(Signature of Co-Author)

To Whom It May Concern

I, Stefan W. Duchesne have outlined my contributions and the contributions of Co-authors to the chapters in this Thesis that have been published as "*The remnant radio galaxy associated with NGC 1534*", "*SPT-CL J2032−5627: a new Southern double relic cluster observed with ASKAP*", "*Murchison Widefield Array detection of steep-spectrum, diffuse, non-thermal radio emission within Abell 1127*", and "*MWA and ASKAP observations of atypical radio-halo–hosting galaxy clusters: Abell 141 and Abell 3404*", as well as some contribution to Chapter 6, "*Palaeontology with the MWA and ASKAP*" as described.

(Signature of Candidate)

I, as a Co-Author, endorse that the level of contribution indicated by the candidate as in the 'Statement of contribution by Co-authors' is appropriate.

Jack L. B. Line

(Full name of Co-Author)

(Signature of Co-Author)

To Whom It May Concern

I, Stefan W. Duchesne have outlined my contributions and the contributions of Co-authors to the chapters in this Thesis that have been published as "*The remnant radio galaxy associated with NGC 1534*", "*SPT-CL J2032−5627: a new Southern double relic cluster observed with ASKAP*", "*Murchison Widefield Array detection of steep-spectrum, diffuse, non-thermal radio emission within Abell 1127*", and "*MWA and ASKAP observations of atypical radio-halo–hosting galaxy clusters: Abell 141 and Abell 3404*", as well as some contribution to Chapter 6, "*Palaeontology with the MWA and ASKAP*" as described.

[redacted]

(Signature of Candidate)

I, as a Co-Author, endorse that the level of contribution indicated by the candidate as in the 'Statement of contribution by Co-authors' is appropriate.

Zhenghao Zhu

(Full name of Co-Author)

[redacted]

(Signature of Co-Author)

To Whom It May Concern

I, Stefan W. Duchesne have outlined my contributions and the contributions of Co-authors to the chapters in this Thesis that have been published as "*The remnant radio galaxy associated with NGC 1534*", "*SPT-CL J2032−5627: a new Southern double relic cluster observed with ASKAP*", "*Murchison Widefield Array detection of steep-spectrum, diffuse, non-thermal radio emission within Abell 1127*", and "*MWA and ASKAP observations of atypical radio-halo–hosting galaxy clusters: Abell 141 and Abell 3404*", as well as some contribution to Chapter 6, "*Palaeontology with the MWA and ASKAP*" as described.

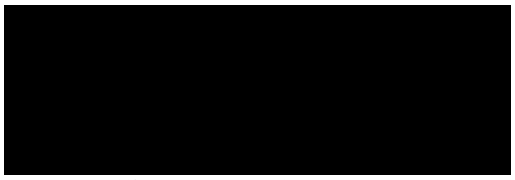

(Signature of Candidate)

I, as a Co-Author, endorse that the level of contribution indicated by the candidate as in the 'Statement of contribution by Co-authors' is appropriate.

Iacopo Bartalucci

(Full name of Co-Author)

(Signature of Co-Author)

To Whom It May Concern

I, Stefan W. Duchesne have outlined my contributions and the contributions of Co-authors to the chapters in this Thesis that have been published as "*The remnant radio galaxy associated with NGC 1534*", "*SPT-CL J2032−5627: a new Southern double relic cluster observed with ASKAP*", "*Murchison Widefield Array detection of steep-spectrum, diffuse, non-thermal radio emission within Abell 1127*", and "*MWA and ASKAP observations of atypical radio-halo–hosting galaxy clusters: Abell 141 and Abell 3404*", as well as some contribution to Chapter 6, "*Palaeontology with the MWA and ASKAP*" as described.

(Signature of Candidate)

I, as a Co-Author, endorse that the level of contribution indicated by the candidate as in the 'Statement of contribution by Co-authors' is appropriate.

Gabriel W. Pratt

(Full name of Co-Author)

(Signature of Co-Author)

To Whom It May Concern

I, Stefan W. Duchesne have outlined my contributions and the contributions of Co-authors to the chapters in this Thesis that have been published as "*The remnant radio galaxy associated with NGC 1534*", "*SPT-CL J2032−5627: a new Southern double relic cluster observed with ASKAP*", "*Murchison Widefield Array detection of steep-spectrum, diffuse, non-thermal radio emission within Abell 1127*", and "*MWA and ASKAP observations of atypical radio-halo–hosting galaxy clusters: Abell 141 and Abell 3404*", as well as some contribution to Chapter 6, "*Palaeontology with the MWA and ASKAP*" as described.

[redacted]

(Signature of Candidate)

I, as a Co-Author, endorse that the level of contribution indicated by the candidate as in the 'Statement of contribution by Co-authors' is appropriate.

Torrance Hodgson

(Full name of Co-Author)

[redacted]

(Signature of Co-Author)

To Whom It May Concern

I, Stefan W. Duchesne have outlined my contributions and the contributions of Co-authors to the chapters in this Thesis that have been published as "*The remnant radio galaxy associated with NGC 1534*", "*SPT-CL J2032−5627: a new Southern double relic cluster observed with ASKAP*", "*Murchison Widefield Array detection of steep-spectrum, diffuse, non-thermal radio emission within Abell 1127*", and "*MWA and ASKAP observations of atypical radio-halo–hosting galaxy clusters: Abell 141 and Abell 3404*", as well as some contribution to Chapter 6, "*Palaeontology with the MWA and ASKAP*" as described.

[redacted]

(Signature of Candidate)

I, as a Co-Author, endorse that the level of contribution indicated by the candidate as in the 'Statement of contribution by Co-authors' is appropriate.

Amanda Gloria Wilber

(Full name of Co-Author)

[redacted]

(Signature of Co-Author)

Peer-reviewed papers

The remnant radio galaxy associated with NGC 1534

The paper titled '*The remnant radio galaxy associated with NGC 1534*' is re-produced here in its form as accepted for publication in the Publications of Astronomical Society of Australia published by Cambridge University Press (CUP). The accepted article is re-produced with permission from Cambridge University Press [6] in line with the CUP 'Green Open Access' policy as agreed to in the signed License To Publish [7] prior to publication. Content is © Astronomical Society of Australia 2019. The version of record is available through CUP at: https://doi.org/10.1017/pasa.2018.26. Acknowledged contributions from Co-authors are outlined in the 'Statement of contribution by Co-authors'. This accepted article also appears on arXiv.org at https://arxiv.org/abs/1806.09255 [8].

[6] https://www.cambridge.org/about-us/rights-permissions/faqs/

[7] https://www.cambridge.org/core/services/open-access-policies/open-access-journals/green-open-access-policy-for-journals

[8] Note the appearance is slightly modified in the present version due to my own update to the PASA LaTeX template, keeping a theme consistent with the main body of the Thesis.

LaTeX document typeset by the authors from a modified LaTeX template from the *Publications of the Astronomical Society of Australia* (PASA).
Current document status: **accepted for publication in PASA:** https://doi.org/10.1017/pasa.2018.26.

Research Paper

The remnant radio galaxy associated with NGC 1534

S. W. Duchesne[1,2,3] and M. Johnston-Hollitt[1,2]

[1]International Centre for Radio Astronomy Research (ICRAR), Curtin University, Bentley, WA 6102, Australia
[2]Peripety Scientific Ltd., PO Box 11355 Manners Street, Wellington, 6142, New Zealand
[3]School of Chemical and Physical Sciences, Victoria University of Wellington, P. O. Box 600, Wellington 6140, New Zealand

Abstract

Large-scale, 'dead' radio galaxies are almost as rare as those hosted by dusty disk galaxies. The emission surrounding the lenticular galaxy NGC 1534 is one such example, and in this paper we present a followup of the remnant radio emission surrounding the galaxy with the Australia Telescope Compact Array in conjunction with data from the Murchison Widefield Array (MWA). We find that NGC 1534 has no significant compact emission suggesting a lack of an active galactic nucleus (AGN), and instead find low-power radio emission tracing its star-formation history. The radio-derived star-formation rate is found to be consistent with that derived via mid-infrared emission at $SFR_{1.4} = 0.38 \pm 0.03$ M$_\odot$ yr^{-1}, further pointing towards a lack of nuclear activity. The spectral energy distribution of the large-scale emission is well-fit by a continuous injection model with an additional 'off' component, implying the emission is indeed no longer fuelled by any injection of relativistic electrons. In particular, we find that the spectral age of the emission is on the order of $\sim$ 203 Myr, having been active for only $\sim$ 44 Myr. Polarimetric analysis points to both a large-scale magneto-ionic foreground associated with the Galaxy with a Faraday depth of +33 rad m^{-2} and a component associated with the northern lobe of the radio emission at -153 rad m^{-2}. The magnetic field structure of the northern lobe shows an unusual circular structure of unknown origin. We discuss that while such sources are rare, combined low and high frequency radio surveys with high surface-brightness sensitivities are expected to greatly increase their numbers in the coming decade and this combined with panchromatic data from new optical and infrared observations should provide a wealth of information on the hosts of this emission.

Keywords: galaxies: individual (NGC 1534)—radio continuum: galaxies—galaxies: active

1. Introduction

The active galactic nucleus (AGN) of a radio galaxy has a typical lifetime on the order of $\sim 10^8$ yr (Cordey, 1986). These finite lifetimes give rise to an observationally rare stage of a radio galaxy's life where the radio plasma forming the lobes may remain visible after the core has shut down and the supply of freshly accelerated plasma provided to the lobes by the resultant jets has ceased. As energy loss due to synchrotron radiation is proportional to square of the electron energy, the highest-energy electrons lose energy more quickly (see Pacholczyk, 1970), and these remnant lobes are usually observed with steep spectral indices, α [1], above some time-dependent break frequency (Parma et al., 2007; Murgia et al., 2011; de Gasperin et al., 2014; Brienza et al., 2016). Such dying sources have predominantly been found within the dense environment of galaxy clusters where it is thought the external pressure from the intra-cluster medium (ICM) is able to stall the dissipation of the lobes (Murgia et al., 2011). However, examples of dead and dying radio sources outside of clusters have been found (e.g. de Gasperin et al., 2014; Brienza et al., 2016) and such sources in under dense environments have the potential to reach sizes in excess of > 700 kpc becoming so-called giant radio galaxy (GRG; e.g., Saripalli et al. 2005). A GRG with an active AGN located in the field is expected to have a low surface brightness, and a dying, fading source much more so. Before the advent of low-frequency radio interferometers such as the Murchison Widefield Array (MWA; Tingay et al., 2013; Bowman et al., 2013) and the LOw-Frequency ARray (LOFAR; van Haarlem et al., 2013), such sources—except in rare cases—were rendered mostly undetectable due to their steep spectra in the GHz regime (see e.g. Cordey, 1987; Giovannini et al., 1988).

A second class of radio galaxy with—at present—low known numbers are dust-rich disk galaxies (lenticular and spiral) with large-scale radio lobes. Radio-loud AGN typically reside within large elliptical galaxies, whereas the denser material within spiral and lenticular galaxies may impede jet propagation, resulting in the sub-kpc–scale jets often seen in Seyfert AGN (e.g Ulvestad et al., 1981; Gallimore et al., 2006). At present there are only 9 spiral (Ledlow et al., 1998; Hota et al., 2011; Bagchi et al., 2014; Mao et al., 2015; Singh et al., 2015; Mulcahy et al., 2016) and 4 lenticular (Burbidge & Burbidge 1957; Cooper et al. 1965; Ekers et al. 1978, Johnston-Hollitt et al. submitted) galaxies hosting large-scale radio emission, and the cause of their lack of detection is not clear as their radio powers, while lower on average than equivalent size radio galaxies, are still high enough to be detected by most radio instruments (Johnston-Hollitt et al., submitted).

NGC 1534 is a lenticular galaxy at a redshift of $z = 0.017816$ (da Costa et al., 1991) and is part of the HDC 269 and LDC 292 galaxy groups (Crook et al., 2007). Hurley-Walker et al. (2015) serendipitously discovered remnant radio emission surrounding

[1]The spectral index, α, is defined via $S \propto \nu^{\alpha}$, where S is the flux density at frequency ν.

Table 1 Properties of the wide GLEAM subbands. The central frequency, ν_c is that specified in the FITS header of the survey products. The rms noise, σ_{rms}, is calculated at the reference pixel of the FITS images, which are centred on NGC 1534.

Band	ν_c (MHz)	Beam shape ($'\times'$, $^\circ$)	σ_{rms} (mJy beam^{-1})
072-103	87.675	5.4×5.0, -3.1	49.1
103-134	118.395	4.0×3.6, 2.8	24.9
139-170	154.235	3.1×2.7, -5.4	15.6
170-231	200.315	2.6×2.3, -1.8	13.9

NGC 1534 with the MWA. The large field of view of the observation and the sensitivity to large-scale structure enabled its detection. The low-surface brightness sensitivity of the MWA is due to the large number of short baselines between the antenna tiles, with a minimum baseline length of 7.7 m and 689 baselines < 60 m. In Phase I, the MWA had a maximum baseline of 2873.3 m, which at the MWA operating frequencies results in arcmin-scale synthesized beams. Despite this resolution limitation, large-scale extended structures can be studied in great detail due to the instrument's large fractional bandwidth, with individual observations able to observe with instantaneous bandwidths of 30.72 MHz. Hurley-Walker et al. (2015) considered the remnant radio plasma most likely associated with NGC 1534, considering it to be ancient lobes from a past cycle of core activity. This conclusion was motivated by the steep spectral index found, $\alpha_{185}^{843} = -2.1$, along with the general agreement in alignment between NGC 1534 and the remnant emission.

In this paper we present follow-up observations of the source with the Australia Telescope Compact Array (ATCA; Frater et al., 1992) in the 16 cm (2.1 GHz) and 15 mm (17 and 19 GHz) bands as well as a complementary low-frequency analysis with data from the GaLactic and Extragalactic All-sky MWA survey (GLEAM; Wayth et al., 2015).

This paper assumes a flat ΛCDM cosmology, with $H_0 = 67.7$ km s^{-1} Mpc^{-1}, $\Omega_m = 0.307$, and $\Omega_\Lambda = 1 - \Omega_m$ (Planck Collaboration et al., 2016). At the redshift of NGC 1534, 1 arcmin corresponds to 22.4 kpc. For the calculation of image rms noise, we use the Background and Noise Estimation tool, `bane` [2], part of the `AegeanTools` software package (Hancock et al., 2012, 2018).

2. Data

2.1. *MHz-frequencies—MWA*

The remnant emission surrounding NGC 1534 was originally detected serendipitously with the MWA at 185 MHz during a calibration pointing towards PKS B0408-658 (Hurley-Walker et al., 2015). We confirm the detection of the emission with data spanning 72–231 MHz from the GLEAM survey. GLEAM is a recently completed survey of the southern sky ($\delta_{J2000} < +25$) performed with the Phase I MWA using a drift scan imaging method to reduce primary beam calibration issues (Wayth et al., 2015). The survey covers the frequency range 72–231 MHz with a declination- and band-dependent synthesized beam and sensitivities. One of the main products of the survey is the availability of three 30.72 MHz-bandwidth wideband images (hereafter 30-MHz subband images) as well as a single, more sensitive 60-MHz wideband image centred on 200.315 MHz (hereafter the 200-MHz band/image). Currently, imaging has been performed with a robust parameter of −1 in the 'Briggs' weighting scheme (Briggs, 1995)—close to uniform weighting. The remnant radio emission is detected in the 200-MHz image. Fig. 1 shows the 200-MHz contours overlaid on the RGB optical image from the Digitised Sky Survey (DSS2). Additionally, the emission is detected in the three 30-MHz wideband images providing additional flux densities across the MWA band. GLEAM image properties are summarised in Table 1 and full imaging details can be found in Hurley-Walker et al. (2017).

2.2. *ATCA observations at 2.1 GHz*

ATCA observations with the Compact Array Broadband Backend (CABB; Wilson et al., 2011) of the remnant emission and NGC 1534 were carried out at 2.1, 17, and 19 GHz. Table 2 summarises the properties of the observations. The 2.1-GHz observations were carried out in 2014 and 2017 with the EW367 and H75 (PI Johnston-Hollitt), and H168 (PI Duchesne) configurations as part of project code CX287. PKS B1934-638 is used as the bandpass, gains, and flux calibrator, and PKS B0302-623 is used for phase calibration for the EW367 and H75 observations and PKS 0407-658 is used for the H168 observation. The use of PKS 0407-658 resulted in a loss of all antenna 6 data from this observation as the longer baselines show structure in the calibrator. Additionally, antenna 4 was unavailable for the 2.1-GHz H168 observations due to maintenance. Observations were performed as a 3-pointing mosaic to ensure the full extent of the emission was covered.

2.2.1. *Calibration and flagging*

Data reduction follows standard reduction procedure using the software package `miriad` (Sault et al., 1995). In the following we briefly outline the process. The data are imported into `miriad` and bands with known RFI or self-generating interference are flagged, along with the 40 edge channels of the initial 2049 due to bandpass rolloff. The 2.1-GHz data are split into four subbands centred at 1510, 1942, 2375, and 2807 MHz, which are chosen to be 432 MHz to give equal frequency coverage based on the non-flagged channels. Calibration, and further RFI flagging, is performed for each of the subbands and pointings individually. We find that the lowest subband, at 1510 MHz, is more heavily affected by RFI reducing the usable data and resulting in a lessened sensitivity compared to the other bands. This is a common problem in the 1100–1400 MHz part of the 2.1-GHz band for the ATCA [3] and has been noted by several authors (e.g. Martinez Aviles et al., 2016, 2018; Shakouri et al., 2016). RFI flagging makes use of the `miriad` task `pgflag`, which utilises the `SumThreshold` method for detecting RFI in the u–v data (Offringa et al., 2012). Calibration follows by first solving for complex gains and bandpass using the appropriate calibrator, then solving for complex gains and leakages

[2] https://github.com/PaulHancock/Aegean/wiki/BANE

[3] http://www.narrabri.atnf.csiro.au/observing/users_guide/html/atug.htmlInterference

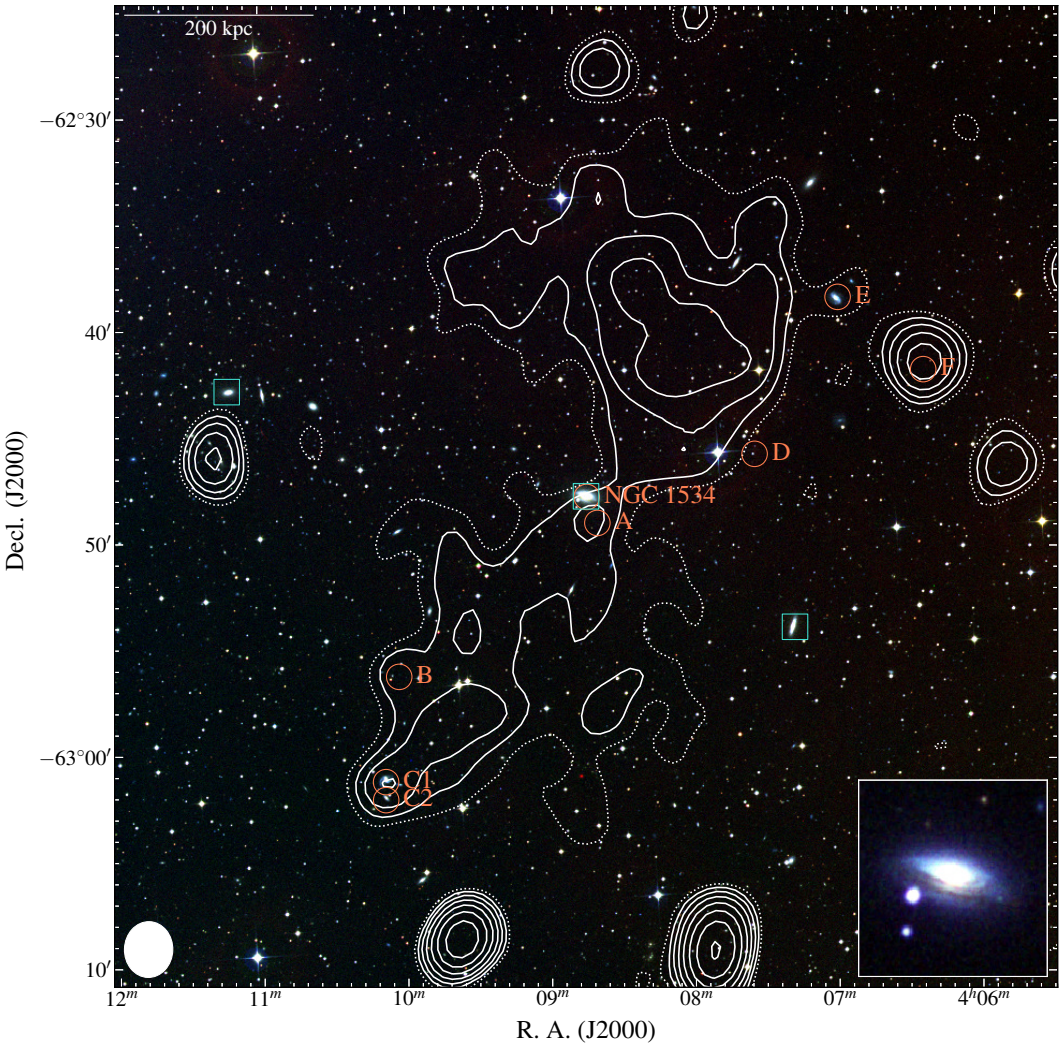

Figure 1. The region surrounding NGC 1534. The background is an RGB image formed using the IR, red, and blue bands of the Digitized Sky Survey 2 (DSS2), and the contours overlaid are from the GLEAM survey at 200 MHz. Solid, white contours begin at 42.2 $\mathrm{mJy\,beam^{-1}}$ ($3\sigma_{\mathrm{rms}}$) increasing with $\sqrt{2}$. The dotted white contour is at $2\sigma_{\mathrm{rms}}$. The GLEAM data will be discussed in Section 2.1. The linear scale is at the redshift of NGC 1534, and the inset is an RGB image formed using images generated by SuperCOSMOS (Hambly et al., 2001a,b,c). Various sources are marked on the figure: orange circles are those that show significant radio emission that may add to low-resolution flux density measurements, discussed in Section 3.1; cyan squares are part of the group HDC 269, discussed in Section 4.3. Other sources detected in the GLEAM image in this field are miscellaneous radio sources not discussed here. The white ellipse is the shape of the synthesised beam of the GLEAM data.

Table 2 Details for the ATCA observations. The scan time for mosaics is given as the total scan time for all three pointings. The frequency, ν, is the observing frequency. A 2 GHz bandwidth is used for each observing frequency.

Configuration	Date	ν (GHz)	$t_{\rm scan}$ (min)	Max. angular scale (arcmin)	Pointings ($\alpha_{\rm J2000}$, $\delta_{\rm J2000}$)
EW367	2014 Feb 25, 2014 Feb 26	2.1	690	13.0	$04^{\rm h}07^{\rm m}47\overset{\rm s}{.}875$, $-62°36'14\overset{''}{.}15$
H75	2014 Apr 4	2.1	150	19.6	$04^{\rm h}08^{\rm m}46\overset{\rm s}{.}099$, $-62°47'51\overset{''}{.}11$
H168	2017 Sept 28	2.1	270	18.7	$04^{\rm h}09^{\rm m}45\overset{\rm s}{.}091$, $-62°59'26\overset{''}{.}27$
H168	2016 Sept 3	17,19	315	1.1,1.2	$04^{\rm h}08^{\rm m}46\overset{\rm s}{.}070$, $-62°47'51\overset{''}{.}30$

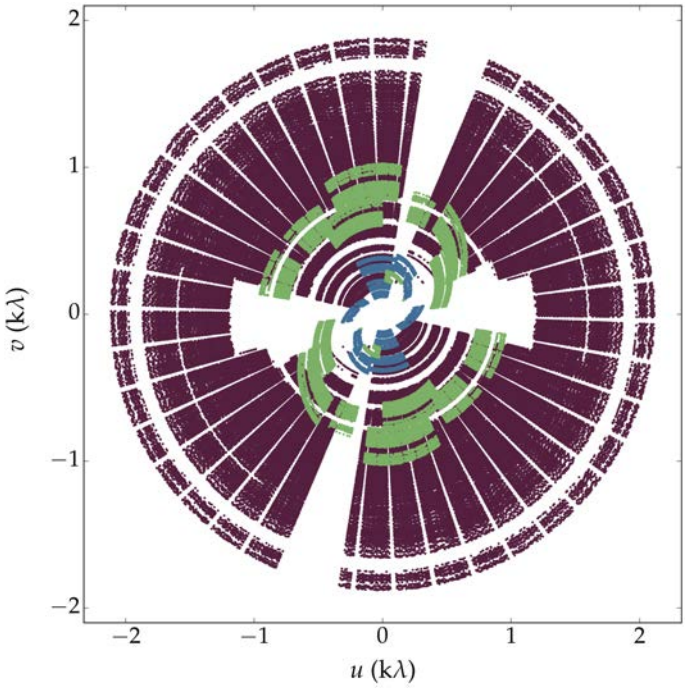

Figure 2. The u–v coverage for a single pointing of the combined EW367 (mauve), H75 (blue), and H168 (green) mosaic observations excluding antenna 6. Note that antenna 2 is missing from all H75 data, and antenna 4 is missing from all H168 data. This is for the 1510-MHz subband which features the most visibility flagging due to RFI.

on the secondary calibrators, finally applying a fluxscale correction based on PKS B1934-638 and copying calibration solutions to the NGC 1534 pointings. After data are calibrated and flagged, we use a number of imaging processes to make subband and full-band images. Fig. 2 shows the combined u–v coverage for a single pointing (pointing 1) of the combined EW367, H75, and H168 data for the 1510-MHz subband after flagging.

2.2.2. *High-resolution imaging*

The first set of subband images we produced used the full set of visibilities and use a 'Briggs' weighting scheme with robust parameter of 0 giving a balance between resolution and sensitivity. As the synthesized beam changes considerably across the bands we use the multi-frequency deconvolution task, `mfclean` (Sault & Wieringa, 1994). After deconvolution, we perform one cycle of phase-only self-calibration, CLEANing for more iterations in the second run of `mfclean`. For the mosaic observation, this procedure is performed for each pointing, and the clean models, beam, and dirty maps are individually combined via the task `restor`. Finally the pointings are linearly mosaicked together with the task `linmos`. We also created a stacked full-band image by combining each pointing and subband image which maximises sensitivity which is shown in Fig. 3. The properties of images produced are listed in Table 3. The remnant lobe emission is not detected though we find that NGC 1534 itself is detected across the 2.1-GHz band.

2.2.3. *Lower-resolution imaging*

We also made two sets of images without antenna 6 (hence removing baselines > 367 m) to maximise sensitivity to large-scale structures. The procedure is the same as for the high-resolution images except we use a robust parameter of +0.5 to further increase sensitivity at a small cost to beam shape and do not phase calibrate, as the significant residual phase errors were only present on baselines involving antenna 6. We designate this first set as 'medium-resolution' images and they have a common beam size of $88'' \times 73''$. The second set of images follows the first, but were convolved with a Gaussian kernel to match the resolution of the 200-MHz GLEAM wideband from which we measure the flux density of the remnant emission. These images are designated as 'low resolution' and they have a common beam size of $157'' \times 136''$. The northern emission is well-detected in the 1510- and 1942-MHz low- and medium-resolution images, though approaches the $3\sigma_{\rm rms}$ detection limit in the 2375- and 2807-MHz images. Fig. 4 shows the 1510-MHz medium-resolution image with the northern emission visible. The emission from the southern lobe is also detected in the 1510-MHz medium- and low-resolution images. The image properties are listed in Table 3.

2.3. *ATCA observations at 17 and 19 GHz*

Complementary to the 2.1-GHz observations of the entire source, an observation at 17 and 19 GHz of the core of NGC 1534 was carried out with the H168 configuration in 2016 (Project Code CX366; PI Hurley-Walker). This was a single pointing, with NGC 1534 at the phase centre. The primary beam in this band is significantly smaller and only encompasses NGC 1534 and the nearby radio source, SUMSS J040841-624908 (Source A in Fig. 1). These observations were performed in an attempt to constrain the spectral index of NGC 1534, the putative host of the radio emission. This observation similarly used PKS B1934-638 for flux calibration, though required PKS B1921-293 for bandpass calibration and PKS B0516-621 for both phase and pointing calibration. The observation details are

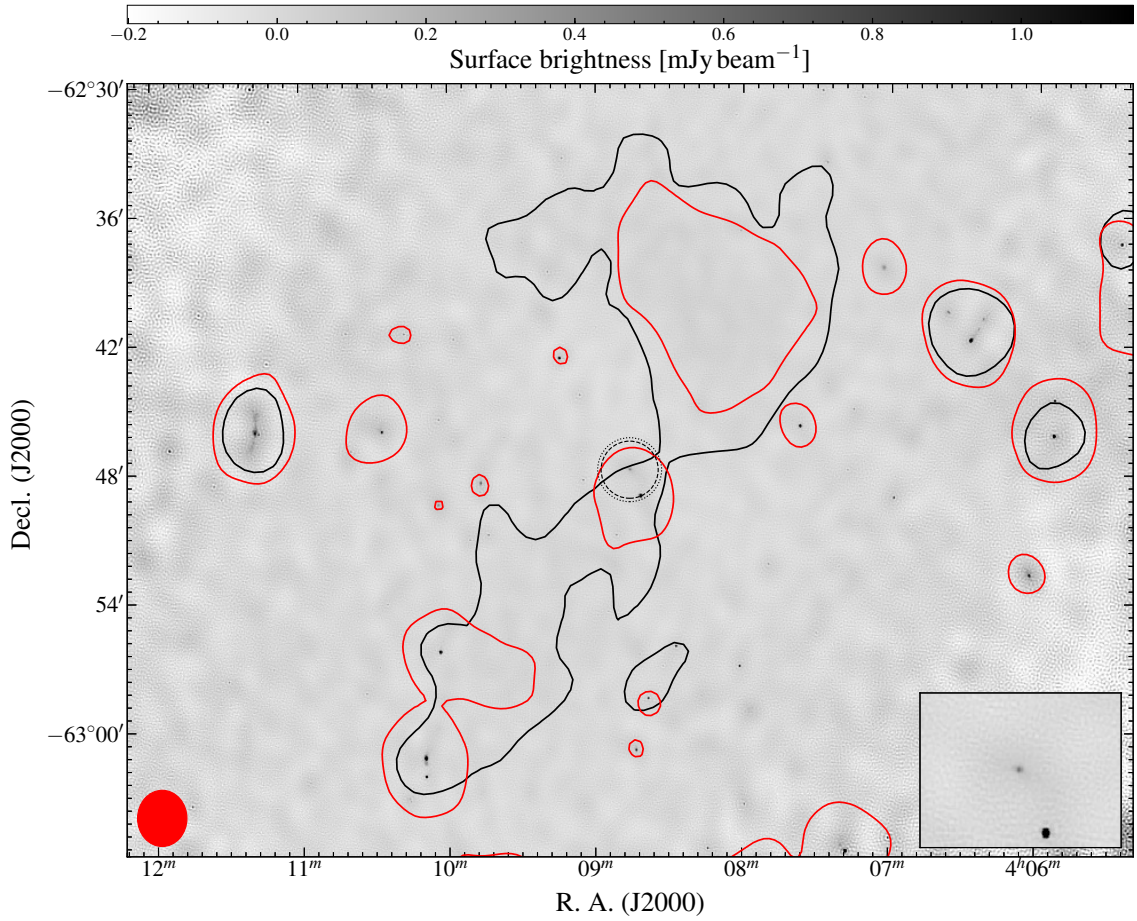

Figure 3. High-resolution, stacked 2200-MHz ATCA image. The single, black contour is the GLEAM 200-MHz image at 43 mJy beam^{-1}, and the single, red contour is the low-resolution 1510-MHz ATCA image at 1.41 mJy beam^{-1}. The red ellipse in the lower-left is the beam shape of the low-resolution 1510-MHz image, and the black, dotted and dashed circles at the centre are the primary beams at 17 and 19 GHz, respectively. The inset shows this same central region.

Table 3 ATCA image properties. The rms noise is the average at the centre of the map, as calculated by `bane`. For the 2200-MHz full-band image the higher-resolution, normally weighted images are convolved to a common beam shape (approximately equivalent to the 1510-MHz subband). The max angular scale is estimated from the minimum baseline of the H75 array (43 m without antenna 2) for the 2.1-GHz band images. Note that medium- and low-resolution images use a robust parameter of +0.5 whereas higher-resolution images use a robust parameter of 0. Values in parenthesis are for (medium-resolution) and [low-resolution] images.

Band	ν_c (MHz)	$\Delta\nu$ (MHz)	Beam shape (a) ($''\times''$,°)	$\sigma_{\mathrm{rms},I}$ (μJy beam^{-1})	$\sigma_{\mathrm{rms},QU}$ (b) (μJy beam^{-1})	Max. angular scale (arcmin)
1510	1485.275	432	5.1×4.6, 43	37(270)[470]	100	19.4
1942	1935.249	432	4.3×3.7, 59	34(150)[330]	50	15.0
2375	2361.121	432	3.6×2.9, 67	46(120)[265]	42	12.3
2807	2801.353	432	3.3×2.8, 62	41(110)[230]	40	10.4
2200	2200.495	1728	5.3×4.6, 0	21	-	13.3
17000	16852.728	1849	0.72×0.30, −0.7 (13.2×10.5, 74)	18 (28)	-	1.2
19000	19090.607	1849	0.64×0.26, −0.6 (11.8×9.4, 74)	20 (23)	-	1.0

Notes. (a) Medium- and low-resolution images have common beam shapes, unless otherwise specified: ($88''\times78''$) [$157''\times136''$]. (b) For $88''\times73''$ images.

presented in Table 2.

2.3.1. Calibration, flagging, and imaging

The 17 and 19 GHz data reduction followed a similar procedure to the 2.1-GHz reduction, though RFI is less problematic and subbands are not made due to the smaller fractional bandwidth. As

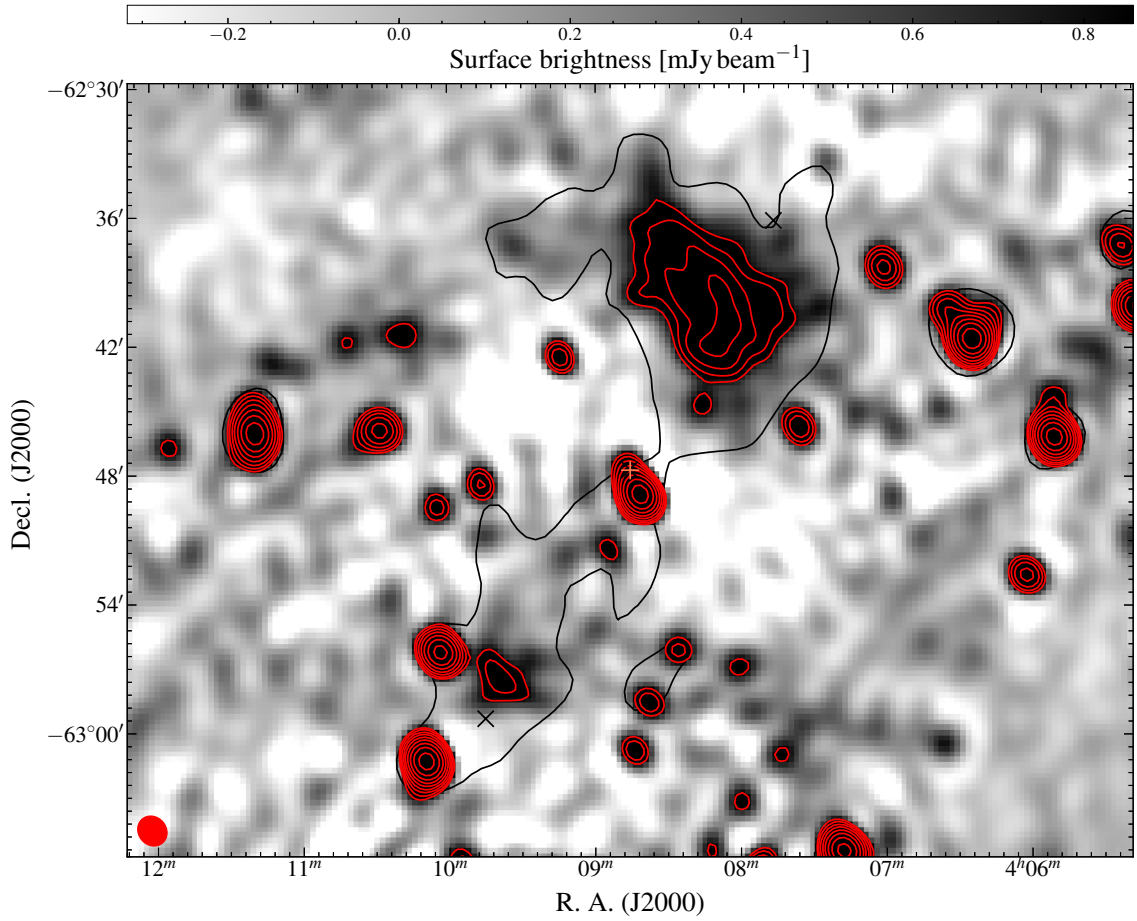

Figure 4. Medium-resolution ($88'' \times 73''$) 1510-MHz subband ATCA image. The single, black contour is as in Fig. 3. The red contours are the 1510-MHz medium-resolution image, beginning at 810 μJy beam^{-1} and increasing with factors of $\sqrt{2}$. The red ellipse in the lower-left is the beam shape of the 1510-MHz image. The black crosses are the mosaic pointing centres, and the orange '+' indicates the position of NGC 1534.

with the 2.1-GHz data, we make high-resolution, robust 0 images as well as medium-resolution, robust +0.5 images without antenna 6. The 17-GHz images are shown in Fig. 5, and image properties are listed in Table 3. Note that there was no emission detected in the 19 GHz image and thus it is not considered any further.

3. Analysis

3.1. *Radio flux density*

We measured the integrated radio flux density of the remnant emission from the GLEAM subbands and also estimated limits from the 2.1 GHz ATCA data. We begin by estimating contribution of flux density from interloping radio sources.

3.1.1. Interloping radio sources

We measure the flux densities of the sources labelled in Fig. 1 across our ATCA subband images, as well as from 843-MHz data taken from the Sydney University Molonglo Sky Survey (SUMSS; Bock et al., 1999; Mauch et al., 2003). Table 4 summarises the flux density measurements, spectral indices, and gives the names of the sources. Fig. 6 plots the spectral energy distribution (SED) of each source. Source E is not a point source at the full resolution of the ATCA images and so we measure flux densities for this source from the low-resolution ATCA subbands, and Source F has extended emission to the north west in the high resolution ATCA images. We use two methods for source measurements: for confirmed point sources, we utilise the source-finding, measuring, and characterising software, `aegean` (Hancock et al., 2012, 2018) with a detection threshold of $6\sigma_{\rm rms}$ and source growth threshold of $3\sigma_{\rm rms}$. Thus we are making sure sources are detected above $6\sigma_{\rm rms}$ and that they are being measured out to $3\sigma_{\rm rms}$. For other sources we use an in-house `python` code to identify connected pixels that comprise an extended source—using a flood-fill algorithm as in `aegean` and measuring integrated flux density in the same manner as the source-finding software `duchamp` (Whiting, 2012). Error calculations are made using rms maps generated by BANE, allowing the rms to vary across the source, yielding

$$\sigma_{S_\nu} = \sqrt{(fS_\nu)^2 + \left(\sum_i \sigma_{{\rm p},i}\right)^2} \quad [{\rm Jy}]\,, \tag{1}$$

where $\sigma_{{\rm p},i}$ is the rms at a specific pixel in Jy pixel^{-1}, and f the additional uncertainty for the flux scale/calibration uncertainties of

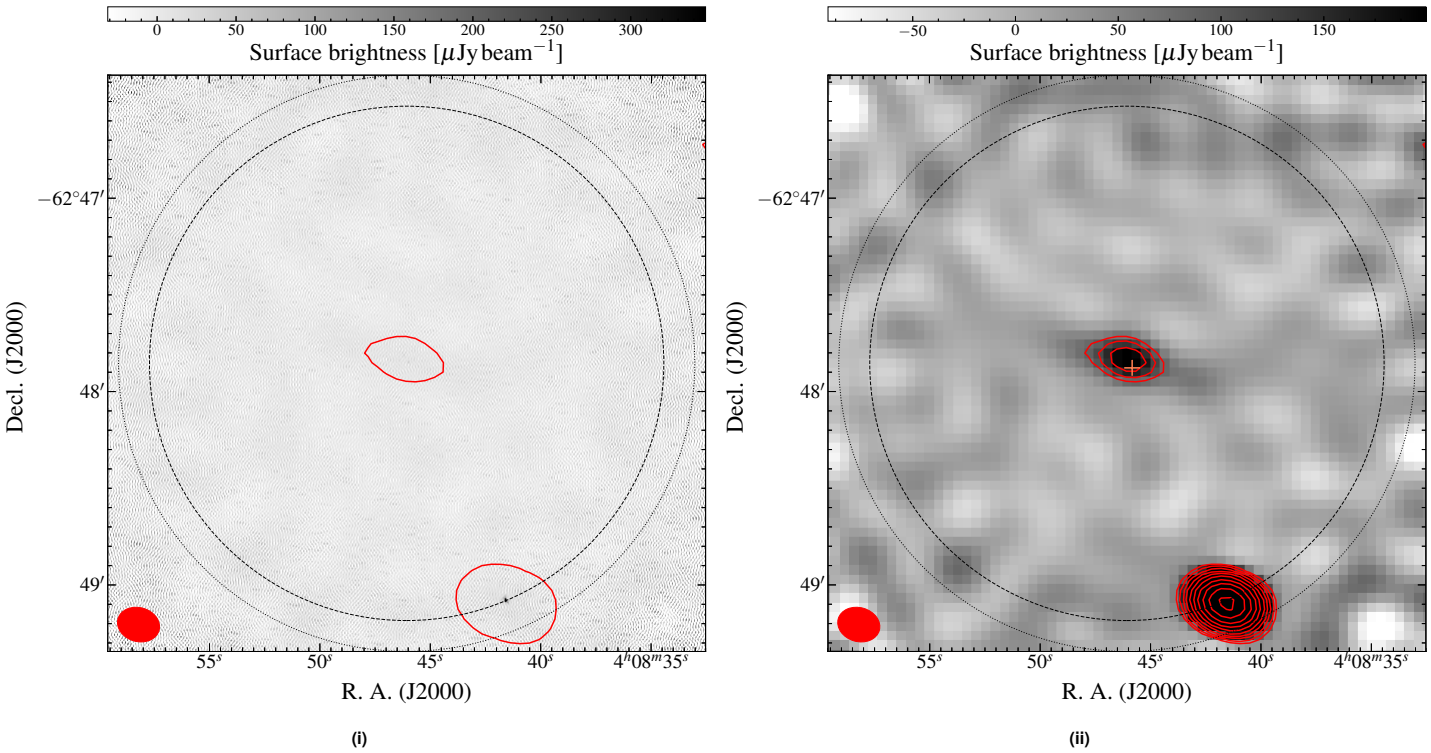

Figure 5. 17 GHz ATCA images. (i): High-resolution, robust 0 image. (ii): Medium-resolution, robust +0.5 image. The red contour(s) in both images are of the medium-resolution 17-GHz image starting at 84 μJy beam^{-1}. The dotted and dashed circles are the FWHM of the ATCA primary beam at 17 and 19 GHz, respectively, and the red ellipse in the lower-left corner is the beam shape of the 17-GHz medium-resolution image. The orange '+' in (ii) is the position of NGC 1534.

Table 4 Spectral properties of sources marked in Fig. 1. These sources, along with the core of NGC 1534, are the main sources of additional flux density GLEAM images. Integrated flux densities in the ATCA subbands are measured down to $3\sigma_{\rm rms}$, where $\sigma_{\rm rms}$ is computed for each pixel by `bane` except in the case of NGC 1534 where we measure down to $2\sigma_{\rm rms}$. The spectral index is calculated between the lowest- and highest-frequency measurements. Dashes in the flux density columns indicate no measurement available. 843-MHz measurements are made using `aegean`/`python` except for Sources C1/C2.

ID	Name	S_{843} (mJy)	S_{1510} (mJy)	S_{1942} (mJy)	S_{2375} (mJy)	S_{2807} (mJy)	S_{17000} (mJy)	α
A	SUMSS J040841-624908	18.5 ± 1.4	12.99 ± 0.27	10.70 ± 0.22	8.89 ± 0.18	7.96 ± 0.16	2.28 ± 0.06	−0.71 ± 0.01
B	SUMSS J041003-625615	14.5 ± 1.4	8.46 ± 0.18	6.36 ± 0.13	5.36 ± 0.12	4.58 ± 0.10	-	−0.96 ± 0.04
C1	2MASX J04100936-6301152	27.8 ± 2.6 (a)	15.34 ± 0.41	12.99 ± 0.32	11.21 ± 0.30	10.06 ± 0.25	-	−0.67 ± 0.05
C2	2MASX J04100935-6302062		3.86 ± 0.10	3.06 ± 0.08	2.74 ± 0.08	2.40 ± 0.07	-	−0.73 ± 0.06
D	GALEXASC J040736.82-624549.3	-	2.69 ± 0.09	3.68 ± 0.12	3.83 ± 0.15	4.22 ± 0.15	-	0.69 ± 0.07
E	PGC 014482	-	2.05 ± 0.32	1.77 ± 0.20	1.53 ± 0.17	0.99 ± 0.14	-	-
F	SUMSS J040627-624144	21.6 ± 1.6 (b)	9.70 ± 0.20	7.21 ± 0.16	4.64 ± 0.14	2.69 ± 0.15	-	-
-	NGC 1534	-	2.20 ± 0.16	1.39 ± 0.09	-	1.12 ± 0.09	0.301 ± 0.048	−0.79 ± 0.08

Notes. (a) Total flux density of C1 and C2 from the SUMSS catalogue (Murphy et al., 2007); not used in fitting the spectral index. (b) Total flux density of Source F and nearby sources; not used in fitting.

the specific map.

Source A is a curious case as measuring the peak flux density and comparing to the integrated flux density shows a significant discrepancy in the SUMSS data. The integrated flux density is lower, at $S_{843} = 13 \pm 2$ mJy (cf. 843-MHz peak flux density measurement in Table 4). The discrepancy is likely due the source's location within a negative bowl resulting in an underestimated flux density measurement. For consistency, we measure the peak flux density values of Source A for all measurements, and note that in all images Source A is unresolved. Further, Source A is at the edge of the 19-GHz primary beam, thus we do not measure the flux density in this band. For the emission from NGC 1534, the full resolution ATCA images show little nuclear activity, but detects extended emission in the disk of the galaxy, likely from star formation. We note the lower sensitivity of the 2375-MHz image made measurement of the the NGC 1534 emission problematic and no measurement there is provided. Most of the sources show typical powerlaw spectra of radio galaxies, with SEDs fit by

$$S_\nu = C\nu^\alpha\,, \tag{2}$$

where α is the spectral index and C the flux normalisation. For Sources E and F, the SEDs show significant curvature and are fit by a generic curved powerlaw model of the form

$$S_\nu = C\nu^\alpha e^{q(\ln\nu)^2}\,, \tag{3}$$

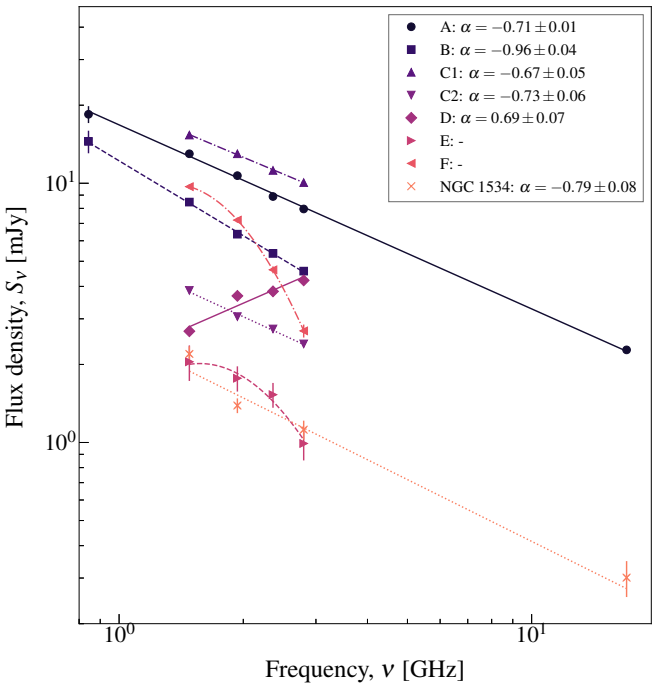

Figure 6. The SEDs of sources within the remnant emission. The data are also presented in Table 4.

where α is the equivalent spectral index in the case of no curvature, and q is the curvature index (e.g. Duffy & Blundell, 2012; Callingham et al., 2017). In Table 4 we only report the power law index when using Eq. 2.

Fitting is done via non-linear weighted least squares methods using the Lavenberg-Marquart algorithm implemented in `lmfit` (Newville et al., 2014). The errors on the flux density measurements are the quadrature sum of the `aegean/python` measurements with the percentage uncertainty associated with the maps (as in Eq. 1 for the in-house `python` code). For the ATCA, this is 2 % (see e.g. Venturi et al., 2000; Johnston-Hollitt et al., 2008), and for the SUMSS map this is 3 % (Mauch et al., 2003).

The power law model fit for NGC 1534 suggests a 1.4-GHz flux density of 1.97 ± 0.15. This translates to a 1.4-GHz power of $P_{1.4} = (1.5 \pm 0.1) \times 10^{21}$ W Hz^{-1}.

3.1.2. The remnant radio emission

We measure the integrated flux densities of the northern lobe from the GLEAM wideband images as well as the 1510- and 1942-MHz low-resolution ATCA images. Due to the blended nature of compact and extended emission within the southern lobe at MWA frequencies, we measure the integrated flux densities of the total emission in the GLEAM images, subtracting the northern lobe contribution for the initial estimate of the flux density of the southern lobe. As the southern lobe is only well-detected, and not blended in the 1510-MHz medium-resolution image, we measure it there. 2375- and 2807-MHz lower limits are placed on the northern lobe based on vague detection at $2\sigma_{\rm rms}$. similarly, a lower limit at 1942-MHz is placed on the southern lobe, though 2375- and 2807-MHz upper limits are not estimated here due to confusion with compact sources.

Table 5 Flux density measurements of the total, northern, and southern lobe emission. Flux densities are measured out to $2\sigma_{\rm rms}$ as per Hurley-Walker et al. (2015).

Band (MHz)	$S_\nu^{\rm north}$ (mJy)	$S_\nu^{\rm south}$ (mJy)	$S_\nu^{\rm total}$ (mJy)	Reference
88	2270 ± 220	840 ± 400	2110 ± 330	(a)
118	1910 ± 180	740 ± 320	2650 ± 260	(a)
154	1670 ± 150	720 ± 270	2390 ± 230	(a)
408	520 ± 104	300 ± 60	820 ± 120	(b)
843	130 ± 20	80 ± 20	210 ± 30	(b)
1400	< 45	< 27	< 72	(b)
1510	35 ± 1	> 10.2	> 45 ± 1	(a)
1942	13.4 ± 0.7	-	> 13.4 ± 0.7	(a)
2375	> 2.8	-	> 2.8	(a)
2807	> 1.9	-	> 1.9	(a)

References. (a) This work; (b) Hurley-Walker et al. (2015).

Flux densities for the extended emission are measured using the in-house `python` code, where we limit measured pixels to those above $2\sigma_{\rm rms}$ This $\sigma_{\rm rms}$ cut is chosen for consistency with Hurley-Walker et al. (2015) and because we have prior knowledge that the emission is of particularly low surface brightness. We consider the rms noise on a pixel-by-pixel basis using `bane`. `bane` uses sparse pixel grids to account for instances where noise may change rapidly across the image. Uncertainties in flux density measurements are given by Eq. 1. We use the model parameters of the interloping sources to extrapolate to MWA frequencies for subtraction from GLEAM images, where appropriate. This is not necessary for the ATCA subband images as no significant interloping sources are found within the emission region at these frequencies. Table 5 summarises the measured flux densities, with additional literature data measured by Hurley-Walker et al. (2015) from SUMSS (Bock et al., 1999; Mauch et al., 2003), a re-processed Molonglo Reference Catalogue image (Large et al., 1981), and an upper limit from CHIPASS [4] (Calabretta et al., 2014).

Using the 200-MHz GLEAM image and the 1510-MHz low-resolution ATCA image, we estimate the projected size of the emission assuming it is indeed emission associated with NGC 1534. The projection separation between the peaks in the northern and southern lobes is ~ 20 arcmin which translates to a projected linear size of ~ 450 kpc at the redshift of NGC 1534. This is smaller than the size found by Hurley-Walker et al. (2015) though their estimate includes Source C1/C2 and extends further north. We do not include Source C1/C2 as there is no evidence that the emission continues beyond the southern peak at 1510 MHz. However, the emission may continue further northwest, in which case the projected size may be up to ~ 610 kpc. We cannot be sure this is the case, as there are a number of faint point sources which may be contributing to the morphology of the emission at the northwestern end.

3.1.3. The spectral energy distribution

In the frequency regime measured here, the SED is not described by a simple powerlaw model, and instead we consider the continuous

[4] http://www.atnf.csiro.au/research/CHIPASS/

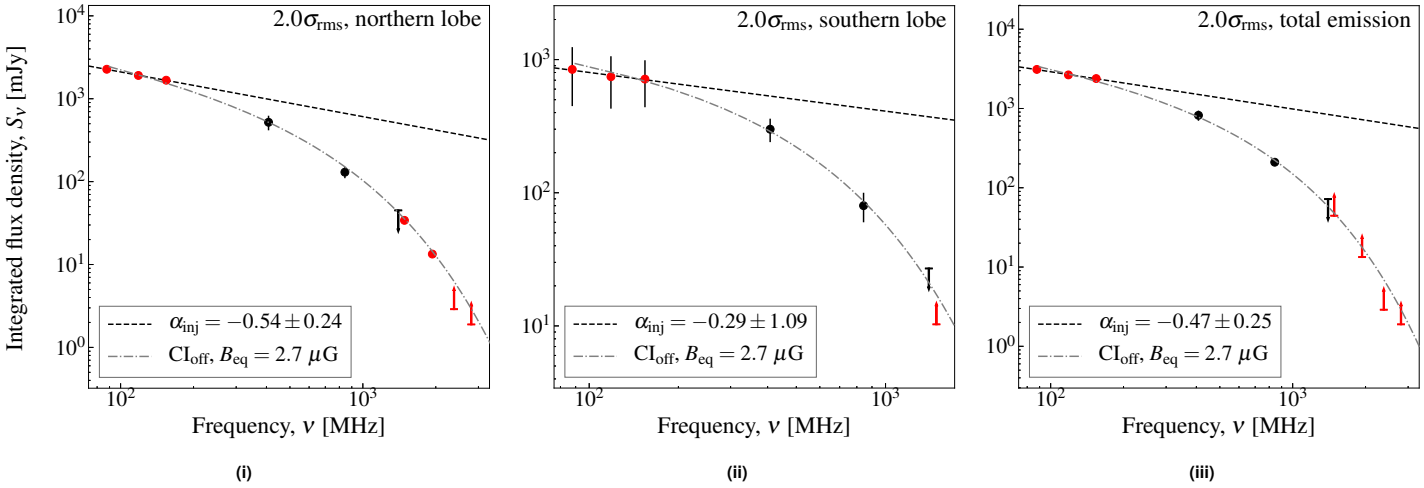

Figure 7. The SED of the emission surrounding NGC 1534 after a $2\sigma_{\rm rms}$ cut to the pixels. (i): emission from the northern lobe. (ii): emission from the southern lobe. (iii): combined emission from the northern and southern lobes. Measured flux densities have sources subtracted, where appropriate, based on spectral indices derived in Section 3.1.1. A CI$_{\rm off}$ model is fit for the northern and southern lobes separately, then for the combined emission. Limits are indicated by arrows, points in black are from the literature (see Table 5), and points in red are measured in this work. Limits are not used in the fitting process.

injection (CI) models (Kardashev, 1962; Pacholczyk, 1970; Jaffe & Perola, 1973) implemented in the Broadband Radio Astronomy ToolS (BRATS; Harwood et al., 2013, 2015) package [5]. The standard CI model is fit under the assumption the magnetic field is in equiparition with the emitting electron population. We assume that the AGN has switched off, as the ATCA data suggest no prominent nuclear activity—hence, we fit the CI$_{\rm off}$ model which describes remnant radio emission described in Komissarov & Gubanov (1994) as a modification to the CI model as described in Jaffe & Perola (1973). For CI$_{\rm off}$ fitting we assume the emission is at the redshift of NGC 1534.

In fitting we require an injection index, $\alpha_{\rm inj} = \left(1 - \delta_{\rm inj}\right)/2$, that describes the observed emission from a continuous injection of fresh electrons with a power law energy distribution of index $\delta_{\rm inj}$, assuming synchrotron and inverse-Compton losses. Fig. 7 shows power law fits to the GLEAM subband data from which we obtain $\alpha_{\rm inj}$, which is valid if a break frequency, $\nu_{\rm b}$, occurs above this regime, further motivated by no clear break seen across the GLEAM bands. We also require an estimate of the equipartition magnetic field, $B_{\rm eq}$. The choice of $B_{\rm eq}$ is motivated by Equation 2 of Miley (1980) and from Jamrozy et al. (2004) we use,

$$B_{\rm eq} = 7.91 \left[\frac{1+k}{(1+z)^{\alpha-3}} \frac{S}{\nu^{\alpha} \theta_x \theta_y l} \frac{\nu_{\rm max}^{\alpha+\frac{1}{2}} - \nu_{\rm min}^{\alpha+\frac{1}{2}}}{\alpha + 0.5} \right]^{\frac{2}{7}} \ [\mu{\rm G}] \, . \quad (4)$$

where k is the relativistic proton–electron energy ratio, θ_x and θ_y are the size of the source on the sky in arcseconds, l is the line-of-sight depth, and $\nu_{\rm max}$ and $\nu_{\rm min}$ are the integration bounds for the luminosity and are chosen to be $\nu_{\rm max} = 100$ GHz and $\nu_{\rm min} = 0.01$ GHz. Here we choose k to be 100 (e.g Moffet, 1975) though could be anywhere between 1 and 2000 (Pacholczyk, 1970). The choice of k is not overly important as the impact in this range is a change of less than an order of magnitude (0.9 μG $\lesssim B_{\rm eq} \lesssim$ 6 μG for $1 \leq k \leq 2000$). We estimate the size of the northern lobe as $\theta_x = 570$ arsec, $\theta_y = 340$ arcsec on the sky and we assume a line-of-sight depth of $l = 127$ kpc. We choose 118 MHz as the reference frequency, and assume $\alpha = \alpha_{\rm inj}$. We estimate $B_{\rm eq} \approx 2.7$ μG for the northern lobe, and in the absence of indication of any asymmetry in the environment that would result in lobe asymmetry we make the assumption that the southern lobe has an equivalent magnetic field strength, as we cannot estimate its magnetic field via Eq. 4 without better knowledge of the extent of the emission (see e.g. Fig. 1, 3, and 4). We will only report here on the northern lobe fitting results, though for completeness show all fits in Fig. 7.

Fig. 7(i)–(iii) show the SEDs of the northern lobe, southern lobe, and total emission, along with model fits. We find that, given $\alpha_{\rm inj} = -0.54$ for the northern lobe emission, a total source age is found to be $t_{\rm s} = 203 \pm 5$ Myr with an injection time of $t_{\rm on} = 44 \pm 5$ Myr and time since it switched off of $t_{\rm off} = 158 \pm 2$ Myr. Note that quoted errors are simply those from model fitting, and the true uncertainties are much greater as many assumptions are made in this process. Notably, our value of $t_{\rm s}$ suggests a break frequency of $\sim$ 502 MHz (see e.g. Equation 1 of Alexander & Leahy, 1987), above the GLEAM frequency coverage validating our choice of $\alpha_{\rm inj}$ found from those data. As discussed in Harwood (2017), these times should be considered as 'characteristic'. From the CI$_{\rm off}$ model of the northern lobe, we estimate the 1.4-GHz flux density as $S_{1.4}^{\rm north} \approx 41$ mJy. Assuming the source size is the same as at the 1.51-GHz size of ~ 60 arcmin^2, then the surface brightness is ~ 0.7 mJy arcmin^{-2}. Assuming NGC 1534 is the original host, and assuming the true emission is represented by a symmetric set of lobes of flux density $2 \times S_{1.4}^{\rm north}$, the core-to-lobe luminosity ratio is $P_{1.4}^{\rm core}/P_{1.4}^{\rm lobe} \approx 0.02$.

Assuming the host of the emission is NGC 1534 and with a distance of 230 kpc from northern lobe centre (i.e. the equivalent hotspot) to NGC 1534, the minimum velocity of the lobe must be $\sim 0.014c$, which is on the same order of magnitude as FR-II

[5] http://www.askanastronomer.co.uk/brats/

(Fanaroff & Riley, 1974) sources (e.g. Liu et al., 1992).

One should be cautious comparing integrated flux densities of maps with different u–v coverage. As there are differences between not only the MWA and ATCA observations, but also the Molonglo and ATCA observations, we may be biasing the spectrum to be much steeper above 1 GHz. This high-frequency, steep-spectrum bias suggests the $t_{\rm off}$ estimate is an upper limit, as the true age will be younger with a flatter high-frequency spectrum. Further ATCA observations to fill in the u-v plane would be required to confirm this. We note that Hurley-Walker et al. (2015) find a significantly higher integrated flux density at 185-MHz than what is suggested here, however, subsequent improvements to the MWA primary beam model and general flux scale used by Hurley-Walker et al. (2017) can account for this discrepancy.

3.2. *Polarimetry*

The ATCA operates with linear XX, YY, XY, and YX cross-correlations which allow measurement of Stokes I, Q, U, and V, thus we investigate the polarisation properties of the emission surrounding NGC 1534. We are interested in the linear polarization defined via Stokes Q and U,

$$P = Q + iU\,, \tag{5}$$

with, assuming no circularly polarized emission (Stokes V), the total polarization intensity

$$\|P\| = \sqrt{Q^2 + U^2}\,. \tag{6}$$

3.2.1. *Rotation measure synthesis*

As the 2.1-GHz data have a large fractional bandwidth and reasonably small channels, we perform rotation measure synthesis (RM-synthesis; Brentjens & de Bruyn, 2005)—a method to investigate rotation measure on a non-contiguous spectrum, building on the rotation measure work of Burn (1966). As in Burn (1966), Brentjens & de Bruyn (2005) define the Faraday depth, ϕ, via

$$\phi(\boldsymbol{r}) = 0.81 \int_{\rm there}^{\rm here} n_{\rm e}\boldsymbol{B}\cdot{\rm d}\boldsymbol{r} \quad [{\rm rad\,m^{-2}}]\,, \tag{7}$$

where $n_{\rm e}$ is the electron density in cm^{-2}, $\boldsymbol{B}$ is the intervening magnetic field in μG, and d$\boldsymbol{r}$ is an infinitesimal path length in pc. Though we cannot usually measure the electron density, the sign of the Faraday depth gives the average magnetic field direction, where a negative ϕ is given by a magnetic field in the direction of the observer. Additionally, the Faraday depth spectrum may show other sources along the line of sight. Intrinsic source rotation measure is defined as

$$RM_0 = \frac{{\rm d}\chi_{\rm P}}{{\rm d}{\lambda_{\rm obs}}^2}\,(1+z)^2 - RM_{\rm gal} - RM_{\rm other} \quad [{\rm rad\,m^{-2}}]\,, \tag{8}$$

where $\lambda_{\rm obs}$ is the observed wavelength, and z is the redshift of the source in question, $RM_{\rm gal}$ is RM contribution from Galactic Faraday rotation and $RM_{\rm other}$ is the RM contribution from other foreground or background sources. The rotation measure gives insight into the source magnetic field as well as any intervening or background magnetic field sources.

For RM-synthesis, we use the EW367 ATCA data and create Stokes Q and U cubes with axes $\alpha_{\rm J2000}$, $\delta_{\rm J2000}$, and ν, where ν represents a single channel of 1 MHz. Only the EW367 observation is used as it had the least flagging due to RFI which enabled a larger fractional bandwidth/more individual channels to be used at only a small loss to sensitivity and u–v coverage. Each plane in the cube, corresponding to a 1 MHz channel of the original 2.1-GHz data, are imaged to the same dimensions—no CLEANing is done on the 1-MHz images. Primary beam corrections are applied for each plane at the given frequency, though pixels outside the FWHM of the primary beam of the highest frequency 1-MHz image are blanked in the output FITS cubes, thus we do not expect noise to vary significantly across the planes. The imaging is done on a per-pointing basis, with each plane a mosaic using `linmos` as in Section 2.2.2. For channels where all data are flagged, we skip those in the cube-forming/imaging process and move on to the next channel.

The Q and U cubes, along with a list containing frequencies for each plane, are then used by the RM-synthesis code developed by M. A. Brentjens [6] to generate a Rotation Measure Transfer Function (RMTF, also known as the rotation measure synthesis function, shown in Fig. 8(i)) and cube of $\alpha_{\rm J2000}$, $\delta_{\rm J2000}$, and Faraday depth ϕ in units of the Faraday dispersion function, $F(\phi)$. The resolution chosen for synthesising RM is 1 rad m^{-2}. We synthesised the Faraday dispersion in the range $-1650 \leq \phi \leq +1650$, The top panel of Fig. 8 shows the RMTF. The polarised intensity, $\|P\|$ in Jy beam^{-1} rmtf^{-1}, is equal to the Faraday dispersion function, $F(\phi)$, in the case of sources that are discrete in ϕ (de Bruyn & Brentjens, 2005).

Fig. 8(ii) shows the Faraday depth spectra of three representative pixels: within the northern lobe ($04^{\rm h}08^{\rm m}29\overset{\rm s}{.}7, -62°38'56\overset{''}{.}8$), the southern lobe ($04^{\rm h}09^{\rm m}39\overset{\rm s}{.}7, -62°58'08\overset{''}{.}9$), and Source A ($04^{\rm h}08^{\rm m}42\overset{\rm s}{.}0, -62°33'00\overset{''}{.}8$). The north and south lobe pixels have peaks at a Faraday depth of +33 and +34 rad m^{-2}, respectively, and Source A shows a peak at −12 rad m^{-2}. The main peak in the north and south lobes is close to the estimated Galactic foreground RM of +27 rad m^{-2} (Oppermann et al., 2015, but see also Oppermann et al. 2012). This Galactic foreground value is taken from an average value within 1000 arcsec of NGC 1534, which comprises approximately four pixels of the `HEALPix` image of the Galactic Faraday depth produced by Oppermann et al. (2015). Fig. 9(ii) shows the plane in the Faraday depth cube at $\phi = +33$, showing large-scale emission beyond the size of the emission from NGC 1534, further suggesting Galactic (or otherwise foreground) origin rather than the intrinsic magneto-ionic plasma of NGC 1534's lobes. Fig. 9(i) shows the second isolated peak in the Faraday depth spectrum of the northern lobe pixel (marked in Fig. 8(ii)) at −153 rad m^{-2}. We do not have enough information about the intergalactic medium to know with 100 per cent certainty whether this peak corresponds to a non-Galactic screen external to the radio plasma, or to the radio lobe itself. However, as the position corresponds to the peak

[6] https://github.com/brentjens/rm-synthesis

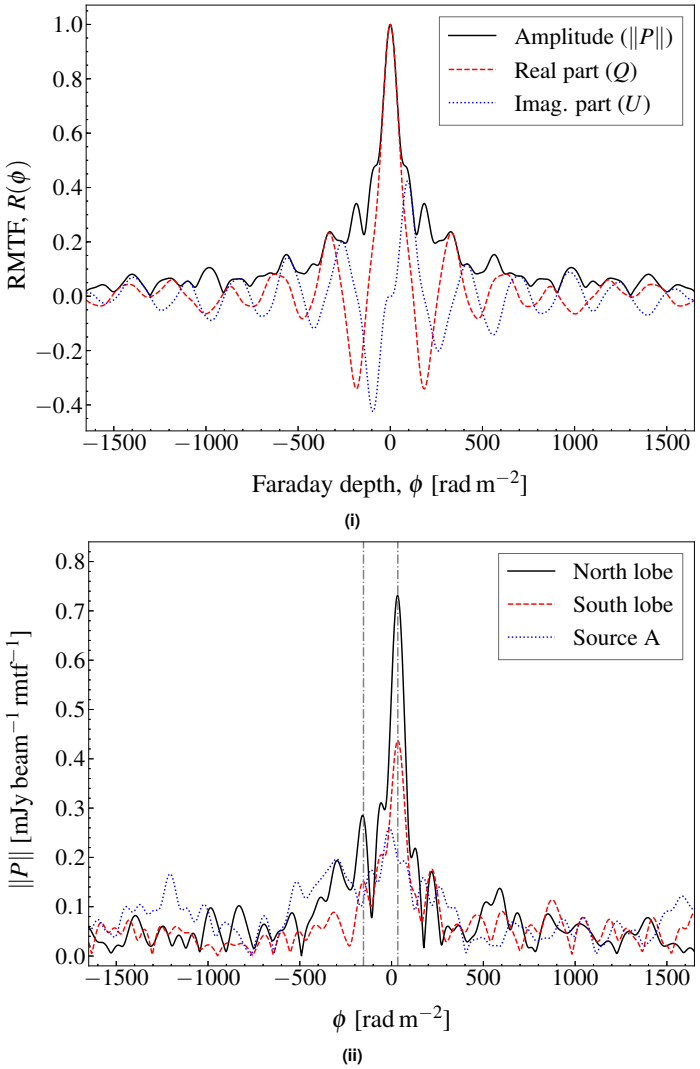

Figure 8. (i): the RMTF between $-1650 \leq \phi \leq 1650$. (ii): the polarised intensity along the Faraday depth cube of 3 pixels corresponding to a pixel within the northern lobe (black, solid—$04^{\rm h}08^{\rm m}29\overset{\rm s}{.}7, -62°38'56\overset{''}{.}8$), within the southern lobe (red, dashed—$04^{\rm h}09^{\rm m}39\overset{\rm s}{.}7, -62°58'08\overset{''}{.}9$), and Source A (blue, dotted—$04^{\rm h}08^{\rm m}42\overset{\rm s}{.}0, -62°33'00\overset{''}{.}8$). Marked with vertical lines are peaks of interest in the Faraday depth spectrum. In both panels, the resolution in ϕ is 1 rad m^{-2}. The vertical lines represent the two detected RM features at -153 and $+33$ rad m^{-2}.

brightness of the polarised emission in the lobes, it is likely to be associated with the radio galaxy itself.

3.2.2. Continuum polarimetry

We follow a similar imaging procedure as in Section 2.2.3 (i.e., without antenna 6). The Stokes I images are deconvolved in a similar manner to the Stokes I images of Section 2.2.3, though for the Stokes Q and U images we use the complex implementation of the Steer-Dewdney-Ito (SDI; Steer et al., 1984) CLEAN algorithm offered by the task `cclean` (Pratley & Johnston-Hollitt, 2016). The SDI CLEAN algorithm is better at CLEANing extended sources than the traditional Hogböm (Högbom, 1974) or Clark (Clark, 1980) CLEAN algorithms as used by `mfclean`. Complex CLEAN acts on both Stokes Q and U in a dependent fashion. As linear polarisation, P, is a complex quantity, the complex CLEAN algorithm properly accounts for this complex vector nature of the signal. We produce total polarisation intensity maps ($\|P\|$), shown in Fig. 10, overlaid with vectors of magnitude proportional to the fractional polarisation, $m_P = \|P\|/I$, and directions representing the apparent magnetic field, $\chi_P + \pi/2 - RM\lambda^2$, where χ_P is the electric vector position angle defined via

$$\chi_P = \frac{1}{2} \arctan \frac{U}{Q}, \tag{9}$$

and RM is the total line-of-sight RM. In making polarization images (intensity, fractional polarization, and position angle) we use a $3\sigma_{{\rm rms},QU}$, $3\sigma_{{\rm rms},I}$ cut to the intensity and a $3\sigma_{\rm rms} = 10$ degree cut to the position angle. This results in no detected polarised emission from the 2375- and 2807-MHz bands. Fig. 10(i) and 10(ii) show the polarisation intensity maps for the 1510- and 1942-MHz bands, respectively, with vectors of magnitude defined by the factional polarisation and magnetic field directions. We de-rotate the position angles based on an assumed Galactic Faraday depth of +33 rad m^{-2} and for the additional peak at -153 rad m^{-2} (see Section 3.2.1). The average fractional polarisation across the source in the 1510- and 1942-MHz bands is 42 ± 14 and 43 ± 14 %, respectively, and in the higher bands little polarization is detected, following the Stokes I images. The field directions appear curled which is not typically seen in the intrinsic magnetic fields of radio galaxy lobes (e.g. Bridle & Perley, 1984), unless the lobe is bent or twisted (e.g. Laing et al., 2008), however, the curling seen here would require the northern lobe to have fallen completely back in on itself.

4. Discussion

NGC 1534 represents the rare chance to study a relatively near-by radio galaxy with diffuse low-surface brightness emission. It is peculiar for a number of reasons including its position in the field, not a cluster, and the seeming discrepancy between the position of the optical galaxy and typical position for radio emissions appears to be slightly offset. Here we consider the properties of NGC 1534 and the environment that surrounds it and argue that it is not inconsistent that if the AGN has switched off, we could see a drift in the position of the source in the loose group environment which could account for the slight misalignment of optical host and radio jet positions.

4.1. *Radio emission from disk galaxies in the NGC 1534 field*

Radio emission is detected in four disk galaxies in the NGC 1534 field, including NGC 1534 itself. Fig. 11(i)–(iii) show the relevant galaxies with 2.2-GHz contours overlaid. NGC 1534 and Source E show typical diffuse emission consistent with low nuclear activity, however both Source C1 and C2 have reasonably strong nuclear activity, with Source C1 showing extensions north and south. Sources C1 and C2 are reported as part of the galaxy triple AM 0409−630 ($z = 0.0481 \pm 0.0002$; Strauss et al., 1992), though no redshift is directly available for Source C2. At this redshift, the extension seen in the radio structure of Source C1 are of the

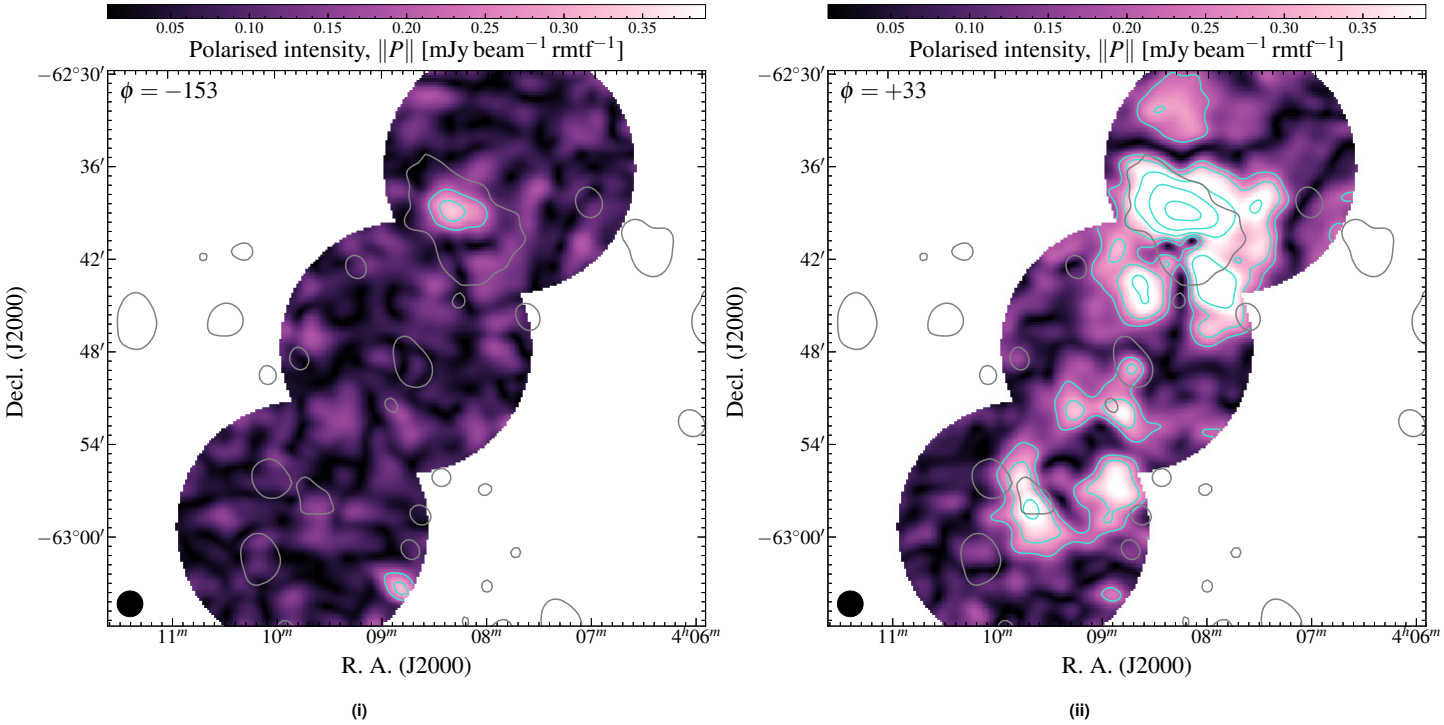

Figure 9. Planes in the Faraday depth cube as indicated in Fig. 8(ii). (i): $\phi = -153$. (ii): $\phi = +33$. In both panels, the single black contour is of the medium-resolution 1510-MHz image at 810 μJy beam^{-1}. The turquoise contours are the linear polarization intensity at the specific Faraday depth, beginning at 210 μJy beam^{-1} rmtf^{-1} and increasing with factors of $\sqrt{2}$. The black ellipse in the lower-left corner is the beam shape of the Faraday depth cube. Both images share the same linear colour scale.

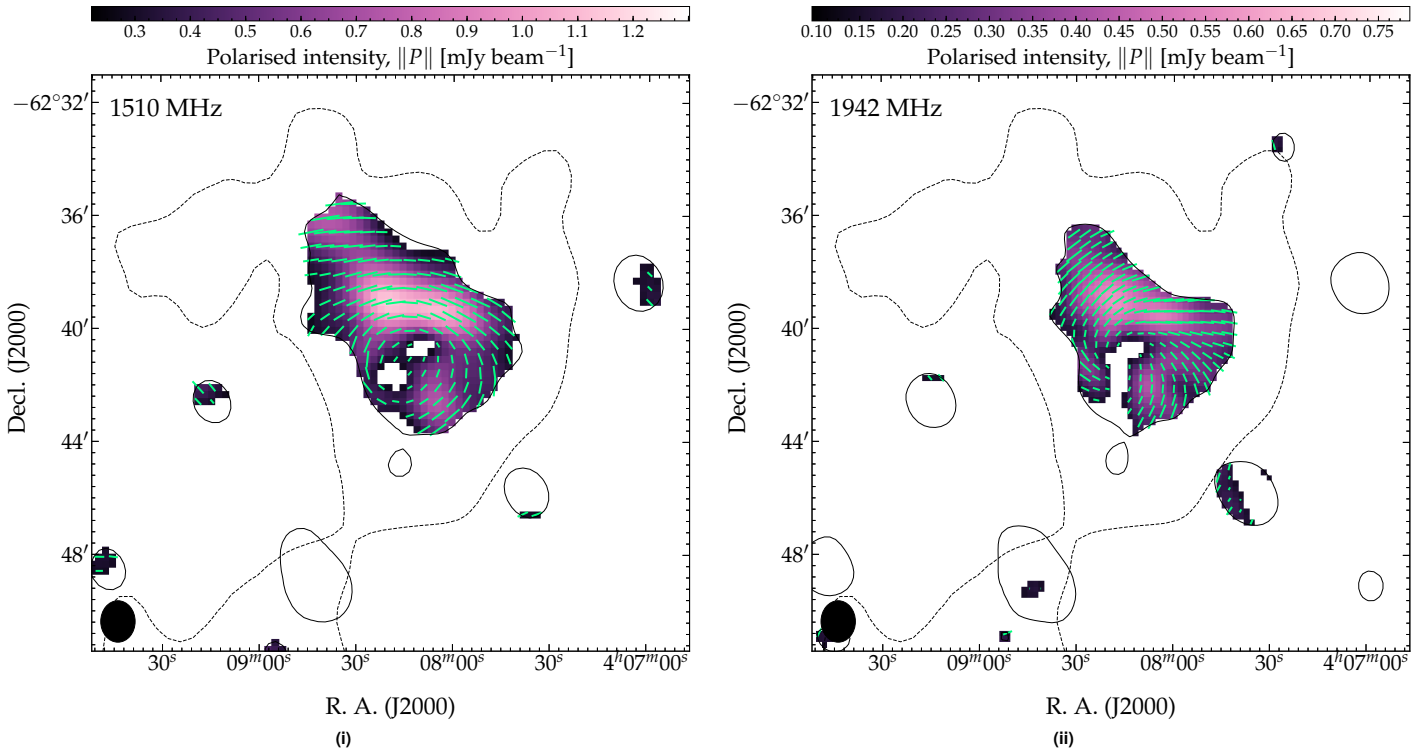

Figure 10. Polarization images. (i): 1510-MHz subband image. (ii): 1942-MHz subband image. The background in both panels is the total linear polarization intensity map (i.e. $\|P\| = \sqrt{Q^2 + U^2}$) which is overlaid with a single black, dashed GLEAM 200-MHz contour at $3\sigma_{\rm rms}$ and a single black, solid ATCA Stokes I contour at $3\sigma_{\rm rms}$ of the medium-resolution image. The fields are the B-field and the vector lengths are proportional to m_P where 5 pixels correspond to $m_P = 1$. The position angles are corrected for Galactic Faraday rotation, assuming $\phi_{\rm gal} = +33$ rad m^{-2}, and an additional Faraday screen at $\phi = -153$ rad m^{-2}.

Table 6 Mid-infrared properties of NGC 1534 from *WISE* (Cutri et al., 2013). For these data we estimate a spectral index of 0.2 for obtaining correction factors for magnitude to flux density conversion and for estimating luminosity, L_ν. The Solar luminosity, $L_\odot$, is taken to be 3.839×10^{33} W as per Jarrett et al. (2013).

Band	λ (μm)	$m_{\rm Vega}$ (mag)	S_ν (mJy)	νL_ν ($\times 10^9\,L_\odot$)
$W1$	3.4	10.365 ± 0.022	22.12 ± 0.45	-
$W2$	4.6	10.377 ± 0.019	12.14 ± 0.21	-
$W3$	12	8.193 ± 0.019	16.73 ± 0.29	0.763 ± 0.013
$W4$	22	6.567 ± 0.050	19.75 ± 0.91	0.491 ± 0.023

order 10 kpc. Additionally, further extension in the radio emission traces the central portion of the bar. Source E is part of the triple AM 0406−624, though itself has no redshift. Its triple members, PGC 014488 and LEDA 075047 have redshifts $z = 0.0189 \pm 0.0002$ and $z = 0.0193 \pm 0.0002$ (Jones et al., 2009), respectively. If the triple association is correct, then we estimate a redshift of $z \sim 0.0191$. At this redshift, the separation from NGC 1534 is only ~ 380 km s^{-1}. This implies a loose group association.

Importantly, we see from Figures 5 and 11 that the radio emission from the core NGC 1534 is extended and diffuse, even at high frequencies. It is therefore very likely to be the result of only star formation in the disk of the galaxy, and there is no significant AGN present in the NCG 1534 core.

4.2. *Star formation in NGC 1534*

As mentioned above, our ATCA images at 2.1 and 17 GHz clearly show that the main component of radio emission from NGC 1534 is extended and diffuse, likely originating within the disk from star formation rather than from any significant nuclear activity. We can test the validity of this assertion by comparing the mid-infrared star-formation rate (SFR) estimators via *Widefield Infrared Survey Explorer* (*WISE*; Wright et al., 2010; Mainzer et al., 2011) measurements (e.g. Jarrett et al., 2013) with the 1.4-GHz SFR estimator via our 2.1-GHz ATCA measurements (Condon, 1992; Hopkins et al., 1998; Cram et al., 1998). At present, one must be cautious when using radio luminosity a SFR estimator as doing so assumes all radio emission is directly related to past star formation and not AGN or other nuclear activity. In the case of a normal radio galaxy with typical double-lobed structure, the AGN component will dramatically dominate the comparatively feeble radio emission from supernova remnants thus providing a massively overestimated SFR. Likewise, infrared SFR estimators will run into similar problems, though much less dramatically.

Fortunately, NGC 1534 is detected in all four bands of the *WISE* all-sky catalogue, AllWISE (Cutri et al., 2013). *WISE* has bands $W1$–4, corresponding to wavelengths 3.4, 4.6, 12, and 22 μm. Table 6 presents $W1$–4 band Vega-calibrated magnitudes as well as flux densities and luminosities assuming a spectral index across the $W1$–4 bands of 0.2. With comparison to Figure 11 of Yan et al. (2013), we can see from *WISE* colours $W1 - W2 = -0.012$ and $W2 - W3 = 2.184$ that NGC 1534 may indeed have some form of nuclear activity, though may also be considered as star-forming. With reference to Equation 2 of Jarrett et al. (2013), we estimate the SFR from the $W4$ measurement: $SFR_{22} = 0.37 \pm 0.04$ M$_\odot$ yr^{-1}. Note that the *WISE* $W4$ band traces mostly the warm interstellar medium dust emission and is a lower estimate of the full SFR.

For the 1.4-GHz SFR, we use the 1.4-GHz power of NGC 1534 derived in Section 3.1.1. We use the 1.4-GHz SFR estimator of Hopkins (1998, Equation 7.1; adapted from Condon 1992) to estimate $SFR_{1.4} = 0.38 \pm 0.03$ M$_\odot$ yr^{-1}, which is valid for the non-thermal synchrotron component, mostly tracing supernova remnants and is valid for stars with $M \geq 5$ M$_\odot$. This value is in good agreement to SFR_{22} derived from *WISE* results. The agreement in these two estimators suggests a lack significant emission from an AGN and further suggests NGC 1534, if the original host of the radio lobes, is no longer fuelling them.

4.3. *A dead radio galaxy*

Hurley-Walker et al. (2015) consider NGC 1534 to be a previously active radio galaxy, with the emission seen surrounding it the remnants of the ancient lobes. The ATCA observations of NGC 1534 point toward a lack of AGN activity, which, coupled with the offset of NGC 1534 from the centre of the lobes, suggests a dying—or dead—radio galaxy. Such an object is less common outside of galaxy clusters (e.g. Cordey, 1987; Murgia et al., 2011). The spectral properties of the lobes of NGC 1534 are consistent with the cluster-based dead radio galaxy sample of Murgia et al. (2011) as well as non-cluster based examples (e.g. Jamrozy et al., 2004; Parma et al., 2007; Brienza et al., 2016). However, in dense cluster environments the radio plasma becomes confined and the lobe size also remains much smaller (Murgia et al., 2011). In the case of NGC 1534, we have emission $\gtrsim 600$ kpc outside of any dense environment which provides an interesting example of a dead field radio galaxy.

The emission surrounding NGC 1534 has many similarities with the remnant emission 'blob1' (Brienza et al., 2016)—namely its location in an underdense environment, its projected size, and the spectral energy distribution. The $t_{\rm off}/t_{\rm s}$ ratio of its 'characteristic time', 0.8, is also similar, however, the spectral age determined through CI$_{\rm off}$ modelling may be poorly represented (see e.g. Harwood, 2017). Assumptions such as a constant magnetic field over the lifetime of the source or a constant spectrum over the extent of the source can lead to uncertain spectral ages (see e.g. Harwood, 2017; Harwood et al., 2017; Turner et al., 2018a,b), and adiabatic losses will result in an underestimate to the dynamical age (particularly in an underdense medium; Blundell & Rawlings, 2000). Work has been done to incorporate adiabatic losses into radio galaxy spectral models (see Godfrey et al., 2017; Heesen et al., 2018), and model fitting across the extent of a resolved source can alleviate the issues with integrated spectra (e.g. Harwood, 2017, and Harwood et al. 2013, 2015 with the use of `brats` in this regard). Additionally, Turner et al. (2018b) discuss how the CI spectrum can be modelled independent of the magnetic field, though note that the magnetic field strength is required for an estimate of the source's synchrotron age. Interestingly, we see that the intrinsic magnetic field of dead radio galaxies does not differ much based on environment (assuming a fixed magnetic field strength)—from a mixture of cluster and

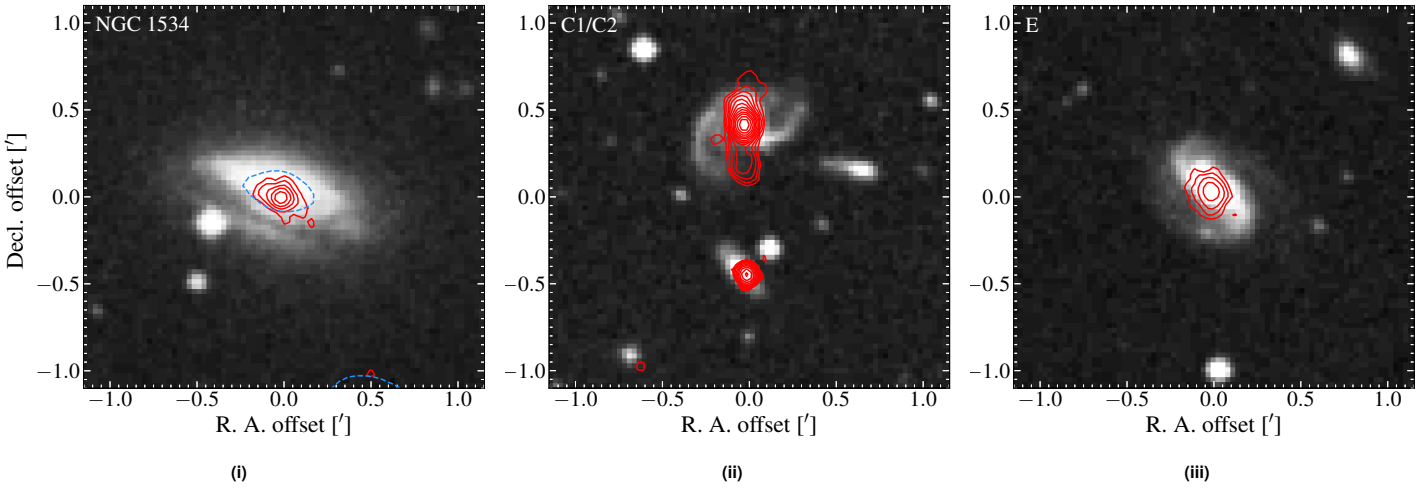

Figure 11. Disk galaxies in the NGC 1534 field with significant radio emission at 2.2 GHz. (i): NGC 1534. (ii): Sources C1 and C2. (iii): Source E. The background images are the blue band UKST images, and the solid, red contours are from the 2.2-GHz wideband ATCA image, beginning at $3\sigma_{\rm rms}$ for NGC 1534 and $4\sigma_{\rm rms}$ for Sources C1/C2 and E. The dashed, blue contour in (i) is the 17-GHz medium-resolution image at $3\sigma_{\rm rms}$.

non-cluster sources, for both the samples of Parma et al. (2007) and Murgia et al. (2011), a mean equipartition magnetic field of $\sim$ 13 μG exists, though note that their equipartition calculations use a fixed energy range rather than a fixed frequency range as used here, and are up to a factor of two larger. Additionally, 'blob1' has 1 μG (Brienza et al., 2016), emission surrounding NGC 5580 and NGC 5588 in a poor group has 2.5 μG (de Gasperin et al., 2014, though note the authors are uncertain of its classification), and the archetypcal B2 0924+30 in the poor cluster ZwCL 0926.5+30.26 (Ekers et al., 1975; Cordey, 1987; Jamrozy et al., 2004; Shulevski et al., 2017) with $B_{\rm eq}$ ranging from 0.89–1.6 μG, which is consistent with $B_{\rm eq} \approx 2.7$ μG we find for NGC 1534.

With so few examples of of dead radio galaxies outside of rich clusters, adding counts to this population will only help in understanding the life-cycles of radio galaxies.

4.4. *The group environment*

NGC 1534 is catalogued as part of the HDC 269 and LDC 292 galaxy groups (Crook et al., 2007), which have line-of-sight velocity dispersions 119.3 and 198.7 km s^{-1}. The high density group, HDC 269, has three members: NGC 1534 itself, NGC 1529, and 2MASX J04111365-6242521; locations of these group members are indicated on Fig. 1 as cyan squares. The group velocity is calculated to be 5201 km s^{-1} (Crook et al., 2007). If NGC 1534 is indeed the host, then we see from the offset position of the optical galaxy and the thinnest point of the radio emission that NGC 1534 must have moved from its old lobes, leaving the radio plasma to gradually diffuse and lose energy to the intergalactic medium. The shortest timescale available for NGC 1534 for movement is if all velocity is in the transverse direction. If we assume that the transverse velocity is no more than its radial velocity, we can assume that the projected transverse velocity is given by the velocity dispersions which allows us to determine the maximum distance NGC 1534 could have drifted from it's original position or alternatively the minimum age of the emission had NCG 1534 drifted this far, assuming the greatest possible transverse velocity. Assuming the pinching point between the lobes was the original location of NGC 1534, we calculate a projected separation of 1.72 arcmin corresponding to 38.5 kpc. With our assumed projected transverse velocities, this indicates a minimum age of the emission (and since NGC 1534 stopped producing it) of 190 Myr (or 316 Myr). Given that this is an underdense environment, the relic plasma will continue to move along the same path as NGC 1534, which pushes these times up further, and movement in any direction not transverse will do the same. This time scale is on the same order as the 'off' spectral age of $\sim$ 158 Myr making it plausible that NGC1534 is the original host, despite the now imperfect alignment of the galaxy and the emission.

4.5. *Implications for furture studies*

It is worth noting that originally, the emission was not found in a survey but as part of a set of targeted observations. However, surveys such as GLEAM, the TFIR GMRT [7] Sky Survey (TGSS alternate data release 1; Intema et al., 2017), the LOFAR Multifrequency Snapshot Sky Survey (MSSS; Heald et al., 2015) and the LOFAR Two-metre Sky Survey (LoTSS; Shimwell et al., 2017), are providing the low frequency observations required to uncover a heretofore unseen population of faint, steep-spectrum sources. With GLEAM (and the MWA in general), the u–v coverage offered by its short baseline observations allow for the detection of low-surface brightness, large-scale emission and where there exists overlap with the TGSS, there is the benefit of complementary, higher-resolution data to confirm, e.g., cores or other compact structure within the emission. However, while emission with such large angular extent such as that presented here is comparatively rare, such low surface-brightness sources do not have to be so large. Smaller-scale, low surface-brightness emission (at higher redshift or otherwise) may

[7] Tata Institute of Fundamental Research Giant Metrewave Radio Telescope

be missed if using only the low-resolution GLEAM survey, though this may be alleviated somewhat with upcoming MWA Phase II surveys using the extended tile configuration, which will have a resolution on the order of two times that of GLEAM at a small cost to surface brightness sensitivity (Wayth et al., in preparation).

Remnant emission like that around NGC 1534 (or 'blob1'; Brienza et al., 2016) would likely be missed in surveys focused within a small frequency band such as that offered by GLEAM due to their reasonably flat low-frequency spectra. It has been suggested (Murgia et al., 2011; Brienza et al., 2016, 2017, but see also Sohn et al. 2003) that using the spectral curvature, SPC = $\alpha_{\rm high} - \alpha_{\rm low}$, where $\alpha_{\rm high}$ and $\alpha_{\rm low}$ are high- and low-frequency spectral indices, respectively, would be a useful tool in detecting dead radio galaxies, as SPC < -0.5 implies a non-active source. Such a diagnostic tool requires a good choice of $\alpha_{\rm high}$ and $\alpha_{\rm low}$, though Harwood (2017) note that even this may not be sufficient due to the different $\alpha_{\rm inj}$ between FR-I and FR-II sources. Furthermore, such a survey would require high- and low-frequency data and at present the most sensitive, higher frequency southern sky counterpart to GLEAM is SUMSS, which may not be high enough in frequency. The upcoming Evolutionary Map of the Universe (EMU; Norris et al., 2011) with the Australia Square Kilometre Array Pathfinder (ASKAP; Johnston et al., 2007) is expected to have a rms sensitivity on the order of 10 µJy beam^{-1}. This, coupled with its low-surface–brightness sensitivity and the frequency range 1130–1430 MHz, will give another high-frequency counterpart to GLEAM (and future MWA Phase II surveys) for searches of remnant radio galaxies, paving the way to vastly increase the detection rate of this population.

Within the context of searching for radio lobes of disk galaxies (e.g. Singh et al., 2015), the larger and possibly faint lobes of giant radio galaxies (e.g. Saripalli et al. 2005), or searching for dead radio sources (e.g. Murgia et al., 2011), the low frequency surveys can be paired with optical surveys such as Pan-STARRS1 (Panoramic Survey Telescope And Rapid Response System; Kaiser et al. 2010, PS1; Tonry et al. 2012, Chambers et al. 2016) for $\delta > -30°$ or the SkyMapper Southern Sky Survey (SMSS; Wolf et al. in preparation [8]) for $\delta \lesssim +2°$ for confirmation of the optical host. On top of the additional depth of the surveys, PS1 has five optical bands from near infrared to blue and SMSS has six from NIR to NUV allowing better estimation of photometric redshifts which is vital when spectroscopic redshifts are unavailable. Further in the future, southern spectroscopic surveys such as the Taipan Galaxy Survey (da Cunha et al., 2017), in conjunction with SMSS will provide an analogue to the Sloan Digital Sky Surveys (SDSS; York et al., 2000, specifically surveys such as the Legacy Survey; Abazajian et al. 2009) and will facilitate surveys for disk galaxies hosting large-scale radio emission as well as surveys of dead or dying radio sources.

5. Conclusion

In this paper we have presented follow-up observations with the ATCA of the remnant emission surrounding the lenticular galaxy NGC 1534 originally detected by Hurley-Walker et al. (2015). We combined this with new low frequency MWA data to study the emission from 72 MHz to 19 GHz, including polarimetric study in the ATCA 16 cm band. We summarise the main results here.

- We find the northern lobe to be well-fit by a $\rm CI_{off}$ model with a fixed $B_{\rm eq} \approx 2.7$ µG and $\alpha_{\rm inj} = 0.54 \pm 0.24$, obtain an estimate of the spectral age of the emission on the order of ~ 203 Myr, having been active for only ~ 44 Myr.
- The ATCA 2.1- and 17-GHz data corroborate the notion that NGC 1534 has no significant core emission, with low-brightness, diffuse emission seen from the galaxy with no compact counterpart.
- We find consistency between the radio and mid-infrared derived star-format rates for NGC 1534 with $SFR_{1.4} = 0.38 \pm 0.03$ $\rm M_\odot\,yr^{-1}$ and $SFR_{22} = 0.37 \pm 0.04$ $\rm M_\odot\,yr^{-1}$, consistent with a lack of significant nuclear activity.
- The northern lobe is shown to be highly linearly polarised at 1510 and 1942 MHz, with $m_{\rm P,1510} = 42 \pm 13$ % and $m_{\rm P,1942} = 43 \pm 14$ %.
- RM-synthesis of the region detects a significant Galactic foreground screen at +33 rad m^{-2} with an additional peak in the Faraday spectrum of the northern lobe at -153 rad m^{-2}.
- Analysis of the position of NGC 1534 with the improved expected position of the host galaxy suggests that the host has drifted away from its original position over a time period commensurate with the cessation of AGN activities.

From these findings, we see that the lenticular galaxy NGC 1534 and the surrouding emission is consistent with remnant radio galaxies, we confirm its classificaton as a rare 'dead' radio galaxy not associated with a galaxy cluster. It additionally sits with the rare class of radio galaxies associated with dusty disk galaxies. With such a wealth of data soon available from upcoming and currently underway sky surveys at multiple wavelengths, we expect to be able to greatly expand both the number of such sources detected and using the panchromatic data available, better understand their host systems.

Acknowledgements. SWD acknowledges a Doctoral Scholarship from Victoria University of Wellington and an Australian Government Research Training Programme scholarship administered through Curtin University. The Australia Telescope Compact Array is part of the Australia Telescope National Facility which is funded by the Australian Government for operation as a National Facility managed by CSIRO. The authors would like to thank the anonymous referee for helpful comments and suggestions that helped to improve this paper.

This research made use of `astropy`, a community-developed core `python` package for Astronomy (Astropy Collaboration et al., 2013), along with `aplpy`, an open-source plotting package for `python` hosted at `http://aplpy.github.com`. This research also made use of `NumPy` (van der Walt et al., 2011), `matplotlib` (Hunter, 2007), and `iPython` (Pérez & Granger, 2007) which are part of the `SciPy` library for `python`: `https://www.scipy.org/`. This research has made use of the VizieR catalogue access tool, CDS, Strasbourg, France. The original description of the VizieR service was described in Ochsenbein et al. (2000).

[8] `http://skymapper.anu.edu.au/surveys/skymapper-southern-sky-survey/`

This research also made use of the NASA/IPAC Extragalactic Database (NED) which is operated by the Jet Propulsion Laboratory, California Institute of Technology, under contract with the National Aeronautics and Space Administration. The Digitized Sky Surveys were produced at the Space Telescope Science Institute under U.S. Government grant NAG W-2166. The images of these surveys are based on photographic data obtained using the Oschin Schmidt Telescope on Palomar Mountain and the UK Schmidt Telescope. The plates were processed into the present compressed digital form with the permission of these institutions.

References

Abazajian K. N., et al., 2009, ApJS, 182, 543
Alexander P., Leahy J. P., 1987, MNRAS, 225, 1
Astropy Collaboration et al., 2013, A&A, 558, A33
Bagchi J., et al., 2014, ApJ, 788, 174
Blundell K. M., Rawlings S., 2000, AJ, 119, 1111
Bock D. C.-J., Large M. I., Sadler E. M., 1999, AJ, 117, 1578
Bowman J. D., et al., 2013, PASA, 30, 31
Brentjens M. A., de Bruyn A. G., 2005, A&A, 441, 1217
Bridle A. H., Perley R. A., 1984, ARA&A, 22, 319
Brienza M., et al., 2016, A&A, 585, A29
Brienza M., et al., 2017, A&A, 606, A98
Briggs D. S., 1995, in American Astronomical Society Meeting Abstracts. p. 1444
Burbidge G. R., Burbidge E. M., 1957, ApJ, 125, 1
Burn B. J., 1966, MNRAS, 133, 67
Calabretta M. R., Staveley-Smith L., Barnes D. G., 2014, PASA, 31, e007
Callingham J. R., et al., 2017, ApJ, 836, 174
Chambers K. C., et al., 2016, preprint, (arXiv:1612.05560)
Clark B. G., 1980, A&A, 89, 377
Condon J. J., 1992, ARA&A, 30, 575
Cooper B. F. C., Price R. M., Cole D. J., 1965, Australian Journal of Physics, 18, 589
Cordey R. A., 1986, MNRAS, 219, 575
Cordey R. A., 1987, MNRAS, 227, 695
Cram L., Hopkins A., Mobasher B., Rowan-Robinson M., 1998, ApJ, 507, 155
Crook A. C., Huchra J. P., Martimbeau N., Masters K. L., Jarrett T., Macri L. M., 2007, ApJ, 655, 790
Cutri R. M., et al., 2013, Technical report, Explanatory Supplement to the AllWISE Data Release Products. University of California, Los Angeles, and the Jet Propulsion Laboratory/California Institute of Technology
Duffy P., Blundell K. M., 2012, MNRAS, 421, 108
Ekers R. D., Fanti R., Lari C., Ulrich M.-H., 1975, Nature, 258, 584
Ekers R. D., Goss W. M., Kotanyi C. G., Skellern D. J., 1978, A&A, 69, L21
Fanaroff B. L., Riley J. M., 1974, MNRAS, 167, 31P
Frater R. H., Brooks J. W., Whiteoak J. B., 1992, Journal of Electrical and Electronics Engineering Australia, 12, 103
Gallimore J. F., Axon D. J., O'Dea C. P., Baum S. A., Pedlar A., 2006, AJ, 132, 546
Giovannini G., Feretti L., Gregorini L., Parma P., 1988, A&A, 199, 73
Godfrey L. E. H., Morganti R., Brienza M., 2017, MNRAS, 471, 891
Hambly N. C., et al., 2001a, MNRAS, 326, 1279
Hambly N. C., Irwin M. J., MacGillivray H. T., 2001b, MNRAS, 326, 1295
Hambly N. C., Davenhall A. C., Irwin M. J., MacGillivray H. T., 2001c, MNRAS, 326, 1315
Hancock P. J., Murphy T., Gaensler B. M., Hopkins A., Curran J. R., 2012, MNRAS, 422, 1812
Hancock P. J., Trott C. M., Hurley-Walker N., 2018, PASA, 35, e011
Harwood J. J., 2017, MNRAS, 466, 2888
Harwood J. J., Hardcastle M. J., Croston J. H., Goodger J. L., 2013, MNRAS, 435, 3353
Harwood J. J., Hardcastle M. J., Croston J. H., 2015, MNRAS, 454, 3403
Harwood J. J., et al., 2017, MNRAS, 469, 639
Heald G. H., et al., 2015, A&A, 582, A123
Heesen V., et al., 2018, MNRAS, 474, 5049
Högbom J. A., 1974, A&AS, 15, 417
Hopkins A. M., 1998, PhD thesis, School of Physics, University of Sydney, NSW, 2006, Australia
Hopkins A. M., Mobasher B., Cram L., Rowan-Robinson M., 1998, MNRAS, 296, 839
Hota A., et al., 2011, MNRAS, 417, L36
Hunter J. D., 2007, Computing in Science & Engineering, 9, 90
Hurley-Walker N., et al., 2015, MNRAS, 447, 2468
Hurley-Walker N., et al., 2017, MNRAS, 464, 1146
Intema H. T., Jagannathan P., Mooley K. P., Frail D. A., 2017, A&A, 598, A78
Jaffe W. J., Perola G. C., 1973, A&A, 26, 423
Jamrozy M., Klein U., Mack K.-H., Gregorini L., Parma P., 2004, A&A, 427, 79
Jarrett T. H., et al., 2013, AJ, 145, 6
Johnston-Hollitt M., Sato M., Gill J. A., Fleenor M. C., Brick A.-M., 2008, MNRAS, 390, 289
Johnston S., et al., 2007, PASA, 24, 174
Jones D. H., et al., 2009, MNRAS, 399, 683
Kaiser N., et al., 2010, in Ground-based and Airborne Telescopes III. p. 77330E, doi:10.1117/12.859188
Kardashev N. S., 1962, Soviet Ast., 6, 317
Komissarov S. S., Gubanov A. G., 1994, A&A, 285
Laing R. A., Bridle A. H., Parma P., Feretti L., Giovannini G., Murgia M., Perley R. A., 2008, MNRAS, 386, 657
Large M. I., Mills B. Y., Little A. G., Crawford D. F., Sutton J. M., 1981, MNRAS, 194, 693
Ledlow M. J., Owen F. N., Keel W. C., 1998, ApJ, 495, 227
Liu R., Pooley G., Riley J. M., 1992, MNRAS, 257, 545
Mainzer A., et al., 2011, ApJ, 731, 53
Mao M. Y., et al., 2015, MNRAS, 446, 4176
Martinez Aviles G., et al., 2016, A&A, 595, A116
Martinez Aviles G., et al., 2018, A&A, 611, A94
Mauch T., Murphy T., Buttery H. J., Curran J., Hunstead R. W., Piestrzynski B., Robertson J. G., Sadler E. M., 2003, MNRAS, 342, 1117
Miley G., 1980, ARA&A, 18, 165
Moffet A. T., 1975, Strong Nonthermal Radio Emission from Galaxies. the University of Chicago Press, p. 211
Mulcahy D. D., et al., 2016, A&A, 595, L8
Murgia M., et al., 2011, A&A, 526, A148
Murphy T., Mauch T., Green A., Hunstead R. W., Piestrzynska B., Kels A. P., Sztajer P., 2007, MNRAS, 382, 382
Newville M., Stensitzki T., Allen D. B., Ingargiola A., 2014, LMFIT: Non-Linear Least-Square Minimization and Curve-Fitting for Python, doi:10.5281/zenodo.11813, https://doi.org/10.5281/zenodo.11813
Norris R. P., et al., 2011, PASA, 28, 215
Ochsenbein F., Bauer P., Marcout J., 2000, A&AS, 143, 23
Offringa A. R., van de Gronde J. J., Roerdink J. B. T. M., 2012, A&A, 539, A95
Oppermann N., et al., 2012, A&A, 542, A93
Oppermann N., et al., 2015, A&A, 575, A118
Pacholczyk A. G., 1970, Radio astrophysics. Nonthermal processes in galactic and extragalactic sources. Series of Books in Astronomy and Astrophysics, San Francisco: Freeman, 1970
Parma P., Murgia M., de Ruiter H. R., Fanti R., Mack K.-H., Govoni F., 2007, A&A, 470, 875
Pérez F., Granger B. E., 2007, Computing in Science & Engineering, 9, 21
Planck Collaboration et al., 2016, A&A, 594, A13
Pratley L., Johnston-Hollitt M., 2016, MNRAS, 462, 3483
Saripalli L., Hunstead R. W., Subrahmanyan R., Boyce E., 2005, AJ, 130, 896
Sault R. J., Wieringa M. H., 1994, A&AS, 108
Sault R. J., Teuben P. J., Wright M. C. H., 1995, in Shaw R. A., Payne H. E., Hayes J. J. E., eds, Astronomical Society of the Pacific Conference Series Vol. 77, Astronomical Data Analysis Software and Systems IV. p. 433 (arXiv:astro-ph/0612759)
Shakouri S., Johnston-Hollitt M., Pratt G. W., 2016, MNRAS, 459, 2525
Shimwell T. W., et al., 2017, A&A, 598, A104

Shulevski A., et al., 2017, A&A, 600, A65
Singh V., Ishwara-Chandra C. H., Sievers J., Wadadekar Y., Hilton M., Beelen A., 2015, MNRAS, 454, 1556
Sohn B. W., Klein U., Mack K.-H., 2003, A&A, 404, 133
Steer D. G., Dewdney P. E., Ito M. R., 1984, A&A, 137, 159
Strauss M. A., Huchra J. P., Davis M., Yahil A., Fisher K. B., Tonry J., 1992, ApJS, 83, 29
Tingay S. J., et al., 2013, PASA, 30, 7
Tonry J. L., et al., 2012, ApJ, 750, 99
Turner R. J., Rogers J. G., Shabala S. S., Krause M. G. H., 2018a, MNRAS, 473, 4179
Turner R. J., Shabala S. S., Krause M. G. H., 2018b, MNRAS, 474, 3361
Ulvestad J. S., Wilson A. S., Sramek R. A., 1981, ApJ, 247, 419
Venturi T., Bardelli S., Morganti R., Hunstead R. W., 2000, MNRAS, 314, 594
Wayth R. B., et al., 2015, PASA, 32, 25
Whiting M. T., 2012, MNRAS, 421, 3242
Wilson W. E., et al., 2011, MNRAS, 416, 832
Wright E. L., et al., 2010, AJ, 140, 1868
Yan L., et al., 2013, AJ, 145, 55
York D. G., et al., 2000, AJ, 120, 1579
da Costa L. N., Pellegrini P. S., Davis M., Meiksin A., Sargent W. L. W., Tonry J. L., 1991, ApJS, 75, 935
da Cunha E., et al., 2017, PASA, 34, e047
de Bruyn A. G., Brentjens M. A., 2005, A&A, 441, 931
de Gasperin F., Intema H. T., Williams W., Brüggen M., Murgia M., Beck R., Bonafede A., 2014, MNRAS, 440, 1542
van Haarlem M. P., et al., 2013, A&A, 556, A2
van der Walt S., Colbert S. C., Varoquaux G., 2011, Computing in Science & Engineering, 13, 22

SPT-CL J2032−5627: a new Southern double relic cluster observed with ASKAP

The paper titled '*SPT-CL J2032−5627: a new Southern double relic cluster observed with ASKAP*' is re-produced here in its form as accepted for publication in the Publications of Astronomical Society of Australia published by Cambridge University Press (CUP). The accepted article is re-produced with permission from Cambridge University Press [9] in line with the CUP 'Green Open Access' policy as agreed to in the signed License To Publish [10] prior to publication. Content is © The Author(s), 2021. Published by Cambridge University Press on behalf of the Astronomical Society of Australia. The version of record is available through CUP at: https://doi.org/10.1017/pasa.2020.51. Contributions from Co-authors are outlined in the previous section. This accepted article also appears on arXiv.org at https://arxiv.org/abs/2008.00660 [11].

[9] https://www.cambridge.org/about-us/rights-permissions/faqs/

[10] https://www.cambridge.org/core/services/open-access-policies/open-access-journals/green-open-access-policy-for-journals

[11] Note the appearance is slightly modified in the present version as an update to the PASA LaTeX template.

LaTeX document typeset by the authors from a modified LaTeX template from the *Publications of the Astronomical Society of Australia* (PASA).
Current document status: **accepted for publication in PASA:** `https://doi.org/10.1017/pasa.2020.51`.

Research Paper

SPT-CL J2032−5627: a new Southern double relic cluster observed with ASKAP

S. W. Duchesne[1]*, M. Johnston-Hollitt[1,2], I. Bartalucci[3,4], T. Hodgson[1], and G. W. Pratt[3]
[1]International Centre for Radio Astronomy Research (ICRAR), Curtin University, Bentley, WA 6102, Australia
[2]Curtin Institute for Computation, Curtin University, GPO Box U1987, Perth, WA 6845, Australia
[3]AIM, CEA, CNRS, Université Paris-Saclay, Université Paris Diderot, Sorbonne Paris Cité, F-91191 Gif-sur-Yvette, France
[4]INAF - Istituto di Astrofisica Spaziale e Fisica Cosmica di Milano, Via A. Corti 12, 20133 Milano, Italy

Abstract

We present a radio and X-ray analysis of the galaxy cluster SPT-CL J2032−5627. Investigation of public data from the Australian Square Kilometre Array Pathfinder (ASKAP) at 943 MHz shows two previously undetected radio relics at either side of the cluster. For both relic sources we utilise archival Australia Telescope Compact Array (ATCA) data at 5.5 GHz in conjunction with the new ASKAP data to determine that both have steep integrated radio spectra ($\alpha_{\rm SE} = -1.52 \pm 0.10$ and $\alpha_{\rm NW,full} = -1.18 \pm 0.10$ for the southeast and northwest relic sources, respectively). No shock is seen in XMM-*Newton* observations, however, the southeast relic is preceded by a cold front in the X-ray–emitting intra-cluster medium. We suggest the lack of a detectable shock may be due to instrumental limitations, comparing the situation to the southeast relic in Abell 3667. We compare the relics to the population of double relic sources and find they are located below the current power–mass (*P*–*M*) scaling relation. We present an analysis of the low-surface brightness sensitivity of ASKAP and the ATCA, the excellent sensitivity of both allow the ability to find heretofore undetected diffuse sources, suggesting these low-power radio relics will become more prevalent in upcoming large-area radio surveys such as the Evolutionary Map of the Universe (EMU).

Keywords: galaxies: clusters: individual: SPT-CL J2032-5627 – large-scale structure of the Universe – radio continuum: general – X-rays: galaxies: clusters

1. Introduction

Clusters of galaxies are the largest virialized systems in the Universe (e.g. Peebles, 1980; Oort, 1983), and can best be described as gravitational potential wells comprised predominantly of dark matter (e.g. Blumenthal et al., 1984), hosting tens to thousands of optically luminous galaxies embedded in an X-ray emitting plasma. Galaxy clusters form hierarchically through accretion and highly energetic merger events, and in the Λ Cold Dark Matter (ΛCDM) cosmology, energy is provided to the intra-cluster medium (ICM) through the infall of ICM gas into the potential well of the cluster dark matter halo (see e.g. Kravtsov & Borgani, 2012, for a review). The energy provided to the ICM creates shocks, adiabatic compression, and turbulence within the ICM, as well as providing additional thermal energy to the ICM gas.

Within predominantly unrelaxed (e.g. merging) galaxy clusters, large-scale ($\sim$ 1 Mpc) radio synchrotron emission has been observed, often either coincident with the centrally located X-ray–emitting ICM plasma (so-called *giant radio halos*, e.g. in the Coma Cluster; Willson 1970, or the halo in Abell 2744; Govoni et al. 2001), or peripherally located and co-spatially with X-ray–detected shocks (*radio relics* or *radio shocks*, e.g. the double relic system in Abell 3667; Johnston-Hollitt 2003; Finoguenov et al. 2010). These sources are characterised by not only their large spatial scales, but also their steep, approximately power law synchrotron spectra, with a lack of obvious host galaxy (for a review see van Weeren et al., 2019). Additionally, smaller-scale ($\lesssim$ 400 kpc), steep-spectrum radio emission is seen within clusters classified as either *mini-halos* (see e.g. Giacintucci et al., 2017, 2019) or *radio phoenices* (see e.g. Slee et al., 2001b, and see also Enßlin & Gopal-Krishna 2001) which have some observational similarities (e.g. steep spectrum, low surface brightness) to their larger cousins which can make them difficult to differentiate in some cases.

Such large-scale cluster emission is thought to be generated via in situ acceleration (or *re*-acceleration) of particles. In the case of radio relics (or radio shocks), the (re-)acceleration process is thought to be primarily diffusive-shock acceleration (DSA; see e.g. Axford et al. 1977; Bell 1978a,b; Blandford & Ostriker 1978; and, e.g. Jones & Ellison 1991). DSA is largely consistent with the observed radio properties, and while a lack of observed γ-rays seen co-spatially with radio relics challenges simulations of this process, under certain shock and environmental conditions, e.g. specific shock orientations (Wittor et al., 2017), lower (re-)acceleration efficiency (Vazza et al., 2016), or injection of fossil electrons from cluster radio galaxies (Pinzke et al., 2013), DSA may still be invoked. If radio relics are truly generated from shocks in the ICM, then we may consider the observed double relic systems, hosting two relics on opposites sides of the host cluster, a suitable laboratory to explore the underlying physics of cluster mergers and the

*email: `stefan.duchesne.astro@gmail.com`

resultant emission. In double relic systems, the merger is thought to be not only between two significant subclusters, but also the merger axis is likely to be close to the plane of sky so projection-related effects (e.g. relic size, location, and brightness) are minimised and these important physical parameters can be more accurately derived providing a more complete understanding of the relationships between radio relics and their host clusters (e.g. Johnston-Hollitt et al., 2008; Bonafede et al., 2012; de Gasperin et al., 2014b).

1.1. *SPT-CL J2032−5627*

SPT-CL J2032−5627 is a galaxy cluster detected with the South Pole Telescope (SPT) as part of the SPT Cluster survey using the Sunyaev–Zel'dovich (SZ) effect to identify massive, distant clusters (Song et al., 2012). Song et al. (2012) report a redshift of $z = 0.284$ via spectroscopy of cluster members. The corresponding *Planck* catalogue of SZ sources (Planck Collaboration et al., 2015) reports an SZ-derived mass of $M_{\rm SZ} = 5.74^{+0.56}_{-0.59} \times 10^{14}$ $M_\odot$. The cluster had previously been detected via X-ray (RXC J2032.1−5627; Böhringer et al., 2004) and had been cross-matched with Abell 3685 (at $z = 0.062$; Struble & Rood 1999). We suggest that the redshift associated with Abell 3685 is derived from an isolated foreground galaxy (2MASS J20321605−5625390, indicated on Fig. 1 as "C"). It is unclear whether Abell 3685 is a distinct foreground cluster or if there is only a single cluster a $z = 0.284$ along the line of sight. Bulbul et al. (2019) report an X-ray–derived mass of $M_{\rm X,500} = 4.77^{+0.71}_{-0.63} \times 10^{14}$ $M_\odot$ for SPT-CL J2032−5627, consistent with the SZ-derived mass.

In this work we report on the detection of two heretofore unknown radio relic sources within SPT-CL J2032−5627. A number of Australian radio telescopes have covered the cluster in a combination of surveys and pointed observations, namely: the Australia Telescope Compact Array (ATCA; Frater et al., 1992), the Molonglo Observatory Synthesis Telescope (MOST; Mills, 1981), the Murchison Widefield Array (MWA; Tingay et al., 2013; Wayth et al., 2018), and the Australian Square Kilometre Array Pathfinder (ASKAP; Johnston et al., 2007, 2008; DeBoer et al., 2009). Along with the radio data, archival XMM-*Newton* data are available. This paper will describe the diffuse radio sources found in and around the cluster within the context of the X-ray emission from the cluster core. In this paper we assume a flat ΛCDM cosmology with $H_0 = 70$ km s^{-1} Mpc^{-1}, $\Omega_{\rm m} = 0.3$, and $\Omega_\Lambda = 1 - \Omega_{\rm m}$. At the redshift of SPT-CL J2032−5627, $1'$ corresponds to 257 kpc.

2. Data

2.1. *Radio*

2.1.1. Australian Square Kilometre Array Pathfinder

The ASKAP Evolutionary Map of the Universe (EMU; Norris et al., 2011) aims to observe the whole sky visible to ASKAP down to 10 μJy beam^{-1}, though observing and processing is still underway. ASKAP's phased array feeds (PAF; Chippendale et al., 2010; Hotan et al., 2014; McConnell et al., 2016) allow 36 independently-formed ~ 1 degree field-of-view (FoV) primary beams to be pointed on the sky within the ~ 30 deg^2 PAF FoV, making it a suitable instrument for survey work. Recently, a pilot set of observations for EMU were released, with calibrated visilibities made publicly available via the CSIRO [1] ASKAP Science Data Archive (CASDA; Chapman et al., 2017). Prior to retrieving from CASDA, data go through radio frequency inteference (RFI) flagging, bandpass-calibration, and averaging using the `ASKAPsoft` [2] pipeline on the Pawsey Supercomputing Centre in Perth, Western Australia. For this observation (ID SB9351) ASKAP's 36 primary beams are formed into a "6 by 6" footprint, covering $\sim 6^\circ \times 6^\circ$. Each of these beams are processed and calibrated individually prior to co-adding in the image plane. PKS B1934-638 is used for bandpass and absolute flux calibration, and the data are averaged to 1 MHz after calibration with a full bandwidth of 288 MHz. Observation details are presented in Table 1. After data are retrieved from CASDA, data are imaged using the widefield imager `WSClean` [3] (Offringa et al., 2014; Offringa & Smirnov, 2017). For each beam we generate deep images using the "Briggs" (Briggs, 1995) weighting with robustness parameter $+0.25$, splitting the full ASKAP bandwidth into six subbands of $\Delta\nu = 48$ MHz, all convolved to a common resolution of $16.2'' \times 16.2''$ matching the resolution in the lowest-frequency band. We use the multi-scale CLEAN algorithm to ensure extended sources are accurately modelled. An additional full-bandwidth image is made for each beam, as well as an additional full-bandwidth image with uniform weighting resulting in a resolution of $8'' \times 8''$.

Initial imaging showed the presence of three discrete sources within the extended emission which prompted the need for compact-source–subtracted images. After trialling a number of methods—including source modelling via their spectral energy distributions (SEDs) and subtracting visibilities after imaging compact sources via a hard u–v cut—we found that using CLEAN masks around the diffuse radio sources to be most effective. For this, we re-image the calibrated data with robust $+0.25$ weighting, and using a CLEAN mask that excludes all diffuse emission we ensure that no diffuse emission is included in the CLEAN component model. We then subtracted the frequency-dependent CLEAN component model before imaging the data with a robust $+0.5$ weighting with an additional 20 arcsec Gaussian taper to enhance the diffuse emission. We only generate four source-subtracted subband images to improve the signal-to-noise ratio ($\Delta\nu = 72$ MHz), specifically for the northern components of the emission. Note that cleaning prior to subtraction is done to the same depth as the robust $+0.25$ subbands, and no residual sources are present in the subband images within the CLEAN mask region above the noise. We note for completeness that in the fullband images, residual emission can be seen around some (specifically extended) sources (see Fig. 3) though this full-band image is not used for flux density measurements. All low-resolution subbands are convolved to a common resolution of $36'' \times 36''$.

[1] Commonwealth Scientific and Industrial Research Organisation
[2] https://www.atnf.csiro.au/computing/software/askapsoft/sdp/docs/current/pipelines/introduction.html
[3] https://sourceforge.net/p/wsclean/wiki/Home/

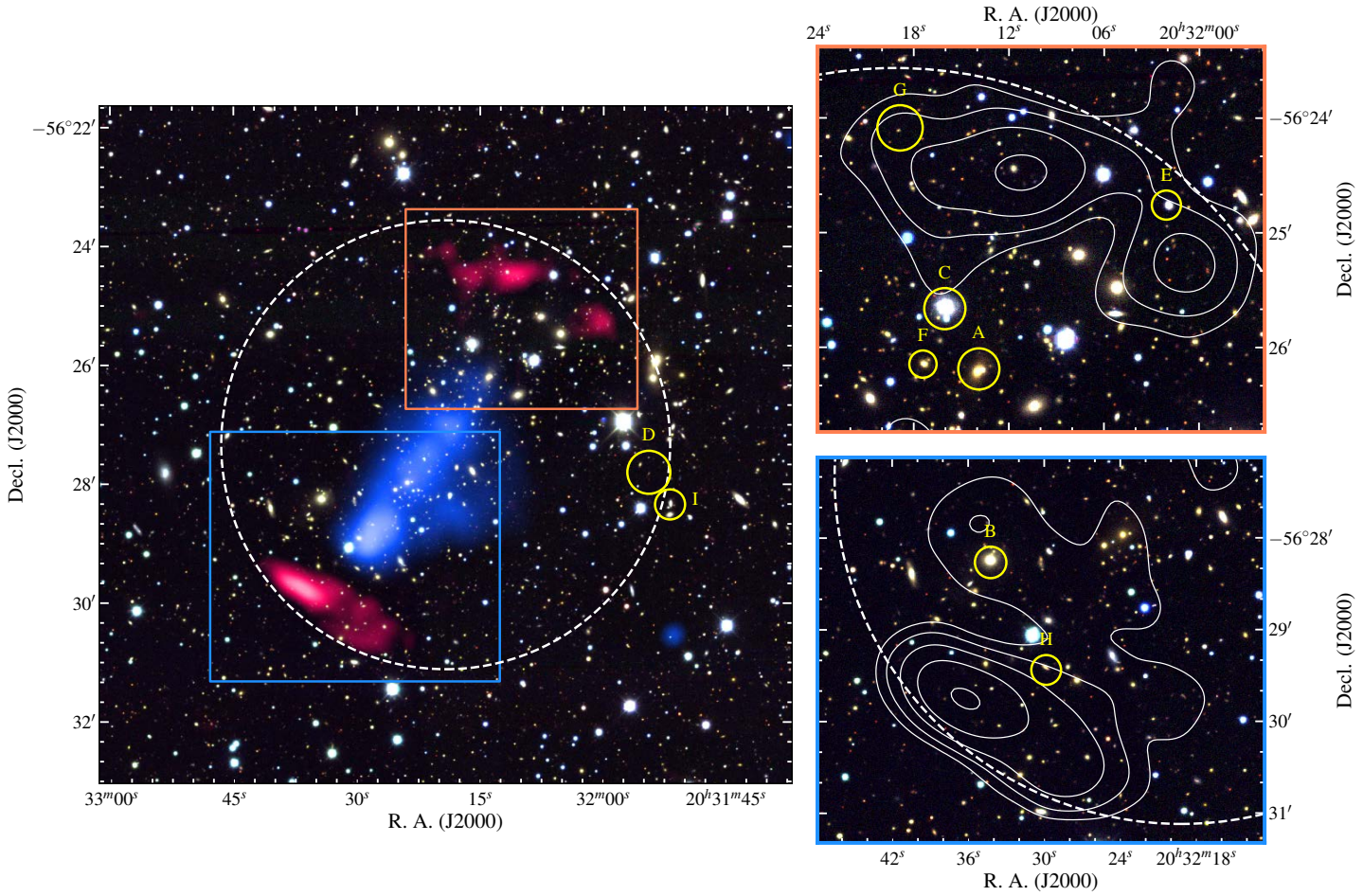

Figure 1. SPT-CL J2032−5627: The background is an RGB image make using the *i*, *r*, and *g* bands of the Dark Energy Survey Data Release 1 (DES DR1; Abbott et al., 2018; Morganson et al., 2018; Flaugher et al., 2015). In the left panel 0.943 GHz ASKAP robust +0.25 source-subtracted data are shown (magenta, 16.2″ resolution) overlaid with XMM-*Newton* data (blue). The side panels feature discrete-source–subtracted, low resolution (36″) ASKAP data, starting at $3\sigma_{\rm rms}$ ($\sigma_{\rm rms} = 54$ μJy beam^{-1}) and increasing with factors of 2. The white, dashed circle is centered on SPT-CL J2032−5627 and has a radius of 1 Mpc. The labelled objects are the main contaminating sources and are discussed in the text, but are not an exhaustive list of subtracted discrete sources. The locations of the right panels are shown in the left panel with blue (bottom, southeast relic) and orange (top, northwest relic) boxes. ASKAP and XMM-*Newton* data are described in Sections 2.1.1 and 2.2, respectively.

For each beam we perform a cross-match with a sky model generated from the GaLactic and Extragalactic All-sky MWA survey (GLEAM; Wayth et al., 2015; Hurley-Walker et al., 2017) and Sydney University Molonglo Sky Survey (SUMSS; Bock et al., 1999; Mauch et al., 2003) and extrapolate the measured SEDs of sources to 943 MHz. We find a ~ 5 per cent standard deviation in measured flux densities compared to the extrapolated flux densities of the $\sim$ 30–40 brightest sources in each beam. SPT-CL J2032−5627 falls within the half-power point of four of the 36 beams (6, 7, 13, and 14). We find the flux scale in the robust +0.25 images of beam 6 to be $\sim 10\%$ higher than the other three beams; as we are unable to identify the cause of this discrepancy and because its inclusion makes little difference to the resultant mosaic, beam 6 is removed for all image sets. For each subband and the fullband image (robust +0.25 and source-subtracted), the three remaining beams are mosaicked, weighted by the square of the primary beam response (a circular Gaussian with full-width at half-maximum proportional to $1.09\lambda/D$, where D is the dish diameter; A. Hotan, priv. comms.). Fig. 1 shows the fullband ASKAP data as contours, with the smaller highlight panels showing the source-subtracted data, with discrete sources labelled. A source-subtracted robust +0.25 image is presented in the left panel of Fig. 1 though is not used for quantitative analysis.

2.1.2. *Australia Telescope Compact Array 4 cm observations*

SPT-CL J2032−5627 was observed in 2009 with the ATCA using the Compact Array Broadband Back-end (CABB; Wilson et al., 2011) for project C1563 (PI Walsh). The 4-cm band observations have dual instantaneous frequency measurements centered at 5.5 and 9 GHz with 2.049 GHz bandwidth. The cluster was observed for $\sim$ 42 minutes in the H75 configuration (maximum baseline 4408 m; minimum baseline 31 m). The H75 configuration has a significant gap between the sixth antenna and the more compact core formed by the remaining antennas which results in a sampling function/point-spread function that can become difficult to accu-

Table 1 Details for the ASKAP and ATCA observations.

Telescope	Dates	$N_{\rm ants}$ [(a)]	$B_{\rm max}$ [(b)] (m)	τ [(c)] (min)	$\Delta\nu$ [(d)] (GHz)	$\nu_{\rm c}$ [(e)] (GHz)	$\theta_{\rm max}$ [(f)] ($'$)	$\sigma_{\rm rms}$ (μJy beam^{-1})
ASKAP	18-07-2019	36	6 000	600	0.288	0.943	49	60(31)[54] [(h)]
ATCA(H75)	02-10-2009	5[(g)]	89	42	2.049	5.5 9.0	6.0 3.7	103(100)[60][(i)] 125 [(i)]

Notes.
(a) Number of antennas. (b) Maximum baseline for observation. (c) Total integration time. (d) Bandwidth. (e) Central frequency. (f) Maximum angular scale that the observation is sensitive to. (g) The sixth antenna is not used due to poor u–v coverage. (h) Root-mean-square (rms) noise in the full-bandwidth uniform(robust 0.25)[robust +0.5, tapered] ASKAP image. (i) rms noise in the uniform(robust 0.0)[natural] ATCA images.

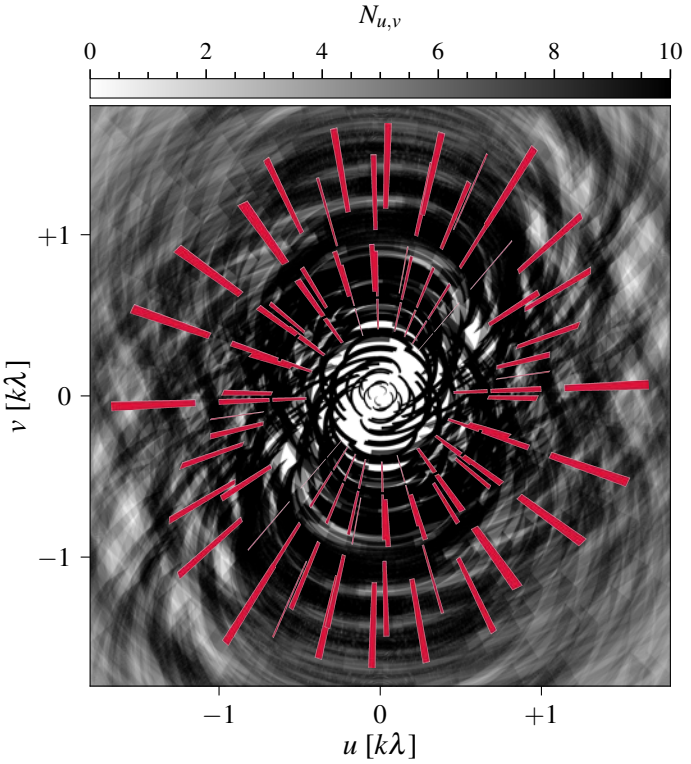

Figure 2. u–v coverage for the 835.5 MHz ASKAP subband (black, $\Delta\nu = 72$ MHz) and 5.5-GHz ATCA fullband (red, $\Delta\nu = 2.049$ GHz) data within -1.8 k$\lambda \leq u \leq 1.8$ kλ and -1.8 k$\lambda \leq v \leq 1.8$ kλ. The ASKAP data are represented as a density (λ^{-2}).

rately deconvolve when imaging [4]. Additionally, because of the shorter observing time the baselines formed with the sixth antenna are significantly elongated in u–v space. We remove antenna 6 prior to self-calibration and imaging for this reason. The observation was performed in "u–v cuts" mode to maximise u–v coverage (see Fig. 2 for a u–v coverage plot with comparison to the ASKAP u–v coverage). Observation details are presented in Table 1. Processing for these data utilise the `miriad` software suite (Sault et al., 1995) as well as `WSClean` and `CASA` for imaging and self-calibration. For initial bandpass and gain calibration, we follow the procedure of Duchesne & Johnston-Hollitt (2019) for the 4-cm data, using PKS B1934−638 as the bandpass and absolute flux calibrator and PKS 1941−554 for phase calibration. `WSClean` is used to generate model visibilities which are then used by the `CASA` task `gaincal` to perform phase-only self-calibration over three iterations, with solution intervals of 300, 120, and 60 s. We only consider Stokes I for this analysis as the resolution of the H75 configuration without antenna 6 is too poor for resolved polarimetry and the observation length prohibits good parallactic angle coverage.

While radio relics are rarely detected above 4 GHz (except in the particularly bright cases e.g. Slee et al. 2001a; Loi et al. 2017), initial imaging at a 'Briggs' robust 0.0 weighting (Fig. 3(i)) revealed residual emission in the vicinity of the relic sources. To determine the nature of this emission, we subtracted the compact components. This is done by imaging the data with a uniform weighting, creating a CLEAN mask that targets only the brightest sources (A, B, and D in Fig. 3(i)), and CLEANing down to $1\sigma_{\rm rms}$ within this mask. The CLEAN model components of these bright, compact sources are subtracted, revealing residual diffuse emission. The remaining discrete sources shown in Fig. 3(i) are not subtracted at this stage. This process results in some over-subtraction of the diffuse emission at the location of source B, though this over-subtraction will be minimal due to the lack of evidence of the diffuse emission in the uniform image. Within the full-width at half maximum (FWHM) of the primary beam no additional residuals are seen in the source-subtracted image to suggest further contamination from poor subtraction except at the location of source F (see Fig. 3(ii)).

To maximise sensitivity here we image the full 2-GHz band with a natural weighting. The resultant source-subtracted 5.5-GHz image is shown in Fig. 3(ii) overlaid on the ASKAP data. Note that 5.5-GHz emission is seen from source F (denoted in Fig. 1) and some low-level residual emission remains from other cluster sources. Additionally, the subtraction of source B is not perfect. Additional uniformly weighted, non–source-subtracted images were made at 5.5- and 9-GHz to measure the SEDs of sources A and B.

2.2. *X-ray*

SPT-CL J2032−5627 was observed by XMM-*Newton* using the European Photon Imaging Camera (EPIC; Turner et al. 2001 and Strüder et al. 2001) for 32 ks (Obs. ID 0674490401). The data

[4] For antenna 6 to be useful in this configuration, additional observations in other ATCA configurations should be used.

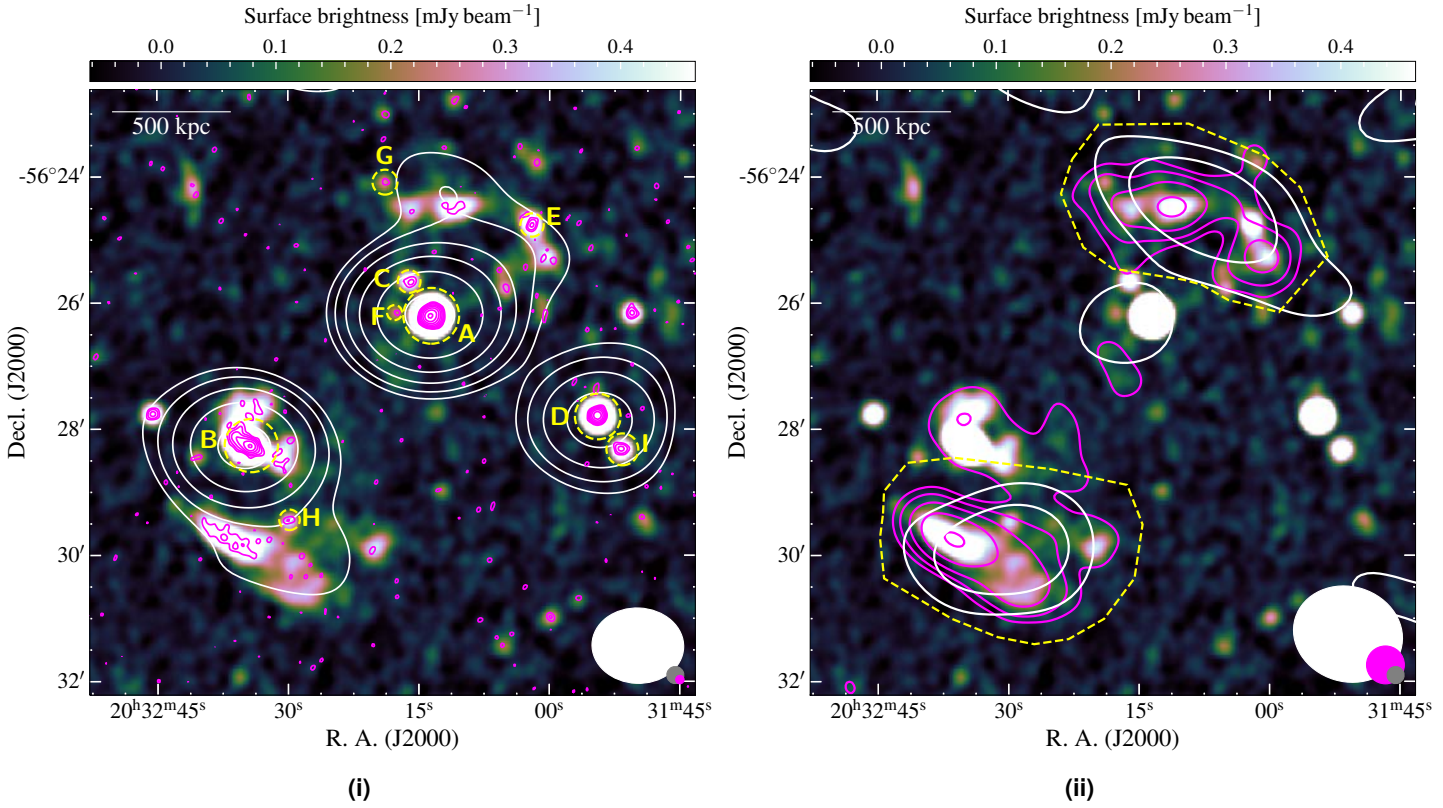

Figure 3. Radio data for SPT-CL J2032−5627. The background image is the fullband ASKAP 16.2″ data. All contours start at $3\sigma_{\rm rms}$ and increase with factors of 2. The contours are as follows: (i) ASKAP 8″, magenta, starting at 180 μJy beam^{-1}; ATCA 5.5-GHz robust 0.0 image, white, starting at 300 μJy beam^{-1}. (ii) ASKAP 36″ source-subtracted, magenta, starting at 162 μJy beam^{-1}; ATCA 5.5-GHz source-subtracted naturally-weighted, white, starting at 180 μJy beam^{-1}. Yellow labels in (i) are discrete sources discussed in the text (Section 3.1). Yellow, dashed regions in (ii) are the flux density integration regions for the NW and SE relics. The beam shapes are shown as ellipses in the bottom right corner, with grey corresponding to the background map. The linear scale in the top left corner is at $z = 0.284$.

were retrieved from the archive and reprocessed using the Science Analysis System version 18.0.0, using the latest calibration files available as of December 2019. High energy particle contamination was reduced by removing events for which the PATTERN keyword was > 4 and > 13 for the MOS1,2 and PN cameras, respectively. Observation intervals affected by flares were identified and removed from the analysis following the prescriptions detailed in Pratt et al. (2007). The cleaned exposure times are 27.7 ks and 20.7 ks for MOS1,2 and PN cameras, respectively. Point sources were identified following the procedures described in Bogdán et al. (2013), and removed from the subsequent analysis.

After these procedures, data taken by the three cameras were combined to maximise the signal-to-noise, and arranged in datacubes. Exposure maps and models of the sky and instrumental background were computed as described in Bourdin & Mazzotta (2008), Bourdin et al. (2013) and Bogdán et al. (2013).

3. Results

The two relics are clearly detected in the ASKAP data as well as the source-subtracted 5.5-GHz ATCA data. Fig. 1 shows the location of the relic sources (top right, bottom right panels), and the top panel in that figure indicates where additional emission from the NW relic may be located (surrounding source E). The two relics are located ~ 850 and ~ 800 kpc from the reported cluster centre in the SE and NW, respectively. Fig. 3 shows the radio data used here, showing the full resolution ASKAP data with lower resolution ASKAP contours overlaid along with the source-subtracted 5.5-GHz ATCA data. From the ASKAP data we estimate the projected extent of the emission: SE relic, 2.77′ (731 kpc at $z = 0.284$), NW relic, 1.71′ (447 kpc, main eastern portion) and 1.58′ (413 kpc, secondary western portion). While there is a compact source (E) within the emission to the west of the NW relic, it is not clear whether the emission surrounding E is associated with the NW relic or not. In the event that it is, then the relic forms a continuous structure with a total projected linear size is 860 kpc.

3.1. *Other radio sources*

The ASKAP data reveal a number of radio sources projected onto the cluster system. As well as the diffuse sources, we will discuss an additional nine sources within the images, labelled A–I, shown on Fig. 1 and Fig. 3. We note the source names and redshifts (where available) in Table 2. For sources A, B, and D we measure the integrated flux densities in the ASKAP and ATCA 5.5- and 9-GHz data. The spectra of A and B show curvature and are fit

Table 2 Compact/intervening radio sources in the field of SPT-CL J2032−5627.

ID.	Name	z	α (b)	q (c)
A	2MASS J20321413−5626117	0.2844 ± 0.0002 (d)	-0.64 ± 0.07	-0.07 ± 0.03
B	2MASX J20323421−5628162	-	-0.38 ± 0.08	-0.12 ± 0.04
C	2MASS J20321605−5625390	0.0621 ± 0.0001 (d)	-1.24 ± 0.81	-
D	SUMSS J203154−562749	-	-0.92 ± 0.05	-
E	WISEA J203202.07−562445.0	-	-1.07 ± 0.59	-
F (a)	2MASS J20321740−5626084	0.2841 ± 0.0002 (d)	-	-
G	WISEA J203219.10−562405.9	-	-0.06 ± 1.04	-
H	WISEA J203229.85−562925.9	-	-1.55 ± 0.98	-
I	WISEA J203151.76-562818.3	-	-0.29 ± 0.57	-

Notes. (a) No SED measured as it is too faint in the ASKAP subbands. (b) $S_\nu \propto \nu^\alpha$. (c) $S_\nu \propto \nu^\alpha e^{q \ln \nu^2}$. (d) Ruel et al. (2014).

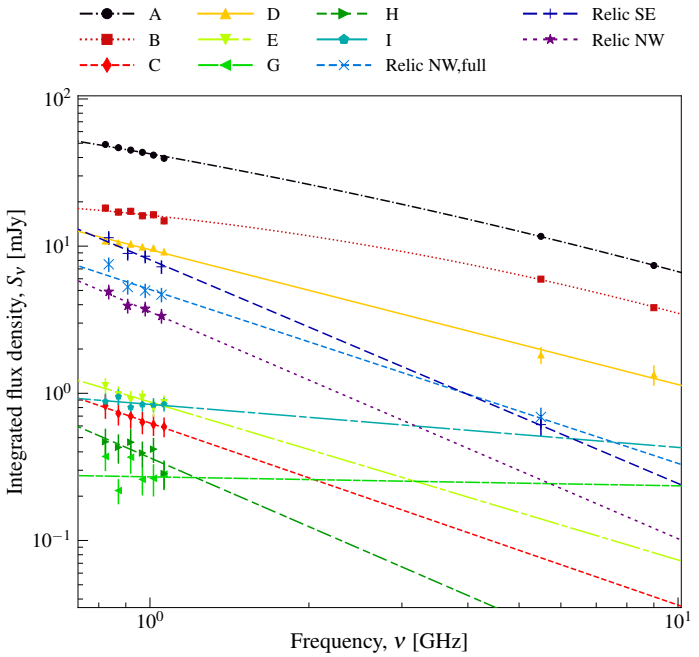

Figure 4. SEDs of compact radio sources in the cluster field. Sources A and B are fitted with generic curved power law models while the remaining sources are with a normal power law. Model parameters are reported in Table 2 and 3 for the discrete sources and relics, respectively.

with a generic curved power law model of the form

$$S_\nu \propto \nu^\alpha e^{q(\ln \nu)^2}, \quad (1)$$

where q is a measure of the curvature and for $q = 0$ the model reduces to a standard power law ($S \propto \nu^\alpha$). For the remaining sources we measure flux densities only from the ASKAP data and all sources except A and B are fit with generic power law models.

Fig. 4 shows SEDs of each of these sources along with the fitted models, and the fitted model parameters are shown in Table 2. As sources A, B, and D+I are point-like sources in the ATCA uniformly weighted images, we use the `aegean` source-finding software [5] (Hancock et al., 2012, 2018) to obtain flux density measurements at 5.5 and 9 GHz. As source D and I become a single point-like source in the ATCA data, we subtract the extrapolated contribution of source I from the `aegean` measurement to obtain flux density measurements at 5.5 and 9 GHz for source D alone. Note that the contributions of sources C and F to the measurement of source A in the ATCA data are significantly less than the errors and are not considered further. Due to the complexity of source B and `aegean` failing to fit the fainter discrete sources, in the ASKAP images we directly measure the flux densities by integrating over regions containing the relevant sources.

[5] https://github.com/PaulHancock/Aegean/tree/master/AegeanTools

Table 3 Relic emission flux density measurements and physical properties.

Relic	ν (MHz)	S_ν (mJy)	α	LLS (kpc)	$\sigma_{\rm rms}$ [(a)] (μJy beam^{-1})
SE	835.5	11.4 ± 0.7	-1.52 ± 0.10	731	109
	907.5	8.92 ± 0.53			84
	979.5	8.54 ± 0.51			75
	1051.5	7.24 ± 0.44			68
	5500.0	0.61 ± 0.10			60
NW	835.5	4.91 ± 0.37	-1.54 ± 0.45	447	100
	907.5	3.95 ± 0.30			82
	979.5	3.76 ± 0.28			77
	1051.5	3.35 ± 0.25			72
	5500.0	$< 0.69 \pm 0.10$			60
NW, full	835.5	7.52 ± 0.53	-1.18 ± 0.10	860	101
	907.5	5.28 ± 0.38			82
	979.5	4.99 ± 0.36			77
	1051.5	4.68 ± 0.36			72
	5500.0	0.69 ± 0.10			60

Notes. (a) Average rms over the source.

3.2. *Radio relic spectral energy distribution*

Within the ASKAP source-subtracted, tapered subband images ($\Delta\nu = 72$ MHz) we integrate the flux density within bespoke polygon regions for each relic source (shown as yellow dashed regions in Fig. 3(ii)). For estimating the uncertainty, we use the Background And Noise Estimation tool (`BANE`; Hancock et al., 2012) to estimate the map rms noise and add an additional uncertainty

based on the flux scale and primary beam correction of 5%. Due to the complex nature of the NW relic source, we measure two different regions, the first being only the most eastern portion of the NW relic, and the second including the emission surrounding source E.

Additionally, we use the residual, source-subtracted 5.5-GHz maps as described in Section 2.1.2 to measure the integrated flux densities of the two relics in the 5.5-GHz map, also integrating the flux within bespoke polygon regions. The regions used here are larger than those used for the ASKAP data due to the difference in resolution. For the first NW relic measurement (i.e. the eastern component) we consider the full 5.5-GHz measurement as an upper limit as we are unable to subtract the contribution from the emission surrounding source E. We add an additional flux scale uncertainty of 10% for these data due to the inherent uncertainty in the source-subtraction with incomplete *u*–*v* data combined with the low resolution of the H75 array and ratio of the primary beam and restoring beams ($\sim 5:1$) and considering the relic sources lie toward the FWHM of the primary beam. Additionally, we subtract the estimated flux density contribution from source E, G, and H, which are not subtracted in visibilities for the 5.5-GHz data.

Fitting a normal power law to the two relic SEDs yields spectral indices of $\alpha_{\rm SE} = -1.52 \pm 0.10$, $\alpha_{\rm NW} = -1.54 \pm 0.45$, and $\alpha_{\rm NW,full} = -1.18 \pm 0.10$, where $\alpha_{\rm NW,full}$ is the spectral index for the NW relic including the emission surrounding source E. We estimate the 1.4-GHz power of the relics from these spectral indices: $P_{1.4}^{\rm SE} = (14.0 \pm 1.6) \times 10^{23}$ W Hz^{-1}, $P_{1.4}^{\rm NW} = (6.2 \pm 1.8) \times 10^{23}$ W Hz^{-1}, and $P_{1.4}^{\rm NW,full} = (9.1 \pm 1.0) \times 10^{23}$ W Hz^{-1}. The measured data and fits are shown in Fig. 4 and presented in Table 3 for the relic sources.

3.3. *X-ray cartography*

The wavelet-filtered, exposure-corrected, and smoothed X-ray image, overlaid with contours from the ASKAP data, is shown in Fig. 5(i). The X-ray morphology of the cluster appears disturbed, with a major axis of elongation along the SE–NW direction. There is a clear bright structure in the centre of the cluster with a tail elongated in the NW direction.

We investigated the projected temperature distribution of the ICM by producing a temperature map using the wavelet filtering approach described in Bourdin et al. (2004) and Bourdin & Mazzotta (2008); the result is shown in Fig. 5(ii).

The NW region does not show any particular features, the mean temperature being ~ 5 keV with no strong spatial variation. The SE region, in contrast, is characterised by the presence of a distinct cold spot at ~ 4 keV, which is spatially coincident with the X-ray brightness peak. This cold spot is surrounded in the SW direction by a bow-like hotter region at ~ 6 keV. The transition between the cold and the hot regions corresponds to a clear drop in the surface brightness visible in the cluster image. This configuration suggests the possible presence of a cold front, resembling that found by Bourdin & Mazzotta (2008) in Abell 2065. However, the radio relic contours follow the SE bow-like hot region, and could therefore signal the presence of a shock related to the merger.

The typical signature of a cold front is a sudden and sharp drop in the ICM brightness map that produces a change of slope in the surface brightness radial profile. This change of slope is translated into a clear jump-like feature in the deprojected density profile, across which the pressure remains constant i.e. the pressure profile does not show features across the cold front. In contrast, the presence of a shock produces a similar signature in the surface brightness and density profiles, but also a jump in the pressure profile. To clarify the nature of the bow-like structure we extracted surface brightness and temperature profiles from annular sectors shown in both panels of Fig. 5 using the radio contours as anchors.

3.4. *X-ray and radio surface brightness profiles*

We extracted background-subtracted, exposure- and vignetting-corrected X-ray brightness profiles in the $[0.5-2.5]$ keV band along the sectors highlighted in Fig. 5. The profiles were binned using a logarithmic bin factor of 1.015, with a mean bin width of 2 arcesc corresponding to 9.2 kpc. These profiles are shown in Fig. 6, where we also overlay the radio surface brightness profiles in the same regions from the full bandwidth ASKAP image as shown in Fig. 3. The presence of a sudden change of the slope in the X-ray surface brightness profile could potentially reveal the existence of a shock. Interior to the position of the radio relic, the X-ray surface brightness profile of the NW sector is noisy and does not show significant features. The radio relic profile peaks at ~ 3.3 arcmin, where we again do not see any correspondence with any obvious feature in the X-ray profile.

The SE profile appears flat below 2 arcmin and then starts dropping. The point where the SE profile slope changes corresponds to the end of the very bright spot that can be seen in Fig. 5(ii). There is a first change of surface brightness slope at ~ 2.5 arcmin matching the position of the bow-like structure. We identified the exact position by fitting the data with a broken power law model in the $[2-4]$ range, following the prescription of Bourdin & Mazzotta (2008). The EPIC point-spread function (PSF) is taken into account in the fitting procedures. The result is shown with a solid blue line in Fig. 6(ii). The change of the slope occurs at 2.272 ± 0.014 arcmin (578 ± 4 kpc). This position is shown with a red solid line in the SE sector in the left panel of Fig. 5, and corresponds to the sharp edge in the brightness map and to the bow-like structure in the temperature map. We extracted the temperature in the two bins of the SE annular sector shown in Fig. 5(ii) obtaining $4.08^{+0.38}_{-0.36}$ keV and $8.50^{+9.47}_{-3.51}$ keV in the upper and lower bin, respectively. We then deprojected the density and the temperature profiles following Bourdin & Mazzotta (2008). We investigated the nature of the slope change by looking at the pressure profile, shown in Fig. 7. The profile across this feature appears to be smooth, as we would expect in the case of a cold front. We also fitted the surface brightness profile using the density model proposed by Vikhlinin et al. (2006, their equation 3) and set the core term, n_{02}, to 0. We compared the result of this fit with the broken power law by using the F-test which yields a value of 16.36 and probability of 0.0049. These values suggest that the use of a double power law model significantly improves the fit. For the reasons discussed above we can interpret this first change in surface brightness slope as being

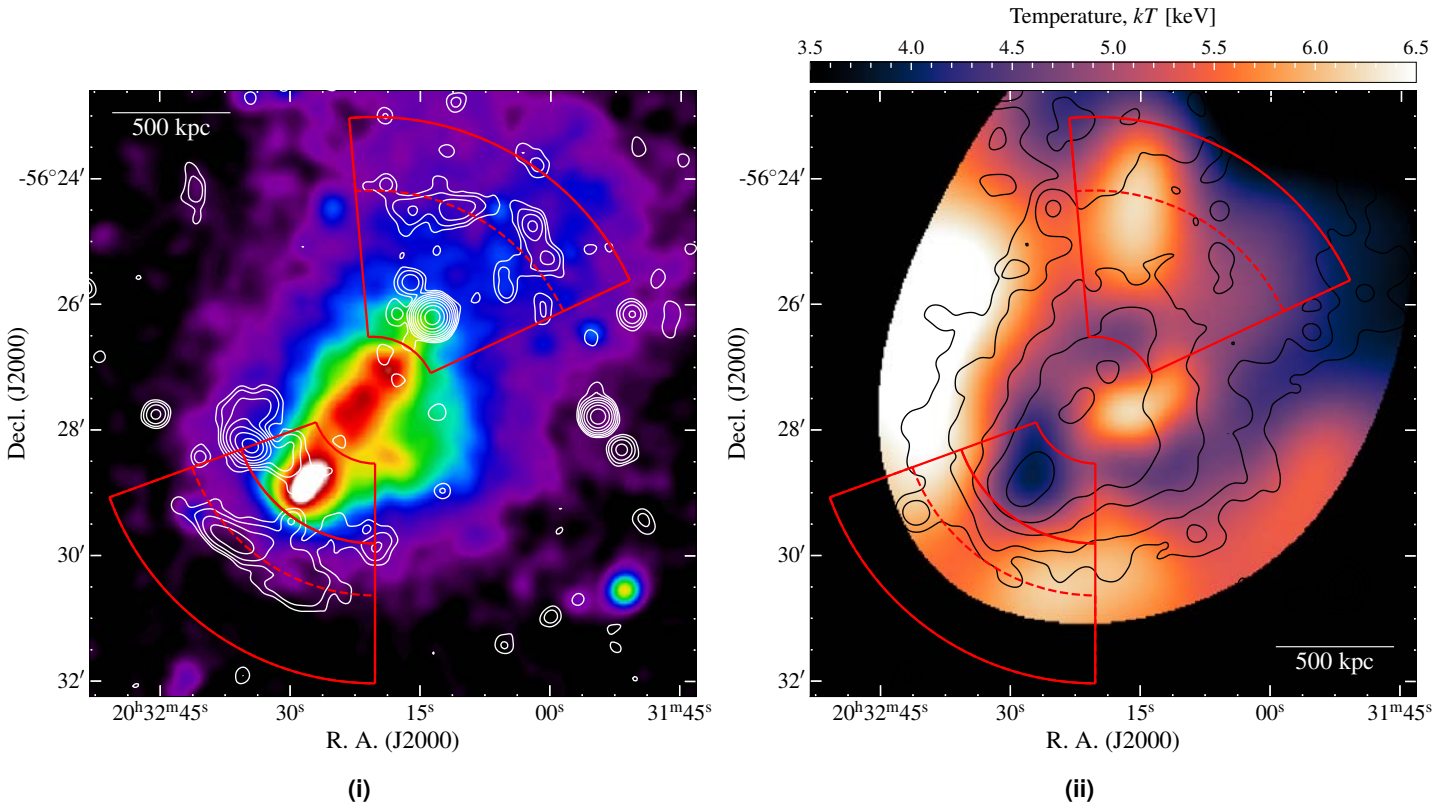

Figure 5. (i) exposure-corrected, background-subtracted, and smoothed X-ray image of SPT-CL J2032−5627. The white contours are the 16.2″ fullband ASKAP image, starting at $3\sigma_{\rm rms}$ ($\sigma_{\rm rms} = 31$ μJy beam^{-1}). The sectors shown in red are those used for surface brightness profiles. The linear scale in the bottom right corner is at $z = 0.284$. (ii) Temperature map of the cluster, with sectors used for surface brightness profile analysis overlaid as in (i). The dashed red arcs within the sectors are at the peak radio locations of the relics, and the solid red arc in the SE sector is the location of a cold front. The black contours are from the smoothed X-ray image. The wavelet filtering algorithms used to obtain these maps are described in Bourdin et al. 2004; Bourdin & Mazzotta 2008; Bourdin et al. 2013.

due to the presence of a cold front.

The radio profile in the SE peaks at ~ 3.3 arcmin. The X-ray surface brightness profile slope seems to change again around this point and the model of the broken power law is on average above the data points beyond 3.3 arcmin. Unfortunately, the data are insufficiently deep to determine the position of this feature, or to extract a temperature profile. The radio relic peak matching a possible change of slope of the X-ray brightness suggests the presence of a shock, and a deeper X-ray observations of the cluster could allow us to confirm this.

Interestingly, the SE profile and the overall scenario suggested by the SE profile are very similar to the case of Abell 2146 (Russell et al., 2010, 2012). The geometry of the cluster is similarly disturbed and our SE profile resembles the profiles shown in Fig. 5 of Russell et al. (2010). Additionally, Hlavacek-Larrondo et al. (2018) report large-scale radio emission in Abell 2146, though it is not clear whether the radio emission found corresponds to radio relics, a radio halo, or a combination thereof (see also Hoang et al., 2019).

4. Discussion

4.1. *Connection of relic emission to active cluster radio sources*

To date a number of radio relic-like sources have been found in clusters with emission connected to apparently active radio galaxies (see e.g. Bonafede et al., 2014; Shimwell et al., 2015; van Weeren et al., 2017; Gasperin et al., 2017), however, the exact mechanism that energises the particle population in these cases is not clear. We will briefly consider the possibility that the SE and NW relic sources in SPT-CL J2032−5627 are associated with active cluster sources, where a shock passing through a population of low-energy electrons (e.g. old radio lobes) imparts energy to re-accelerate the electron population (either through DSA or adiabatic compression).

SE relic. Source B is an FR-I radio galaxy associated with 2MASX J20323421−5628162 with jets oriented roughly NE–SW (the same orientation as the SE relic source, see Fig. 3(i)). The host galaxy has no reported redshift, but has a lower magnitude than the surrounding galaxies in SPT-CL J2032−5627. The host galaxy has *WISE* [6] $W1$ ($W2$) magnitudes of 13.597 ± 0.025 (13.365 ± 0.030) compared to the mean for the 31 cluster members of 15.8 ± 1.0 (15.6 ± 1.0). We do not consider that this galaxy should be sig-

[6] Wide-field Infrared Survey Explorer; Wright et al. (2010)

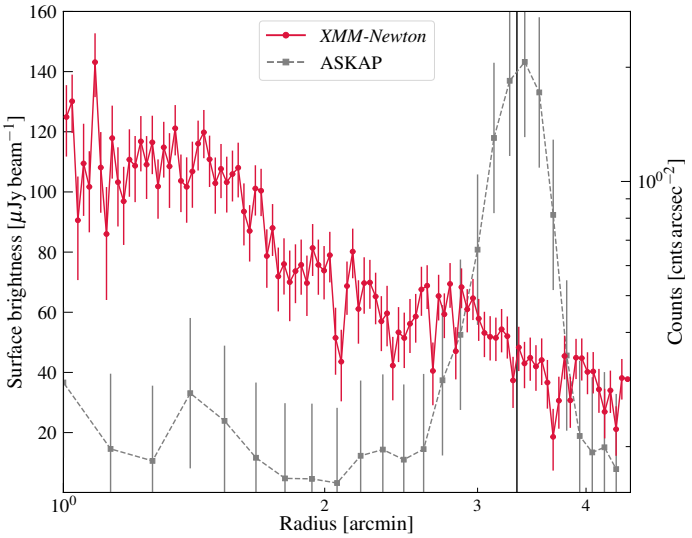

(i) NW profile.

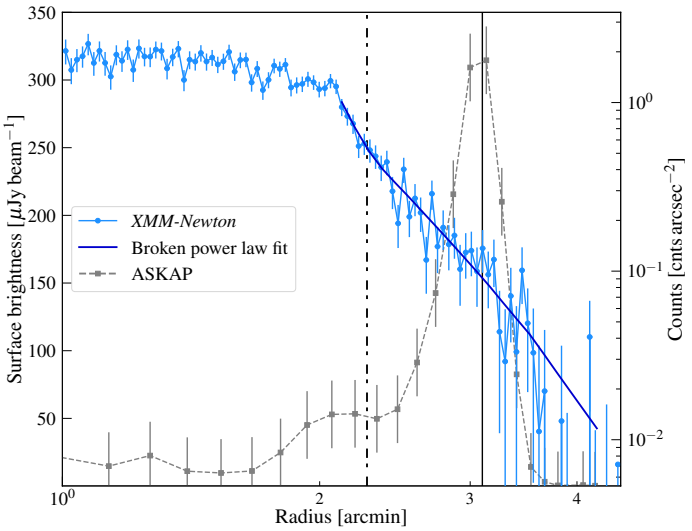

(ii) SE profile.

Figure 6. X-ray and radio surface brightness profiles in the directions of the NW (i) and SE (ii) relic regions. The solid, vertical lines are the peak locations of the radio emission, and the dot-dashed, vertical line in (ii) is the location of a cold front. The broken power law fit to the SE profile is shown in (ii) as a solid, dark blue line.

nificantly brighter than the cluster members, and given it is not near the centre of the cluster it is unlikely this is the BCG of SPT-CL J2032−5627. Given the difference in *WISE* magnitudes, we suspect that this galaxy is not a cluster member. Similarly, source C ($z = 0.0621$; Ruel et al. 2014) has *WISE* magnitudes 14.057 ± 0.037 (13.894 ± 0.044), at the redshift of the reported foreground cluster Abell 3685 ($z = 0.0620$; Struble & Rood 1999), though note that Abell 3685 is considered a richness [0] cluster, but only has a single galaxy with a confirmed redshift. We conclude that there is no cluster at the reported redshift and location of Abell 3685. If the SE relic originated in source B, the lack of physical connection would suggest some episodic activity wherein the the SE relic would have

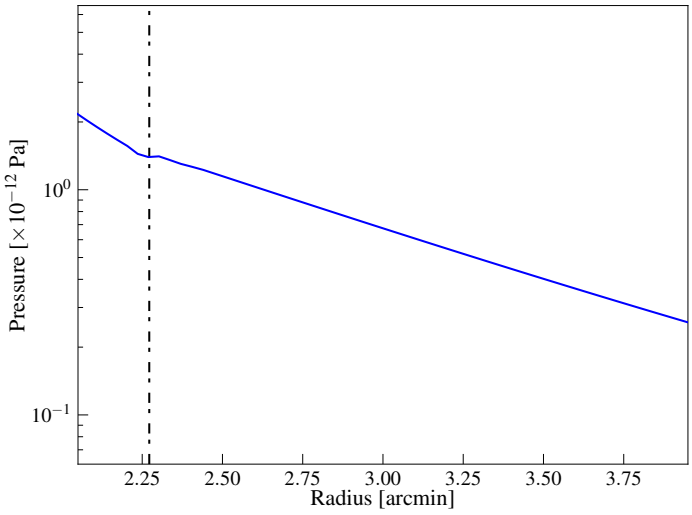

Figure 7. Derived pressure profile through the SE sector as discussed in the text. The dot-dashed, vertical line is the cold front location as in Fig. 6(ii). Note the radial range covers 2–4 arcmin.

faded and would require some ICM-related re-acceleration from shock physics (i.e. a relic).

NW relic. Source E is the likeliest candidate for a host for the NW relic, however, the orientation of the east component of the NW relic is almost perpendicular with respect to the western component (see e.g. Fig. 3(i)), which would require E be a wide-angle tailed (WAT) radio source. Such WAT sources typically occur in cluster environments (e.g. Mao et al., 2009; Pratley et al., 2013) and it is thought the ram pressure of the ICM on the lobes generates the observed morphology (Burns, 1998). Usually, this occurs during infall into the cluster but such a morphology may also occur after a radio galaxy has passed through the cluster centre. The asymmetry in the two NW relic components with respect to source E suggests that this is less likely to be an active WAT source, and the spectral index of the western relic component is sufficiently steep to preclude its classification as a normal radio lobe.

4.2. *A merging system*

The X-ray morphology clearly shows that this is a disturbed system. The X-ray image confirms the merging axis along the SE–NW direction suggested by the position of the radio relics. Assuming DSA and using the derived spectral indices for the two relic sources, we can estimate the Mach number, $\mathscr{M}$, of any shock that has generated them via (see e.g. Blandford & Eichler, 1987)

$$\mathscr{M} = \sqrt{\frac{2\alpha_{\rm inj} + 3}{2\alpha_{\rm inj} - 1}}, \qquad (2)$$

where $\alpha_{\rm inj}$ is the emission injection index of the power law distribution of relativistic electrons. Without making an assumption on the injection index, we use the integrated spectral indices of the relics to determine lower limits to the Mach numbers, finding $\mathscr{M}_{\rm SE} \geq 1.7 \pm 0.1$, $\mathscr{M}_{\rm NW,full} \geq 2.0 \pm 0.1$, and $\mathscr{M}_{\rm NW} \geq 1.7 \pm 0.6$. For the full NW source and the SE source, the integrated spectral

Table 4 Best-fit parameters to *P*–*M* relation for dRS sources list in Table 3.

Method	A	B	$\sigma_{\rm raw}$
Individual dRS			
$P_{1.4}\|M_{500}$	2.67 ± 0.48	-14.70 ± 7.12	0.47
$M_{500}\|P_{1.4}$	3.50 ± 0.58	-27.00 ± 8.48	0.57
bis.	3.03 ± 0.47	-20.10 ± 6.90	0.51
orth.	3.42 ± 0.57	-25.80 ± 8.38	0.56
Summed dRS			
$P_{1.4}\|M_{500}$	2.55 ± 0.55	-12.70 ± 8.02	0.42
$M_{500}\|P_{1.4}$	2.66 ± 0.65	-14.30 ± 9.53	0.42
bis.	2.61 ± 0.54	-13.50 ± 7.92	0.41
orth.	2.65 ± 0.62	-14.10 ± 9.06	0.41

Notes. The *P*–*M* relation is fit in the form $\log(P_{1.4}) = A\log(M_{500}) + B$.

indices are consistent with those found for other double radio relics [7] (hereafter dRS) sources (with a mean value of $\langle\alpha\rangle \approx -1.2$ for the current sample of dRS sources; see Appendix A), and by construction the derived Mach numbers are as well (see e.g. figure 24 of van Weeren et al., 2019).

Unfortunately the X-ray data is insufficient to probe for evidence of shocks. While some relic and double relic sources have been found to correlate to an X-ray–detected shock (e.g. Mazzotta et al., 2011; Finoguenov et al., 2010; Akamatsu et al., 2012; Akamatsu & Kawahara, 2013; Botteon et al., 2016b,a), this is not true for all relic sources. This could partly be due to data quality issues, as often the exposures are insufficiently deep to allow extraction of temperature profiles at the large cluster-centric distances at which radio relics are found. Projection effects could also hamper the detection of a shock. If the merging axis is inclined along the line of sight, the projected surface brightness map will not highlight any noticeable feature, and any shock surface will be smeared out in the surface brightness profiles. However, geometrical considerations would suggest that in double-relic systems it is likely that the merging axis is not significantly inclined along the line of sight. Finally, the shock surface thickness may not correspond to a sharp edge but to a much wider and more complex structure that in combination with projection effects could be difficult to detect even with a deep observation (e.g. van Weeren et al., 2010). A deeper X-ray observation allowing the extraction of temperature profiles and surface brightness profiles with better photon statistics will allow us to discuss quantitatively these possibilities.

4.3. *Double relic scaling relations*

de Gasperin et al. (2014a; hereafter DVB14) investigated the scaling relation of dRS 1.4-GHz power with the mass of the cluster ($P_{1.4}$–M_{500}). DVB14 derive, from merger simulations of X-ray–emitting clusters (Poole et al., 2006), a relationship of the form

[7] Double radio relics in this context are the same as the "double radio shocks" (dRS) described in van Weeren et al. (2019).

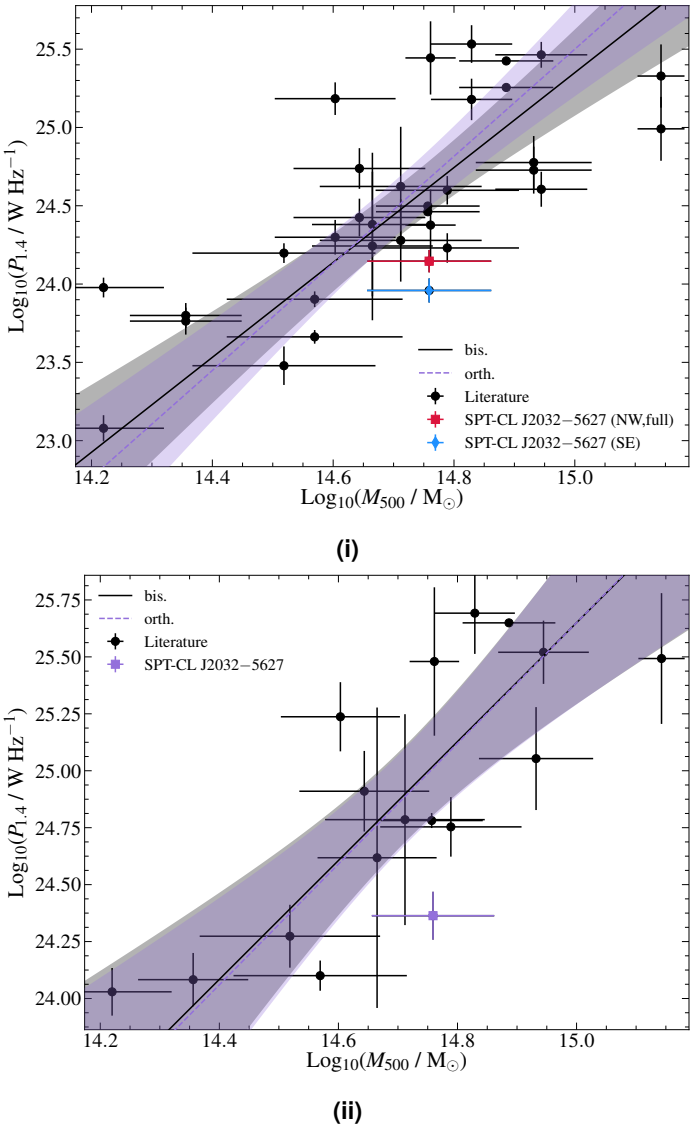

Figure 8. *P*–*M* for cluster systems hosting double relics (see Table 3). (i) Counting relics as individual sources. (ii) Sum of power from both relics. We show the fitting results for the bisector (black-solid, grey-shaded) and orthogonal (purple-dashed, purple-shaded) methods, with shaded 95 per cent confidence intervals. Table 4 presents the best fit values for the relation $\log(P_{1.4}) = A\log(M_{500}) + B$.

$P \propto M^{5/3}$ but require a number of assumptions including spherical symmetry and the mass–temperature relation for X-ray–emitting clusters ($T \propto M^{2/3}$; Pratt et al. 2009) which is largely based on relaxed galaxy clusters. Additionally, DVB14 use a simulation of 20 merging clusters, simulating relics at shocks and varying the magnetic field (uniform field, a model derived from the Coma Cluster, and an equipartition model) and find steeper relations ($P \propto M^{3.02\pm0.96}$, $P \propto M^{4.73\pm1.78}$, and $P \propto M^{6.43\pm1.84}$, respectively). The uniform magnetic field model from simulations is consistent with the the empirical relation they find ($P \propto M^{2.60\pm0.45}$) when the total double relic power for each system is taken into account.

We update the the $P_{1.4}$–M_{500} scaling relation with the current sample of dRS from van Weeren et al. (2019, see Table 6 for

values and references) and calculate radio power from available flux densities and spectral indices. In cases where multiple flux density measurements and spectral indices are available we extrapolate to 1.4 GHz from the closest measurement to 1.4 GHz unless a lack of u–v coverage is a concern. For radio relics without a measured spectral index we assume an average spectral index of $\langle\alpha\rangle = -1.2 \pm 0.3$. We use the Bivariate Estimator for Correlated Errors and intrinsic Scatter (BCES) method (Akritas & Bershady, 1996) [8] to determine the best-fit parameters to the scaling relation of the form $\log(P_{1.4}) = A\log(M_{500}) + B$. The BCES method can be performed assuming either M_{500} or $P_{1.4}$ as the independent variable ($P_{1.4}|M_{500}$ and $M_{500}|P_{1.4}$, respectively), with a bisector method, or with an orthogonal method that minimises the squared orthogonal distances. While one might expect that radio relic power is dependent on cluster mass, given the large, equivalent uncertainties on each quantity we present all BCES methods for ease of comparison to other works (e.g. DVB14 use bisector). Table 4 lists the best-fit values, and Fig. 8(i) shows the relation treating each relic in the dRS system as individual objects, and Fig. 8(ii) shows the same relation but treating the whole dRS system as a single object with best-fit bisector and orthogonal lines. The summed power case shows both consistency with DVB14 and between the bisector and orthogonal methods. We note that while consistent with the general scatter in the dRS systems, SPT-CL J2032−5627 is a lower-brightness dRS system and falls below the best-fit scaling relation.

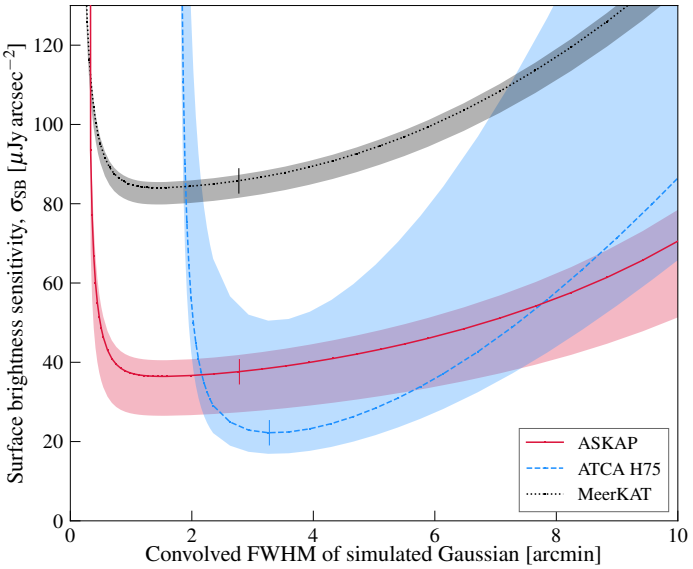

Figure 9. Surface brightness sensitivity comparison between ASKAP, ATCA H75, and a MeerKAT observation as described in the text. The data are scaled to 1.4 GHz using $\alpha = -1.2$ and the shaded regions indicate a range of spectral indices, $-1.8 \leq \alpha \leq -1.0$. The angular scale (FWHM) has been convolved with the major axis of the restoring beam (ASKAP: 16.2 arcsec; ATCA H75: 105 arcsec; MeerKAT: 10.9 arcsec, assuming circular beams). The vertical notches on each dataset indicate the angular size of the SE relic after convolution with the major axis of the restoring beam.

4.4. *Telescope capabilities in the era of Square Kilometre Array precursors*

Two of the greatest outstanding mysteries associated with radio relic and halo generation are the source of the seed electron populations and the precise acceleration mechanisms at work. Previously, the rarity of radio relics and the lack of detailed observations over a range of frequencies has hampered efforts to understand the source generation mechanism. Radio relics are not generally detected above 4 GHz (see e.g. van Weeren et al., 2019), and even dedicated attempts to detect such emission in some of the brightest known relics has been unsuccessful with the previous generation of telescopes (e.g. 4.8 GHz observations of the northwest relic in A3667 by Johnston-Hollitt, 2003). Here however, given the u–v coverage offered by the compact H75 configuration of the ATCA we are able to make a detection prompting us to consider the likelihood of similar high frequency detections in the era of next generation telescopes, particularly precursors to the Square Kilometre Array (SKA).

4.4.1. *ASKAP and the ATCA H75 array*

We compare the surface brightness sensitivity of the ATCA 5.5-GHz and ASKAP observations (observation details in Table 1) by simulating for each observation a range of circular Gaussian sources of varying FWHM but constant peak, P, in Jy deg^{-2}. The various Gaussians are each simulated and imaged separately with `wsclean` using the otherwise empty `MODEL_DATA` column of the respective datasets. We use the same imaging parameters as in the original robust +0.25 (ASKAP) and naturally-weighted (ATCA H75) images. The peak surface brightness, $S_{\rm peak}$, in Jy beam^{-1} is then measured from the map without CLEANing. For a $3\sigma_{\rm rms}$ detection the surface brightness sensitivity can be estimated via $\sigma_{\rm SB} = 3\sigma_{\rm rms}\left(P/S_{\rm peak}\right)$ (see Section 4 of Hodgson et al., 2020, for further details).

To compare ASKAP to ATCA we rescale the measured peak surface brightness to 1.4 GHz using $\alpha = -1.2$ but also compare a range from $-1.8 \leq \alpha \leq -1.0$. Fig. 9 shows $\sigma_{\rm SB}$ for these datasets over a range of convolved FWHM between 0 and 10 arcmin. While the same Gaussian sources are simulated for each dataset, after convolution with the PSF of each observation the Gaussian sources in the ATCA H75 images have larger FWHM. Immediately we can see that the H75 data, even for such a short observation, provides good surface brightness sensitivity largely due to the size of the PSF without antenna 6. Additionally, the angular size of the SE relic in the H75 images occurs at the most sensitive scale for the observation. One thing to note here is that the primary beam FWHM of the ATCA at 5.5 GHz is $\sim$ 10 arcmin, which limits the angular scale sensitivity without mosaicking.

4.4.2. *ASKAP and MeerKAT within the context of all-sky surveys*

ATCA is limited in its extended source surveying capability by the small FoV and the limited baselines any single array configuration provides. ASKAP surveys such as EMU, with 10-hr observations covering $\sim$ 36 deg^2 and excellent u–v coverage (see Fig. 2), are be-

[8] `http://www.astro.wisc.edu/~mab/archive/stats/stats.html`

ginning to provide the much-needed increase to numbers of diffuse cluster sources (e.g. HyeongHan et al. 2020; Wilber et al. 2020, Duchesne et al. in prep., this work). Recently, MeerKAT [9] (Jonas, 2009; Jonas & MeerKAT Team, 2016) [10] with an increase in overall sensitivity compared to ASKAP—largely due to an increased instantaneous bandwidth and its 64 antennas—is providing excellent observations of faint synchrotron structures (e.g. filaments in radio galaxies; Ramatsoku et al., 2020), suggesting MeerKAT will be a powerful instrument for detailed observations of diffuse cluster emission at frequencies on the order of 1 GHz.

While MeerKAT is able to provide deeper imaging than ASKAP, its single ~ 1 deg instantaneous FoV limits its ability to cover the sky at a similar rate to ASKAP. At the same surveying rate as ASKAP, MeerKAT L-band would require integration times of ~ 16.7 min per pointingassuming individual pointings match the present ASKAP PAF footprint which includes a 0.9 deg separation between the 36 individual primary beams. With a robust 0.0 weighting images would reach an rms noise of ~ 14.1 μJy beam^{-1} [11], close to the lower limit expected from the EMU survey. Assuming this integration time we use the `simms` [12] package to simulate an observation of a source transiting through zenith with a 1.284 GHz central frequency over the full bandwidth available. Additional details of the simulated observation are shown in Table 5. Note that we used the full 64 antennas for sensitivity calculation and data simulation rather than the 60 typically used.

We repeat the simulation of Gaussian sources of varying FWHM as with the ASKAP and ATCA data, and show on Fig. 9 the equivalent surface brightness sensitivity limits for robust 0.0 imaging. This illustrates that an equivalent survey would not match ASKAP's surface brightness sensitivity for large-scale structures. We note that when $S_{\rm peak}$ is measured from the CLEANed MeerKAT images this results in a decrease in $S_{\rm peak}$ which increases $\sigma_{\rm SB}$ by up to $\sim 30\%$, dependent on simulated Gaussian FWHM. Comparatively, $\sigma_{\rm SB}$ *decreases* for the ATCA H75 maps (by up to $\sim 50\%$) and slightly increases for ASKAP (by up to $\sim 6\%$), which does not appreciably change the conclusions drawn from Fig. 9. An additional note here is that changing imaging weighting or adding additional tapering would increase the sensitivity to large-scale structures, though a general all-sky survey would likely optimise for point source sensitivity. This difference suggests that ASKAP will be be an excellent survey instrument for uncovering new diffuse sources within (and outside of) galaxy clusters, while MeerKAT and the ATCA will remain excellent complementary instruments for deeper follow-up observations at frequencies of 1 GHz and higher.

5. Summary

Using recently released ASKAP observations we have identified a new radio relic in the cluster SPT-CL J2032−5627, with a secondary relic on the opposite side of the cluster. The radio relics are detected in both the new ASKAP data at ~ 900 MHz and archival ATCA 5.5-GHz observations. The relics have power law spectra between 800–5500 MHz, with $\alpha_{\rm SE} = -1.52 \pm 0.10$ and $\alpha_{\rm NW,full} = -1.18 \pm 0.10$, consistent with many examples of radio relics. The relic properties are largely consistent with the established relic population, though they lie slightly below the *P–M* scaling relation for double relic systems.

The cluster itself is morphologically disturbed, as shown by the X-ray emission from the ICM as seen by XMM-*Newton*. Though no shocks are detected in the X-ray surface brightness profiles, a temperature map reveals a potential cold front preceding the SE relic sources. A lack of detectable shock at the radio relic locations may be due to a complex shock structure, perhaps formed of multiple shocks along the line of sight, or insufficient depth of the available XMM-*Newton* data.

Despite radio relics featuring steep radio spectra, ASKAP surveys such as EMU will uncover a heretofore unseen radio relic population in the Southern Sky, at this surface-brightness sensitivity with many cluster systems predicted to host such objects at low power (e.g. Nuza et al., 2012).

Such a sample of radio relics could be followed up by deep MeerKAT, ASKAP and/or even ATCA observations, utilising the full frequency range provided by the instruments (either instantaneously with MeerKAT or as multiple observations across the band with ASKAP), providing wide-frequency information vital to finally understanding the acceleration mechanisms at work in clusters to generate these sources.

Acknowledgements. The authors would like to thank the anonymous referee for their comments and suggestions that have helped to improve this manuscript. SWD acknowledges an Australian Government Research Training Program scholarship administered through Curtin University. IB acknowledges financial contribution from contract ASI-INAF n. 2017-14-H.0. GWP acknowledges the French space agency, CNES. The Australian SKA Pathfinder is part of the Australia Telescope National Facility which is managed by CSIRO. Operation of ASKAP is funded by the Australian Government with support from the National Collaborative Research Infrastructure Strategy. ASKAP uses the resources of the Pawsey Supercomputing Centre. Establishment of ASKAP, the Murchison Radio-astronomy Observatory and the Pawsey Supercomputing Centre are initiatives of the Australian Government, with support from the Government of Western Australia and the Science and Industry Endowment Fund. We acknowledge the Wajarri Yamatji people as the traditional owners of the Observatory site. We acknowledge the Pawsey Supercomputing Centre which is supported by the Western Australian and Australian Governments. This paper includes archived data obtained through the Australia Telescope Online Archive (`http://atoa.atnf.csiro.au/`).

This research made use of a number of `python` packages: `aplpy` (Robitaille & Bressert, 2012), `astropy` (Astropy Collaboration et al., 2013; Price-Whelan et al., 2018), `matplotlib` (Hunter, 2007), `numpy` (van der Walt et al., 2011), `scipy` (Jones et al., 2001), and `cmasher` (van der Velden, 2020).

This research has made use of the NASA/IPAC Extragalactic Database (NED), which is operated by the Jet Propulsion Laboratory, California Institute of Technology, under contract with the National Aeronautics and Space Administration. This work makes use of the `cubehelix` family

[9] Karoo Array Telescope.

[10] See Mauch et al. 2020 for further technical details.

[11] For MeerKAT sensitivity calculations, see the online sensitivity calculator provided by the South African Radio Astronomy Observatory, based on real observations: `https://archive-gw-1.kat.ac.za/public/tools/continuum_sensitivity_calculator.html`

[12] `https://github.com/ratt-ru/simms`

Table 5 Details of the simulated MeerKAT data, using a robust 0.0 image weighting.

τ (a) (min)	$\Delta\nu$ (GHz)	ν_c (GHz)	SEFD (a) (b) (Jy)	N_{ants} (c)	σ_{rms} (a) (μJy beam^{-1})	θ_{minor} (a) (d) ($''$)
16.7	0.856	1.284	420	64	14.1	10.9

Notes. (a) Value from the MeerKAT sensitivity calculator as described in the text. Columns are similar to those in Table 1 with the addition of: (b) Average system equivalent flux density used for scaling the rms noise from observed values. (c) Note the default for the sensitivity calculator is $N_{ants} = 60$. (d) Size of the minor axis for the synthesized beam.

of colourmaps (Green, 2011).

This project used public archival data from the Dark Energy Survey (DES). Funding for the DES Projects has been provided by the U.S. Department of Energy, the U.S. National Science Foundation, the Ministry of Science and Education of Spain, the Science and Technology FacilitiesCouncil of the United Kingdom, the Higher Education Funding Council for England, the National Center for Supercomputing Applications at the University of Illinois at Urbana-Champaign, the Kavli Institute of Cosmological Physics at the University of Chicago, the Center for Cosmology and Astro-Particle Physics at the Ohio State University, the Mitchell Institute for Fundamental Physics and Astronomy at Texas A&M University, Financiadora de Estudos e Projetos, Fundação Carlos Chagas Filho de Amparo à Pesquisa do Estado do Rio de Janeiro, Conselho Nacional de Desenvolvimento Científico e Tecnológico and the Ministério da Ciência, Tecnologia e Inovação, the Deutsche Forschungsgemeinschaft, and the Collaborating Institutions in the Dark Energy Survey. The Collaborating Institutions are Argonne National Laboratory, the University of California at Santa Cruz, the University of Cambridge, Centro de Investigaciones Energéticas, Medioambientales y Tecnológicas-Madrid, the University of Chicago, University College London, the DES-Brazil Consortium, the University of Edinburgh, the Eidgenössische Technische Hochschule (ETH) Zürich, Fermi National Accelerator Laboratory, the University of Illinois at Urbana-Champaign, the Institut de Ciències de l'Espai (IEEC/CSIC), the Institut de Física d'Altes Energies, Lawrence Berkeley National Laboratory, the Ludwig-Maximilians Universität München and the associated Excellence Cluster Universe, the University of Michigan, the National Optical Astronomy Observatory, the University of Nottingham, The Ohio State University, the OzDES Membership Consortium, the University of Pennsylvania, the University of Portsmouth, SLAC National Accelerator Laboratory, Stanford University, the University of Sussex, and Texas A&M University. Based in part on observations at Cerro Tololo Inter-American Observatory, National Optical Astronomy Observatory, which is operated by the Association of Universities for Research in Astronomy (AURA) under a cooperative agreement with the National Science Foundation.

A. Literature data

In this section we provide the literature data used in Section 4.3. For all sources we estimate power from flux density measurements and the reported spectral indices. Where multiple indices and flux density measurements are available, we choose values from the literature that are closest to 1.4 GHz (where no serious u–v coverage problems exist). Additionally, for clusters without a measured spectra index assume a spectral index based on the mean of the sample ($\langle\alpha\rangle = -1.2 \pm 0.3$). Mass measurements are taken from SZ measurements where available (e.g. via Planck Collaboration et al. 2015) or from X-ray measurements if SZ-proxy mass estimates are not available.

References

Abbott T. M. C., et al., 2018, ApJS, 239, 18
Akamatsu H., Kawahara H., 2013, PASJ, 65, 16
Akamatsu H., de Plaa J., Kaastra J., Ishisaki Y., Ohashi T., Kawaharada M., Nakazawa K., 2012, PASJ, 64, 49
Akritas M. G., Bershady M. A., 1996, ApJ, 470, 706
Astropy Collaboration et al., 2013, A&A, 558, A33
Axford W. I., Leer E., Skadron G., 1977, in International Cosmic Ray Conference. p. 132
Bell A. R., 1978a, MNRAS, 182, 147
Bell A. R., 1978b, MNRAS, 182, 443
Blandford R., Eichler D., 1987, Phys. Rep., 154, 1
Blandford R. D., Ostriker J. P., 1978, ApJ, 221, L29
Blumenthal G. R., Faber S. M., Primack J. R., Rees M. J., 1984, Nature, 311, 517
Bock D. C. J., Large M. I., Sadler E. M., 1999, AJ, 117, 1578
Bogdán Á., et al., 2013, ApJ, 772, 97
Böhringer H., et al., 2004, A&A, 425, 367
Bonafede A., Giovannini G., Feretti L., Govoni F., Murgia M., 2009, A&A, 494, 429
Bonafede A., et al., 2012, MNRAS, 426, 40
Bonafede A., Intema H. T., Brüggen M., Girardi M., Nonino M., Kantharia N., van Weeren R. J., Röttgering H. J. A., 2014, ApJ, 785, 1
Botteon A., Gastaldello F., Brunetti G., Dallacasa D., 2016a, MNRAS: Letters, 460, L84
Botteon A., Gastaldello F., Brunetti G., Kale R., 2016b, MNRAS, 463, 1534
Bourdin H., Mazzotta P., 2008, A&A, 479, 307
Bourdin H., Sauvageot J. L., Slezak E., Bijaoui A., Teyssier R., 2004, A&A, 414, 429
Bourdin H., Mazzotta P., Markevitch M., Giacintucci S., Brunetti G., 2013, ApJ, 764, 82
Briggs D. S., 1995, PhD thesis, The New Mexico Institute of Mining and Technology, Socorro, New Mexico
Bulbul E., et al., 2019, ApJ, 871, 50
Burns J. O., 1998, Science, 280, 400
Chapman J. M., Dempsey J., Miller D., Heywood I., Pritchard J., Sangster E., Whiting M., Dart M., 2017, CASDA: The CSIRO ASKAP Science Data Archive. p. 73
Chippendale A. P., O'Sullivan J., Reynolds J., Gough R., Hayman D., Hay S., 2010, in Phased Array Systems and Technology (ARRAY. pp 648–652, doi:10.1109/ARRAY.2010.5613298
DeBoer D. R., et al., 2009, IEEE Proceedings, 97, 1507
Duchesne S. W., Johnston-Hollitt M., 2019, PASA, 36, e016
Enßlin T. A., Gopal-Krishna 2001, in Laing R. A., Blundell K. M., eds, Astronomical Society of the Pacific Conference Series Vol. 250, Particles and Fields in Radio Galaxies Conference. p. 454 (arXiv:astro-ph/0010600)
Feretti L., Schuecker P., Böhringer H., Govoni F., Giovannini G., 2005, A&A, 444, 157
Finoguenov A., Sarazin C. L., Nakazawa K., Wik D. R., Clarke T. E., 2010, ApJ, 715, 1143
Flaugher B., et al., 2015, AJ, 150, 150
Frater R. H., Brooks J. W., Whiteoak J. B., 1992, Journal of Electrical and Electronics Engineering Australia, 12, 103
Gasperin F. d., et al., 2017, Science Advances, 3, e1701634

Table 6 Clusters with dRS sources used in Section 4.3.

Cluster	z	M_{500} ($\times 10^{14}$ $M_\odot$)	Relic No.	α	$P_{1.4}$ ($\times 10^{23}$ W Hz^{-1})	References (a)
Abell 3376	0.046	2.27 ± 0.21 (b)	1	-1.82 ± 0.06	6.3 ± 0.5	(e)
			2	-1.70 ± 0.06	5.8 ± 0.5	(e)
Abell 3667	0.056	5.77 ± 0.24 (b)	1	-0.90 ± 0.10	23.8 ± 5.4	(f)
			2	-0.90 ± 0.10	278.0 ± 65.0	(f)
Abell 3365	0.093	1.66 ± 0.17 (c)	1	-1.20 ± 0.30	9.5 ± 0.6	(g)/-
			2	-1.20 ± 0.30	1.2 ± 0.1	(g)/-
ZwCl 0008.8+5215	0.103	3.30 ± 0.50 (b)	1	-1.59 ± 0.06	15.8 ± 1.0	(h)
			2	-1.49 ± 0.12	3.0 ± 0.4	(h)
Abell 1240	0.159	3.71 ± 0.54 (b)	1	-1.20 ± 0.10	4.6 ± 0.2	(i)
			2	-1.30 ± 0.20	8.0 ± 0.4	(i)
Abell 2345	0.176	5.71 ± 0.49 (b)	1	-1.50 ± 0.10	29.0 ± 0.7	(i)
			2	-1.30 ± 0.10	31.5 ± 0.8	(i)
CIZA J2242.8+5301	0.192	4.01 ± 0.40 (c)	1	-1.06 ± 0.04	152.7 ± 15.9	(j)
			2	-1.29 ± 0.04	19.9 ± 2.2	(j)
RXC J1314.4−2515	0.244	6.15 ± 0.73 (b)	1	-1.40 ± 0.09	17.0 ± 1.6	(k)/(l)
			2	-1.41 ± 0.09	39.7 ± 3.6	(k)/(l)
ZwCl 2341.1+0000	0.270	5.15 ± 0.69 (b)	1	-0.49 ± 0.18	19.0 ± 5.0	(m)
			2	-0.76 ± 0.17	42.0 ± 16.0	(m)
SPT-CL J2032−5627	0.284	5.74 ± 0.59 (d)	1	-1.18 ± 0.10	9.1 ± 1.0	this work
			2	-1.52 ± 0.10	14.0 ± 1.6	this work
PSZ1 G096.89+24.17	0.300	4.40 ± 0.48 (b)	1	-1.20 ± 0.30	26.6 ± 3.2	(n)/-
			2	-1.20 ± 0.30	54.7 ± 7.1	(n)/-
PSZ1 G108.18−11.53	0.335	7.70 ± 0.60 (b)	1	-1.25 ± 0.02	266.0 ± 1.9	(o)
			2	-1.28 ± 0.02	180.0 ± 1.6	(o)
MACS J1752.0+4440	0.367	6.75 ± 0.45 (d)	1	-1.21 ± 0.06	341.0 ± 41.0	(p)
			2	-1.12 ± 0.07	151.0 ± 20.0	(p)
PSZ1 G287.0+32.9	0.390	13.89 ± 0.54 (b)	1	-1.36 ± 0.21	213.0 ± 43.0	(q)
			2	-1.33 ± 0.21	98.0 ± 20.0	(q)
MACS J1149.5+2223	0.544	8.55 ± 0.82 (b)	1	-1.15 ± 0.08	53.4 ± 8.0	(p)
			2	-0.75 ± 0.08	59.7 ± 10.1	(p)
MACS J0025.4−1222	0.586	4.62 ± 0.46 (c)	1	-1.20 ± 0.30	17.5 ± 8.3	(r)/-
			2	-1.20 ± 0.30	24.0 ± 11.0	(r)/-
ACT-CL J0102−4915	0.870	8.80 ± 0.67 (b)	1	-1.19 ± 0.09	291.0 ± 24.0	(s)
			2	-1.40 ± 0.10	40.3 ± 4.5	(s)

Notes. (a) flux density/α. "-" = $\langle\alpha\rangle$. *References.* (b) Planck Collaboration et al. (2015). (c) Piffaretti et al. (2011); assume 10 per cent uncertainty on mass estimate. (d) Planck Collaboration et al. (2016). (e) Kale et al. (2012). (f) Hindson et al. (2014). (g) van Weeren et al. (2011a). (h) van Weeren et al. (2011b). (i) Bonafede et al. (2009). (j) van Weeren et al. (2010). (k) Feretti et al. (2005). (l) Venturi et al. (2007). (m) van Weeren et al. (2009). (n) de Gasperin et al. (2014a). (o) de Gasperin et al. (2015). (p) Bonafede et al. (2012). (q) Bonafede et al. (2014). (r) Riseley et al. (2017). (s) Lindner et al. (2014).

Giacintucci S., Markevitch M., Cassano R., Venturi T., Clarke T. E., Brunetti G., 2017, ApJ, 841, 71
Giacintucci S., Markevitch M., Cassano R., Venturi T., Clarke T. E., Kale R., Cuciti V., 2019, ApJ, 880, 70
Govoni F., Feretti L., Giovannini G., Böhringer H., Reiprich T. H., Murgia M., 2001, A&A, 376, 803
Green D. A., 2011, Bulletin of the Astronomical Society of India, 39, 289
Hancock P. J., Murphy T., Gaensler B. M., Hopkins A., Curran J. R., 2012, MNRAS, 422, 1812
Hancock P. J., Trott C. M., Hurley-Walker N., 2018, PASA, 35, e011
Hindson L., et al., 2014, MNRAS, 445, 330
Hlavacek-Larrondo J., et al., 2018, MNRAS, 475, 2743
Hoang D. N., et al., 2019, A&A, 622, A21
Hodgson T., Johnston-Hollitt M., McKinley B., Vernstrom T., Vacca V., 2020, PASA, 37, e032
Hotan A. W., et al., 2014, PASA, 31, e041
Hunter J. D., 2007, Computing in Science and Engineering, 9, 90
Hurley-Walker N., et al., 2017, MNRAS, 464, 1146
HyeongHan K., et al., 2020, arXiv e-prints, p. arXiv:2007.08244
Johnston-Hollitt M., 2003, PhD thesis, University of Adelaide
Johnston-Hollitt M., Hunstead R. W., Corbett E., 2008, A&A, 479, 1
Johnston S., et al., 2007, PASA, 24, 174
Johnston S., et al., 2008, Experimental Astronomy, 22, 151
Jonas J. L., 2009, IEEE Proceedings, 97, 1522
Jonas J., MeerKAT Team 2016, in MeerKAT Science: On the Pathway to the SKA. p. 1
Jones F. C., Ellison D. C., 1991, Space Sci. Rev., 58, 259
Jones E., Oliphant T., Peterson P., et al., 2001, SciPy: Open source scientific tools for Python, http://www.scipy.org/
Kale R., Dwarakanath K. S., Bagchi J., Paul S., 2012, MNRAS, 426, 1204
Kravtsov A. V., Borgani S., 2012, ARA&A, 50, 353
Lindner R. R., et al., 2014, ApJ, 786, 49
Loi F., et al., 2017, MNRAS, 472, 3605
Mao M. Y., Johnston-Hollitt M., Stevens J. B., Wotherspoon S. J., 2009, MNRAS, 392, 1070
Mauch T., Murphy T., Buttery H. J., Curran J., Hunstead R. W., Piestrzynski B., Robertson J. G., Sadler E. M., 2003, MNRAS, 342, 1117
Mauch T., et al., 2020, ApJ, 888, 61
Mazzotta P., Bourdin H., Giacintucci S., Markevitch M., Venturi T., 2011, Mem. Soc. Astron. Italiana, 82, 495
McConnell D., et al., 2016, PASA, 33, e042
Mills B. Y., 1981, Proceedings of the Astronomical Society of Australia, 4, 156
Morganson E., et al., 2018, PASP, 130, 074501
Norris R. P., et al., 2011, PASA, 28, 215
Nuza S. E., Hoeft M., van Weeren R. J., Gottlöber S., Yepes G., 2012, MNRAS, 420, 2006
Offringa A. R., Smirnov O., 2017, MNRAS, 471, 301
Offringa A. R., McKinley B., Hurley-Walker et al., 2014, MNRAS, 444, 606
Oort J. H., 1983, ARA&A, 21, 373
Peebles P. J. E., 1980, The large-scale structure of the universe. Princeton Univ. Press, Princeton, N. J.
Piffaretti R., Arnaud M., Pratt G. W., Pointecouteau E., Melin J.-B., 2011, A&A, 534, A109
Pinzke A., Oh S. P., Pfrommer C., 2013, MNRAS, 435, 1061
Planck Collaboration et al., 2015, A&A, 581, A14
Planck Collaboration et al., 2016, A&A, 594, A27
Poole G. B., Fardal M. A., Babul A., McCarthy I. G., Quinn T., Wadsley J., 2006, MNRAS, 373, 881
Pratley L., Johnston-Hollitt M., Dehghan S., Sun M., 2013, MNRAS, 432, 243
Pratt G. W., Böhringer H., Croston J. H., Arnaud M., Borgani S., Finoguenov A., Temple R. F., 2007, A&A, 461, 71
Pratt G. W., Croston J. H., Arnaud M., Böhringer H., 2009, A&A, 498, 361
Price-Whelan A. M., et al., 2018, AJ, 156, 123
Ramatsoku M., et al., 2020, A&A, 636, L1
Riseley C. J., Scaife A. M. M., Wise M. W., Clarke A. O., 2017, A&A, 597, A96
Robitaille T., Bressert E., 2012, APLpy: Astronomical Plotting Library in Python, Astrophysics Source Code Library (ascl:1208.017)
Ruel J., et al., 2014, ApJ, 792, 45
Russell H. R., Sanders J. S., Fabian A. C., Baum S. A., Donahue M., Edge A. C., McNamara B. R., O'Dea C. P., 2010, MNRAS, 406, 1721
Russell H. R., et al., 2012, MNRAS, 423, 236
Sault R. J., Teuben P. J., Wright M. C. H., 1995, in Shaw R. A., Payne H. E., Hayes J. J. E., eds, Astronomical Society of the Pacific Conference Series Vol. 77, Astronomical Data Analysis Software and Systems IV. p. 433 (arXiv:astro-ph/0612759)
Shimwell T. W., Markevitch M., Brown S., Feretti L., Gaensler B. M., Johnston-Hollitt M., Lage C., Srinivasan R., 2015, MNRAS, 449, 1486
Slee O. B., Roy A. L., Murgia M., Andernach H., Ehle M., 2001a, AJ, 122, 1172
Slee O. B., Roy A. L., Murgia M., Andernach H., Ehle M., 2001b, AJ, 122, 1172
Song J., et al., 2012, ApJ, 761, 22
Struble M. F., Rood H. J., 1999, ApJS, 125, 35
Strüder L., et al., 2001, A&A, 365, L18
Tingay S. J., et al., 2013, PASA, 30, 7
Turner M. J. L., et al., 2001, A&A, 365, L27
Vazza F., Brüggen M., Wittor D., Gheller C., Eckert D., Stubbe M., 2016, MNRAS, 459, 70
Venturi T., Giacintucci S., Brunetti G., Cassano R., Bardelli S., Dallacasa D., Setti G., 2007, A&A, 463, 937
Vikhlinin A., Kravtsov A., Forman W., Jones C., Markevitch M., Murray S. S., Van Speybroeck L., 2006, ApJ, 640, 691
Wayth R. B., et al., 2015, PASA, 32, 25
Wayth R. B., et al., 2018, PASA, 35
Wilber A. G., Johnston-Hollitt M., Duchesne S. W., Tasse C., Akamatsu H., Intema H., Hodgson T., 2020, PASA, 37, e040
Willson M. A. G., 1970, MNRAS, 151, 1
Wilson W. E., et al., 2011, MNRAS, 416, 832
Wittor D., Vazza F., Brüggen M., 2017, MNRAS, 464, 4448
Wright E. L., et al., 2010, AJ, 140, 1868
de Gasperin F., van Weeren R. J., Brüggen M., Vazza F., Bonafede A., Intema H. T., 2014a, MNRAS, 444, 3130
de Gasperin F., van Weeren R. J., Brüggen M., Vazza F., Bonafede A., Intema H. T., 2014b, MNRAS, 444, 3130
de Gasperin F., Intema H. T., van Weeren R. J., Dawson W. A., Golovich N., Wittman D., Bonafede A., Brüggen M., 2015, MNRAS, 453, 3483
van Weeren R. J., et al., 2009, A&A, 506, 1083
van Weeren R. J., Röttgering H. J. A., Brüggen M., Hoeft M., 2010, Science, 330, 347
van Weeren R. J., Hoeft M., Röttgering H. J. A., Brüggen M., Intema H. T., van Velzen S., 2011a, A&A, 528, A38
van Weeren R. J., Brüggen M., Röttgering H. J. A., Hoeft M., Nuza S. E., Intema H. T., 2011b, A&A, 533, A35
van Weeren R. J., et al., 2017, Nature Astronomy, 1, 0005
van Weeren R. J., de Gasperin F., Akamatsu H., Brüggen M., Feretti L., Kang H., Stroe A., Zandanel F., 2019, Space Sci. Rev., 215, 16
van der Velden E., 2020, The Journal of Open Source Software, 5, 2004
van der Walt S., Colbert S. C., Varoquaux G., 2011, Computing in Science Engineering, 13, 22

Murchison Widefield Array detection of steep-spectrum, diffuse, non-thermal radio emission within Abell 1127

[12] https://www.cambridge.org/about-us/rights-permissions/faqs/

[13] https://www.cambridge.org/core/services/open-access-policies/open-access-journals/green-open-access-policy-for-journals

[14] Note the appearance is slightly modified in the present version as an update to the PASA LaTeX template.

LaTeX document typeset by the authors from a modified LaTeX template from the *Publications of the Astronomical Society of Australia* (PASA).
Current document status: **accepted for publication in PASA:** https://doi.org/10.1017/pasa.2020.29.

Research Paper

Murchison Widefield Array detection of steep-spectrum, diffuse, non-thermal radio emission within Abell 1127

S. W. Duchesne[1]*, M. Johnston-Hollitt[1], Z. Zhu[2], R. B. Wayth[1], J. L. B. Line[1,3]
[1]International Centre for Radio Astronomy Research (ICRAR), Curtin University, Bentley, WA 6102, Australia
[2]School of Physics and Astronomy, Shanghai Jiao Tong University, 800 Dongchuan Road, Minhang, Shanghai 200240, People's Republic of China
[3]ARC Centre of Excellence for All Sky Astrophysics in 3 Dimensions (ASTRO 3D)

Abstract

Diffuse, non-thermal emission in galaxy clusters is increasingly being detected in low-frequency radio surveys and images. We present a new diffuse, steep-spectrum, non-thermal radio source within the cluster Abell 1127 found in survey data from the Murchison Widefield Array (MWA). We perform follow-up observations with the 'extended' configuration MWA Phase II with improved resolution to better resolve the source and measure its low-frequency spectral properties. We use archival Very Large Array S-band data to remove the discrete source contribution from the MWA data, and from a power law model fit we find a spectral index of -1.83 ± 0.29 broadly consistent with relic-type sources. The source is revealed by the Giant Metrewave Radio Telescope (GMRT) at 150 MHz to have an elongated morphology, with a projected linear size of 850 kpc as measured in the MWA data. Using *Chandra* observations we derive morphological estimators and confirm quantitatively that the cluster is in a disturbed dynamical state, consistent with the majority of phoenices and relics being hosted by merging clusters. We discuss the implications of relying on morphology and low-resolution imaging alone for the classification of such sources and highlight the usefulness of the MHz to GHz radio spectrum in classifying these types of emission. Finally, we discuss the benefits and limitations of using the MWA Phase II in conjunction with other instruments for detailed studies of diffuse, steep-spectrum, non-thermal radio emission within galaxy clusters.

Keywords: galaxies: clusters: individual: Abell 1127 – large-scale structure of the Universe – radio continuum: general – X-rays: galaxies: clusters

1. Introduction

Clusters of galaxies are large virialized structures that reside at the intersection of cosmic filaments. The formation of galaxy clusters is thought to be hierarchical through mergers and accretion (Peebles, 1980), and cluster mergers represent some of the largest, most energetic collisions in the known Universe. Clusters have been found to host a number of radio emitting sources with steep synchrotron emission spectra implying aged electron populations (see e.g. Pacholczyk, 1970; Tribble, 1993; Enßlin & Gopal-Krishna, 2001; Kempner et al., 2004). Both centrally-located *radio halo* sources and peripherally-located *radio relic* sources are thought to be associated with inter-cluster mergers or otherwise similarly energetic and turbulent events (see van Weeren et al., 2019, for a review).

Halos, relics, and other types of steep-spectrum cluster sources have been well-studied over the last two decades. Enßlin & Gopal-Krishna (2001) propose for radio relics that adiabatic compression of remnant radio galaxy lobes by shocks in the intra-cluster medium (ICM) is responsible for radio relic sources such as that in Abell 85 (Slee & Reynolds, 1984; Slee et al., 2001) or Abell 4038 (Slee & Roy, 1998), however, for megaparsec-scale radio relics a different physical process may be the cause. Diffusive shock acceleration (DSA; Fermi, 1949; Jones & Ellison, 1991) is consistent with the spectral features of megaparsec-scale radio relics (see e.g. Johnston-Hollitt, 2003; van Weeren et al., 2010, 2016) and shocks have been observed at the locations of some relics. These two types of relics are distinguished as *phoenices* and *radio shocks* (see van Weeren et al., 2019, but also Kempner et al. 2004). Radio halo type sources can also be broken into two classes: *giant radio halos* and *mini-halos*; the distinction here is less about physical process as both are thought to be caused by turbulence in the ICM through a second order Fermi process (Fermi, 1954; Brunetti et al., 2001; Gitti et al., 2015).

While the physical (re-)acceleration mechanisms are understood, the origin of the seed electrons for the emission is still not entirely clear. The synchrotron-emitting electrons have been proposed as the thermal pool of electrons in ICM (i.e. the hot plasma, though this has issues related to Coulomb losses; Petrosian 2001), left-over from old active galactic nuclei (AGN; see e.g. Shimwell et al., 2015; van Weeren et al., 2017; de Gasperin et al., 2017), or electrons created in proton-proton collisions (Dennison, 1980). The seed for phoenices and mini-halos are almost certainly AGN, despite any difference in final (re-)acceleration process, the larger-scale halos and relics may require a similar origin.

As halos, relics, and similar types of emission are usually detected with low surface brightness and steep, mostly power law spectra, radio interferometers such as the Murchison Widefield Array (MWA; Tingay et al., 2013) in remote Western Australia are well-suited at detecting and characterising such emission (e.g. Hindson et al., 2014; George et al., 2017; Duchesne et al., 2017; Zheng

*email: stefan.duchesne.astro@gmail.com

et al., 2018). In 2017, the GaLactic and Extragalactic All-sky MWA survey (Wayth et al., 2015; Hurley-Walker et al., 2017) was released, unveiling myriad new candidate halos and relics (Johnston-Hollitt et al., in preparation), as well as giving unprecedented spectral coverage to previously detected halos and relics in the Southern Sky.

One such galaxy cluster, Abell 1127, was found to host diffuse radio emission within the 72–231 MHz GLEAM survey images, and was found as part of a targeted search for halos and relics within clusters from the Abell catalogues (ACO; Abell et al., 1989), the Meta-Catalogue of X-ray detected Clusters of galaxies (MCXC; Piffaretti et al., 2011), and the *Planck* Sunyaev–Zel'dovich cluster catalogue (PSZ1; Planck Collaboration et al., 2015). This particular example is complete with archival X-ray data from the *Chandra* observatory and given its location above the equator has good coverage from northern optical surveys.

In this paper we will investigate the diffuse radio source within Abell 1127 (located at $10^{\rm h}54^{\rm m}14\overset{\rm s}{.}4$, $+14°38'34\overset{''}{.}8$) and the cluster itself, from radio to X-ray wavelengths to determine its nature. We assume a Lambda Cold Dark Matter cosmology, with $H_0 = 70\ {\rm km\,s^{-1}\,Mpc^{-1}}$, $\Omega_{\rm m} = 0.3$, and $\Omega_\Lambda = 1 - \Omega_{\rm m}$.

1.1. *Abell 1127 and associated clusters*

Abell 1127 ($10^{\rm h}54^{\rm m}09^{\rm s}$, $+14°40'00''$; Abell et al., 1989) is detected as a *Planck*-SZ source ($10^{\rm h}54^{\rm m}18\overset{\rm s}{.}1$ $+14°39'21''$, with positional uncertainty of $\sim$ 2.4 arcmin; Planck Collaboration et al. 2016), designated PSZ2 G231.56+60.03. A spectroscopic redshift is reported by Wen et al. (2012) of $z_{\rm spec} = 0.2994$. However, the cluster is also used as part of the SOAR [1] Gravitational Arc Survey (SOGRAS; Furlanetto et al., 2013) wherein a photometric redshift of $z_{\rm phot} = 0.328$ is determined. Despite the difference in redshift we consider this a single cluster system. The system has not previously been described as merging, and no diffuse, non-thermal radio emission has been found to be associated with the cluster.

2. Data

A plethora of all-sky and large-area astronomical surveys are available, many of which we make use of here. As well as survey data, we have dedicated observations with the MWA and archival data from the *Chandra* X-ray observatory and the Karl G. Jansky Very Large Array (VLA). We will introduce and describe the various data products in this section.

2.1. *Surveys*

2.1.1. Radio surveys

Three radio surveys are used explicitly in this work: The NRAO [2] VLA Sky Survey (NVSS; Condon et al., 1998), which covers the entire sky north of $\delta_{\rm J2000} \geq -40°$ at 1.4 GHz; the Faint Images of the Radio Sky at Twenty-centimeters (FIRST; Becker et al., 1995; White et al., 1997; Helfand et al., 2015), mostly located in the Northern Sky and also at 1.4 GHz, the TIFR GMRT [3] Sky Survey Alternative Data Release (TGSS-ADR1; Intema et al., 2017), covering the sky north of $\delta_{\rm J2000} \gtrsim -53°$ centred at 150 MHz. We also utilise low-resolution images from both the NVSS and TGSS ADR1 by convolving full-resolution images to a final resolution of 100 arcsec × 100 arcsec to match closely to MWA-2 data.

2.1.2. Optical surveys

The region surrounding the Abell 1127 system is covered by the Sloan Digital Sky Survey Data III, Data Release 12 (SDSS III, DR12; York et al., 2000; Eisenstein et al., 2011; Alam et al., 2015), with 158 sources with redshifts available within 7 Mpc of the diffuse radio source of interest.

2.2. *VLA S-band data*

In June 2017 Abell 1127 was observed with the VLA in S-band (2–4 GHz) in the C configuration for $\sim$ 24 min (Proposal ID 17A-308, PI T. Cantwell). S-band is split into 16 subbands of 128 MHz, and each subband is calibrated independently. Calibration and radio frequency interference (RFI) flagging is performed following standard procedures for VLA data using the Common Astronomy Software Applications (`CASA`) package (McMullin et al., 2007). 3C 286 is used for flux scale calibration using the Perley & Butler (2017) scale (itself based on the flux density scale of Baars et al., 1977), and 3C 241 is used for phase calibration, bracketing the source observations. Eight subbands are not used due to RFI contamination or calibration problems. The remaining eight subbands are imaged using the widefield imager `WSClean` (Offringa et al., 2014; Offringa & Smirnov, 2017) [4], jointly deconvolving the 8 subbands and creating a model in each band which is used for self-calibration with `CASA`. We perform three rounds of phase-only self-calibration followed by a round of phase and amplitude self-calibration. Data are imaged with a natural weighting, providing the best sensitivity to point sources in this configuration, creating a fullband image centered at 3.063 GHz. No extended emission is seen at the location of the diffuse emission seen in the GLEAM data. We subtract the naturally-weighted model from the visibilities and re-image with a 25 arcsec Gaussian taper to try to highlight extended structure, finally convolving the resulting image to a final resolution of 100 arcsec×100 arcsec. The naturally-weighted image prior to source subtraction is shown in Fig. 4(i).

2.3. *MWA-2 data*

Abell 1127 was observed as part of a MWA project G0045 [5] during the 2018A observing semester. During this semester, the MWA was operating in the 'extended' configuration, part of the Phase II upgrade (Wayth et al., 2018, hereafter MWA-2) that occurred in 2017 adding tiles (antennas) out to $\sim$ 5 km improving the resolution of the array at a small cost to surface brightness sensitivity. Fig. 1 shows the monochromatic u–v coverage for a single 2-minute

[1] Southern Astrophysical Research telescope
[2] National Radio Astronomy Observatory
[3] Tata Institute for Fundamental Research Giant Metrewave Radio Telescope
[4] https://sourceforge.net/p/wsclean/wiki/Home/
[5] Details of MWA projects can be found at http://www.mwatelescope.org/data/observing.

Table 1 MWA-2 observational details for Abell 1127.

Date (UTC)	$N_{88\ \mathrm{MHz}}$ (a)	$N_{118\ \mathrm{MHz}}$	$N_{154\ \mathrm{MHz}}$	$N_{185\ \mathrm{MHz}}$	$N_{216\ \mathrm{MHz}}$	Project (b)	Comments (d)
2018-01-17	13/13	14/14	14/14	12/14	14/14	G0045	Good.
2018-01-18	0/14	11/14	9/14	8/14	13/14	G0045	Poor ionosphere.
2018-01-26	0/6	6/6	5/5	2/5	4/5	G0008	Variable ionosphere.
2018-02-01	0/6	0/6	2/5	2/5	4/5	G0008	Poor ionosphere.
2018-03-03	1/6	6/6	5/5	4/4	5/5	G0008	Poor ionosphere.
2018-05-07	5/5	5/5	4/4	4/4	4/4	G0008	Good.
2018-05-26	5/5	5/5	4/4	4/4	2/4	G0008	Good.
Totals (c)	24/55	47/56	43/51	36/50	46/51	...	...

Notes. (a) Ratio of snapshots used to snapshots observed for a given night and frequency, with each snapshot 112–120s of data. (b) G0008 is GLEAM-eXtended, and G0045 is the dedicated cluster project. (c) Total snapshots used after discarding snapshots with issues including poor ionospheric conditions, too few tiles, or particularly bad RFI. (d) User determined qualitative assessment of the datasets.

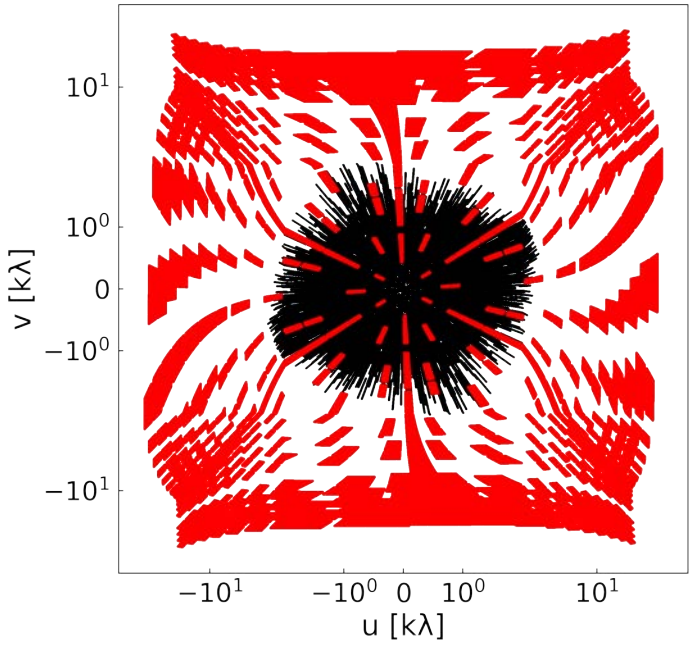

Figure 1. The typical *u*–*v* coverage of a single 2-min snapshot at 154 MHz (the central band) with 30 MHz bandwidth (black) with the VLA S-band *u*–*v* coverage overlaid (red). Note the symmetric logarithmic scale used for both axes to highlight the overlap.

snapshot at 154 MHz illustrating the completeness of the *u*–*v* coverage with the MWA-2. In addition to the G0045 observations, we make use of snapshots taken as part of the MWA-2 GLEAM survey (GLEAM-eXtended) where they overlap with the position of A1127 to increase sensitivity. Pertinent observation information is provided in Table 1. A set of between 50 and 56 2-minute snapshots for each of the five observing frequencies (at 88, 118, 154, 185, and 216 MHz) were taken across the two projects and across a number of observing nights, though in practice because of poor ionospheric conditions some snapshots were rendered unusable [6]. Over half of the snapshots taken in the lowest frequency band were rendered unusable with current processing techniques.

Data processing is largely done using the purpose-written Phase II Pipeline (`piip` [7]) and `skymodel` [8] code once data have been pre-processed. The following sections outline this process and the various software involved.

2.3.1. *Pre-processing*

Data are recorded by the telescope in 2-minute snapshots as the primary beam varies with time and this allows primary beam correction with current tools. The downside of this observing strategy is that each 2-minute snapshot must be calibrated and imaged individually. Data processing is performed at the Pawsey Supercomputing Centre [9] in Perth, Western Australia, which conveniently also hosts the raw visibilities sent directly via fiber from the Murchison Radio-astronomy Observatory (MRO). For each snapshot, the following process is used to generate a calibrated, primary beam corrected image: data are staged using the MWA All Sky Virtual Observatory [10]. The MWA ASVO system converts raw telescope products to the more standard "MeasurementSet" format using the `cotter` software developed by A. O. Offringa, and performs preliminary radio-frequency inference (RFI) flagging using the `AOFlagger` software (Offringa et al., 2012) [11]. Additional bad tiles and channels are manually flagged prior to calibration, then again prior to imaging if any bad data present itself.

2.3.2. *Initial calibration*

As the field of view of the MWA at all frequencies is > 20 degrees, every snapshot contains a large number of sources which often allows infield calibration, which is made even easier when bright extra-galactic sources (e.g. Virgo A) lie within the main lobe of the primary beam. Generally MWA calibration requires peeling of bright (> 25 Jy) sources outside of the image field of view, and

[6] Development for direction-dependent calibration of MWA data is underway to help alleviate ionospheric problems, though software and tools to reliably do this are not currently available.

[7] https://gitlab.com/Sunmish/piip

[8] https://github.com/Sunmish/skymodel

[9] https://pawsey.org.au

[10] ASVO: https://asvo.mwatelescope.org/

[11] https://sourceforge.net/p/aoflagger/wiki/Home/

in the case of this field the Galactic Plane becomes a source of sidelobe noise at the high end of the MWA band. To counter this, after initial calibration the side lobes of the 185- and 216-MHz bands are imaged on multiple angular scales and their CLEAN component models (Gaussian and point sources) are subtracted from the visibilities. Note that all CLEAN components within the sidelobe are subtracted, including non-Galactic discrete sources. Despite Virgo A being within and near the field of interest, it either lies within the primary beam mainlobe at low frequencies (88- and 118-MHz) or outside enough to be nulled at higher frequencies (154-, 185-, and 216-MHz).

In these observations, we use 100–200 sources for infield calibration, depending on frequency (with more sources used at low frequency due to the larger field view). Calibration is performed with an implementation of the full-Jones `Mitchcal` algorithm, developed for MWA calibration specifically as described by Offringa et al. (2016), which produces static phase offsets via least-squares fitting for each MWA tile. The sky model used for calibration is generated using a cross-match between GLEAM, NVSS, and TGSS (using the Positional Update and Matching Algorithm, `PUMA`; Line et al. 2017) with flux densities and the required frequency estimated by either fitting a generic curved or normal power law to the catalogue flux density measurements, or using an average spectral index of $\langle\alpha\rangle = -0.77$ and assuming a normal power law model. Given the density of measurements provided by the GLEAM Extra-Galactic Catalogue (GLEAM EGC; Hurley-Walker et al., 2017), flux densities are heavily weighted by these measurements which are based on the Baars et al. (1977) flux density scale, but positions are more heavily weighted by the NVSS positions where available.

2.3.3. Self-calibration and imaging

After initial calibration, a single round of phase and amplitude self-calibration is performed by first doing a shallow CLEAN using `WSClean` which makes use of a *w*-stacking technique to ensure the large field-of-view is properly imaged. This round of CLEAN stops at a threshold of 5 times the local noise. Imaging during self-calibration is done in an "8 channels out" mode, where CLEANing is performed on 8 subbands (each with $\Delta\nu = 3.84$ MHz) which allows for a self-calibration model that has frequency-dependence at that sampling. The model generated by `WSClean` is then used by the previously described calibration software to once again calibrate the data. This usually significantly improves the residual calibration artefacts from the first iteration. Deeper CLEANing is then performed again using `WSClean` with a 'Briggs' robust +1.0 weighting, this time down to an initial threshold of $3\sigma_{\rm rms}$ and a final threshold of $1\sigma_{\rm rms}$. Here we use a "4 channels out" mode (CLEANing subbands of $\Delta\nu = 7.68$ MHz), which addresses the issue of a changing point-spread function (PSF) as a function of frequency, thus reducing amplitude errors which become particularly more problematic around bright sources. Primary beam corrections are applied to each snapshot, using the Full Embedded Element primary beam model (Sokolowski et al., 2017), generating astronomical Stokes *I* primary beam-corrected images. Note that a set of images are also produced at a 'Briggs' robust 0.0 weighting but are not used.

2.3.4. Astrometric and flux scale corrections

For each 2-min snapshot Stokes I image, a pixel-based position correction is done to account for first-order ionospheric effects. This is achieved using `fits_warp.py` (Hurley-Walker & Hancock, 2018), which compares an initial image catalogue generated by the `aegean` [12] source-finding software (Hancock et al., 2012, 2018) with a reference catalogue, in this case generated by combining the NVSS, TGSS, and GLEAM catalogues. A pixel-based shift is performed based on the angular separation of sources, and cubic interpolation is used to create an effective screen to shift pixels by. Any snapshots that have significantly higher noise or show more complex ionospheric distortions are at this stage discarded.

Finally, each snapshot at each frequency has a slightly different flux scale that must be normalised. The initial calibration is performed with respect to both the GLEAM EGC (Hurley-Walker et al., 2017) (along with other radio sky surveys) as well as select multi-component and point-source models from earlier MWA Phase I data of particularly bright sources (e.g. Virgo A). This initial flux scale is more heavily determined by the initial bright source models, which vary from the GLEAM catalogue by up to 50 per cent and so final image-based bootstrapping is required to tie the flux scale more closely to the GLEAM EGC. Additionally, we suspect that there are residual primary beam model errors present in the data, which have a position dependence which is corrected for simultaneously. This process uses in-house code written for this purpose and is described in more detail in Appendix B.

2.3.5. Stacking the 2-min snapshots

To re-grid images prior to co-addition, we make use of the `regrid` task within the `miriad` software suite (Sault et al., 1995). We generate three separate stacked images: 1) Stokes *I* images weighted by the primary beam response, 2) the effective Stokes *I* response images corresponding to the weighted Stokes *I* image, and 3) the effective PSF map weighted as per the previous two stacked images. In practice, this PSF map incorporates a total flux preserving factor (see Appendix A for determination of the correction factor) within an effective major axis for the PSF which is all that is required when measuring total or integrated flux densities, hence the position angle is not well defined. Note that peak flux (i.e. surface brightness) is always preserved. Fig. 2 shows the output from creating mosaics for the 154-MHz data, with the Stokes *I* image, effective PSF major axis map, noise map, and summed Stokes *I* primary beam. While our pipeline produces individual snapshots of the $\Delta\nu = 30.72$ MHz bands as well as the $\Delta\nu = 7.68$ MHz subbands generated during "4 channels out" CLEANing, we only use stacked mosaics of the $\Delta\nu = 30.72$ MHz images due to the signal-to-noise ratio constraints of our source of interest in the higher frequency bands (see Section 3.2.2). The final mosaic properties are presented in Table 2 and the images centered on Abell 1127 are shown in Fig. 3. Note that some image properties vary over the map (e.g. PSF) so we report the value at the position of Abell 1127.

[12] https://github.com/PaulHancock/Aegean

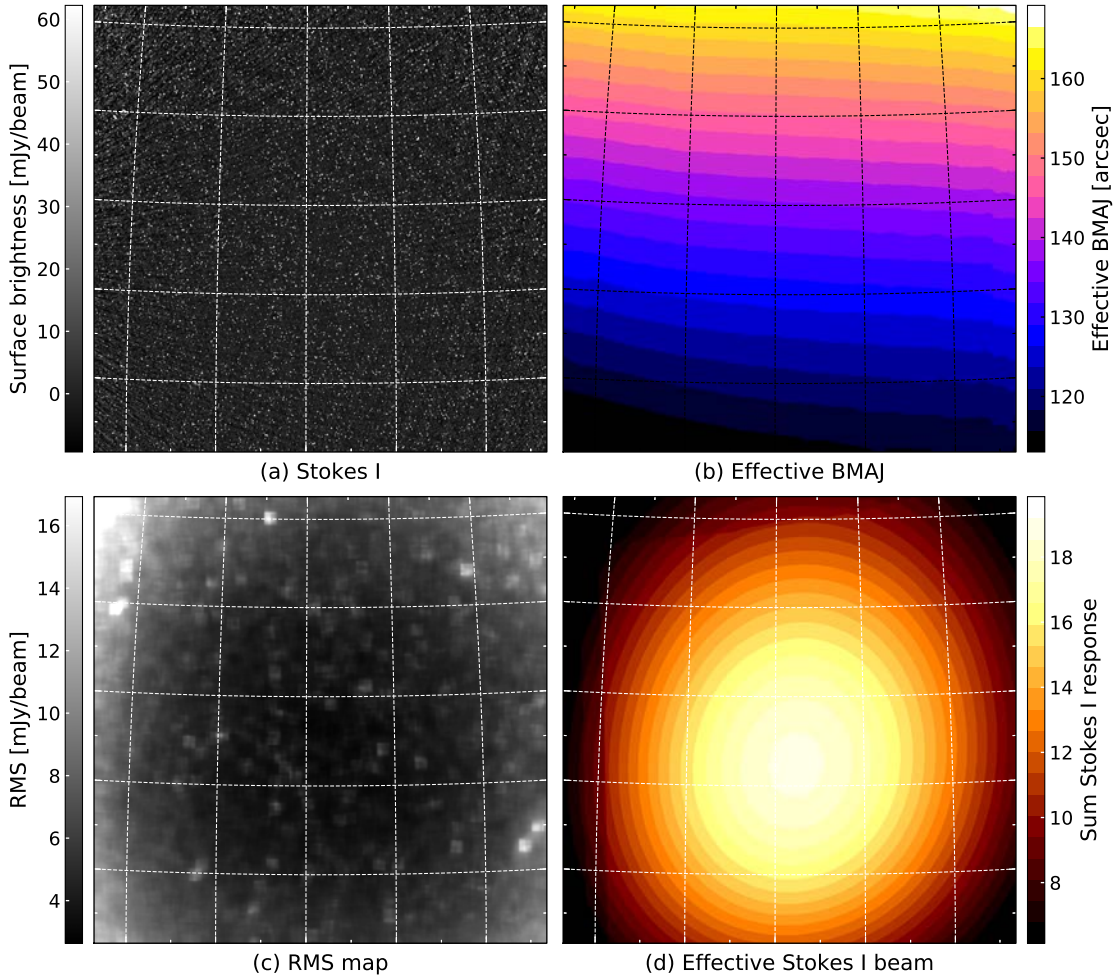

Figure 2. Output from stacking and re-gridding for the 30-MHz band centered on 154 MHz. Note the images cover a $\sim 25^\circ$ by $\sim 25^\circ$ region.

2.4. Chandra *data*

A1127 (as RM J105417.5+143904.2) was observed with the Advanced CCD Imaging Spectrometer (ACIS-I) instrument on the *Chandra* observatory with 10.46 ks of exposure time (Obs. ID 17160, PI: Eduardo Rozo). These archival data were retrieved from the *Chandra* Data Archive (CDA). We analyzed the data obtained from the S0-3 chips of ACIS. We followed the standard *Chandra* data reduction process and used the `CIAO` [13] (version v4.11 with CALDB v4.8.2; Fruscione et al. 2006) script `chandra_repro` to generate the level-2 event file. We examined the light curves extracted in 0.5–12.0 keV from source-free regions near CCD edges and exclude the time intervals during which the count rates deviate from the mean values by 20 per cent. The CIAO tool `celldetect` is used to identify and exclude the point sources detected on the S0-3 chips and finally `flux_image` is used to generate the exposure map to correct for the vignetting and exposure time fluctuations.

3. Results

[13] *Chandra* Interactive Analysis of Observations

3.1. *The optical and X-ray core*

The core of the cluster system can be characterised by both an optical concentration of galaxies as well as an X-ray–emitting plasma. Fig. 5 shows the SDSS data of the cluster region, with an inset zoom-in on the BCG and surrounding galaxies ("A1-2", "B", and "C"). The BCG, "B", is 2MASX J10541751+1439041 (hereafter 2MASX J1504). 2MASX J1504 is reported with a spectroscopic redshift of $z = 0.299437 \pm 0.000054$ from DR12 of the SDSS.

Fig. 6 shows the reprocessed archival *Chandra* data with radio contours overlaid. For display purposes we smooth the X-ray image by convolving with a $\sigma = 18$ arcsec Gaussian kernel using the `CIAO` task `asmooth`. The image itself provides two interesting things to note: 1) the X-ray distribution is not circular, and 2) the emission is divided into two clumps, with the main, eastern clump containing the peak of the surface brightness and the secondary, western clump being much fainter. The void between the clumps coincides with the peak of the radio emission.

We analyse the un-smoothed *Chandra* image with the X-ray

Table 2 Details of the MWA-2 observations and resultant images.

Band (MHz)	ν_c (a) (MHz)	t_{scan} (b) (min)	PSF (c) ($''\times''$)	$\sum A_I$ (d)	σ_{rms} (e) (mJy beam^{-1})	Δ_{flux} (f) %
72–103	88	38	241.1×179.6	10.1	18.4	5.6
103–134	118	82	176.4×131.2	18.1	7.1	3.5
139–170	154	74	136.2×101.0	18.0	3.7	3.7
170–200	185	60	111.3×82.5	15.1	3.4	4.1
200–231	216	92	96.7×71.5	10.6	3.9	5.0

Notes. (a) Central observing frequency. (b) Total scan length of data used in imaging. (c) Effective PSF at the source location. (d) The summed Stokes *I* primary beam response of the stacked image, where $A_I = 1$ is the peak response for a 2-min observation at zenith. (e) Local rms at the location of Abell 1127. (f) % uncertainty on the flux scale compared to the input calibration model.

Table 3 Sources detected in the SDSS images at the center of the cluster region.

ID	Name	z
A1	GALEXASC J105418.23+143902.3	-
A2	SDSS J105418.12+143902.0	-
B	2MASX J10541751+1439041	0.2994
C	2MASX J10541735+1439012	-
D	SDSS J105415.58+143914.8	-
E	2MASS J10541703+1438353	-

surface brightness analysis software, `proffit` [14] (Eckert et al., 2011). We use circular annuli to determine an azimuthally averaged surface brightness profile. As the un-smoothed image has no well-defined peak, we use the smoothed image to define the centre of the surface-brightness profile (corresponding to coordinates $10^h54^m17\overset{s}{.}3$, $+14°38'49''$). The profile is measured out to 6 arcmin (1.6 Mpc at $z_{spec} = 0.2994$, however this radius is chosen as it is the edge of the image), with counts initially binned in 4 arcsec annuli. These bins are adjusted to ensure a signal-to-noise ratio of at least 10 per bin, resulting in 8–16 arcsec bins with > 100 counts per bin. We assume a constant background over the image, and define the annuli with radii $4.5' < r \leq 6'$ to consist of only background counts from visual inspection and fit these bins with a constant profile. This is $I_b = (1.095 \pm 0.034) \times 10^{-5}$ counts s^{-1} cm^{-2} arcmin^{-2} and is subtracted from the surface brightness profile. For the background-subtracted annuli with radii $r \leq 4.5'$, we find that a standard β model (Cavaliere & Fusco-Femiano, 1976) fits the surface brightness profile well (with $\chi_{red} = 1.27$). The results of the surface brightness profile fitting and background subtraction are shown in Fig. 7. We perform a similar surface brightness analysis across the southwest X-ray clump as indicated by the red, dashed wedge region in Fig. 6. This profile is shown in Fig. 7 and the location of the peak radio emission in the TGSS ADR1 image is also plotted for reference. The peak radio emission occurs immediately as the X-ray separates into the southwestern clump.

We calculate the centroid shift, w (e.g. Poole et al., 2006, but see also Mohr et al. 1993) with an outer radius set to 1.87 arcmin, corresponding to 500 kpc (see Cassano et al., 2010), resulting in $w_{500} = 0.072$. For further comparison to literature data, we estimate the centroid shift within R_{500} [15]. We estimate $R_{500} \sim 920$ kpc from a 0.5–2.0 keV X-ray luminosity of $L_X \sim 3.6 \times 10^{44}$ erg s^{-1} as measured from flux within the cluster region, using R_{500}–L_X relations (Böhringer et al., 2007, but see also Arnaud et al. 2005); we find $w_{920} = 0.02R_{500}$. Additionally, we calculate the surface brightness concentration parameter (see e.g. Santos et al., 2008) in two ways: within 100 kpc and 500 kpc (0.37 and 1.87 arcmin, respectively, as per Cassano et al. 2010) and within 40 kpc and 400 kpc (0.15 and 1.50 arcmin, respectively, as per Santos et al. 2008), thus finding $c_{100/500} = 0.105$ and $c_{40/400} = 0.022$.

3.2. *Radio emission*

3.2.1. *Radio morphology and discrete sources*

The full-resolution TGSS ADR1 image at 150 MHz shows an elongated radio structure near the optical centre of the cluster system (see Fig. 5). Given the concentration of optical sources, it is difficult to confirm if one or more of the optical galaxies in the region is the host of the emission, however, no discrete radio sources are seen within the TGSS-detected emission either in the FIRST survey image or the VLA S-band image (Fig. 4). Optical source "D" (Fig. 5) sits within the TGSS emission and at first glance appears to correspond to a peak in the TGSS image with $S_{150\,MHz} \sim 12$ mJy beam^{-1}. However, no discrete source is detected in the VLA S-band image above $3\sigma_{rms}$ ($\sigma_{rms} = 11.5$ μJy beam^{-1}) at this position. If this component of the full extended emission is a discrete source, it would require $\alpha < -1.9$ to result in a non-detection in the VLA S-band image. Given this would be an unusually steep spectrum core, we assume the peak 150-MHz emission co-spatial with "D" is not associated with "D" and is part of the extended emission.

The VLA S-band data reveal six discrete radio sources, including Source "E", within the measured region in the MWA-2 images. Source "E" is shown in the insets of Fig. 4 and other discrete sources are indicated by cyan circles in Fig. 4(i), though the additional discrete sources are not detected in the FIRST survey image. Source "E" is not detected in the TGSS image above 9.4 mJy ($3\sigma_{rms}$) but based on the spectral index between the FIRST and VLA S-band

[14] http://www.isdc.unige.ch/~deckert/newsite/Proffit.html

[15] R_{500} corresponds to the radius within which the mean mass density is 500 times the critical density of the Universe.

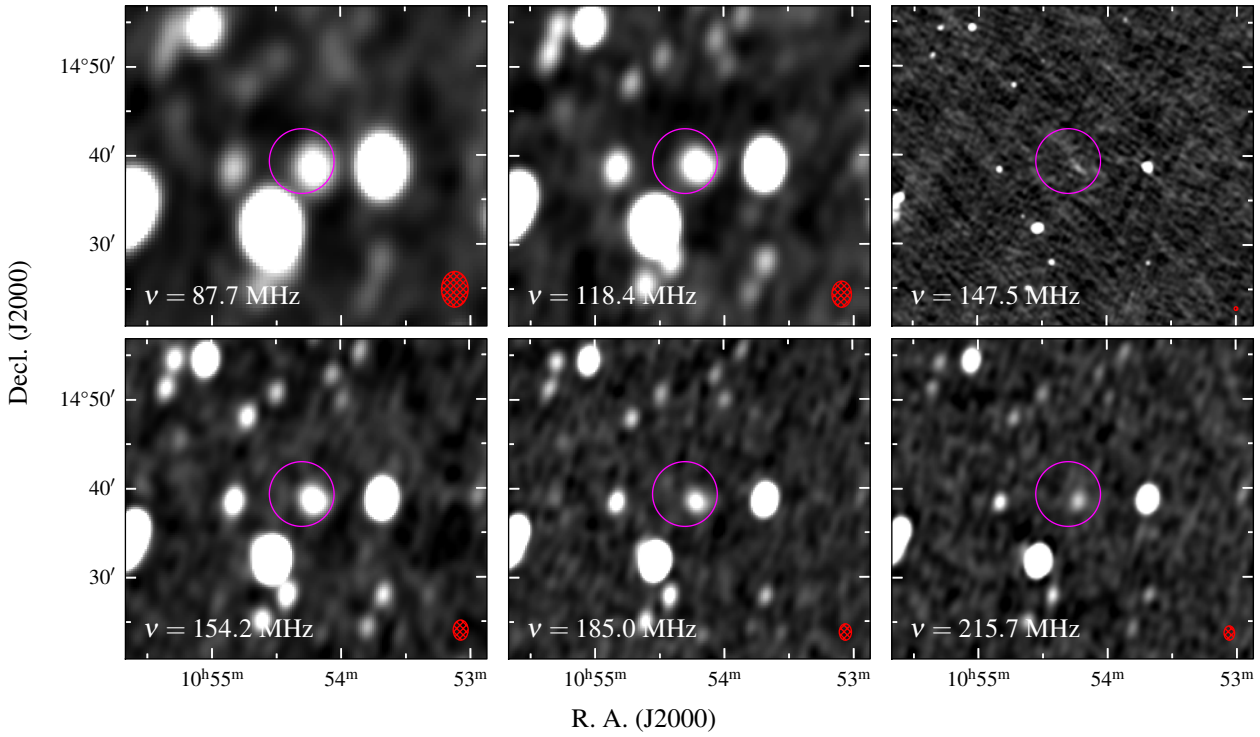

Figure 3. The MWA-2 robust +1.0 stacked mosaics for the MWA field containing Abell 1127 across the five frequencies, with the TGSS ADR1 image in the top right. The greyscale maps are all linear stretches between $-3\sigma_{\rm rms}$ and $15\sigma_{\rm rms}$ (see Table 4 for values for each image). The magenta circle is centered on PSZ2 G231.56+60.03 and has a radius of 1 Mpc. The red, hatched ellipses in the lower right corners are the effective PSF size for each map at this position.

data ($\alpha_{\rm E} = -0.8 \pm 0.2$) , assuming a power law, the source would be just detectable at $\sim 4\sigma_{\rm rms}$ significance in the TGSS image.

We measure the full extent of the diffuse source in the MWA-2 154-MHz image: the deconvolved largest angular size is determined to be 3.2 arcmin measured out to $2\sigma_{\rm rms}$, corresponding to a projected linear size of 850 kpc.

3.2.2. Radio spectral energy distribution and power

We measure the spectral energy distribution of the source between 88–3063 MHz using the MWA-2, TGSS, NVSS, and VLA S-band data. We measure the integrated flux density of the source in the MWA-2 and TGSS data by integrating over a circular aperture centered on the source. We mask pixels below $2\sigma_{\rm rms}$, and the measurement uncertainty, σ_S, is defined via

$$\sigma_S = \sqrt{\frac{\Omega_{\rm pixel}\langle\Omega_{\rm beam}\rangle}{N_{\rm pixel}}} \sum_{i=0}^{N_{\rm pixel}} \frac{\sigma_{{\rm rms},i}}{\Omega_{{\rm beam},i}} \quad [{\rm Jy}]\,, \qquad (1)$$

where $\Omega_{\rm pixel}$ is the constant pixel solid angle, $\Omega_{\rm beam}$ is the varying beam solid angle, and $\sigma_{\rm rms}$ is the map rms. While the synthesized beam does vary in size across these MWA-2 mosaics, in practice the variation across our source of interest is minute. Note that the 216-MHz band of the MWA-2 data is considered a lower limit as the shape of the source changes significantly enough that we suspect the entirety of the source is not detected in this band. Inspecting the highest frequency subband ($\nu_{\rm c} = 227$ MHz) shows only a hint of signal at the $3\sigma_{\rm rms}$ level.

For the MWA-2 data, we correct a CLEAN bias by adding 14–48 mJy to each measurement (see Appendix C for details). Additionally, we estimate the possible contribution from the unnamed discrete S-band sources by extrapolating to MWA frequencies assuming $\alpha_{\rm discrete} = -0.77$. We find the contribution is small (at the level of the noise) so include this as additional uncertainty in the measurements. The total uncertainty of an integrated flux density measurement is the quadrature sum of the measurement uncertainty, flux scale uncertainty, and discrete source uncertainty. The contribution from source "E" is also estimated from $\alpha_{\rm E} \sim -0.8$ and is subtracted. The low-resolution TGSS ADR1 flux density measurement is consistent with the MWA-2 measurement at 154 MHz within the estimated uncertainties. Finally, assuming the angular size of the emission in the MWA-2 154-MHz map is the true size, we estimate a 3σ upper limit from the low-resolution NVSS and VLA discrete-source–subtracted S-band maps which have constant rms noises of 1.25 and 0.082 mJy beam^{-1}, respectively. Table 4 presents the flux densities measurements and the various measurement corrections for each band.

We fit a generic power law model to the MWA-2 data between 88–185 MHz using the Levenberg–Marquardt algorithm for non-linear least-squares fitting implemented in `lmfit` (Newville et al., 2014). The best-fit power law model yields a spectral index of

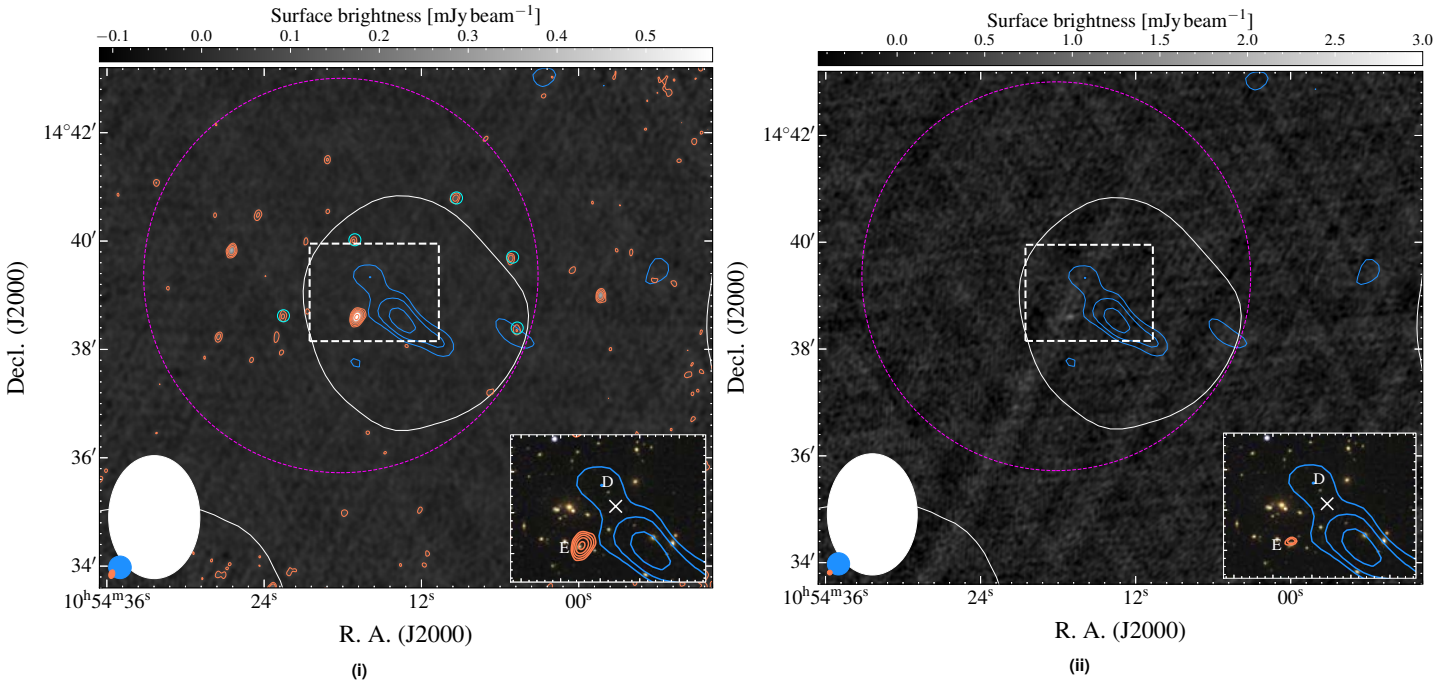

Figure 4. VLA GHz view of the cluster region. (i) The background is the 3.063 GHz VLA S-band map prior to source-subtraction. Orange contours start at $4\sigma_{\rm rms}$ ($\sigma_{\rm rms} = 11.5\ \mu$Jy beam^{-1}) increasing with factors of 2. The cyan circles denote discrete sources that affect the MWA measurements as discussed in the main text. (ii) FIRST survey image background of the same region. In both panels the magenta circle is as in Fig. 3. The single white contour is the 154-MHz MWA-2 data at $3\sigma_{\rm rms}$, and the blue contours are the TGSS data starting at $3\sigma_{\rm rms}$ increasing with factors of $\sqrt{2}$. The coloured ellipses in the lower right of each panel are of the respective beam shapes, with smallest, orange beam being the VLA data. The dashed, white box indicates the location of the inset panels. Sources "E" and "D" are discussed in the text.

Table 4 Flux density measurements of the diffuse radio source with required corrections.

Band	$\nu_{\rm c}$ (MHz)	S_ν (mJy)	$S_{\rm bias}$ (mJy)	$\Delta S_{\rm discrete}$ (mJy)	$S_{\rm E}$ (mJy)	$\sigma_{\rm rms}$ (mJy beam^{-1})
TGSS (a)	147.5	150 ± 50	-	6	< 12.2	25
NVSS (a)	1400	< 15	-	0	1.85 ± 0.24	1.2
S-band (a)	3063	< 0.9	-	0	0.96 ± 0.05	0.082
MWA-2						
72–103	87.7	341 ± 54	48	9	19	18
103–134	118.4	188 ± 29	20	7	15	9
139–170	154.2	122 ± 19	10	6	12	5
170–200	185.0	86 ± 15	12	5	10	4
200–231	215.7	> 55	14	5	9	4

Note. (a) Based on low-resolution image (100 arcsec × 100 arcsec).

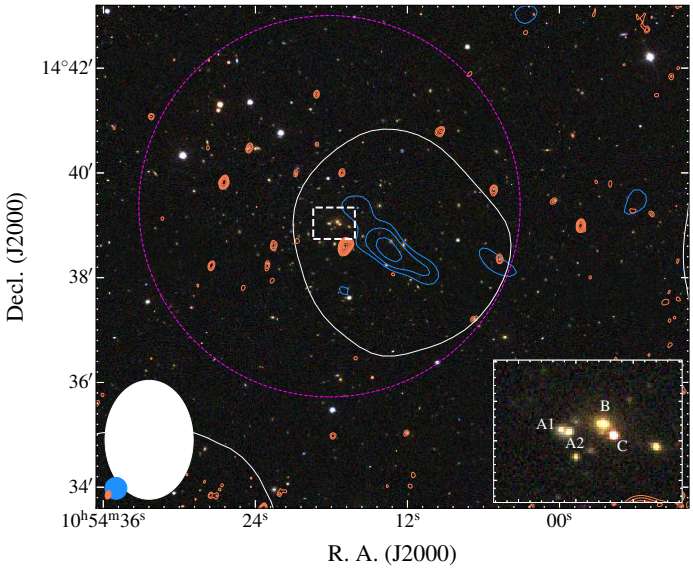

Figure 5. The background is a three-colour (red-green-blue) image made from the i, r, and g bands of the SDSS. The contours and features in the image are as in Fig. 4(i), though the inset location is focused on the cluster centre. The dashed box in the centre of the cluster is enlarged in the inset shown on the bottom right.

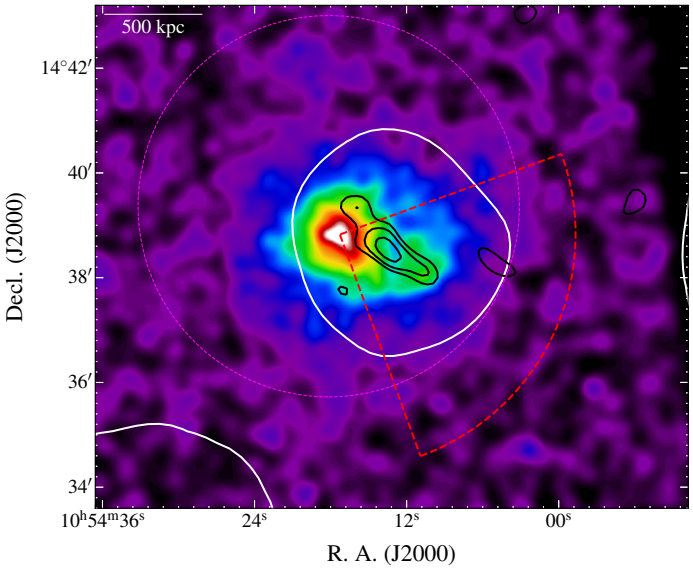

Figure 6. The *Chandra* X-ray map smoothed with a $\sigma = 18$ arcsec Gaussian kernel. The overlaid white contour is from the 154-MHz MWA-2 image at $3\sigma_{\rm rms}$. The overlaid black contours are the 150-MHz TGSS ADR1 image, with contours also starting at $3\sigma_{\rm rms}$. The dashed, magenta circle is the same as in Fig. 3, and the dashed, red wedge indicates the region used to extract the surface brightness profile through the southwest X-ray clump (blue points in Fig. 7).

$\alpha = -1.83 \pm 0.29$ for the source. This fit is shown in Fig. 8. Using the MWA-2 model fit we estimate the 1.4-GHz flux density of the extended source to be $S_{1.4\ \rm GHz} \sim 2$ mJy, which gives a monochromatic power of $P_{1.4\ \rm GHz} \sim 7 \times 10^{23}$ W Hz^{-1} if indeed the emission is at the redshift of the BCG ($z = 0.2994$), and using the spectral index determined above.

4. Discussion

4.1. *A dynamic system*

The clumping of the X-ray emission and general extension to the west suggests an un-relaxed system. We can attempt to quantify this by comparing the morphological parameters $c_{100/500} = 0.105$ ($c_{40/400} = 0.022$) and $w_{500} = 0.072$ ($w_{920} = 0.02 R_{500}$) and with other clusters. The surface brightness concentration parameter is a good indicator of cool-core systems (Santos et al., 2008) and here we note that $c_{40/400} = 0.026$ is below values typically seen in cool-core systems (with $c_{40/400} \gtrsim 0.75$). Poole et al. (2006) find that for simulated data the centroid shift, w, is a good indicator that a cluster has been disturbed, presumably by merger-related activity. Pratt et al. (2009) define a disturbed system as having $w > 0.01 R_{500}$ from a representative sample of 31 X-ray–emitting, nearby clusters (i.e. the REXCESS [16] sample), suggesting that Abell 1127 is morphologically disturbed. Additionally, the measured values for w_{500} and $c_{100/500}$ place the cluster in the quadrant of merging clusters in Figure 1(a) from Cassano et al. (2010), most of which have been found to host giant radio halos. The *Chandra* data provide good support for the cluster system being in a morphologically disturbed state (corresponding to merger activity). In addition to this, the peak emission of the radio source in the TGSS ADR1 image sits immediately before the transition between the main X-ray–emitting clump and the fainter southwestern clump.

[16] Representative *XMM-Newton* Cluster Structure Survey

4.2. *Classification of the diffuse radio source*

While there are numerous optical galaxies within the emission region of the extended, diffuse radio emission there is no radio core detected. This, combined with the steep observed radio spectrum precludes the extended source from being a normal, active radio galaxy. The steep radio spectrum of the source suggests an aged population of electrons, fading or perhaps re-accelerated from merger-related activity within the ICM. Merging clusters have been found to host radio halos and relics (see e.g. Cassano et al., 2013). While the source is unlikely to be a giant radio halo, given its offset from the X-ray emission peak, we consider the possibility of a relic-like radio source.

Unfortunately the source is not resolved enough with the current data to perform a resolved spectral study to explore possible radio shock origins (e.g. van Weeren et al., 2010; Hindson et al., 2014; de Gasperin et al., 2014) including re-acceleration or re-energisation (e.g. Bonafede et al., 2014; de Gasperin et al., 2017), however, if the source is a relic generated from a shock, it is likely oriented at some angle between the cluster and observer, and shock-driven relic features such as a spectral gradients may not be present or observable. The integrated spectrum is steeper than most radio relics associated with shocks (with the current sample mean $\alpha = -1.2 \pm 0.2$; van Weeren et al. 2019 and references therein), but does share observed properties of the relic source in RXC J1234.2+0947 (Kale et al., 2015); a similar steep spectrum relic-like source with no observed connection to a shock. Such

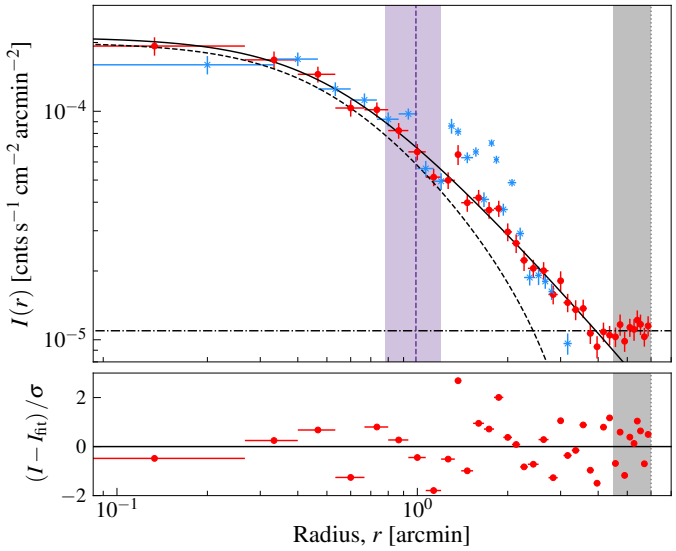

Figure 7. Surface brightness profile of the X-ray emission associated with Abell 1127. For the azimuthally averaged profile (red circles), two models are fit at separate radii: a β model for $r \leq 4.5'$ (dashed line) fit to background subtracted data, and a constant model for $4.5' < r \leq 6'$ (dot-dash line) to determine the background. The solid line is the combination of the background-subtracted β model and the constant background. The grey, shaded region indicates the background fitting region. The horizontal bars indicate the radial bin widths. The blue points correspond to a radial surface brightness profile across the southwest X-ray clump (red, dashed region in Fig. 6), and the vertical, dashed purple line marks the peak emission of the radio source in the TGSS ADR1 image, with the purple shaded region indicating the beam size.

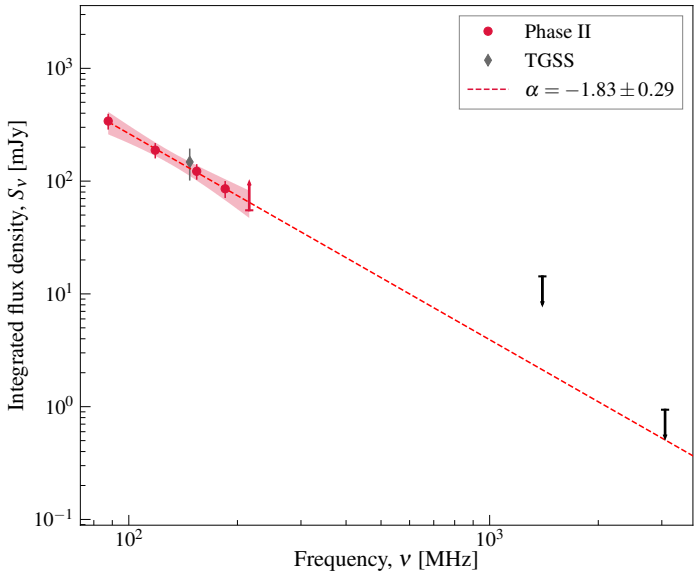

Figure 8. The spectral energy distribution of the diffuse radio source from 88–3063 MHz. The black upper limits are from the low-resolution NVSS and VLA source-subtracted S-band images. Note the lower limit at 216-MHz. The power law fit to the MWA-2 data is shown as the dashed, red line. Limits are not used in fitting. The TGSS measurement is also shown for completeness, but not used in fitting. The shaded region corresponds to the 95% confidence interval.

steepness is more often seen in "roundish" radio relics or phoenices, thought to be energised by adiabatic compression due to small-scale shocks (Kempner et al., 2004), possibly from cluster mergers. We do not rule out a merger-related relic classification based on the present data.

An alternative explanation is that of remnant (non–re-accelerated) electrons from a long-dead radio galaxy—confirmation of this would require, at the least, access to a higher-frequency detection of the emission to confirm spectral steepening (see e.g. Murgia et al., 2011; Duchesne & Johnston-Hollitt, 2019). Potential hosts for such a scenario are sources "B" (the BCG) or "E", with "E" the most likely candidate based on existing detected emission at 1.4 GHz. In either case this requires some separation of the radio lobes from the host and, assuming a maximum projected velocity of 1000 km s^{-1} (away from the diffuse radio source) requires a travel time of $\gtrsim$ 200 Myr.

While we may speculate on the nature of the emission, from the data at hand it is impossible to confirm its precise classification.

4.3. *Towards an SED-based taxonomy: current limitations*

SED sampling is sorely missing in many studies of diffuse, non-thermal radio cluster emission. Some examples exist of well-sampled spectra, though it is only the brightest examples of diffuse cluster emission, such as the radio halo in the Coma Cluster (e.g. Schlickeiser et al., 1987; Thierbach et al., 2003), or the relic-type source in Abell 85 (Slee et al., 2001) or Abell 4038 (Slee et al., 2001; Kale et al., 2018), that have well-studied and sampled spectra which allow the distinction between synchrotron emission models for the sources. The MWA provides good fractional bandwidth at MHz-frequencies, however, cannot be used alone to fully confirm integrated emission models. For completeness, additional data at GHz-frequencies would be required to distinguish between various emission model with breaks or curves in logarithmic space between MHz and GHz frequencies.

The most significant limit of MWA data (even in its Phase II 'extended' configuration) is the angular resolution. This is limiting for two reasons: 1) the intrusion of discrete sources within the larger-scale cluster emission, and 2) the limited ability to perform resolved spectral studies. The first limitation can be bypassed by incorporating complementary higher-resolution observations or survey data as used in this work. In the near future, the Australian Square Kilometre Array Pathfinder (ASKAP; Johnston et al., 2007, 2008) will be providing the Evolutionary Map of the Universe (EMU; Norris et al., 2011) survey, covering the Southern Sky up to +30° declination, complementing the coverage offered by the MWA. At a frequency of $\sim$ 900 MHz, resolution of 10 arcsec, and expected noise of 10 μJy beam^{-1}, we will be able to provide better analysis of intruding discrete sources than what is provided here with the current VLA S-band data and FIRST survey images. Additionally, where there is overlap between the MWA and TGSS (and by extension the the newly upgraded GMRT; Gupta et al. 2017) we can immediately rule out bright compact sources within the emission or that make up the emission. The second limitation is not bypassable with the current array, but still resolved spectral studies can be performed on the nearest, largest sources (e.g. Hindson et al., 2014). For resolved spectral studies, a combination of instruments

such as the LOw Frequency ARray (LOFAR; van Haarlem et al., 2013), (u)GMRT, and VLA have been used to good effect with deep observations (e.g. de Gasperin et al., 2017; Di Gennaro et al., 2018), noting the appropriate caveats in regards to matching u–v coverage.

5. Summary

In this paper we have presented observations of a steep-spectrum, diffuse radio source in the cluster Abell 1127. The data include dedicated MWA-2 observations, and archival VLA (S-band) and *Chandra* data, as well as survey data from the TGSS, FIRST, and NVSS, and SDSS. With the available data, we are unable to unambiguously classify the radio source, but we report on the following properties:

1. steep radio spectrum, $\alpha = -1.83 \pm 0.29$, up to GHz-frequencies,
2. projected linear extent 850 kpc,
3. hosting cluster is morphological disturbed,
4. no obvious radio core.

These features are consistent with radio relics, phoenices, as well as remnant radio galaxies, and places this in a growing category of similar diffuse cluster sources which are not able to be precisely categorised with present data (e.g. Shakouri et al., 2016; Duchesne et al., 2017, and a number of references within van Weeren et al. 2019).

We have described a data-reduction pipeline for MWA-2 continuum data based on the pipeline used for the GLEAM survey, with improvements to the calibration and overall flux scale and improvements to how the re-projected PSF is handled during image stacking/mosaicking.

Despite additional long baselines provided by the MWA-2 "extended" configuration, MWA data are still limited in angular resolution ($\gtrsim$ 50 arcsec). We have showed that despite this limiting angular resolution, with complementary high resolution observations to remove discrete source contribution, we can investigate diffuse cluster sources. In the near future, the sky observable to the MWA will have complementary $\sim$ 10 arcsec resolution data with sufficient sensitivity to disentangle underlying point source populations as well as the necessary surface-brightness sensitivity to detect diffuse cluster sources.

Acknowledgements. The authors would like the thank Davide Picchieri and Susannah R. Keel for identifying the source of interest. The authors would also like to the thank the anonymous referee for their useful comments that have improved the quality of this paper.

SWD acknowledges an Australian Government Research Training Program scholarship administered through Curtin University. ZZ is supported by the National Science Foundation of China (grant No. 11433002, 11835009).

This scientific work makes use of the Murchison Radio-astronomy Observatory, operated by CSIRO. We acknowledge the Wajarri Yamatji people as the traditional owners of the Observatory site. Support for the operation of the MWA is provided by the Australian Government (NCRIS), under a contract to Curtin University administered by Astronomy Australia Limited.

We acknowledge the Pawsey Supercomputing Centre which is supported by the Western Australian and Australian Governments.

This research has made use of data obtained from the Chandra Data Archive and software provided by the Chandra X-ray Center (CXC) in the application package `CIAO`.

The National Radio Astronomy Observatory is a facility of the National Science Foundation operated under cooperative agreement by Associated Universities, Inc. This research made use of a number of `python` packages: `aplpy` (Robitaille & Bressert, 2012), `astropy` (Astropy Collaboration et al., 2013; Price-Whelan et al., 2018), `matplotlib` (Hunter, 2007), `numpy` (van der Walt et al., 2011) and `scipy` (Jones et al., 2001).

This research has made use of the NASA/IPAC Extragalactic Database (NED), which is operated by the Jet Propulsion Laboratory, California Institute of Technology, under contract with the National Aeronautics and Space Administration.

Funding for SDSS-III has been provided by the Alfred P. Sloan Foundation, the Participating Institutions, the National Science Foundation, and the U.S. Department of Energy Office of Science. The SDSS-III web site is `http://www.sdss3.org/`. SDSS-III is managed by the Astrophysical Research Consortium for the Participating Institutions of the SDSS-III Collaboration including the University of Arizona, the Brazilian Participation Group, Brookhaven National Laboratory, Carnegie Mellon University, University of Florida, the French Participation Group, the German Participation Group, Harvard University, the Instituto de Astrofisica de Canarias, the Michigan State/Notre Dame/JINA Participation Group, Johns Hopkins University, Lawrence Berkeley National Laboratory, Max Planck Institute for Astrophysics, Max Planck Institute for Extraterrestrial Physics, New Mexico State University, New York University, Ohio State University, Pennsylvania State University, University of Portsmouth, Princeton University, the Spanish Participation Group, University of Tokyo, University of Utah, Vanderbilt University, University of Virginia, University of Washington, and Yale University.

References

Abell G. O., Corwin Jr. H. G., Olowin R. P., 1989, ApJS, 70, 1
Alam S., et al., 2015, ApJS, 219, 12
Arnaud M., Pointecouteau E., Pratt G. W., 2005, A&A, 441, 893
Astropy Collaboration et al., 2013, A&A, 558, A33
Baars J. W. M., Genzel R., Pauliny-Toth I. I. K., Witzel A., 1977, A&A, 500, 135
Becker R. H., White R. L., Helfand D. J., 1995, ApJ, 450, 559
Bertin E., Mellier Y., Radovich M., Missonnier G., Didelon P., Morin B., 2002, in Bohlender D. A., Durand D., Handley T. H., eds, Astronomical Society of the Pacific Conference Series Vol. 281, Astronomical Data Analysis Software and Systems XI. p. 228
Böhringer H., et al., 2007, A&A, 469, 363
Bonafede A., Intema H. T., Brüggen M., Girardi M., Nonino M., Kantharia N., van Weeren R. J., Röttgering H. J. A., 2014, ApJ, 785, 1
Brunetti G., Setti G., Feretti L., Giovannini G., 2001, MNRAS, 320, 365
Cassano R., Ettori S., Giacintucci S., Brunetti G., Markevitch M., Venturi T., Gitti M., 2010, ApJ, 721, L82
Cassano R., et al., 2013, ApJ, 777, 141
Cavaliere A., Fusco-Femiano R., 1976, A&A, 49, 137
Condon J. J., Cotton W. D., Greisen E. W., Yin Q. F., Perley R. A., Taylor G. B., Broderick J. J., 1998, AJ, 115, 1693
Dennison B., 1980, ApJ, 239, L93
Di Gennaro G., et al., 2018, ApJ, 865, 24
Duchesne S. W., Johnston-Hollitt M., 2019, PASA, 36, e016
Duchesne S. W., Johnston-Hollitt M., Offringa A. R., Pratt G. W., Zheng Q., Dehghan S., 2017, preprint, (`arXiv:1707.03517`)
Eckert D., Molendi S., Paltani S., 2011, A&A, 526, A79

Eisenstein D. J., et al., 2011, AJ, 142, 72
Enßlin T. A., Gopal-Krishna 2001, A&A, 366, 26
Fermi E., 1949, Physical Review, 75, 1169
Fermi E., 1954, ApJ, 119, 1
Fruscione A., et al., 2006, in Proc. SPIE. p. 62701V, doi:10.1117/12.671760
Furlanetto C., et al., 2013, MNRAS, 432, 73
George L. T., et al., 2017, MNRAS,
Gitti M., et al., 2015, in Advancing Astrophysics with the Square Kilometre Array (AASKA14). p. 76 (arXiv:1412.5664)
Gupta Y., et al., 2017, Current Science, 113, 707
Hancock P. J., Murphy T., Gaensler B. M., Hopkins A., Curran J. R., 2012, MNRAS, 422, 1812
Hancock P. J., Trott C. M., Hurley-Walker N., 2018, PASA, 35, e011
Helfand D. J., White R. L., Becker R. H., 2015, ApJ, 801, 26
Hindson L., et al., 2014, MNRAS, 445, 330
Hunter J. D., 2007, Computing in Science and Engineering, 9, 90
Hurley-Walker N., Hancock P. J., 2018, Astronomy and Computing, 25, 94
Hurley-Walker N., et al., 2017, MNRAS, 464, 1146
Intema H. T., Jagannathan P., Mooley K. P., Frail D. A., 2017, A&A, 598, A78
Johnston-Hollitt M., 2003, PhD thesis, University of Adelaide
Johnston S., et al., 2007, PASA, 24, 174
Johnston S., et al., 2008, Experimental Astronomy, 22, 151
Jones F. C., Ellison D. C., 1991, Space Sci. Rev., 58, 259
Jones E., Oliphant T., Peterson P., et al., 2001, SciPy: Open source scientific tools for Python, http://www.scipy.org/
Jones E., Oliphant T., Peterson P., et al., 2001–2017, SciPy: Open source scientific tools for Python, http://www.scipy.org/
Kale R., et al., 2015, A&A, 579, A92
Kale R., Parekh V., Dwarakanath K. S., 2018, MNRAS, 480, 5352
Kempner J. C., Blanton E. L., Clarke T. E., Enßlin T. A., Johnston-Hollitt M., Rudnick L., 2004, in Reiprich T., Kempner J., Soker N., eds, The Riddle of Cooling Flows in Galaxies and Clusters of galaxies. (arXiv:astro-ph/0310263)
Line J. L. B., Webster R. L., Pindor B., Mitchell D. A., Trott C. M., 2017, Publications of the Astronomical Society of Australia, 34, e003
McMullin J. P., Waters B., Schiebel D., Young W., Golap K., 2007, in Shaw R. A., Hill F., Bell D. J., eds, Astronomical Society of the Pacific Conference Series Vol. 376, Astronomical Data Analysis Software and Systems XVI. p. 127
Mohr J. J., Fabricant D. G., Geller M. J., 1993, ApJ, 413, 492
Murgia M., et al., 2011, A&A, 526, A148
Newville M., Stensitzki T., Allen D. B., Ingargiola A., 2014, LMFIT: Non-Linear Least-Square Minimization and Curve-Fitting for Python, doi:10.5281/zenodo.11813, https://doi.org/10.5281/zenodo.11813
Norris R. P., et al., 2011, PASA, 28, 215
Offringa A. R., Smirnov O., 2017, MNRAS, 471, 301
Offringa A. R., van de Gronde J. J., Roerdink J. B. T. M., 2012, A&A, 539, A95
Offringa A. R., et al., 2014, MNRAS, 444, 606
Offringa A. R., et al., 2016, MNRAS, 458, 1057
Pacholczyk A. G., 1970, Radio astrophysics. Nonthermal processes in galactic and extragalactic sources. Series of Books in Astronomy and Astrophysics, San Francisco: Freeman, 1970
Peebles P. J. E., 1980, The large-scale structure of the universe. Princeton Univ. Press, Princeton, N. J.
Perley R. A., Butler B. J., 2017, ApJS, 230, 7
Petrosian V., 2001, ApJ, 557, 560
Piffaretti R., Arnaud M., Pratt G. W., Pointecouteau E., Melin J.-B., 2011, A&A, 534, A109
Planck Collaboration et al., 2015, A&A, 581, A14
Planck Collaboration et al., 2016, A&A, 594, A27
Poole G. B., Fardal M. A., Babul A., McCarthy I. G., Quinn T., Wadsley J., 2006, MNRAS, 373, 881
Pratt G. W., Croston J. H., Arnaud M., Böhringer H., 2009, A&A, 498, 361
Price-Whelan A. M., et al., 2018, AJ, 156, 123
Robitaille T., Bressert E., 2012, APLpy: Astronomical Plotting Library in Python, Astrophysics Source Code Library (ascl:1208.017)
Santos J. S., Rosati P., Tozzi P., Böhringer H., Ettori S., Bignamini A., 2008, A&A, 483, 35
Sault R. J., Teuben P. J., Wright M. C. H., 1995, in Shaw R. A., Payne H. E., Hayes J. J. E., eds, Astronomical Society of the Pacific Conference Series Vol. 77, Astronomical Data Analysis Software and Systems IV. p. 433 (arXiv:astro-ph/0612759)
Schlickeiser R., Sievers A., Thiemann H., 1987, A&A, 182, 21
Shakouri S., Johnston-Hollitt M., Pratt G. W., 2016, MNRAS, 459, 2525
Shimwell T. W., Markevitch M., Brown S., Feretti L., Gaensler B. M., Johnston-Hollitt M., Lage C., Srinivasan R., 2015, MNRAS, 449, 1486
Slee O. B., Reynolds J. E., 1984, Proceedings of the Astronomical Society of Australia, 5, 516
Slee O. B., Roy A. L., 1998, MNRAS, 297, L86
Slee O. B., Roy A. L., Murgia M., Andernach H., Ehle M., 2001, AJ, 122, 1172
Sokolowski M., et al., 2017, PASA, 34, e062
Thierbach M., Klein U., Wielebinski R., 2003, A&A, 397, 53
Tingay S. J., et al., 2013, PASA, 30, 7
Tribble P. C., 1993, MNRAS, 261, 57
Wayth R. B., et al., 2015, PASA, 32, 25
Wayth R. B., et al., 2018, PASA, 35
Wen Z. L., Han J. L., Liu F. S., 2012, ApJS, 199, 34
White R. L., Becker R. H., Helfand D. J., Gregg M. D., 1997, ApJ, 475, 479
York D. G., et al., 2000, AJ, 120, 1579
Zheng Q., Johnston-Hollitt M., Duchesne S. W., Li W. T., 2018, MNRAS, 479, 730
de Gasperin F., van Weeren R. J., Brüggen M., Vazza F., Bonafede A., Intema H. T., 2014, MNRAS, 444, 3130
de Gasperin F., et al., 2017, Science Advances, 3, e1701634
van Haarlem M. P., et al., 2013, A&A, 556, A2
van Weeren R. J., Röttgering H. J. A., Brüggen M., Hoeft M., 2010, Science, 330, 347
van Weeren R. J., et al., 2016, ApJ, 818, 204
van Weeren R. J., et al., 2017, Nature Astronomy, 1, 0005
van Weeren R. J., de Gasperin F., Akamatsu H., Brüggen M., Feretti L., Kang H., Stroe A., Zandanel F., 2019, Space Sci. Rev., 215, 16
van der Walt S., Colbert S. C., Varoquaux G., 2011, Computing in Science Engineering, 13, 22

A. The effective point spread function

The effective PSF is not well defined in images after regridding and reprojecting with current software (e.g. `regrid` from `miriad`; Sault et al. 1995, or `SWarp` Bertin et al. 2002). This problem is exacerbated by a shift of reference coordinates over tens of degrees, and by the large field of view of the MWA. To ensure the reprojected PSF is defined correctly for integrated flux density measurements, we define an effective PSF correction factor, f_{regrid}, dependent on final projection, to determine the effective PSF area. This factor is

$$f_{\mathrm{regrid}} = \begin{cases} \sqrt{\dfrac{1-l^2-m^2}{1-l'^2-m'^2}} & \text{if } \texttt{SIN}, \\ \sqrt{1-l^2-m^2} & \text{if } \texttt{ZEA}, \end{cases} \tag{2}$$

where l, m are the direction cosines with respect to the original image reference coordinates and l', m' with respect to the new image reference coordinates. Note that this assumes the original images are in a `SIN` projection as output by `wsclean`. For the work here we have final reprojected images in the `SIN` projection, however, it is common with MWA data to also produce mosaics with the `ZEA` projection (see e.g. GLEAM; Hurley-Walker et al., 2017). Naturally the `ZEA` correction only takes the `SIN` component from the original image due to the equal area definition of the `ZEA` projection.

An additional concern regarding the PSF and measuring integrated flux densities was found in the `aegean` source-finding software. Prior to commit `6cd5bac` [17] calculation of the PSF size was done assuming a distortion due to projection and, optionally, with an additional latitude-dependent correction if not in the `SIN` projection. These factors produced an approximate correction that became worse radially from the image reference coordinates. Removing these factors and applying $f_{\rm regrid}$ to the effective PSF area (when data have been reprojected) produces the expected results.

We demonstrate these two effects (general reprojection corrections and removal of PSF size calculations by `aegean`) by selecting two 88-MHz snapshots—a low-elevation snapshot (from this work) and a zenith-pointed snapshot (a "best-case" example)—to simulate grids of 1 Jy point sources across the field of view without noise. We then image the data using `wsclean` as with real data (including the use of a shift of phase centre to zenith), and reproject each resultant snapshot to an example set of coordinates that would be used when generating mosaics. Once images are prepared, we source-find with `aegean`: first with the old version of `aegean`, then without the internal PSF calculations and using $f_{\rm regrid}$ for the reprojected images. Fig. 9 shows the results of the source-finding on the various images (original `SIN`, reprojected `SIN`, and reprojected `ZEA`). Note that a < 1 per cent error remains after the correction, however, it is likely this falls within the expected error from the interpolation done during the reprojection process. Visual inspection of simulated point sources makes it clear that $f_{\rm regrid}$ applied to the PSF major axis mimics the reprojected point sources.

Post commit `6cd5bac`, `aegean` does not attempt to calculate the size of the PSF, leaving the user to supply an appropriate PSF map if needed [18], and `python` code is available in `piip` (see Section 2.3) to generate PSF maps with $f_{\rm regrid}$ applied. This is done as part of the mosaicking for this work. Note that at the time of writing work is being done on `aegean` (from February 2020) to incorporate correct calculations of PSF and pixel sizes across an image for `SIN` projection images. From February 2020 up to commit `d453938` the $f_{\rm regrid}$ factors derived for `SIN` PSF maps are identical to those derived for `ZEA` and $f_{\rm regrid}$ for `ZEA` re-gridded images remains the same.

B. MWA flux scale corrections

After ensuring PSF-related effects are removed, there are still other issues that arise in real MWA data reduction that result in final image flux scales not being consistent with the input amplitude calibration model. The effect is largely only problematic at low-elevations, which leads to the suspicion that the primary beam model used in correcting the individual snapshots is not accurately defined for these low-elevation pointings. The individual snapshots have differing pointings and so the final primary beam correction is slightly different between them. To correct this effect, we use an in-house developed `python` code `flux_warp` [19] to *finalise* the primary beam correction. The basic premise of `flux_warp` is to take an image, image catalogue with measured flux densities, and a model catalogue of the sky to compare to, then create a screen to multiply the image by to correct, for example, primary-beam related problems. In principle a variety of model sky catalogues can be used but for this work we use the same model sky catalogue used for calibration, without bright extended sources (e.g. Virgo A). The screen can be created using a number of methods:

1. (SNR-weighted) mean or median,
2. (SNR-weighted) 1-D polynomial fit to declination or elevation,
3. (SNR-weighted) 2-D polynomial fit to image pixel coordinates, or
4. Interpolation using linear radial basis function, pure 2-D linear, or nearest-neighbour methods.

While the beam effects appear elevation-dependent, we find that for these data this fitting does not reduce residuals as well as a linear radial basis function (RBF) interpolation (see `scipy.interpolation.Rbf` [20]; Jones et al. 2017) method, thus we use this RBF method to determine appropriate flux-scale corrections to apply over the individual snapshots. For each snapshot, a number of "calibrator" sources are chosen satisfying

$$S_{{\rm cal},\nu} \geq 1 \text{ Jy} \left(\frac{\nu}{88 \text{ MHz}}\right)^{-0.77}, \tag{3}$$

where ν is effective frequency of the image and $S_{{\rm cal},\nu}$ is the flux density of the source. Additionally, we impose a constraint that only 1000 sources may be selected with the brightest sources preferentially chosen. This source number limit is largely due to computational time constraints. The exact number of "calibrators" chosen for each snapshots varies between 50 and 1000, with the higher frequency bands typically on the lower side. Of the 50–1000 calibrator sources initially selected, 25 per cent of these from the faint end of the set are reserved for testing the model and are not used in determining the model.

Fig. 10 shows the derived correction factor map (where corrected data is the original data divided by the correction factor map) with the calibrator and test sources overlaid. Fig. 11 shows the residuals of the calibrator and test sources at their locations on the correction factor map. For this particular snapshot example (Obs. ID 1200252120), the flux density threshold for calibrator sources was moved to 2.14 Jy (with maximum flux density 129 Jy) for 750 calibrators, and the flux density range for the 250 test sources was 1.77 Jy $< S <$ 2.14 Jy. During a run of `flux_warp`, a number of basic statistics are computed prior to creating the correction factor screen including fitting a normal distribution to the log-ratios (i.e. $\log\left[S_{\rm image}/S_{\rm model}\right]$). Fig. 12 shows this fitting to the log-ratios and residuals showing the improvement in the calibrators and test sources.

One final use of the `flux_warp` is performing quality assurance on the stacked mosaics, where we determine the standard deviation

[17] https://github.com/PaulHancock/Aegean/commit/6cd5bac42405a654c26f43d6971b893444fdd1c7

[18] This is more appropriate than `aegean` trying to determine direction cosines with no knowledge of the original projection.

[19] https://gitlab.com/Sunmish/flux_warp

[20] https://docs.scipy.org/doc/scipy/reference/generated/scipy.interpolate.Rbf.html

Table 5 Fitted bias correction parameters for each MWA-2 band for $S_{\mathrm{bias,compact}} = A \times \mathrm{SNR} + B$.

Band	A (mJy)	B (mJy)
72–103	−1.2	62.2
103–134	−0.54	25.1
139–170	−0.36	14.1
170–200	−0.23	11.0
200–231	−0.34	13.3

of the measured integrated flux densities from our input model to estimate the intrinsic uncertainty in our absolute flux calibration. This results in attributing a few per cent flux scale error to each mosaic (see Table 2).

C. CLEAN bias

In comparing the MWA MWA-2 data to the TGSS data in the same region, we found that integrated flux densities were biased towards lower values. In the low-SNR case, this bias pushed the integrated flux density well below the peak flux in the map. We consider this (at least in part) due to CLEAN bias (see e.g. Becker et al., 1995; White et al., 1997; Condon et al., 1998), though note that the observed bias will have some contribution from the inherent bias in measuring integrated flux densities without, e.g., Gaussian fitting (as in the case for measuring the flux density of the source in Abell 1127).

We correct this by fitting the offset $S_{\mathrm{peak}} - S_{\mathrm{int}}$ for compact sources ($S_{\mathrm{int}}/S_{\mathrm{peak}} < 1.2$) with a linear function of the form $S_{\mathrm{bias,compact}} = A \times \mathrm{SNR} + B$ for each MWA-2 image. For measuring source flux densities, we use a floodfill approach out to $2\sigma_{\mathrm{rms}}$ rather than Gaussian fitting to mimic the technique used in measuring the diffuse cluster source. Gaussian fitting would hide the issue, as the integrated flux density of a Gaussian source is measured from its fitted peak flux, and major/minor axes and does not directly measure the pixel values.

Table 5 reports the bias-correcting parameters. Note that for an extended source, we assume that the bias scales with fractional peak, i.e. $S_{\mathrm{bias}} = S_{\mathrm{bias,compact}} \times \left(S_{\mathrm{int}}/S_{\mathrm{peak}}\right)$, becoming worse for low surface brightness sources. Note that due to the convention used the final integrated flux density is defined as $S_{\mathrm{int,corrected}} = S_{\mathrm{int}} + S_{\mathrm{bias}}$.

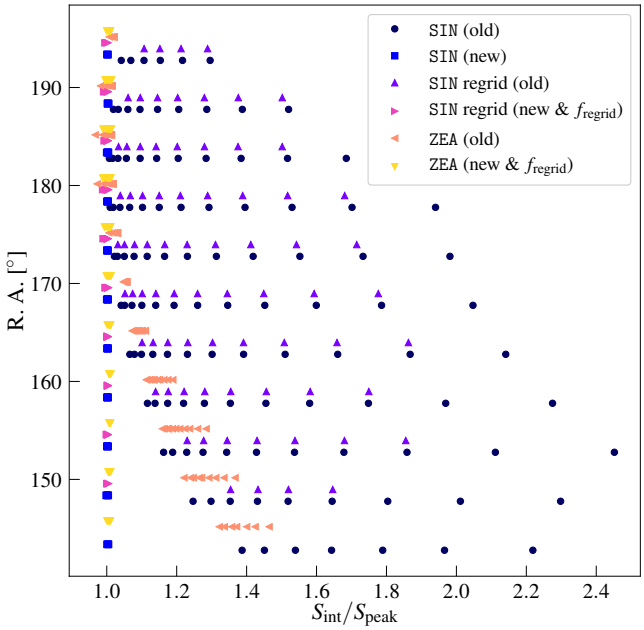

(i) Low-elevation pointing, RA dependence.

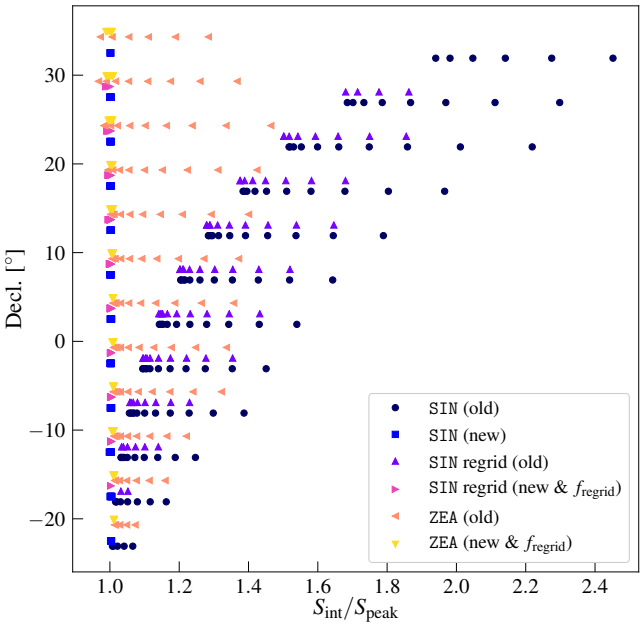

(ii) Low-elevation pointing, declination dependence.

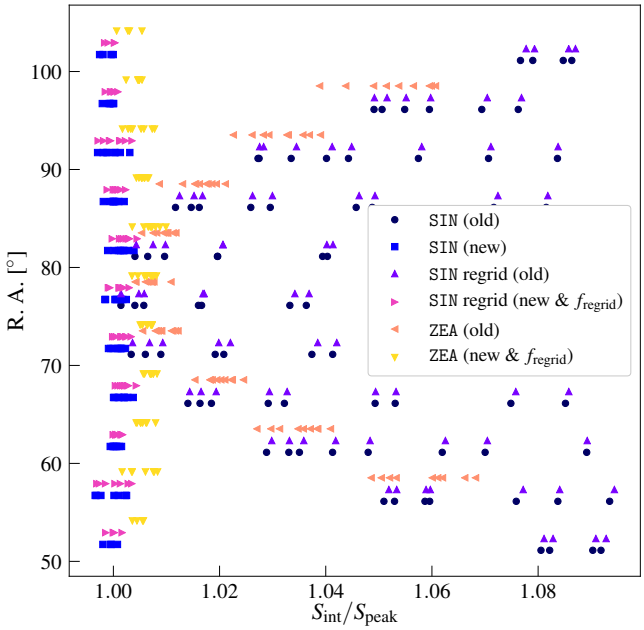

(iii) Zenith pointing, RA dependence.

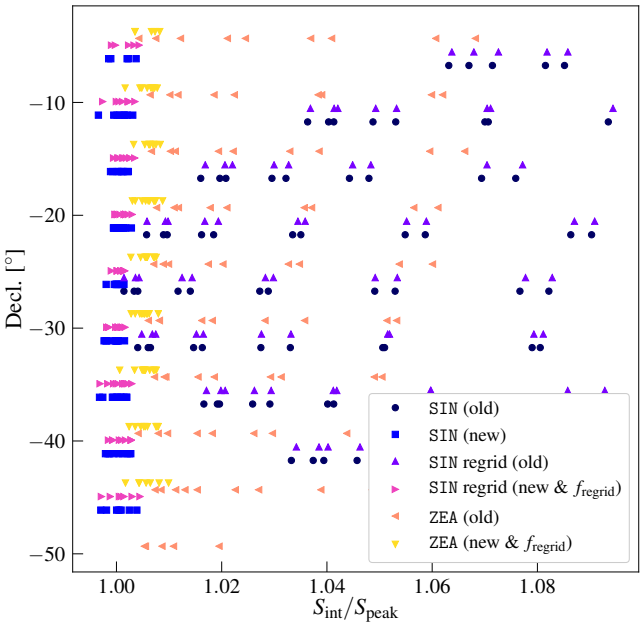

(iv) Zenith pointing, declination dependence.

Figure 9. The various effects on integrated flux density measurements. Note the datasets are shifted by an arbitrary 36′ for clarity. The ZEA projection is only used after reprojecting as the imaging software does not natively generate ZEA images. (i) and (ii): Low-elevation snapshot (from this work) where the snapshot is reprojected to a different set of coordinates, showing the RA and declination dependence, respectively. (iii) and (iv): A zenith-pointed snapshot (used as a "best-case" example only) where the reprojection does not change the reference coordinate significantly, showing for the RA and declination dependence, respectively. Note the different scales of $S_{\mathrm{int}}/S_{\mathrm{peak}}$ between the two pointings.

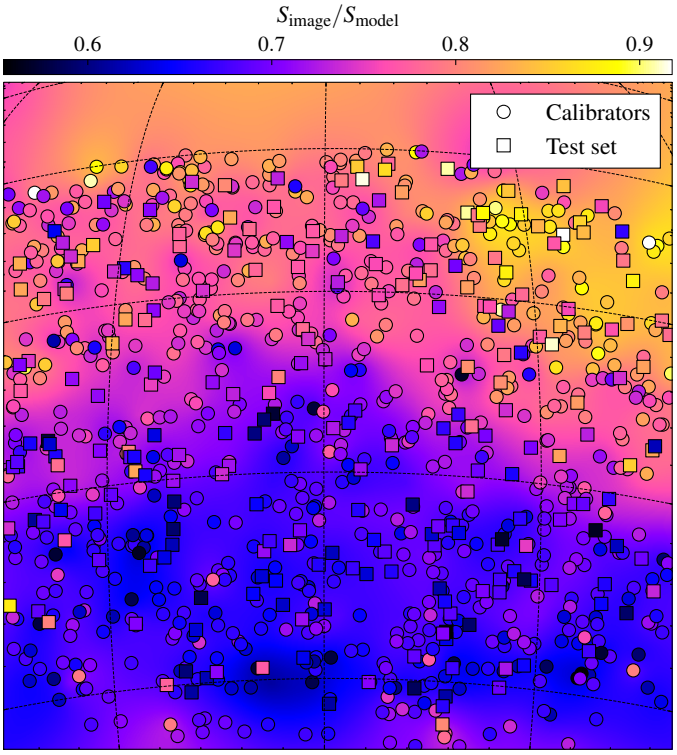

Figure 10. Example output showing the derived RBF interpolated correction factor map that is applied to the snapshot image with calibrator and test sources overlaid. The colour scale for the map and sources is the same. Note this image represents the full imaged region at 88 MHz which is $\sim 44° \times 44°$.

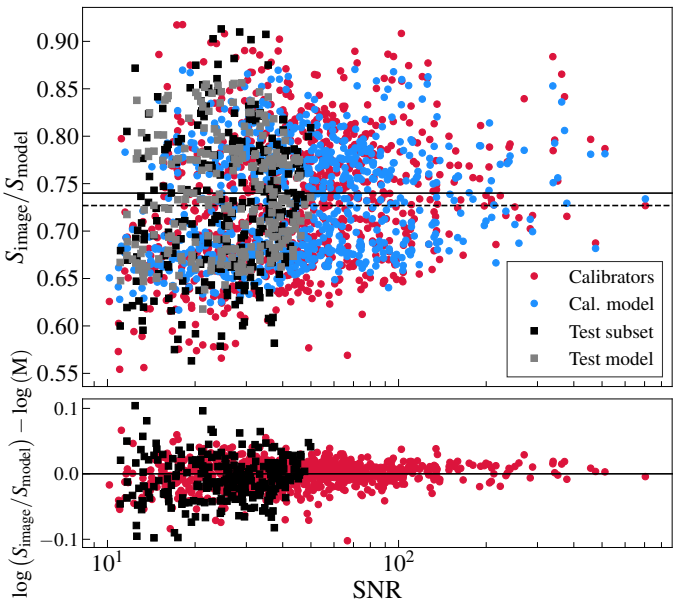

Figure 11. Example output showing the residuals between the calibrator and test sources when inspecting their new measured flux densities after applying the correction factor map, where M is the model factor, and the black solid and dashed lines are the mean and median factors, respectively.

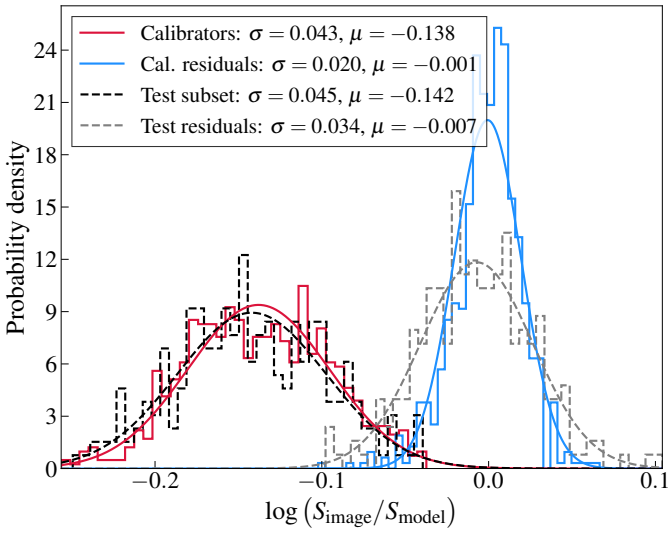

Figure 12. Example output showing the histogram of the log-ratios and their residuals after creating the correction factor map.

MWA and ASKAP observations of atypical radio-halo–hosting galaxy clusters: Abell 141 and Abell 3404

The paper titled '*MWA and ASKAP observations of atypical radio-halo–hosting galaxy clusters: Abell 141 and Abell 3404*' is re-produced here in its form as accepted for publication in the Publications of Astronomical Society of Australia published by Cambridge University Press (CUP). The accepted article is re-produced with permission from Cambridge University Press [15] in line with the CUP 'Green Open Access' policy as agreed to in the signed License To Publish [16] prior to publication. Content is © The Author(s), 2021. Published by Cambridge University Press on behalf of the Astronomical Society of Australia. The version of record is available through CUP at: https://doi.org/10.1017/pasa.2021.24. Contributions from Co-authors are outlined in the previous section. This accepted article also appears on arXiv.org at https://arxiv.org/abs/2103.08282. [17].

[15] https://www.cambridge.org/about-us/rights-permissions/faqs/

[16] https://www.cambridge.org/core/services/open-access-policies/open-access-journals/green-open-access-policy-for-journals

[17] Note the appearance is slightly modified in the present version as an update to the PASA LaTeX template.

LaTeX document typeset by the authors from a modified LaTeX template from the *Publications of the Astronomical Society of Australia* (PASA).
Current document status: **accepted for publication in PASA: in press**.

Research Paper

MWA and ASKAP observations of atypical radio-halo–hosting galaxy clusters: Abell 141 and Abell 3404

S. W. Duchesne[1]*, M. Johnston-Hollitt[1,2], and A. G. Wilber[1]
[1]International Centre for Radio Astronomy Research (ICRAR), Curtin University, Bentley, WA 6102, Australia
[2]Curtin Institute for Computation, Curtin University, GPO Box U1987, Perth, WA 6845, Australia

Abstract

We report on the detection of a giant radio halo in the cluster Abell 3404 as well as confirmation of the radio halo observed in Abell 141 (with linear extents ∼ 770 kpc and ∼ 850 kpc, respectively). We use the Murchison Widefield Array (MWA), the Australian Square Kilometre Array Pathfinder (ASKAP), and the Australia Telescope Compact Array (ATCA) to characterise the emission and intervening radio sources from ∼ 100–1000 MHz; power law models are fit to the spectral energy distributions with spectral indices $\alpha_{88}^{1110} = -1.66 \pm 0.07$ and $\alpha_{88}^{943} = -1.06 \pm 0.09$ for the radio halos in Abell 3404 and Abell 141, respectively. We find strong correlation between radio and X-ray surface brightness for Abell 3404 but little correlation for Abell 141. We note each cluster has an atypical morphology for a radio-halo–hosting cluster, with Abell 141 having been previously reported to be in a pre-merging state, and Abell 3404 is largely relaxed with only minor evidence for a disturbed morphology. We find that the radio halo powers are consistent with the current radio halo sample and P_ν–M scaling relations, but note that the radio halo in Abell 3404 is an ultra-steep–spectrum radio halo (USSRH) and, as with other USSRHs lies slightly below the best-fit $P_{1.4}$–M relation. We find that an updated scaling relation is consistent with previous results and shifting the frequency to 150 MHz does not significantly alter the best-fit relations with a sample of 86 radio halos. We suggest that the USSRH halo in Abell 3404 represents the faint class of radio halos that will be found in clusters undergoing weak mergers.

Keywords: galaxies: clusters: individual: (Abell 141, Abell 3404) – large-scale structure of the Universe – radio continuum: general – X-rays: galaxies: clusters

1. Introduction

Galaxy clusters represent ideal laboratories for investigating large-scale structure formation. As the largest virialized systems in the Universe, galaxy clusters are located at the nodes of the Cosmic Web and are assembled through hierarchical structure formation (Peebles, 1980); accretion of matter from filaments and mergers between clusters releases energy into the intra-cluster medium (ICM) to be transferred into various non-thermal processes (see e.g. Sarazin, 2002; Keshet et al., 2004; Brunetti & Jones, 2014). Resultant shocks and turbulence in the ICM are thought to energise electrons to emit synchrotron radio emission over large scales with steep power law spectra ($\alpha \lesssim -1$; see e.g. Brunetti et al. 2008; Brunetti & Jones 2014; van Weeren et al. 2019) in the micro-Gauss–level magnetic fields permeating the clusters (see e.g. Clarke et al., 2001; Brüggen et al., 2012, and Donnert et al. 2018 for a recent review).

The observed radio emission from ICM-based turbulence and shocks can be broken down into four main categories, with somewhat blurred lines between definitions (see e.g. Kempner et al., 2004; van Weeren et al., 2019, for taxonomic discussion). Mega-parsec–scale *radio relics* are found in the low-density environments of cluster outskirts (e.g. in Abell 3667, Johnston-Hollitt 2003; CIZA J2242.8+5301, van Weeren et al. 2010; PSZ1 G096.89+24.17 de Gasperin et al. 2014; SPT-CL J2032−5627, Duchesne et al. 2021a)—shocks in the ICM are thought to energise electrons via diffusive-shock acceleration (DSA and related processes, e.g. Blandford & Eichler 1987) and relics have been observed to align with shocks detected via X-ray temperature and surface brightness discontinuities (e.g. Mazzotta et al., 2011; Akamatsu et al., 2015; Eckert et al., 2016). Smaller-scale ($\lesssim$ 400 kpc) relic sources called *phoenices* are thought to be the revived corpses of ancient, lobed radio galaxies, with the radio plasma re-energised by adiabatic compression via small-scale ICM turbulence and shocks (Enßlin & Gopal-Krishna, 2001, furthermore, see Slee et al. 2001; de Gasperin et al. 2015 for examples) or gentle re-energisation of radio plasma from single (de Gasperin et al., 2017) or multiple electron populations (Hodgson et al., 2021). Phoenices are typically located closer to the cluster centre, and feature steeper spectra, with steepening beyond ∼ 1 GHz. *Mini-halos* are smaller ($\lesssim$ 400 kpc), centrally-located, steep-spectrum patches of diffuse emission often found surrounding a radio-loud active galactic nucleus (AGN) associated with the brightest cluster galaxy (BCG). These sources are predominantly found in relaxed cool-core clusters, thought to form through the inner sloshing of the ICM gas, with seed electrons fuelled by the embedded AGN (see e.g. Giacintucci et al., 2017, 2019). Finally, *giant radio halos* ($\gtrsim$ 1 Mpc) are found in the centres of massive, merging clusters and are thought to also form through ICM turbulence generated by the merger process (e.g. in Abell 2255,

*email: stefan.duchesne.astro@gmail.com
$S_\nu \propto \nu^\alpha$
Also called radio *shocks*: van Weeren et al. (2019).

Harris et al. 1980; 1E 0657−56, Liang et al. 2000; Abell 2163, Feretti et al. 2001; Abell 523, Giovannini et al. 2011). It has been suggested that mini-halos may transition into giant radio halos during mergers: the emitting cosmic ray electrons of mini-halos being transported throughout the cluster volume and re-accelerated via ICM turbulence (Brunetti & Jones, 2014). Observations suggest radio halos are transient phenomena—Donnert et al. (2013) showed that the range of spectral and morphological shapes seen in observed halos can, in part, be attributed to when they occur during a merger.

Historically, radio halo detections have been uncommon in clusters and the number of sources has, until recently, remained low. This was due in part to observational biases and limitations; many historic surveys were performed at 1.4 GHz, missing steep-spectrum emission only visible at lower frequencies. With the current generation of radio telescopes, telescope upgrades, increases in sensitivity, and low-frequency operation are helping to reveal a new population of radio halos (e.g. Duchesne et al., 2021b; Cassano et al., 2019; HyeongHan et al., 2020; Wilber et al., 2020; Di Gennaro et al., 2020; Hoeft et al., 2020; van Weeren et al., 2020; Knowles et al., 2021; Hodgson et al., 2021) and to clarify the nature of previously detected systems (e.g. Botteon et al., 2020c; Bonafede et al., 2020).

In this paper we present new observations of two clusters with candidate radio halo emission, originally detected in MWA data, now followed-up with the Australia Telescope Compact Array (ATCA; Frater et al., 1992), the Australian Square Kilometre Array Pathfinder (ASKAP; Hotan et al., 2021), and the recently upgraded Murchison Widefield Array (Tingay et al., 2013) in its new "phase 2" extended baseline configuration (Wayth et al., 2018, hereafter "MWA-2"). In this work we assume a flat Λ cold dark matter cosmology with $H_0 = 70\ \mathrm{km\,s^{-1}\,Mpc^{-1}}$, $\Omega_\mathrm{M} = 0.3$, and $\Omega_\Lambda = 1 - \Omega_\mathrm{M}$.

1.1. *Abell 141*

During a search for diffuse, non-thermal emission in a selection of galaxy clusters within a large MWA image at 168 MHz covering the Epoch of Reionization 0-hour field (EoR0; Offringa et al., 2016), Duchesne et al. (2021b) reported the detection of a giant radio halo in the massive, merging galaxy cluster Abell 141 (Abell, 1958; Abell et al., 1989). Using the Giant Metrewave Radio Telescope (GMRT), Venturi et al. (2007) reported the non-detection of a radio halo in Abell 141 at 610 MHz. Using the low resolution MWA data and the GMRT limit, Duchesne et al. (2021b) reported a spectral index limit of $\alpha^{610\ \mathrm{MHz}}_{168\ \mathrm{MHz}} < -2.1$, making it one of the steepest-spectrum radio halo detected to date, tied with the radio halo in Abell 521 ($\alpha^{610\ \mathrm{MHz}}_{240\ \mathrm{MHz}} \approx -2.1$; Brunetti et al. 2008). Caglar (2018) investigated the X-ray properties of the cluster, which show both a bi-modal X-ray distribution as well as a bi-modal optical distribution (Dahle et al., 2002). The cluster is also detected in *Planck* Sunyaev–Zel'dovich (PSZ) surveys as PSZ2 G175.69−85.98 (Planck Collaboration et al., 2016a) and is reported to have an SZ-derived mass of $5.67^{+0.36}_{-0.40} \times 10^{14}\ \mathrm{M}_\odot$. The cluster is reported to have a redshift of 0.23 (Struble & Rood, 1999) where 1 arcmin corresponds to 221 kpc in scale. We show an updated composite image of Abell 141 in Fig. 1 with data described in Section 2.3 and 2.4.

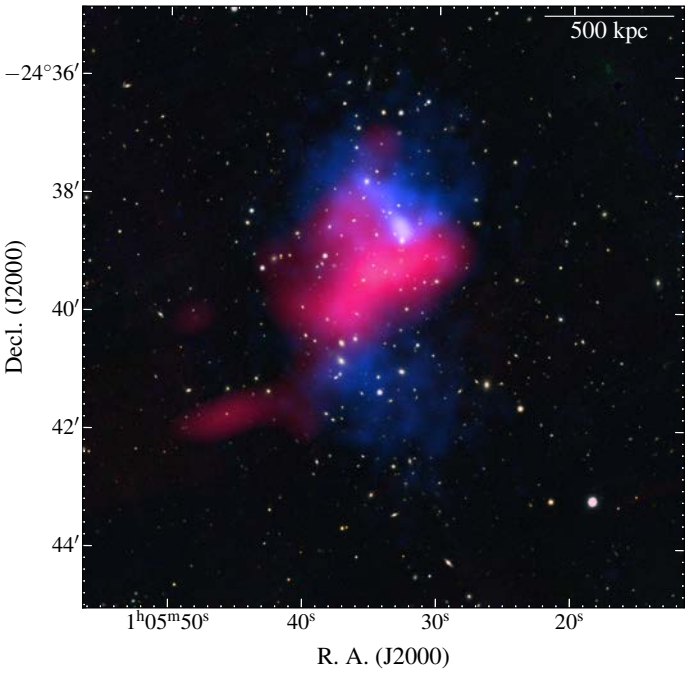

Figure 1. Composite image of Abell 141. Background optical data are from the Pan-STARRS survey, data release 1 (bands *r*, *i*, *z*; Kaiser et al., 2010; Tonry et al., 2012) with *Chandra* (blue, Section 2.4) and source-subtracted ASKAP (red, Section 2.3) maps overlaid. The linear scale is at the redshift of the cluster.

1.2. *Abell 3404*

Abell 3404 was found to host unclassified extended emission permeating the cluster in GaLactic and Extragalactic All-sky MWA (GLEAM; Wayth et al., 2015; Hurley-Walker et al., 2017) data at 200 MHz from a search for diffuse cluster emission within clusters from the Meta-Catalogue of X-ray detected galaxy Clusters (MCXC; Piffaretti et al., 2011). Although the emission is elongated, typical of the morphologies of radio relics, its location at the centre of cluster suggested a halo-type source. The low resolution of the GLEAM data resulted in significant blending of the extended emission with nearby point sources and made it impossible to confirm its nature. Shakouri et al. (2016) investigated the cluster using the Australia Telescope Compact Array (ATCA; Frater et al., 1992) as part of the ATCA REXCESS Diffuse Emission Survey (ARDES), though they found no evidence of a radio halo or other diffuse radio source. In advance of this publication, Brüggen et al. (2021) noted the detection of diffuse emission in Abell 3404 on the edge of a widefield observation of the cluster system Abell 3391-95 but leave the detailed characterisation to this work. The cluster has an SZ-derived mass of $7.96^{+0.23}_{-0.21} \times 10^{14}\ \mathrm{M}_\odot$ and redshift $z = 0.1644$ (Planck Collaboration et al., 2016a). At the cluster redshift 1 arcmin corresponds to 170 kpc in scale. A composite image of Abell 3404 is shown in Fig. 2.

Representative *XMM-Newton* Cluster Structure Survey (Böhringer et al., 2007).

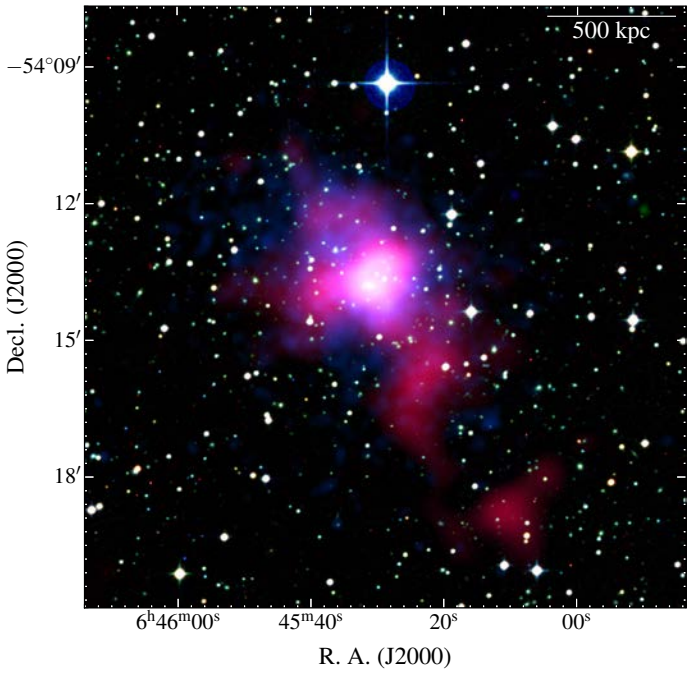

Figure 2. Composite image of Abell 3404. Background optical data are from the SuperCOSMOS Sky Survey (Hambly et al., 2001a,b,c). Radio and X-ray data overlaid as in Fig. 1. The linear scale is at the redshift of the cluster.

2. Data & methods

New data presented in this work are described in the following sections. A summary of observations used in this work and described in this section is presented in Table 1. We also provide representative plots of the *u*–*v* coverage for all datasets in Appendix A.

2.1. *MWA-2*

2.1.1. Data processing

Both Abell 141 and Abell 3404 were observed with the MWA-2 as part of a follow-up of candidate radio halos and relics detected with the GLEAM survey. The observations covered five frequency bands (of 30-MHz bandwidth): 88, 118, 154, 185, and 216-MHz. Observation details are presented in Table 1. The MWA data are processed following Duchesne et al. (2020). Briefly, MWA data are observed in a 2-minute snapshot observing mode, with each 2-minute snapshot calibrated and imaged independently and stacked in the image plane at the end.

We use in-field calibration on a global sky model generated from the GLEAM, NVSS, and SUMSS catalogues (where survey coverage is available) using the `Mitchcal` algorithm (see Offringa et al., 2016). The calibrated data are then imaged using `WSClean` (Offringa et al., 2014; Offringa & Smirnov, 2017) to perform amplitude and phase self-calibration before imaging again to a lower threshold (i.e. CLEANing more deeply). After initial primary beam correction using the most recent Full-Embedded Element model (Sokolowski et al., 2017) these CLEANed images are then corrected for ionosphere-related astrometric shifts using `fits_warp.py` (Hurley-Walker & Hancock, 2018) and finally corrected for residual primary beam errors and flux scale errors with `flux_warp` (Duchesne et al., 2020) to ensure a common flux scaling across snapshots. The snapshots are then co-added, weighted by the square of the primary beam response and local noise.

We make a number of image sets for multiple purposes: a) using an image weighting with a 'Briggs' robustness parameter of 0.0 for a maximum resolution image, b) robust = +2.0, and c) robust = +1.0 with an additional 120 arcsec Gaussian taper applied to produce a more common sensitivity between the five frequencies and to enhance the low surface-brightness emission in individual snapshots further. We find that, because of the slight difference in inner *u*–*v* sampling between the five frequencies (see Appendix A, Figs. 11(i)–(v) and 12(i)–(v)) the 88- and 118-MHz images do not require additional tapering, though for Abell 3404 we find we can use the robust = +2.0 images for flux density measurement without additional confusion.

Fig. 3(i) and 3(ii) show the $3\sigma_{\rm rms}$ contours of the robust = +2.0, 118-MHz image and the robust = 0.0, 216-MHz image of Abell 141, respectively. Similarly, Fig. 4(i) shows the $3\sigma_{\rm rms}$ contour of the robust = +2.0, 118-MHz image of Abell 3404 and Fig. 4(ii) shows the $3\sigma_{\rm rms}$ contour of the robust = 0.0, 216-MHz image.

2.1.2. Measuring dirty flux density

Snapshot imaging results in residual dirty flux (i.e. emission that has not been deconvolved by the CLEAN algorithm) that becomes significant in final stacked images as the CLEANing depth is set in the individual snapshot images. Using multiscale CLEAN can mitigate this somewhat as the root-mean-square (rms) noise on larger scales allows CLEANing of large structures below the point-source CLEAN depth. The result is measurement of residual dirty flux, which 1) has a point spread function (PSF) that differs from the restoring beam and 2) the dirty flux may be reduced or increased compared to the equivalent CLEAN flux due to complex PSF sidelobe interactions. We assume that the PSF difference is small—i.e. the fitted restoring beam is an accurate representation of the PSF. To test the difference in measured dirty to CLEAN flux density, we simulate 2-d circular Gaussian sources in all snapshots with an arbitrary S = 1 Jy with varying full-width at half maximum (FWHM) sizes, ranging from 5″ to 575″ in 30″ intervals and measure the integrated flux density in the dirty and CLEANed maps. We find that the ratios of measured $S_{\rm p,dirty}/S_{\rm p,CLEAN}$ (peak) and $S_{\rm dirty}/S_{\rm CLEAN}$ (integrated) decrease down to ~0.5–0.6 for structures up to 10 arcmin for the Abell 3404 data, but increase by only a few per cent for Abell 141. We show the robust = +2.0 results in Fig. 5.

To correct for this, we create separate CLEAN component model and residual stacked images to match the restored stacked image. When measuring S for real sources, we use the restored image to guide the integration region, but sum the CLEAN model and add the integrated residuals with a correction factor applied to the residual flux density determined by the size of the emission region. The correction factor is determined by the convolved source size

`https://github.com/nhurleywalker/fits_warp`
`https://gitlab.com/Sunmish/flux_warp`

Table 1 Details of the radio observations of Abell 141 and Abell 3404.

Telescope	ν_c [a] (MHz)	$\Delta\nu$ [b] (MHz)	θ_{max} [c] (arcmin)	τ [d] (min)	Dates
Abell 141					
MWA-2	88	30	60	64	2017 Nov 03,04, Dec 22, 2018 Jan 06
MWA-2	118	30	60	68	2017 Nov 03,04, Dec 22, 2018 Jan 06
MWA-2	154	30	60	64	2017 Nov 03,04,Dec 22, 2018 Jan 06
MWA-2	185	30	60	62	2017 Nov 03,04, Dec 22, 2018 Jan 06
MWA-2	216	30	60	60	2017 Nov 03,04, Dec 22, 2018 Jan 06
ASKAP	943	288	49	2145	2020 Apr 03,04, Jul 03,04, Nov 28
ATCA (CABB)	2100	1500 [e]	5.7	928	2015 May 05,10,15,16
Abell 3404					
MWA-2	88	30	60	58	2018 Jan 10, Feb 18,21, Mar 04,13
MWA-2	118	30	60	42	2018 Jan 10, Feb 18, Mar 04,13
MWA-2	154	30	60	58	2018 Jan 10, Feb 18,21, Mar 04,13
MWA-2	185	30	60	42	2018 Jan 10, Feb 18,21, Mar 13
MWA-2	216	30	60	38	2018 Jan 10, Feb 18,21, Mar 13
ASKAP	1013	288	35	689	2019 Mar 22
ATCA (pre-CABB)	1344	128	35	374	2007 Jun 10–16, Jul 26,28–30, Aug 02
ATCA (pre-CABB)	1432	128	35	374	2007 Jun 10–16, Jul 26,28–30, Aug 02
ATCA (CABB)	2100	1400 [e]	25	103	2013 Jun 21–23

[a] Central observing frequency.
[b] Observation bandwidth.
[c] Maximum angular scale observation is sensitive to at the respective central frequency with a u–v limit employed during imaging.
[d] Total observing time.
[e] Originally a 2049 MHz band, significant RFI flagging reduces the usable bandwidth.

and estimated from the nearest simulated ratio of $S_{\rm dirty}/S_{\rm CLEAN}$.

2.2. *ATCA*

Abell 3404 was observed with both the Compact Array Broadband Backend (CABB; Wilson et al., 2011) and the ATCA correlator prior to the CABB installation (hereafter "pre-CABB", Project Codes C1683 and C2837; Johnston-Hollitt et al., 2007, 2013). The observation details are listed in Table 1, though note for both the CABB and pre-CABB observations Abell 3404 was observed in a "u–v cuts" mode at a range of hour-angles, but not filling in the u–v plane significantly. The pre-CABB and CABB data have different phase centres, and the lower end of the CABB data are flagged due to RFI so the two data sets are imaged independently. Abell 141 was observed with the CABB (Project Code C2915; Shimwel et al., 2015), though two configurations were used: 1.5C and 6A, with maximum/minimum baselines of 4500/77 and 5939/337 m, respectively.

Calibration for all ATCA data follows standard data reduction procedures using `miriad` (Sault et al., 1995). Bandpass and absolute flux calibration is performed using the standard ATCA centremetre calibrator, PKS B1934-638, and appropriate secondary calibrators bracket the source observations, used for complex gain and phase calibration. We perform two rounds of self-calibration on each dataset, using `WSClean` to create initial CLEAN component models and the Common Astronomy Software Applications (`CASA`; McMullin et al., 2007) task, `gaincal`, to solve for phase-only gain solutions on successively shorter intervals (i.e. 120 s and 30 s). Additionally, final imaging for the Abell 3404 data removes the longest baselines formed with antenna 6 to achieve a more well-behaved point spread function. Imaging for all datasets is otherwise similar, utilising a 'Briggs' robustness parameter of 0.0, and splitting the full CABB bands into smaller subbands. Note that significant RFI flagging occurs in the 16-cm band for the ATCA data and the final usable band for CABB observations is $\sim$ 1.5 GHz and is split into subbands of $\Delta\nu$ = 300 MHz for discrete source measurements.

Fig. 3(ii) shows the robust = 0.0 full-band 2.2-GHz ATCA map for Abell 141 convolved to 18 arcsec. Fig. 4(ii) shows the similar 2.4-GHz full-band map for Abell 3404.

2.3. *ASKAP*

ASKAP operates between 700–1800 MHz and features a Phased Array Feed (PAF; DeBoer et al., 2009; Hotan et al., 2014; McConnell et al., 2016) allowing the creation of 36 independent primary beams which can be arranged in a number of different footprints to create large $7^\circ \times 7^\circ$ mosaics in "6 by 6" primary beam footprints. ASKAP has recently been used to complete some observations for early science and survey projects (e.g. the Evolutionary Map of the Universe, EMU; Norris et al., 2011). Abell 3404 and Abell 141 feature in early science observations, however, both Abell 141 and Abell 3404 sit

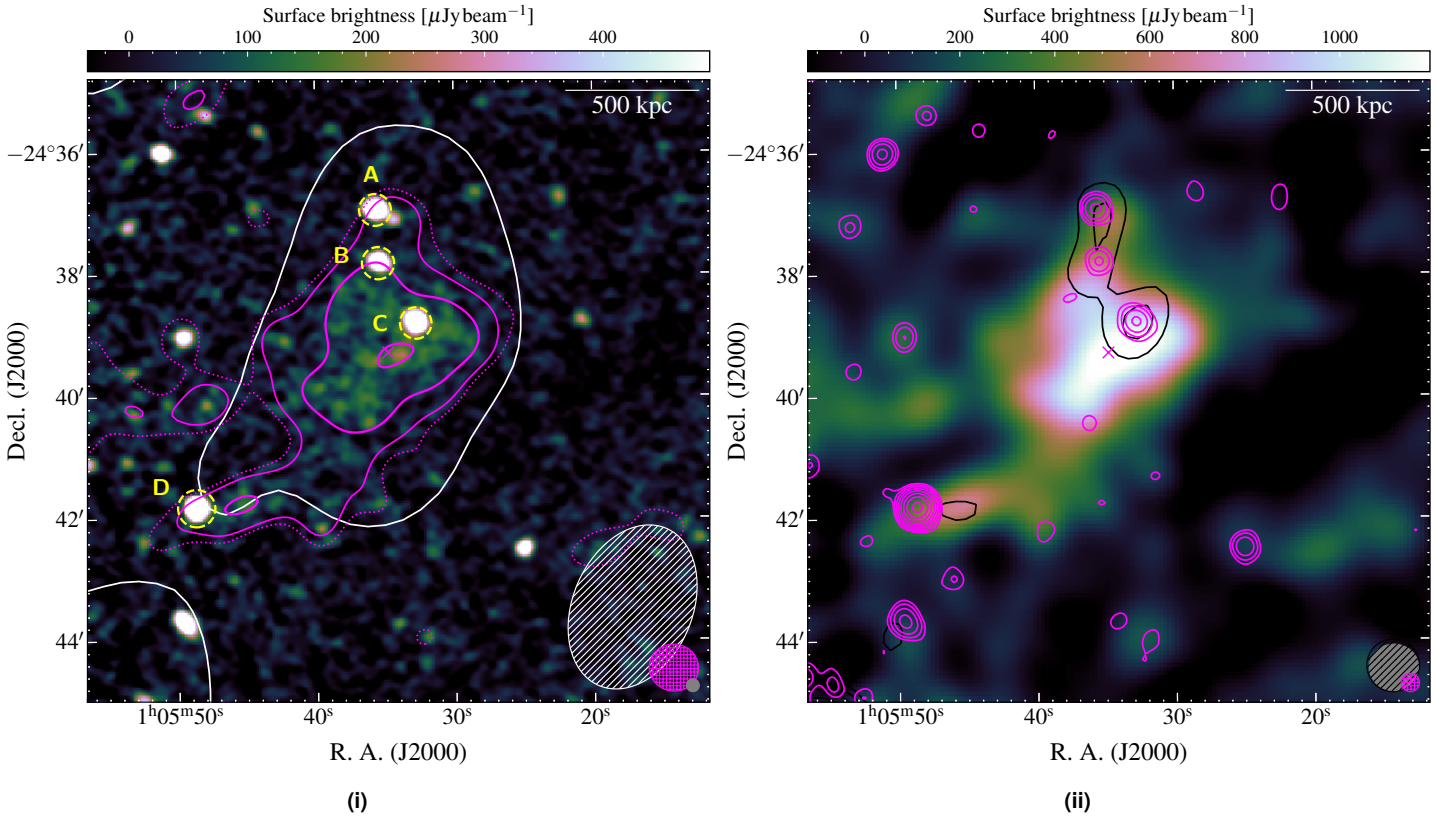

Figure 3. Abell 141 radio maps. (i): ASKAP, 943-MHz image at robust = +0.25. The overlaid contours are as follows: MWA-2, 118-MHz robust = +2.0 image, single white contour at $3\sigma_{\rm rms}$ (4.7 mJy beam^{-1}); ASKAP, 943-MHz source-subtracted image, solid magenta contours starting from $3\sigma_{\rm rms}$ ($\sigma_{\rm rms}$ = 0.105 mJy beam^{-1}), increasing with increments of 2 with a single dotted magenta contour at $2\sigma_{\rm rms}$. Sources subtracted after SED modelling are labelled. (ii): ASKAP, 943-MHz source-subtracted image with contours as follows: MWA-2, 216-MHz robust = 0.0, black contours starting at $3\sigma_{\rm rms}$ (11.4 mJy beam^{-1}); ATCA full-band image at robust = 0.0, magenta contours starting at $3\sigma_{\rm rms}$ ($\sigma_{\rm rms}$ = 27 μJy beam^{-1}). For both figures the resolution of each image is shown in the bottom right corner, with the grey ellipse corresponding to the background map. The linear scale in the top right is at the redshift of the cluster.

towards the edges of primary beams. The ASKAP data are publicly available and are retrieved from the CSIRO ASKAP Science Data Archive (CASDA; Chapman et al., 2017). Prior to being made available through CASDA, the `ASKAPsoft` pipeline uses daily observations of PKS B1934-638 for bandpass calibration, with each of the 36 beams being calibrated independently. Additionally, the data are averaged to 1 MHz/10 s spectral/temporal resolution. The full bandwidth for each observation is 288 MHz. We summarize additional observation details in Table 1.

2.3.1. ASKAP—Abell 3404

The ASKAP Scheduling Block (SB)8275 (Harvey-Smith et al., 2018) has two overlapping beams containing Abell 3404 (beam 17 and 23) with a central observing frequency of $\nu_{\rm c}$ = 1013.5 MHz. We follow a similar self-calibration process to the ATCA data described in Section 2.2, though this calibration does not reduce the well-known, but not currently understood artefacts that appear around bright sources at a ∼ 1 per cent level. For the two beams containing Abell 3404, these artefacts are negligible and do not interfere with the cluster. Imaging is performed using `WSClean`, and we image by splitting the data into 4 subbands of $\Delta\nu$ = 72 MHz, jointly CLEANing in the fullband multi-frequency synthesis (MFS) image. Imaging for these data is done by first masking the diffuse emission within the cluster region, ensuring all discrete sources *are* included in the CLEAN process. The initial image weighting is robust = +0.5, which we found to be most accurate for modelling the discrete cluster sources. The second image set we produce are the re-imaged residuals convolved with a 25 arcsec beam to highlight diffuse cluster emission. Finally, we re-image the residuals with an additional 35 arcsec taper in 3 subbands of $\Delta\nu$ = 96 MHz.

For each image set, we linearly mosaic beams 17 and 23, applying a correction for primary beam attenuation assuming a 2-dimensional Gaussian model that scales with $1.09\lambda/D$ (A. Hotan, priv. comms.) with D = 12 m the diameter of the ASKAP dishes. For quality assurance we compare the spectral energy distribution (SED) of a nearby, bright test source measured by the MWA-2, ATCA, and additional survey data and find that the ASKAP data follow the expected flux density. Additionally, we find an astrometric offset of $\Delta\delta_{\rm J2000} \sim -0.0055$, which we correct in the image World Coordinate System (WCS) metadata. Fig. 4(i) shows the ASKAP full-band robust = +0.5 image with the source-subtracted 35 arcsec tapered image as contours.

Commonwealth Scientific and Industrial Research Organisation
https://www.atnf.csiro.au/computing/software/askapsoft/sdp/docs/current/pipelines/introduction.html

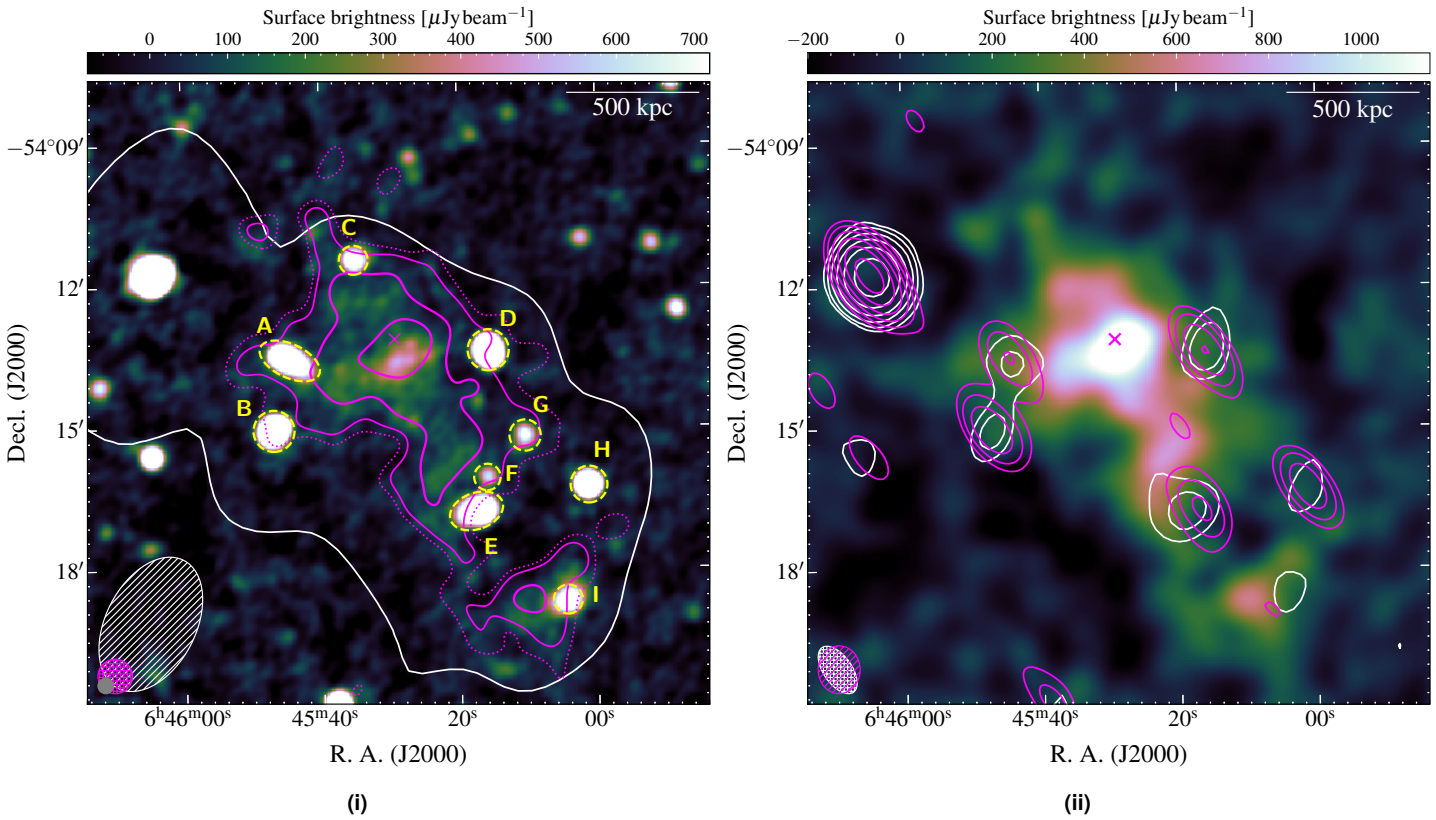

Figure 4. Abell 3404 radio maps. (i): ASKAP, 1013-MHz image at robust = +0.5. The overlaid contours are as follows: MWA-2, 118-MHz robust = +2.0, single white contour at $3\sigma_{\rm rms}$ (6.1 mJy beam^{-1}); ASKAP, 1013-MHz tapered source-subtracted image, solid magenta contours starting from $3\sigma_{\rm rms}$ ($\sigma_{\rm rms}$ = 0.84 mJy beam^{-1}), increasing with increments of 2 with a single dotted magenta contour at $2\sigma_{\rm rms}$. Sources subtracted after SED modelling are labelled. (ii): ASKAP source-subtracted, tapered, with contours as follows: MWA-2, 216-MHz robust = 0.0 image, white contours starting at $3\sigma_{\rm rms}$ ($\sigma_{\rm rms}$ = 6.6 mJy beam^{-1}); ATCA, 2.4-GHz robust = 0.0 image, magenta contours starting at $3\sigma_{\rm rms}$ ($\sigma_{\rm rms}$ = 0.24 mJy beam^{-1}). The ellipses in the the lower left are as in Fig. 3 and the linear scale is at the redshift of the cluster.

2.3.2. *ASKAP–Abell 141*

Abell 141 is present on the edge of a beam (23) in a number of ASKAP observations . After an initial round of imaging with all available observations we find most of the observations contain significant radial artefacts crossing the cluster from a nearby bright source which is unable to be removed via direction-independent calibration. We find the SB12704, SB15191, and SB18925 observations do not show significant artefacts and combine those observations for further joint imaging. We opted to self-calibrate the data, generating a combined, jointly-deconvolved model image of the three datasets then self-calibrating each dataset individually based on the combined model. Initial imaging was carried out similarly to the Abell 3404 data, masking the cluster diffuse emission. The difference in this imaging process is we use a robust = +0.25 weighting scheme, which for these observations provided a better model of the cluster discrete sources. Additionally, we find that since the diffuse emission is much fainter than in Abell 3404, and because the cluster lies further from the primary beam centre, we only consider the fullband re-imaged residual visibilities rather than the subbands produced while CLEANing. As there is only a single primary beam, mosaicking is not required, however, a primary beam correction is applied. Because the source lies to the edge of the beam, we compare the ASKAP flux densities of sources across the image to extrapolated flux densities derived from the ATCA subband images and the catalogue used for MWA-2 flux scaling (independently, see Duchesne et al. 2020 for details of the calibration catalogue). For comparison with the MWA catalogue, the data are first convolved to a common resolution. We find the flux densities of sources do not deviate beyond ∼ 10 per cent. We find no discernible astrometric offset for these data.

The full-band, robust = +0.25 image is shown in Fig. 3(i) with the source-subtracted, 45 arcsec robust = +0.25 image as contours in Fig. 3(i) and the background in Fig. 3(ii).

2.4. *Chandra*

Both clusters have been observed with the Advanced CDD Imaging Spectrometer (ACIS-I) on the *Chandra* X-ray observatory. We obtain both datasets (Abell 141: Obs. ID 9410, PI: Smith, 19.91 ks; Abell 3404: Obs. ID 15301, PI: Murray, 9.96 ks) from the *Chandra* data archive and use the `CIAO` software suite (v4.12, with CALDB v4.9.1; Fruscione et al., 2006) to process the data fol-

SB9602, SB9649, SB9910, SB10463, SB12704, SB15191, SB18912, SB18925; (Murphy et al., 2019), as part of a gravitational wave follow-up programme, with an average of 8–10-h per observation with similar u–v tracks.

Calibration database.

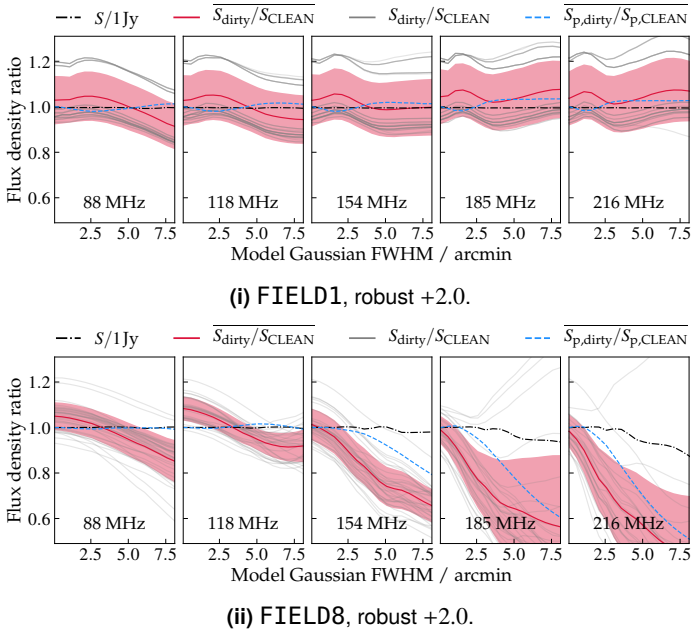

Figure 5. Comparison of dirty and CLEANed flux densities in the robust +2.0 MWA-2 images as a function of source FWHM for simulated Gaussian sources. Note that individual snapshot $S_{\rm dirty}/S_{\rm CLEAN}$ ratios are shown as transparent grey lines with the mean value plotted as a solid red line, and a shaded region corresponding to the standard deviation between snapshots.

lowing standard *Chandra* data reduction procedures, using the task `chandra_repro` to generate the level-2 event file. From this we generate count and exposure-corrected flux images using the task `fluximage` applying 1 arcsec binning for the full energy band ([0.5–7] keV). We use `wavdetect` to identify point-like sources in the images and remove them, finally creating images in the [0.5–2] kev band. For Abell 141, as there is an AGN at the centre of the northern sub-cluster that is subtracted, we fill in the removed component using the task `dmfilth`. Additional smoothing with a $\sigma = 6$ arcsec 2-dimensional Gaussian kernel is applied to the exposure-corrected image, using the task `aconvolve`. The [0.5–2] kev exposure-corrected, smoothed, and source-subtracted *Chandra* images are shown in Fig. 6 for each cluster.

3. Results & discussion

3.1. *Morphology*

The ASKAP and MWA-2 data show clear evidence of central diffuse emission and additional extended peripheral structures in Abell 141 and Abell 3404 (see Fig. 3(i), 4(i), 6(i), and 6(ii)), not necessarily associated with any particular radio galaxy, though it is unclear if these components are associated with the central diffuse sources. No diffuse radio emission is detected in the ATCA data for either cluster (Fig. 3(ii) and Fig. 4(ii)). We show the exposure-corrected, smoothed X-ray maps in Fig. 6 to highlight the morphology of the clusters and the co-location of the radio emission.

3.1.1. *Abell 141*

The central, diffuse radio emission in Abell 141 has a slightly elongated morphology as seen in the source-subtracted ASKAP data, with an extension towards the southeast becoming a distinct peripheral component (yellow, dashed box in Fig. 6(i)). The radio emission fills the volume between two X-ray sub-clusters, and extends into the northern sub-cluster. Excluding the peripheral source, we measure the size of the central diffuse emission in Abell 141 from N–S and E–W within $2\sigma_{\rm rms}$ contours finding deconvolved dimensions of 4.2 arcmin and 3.7 arcmin, respectively, corresponding to a linear size of 910 kpc and 790 kpc. We will consider the mean linear extent to be 850 kpc. Additionally, the SE peripheral component has a maximum projected extent of 2.6 arcmin, corresponding to 550 kpc.

3.1.2. *Abell 3404*

The central diffuse emission in Abell 3404 is also elongated and we similarly see peripheral extended components that may not be associated with the central diffuse source—these are most prominent in the 25 arcsec source-subtracted ASKAP image (contours in Fig. 6(ii), indicated by yellow, dashed rectangles). The peak of the central radio emission is co-located with the X-ray peak, and the radio emission generally fills the X-ray–emitting area. The size of the central diffuse source is measured in the ASKAP source-subtracted, 35 arcsec tapered image within $2\sigma_{\rm rms}$ contours as above, finding angular sizes in the N–S and E–W directions of 5.3 arcmin and 3.9 arcmin, respectively, corresponding to linear sizes of 900 kpc and 660 kpc. We note that the the N–S direction is influenced by additional peripheral components, though it is not clear if these are part of the central emission or not (further discussed in Section 3.4.3). For the estimate of the size the SE component—which is more distinct—is not included. We again will consider the mean linear extent of 770 kpc in the following sections. The NE peripheral component is found to have a maximum projected size of 1.7 arcmin (270 kpc) and the SW component is found to be 1.5 arcmin (230 kpc) in extent.

3.2. *Radio spectral properties*

3.2.1. *Flux densities*

Fig. 3(i) and 4(i) also show relevant discrete sources that are projected onto the clusters within the MWA-2 emission. For the ASKAP data these were subtracted in the visibilities using CLEAN component models (Section 2.3), but in the MWA data their contribution is subtracted from the integrated flux density measurement after extrapolation from their measured SEDs. The central diffuse emission in Abell 3404 from 185–216 MHz is only barely detected above a $3\sigma_{\rm rms}$ significance in the MWA-2 data, with generally poorer image qualities and lack of detection in individual snapshots. As we cannot guarantee significant enough flux is recovered in these images, we opt not to provide measurements for Abell 3404 in the 185- and 216-MHz MWA-2 images. We instead measure the source using the 200-MHz GLEAM image. For Abell 141, we use all MWA-2 bands and re-measure the source in the 169-MHz EoR-0 image (Offringa et al., 2016) and the 200-MHz GLEAM image. We

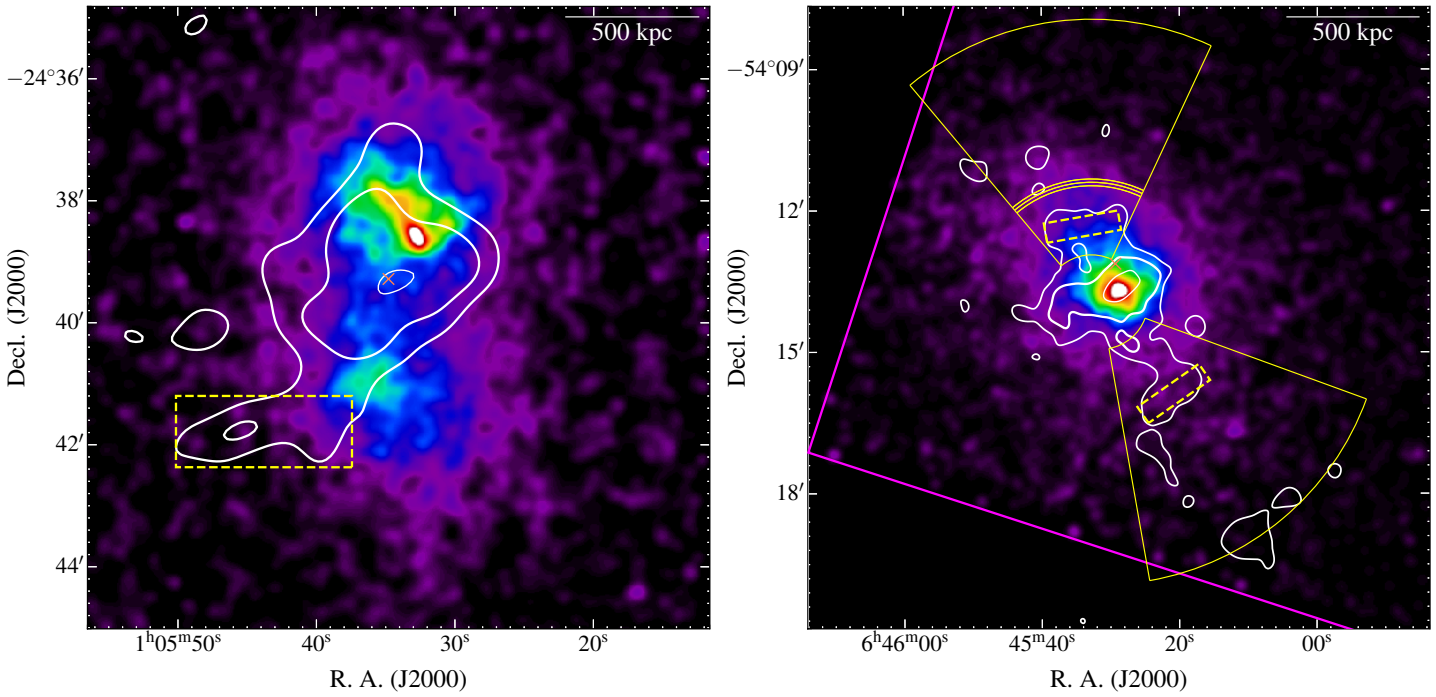

Figure 6. Exposure-corrected, smoothed, point source-subtracted [0.5–2] kev *Chandra* maps with source-subtracted ASKAP contours overlaid. (i) Abell 141: ASKAP contours as in Fig. 3(i), but without the $2\sigma_{\rm rms}$ contour. (ii) Abell 3404: ASKAP contours are the source-subtracted without tapering, but convolved with a 25 arcsec beam (hence, slightly higher resolution than the tapered, source-subtracted map). In (i) the yellow, dashed box indicates the peripheral diffuse source. In (ii) we show the regions within which we extract radio and X-ray surface brightness profiles (yellow sectors) and indicate extended radio components in those profiles (yellow, dashed rectangles) that may indicate radio shocks discussed in Section 3.4.3. The magenta lines indicate the edge of the ACIS-I field-of-view.

find the 169-MHz measurement is lower than reported by Duchesne et al. (2021b) largely due to additional discrete source-subtraction.

Table 2 shows the fitted power law properties of the discrete sources in each cluster. We measure the flux density of the peripheral diffuse sources in Abell 141 and Abell 3404 in the full-band, 25 arcsec ASKAP image, though are unable to provide a spectral index estimate. Individual flux density measurements of the diffuse sources are provided in Table 3, indicating the contributions from discrete sources that are subtracted from the total integrated flux density in the process. The peripheral components in each cluster contribute to the diffuse source measurements as we cannot subtract them from the MWA data and we only provide measurements of the perierphal sources in the full-band ASKAP images. Relevant details of images used for flux density measurements are also provided in Table 3.

3.2.2. *Diffuse source spectral indices*

The central diffuse radio sources can be described by a simple power law between 88 and 943 MHz for Abell 141 and 88 and 1110 MHz for Abell 3404. Fig. 7 plots the measured data as well as the best-fit power law models. The spectral index for the central diffuse source in Abell 3404 ($\alpha_{88}^{1013} = -1.66 \pm 0.07$) pushes it into the "ultra-steep spectrum radio halo" category (defined by $\alpha < -1.5$, USSRH; Cassano et al., 2013). We find that the central emission in Abell 141 has a flatter spectrum than reported by Duchesne et al. (2021b), though this is in part due to the subtraction

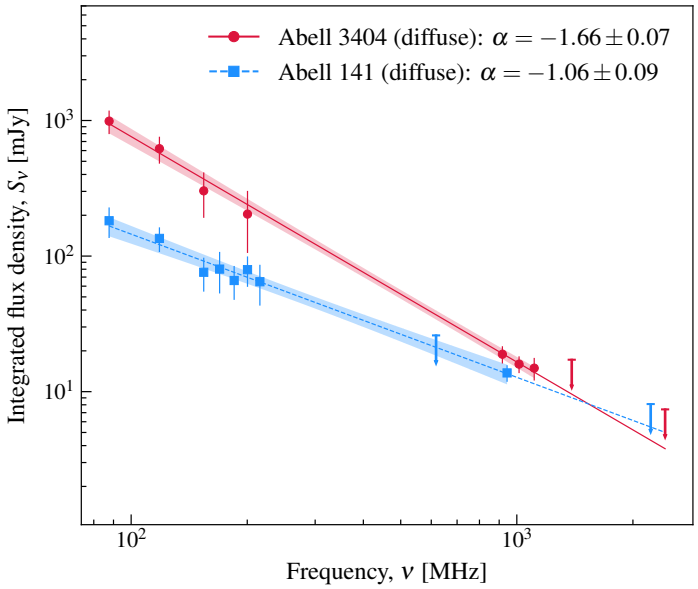

Figure 7. SEDs of the diffuse emission in Abell 141 and Abell 3404. The lines are power law fits, with 95 per cent confidence intervals represented by the shaded regions. Upper limits are represented by arrows. The fits are extrapolated to ATCA frequencies for ease of comparing to ATCA limits.

Table 2 Discrete source SED properties for both clusters.

Source	α	$\Delta\nu$ [a] (MHz)
Abell 141		
A	-1.09 ± 0.07	216–2674
B [b]	-1.44 ± 0.05	147–2674
C	-1.07 ± 0.07	147–2674
D [c]	$+1.18 \pm 0.09$	943–3000
Abell 3404		
A	-0.49 ± 0.11	216–1388
B	-0.35 ± 0.10	216–1388
C	-1.02 ± 0.14	185–1121
D [b]	-0.67 ± 0.18	185–2424
E	-0.65 ± 0.08	216–2424
F [d]	-	-
G [e]	-1	905–1121

[a] Frequency range over which source is modelled.
[b] Fit with a curved power law model.
[c] Inverted spectrum.
[d] Source could not be modelled, but is not distinguishable from "E" in MWA data.
[e] No uncertainty is given as the SED is only over the ASKAP subbands and we do not quantify the internal flux scale uncertainty across the band.

of three discrete sources with steep spectra. We report all derived source properties in Table 4, including source linear size, spectral index, and extrapolated monochromatic power at 1.4 and 0.15 GHz.

3.2.3. Limits on high frequency non-detections

To investigate the non-detections in ATCA data, we obtain upper limits by injecting simulated radio halos into the visibility data. We assume an azimuthally averaged brightness distribution described by Orrú et al. (2007, but see also Murgia et al. 2009; Bonafede et al. 2017), of the form

$$I(r) = I_0 e^{-r/r_e} \quad [\mathrm{Jy\,arcsec^{-2}}], \tag{1}$$

with I_0 the peak brightness, the e-folding radius $r_e = f/R_\mathrm{H}$, and R_H the radio halo radius. A median value of f is found to be 2.6 by Bonafede et al. (2017, based on radio halo samples described by Cassano et al. 2007; Murgia et al. 2009). For the purpose of determining limits, we use the calibrated GMRT data presented by Venturi et al. (2007, 2008) of Abell 141, recalculating the limit for consistency with the current method.

To determine the initial halo brightness and spectrum, we use the brightness from the ASKAP data and spectral index reported in Section 3.2.2. Additionally we find values of f (Eq. 1) to be 2.0 and 1.9 that recover adequate model flux for the Abell 141 and Abell 3404 radio halos, respectively. We use `WSClean` to inject the simulated halo as a function of frequency into the relevant datasets. During imaging of the mock radio halo, we increase brightness by factors of $\sqrt{2}$ until a detection is made. Imaging is done as a two-part process: first the model data are imaged alone, then imaged with the true calibrated data. The imaging of the model alone allows us to investigate the percentage of flux lost due to the u–v sampling. For Abell 141, we image both the ATCA and GMRT data with a 30 arcsec Gaussian taper applied to the visibilities to maximise the likelihood of detection. We find that the ATCA observation of Abell 141 only recovers $\sim$ 20 per cent of the model radio halo flux due to the lack of inner spacings limiting sensitivity on larger scales, with the GMRT observation recovering $\sim$ 60 per cent. For Abell 3404 the flux recovered is $\sim$ 70 per cent and $\sim$ 90 per cent for the pre-CABB and CABB data, respectively. We use the same detection criterion as Bonafede et al. (2017): $D^{\mathrm{mock}}_{2\sigma_\mathrm{rms}} \geq R_\mathrm{H}$, where $D^{\mathrm{mock}}_{2\sigma_\mathrm{rms}}$ is the diameter of the mock radio halo within $2\sigma_\mathrm{rms}$ contours. As per Bonafede et al. (2017), we opt to consider the model radio halo flux density for the limit, as this is the flux density that would be required to make the detection. The resultant limits, along with new limits obtained for the GMRT data (Venturi et al., 2007, 2008) are provided in Table 3, though are not used in fitting in Section 3.2.2.

We note that the limit found for the GMRT data of Abell 141 is higher than what is reported by Venturi et al. (2007, 2008): $\sim$ 7 mJy . This discrepancy is a result of, in part, the $\sim$ 60 per cent of flux lost to u–v sampling, and the difference in the modelled brightness profile, where Venturi et al. use optically thin concentric spheres (see also Brunetti et al., 2007). The remaining difference may be contributed from a different model geometry and spectrum and a bias that occurs when measuring the integrated flux density of low-SNR extended sources (Stroe et al., 2016, but see also Helfer et al. 2003).

Cuciti et al. (2018) perform a similar mock halo analysis for GMRT and Karl G. Jansky Very Large Array (JVLA) data to test flux recovery of incomplete u–v sampling. An important note they make is that the recovered flux density fraction decreases as the mock halo brightness decreases. We note that the flux recovery fraction for our mock halos are based on the limits. Appendix A shows representative u–v coverage plots for the observations used in this work (MWA-2, ASKAP, ATCA, and GMRT). These plots highlight that inner u–v sampling for the GMRT and ATCA (Abell 141) observations is lacking, whereas the MWA-2, ASKAP, and even the pre-CABB and CABB data for Abell 3404 have much more densely sampled inner u–v data. We note, however, that the smaller λ values become less populated toward the higher end of the MWA-2 band. We opt not to provide limits on the MWA-2 data between 185–216 MHz for Abell 3404 due to partial detection of the radio halo combined with significant confusion with discrete sources.

3.3. *Radio–X-ray correlation*

Radio halo brightness (I_R) is often observed to correlate with the X-ray surface brightness (I_X) of the ICM ($I_\mathrm{R} \propto {I_\mathrm{X}}^k$; Govoni et al. 2001). Radio halos are typically observed with a sub-linear slope (e.g. Giacintucci et al., 2005; Rajpurohit et al., 2018; Hoang et al., 2019a; Botteon et al., 2020c; Rajpurohit et al., 2021; Bruno et al.,

Note this value is calculated from the reported limit to the luminosity at 610 MHz, requiring an assumption on the spectral index of -1.3, though the index does not appreciably change the power calculation here.

Table 3 Flux density measurements and limits of the diffuse sources.

Instrument	Weighting	ν (MHz)	Resolution ($''\times''$)	$\langle\sigma_{\rm rms}\rangle$ [a] (mJy beam^{-1})	$S_{{\rm c},\nu}$ [b] (mJy)	S_ν (mJy)
Abell 141 radio halo (+ peripheral source)						
MWA-2	robust 0.0	87.7	130×130	8.6	78 ± 28	182 ± 46
MWA-2	robust +2.0	118.4	168×118	4.7	58 ± 16	135 ± 28
MWA-2	robust +1.0, 120″ taper	154.2	166×147	6.1	45 ± 8	75 ± 21
MWA [c]	uniform	169.6	109×109	4.9	41 ± 6	80 ± 27
MWA-2	robust +1.0, 120″ taper	185.0	150×137	5.1	38 ± 5	66 ± 19
MWA	robust −1.0	200.3	133×126	16.3	35 ± 4	79 ± 20
MWA-2	robust +1.0, 120″ taper	215.7	138×130	5.1	32 ± 3	65 ± 22
GMRT [d]	natural, 30″ taper	617.5	71×56	0.45	-	<26 [e]
ASKAP	robust +0.25, 45″ taper	943.5	49×46	0.14	-	13.7 ± 1.9
ATCA	robust 0.0, 45″ taper	2224.5	44×31	0.052	-	<8.1 [e]
Abell 141 peripheral source (SE)						
ASKAP	robust +0.25, 45″ taper	943.5	49×46	0.15	-	1.7 ± 0.5
Abell 3404 radio halo (+ peripheral sources)						
MWA-2	robust +2.0	87.7	242×157	24.7	130 ± 140	990 ± 190
MWA-2	robust +2.0	118.4	183×114	10.4	120 ± 120	620 ± 140
MWA-2	robust +2.0	154.2	137×86	4.7	100 ± 100	300 ± 110
MWA	robust −1.0	200.3	147×134	8.3	90 ± 91	204 ± 99
ASKAP	robust +0.5, 35″ taper	917.5	36×36	0.15	-	18.9 ± 2.7
ASKAP	robust +0.5, 35″ taper	1013.5	36×36	0.12	-	16.0 ± 2.3
ASKAP	robust +0.5, 35″ taper	1109.5	36×36	0.16	-	14.9 ± 2.8
ATCA	robust 0.0	1388.0	98×38	0.15	-	<21 [e]
ATCA	robust 0.0	2424.0	71×37	0.055	-	<5.7 [e]
Abell 3404 peripheral source (NE)						
ASKAP	robust +0.5	1013.5	25×25	0.074	-	1.3 ± 0.3
Abell 3404 peripheral source (SW)						
ASKAP	robust +0.5	1013.5	25×25	0.065	-	1.4 ± 0.4

[a] Average rms noise within the measured source region.
[b] Confusing source flux that is subtracted from initial measurement based on SEDs reported in Table 2.
[c] EoR-0 field image (Offringa et al., 2016) as used by Duchesne et al. (2021b), re-measured with present integration region and source subtraction, including brightness scaling of 0.69.
[d] Data originally presented by Venturi et al. (2007).
[e] Limit from mock radio halos as described in Section 3.2.3.

Table 4 Derived radio halo properties.

Property	Abell 141	Abell 3404
Linear size (kpc)	850	770
α	-1.06 ± 0.09	-1.66 ± 0.07
$P_{1.4}$ (10^{23} W Hz^{-1})	14.4 ± 2.0	8.6 ± 1.7
$P_{0.15}$ (10^{23} W Hz^{-1})	164 ± 43	350 ± 70

2021); conversely mini-halos have been found to have super-linear slopes (Ignesti et al., 2020). We use the exposure-corrected, source-subtracted, smoothed [0.5–2] kev *Chandra* data along with the low-resolution, source-subtracted ASKAP images to perform a similar analysis for Abell 141 and Abell 3404.

Following a procedure described by Ignesti et al. (2020), we construct grids across the diffuse emission with cell sizes corresponding to the ASKAP beam major axis. For Abell 141 this is 49″, corresponding to 178 kpc and for Abell 3404 this is 44″, corresponding to 124 kpc. We fit the data as $\log_{10}(I_{\rm R}) = k\log_{10}(I_{\rm X}) + C$ using the BCES method with an orthogonal regression. Fig. 8 shows the results for (i) Abell 141 and (ii) Abell 3404. For both, we separate out the contribution from the peripheral components,

Bivariate Correlated Errors and intrinsic Scatter: Akritas & Bershady (1996).

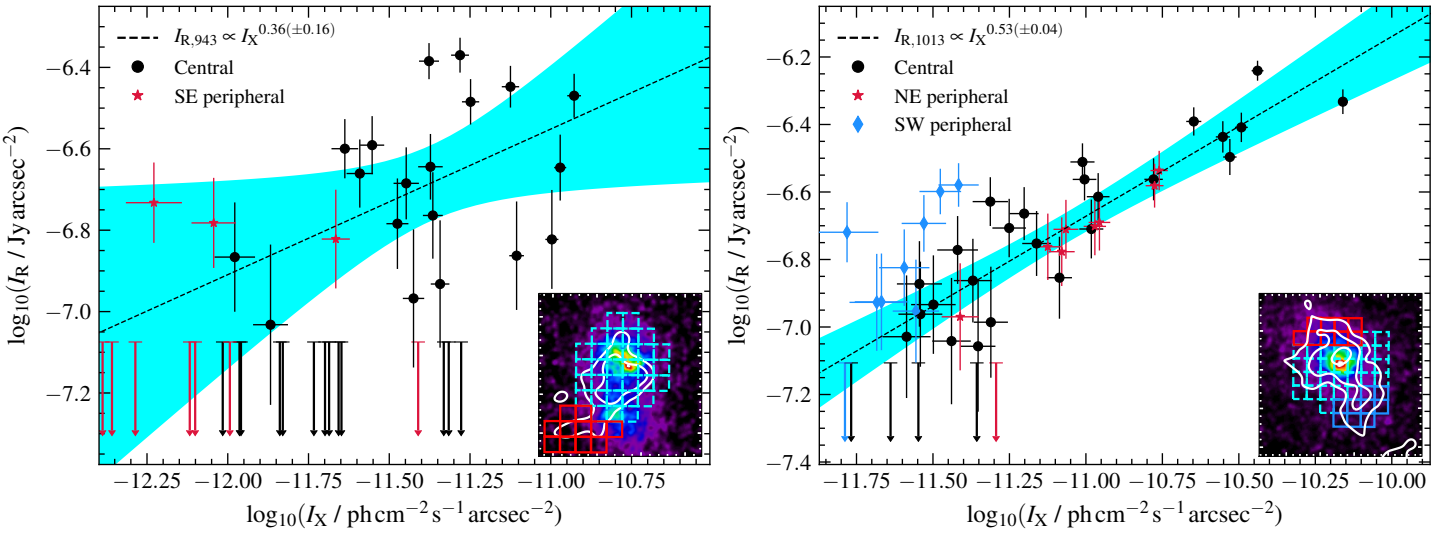

(i) Abell 141. **(ii)** Abell 3404.

Figure 8. Radio–X-ray point-to-point correlation for (i) Abell 141 and (ii) Abell 3404. Upper limits correspond to cells where $I_R < 2\sigma_{rms}$. The black, dashed line is the best-fitting line with a 95 per cent confidence interval shaded in cyan. The insets show the *Chandra* X-ray maps with the source-subtracted ASKAP image overlaid as contours as in Fig. 6(i) and Fig. 4(i) for Abell 141 and Abell 3404, respectively. The cyan boxes on the insets show the cells within which surface brightesses are calculated, and the red and blue cells indicate the locations of the peripheral components.

with each grid shown on the inset for each figure. Abell 3404 shows strong correlation (with Spearman rank-order correlation coefficient, $\rho = 0.89$), and we find a sub-linear trend with $k = 0.53 \pm 0.04$. While many halos have been found with $k \gtrsim 0.6$ (e.g. Govoni et al., 2001; Botteon et al., 2020c; Rajpurohit et al., 2021), we note the steep-spectrum radio halo in MACS J1149.5+2223 is found to have $k \lesssim 0.6$ (Bruno et al., 2021). The SW peripheral component (blue points, Fig. (ii)) appears unassociated whereas the NE component follows the correlation tightly. For the fit the NE component is included. For Abell 141, we find no significant correlation ($\rho = 0.31$). This may indicate a mixture of emission components, though Shimwell et al. (2014) notes, in reference to the Bullet Cluster radio halo showing a similar lack of correlation, this may be due to the halo occurring during a specific stage of a complex merger.

3.4. *Cluster dynamics and source classification*

3.4.1. Abell 141—pre-merger?

The dynamic nature of Abell 141 has been studied extensively by Dahle et al. (2002, in optical) and Caglar (2018, hereafter C18, in X-ray). Dahle et al. (2002) and C18 find that the bi-modal distribution (as seen in the X-ray in Fig. 6(i)) represents two subclusters (labelled A141N and A141S by C18) which have not completed a core-crossing—i.e., the cluster is likely in a pre-merging state. C18 report that X-ray–emitting gas between the two subclusters features a hotspot, which may imply the presence of a shock or shocks. We note that the central diffuse radio emission coincides more with the A141N subcluster, but extends into the region between the subclusters. Most radio halos have been detected in clusters that are in a merging or dynamic state (see e.g. Cassano et al., 2013), with three examples in the literature of likely pre-merger subclusters: Abell 399–401 (Murgia et al., 2010), MACS J0416.1−2403 (Ogrean et al., 2015), and Abell 1758N–S (Botteon et al., 2018). We note in the cases of Abell 399–401 and Abell 1758N–S each subcluster in the corresponding mergers clearly host their own radio halos whereas we do not detect two distinct radio halos in the A141N and A141S subclusters. The emission may represent a bridge between the subclusters rather than a traditional giant radio halo (see Govoni et al., 2019; Botteon et al., 2020a; Hoeft et al., 2020; Bonafede et al., 2021), though due to the resolution of our data we cannot confirm bridge emission distinct from the radio emission that permeates A141N.

A radio relic? Some radio relics have been found to be co-located with shocks detected via X-ray emission (e.g. Bourdin et al., 2013; Akamatsu et al., 2015; Eckert et al., 2016; Di Gennaro et al., 2019). Assuming the central region temperature jump in the X-ray corresponds to a shock, C18 derive a Mach number of $\mathcal{M}_X = 1.69^{+0.41}_{-0.37}$. If we consider that a radio shock traces the same shock structure, and that DSA on a pool of thermal electrons triggers the emission (see e.g. Blandford & Eichler, 1987), a corresponding radio Mach number can be calculated from

$$\mathcal{M}_R = \sqrt{\frac{2\alpha_{inj} - 3}{2\alpha_{inj} + 1}}, \quad (2)$$

assuming that $\alpha = \alpha_{inj} - 0.5$, with α_{inj} the synchrotron injection spectrum index. We find $\mathcal{M}_R = 5.9 \pm 0.9$, inconsistent with the X-ray–derived Mach number. This does not necessarily rule out the possibility of the source being a radio shock, as discussed by van Weeren et al. (2016, 2017) (but see also Hoang et al., 2019b; Lee et al., 2020), a discrepancy in Mach numbers may indicate that the thermal pool electrons are *not* seed electrons for the emission—i.e., pre-accelerated fossil electrons may be accelerated by the

DSA process. In this case the injection spectrum may resemble the observed emission spectrum (van Weeren et al., 2016) with $\alpha = \alpha_{\rm inj}$ and $\mathcal{M}_{\rm R} = 2.1 \pm 0.2$, in agreement with $\mathcal{M}_{\rm X}$. Assuming seed electrons for radio relics originate as fossil electrons rather than thermal pool electrons also alleviates the acceleration efficiency problem for some relics with X-ray detected shocks (see Botteon et al., 2020b, and references therin). Additionally, simulations show radio galaxies in cluster environments can supply fossil electrons for re-acceleration (Vazza et al., 2021). A difference in Mach number may also arise from the X-ray and radio emission preferentially tracing different shocks along a line of sight (see e.g. van Weeren et al., 2016; Rajpurohit et al., 2020, and references therein) or may arise due to turbulence near the shock front (Domínguez-Fernández et al., 2021).

The present data (including lack of polarimetry) do not allow us to rule out a radio relic or radio bridge interpretation, or a combination thereof. We consider the source a radio halo because the observed physical characteristics—including its morphology, location, and SED—are consistent with a radio halo classification.

3.4.2. Abell 3404—dynamics

Fig. 6(ii) shows the exposure-corrected, smoothed, and point-source subtracted [0.5–2] kev *Chandra* map for Abell 3404, where the X-ray emission is slightly elongated. We note that using *XMM-Newton* data Pratt et al. (2009) consider the cluster as non-cool core, but also not morphologically disturbed based on its centroid shift, w (Poole et al., 2006, but see also Mohr et al. 1993), which gives an indication of the dynamic state of the cluster. We repeat the calculation for the present *Chandra* data, using `proffit` (Eckert et al., 2011), subtracting a fitted background of $I_{\rm B} = (1.41 \pm 0.05) \times 10^{-5}$ ph cm^{-2} s^{-1} arcmin^{-2}, finding $w = 0.039$ within $R_{500} = 1280$ kpc (Pratt et al., 2009), smaller than the expected $w > 0.075$ for a disturbed system of this radius. We note that the radio halo detected in Abell S1063 (Xie et al., 2020) is similarly detected in a cluster that is considered morphologically relaxed based on this definition.

We also calculate the concentration parameter, $c_{100/500}$ (and $c_{40/400}$; Santos et al. 2008), defined via

$$c_{r_1/r_2} = \frac{I_{\rm X}\,(r < r_1\ {\rm kpc})}{I_{\rm X}\,(r < r_2\ {\rm kpc})}, \tag{3}$$

with $I_{\rm X}$ the X-ray surface brightness. We find $c_{100/500} = 0.24$ which, in combination with the centroid shift within 500 kpc ($w_{500\ {\rm kpc}} = 0.039$) places the cluster just outside of the halo-hosting quadrant of the $c_{100/500}$–$w_{500\ {\rm kpc}}$ plane shown by Cassano et al. (2010)—no halos appear in clusters with $c_{100/500} > 0.2$. We also find $c_{40/400} = 0.062$, consistent with non-cool–core clusters (Santos et al., 2008). The ambiguity of the X-ray morphological parameters point towards a low-energy/weak merger or a late stage in the merger. For example, a merger between low velocity subclusters or a high mass-ratio between subclusters may result in low-energy mergers. Given the cluster's SZ-derived mass of $7.96^{+0.23}_{-0.21} \times 10^{14}$ M$_\odot$ (Planck Collaboration et al., 2016b) we can infer the presence of a massive subcluster prior to the merger. Such scenarios are expected to generate USSRHs (Brunetti et al., 2008) as observed here.

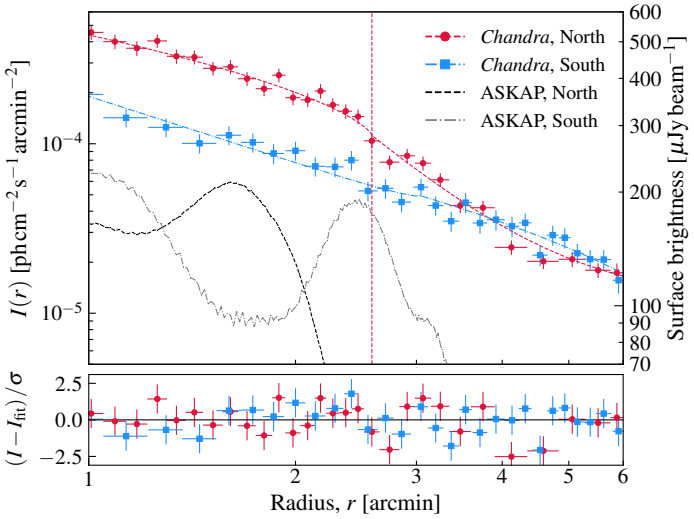

Figure 9. Radio and background-subtracted X-ray surface brightness profile for sectors shown in Fig. 6(ii) for Abell 3404. The radio ordinate clips at $2\sigma_{\rm rms}$. The dashed-red vertical line is at location of the discontinuity in the northern profile.

3.4.3. Abell 3404—radio and X-ray shocks?

Fig. 6(ii) shows two extended diffuse emission regions (indicated with dashed, yellow rectangles) either side of the cluster center. We do not have sufficient fidelity in the ASKAP subband data to investigate the spectral properties or to remove the northern component from the radio halo measurement, though for the purpose of this section we consider the possibility that the two extended structures represent radio shocks.

We investigate that possibility by extracting X-ray and radio surface brightness (SB) profiles along the directions of the relic-like sources (extracted regions shown as yellows sectors in Fig. 6(ii)). For the X-ray data, we use `proffit`, masking the point sources indicated in Fig. 6(ii) with yellow circles. The X-ray SB profiles are binned ensuring each bin is $\geq 10\sigma$ and $\geq 7\sigma$ for the north and south profiles, respectively. The radio SB profile is extracted using in-house `python` code `fluxtools.py` . The extracted profiles in each direction are shown in Fig. 9. We find candidate discontinuities in the X-ray SB profile. We fit standard broken power law models, representing an electron density discontinuity either side of a putative shock (see e.g. Owers et al., 2009; Eckert et al., 2016):

$$\rho(r) = \begin{cases} C r^{-\Gamma_{\rm in}}, & \text{if } r < r_{\rm break} \\ C \dfrac{n_{\rm out}}{n_{\rm in}} r^{-\Gamma_{\rm out}}, & \text{otherwise} \end{cases}, \tag{4}$$

with Γ the power law indices either side of the discontinuity, $j = n_{\rm out}/n_{\rm in}$ the density jump, and C a normalisation factor, and the SB profile is $\rho(r)$ integrated along the line of sight. For the southern profile we find $j_{\rm south} \sim 1$, indicating no evidence for a discontinuity. For the northern profile we obtain $j_{\rm north} = 1.11^{+0.09}_{-0.10}$. The radio source occurs ~ 1 arcmin (~ 170 kpc) from the X-ray discontinuity; in the case of a relic associated with a shock the

http://www.isdc.unige.ch/~deckert/newsite/Proffit.html

https://gist.github.com/Sunmish/198ef88e1815d9ba66c0f3ef3b18f74c

Table 5 Fitted values for the P_ν–M_{500} scaling relations for various methods.

Method	B	σ_B	A	σ_A
	$P_{1.4}$–M_{500}			
$P_{1.4}\|M_{500}$	3.21	0.39	−23.4	5.8
Orthogonal	5.75	0.93	−61.0	13.8
Bisector	4.17	0.46	−37.7	6.8
	$P_{0.15}$–M_{500}			
$P_{0.15}\|M_{500}$	3.15	0.41	−21.2	6.0
Orthogonal	4.76	0.93	−45.0	13.8
Bisector	3.84	0.50	−31.4	7.4

observed discontinuity in the X-ray profile occurs directly after the relic source (and a hard edge may be seen in the radio map), therefore the northern peripheral radio source is unlikely to be a relic associated with a shock.

3.5. *Radio halo* P_ν–M_{500} *scaling relations*

Despite a somewhat atypical X-ray morphology of each cluster, based on the available data we classify both central diffuse radio sources as giant radio halos (for Abell 141, consistent with the classification from Duchesne et al. 2021b). Both Abell 141 and Abell 3404 have similar masses, and their constituent radio halos have similar sizes and brightness at ∼ 1 GHz, however, due to the difference in their SEDs their 1.4- and 0.15-GHz monochromatic luminosities differ by around a factor of two.

Scaling relationships between radio halo power and various (related) cluster properties have been found (see e.g. Liang et al., 2000; Brunetti et al., 2007; Basu, 2012), somewhat explained physically by turbulent (re-)acceleration models for halo formation (Cassano et al., 2013, hereafter C13). A key finding by Brunetti et al. (2009, but see also Cassano et al. 2010, 2013) is the bi-modality to the sample of halo-hosting clusters, where morphologically disturbed (i.e., likely merging) clusters host radio halos, and most relaxed, X-ray–luminous, and massive clusters without halos have upper limits to radio halo power well below the empirical scaling relations.

Recent updates to the power–mass (P_ν–M_{500}) relation (Cassano et al., 2013; Martinez Aviles et al., 2016; Duchesne et al., 2021b; van Weeren et al., 2020; Cuciti et al., 2021) find results largely consistent within reported uncertainties. We update this relation at $\nu = 1.4$ GHz and $\nu = 0.15$ GHz following van Weeren et al. (2020, hereafter vW20). For this work, we incorporate the compiled literature sample of halos reported by C13 and Martinez Aviles et al. (2016), halos in Abell S1121 and Abell 2811 reported by Duchesne et al. (2021b), and new halos reported in the literature from 2017 (Parekh et al., 2017; Wilber et al., 2018; Cassano et al., 2019; Bîrzan et al., 2019; Xie et al., 2020; HyeongHan et al., 2020; Giovannini et al., 2020; Wilber et al., 2020; Hoeft et al., 2020; Hoang et al., 2021; Di Gennaro et al., 2020; van Weeren et al., 2020; Raja et al., 2020; Knowles et al., 2021; Raja et al., 2021), with the exception of the halo in ACT-CL J0528.8−3927 reported by Knowles et al. (2021) as its small size and coincidence with a radio-bright BCG suggests a mini-halo. For consistency, cluster masses are obtained from PSZ measurements where available (Planck Collaboration et al., 2016c, with some masses obtained from the South Pole Telescope; Song et al. 2012; Reichardt et al. 2013), and only clusters with an SZ-derived mass are used. Note all radio halos are scaled to 1.4 and 0.15 GHz with either a measured spectral index or using the full sample mean, $\langle\alpha\rangle = -1.4 \pm 0.2$, following

$$P_{\nu_1} = \frac{4\pi D_L(z)^2}{(1+z)^{1+\alpha}} S_{\nu_{obs}} \left(\frac{\nu_1}{\nu_{obs}}\right)^{\alpha} \quad [\mathrm{W\,Hz^{-1}}], \tag{5}$$

where ν_{obs} is the closest observed frequency, $\nu_1 \in \{0.15, 1.4\}$, and D_L is the luminosity distance of the cluster. We do not distinguish between normal giant radio halos and ultra-steep spectrum radio halos defined by $\alpha < -1.5$ (USSRH) (e.g. Brunetti et al. 2008; C13). We note that integrated flux densities measured by vW20 are integrated from a fitted exponential profile (Eq. 1) rather than measured directly from the maps and may be generally larger than those measured via integration directly from the pixel sum, especially for low-SNR halos.

We fit the radio halo sample assuming a scaling relation at $\nu = 1.4$ GHz and $\nu = 0.15$ GHz with a function of the form $\log_{10}(P_\nu) = B \times \log_{10}(M_{500}) + A$ using the BCES method with an orthogonal regression. For comparison with C13 and vW20 we shift their fitted relations to the relevant frequencies via

$$\log_{10}(P_{\nu_1}) = B \log_{10}(M_{500}) + A - \langle\alpha\rangle \log_{10}\left(\frac{\nu_2}{\nu_1}\right), \tag{6}$$

where ν_2 is the frequency at which the original scaling relation is fit and with $P_{\nu_1} = P_{\nu_2}(\nu_1/\nu_2)^{\langle\alpha\rangle}$. Fig. 10 shows the $P_{1.4}$–M_{500} (10(i)) and $P_{0.15}$–M_{500} (10(ii)) planes with the relevant fits and aforementioned data. Best-fit values for the scaling relation for various methods are shown in Table 5 for comparison with other works.

The updated position of the radio halo in Abell 141 on both the $P_{1.4}$–M_{500} and $P_{0.15}$–M_{500} planes is in agreement with the fitted relations, and the halo in Abell 3404 lies below the $P_{1.4}$–M_{500} relation consistent with the general population of USSRHs (Cassano et al., 2013; Cuciti et al., 2021), but is closer to the fitted $P_{0.15}$–M_{500} relation. We note also that if the halo in Abell 141 was only associated with the A141N subcluster the halo's position on both P_ν–M_{500} relations would be significantly above the best fitting lines. With a sample size of 86 we find (orthogonal) scaling relations consistent with C13 and vW20 at both frequencies within respective uncertainties, but note some deviation from the fit reported by vW20 at 0.15 GHz. Naturally, scaling radio halo powers to frequencies beyond which they are measured introduces additional uncertainties. We also find that the $P_\nu|M_{500}$ fitting is the most consistent method (albeit shallower than for orthogonal), with results from vW20 ($B = 3.84 \pm 0.69$) and Cuciti et al. (2021) ($B = 3.26 \pm 0.74$ for their 'statistical' sample with USSRHs) with

With $M_{X,500} = (3.79 \pm 0.3) \times 10^{14}$ $M_\odot$ (C18).
P_ν the dependent variable and M_{500} the independent variable.

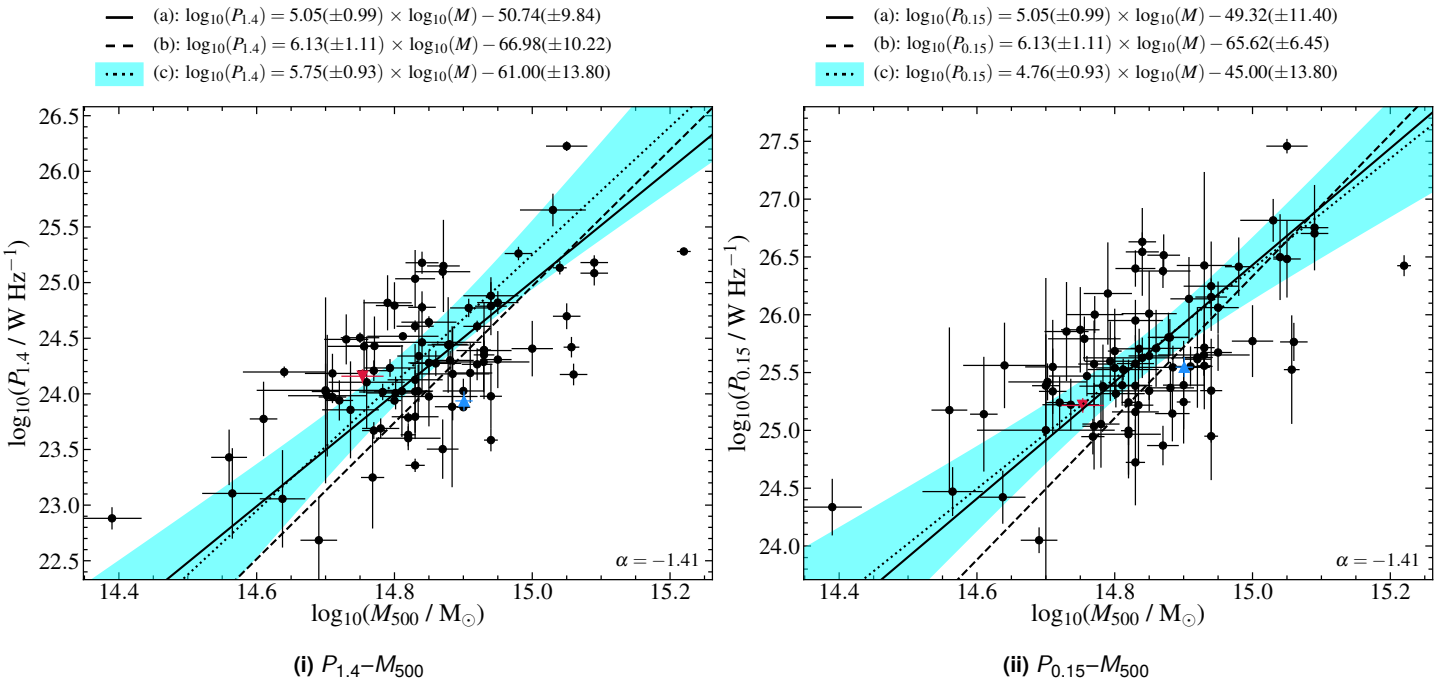

Figure 10. Radio halo $P_{1.4}$–M_{500} relation (i) and $P_{0.15}$–M_{500} relation (ii) with best-fitting orthogonal relations from (a) Cassano et al. (2013) (solid, black), (b) van Weeren et al. (2020) (dashed, black), and (c) this work (dotted, black). Halos are taken from the literature (as discussed in Section 3.5) with the addition of the halo in Abell 3404 (blue, upright triangle) and the updated values for Abell 141 (red, downward triangle), for a total of 86 halos. The shaded regions are 99.7% confidence intervals for fits from this work.

both vW20 and Cuciti et al. (2021) employing smaller, specific samples.

C13 find that inclusion of USSRHs steepens the scaling relation at 1.4 GHz and vW20 find generally steeper relations at 0.15 GHz for radio halos detected around 0.15 GHz (and presumably generally steeper in spectrum). In Equation 6 we re-scale the scaling relation with an assumed mean $\langle\alpha\rangle$, where real observations at lower of higher frequencies may bias the sample selection towards steeper or flatter spectrum sources, respectively, finding opposed slopes to the P_ν–M_{500} relation. Uncertainties are still too significant to confirm this as discussed by vW20.

The concordance between these results and those in the recent literature demonstrates that we are now reaching sufficient sample sizes to have confidence in the scaling relation values. While it has recently been suggested there is little evolution of magnetic field strength as a function of redshift in galaxy clusters and hence a redshift dependence in the power-mass scaling relations are not expected (Di Gennaro et al., 2020), an outstanding question remains regarding if there is a difference in the relations for halos and USSRHs which may be expected from differences in their underlying physics. Yet larger samples of halos, expected in the near future, will allow this to be probed.

4. Summary

We have confirmed the detection of centrally-located diffuse, steep-spectrum cluster radio emission in Abell 141, and ultra-steep spectrum emission in Abell 3404. We have presented new observations from the MWA-2, ASKAP, and ATCA of the clusters, with the central diffuse sources detected with the MWA-2 and ASKAP. We conclude that these central diffuse radio sources can be described as giant radio halos with linear extents of $\sim$ 850 kpc and $\sim$ 770 kpc, for Abell 141 and Abell 3404, respectively. We find that each source has an SED that can be fitted with a normal power law model, with spectral indices of $\alpha_{88}^{943} = -1.06 \pm 0.09$ and $\alpha_{88}^{1110} = -1.66 \pm 0.07$ for Abell 141 and Abell 3404, respectively, making the radio halo in Abell 3404 the first reported USSRH detected with ASKAP. We find no evidence of these sources in pre-CABB and CABB ATCA data, though find the u–v coverage for the observations preclude detection of the radio halos assuming an exponential brightness profile described by the derived spectral index and the measured size and peak brightness in the ASKAP images. Additional peripheral components are detected along with the main central halos, though only for the SW peripheral source in Abell 3404 do we confirm this is not associated with the central halo. No shocks are detected at the locations of the peripheral components in Abell 3404 and they are unlikely to be relics. These peripheral components may be background/foreground radio galaxies, phoenices, or other extended sources and we do not classify them here.

We discuss the morphological properties of the two clusters based on their X-ray emission using *Chandra* data, noting that Abell 141 has previously been found to likely be in a pre-merging state, prior to core passage of the sub clusters. Conversely, we find that the dynamic status of Abell 3404 is likely to be in more relaxed state, either in the late stage of a merger or a low-energy merger. The radio–X-ray surface brightness correlation is explored for each cluster, finding strong correlation for Abell 3404 but no significant correlation for Abell 141. Some of these properties make them

atypical for most radio-halo–hosting clusters, though we find that the radio halos are located in the expected places on the P–M scaling relations at both 1.4 and 0.15 GHz, given their respective spectral properties and cluster masses (considering Abell 141 a single cluster system). We fit the $P_{1.4}$–M_{500} and $P_{0.15}$–M_{500} scaling relations with the current sample of radio halos, finding results consistent with the literature suggesting that we are now converging with a high precision on these relations.

Acknowledgements. We thank T. Venturi for providing the calibrated GMRT dataset of Abell 141. We also thank the anonymous referee for providing valuable feedback and their suggestion to explore the radio–X-ray surface brightness correlation. SWD acknowledges an Australian Government Research Training Program scholarship administered through Curtin University. The Australian SKA Pathfinder is part of the Australia Telescope National Facility which is managed by CSIRO. Operation of ASKAP is funded by the Australian Government with support from the National Collaborative Research Infrastructure Strategy. ASKAP uses the resources of the Pawsey Supercomputing Centre. Establishment of ASKAP, the Murchison Radio-astronomy Observatory and the Pawsey Supercomputing Centre are initiatives of the Australian Government, with support from the Government of Western Australia and the Science and Industry Endowment Fund. Support for the operation of the MWA is provided by the Australian Government (NCRIS), under a contract to Curtin University administered by Astronomy Australia Limited. We acknowledge the Pawsey Supercomputing Centre which is supported by the Western Australian and Australian Governments. This paper includes archived data obtained through the Australia Telescope Online Archive (`http://atoa.atnf.csiro.au/`). This research has made use of data obtained from the *Chandra* Data Archive and the *Chandra* Source Catalog, and software provided by the *Chandra* X-ray Center (CXC) in the application package `CIAO`. This research has made use of the NASA/IPAC Extragalactic Database (NED), which is operated by the Jet Propulsion Laboratory, California Institute of Technology, under contract with the National Aeronautics and Space Administration. This research made use of a number of `python` packages not explicitly mentioned in the main text: `aplpy` (Robitaille & Bressert, 2012), `astropy` (Astropy Collaboration et al., 2013; Price-Whelan et al., 2018), `matplotlib` (Hunter, 2007), `numpy` (van der Walt et al., 2011) and `scipy` (Jones et al., 2001).

References

Abell G. O., 1958, ApJS, 3, 211
Abell G. O., Corwin Jr. H. G., Olowin R. P., 1989, ApJS, 70, 1
Akamatsu H., et al., 2015, A&A, 582, A87
Akritas M. G., Bershady M. A., 1996, ApJ, 470, 706
Astropy Collaboration et al., 2013, A&A, 558, A33
Basu K., 2012, MNRAS, 421, L112
Bîrzan L., et al., 2019, MNRAS, 487, 4775
Blandford R., Eichler D., 1987, Phys. Rep., 154, 1
Böhringer H., et al., 2007, A&A, 469, 363
Bonafede A., et al., 2017, MNRAS, 470, 3465
Bonafede A., et al., 2020, arXiv e-prints, p. arXiv:2011.08856
Bonafede A., et al., 2021, ApJ, 907, 32
Botteon A., et al., 2018, MNRAS, 478, 885
Botteon A., et al., 2020a, MNRAS, 499, L11
Botteon A., Brunetti G., Ryu D., Roh S., 2020b, A&A, 634, A64
Botteon A., et al., 2020c, ApJ, 897, 93
Bourdin H., Mazzotta P., Markevitch M., Giacintucci S., Brunetti G., 2013, ApJ, 764, 82
Brüggen M., Bykov A., Ryu D., Röttgering H., 2012, Space Sci. Rev., 166, 187
Brüggen M., et al., 2021, A&A, 647, A3
Brunetti G., Jones T. W., 2014, International Journal of Modern Physics D, 23, 1430007
Brunetti G., Venturi T., Dallacasa D., Cassano R., Dolag K., Giacintucci S., Setti G., 2007, ApJ, 670, L5
Brunetti G., et al., 2008, Nature, 455, 944
Brunetti G., Cassano R., Dolag K., Setti G., 2009, A&A, 507, 661
Bruno L., et al., 2021, arXiv e-prints, p. arXiv:2103.10110
Caglar T., 2018, MNRAS, 475, 2870
Cassano R., Brunetti G., Setti G., Govoni F., Dolag K., 2007, MNRAS, 378, 1565
Cassano R., Ettori S., Giacintucci S., Brunetti G., Markevitch M., Venturi T., Gitti M., 2010, ApJ, 721, L82
Cassano R., et al., 2013, ApJ, 777, 141
Cassano R., et al., 2019, ApJ, 881, L18
Chapman J. M., Dempsey J., Miller D., Heywood I., Pritchard J., Sangster E., Whiting M., Dart M., 2017, CASDA: The CSIRO ASKAP Science Data Archive. p. 73
Clarke T. E., Kronberg P. P., Böhringer H., 2001, ApJ, 547, L111
Cuciti V., Brunetti G., van Weeren R., Bonafede A., Dallacasa D., Cassano R., Venturi T., Kale R., 2018, A&A, 609, A61
Cuciti V., et al., 2021, A&A, 647, A51
Dahle H., Kaiser N., Irgens R. J., Lilje P. B., Maddox S. J., 2002, ApJS, 139, 313
DeBoer D. R., et al., 2009, IEEE Proceedings, 97, 1507
Di Gennaro G., et al., 2019, ApJ, 873, 64
Di Gennaro G., et al., 2020, Nature Astronomy,
Domínguez-Fernández P., Bruggen M., Vazza F., Banda-Barragan W. E., Rajpurohit K., Mignone A., Mukherjee D., Vaidya B., 2021, MNRAS, 500, 795
Donnert J., Dolag K., Brunetti G., Cassano R., 2013, MNRAS, 429, 3564
Donnert J., Vazza F., Brüggen M., ZuHone J., 2018, Space Sci. Rev., 214, 122
Duchesne S. W., Johnston-Hollitt M., Zhu Z., Wayth R. B., Line J. L. B., 2020, PASA, 37, e037
Duchesne S. W., Johnston-Hollitt M., Bartalucci I., Hodgson T., Pratt G. W., 2021a, PASA, 38, e005
Duchesne S. W., Johnston-Hollitt M., Offringa A. R., Pratt G. W., Zheng Q., Dehghan S., 2021b, PASA, 38, e010
Eckert D., Molendi S., Paltani S., 2011, A&A, 526, A79
Eckert D., Jauzac M., Vazza F., Owers M. S., Kneib J. P., Tchernin C., Intema H., Knowles K., 2016, MNRAS, 461, 1302
Enßlin T. A., Gopal-Krishna 2001, A&A, 366, 26
Feretti L., Fusco-Femiano R., Giovannini G., Govoni F., 2001, A&A, 373, 106
Frater R. H., Brooks J. W., Whiteoak J. B., 1992, Journal of Electrical and Electronics Engineering Australia, 12, 103
Fruscione A., et al., 2006, in Proc. SPIE. p. 62701V, doi:10.1117/12.671760
Giacintucci S., et al., 2005, A&A, 440, 867
Giacintucci S., Markevitch M., Cassano R., Venturi T., Clarke T. E., Brunetti G., 2017, ApJ, 841, 71
Giacintucci S., Markevitch M., Cassano R., Venturi T., Clarke T. E., Kale R., Cuciti V., 2019, ApJ, 880, 70
Giovannini G., Feretti L., Girardi M., Govoni F., Murgia M., Vacca V., Bagchi J., 2011, A&A, 530, L5
Giovannini G., et al., 2020, A&A, 640, A108
Govoni F., Enßlin T. A., Feretti L., Giovannini G., 2001, A&A, 369, 441
Govoni F., et al., 2019, Science, 364, 981
Hambly N. C., et al., 2001a, MNRAS, 326, 1279
Hambly N. C., Irwin M. J., MacGillivray H. T., 2001b, MNRAS, 326, 1295
Hambly N. C., Davenhall A. C., Irwin M. J., MacGillivray H. T., 2001c, MNRAS, 326, 1315
Harris D. E., Kapahi V. K., Ekers R. D., 1980, A&AS, 39, 215
Harvey-Smith L., et al., 2018, ASKAP Data Products for Project AS034 (ASKAP Early Science Broadband Survey): images and visibilities. v1. CSIRO. Data Collection, `httFHp://hdl.handle.net/102.100.100/74037?index=1`
Helfer T. T., Thornley M. D., Regan M. W., Wong T., Sheth K., Vogel S. N., Blitz L., Bock D. C. J., 2003, ApJS, 145, 259
Hoang D. N., et al., 2019a, A&A, 622, A20
Hoang D. N., et al., 2019b, A&A, 622, A21
Hoang D. N., et al., 2021, MNRAS, 501, 576

Hodgson T., Bartalucci I., Johnston-Hollitt M., McKinley B., Vazza F., Wittor D., 2021, ApJ, 909, 198
Hoeft M., et al., 2020, arXiv e-prints, p. arXiv:2010.10331
Hotan A. W., et al., 2014, PASA, 31, e041
Hotan A. W., et al., 2021, PASA, 38, e009
Hunter J. D., 2007, Computing in Science and Engineering, 9, 90
Hurley-Walker N., Hancock P. J., 2018, Astronomy and Computing, 25, 94
Hurley-Walker N., et al., 2017, MNRAS, 464, 1146
HyeongHan K., et al., 2020, ApJ, 900, 127
Ignesti A., Brunetti G., Gitti M., Giacintucci S., 2020, A&A, 640, A37
Johnston-Hollitt M., 2003, PhD thesis, University of Adelaide
Johnston-Hollitt M., Finoguenov A., Böhringer H., Pratt G., Croston J., 2007, Radio Imaging of an X-ray Luminosity Selected Galaxy Cluster Sample (C1683), https://atoa.atnf.csiro.au/
Johnston-Hollitt M., Basu K., Nord M., Hindson L., Shakouri S., 2013, A census of radio emission in a complete SZ-derived cluster sample (C2837), https://atoa.atnf.csiro.au/
Jones E., Oliphant T., Peterson P., et al., 2001, SciPy: Open source scientific tools for Python, http://www.scipy.org/
Kaiser N., et al., 2010, in Ground-based and Airborne Telescopes III. p. 77330E, doi:10.1117/12.859188
Kempner J. C., Blanton E. L., Clarke T. E., Enßlin T. A., Johnston-Hollitt M., Rudnick L., 2004, in Reiprich T., Kempner J., Soker N., eds, The Riddle of Cooling Flows in Galaxies and Clusters of galaxies. p. 335 (arXiv:astro-ph/0310263)
Keshet U., Waxman E., Loeb A., 2004, ApJ, 617, 281
Knowles K., et al., 2021, MNRAS, 504, 1749
Lee W., Jee M. J., Kang H., Ryu D., Kimm T., Brüggen M., 2020, ApJ, 894, 60
Liang H., Hunstead R. W., Birkinshaw M., Andreani P., 2000, ApJ, 544, 686
Martinez Aviles G., et al., 2016, A&A, 595, A116
Mazzotta P., Bourdin H., Giacintucci S., Markevitch M., Venturi T., 2011, Mem. Soc. Astron. Italiana, 82, 495
McConnell D., et al., 2016, PASA, 33, e042
McMullin J. P., Waters B., Schiebel D., Young W., Golap K., 2007, in Shaw R. A., Hill F., Bell D. J., eds, Astronomical Society of the Pacific Conference Series Vol. 376, Astronomical Data Analysis Software and Systems XVI. p. 127
Mohr J. J., Fabricant D. G., Geller M. J., 1993, ApJ, 413, 492
Murgia M., Govoni F., Markevitch M., Feretti L., Giovannini G., Taylor G. B., Carretti E., 2009, A&A, 499, 679
Murgia M., Govoni F., Feretti L., Giovannini G., 2010, A&A, 509, A86
Murphy T., Lenc E., Whiting M., Huynh M., Hotan A., 2019, ASKAP Data Products for Project AS111 (ASKAP Pilot Survey for Gravitational Wave Counterparts): images and visibilities. v1. CSIRO. Data Collection, http://hdl.handle.net/102.100.100/175570?index=1
Norris R. P., et al., 2011, PASA, 28, 215
Offringa A. R., Smirnov O., 2017, MNRAS, 471, 301
Offringa A. R., et al., 2014, MNRAS, 444, 606
Offringa A. R., et al., 2016, MNRAS, 458, 1057
Ogrean G. A., et al., 2015, ApJ, 812, 153
Orrú E., Murgia M., Feretti L., Govoni F., Brunetti G., Giovannini G., Girardi M., Setti G., 2007, A&A, 467, 943
Owers M. S., Nulsen P. E. J., Couch W. J., Markevitch M., Poole G. B., 2009, ApJ, 692, 702
Parekh V., Dwarakanath K. S., Kale R., Intema H., 2017, MNRAS, 464, 2752
Peebles P. J. E., 1980, The large-scale structure of the universe. Princeton Univ. Press, Princeton, N. J.
Piffaretti R., Arnaud M., Pratt G. W., Pointecouteau E., Melin J.-B., 2011, A&A, 534, A109
Planck Collaboration et al., 2016a, A&A, 594, A27
Planck Collaboration et al., 2016b, A&A, 594, A27
Planck Collaboration et al., 2016c, A&A, 594, A27
Poole G. B., Fardal M. A., Babul A., McCarthy I. G., Quinn T., Wadsley J., 2006, MNRAS, 373, 881
Pratt G. W., Croston J. H., Arnaud M., Böhringer H., 2009, A&A, 498, 361
Price-Whelan A. M., et al., 2018, AJ, 156, 123
Raja R., et al., 2020, MNRAS, 493, L28
Raja R., Rahaman M., Datta A., van Weeren R. J., Intema H. T., Paul S., 2021, MNRAS, 500, 2236
Rajpurohit K., et al., 2018, ApJ, 852, 65
Rajpurohit K., et al., 2020, A&A, 636, A30
Rajpurohit K., et al., 2021, A&A, 646, A135
Reichardt C. L., et al., 2013, ApJ, 763, 127
Robitaille T., Bressert E., 2012, APLpy: Astronomical Plotting Library in Python, Astrophysics Source Code Library (ascl:1208.017)
Santos J. S., Rosati P., Tozzi P., Böhringer H., Ettori S., Bignamini A., 2008, A&A, 483, 35
Sarazin C. L., 2002, The Physics of Cluster Mergers. pp 1–38, doi:10.1007/0-306-48096-4_1
Sault R. J., Teuben P. J., Wright M. C. H., 1995, in Shaw R. A., Payne H. E., Hayes J. J. E., eds, Astronomical Society of the Pacific Conference Series Vol. 77, Astronomical Data Analysis Software and Systems IV. p. 433 (arXiv:astro-ph/0612759)
Shakouri S., Johnston-Hollitt M., Pratt G. W., 2016, MNRAS, 459, 2525
Shimwel T., Stroe A., Hoang D., 2015, Ultra-deep observations to map the diffuse radio emission from a sample of merging galaxy clusters (C2915), https://atoa.atnf.csiro.au/
Shimwell T. W., Brown S., Feain I. J., Feretti L., Gaensler B. M., Lage C., 2014, MNRAS, 440, 2901
Slee O. B., Roy A. L., Murgia M., Andernach H., Ehle M., 2001, AJ, 122, 1172
Sokolowski M., et al., 2017, PASA, 34, e062
Song J., et al., 2012, ApJ, 761, 22
Stroe A., et al., 2016, MNRAS, 455, 2402
Struble M. F., Rood H. J., 1999, ApJS, 125, 35
Tingay S. J., et al., 2013, PASA, 30, 7
Tonry J. L., et al., 2012, ApJ, 750, 99
Vazza F., Wittor D., Brunetti G., Brüggen M., 2021, arXiv e-prints, p. arXiv:2102.04193
Venturi T., Giacintucci S., Brunetti G., Cassano R., Bardelli S., Dallacasa D., Setti G., 2007, A&A, 463, 937
Venturi T., Giacintucci S., Dallacasa D., Cassano R., Brunetti G., Bardelli S., Setti G., 2008, A&A, 484, 327
Wayth R. B., et al., 2015, PASA, 32, 25
Wayth R. B., et al., 2018, PASA, 35
Wilber A., et al., 2018, MNRAS, 473, 3536
Wilber A. G., Johnston-Hollitt M., Duchesne S. W., Tasse C., Akamatsu H., Intema H., Hodgson T., 2020, PASA, 37, e040
Wilson W. E., et al., 2011, MNRAS, 416, 832
Xie C., et al., 2020, A&A, 636, A3
de Gasperin F., van Weeren R. J., Brüggen M., Vazza F., Bonafede A., Intema H. T., 2014, MNRAS, 444, 3130
de Gasperin F., Ogrean G. A., van Weeren R. J., Dawson W. A., Brüggen M., Bonafede A., Simionescu A., 2015, MNRAS, 448, 2197
de Gasperin F., et al., 2017, Science Advances, 3, e1701634
van Weeren R. J., Röttgering H. J. A., Brüggen M., Hoeft M., 2010, Science, 330, 347
van Weeren R. J., et al., 2016, ApJ, 818, 204
van Weeren R. J., et al., 2017, Nature Astronomy, 1, 0005
van Weeren R. J., de Gasperin F., Akamatsu H., Brüggen M., Feretti L., Kang H., Stroe A., Zandanel F., 2019, Space Sci. Rev., 215, 16
van Weeren R. J., et al., 2020, arXiv e-prints, p. arXiv:2011.02387
van der Walt S., Colbert S. C., Varoquaux G., 2011, Computing in Science Engineering, 13, 22

A. *u–v* coverage plots

Fig. 11(i)–11(viii) shows *u–v* coverage (in λ, from -3000λ–3000λ) for the Abell 141 data used in this work, excluding MWA-1 data. Similarly Fig. 12(i)–12(ix) show the *u–v* coverage for observations of Abell 3404. We include these plots to highlight the coverage offered by both the MWA and ASKAP in comparison to ATCA and GMRT.

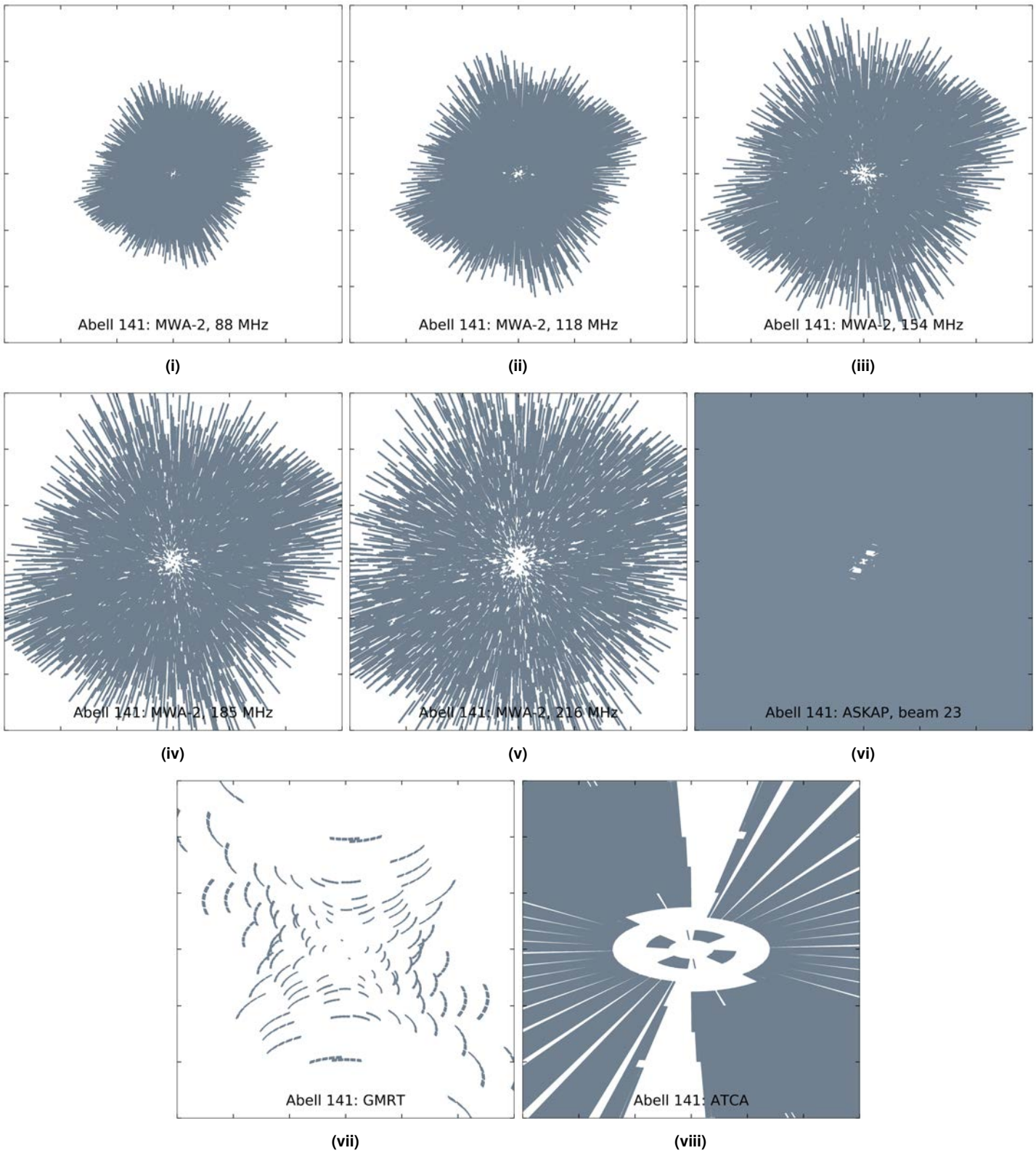

Figure 11. *u*–*v* coverage plots for Abell 141 data. Axes are centered on zero and range from -3000λ to 3000λ. Note that the MWA-2 data are of single 2-min snapshots, representative of the snapshot observations. The true *u*–*v* coverage is slightly more filled in. The observation used for the ASKAP example is SB15191.

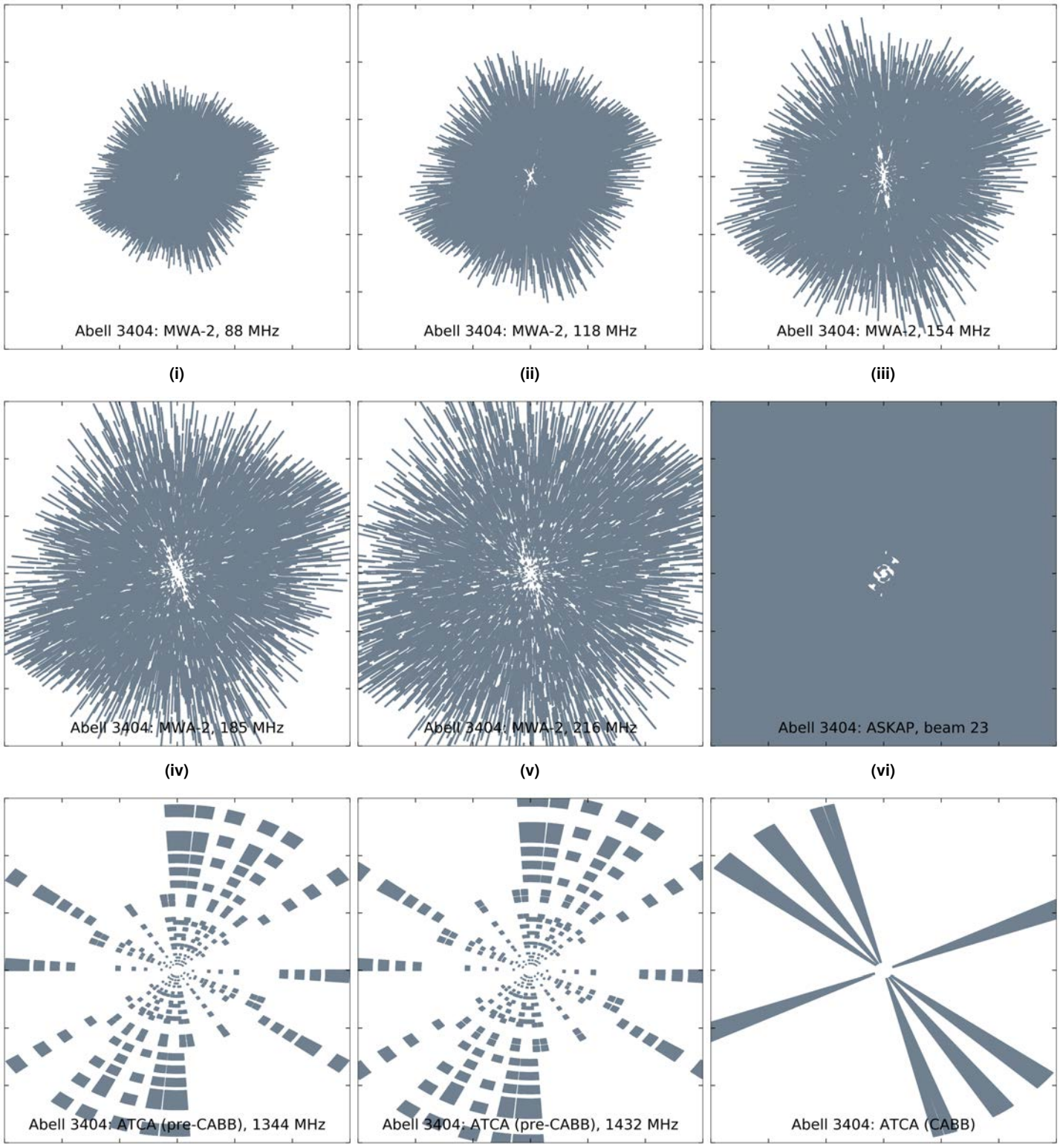

Figure 12. u–v coverage plots for Abell 3404 data. Axes are centered on zero and range from -3000λ to 3000λ.

Low-frequency integrated radio spectra of diffuse, steep-spectrum sources in galaxy clusters: palaeontology with the MWA and ASKAP

The paper titled '*Low-frequency integrated radio spectra of diffuse, steep-spectrum sources in galaxy clusters: palaeontology with the MWA and ASKAP*' is re-produced here in its form as accepted for publication in the Publications of Astronomical Society of Australia published by Cambridge University Press (CUP). The accepted article is re-produced with permission from Cambridge University Press [18] in line with the CUP 'Green Open Access' policy as agreed to in the signed License To Publish [19] prior to publication. Content is © The Author(s), 2021. Published by Cambridge University Press on behalf of the Astronomical Society of Australia. The version of record will be available through CUP at: https://doi.org/10.1017/pasa.2021.45. Contributions from Co-authors are outlined in the previous section. This accepted article also appears on arXiv.org at https://arxiv.org/abs/2103.08282. [20].

I recommend reading the version of this paper at https://arxiv.org/abs/2103.0828 as links between sections, figures, and appendices make navigating the paper easier and are non-functional in this re-produced version here and the version of record published by CUP.

[18] https://www.cambridge.org/about-us/rights-permissions/faqs/

[19] https://www.cambridge.org/core/services/open-access-policies/open-access-journals/green-open-access-policy-for-journals

[20] Note the appearance is slightly modified in the present version as an update to the PASA LaTeX template.

LaTeX document typeset by the authors from a modified LaTeX template from the *Publications of the Astronomical Society of Australia* (PASA).
Current document status: **accepted for publication in PASA: in press**.

Research Paper

Low-frequency integrated radio spectra of diffuse, steep-spectrum sources in galaxy clusters: palaeontology with the MWA and ASKAP

S. W. Duchesne [1]*, M. Johnston-Hollitt[1,2], and I. Bartalucci[3]
[1]International Centre for Radio Astronomy Research (ICRAR), Curtin University, Bentley, WA 6102, Australia
[2]Curtin Institute for Computation, Curtin University, GPO Box U1987, Perth, WA 6845, Australia
[3]INAF - Istituto di Astrofisica Spaziale e Fisica Cosmica di Milano, Via A. Corti 12, 20133 Milano, Italy

Abstract

Galaxy clusters have been found to host a range of diffuse, non-thermal emission components, generally with steep, power law spectra. In this work we report on the detection and follow-up of radio halos, relics, remnant radio galaxies, and other fossil radio plasmas in Southern Sky galaxy clusters using the Murchison Widefield Array and the Australian Square Kilometre Array Pathfinder. We make use of the frequency coverage between the two radio interferometers—from 88 to ∼ 900 MHz—to characterise the integrated spectra of these sources within this frequency range. Highlights from the sample include the detection of a double relic system in Abell 3186, a mini-halo in RXC J0137.2−0912, a candidate halo and relic in Abell 3399, and a complex multi-episodic head-tail radio galaxy in Abell 3164. We compare this selection of sources and candidates to the literature sample, finding sources consistent with established radio power–cluster mass scaling relations. Finally, we use the low-frequency integrated spectral index, α ($S_\nu \propto \nu^\alpha$), of the detected sample of cluster remnants and fossil sources to compare with samples of known halos, relics, remnants and fossils to investigate a possible link between their electron populations. We find the distributions of α to be consistent with relic and halo emission generated by seed electrons that originated in fossil or remnant sources. However, the present sample sizes are insufficient to rule out other scenarios.

Keywords: galaxies: clusters: general – large-scale structure of the Universe – radio continuum: general – X-rays: galaxies: clusters

1. Introduction

Clusters of galaxies are formed through often highly energetic merger events and accretion from filaments of the Cosmic Web. Clusters are comprised of constituent galaxies, X-ray emitting plasmas, and ∼ µG-level magnetic fields (Clarke et al., 2001; Johnston-Hollitt, 2003). In a fraction of clusters, large-scale (∼ 1 Mpc) steep-spectrum ($\alpha \lesssim -1$), diffuse radio emission is observed as centrally-located radio *halos* and peripherally-located radio *relics* (see van Weeren et al., 2019, and references therein). These large-scale synchtrotron-emitting sources are not thought to be presently fuelled by active galactic nuclei (AGN), rather they are assumed to be generated through in situ (re-)acceleration of particles (e.g. Jaffe, 1977; Enßlin et al., 1998). Such sources are observed in predominantly merging, or otherwise morphologically disturbed clusters (e.g. Buote, 2001; Brunetti et al., 2009; Cassano et al., 2010; Botteon et al., 2018; Golovich et al., 2019).

Radio *halos* are generally spatially correlated with the thermal, X-ray–emitting core of the cluster and are observed with morhpologies ranging from circular (e.g. Orrú et al., 2007; Murgia et al., 2009) to more complex and elongated structures (e.g. van Weeren et al., 2012). Radio halos are generally observed to have power law spectra, though some halos with significant spectral coverage show steepening beyond GHz frequencies (Thierbach et al., 2003; Xie et al., 2020; Rajpurohit et al., 2021c). Merger-driven turbulence in the ICM may provide a mechanism for in situ (re-)acceleration of seed particles from either the thermal pool of electrons or from a pre-accelerated population of mildly-relativistic 'fossil' electrons throughout the cluster volume (e.g. Brunetti et al., 2001; Buote, 2001; Brunetti & Jones, 2014).

Radio *relics* occur in the low-density cluster outskirts, where strong shocks in the intra-cluster medium (ICM) are thought to (re-)accelerate electrons through diffusive-shock acceleration (DSA; e.g. Enßlin et al. 1998, and similar processes; e.g. Kang 2015) either originating a 'fossil' electron population (e.g. Markevitch et al., 2005; Kang & Ryu, 2011, 2016) or accelerated from the thermal pool of electrons in the cluster (e.g. Enßlin et al., 1998; Hoeft & Brüggen, 2007). Unlike radio halos, relics are often observed with highly ordered, linearly polarized emission (e.g. Johnston-Hollitt, 2003; van Weeren et al., 2010; Pearce et al., 2017). The integrated spectra of relics are generally power laws (e.g. Hindson et al., 2014; Loi et al., 2017; Rajpurohit et al., 2020; Duchesne et al., 2021a), though few examples exist with curvature beyond GHz frequencies (e.g. Trasatti et al., 2015). In some cases, radio relics have been observed to be located co-spatially with X-ray shocks/surface brightness discontinuities (e.g. Finoguenov et al., 2010; Botteon et al., 2016a; Botteon et al., 2016b).

Along with the large-scale radio halos and relics, other diffuse, non-thermal sources have been observed in clusters with many observational and physical similarities (see e.g. van Weeren et al., 2019, for a review of source types and nomenclature). Radio *mini-halos* are $\lesssim$ 500 kpc synchrotron-emitting regions surrounding

*stefan.duchesne.astro@gmail.com
Where α is defined via $S_\nu \propto \nu^\alpha$.

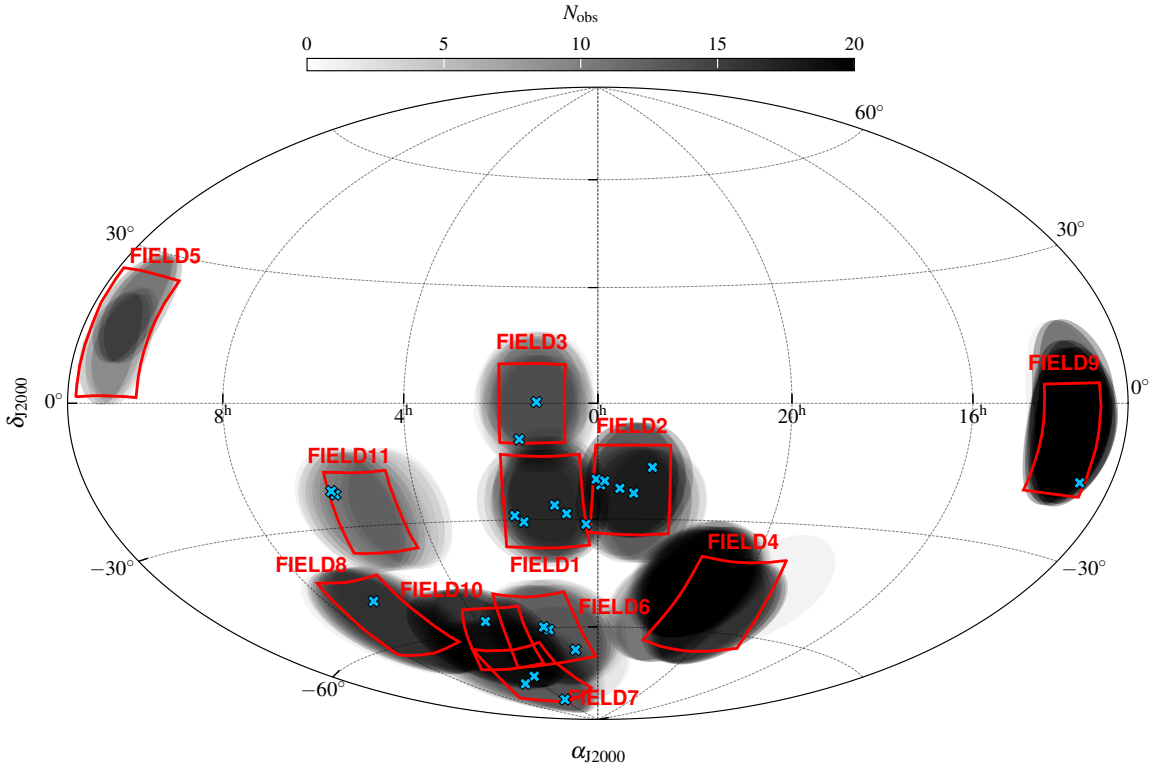

Figure 1. The sky coverage of the MWA-2 diffuse source follow-up survey, with named fields labelled and cluster targets reported in this work noted as blue 'x' marks. Actual MWA-2 pointings at 154 MHz are shown as transparent black circles, indicating relative sensitivity of fields. While no sources from either `FIELD4` or `FIELD5` are reported in this work (as discussed in the text) we show their locations for completeness.

AGN in the centres of some cool-core (CC) clusters (see e.g. Bravi et al., 2016; Giacintucci et al., 2019). Observationally, they appear as small radio halos with similar spectral and morphological properties but are thought to form via re-acceleration of AGN outflow from small-scale turbulence and sloshing within the cluster core (e.g. Gitti et al., 2002). Mini-halos are not typically associated with major mergers.

Beyond the cluster core, smaller-scale relic-like sources of various types are also found: radio *phoenices* or otherwise revived *fossil* sources have been observed (e.g. Slee et al., 2001; Cohen & Clarke, 2011; Giacintucci et al., 2020; Hodgson et al., 2021). These sources are typically on the order of a few hundred kpc in size and vary morphologically. They range from ultra-steep spectrum fossil plasmas that have possibly been revived via shock-driven adiabatic compression (e.g. Enßlin & Gopal-Krishna, 2001; Enßlin & Brüggen, 2002), radio galaxies with shocks passing through an outer lobe/tail, re-energising the radio plasma (e.g. gentle re-energisation; de Gasperin et al. 2017, or less-gentle processes; Bonafede et al. 2014; van Weeren et al. 2017), to true remnant radio galaxies with no evidence of re-energisation and are simply fading from normal energy losses after their AGN have switched off or have entered a low-power state (e.g. Parma et al., 2007; Murgia et al., 2011). Distinguishing between what are effectively radio galaxies at various stages through their life-cycle is difficult and in the case of radio phoenices often the hosting cluster does not show evidence of merger-driven shocks. Finally, in rare cases synchrotron-emitting bridges have been observed between cluster pairs (e.g. Govoni et al., 2019; Botteon et al., 2020a), likely formed through turbulence in the inter-cluster region (Brunetti & Vazza, 2020).

It is not yet clear whether the seed electrons responsible for radio halos and relics are from the thermal pool or from fossils that have diffused into the surrounding ICM—observations of spectra of such sources are beginning to provide answers (e.g. Rajpurohit et al., 2021c,b,a). The current generation of radio interferometers, including the Murchison Widefield Array (MWA; Tingay et al., 2013; Wayth et al., 2018), the Australian Square Kilometre Array Pathfinder (ASKAP; Hotan et al., 2021), the LOw Frequency ARray (LOFAR; van Haarlem et al., 2013), and MeerKAT (Jonas & MeerKAT Team, 2016) are beginning to uncover diffuse cluster sources at higher rates (e.g. Wilber et al., 2020; Duchesne et al., 2020; Di Gennaro et al., 2021; Brüggen et al., 2021; van Weeren et al., 2021; Knowles et al., 2021; Duchesne et al., 2021a; Hodgson et al., 2021; Duchesne et al., 2021b,c), providing unprecedented insight into cluster diffuse source populations, paving the way for future observations with the Square Kilometre Array (SKA). In this work we detail a targeted campaign to follow-up diffuse radio emission in clusters originally detected in MWA surveys, leveraging the wide bandwidth of the MWA to investigate the low-frequency integrated spectra of these sources.

Throughout this paper, we assume a standard Λ Cold Dark

Karoo Array Telescope

Matter cosmology with $H_0 = 70\ \mathrm{km\,s^{-1}\,Mpc^{-1}}$, $\Omega_\mathrm{M} = 0.3$, and $\Omega_\Lambda = 1 - \Omega_\mathrm{M}$. Unless otherwise stated, frequency subscripts and superscripts on quantities are in units of MHz.

2. Data & methods

2.1. *Cluster sample*

Duchesne et al. (2021b, hereafter D21) report a number of candidate diffuse cluster sources detected in a large, deep $45° \times 45°$ MWA image created for foreground modelling of the Epoch of Re-ionization 0-h field (Offringa et al., 2016). Due to the low resolution of the MWA, many of these sources had an uncertain nature. With the upgrade to the Phase 2 'extended' MWA (Wayth et al., 2018, hereafter MWA-2) and the allure of an increase in resolution by a factor of two, we carried out re-observation of a selection of these sources as part of MWA project G0045 with Director's Time observations of two additional fields and the addition of overlapping archival observations.

At the same time, a candidate list of diffuse cluster sources had been prepared based on visual searches of the GaLactic and Extragalactic MWA (GLEAM) survey (Wayth et al., 2015; Hurley-Walker et al., 2017). These searches focused on clusters from the Meta-Catalogue of X-ray detected Clusters (MCXC; Piffaretti et al., 2011), the Abell catalogues (Abell, 1958; Abell et al., 1989), *Planck* Sunyaev–Zel'dovich clusters (Planck Collaboration et al., 2015, 2016), and a handful of miscellaneous clusters serendipitously found to host candidate diffuse emission that are nearby other clusters from the aforementioned catalogues. While the full sample is not within the scope of this work (it would be prohibitive to perform targeted follow-up of close to 200 sources), we present here 31 sources across 9 fields [1]. Due to the large field of view of the MWA ($\sim$ 20 deg at 216 MHz and $\sim$ 60 deg at 88 MHz) we planned MWA-2 observations to cover a total 22 clusters (Table 1). While the 200-MHz wideband GLEAM image is usually sufficient to detect and measure flux density of these sources, the lower-frequency bands become prohibitively confused for use here. The fields observed (labelled `FIELD1`–`11`) are shown on Fig. 1. `FIELD5` and our target source within Abell 1127 were presented in Duchesne et al. (2020), while two sources from the current survey have already been reported: Abell 141 in `FIELD1` and Abell 3404 in `FIELD8` (Duchesne et al., 2021c). While generally we will not report non-detections (or more accurately, non-confirmations) from the non-public candidate list, we will, where available, report any such sources from D21 in Appendix A.

2.2. *Observations with the MWA-2*

For all fields, we observed a range of frequencies, mirroring the GLEAM survey frequency selections: 30-MHz instantaneous bandwidth observations centered on 88, 118, 154, 185, and 216 MHz. Observations are performed in the MWA-standard 'snapshot' observing mode, with 2-min drift-scan snapshots. Each snapshot is calibrated and imaged independently prior to stacking/mosaicking.

Processing of the MWA-2 data follow the recipe described in detail by Duchesne et al. (2020) making use of the purpose-built Phase II Pipeline (`piip`) with constituent software which will be briefly described. Individual snapshots are retrieved from the Pawsey Supercomputing Centre [2] archive using the MWA component of the All-Sky Virtual Observatory [3] which performs general pre-processing and initial RFI flagging with `AOFlagger` [4] (Offringa et al., 2015). After snapshots are retrieved and pre-processed, they are calibrated using an implementation of the `Mitchcal` algorithm (Offringa et al., 2016) using a global sky model as described in Duchesne et al. (2020). Imaging per snapshot is performed with `WSClean` [5] (version 2.9.0; Offringa et al., 2014; Offringa & Smirnov, 2017) using multi-scale CLEANing.

Final images are corrected for astrometry using `fits_warp.py` (version 2.0; Hancock et al., 2018) and the flux scale is set using `flux_warp` [6] (version 1.14). Both of these tools take an input sky model generated by cross-matching and spectral modelling of GLEAM, the NRAO [7] VLA [8] Sky Survey (NVSS; Condon et al., 1998) and/or the Sydney University Molonglo Sky Survey (SUMSS; Bock et al., 1999; Mauch et al., 2003; Murphy et al., 2007) using the Positional Update and Matching Algorithm (PUMA; Line et al., 2017). This sky model is in turn cross-matched to point sources in the snapshot image catalogues to calculate astrometric offsets and flux density discrepancies. Corrections are applied over the snapshots via interpolation between cross-matched sources. Finally, snapshot images are stacked to create mosaics as described in Duchesne et al. (2020). Flux density scale uncertainties are derived by comparing point source flux densities with the PUMA-generated sky model finding $\sim$ 2–10 per cent standard deviation across the observed fields and frequencies. An additional 8 per cent is added in quadrature as inherited from the GLEAM survey, which dominates the flux densities in the sky model. Bulk image details are presented in Table 2.

The 'extended' configuration of the MWA was created with the same number of tiles (i.e. 128) as the Phase I MWA due to limitations of the current correlator. Creating the longer baselines of the MWA-2 therefore required removing a significant number of short baselines, reducing the sensitivity to larger angular scales compared to the Phase I MWA (Hodgson et al., 2020). While the loss of sensitivity for this work is comparatively minimal, we still find that images weighted with a 'Briggs' (Briggs, 1995) robust parameter of $\lesssim +0.5$ begin to significantly lose large-scale flux. Therefore, for flux density measurements we create at set of robust +2.0 images for all fields except `FIELD11` for which we use robust +1.0 [9]. We also create images at 0.0 and +0.5 to leverage the

[1] A total of 11 fields were observed, 1 is presented in Duchesne et al. (2020), and one was not able to be processed.

[2] https://pawsey.org.au/

[3] https://asvo.org.au/

[4] https://gitlab.com/aroffringa/aoflagger

[5] https://gitlab.com/aroffringa/wsclean

[6] https://gitlab.com/Sunmish/flux_warp

[7] National Radio Astronomy Observatory

[8] Very Large Array

[9] There is no functional difference between the robust +1.0 and +2.0 weighting for the MWA-2 data with respect to image resolution and sensitivity, however, the `FIELD11` data were processed at an earlier date for a separate project while more recent data-processing is done at +2.0.

Table 1 Clusters and sources discussed in this work.

Cluster	FIELD	α_{J2000} [1] (J2000)	δ_{J2000} [1] (J2000)	z	M_{500} [2] ($\times 10^{14}$ $M_\odot$)	Type [3]	Ref. [4]
Abell 0122	1	00:57:24	−26:16:50	0.113	1.73	r/F	(a)/(e)/(c)/(d)
Abell 2751	1	00:16:20	−31:21:55	0.107	1.26	r/F	(a)/(b)/(c)/(d)
Abell 2811	1	00:42:09	−28:32:09	0.108	$3.67^{+0.35}_{-0.37}$	cH	(a)/(e)/(f)/(d)
Abell 2496	2	22:51:00	−16:24:24	0.123	$3.36^{+0.30}_{-0.32}$	r	(a)/(b)/(w)/(d)
Abell 2680	2	23:56:28	−21:02:18	0.190	$3.2^{+0.8}_{-1.0}$	cH	(a)/(h)/(i)/(d)
Abell 2693	2	00:02:10	−19:33:18	0.173	$2.1^{+0.5}_{-0.6}$	cH/p	(a)/(h)/-/(d)
Abell S1099	2	23:13:16	−23:08:40	0.110	-	r	(j)/(k)/-/(d)
AqrCC 087	2	23:31:30	−21:55:00	-	-	F	(k)/-/-/-
RXC J2351.0−1954	2	23:51:07	−19:58:52	0.248	$5.60^{+0.59}_{-0.62}$	p, r/F, U	(l)/(l)/(f)/(d)
Abell 0168	3	01:15:12	+00:19:48	0.045	$1.87^{+0.29}_{-0.31}$	R	(a)/(b)/(f)/(m)
RXC J0137.2−0912	3	01:37:15	−09:12:10	0.039	0.95	mH, RG	(n)/(n)/(c)/-
Abell S0112	6	00:57:48	−66:48:44	0.067	1.62	F	(j)/(o)/(c)/-
MCXC J0145.2−6033	6	01:45:12	−60:33:45	0.180	$3.55^{+0.42}_{-0.44}$	cmH	(p)/(p)/(f)/-
MCXC J0154.2−5937	6	01:54:15	−59:39:38	0.360	1.41	cGRG	(q)/(q)/(c)/-
Abell 3186	7	03:52:30	−74:01:51	0.127	$6.44^{+0.24}_{-0.24}$	R, R, cH	(j)/(b)/(f)/-
Abell S0405	7	03:51:09	−82:13:00	0.061	$2.51^{+0.20}_{-0.21}$	r	(j)/(r)/(f)/-
PSZ1 G287.95−32.98	7	04:59:38	−75:47:48	0.250	$5.88^{+0.40}_{-0.41}$	cH	(f)/(s)/(f)/-
Abell 3399	8	06:37:19	−48:28:42	0.203	$4.81^{+0.37}_{-0.39}$	cR, cH	(j)/(t)/(f)/-
MCXC J1253.2−1522	9	12:53:14	−15:22:48	0.046 [5]	0.98	F	(c)/(c)/(c)/-
Abell 3164	10	03:46:10	−57:03:00	0.059	$1.62^{+0.26}_{-0.28}$	F, F, F	(j)/(u)/(f)/-
Abell 3365	11	05:48:50	−21:54:43	0.093	1.66	R, U	(j)/(b)/(c)/(v)
Abell 0550	11	05:52:52	−21:03:25	0.099	$3.87^{+0.25}_{-0.27}$	r	(a)/(r)/(w)/-

[1] Coordinates are shown in units of hours, minutes, seconds, and degrees, arcminutes, arcseconds.
[2] Mass within R_{500}, the radius within which the mean density of the cluster is 500 times the critical density of the Universe.
[3] Detected diffuse source types (either as reported in the literature or as determined in this work): relic (R), halo (H), mini-halo (mH), remnant radio galaxy/AGN (r), miscellaneous fossil plasma/re-accelerated fossil plasma source (e.g. phoenix) (F), candidate (c), point source (p), normal radio galaxy (RG), giant radio galaxy (GRG), unclassified (U).
[4] References for position/z/M_{500}/previously detected diffuse emission: (a) Abell (1958). (b) Struble & Rood (1999). (c) ($M_{X,500}$) Piffaretti et al. (2011). (d) Duchesne et al. (2021b). (e) Zaritsky et al. (2006). (f) ($M_{SZ,500}$) Planck Collaboration et al. (2015). (g) Cavagnolo et al. (2008). (h) Coziol et al. (2009). (i) Wen & Han (2015). (j) Abell et al. (1989). (k) Caretta et al. (2002). (l) Chon & Böhringer (2012). (m) Dwarakanath et al. (2018). (n) Cruddace et al. (2002). (o) Garilli et al. (1993). (p) Schwope et al. (2000). (q) Vikhlinin et al. (1998). (r) De Grandi et al. (1999). (s) Planck Collaboration et al. (2014). (t) Böhringer et al. (2004). (u) Fleenor et al. (2006). (v) van Weeren et al. (2011). (w) Planck Collaboration et al. (2016).
[5] A second system (Abell 1631) is detected at $z = 0.014$ (Coziol et al., 2009)—see cluster entry in Section 3.1 for details.

resolution increase, though these images are typically used for morphological reference only, unless otherwise noted. Fig. 27(i)–(ix) in Appendix D highlight the 'dirty flux' bias introduced due to the snapshot stacking method used which is corrected as described in Section 2.1.2 of Duchesne et al. (2021c). Final imaging details are collected in Table 2. Note FIELD5 was published in Duchesne et al. (2020) and no further sources have been detected in that field so is not discussed here. FIELD4 suffered from significant sidelobe contamination from Cygnus A with the 185- and 216-MHz bands rendered unusable and will not be considered until future observations can be made when Cygnus A is not present in the primary beam sidelobe [1].

2.3. *ASKAP survey data*

2.3.1. *Data and re-processing*

The Rapid ASKAP Continuum Survey (McConnell et al., 2020) at 887 MHz covers the entire sky below $\delta_{J2000} \sim +30°$ and covers all clusters in our sample. The survey has a resolution of ∼ 15 arcsec and noise of ∼ 250–400 μJy beam^{-1}. This imaging is sufficient in most cases to detect discrete source populations within the emission regions in the MWA data. ASKAP data (images and calibrated visibilities) are publicly available through the CSIRO ASKAP Science Data Archive (CASDA; Chapman et al., 2017; Huynh et al., 2020). RACS data products are available under project AS110 (Hotan et al., 2020a).

We are able to obtain slightly higher sensitivity in the RACS images by re-imaging with a robust +0.25 weighting using WSClean which has the added benefit of enhancing any detected diffuse

[1] Note that Cygnus A appeared with an apparent flux of ∼ 800 Jy beam^{-1} at 185 MHz on the horizon for these observations so proved particularly resistant to subtraction/peeling techniques. While images were eventually made, residual errors remain which made the images unusable for this work.

[2] Commonwealth Scientific and Industrial Research Organisation

Table 2 MWA-2 and ASKAP observation and image details. Note due to the large number of separate images produced, there is a large range of values and here we report the minimum and maximum values for each quantity for each field. Exact PSF values used in measurements are provided as part of the online table described in Appendix B.

Field/Name/Project	ν (MHz)	Weighting	τ [a] (min)	PSF [b] ($'' \times ''$)	min($\sigma_{\rm rms}$) (mJy beam^{-1})	$\theta_{\rm max}$ ($'$)
MWA-2 [f]						
FIELD1 [c]	88–216	+2.0	68(56)	$91 \times 65(230 \times 160)$	2.0(8.3)	90
FIELD2		+2.0	62(88)	$94 \times 68(222 \times 165)$	1.4(7.9)	120
		+0.5	60(86)	$60 \times 60(150 \times 148)$	0.83(5.4)	90
FIELD3		+2.0	22(66)	$100 \times 66(248 \times 157)$	3.0(10.9)	120
		0.0	30(46)	$60 \times 53(152 \times 126)$	2.3(7.1)	120
FIELD6		+2.0	24(42)	$63 \times 51(229 \times 145)$	2.3(10.3)	90
		0.0	24(42)	$63 \times 51(145 \times 118)$	2.4(9.7)	90
FIELD7 [c]		+2.0	64(94)	$128 \times 67(321 \times 161)$	4.0(12.2)	120
		0.0	56(86)	$67 \times 52(162 \times 125)$	2.3(7.0)	120
FIELD8 [e]		+2.0	64(94)	$128 \times 67(321 \times 161)$	3.1(16.1)	120
FIELD9		+2.0	124(198)	$96 \times 67(235 \times 163)$	2.0(10.0)	90
		0.0	200(216)	$59 \times 53(140 \times 126)$	1.2(6.1)	120
FIELD10 [c]		+2.0	64(94)	$103 \times 67(254 \times 161)$	2.6(9.9)	120
FIELD11		+1.0	36(38)	$79 \times 61(194 \times 148)$	1.5(9.6)	90
ASKAP [g]						
RACS	887	+0.25	15	$14.5 \times 14.5(22 \times 22)$	0.12(0.18)	10
		0.0	15	$12 \times 12(16 \times 16)$	0.16	10
		+0.25, tapered	15	$39 \times 39(90 \times 90)$	0.31(0.60)	10
VAST	887	+0.25	60	16×16	0.10	20
		0.0	60	13×13	0.075	20
		+0.5, taper	60	50×50	0.16	20
SB25035	887	+0.25	780	21×21	0.25	20
		+0.25, taper	780	60×60	0.70	20
SB15191	943	+0.25	595	12.8×12.8	0.026	20

[a] Range of total stacked times for MWA snapshots, though note that effective sensitivity varies over the map due to mixed primary beam pointings/patterns. For ASKAP observations, this is simply integration time.
[b] Range of major and minor axes of the PSF at the centre of the stacked images for the various images/frequencies.
[c] Alternate imaging published in Duchesne et al. (2021c).
[d] FIELD7 and FIELD10 have significant enough overlap that they are combined for a joint FIELD7+FIELD10 for increased sensitivity, though two individual maps are made centered on each field.
[e] Alternate imaging for this field published in Brüggen et al. (2021) and Duchesne et al. (2021c).
[f] For MWA-2 observations, all fields are observed at 88, 118, 154, 185, and 216 MHz, and in general resolution increases with frequency, sensitivity peaks at 154 MHz except for zenith fields where sensitivity peaks at 216 MHz, and integration time varies across frequencies due to difference in data lost to ionospheric problems or other calibration problems. As discussed in the text, FIELD4 and FIELD5 are not presented in this work.
[g] All ASKAP data are re-imaged.

emission with only a minor loss in resolution. For clusters where discrete sources are strong enough to be subtracted using a suitable u, v cut (ranging from 1700–3000λ, additionally see Knowles et al. 2021 for some discussion of this problem), we subtract discrete sources and re-image with additional tapering—dependent on the scale of the emission—at a robust +0.25 image weighting. For a selection of observations where point sources are either too faint or non-existent, a low-resolution image is made without additional subtraction and intervening source contributions (if any) are subtracted from the flux density measurements. As a quick quality assurance check, we compare any re-processed maps to the RACS survey images and find no significant discrepancies in astrometry or flux scale.

Two clusters in our sample also benefit from being within archival ASKAP observations performed for the ASKAP survey for Variability And Slow Transients (VAST; Murphy et al., 2013) under pilot project AS107 (Murphy et al., 2020). The set up for these observations is similar to RACS, except they have 5–6 $\sim$ 15 min identical pointings which we combine and image as above. These data have some overlap in u, v coverage, so the additional u, v coverage is typically only equivalent to 2–3 additional 15-min observations. Source-subtraction is done in the combined visibilities

and flux densities of points sources are equivalent to within a few per cent of RACS data at the location of the VAST observations.

Abell 0122 features at the centre of a beam in a deep observation, SB25035 (Murphy et al., 2019) . These data are processed identically to images presented of Abell 0141 by Duchesne et al. (2021c) and no flux scale discrepancy is observed. Due to the smaller size of the emission, no low-resolution image is made.

Finally, a single cluster, Abell 3186, is present outside of the full width at half maximum (FWHM) of some beams in a deep, 12-h observation near the Large Magellanic Cloud (SB25035; Hotan et al., 2020b). As the primary beam is not well modelled by a simple 2-d Gaussian $\sim$ 2 deg away from the beam centre, we instead cross-match sources in the image to a catalogue derived from the RACS image in the region, and create a pseudo primary beam correction using `flux_warp` with a linear radial basis function interpolation scheme. This results in flux densities of the surrounding point sources that do not different by more than $\sim$ 10 per cent from RACS. While the point source sensitivity of this image is comparable to the 15-min RACS image, the inner u, v sampling is denser due to the longer synthesis rotation allowing better recovery of extended emission.

While the deep ASKAP observations have a well-sampled u, v plane, as discussed by McConnell et al. (2020), the short $\sim$ 15-min observations performed for RACS do not allow significant sampling of the inner u, v plane due to lack of significant Earth-rotation synthesis (see e.g. their Figure 4 for an example of the u, v coverage, and see e.g. Figure 2 from Duchesne et al. 2021a for an example of the u, v coverage for a 10-h ASKAP observation). While in principle structures up to $\sim$ 10 arcmin can be recovered, the lower sensitivity at this large angular scale only allows the brightest large-scale objects to be recovered fully. Generally the sources we will discuss in this work are sufficiently small to not be heavily affected (with some exceptions, noted where appropriate) and measurements typically agree with spectra obtained from MWA-2 data alone.

General ASKAP imaging details are presented in Table 2, and as with the MWA-2 data a range of imaging properties are reported for the various RACS images made. For non-RACS images, we report the exact properties.

2.4. *Spectral properties*

2.4.1. Intervening source contributions

Due to the low resolution of the MWA (even in its extended configuration) we have to carefully consider contamination from confusing sources. The two main scenarios we consider are case (1) brighter sources blended with the diffuse emission, and/or case (2) faint underlying/intervening sources within the detected MWA emission. Case (1) is simple in the sense that bright sources are easily detected with low resolution surveys such as the NVSS or SUMSS, both with $\sim$ 45 arcsec resolution, or the TIFR GMRT Sky Survey (TGSS; Intema et al., 2017) with $\sim$ 25 arcsec resolution. The RACS survey data are suitable for this purpose also, and the MWA-2 and GLEAM data can also be useful in this case.

In case (1), we can generally detect these brighter sources across multiple frequencies and model their spectra to remove their contribution in the MWA images, fitting a normal power law model of the form

$$S_{\nu,\mathrm{discrete}} = S_{0,\mathrm{discrete}} \, (\nu/\nu_0)^{\alpha} \ , \tag{1}$$

for extrapolation to $S_{\nu,\mathrm{discrete}}$ from a measured flux density $S_{0,\mathrm{discrete}}$. For sources with only two measurements we derive a two-point spectral index rearranging Eq. (1). We did not encounter any intervening discrete sources that required more complex spectral energy distribution (SED) modelling. Uncertainty in the initial discrete source measurements and spectral index are propagated to the extrapolated value.

Case (2) typically involves sources that are only detected in RACS or other higher-resolution data due to the relative sensitivities of the various low-resolution surveys. If multiple data sets are available, we model the SED as above to extrapolate discrete source flux densities at MWA frequencies. For sources without spectral coverage, we assume a spectral index. Typically this is assumed to be $\langle\alpha\rangle = -0.7$, though for some sources we note a non-detection in some MWA-2 bands/TGSS imply flatter spectra and modify the assumed spectral index appropriately. We use a range of α to estimate additional uncertainty in the unknown spectral index, via:

$$S_{\nu,\mathrm{discrete}} = S_{0,\mathrm{discrete}} \nu^{\langle\alpha\rangle} \pm \sigma_{S_{\nu,\mathrm{discrete}}} \quad [\mathrm{Jy}] \, , \tag{2}$$

and

$$\sigma_{S_{\nu,\mathrm{discrete}}} = S_{0,\mathrm{discrete}} \| \nu^{\alpha_{\mathrm{min}}} - \nu^{\alpha_{\mathrm{max}}} \| \quad [\mathrm{Jy}] \, , \tag{3}$$

where $\alpha_{\mathrm{min}} = -1.0$ and $\alpha_{\mathrm{max}} = -0.5$, typically, though may be chosen to reflect limits on point source contributions as seen in TGSS or MWA images. For each source, we report the total confusing flux density contributions that are subtracted, along with associated uncertainty in the online table (see Appendix B for details of the online table).

2.4.2. Flux density measurements

Flux density measurements are predominantly made using the lower-resolution robust +2.0/+1.0 images along with the GLEAM 200-MHz image and select ASKAP images. For certain sources/fields MWA-2 robust 0.0/+0.5 images are used to maximise the signal-to-noise ratio (SNR) for smaller sources. Flux density measurements are performed using in-house code, `fluxtools.py` by integration over a bespoke polygon region enclosing the source at all frequencies. This means the region is large enough to enclose the emission seen in the lowest-resolution images (usually the 88-MHz maps).

As the MWA-2 images are only CLEANed to the noise level in the individual 2-min snapshots, additional consideration is made for the un-deconvolved/'dirty' flux density contribution in the final stacked images. As described in Duchesne et al. (2021c), the measurement of flux density may not be consistent before and after

Additional observations are also available, however, the sensitivity in the single observation used here is sufficient and sensitivity improves only moderately with the additional observations.

Tata Institute for Fundamental Research

Giant Metrewave Radio Telescope

https://gist.github.com/Sunmish/198ef88e1815d9ba66c0f3ef3b18f74c,

CLEANing, and the measurement process has the added complexity of normalising the residual, 'dirty' flux density to the CLEAN flux density. Fig. 27(i)–(ix) in Appendix D show this effect for simulated Gaussian sources of varying size, highlighting the dependence on source size.

Flux density measurements, S_ν, can therefore be described by

$$S_\nu = \begin{cases} S_{\rm CLEAN} + S_{\rm dirty}/f - S_{\nu,\rm discrete}, & \text{for MWA-2} \\ S_{\rm image} - S_{\nu,\rm discrete}, & \text{otherwise} \end{cases} \quad (4)$$

where $S_{\rm CLEAN}$ is the contribution from the stacked CLEAN component model, $S_{\rm dirty}$ is contribution from the stacked residual map, f is the model ratio $\overline{S_{\rm dirty}/S_{\rm CLEAN}}$ determined from simulated Gaussian sources, dependent on source size (Fig. 27(i)–(ix)), and $S_{\rm discrete}$ is the contribution from intervening discrete sources. For the non-MWA-2 images, $S_{\rm image}$ is measured directly from the restored images.

The uncertainty on the flux density measurement, σ_{S_ν}, is estimated as the quadrature sum of the various sources of uncertainty following

$$\sigma_{S_\nu} = \Big[(\sigma_{\rm scale} S_\nu)^2 + (\sigma_{\rm discrete})^2 + N_{\rm beam}\,(\sigma_{\rm rms})^2 + \left(\sigma_{{\rm std},f}\, S_{\rm dirty}\right)^2 \Big]^{0.5}, \quad (5)$$

where $\sigma_{\rm scale}$ is the flux scale uncertainty for the image, $\sigma_{{\rm std},f}$ is the standard deviation in values of f over all snapshots for a given stacked MWA-2 image, $\sigma_{\rm discrete}$ is the uncertainty in the subtracted discrete source contribution, and $N_{\rm beam}$ is the number of independent restoring beams that cover the polygon region used for measurement. Typically the $\sigma_{\rm scale}$ term dominates, as this is $\sim$ 8–10 per cent for all MWA and ASKAP images. The $\left(\sigma_{{\rm std},f}\, S_{\rm dirty}\right)^2$ term is only included for MWA-2 images.

2.4.3. *Spectra and spectral indices*

The measured flux densities and uncertainties are used for modelling the integrated spectra within the observed frequency range. For sources with only MWA-2 data, we find a normal power law (as in Eq. 1) describes the data sufficiently well and provides a spectral index for the source. For sources where additional flux density measurements are available, we find a mixture of power law and curved power law models can be used to describe the observed spectra. We use a generic curved power law model of the form (Duffy & Blundell, 2012)

$$S_\nu \propto \nu^\alpha \exp\left[q\,(\ln \nu)^2\right], \quad (6)$$

where q gives an indication of curvature in the spectrum. For each source we provide a fitted power law model or a curved power law model if appropriate, with the combined MWA-2 and supplementary data. An additional power law model is fit solely to the MWA-2 measurements providing a low-frequency spectral index. Model parameters and uncertainties are estimated via non-linear weighted least-squares curve fitting with the Levenberg–Marquardt algorithm and we report 1σ uncertainties.

Though note in low-SNR cases curvature could be hidden in the noise.

Table 3 X-ray observation properties.

Cluster name	Obs. ID	Exp. time [a] (ks)
RXC J0137.2−0912	0765001101	14.4
Abell S0112	0653880201	42.3
MCXC J0154.2−5937	0109460201	6.3
Abell 3186	0692931401 0723161201	22
Abell S0405	0720250601	8
PSZ1 G287.95−32.98	0762800101	15
Abell 3399	0692933101 [b]	25
Abell 0550	0675470101 0720250101	17

[a] Exposure time after the cleaning procedures described in Section 2.5.
[b] *Chandra* dataset.

2.5. *Archival X-ray observations*

X-ray datasets used in this work were taken using the XMM-*Newton* European Photon Imaging Camera (EPIC, Turner et al. 2001 and Strüder et al. 2001) except for the observation of Abell 3399 which was taken using the Advanced CCD Imaging Spectrometer (ACIS, Garmire et al. 2003) on board of the *Chandra* observatory. The details of data reduction can be found in the Appendix A of Bartalucci et al. (2017). We used the same reduction and cleaning procedures but updated versions of the *Chandra* and XMM-*Newton* analysis software `CIAO` (Fruscione et al., 2006) ver. 4.11 with CALDB 4.8.5 and `SAS` (ver. 15.0) with CCF updated up to March 2021, respectively. The useful exposure times after the cleaning procedures and the observations used are reported in Table 3. The datasets were then arranged in data-cubes and corresponding exposure and background maps were calculated as detailed in Bourdin & Mazzotta 2008, Bourdin et al. 2013 and Bogdán et al. 2013. Point sources were detected using the technique described in Bogdán et al. 2013, visually inspected for false positives or missed sources and then removed from the analysis. Exposure-corrected and background subtracted images are produced in the [0.5–2.5] keV band.

2.6. *Additional survey data*

In addition to the already discussed radio survey images (NVSS, TGSS, SUMSS, and GLEAM), we make use of images from the *ROSAT* All Sky Survey (RASS; Voges et al., 1999) for select clusters without deep *Chandra* or XMM-*Newton* observations and optical data from the SuperCOSMOS Sky Survey (SSS; Hambly et al., 2001a,b,c), the first Pan-STARRS survey (PS1; Tonry et al., 2012; Chambers et al., 2016), and the Dark Energy Survey Data Release 2 (DES DR2; Abbott et al., 2018; Morganson et al., 2018; Flaugher et al., 2015, hereafter DES).

RÖentgen SATellite
Panoramic Survey Telescope And Rapid Response System

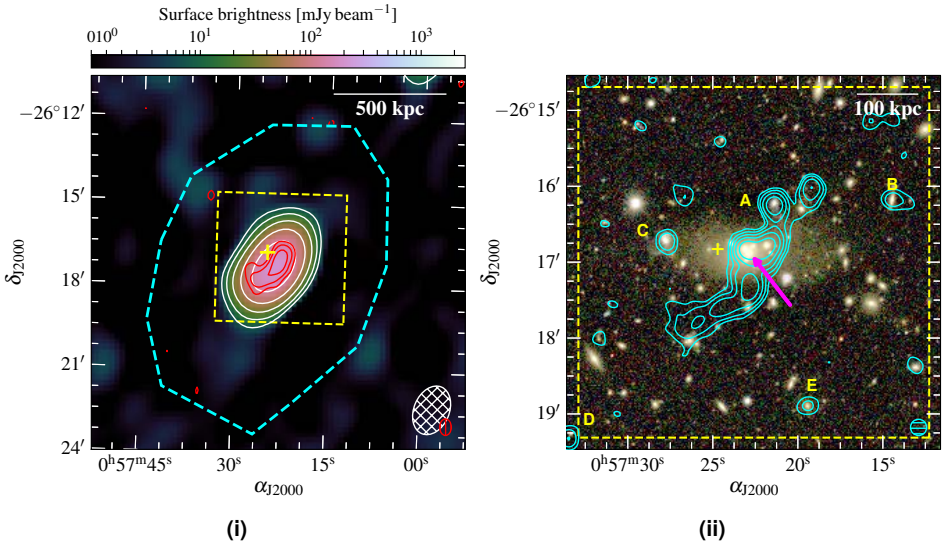

Figure 2. Abell 0122. (i). Background: MWA-2, 185 MHz, robust +2.0 image. (ii). Background: RGB DES image (i, r, g). Where relevant, the white contours are from the background image in (i), in levels of $[\pm3, 6, 12, 24, 48] \times \sigma_{\rm rms}$ ($\sigma_{\rm rms}$ = 2.5 mJy beam^{-1}). Red contours: TGSS image, in levels of $[\pm3, 6, 12, 24, 48] \times \sigma_{\rm rms}$ ($\sigma_{\rm rms}$ = 4.5 mJy beam^{-1}. Cyan contours: deep ASKAP robust +0.25 image, in levels of $[\pm3, 6, 12, 24, 48] \times \sigma_{\rm rms}$ ($\sigma_{\rm rms}$ = 0.026 mJy beam^{-1}). The dashed, yellow box is identical in both panels. The ellipses in the lower corners correspond to the respective beams. Sources discussed in the text are labelled. Linear scale bars are at the redshift of the cluster. The magenta arrow points towards the brightest cluster galaxy (BCG). The yellow cross indicates the reported cluster centre, and the dashed cyan polygon indicates the region used for flux density measurement.

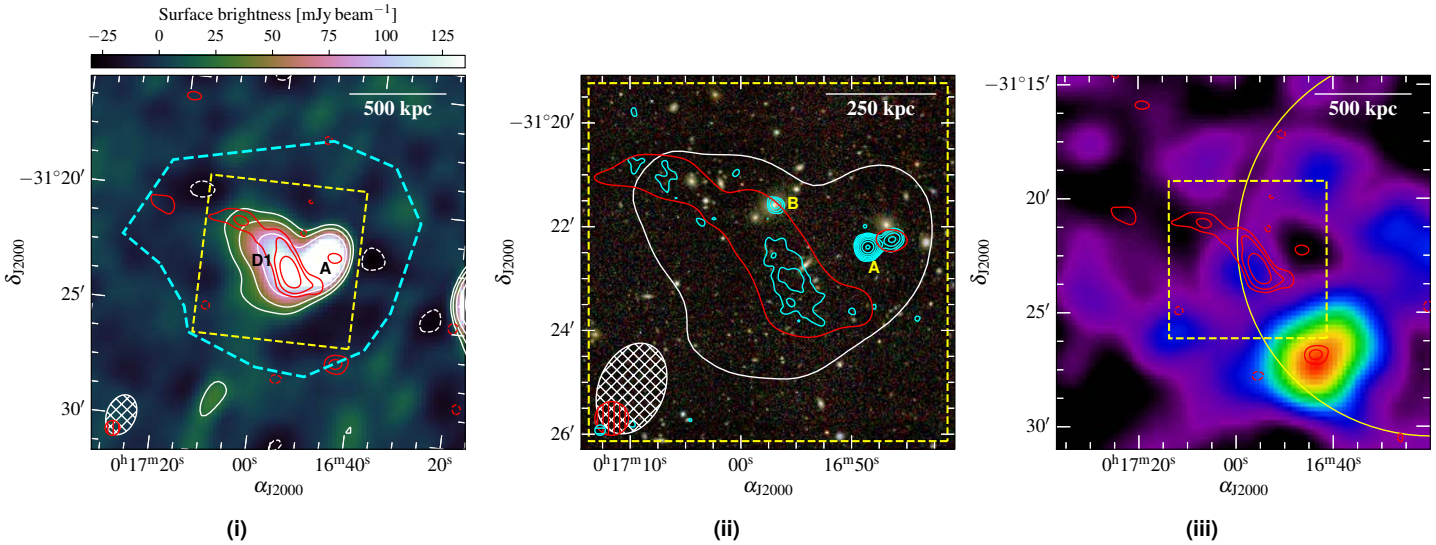

Figure 3. Abell 2751. (i). Background: MWA-2, 185 MHz, robust +2.0 image. (ii). Background: RGB DES image (i, r, g). (iii). Background: Smoothed RASS image. The white contours are as in Fig. 2(i) for the background of (i) ($\sigma_{\rm rms}$ = 7 mJy beam^{-1}), except in (ii) with a single contour at $3\sigma_{\rm rms}$. Red contours: RACS discrete source-subtracted image, $[\pm3, 6, 12, 24, 48] \times \sigma_{\rm rms}$ ($\sigma_{\rm rms}$ = 0.44 mJy beam^{-1}), except in (ii) with a single contour at $3\sigma_{\rm rms}$. Cyan contours: RACS robust +0.25 image, $[\pm3, 6, 12, 24, 48] \times \sigma_{\rm rms}$ ($\sigma_{\rm rms}$ = 0.2 mJy beam^{-1}). The yellow circle in (iii) has a 1 Mpc radius centered on the reported cluster coordinates. Other features are as in Fig. 2.

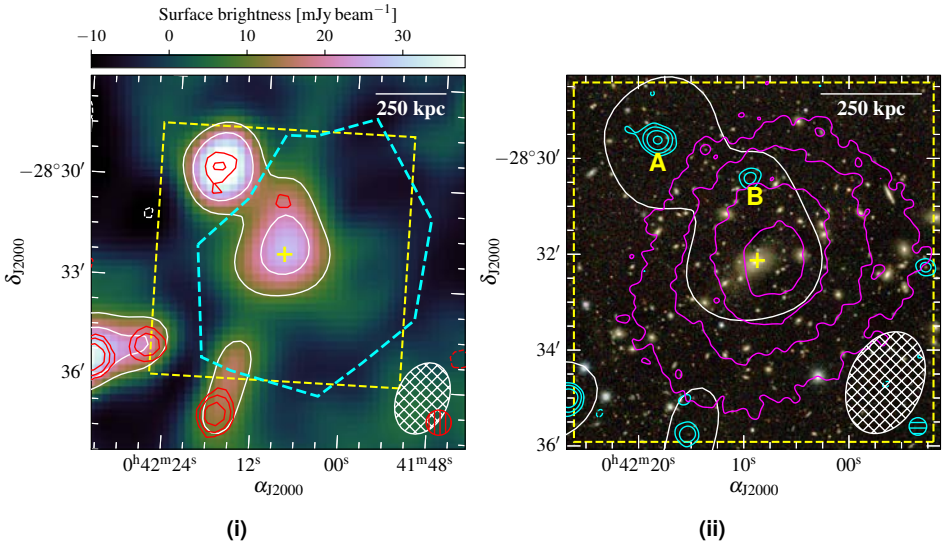

Figure 4. Abell 2811. (i). Background: MWA-2, 154 MHz, robust +2.0 image. (ii). Background: RGB DES image (i, r, g). The white contours are as in Fig. 2(i) for the background of (i) (for $\sigma_{\rm rms}$ = 3.5 mJy beam^{-1}). Red contours: NVSS image, in levels of $[\pm3, 6, 12, 24, 48] \times \sigma_{\rm rms}$ ($\sigma_{\rm rms}$ = 0.45 mJy beam^{-1}. Cyan contours: RACS robust +0.25 image, in levels of $[\pm3, 6, 12, 24, 48] \times \sigma_{\rm rms}$ ($\sigma_{\rm rms}$ = 0.17 mJy beam^{-1}). Magenta contours: exposure-corrected, background-subtracted XMM-*Newton* data as presented in D21. Other image features are as in Fig. 2.

3. Results

3.1. *Individual clusters*

In this section we will describe the individual clusters ordered by observed field. Individual plots of source SEDs are shown in Appendix C and measurements for cluster sources are provided as an online table described in Appendix B.

3.1.1. FIELD1

Abell 0122. (Fig. 2). Reported by D21 as an unclassified steep spectrum source. The source is detected in the MWA-2, TGSS, and deep ASKAP data, shown in Fig. 2(i) and Fig. 2(ii). The deep ASKAP data show a complex source with additional point source contributions (labelled in Fig. 2(ii)) and with contribution from what may be the core of the emission, the brightest cluster galaxy (BCG) (6dF J0057228−261653; Jones et al. 2009) indicated by a magenta arrow in Fig. 2(ii). The projected extent of the source is ∼ 2.6 arcmin (corresponding to ∼ 310 kpc), including the protrusion to the West of Source A. This is slightly smaller than that reported by D21 due to less source blending. The SED between 88–943 MHz is shown in Fig. 26(i), finding curvature between the MWA and ASKAP data after subtraction of the labelled sources, and with a spectral index from 88–216 MHz of $\alpha_{88}^{216} = -1.6 \pm 0.1$. We consider this a remnant radio galaxy, likely associated with the BCG, or otherwise fossil plasma originally from the BCG.

Abell 2751. (Fig. 3). D21 report a relic source on the outskirts of Abell 2751 (D1 in Fig. 3(i)). We show the MWA-2 and RACS discrete source-subtracted images in Fig. 3(i), and the higher-resolution RACS image in Fig. 3(ii) showing the embedded compact source labelled B. The largest angular size (LAS) is 4.7 arcmin corresponding to a largest linear size (LLS) of 580 kpc, slightly smaller than that reported by D21 due to the less confused images. Sources A and B are subtracted from MWA-2 measurements, and we subtract the contribution of B from the measurements presented in D21. A plot of the SED between 88–1400 MHz is shown in Fig. 26(ii) in Appendix C, and we find a well-fit power law distribution with $\alpha_{88}^{1400} = -1.23 \pm 0.06$, consistent with α reported by D21. RASS data shown in the Fig. 3(iii) indicates the bulk ICM sits to the southwest, with D1 oriented almost perpendicular, which is abnormal for large-scale relics (with the exception of the relic source in MACS J1149.5+2223, though the nature of that source is unclear; Bonafede et al. 2012; Bruno et al. 2021). With no evidence of shocks (and an absence of more sensitive X-ray data) we cannot differentiate from relic or fossil electrons/remnant radio galaxy. The reported cluster centre by Abell et al. (1989) is offset from the RASS X-ray peak by ∼ 2 arcmin (∼ 230 kpc); the optical concentration of galaxies is also elongated (Duchesne et al., 2021b, see their Figure 15)—we suggest the system is merging based on these observations, and significant shocks may be present in the cluster volume. We consider this an ambiguous fossil source or remnant.

Abell 2811. (Fig. 4). Halo/mini-halo candidate reported by D21, detected in MWA-2 data up to 185 MHz, with only partial detection at 216 MHz, and no detection in the RACS data (Fig. 4). We measure the integrated flux density across the MWA-2 band, including the 200-MHz GLEAM image, and fit a power law model to the SED (Fig. 26(iii)), finding $\alpha_{88}^{200} = -2.5 \pm 0.4$ ($\alpha_{\rm MWA\text{-}2} = -3.1 \pm 0.5$ for the MWA-2 data only), after subtraction of the contribution of Source B. The 168-MHz measurement reported by D21 is slightly higher than expected due to additional blending with Source A. Additionally, the LAS is 2.7 arcmin (with an LLS of 320 kpc), slightly smaller again due to less blending with Source A. We fit the exposure-corrected and background-subtracted XMM-*Newton* data presented in D21 with a single-β model (Cavaliere & Fusco-Femiano, 1976), and estimate the X-ray morphological parameters, the centroid shift, w (Poole et al., 2006), with an outer radius set to R_{500} = 1.035 Mpc (Piffaretti et al., 2011). We find $w = 0.072 R_{500}$, consistent with disturbed systems (Pratt et al., 2009). Additionally, the surface brightness concentration, $c_{100/500}$ is found to be 0.21, placing it right on the border of merging, halo-hosting clusters (Cassano et al., 2010). Similarly, the centroid shift within 500 kpc is found to be w_{500} = 0.07, placing it outside of halo-hosting quadrant, near Abell 697 which has been reported to host a radio halo (but see also Kempner & Sarazin 2001 Venturi et al., 2008)

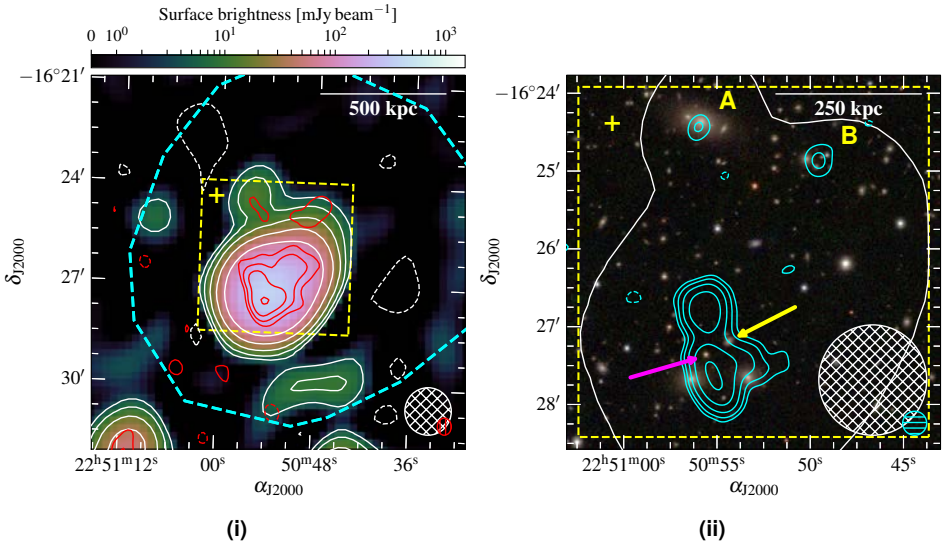

Figure 5. Abell 2496. (i). Background: MWA-2, 185 MHz, robust +0.5 image. (ii). Background: RGB PS1 image (i, r, g). The white contours are as in Fig. 2(i) for the background of (i) (for $\sigma_{\rm rms}$ = 1.5 mJy beam^{-1}). Red contours: TGSS image, in levels of $[\pm3, 6, 12, 24, 48] \times \sigma_{\rm rms}$ ($\sigma_{\rm rms}$ = 4 mJy beam^{-1}). Cyan contours: RACS robust +0.25 image, in levels of $[\pm3, 6, 12, 24, 48] \times \sigma_{\rm rms}$ ($\sigma_{\rm rms}$ = 0.23 mJy beam^{-1}). Other image features are as in Fig. 2.

with an ultra-steep spectrum ($\alpha = -1.5$; Macario et al., 2013), though not as steep as the spectrum for Abell 2811. We also note the concentration parameter, $c_{40/400} = 0.048$, is below what is typically seen in cool-core clusters (CC; Santos et al. 2008, with $c_{40/400} \gtrsim 0.075$). Many of the properties are consistent with a radio halo, however, such a steep spectrum is rare for radio halos: while we consider this an extreme case of an ultra-steep–spectrum radio halo (USSRH) it may be a fossil plasma source projected onto the cluster centre.

3.1.2. FIELD2

Abell 2496. (Fig. 5). Reported by D21 as an unclassifed diffuse cluster source. The MWA-2 and TGSS data in Fig. 5(i) show an extended source, with the RACS data in Fig. 5(ii) showing a clear double-lobed morphology. A small extension is seen in the RACS data in the direction of the larger extension seen in the TGSS and MWA-2 images, tracing an older plasma component. The angular and linear extend of the source is the same as reported in D21. The overall emission is modelled with a normal power law with $\alpha_{88}^{1400} = -1.23 \pm 0.05$ (Fig. 26(i)). The PS1 data show possible hosts between the lobes: WISEA J225055.58−162721.0; indicated by a yellow arrow in Fig. 5(ii), and WISEA J225054.36-162710.7; indicated by a magenta arrow, neither with known redshifts. No distinct radio core is seen. We suggest this is a remnant radio galaxy.

Abell 2680. (Fig. 6). Reported by D21. Fig. 6(i) shows the MWA-2 and TGSS radio data, and Fig. 6(ii) the PS1 data with MWA-2 and RACS data overlaid. The LAS of the source is 3.0 arcmin (with an LLS of 580 kpc), slightly larger than reported by D21 and the reduced confusion enables a better estimate of the size. A single compact source is detected within the emission with RACS (Source A) and is subtracted from subsequent flux density measurements. We are only able to provide measurements in the 88-, 118-, and 154-MHz MWA-2 bands as the cluster is towards the edge of FIELD2 with lessened sensitivity in the higher frequency images. We find $\alpha_{88}^{200} = -1.7 \pm 0.7$ (Fig. 26(v)), consistent with the limited reported by D21. Smoothed RASS data is shown in Fig. 6(iii) highlighting the location of the radio emission relative to the thermal ICM though noting that the RASS data provide limited insight to the morphology of the ICM. From an optical analysis, Wen & Han (2015, but see also Wen et al. 2012) report an R_{500} of 1.26 Mpc which corresponds to mass of $M_{500} = 2.4 \times 10^{14}$ M$_\odot$ following Equation 1 from Wen & Han (2015). As the cluster is detected in the RASS data, a mass is estimated following the procedures described by Tarrío et al. (2016, 2018), resulting in $M_{500} = 3.2^{+0.8}_{-1.0} \times 10^{14}$ M$_\odot$, somewhat consistent with the mass derived from the optical radius. We consider this a candidate halo.

Abell 2693. (Fig. 7). Reported by D21. The candidate radio halo in Abell 2693 is largely similar to that in Abell 2680, with only a faint discrete source detected in the RACS data (Source A) with $S_{\rm A,887} \sim 0.8$ mJy. We provide additional flux density measurements, subtracting the contribution of Source A, to obtain a spectral index of $\alpha_{88}^{200} = -1.5 \pm 0.2$ (Fig. 26(vi)). A mass is derived from the RASS data: $M_{500} = 2.1^{+0.5}_{-0.6} \times 10^{14}$ M$_\odot$, placing Abell 2693 as one of the least massive halo-hosting clusters if confirmed (surpassed only by the 'Ant' cluster; Botteon et al., 2021b). The LAS for the source is 2.0 arcmin (LLS = 370 kpc), marginally smaller than that reported by D21. Alternatively, this may be a point source with $\alpha_{88}^{887} = -2.2 \pm 0.2$.

Abell S1099. (Fig. 8). Reported by D21. MWA-2 radio data shown in Fig. 8(i) and PS1 optical data shown in Fig. 8(ii). RACS data shows no additional discrete sources beyond Source A, which is subtracted from flux density measurements where appropriate with $\alpha_{\rm A,216}^{1400} = -0.5 \pm 0.1$. The resulting spectral index of the diffuse source D1 is found to be $\alpha_{88}^{1400} = -0.87 \pm 0.11$ (Fig. 26(vii)). The lack of obvious core or any clear lobes/hot spots suggests a remnant radio source that has diffused into the surrounding medium. No deep X-ray observations are available, no cluster or source is detected in the RASS image, and there is no detection as a *Planck*-SZ source. We consider this a remnant radio galaxy with the putative host (LEDA 195207) indicated by a magenta arrow on Fig. 8(ii).

Radius within which the mean density of the cluster is 500 times the critical density of the Universe.

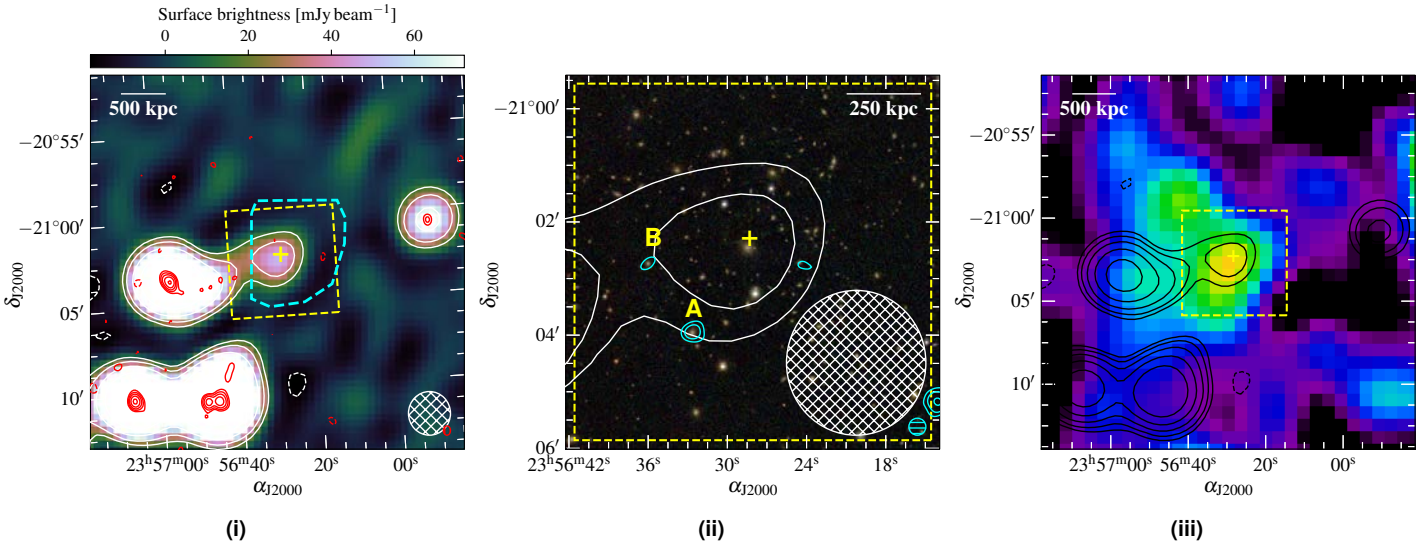

Figure 6. Abell 2680. (i). Background: MWA-2, 88 MHz, robust +0.5 image. (ii). Background: RGB PS1 image (i, r, g). (iii). Background: Smoothed RASS image. The white (black) contours are as in Fig. 2(i) for the background of (i) (with $\sigma_{\rm rms} = 5.5$ mJy beam^{-1}). Red contours: TGSS image, in levels of $[\pm 3, 6, 12, 24, 48] \times \sigma_{\rm rms}$ ($\sigma_{\rm rms} = 3.7$ mJy beam^{-1}). Cyan contours: RACS robust +0.25 image, in levels of $[\pm 3, 6, 12, 24, 48] \times \sigma_{\rm rms}$ ($\sigma_{\rm rms} = 0.25$ mJy beam^{-1}). Other image features are as in Fig. 2.

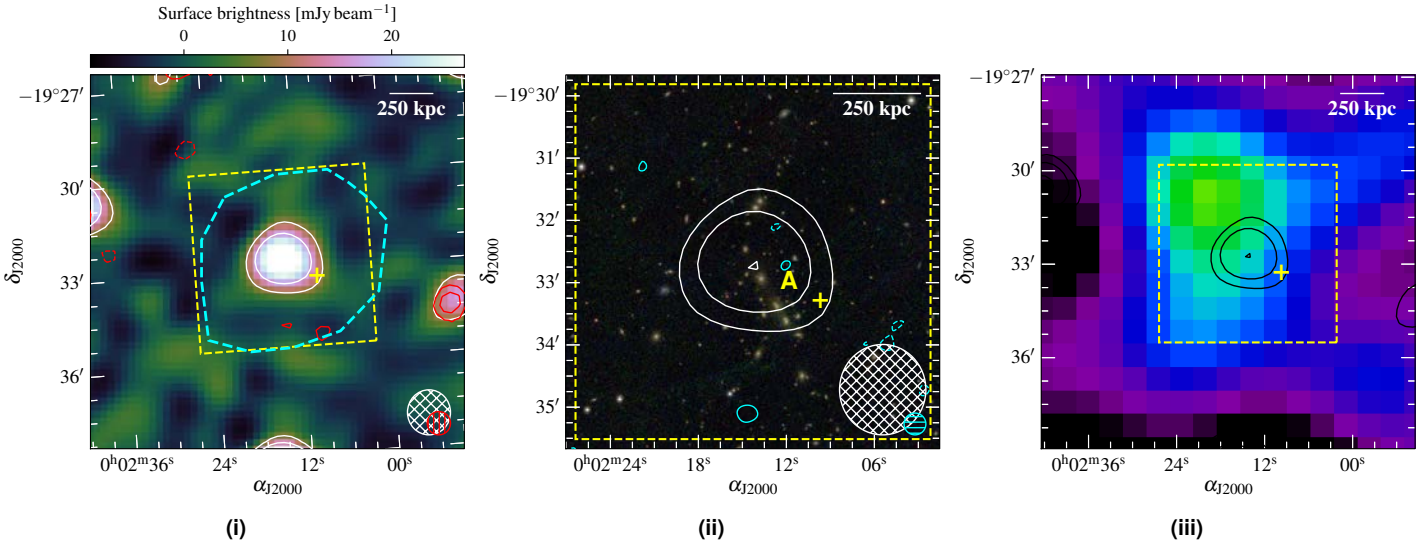

Figure 7. Abell 2693. (i) Background: MWA-2, 154 MHz, robust +0.5 image. (ii). Background: RGB PS1 image (i, r, g). (iii). Background: Smoothed RASS image. The white (black) contours are as in Fig. 2(i) for the background of (i) (with $\sigma_{\rm rms} = 2.8$ mJy beam^{-1}). Red contours: NVSS image as in Fig. 4(i). Cyan contours: RACS robust +0.25 image, in levels of $[\pm 3, 6, 12, 24, 48] \times \sigma_{\rm rms}$ ($\sigma_{\rm rms} = 0.15$ mJy beam^{-1}). Other image features are as in Fig. 2.

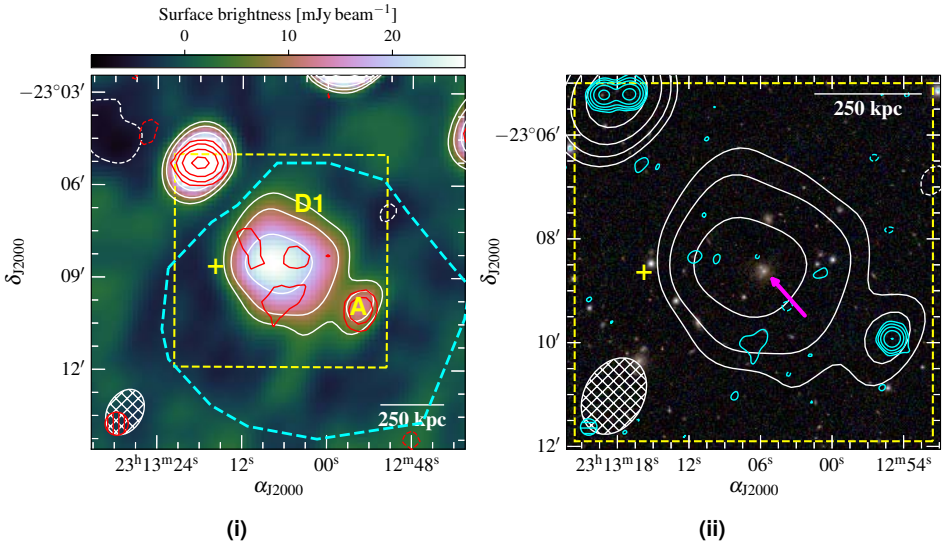

Figure 8. Abell S1099. (i) Background: MWA-2, 216-MHz, robust +2.0 image. (ii) Background: RGB PS1 image (i, r, g). The white contours are as in Fig. 2(i) for the background of (i) (with σ_{rms} = 1.6 mJy beam^{-1}). Red contours: NVSS image as in Fig. 4(i). Cyan contours: RACS robust +0.25 image, in levels of $[\pm 3, 6, 12, 24, 48] \times \sigma_{rms}$ (σ_{rms} = 0.19 mJy beam^{-1}). Other image features are as in Fig. 2.

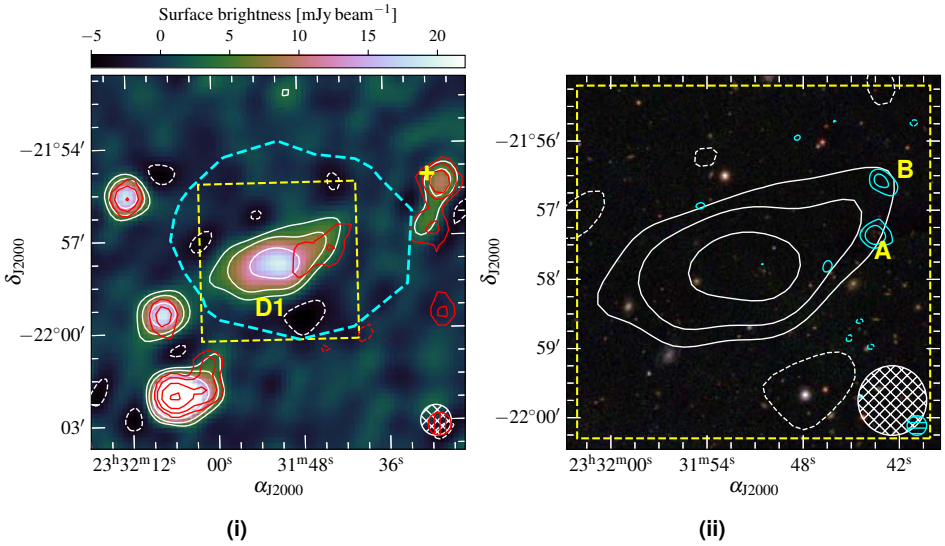

Figure 9. AqrCC 087. (i) Background: MWA-2, 216-MHz, robust +0.5 image. (ii) Background: RGB PS1 image (i, r, g). The white contours are as in Fig. 2(i) for the background of (i) (with σ_{rms} = 1.1 mJy beam^{-1}). Red contours: NVSS image as in Fig. 4(i). Cyan contours: RACS robust +0.25 image, in levels of $[\pm 3, 6, 12, 24, 48] \times \sigma_{rms}$ (σ_{rms} = 0.15 mJy beam^{-1}). Other image features are as in Fig. 2, though note no scalebar is given as no redshift is available for the reported cluster.

AqrCC 087. (Fig. 9). The cluster is reported in the Aquarius cluster catalogue (Caretta et al., 2002), though no redshift is available. Additionally, there is no cross-identification with other cluster catalogues, and as with Abell S1099 no X-ray or SZ observations provide detections. We suggest this is a poor cluster or group. The redshift distribution of galaxies within 1 deg around AqrCC 087 peaks around $z \approx 0.1$. We detect an elongated radio source $\sim$ 5.6 arcmin from the reported cluster centre (Fig. 9(i), $\sim$ 620 kpc at $z = 0.1$) with no obvious optical host (Fig. 9(ii)). The angular size is $\sim$ 4.5 arcmin, which if at $z = 0.1$ is a linear projected extent of $\sim$ 500 kpc. The source is not detected in RACS, with a partial detection in the NVSS image (though note there is confusion with the discrete Source A). Source A is subtracted from subsequent MWA-2 flux density measurements, and we obtain a spectral index of $\alpha_{88}^{216} = -1.7 \pm 0.1$ (Fig. 26(viii)). As with Abell S1099, we consider this likely to be a remnant radio galaxy.

RXC J2351.0−1954 (PSZ1 G057.09-74.45). (Fig. 10). Originally D21 reported three candidate sources: a halo at the centre (labelled D1 in Fig. 10(i)), and two relics: SE (labelled D2, inset Fig. 10(iii)), and NW, (labelled D3, inset Fig. 10(ii)). The candidate halo is shown by the RACS data to be blended sources. The SE candidate relic detected at low significance ($\sim 3\sigma$), though the RACS data show a single compact source within the southern portion of the emission (Source A). The NW candidate relic is partially detected in RACS, with other compact blended sources (B–D in Fig. 10(ii)). Excluding point sources, the LAS of D2 and D3 are 1.9 arcmin (LLS = 230) and 3.5 arcmin (LLS = 430 kpc), respectively. All labelled compact sources are subtracted from MWA measurements where appropriate. The spectral index of D2 is measured to be $\alpha_{D2,88}^{216} = -1.3 \pm 0.3$ (Fig. 26(ix)). D3 shows significant curvature within the MWA band and to 887.5 MHz and is fit with a generic curved model, with a power law model fit across the MWA-2 band: $\alpha_{D3,88}^{216} = -1.2 \pm 0.1$ (Fig. 26(x)).The smoothed RASS image is shown as contours on Fig. 10(i) showing elongation hinting at an un-relaxed ICM, though we consider that D3 is likely a remnant with the classical spectral steepening and D2 is still unconfirmed.

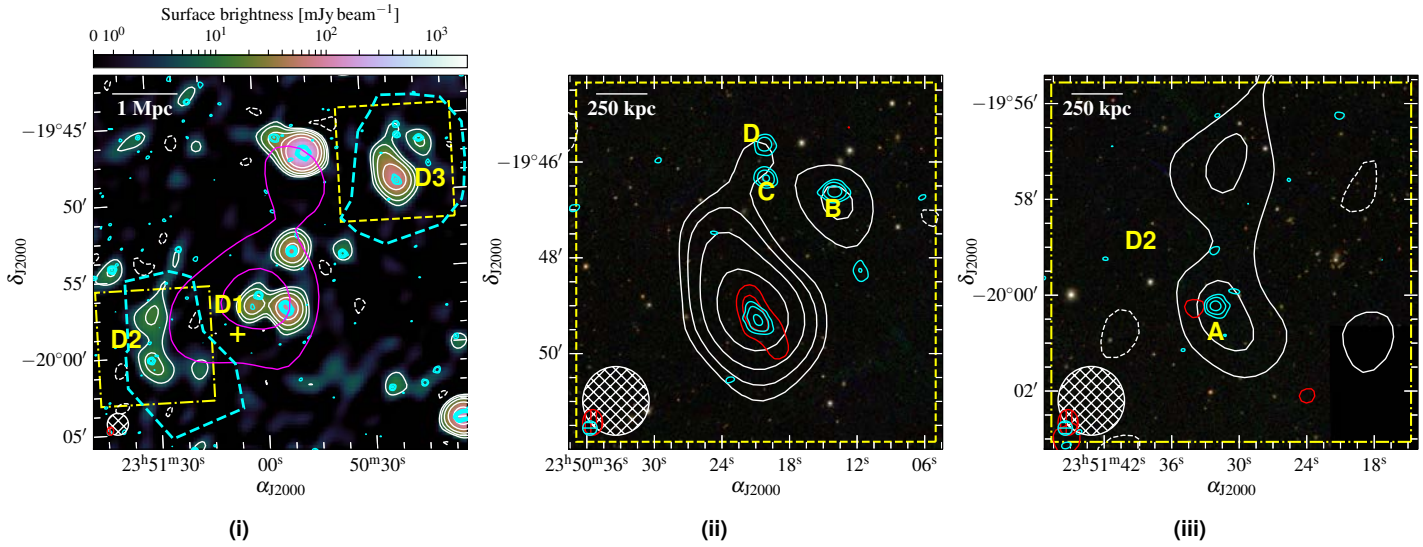

Figure 10. RXC J2351.0−1954. (i) Background: MWA-2, 154-MHz, robust +0.5 image. (ii) and (iii) Background: RGB PS1 image (i, r, g). The white contours are as in Fig. 2(i) for the background of (i) (with $\sigma_{\rm rms}$ = 4.9 mJy beam^{-1}). Red contours: TGSS image, in levels of $[\pm3, 6, 12, 24, 48] \times \sigma_{\rm rms}$ ($\sigma_{\rm rms}$ = 3.6 mJy beam^{-1}. Cyan contours: RACS robust +0.25 image, in levels of $[3, 6, 12, 24, 48] \times \sigma_{\rm rms}$ ($\sigma_{\rm rms}$ = 0.20 mJy beam^{-1}). Magenta contours: smoothed RASS image, increasing with factors of $\sqrt{2}$. Other image features are as in Fig. 2.

3.1.3. FIELD3

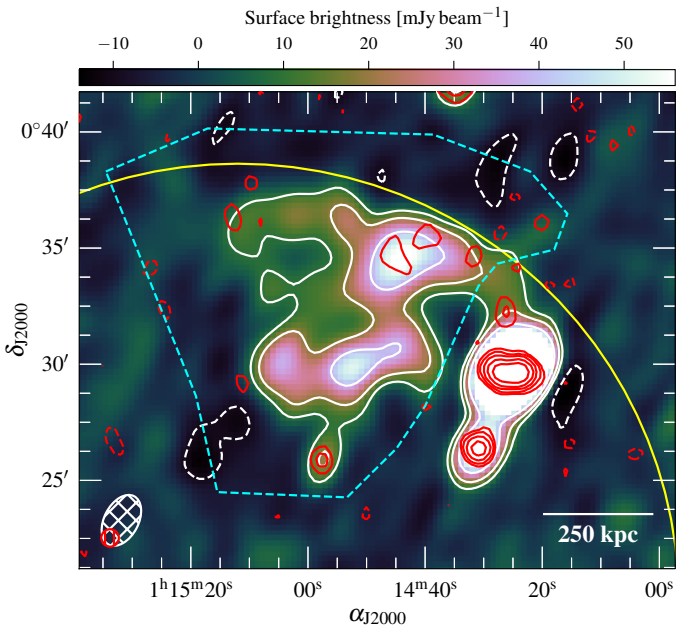

Figure 11. Abell 0168. Background: MWA-2, 154-MHz, robust +2.0 image. The white contours are as in Fig. 2(i) for the background image (with $\sigma_{\rm rms}$ = 3.2 mJy beam^{-1}). Red contours: NVSS, $[\pm3, 6, 12, 24, 48] \times \sigma_{\rm rms}$ ($\sigma_{\rm rms}$ = 0.45 mJy beam^{-1}). Other image features are as in Fig. 2, with a yellow circle with a 1 Mpc radius centered on the cluster.

Abell 0168. Fig. 11 shows the radio relic that was reported by Dwarakanath et al. (2018) and is detected in the MWA-2 data. Dwarakanath et al. (2018) split the total relic source into two distinct components–a large exterior component and a smaller interior component with a steeper spectrum. Here we consider it a single emission region due in part to the limitation of resolution but there also appears to be a fainter diffuse component connecting the two regions. While emission is detected in all MWA-2 bands (see e.g. 118-MHz in Fig. 11), due to the large size (∼ 11.5 arcmin) we note that flux recovery diminishes significantly in the 154-, 185-, and 216-MHz bands. With supplemental GLEAM data and flux densities reported by Dwarakanath et al. (2018), we find the spectral index of the whole relic to be $\alpha_{88}^{608} = -1.50 \pm 0.08$.

RXC J0137.2−0912. (Fig. 12). We report the detection of steep-spectrum emission within RXC J0137.2−0912, shown in Fig. 12(i) in MWA and TGSS data. Fig. 12(ii) shows the optical host of the central compact emission with contours from re-processed VAST data (cyan) overlaid. Fig. 12(iii) shows the extent of the cluster's X-ray emission with archival XMM-*Newton* data, noting some elongation perpendicular to the orientation of the radio emission. The compact emission from Sources A and B is subtracted after extrapolating to MWA-2 frequencies using the VAST and TGSS measurements, and C–E are subtracted assuming $\alpha = -0.7$. A power law SED is modelled, with a spectral index of $\alpha_{88}^{887} = -1.62 \pm 0.07$ (Fig. 26(xii), or $\alpha_{88}^{216} = -1.5 \pm 0.1$ across the MWA band alone). The total angular size of the source is 7.8 arcmin, corresponding to 410 kpc. From the archival XMM-*Newton* data, we find a concentration parameter $c_{40/400} = 0.19$, consistent with cool-core (CC) clusters (where non-CC clusters are found to have $c_{40/400} \lesssim 0.075$; Santos et al. 2008). Based on the likelihood of a CC, the prominent BCG with significant AGN emission, and steep-spectrum diffuse emission surrounding the BCG we suggest the emission is a mini-halo. Some structure in the centre of the cluster gives some evidence for sloshing, and with a centroid shift within R_{500} = 684 kpc (Piffaretti et al., 2011) of $w = 0.037 R_{500}$ suggesting some disturbance (Pratt et al., 2009; Böhringer et al., 2010). While the orientation of the radio emission appears largely perpendicular to the X-ray emission, the extension to the SW in the

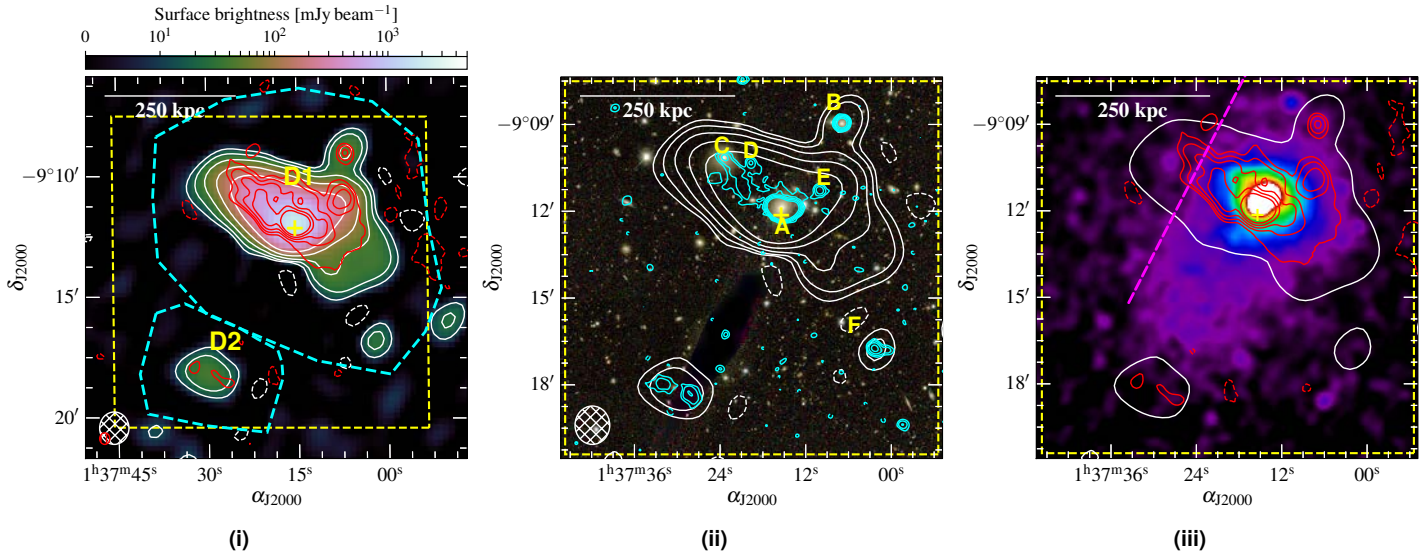

Figure 12. RXC J0137.2−0912. (i) Background: MWA-2, 154-MHz, robust 0.0 image. (ii) Background: RGB DES image (i, r, g). (iii). Background: smoothed XMM-*Newton* EPIC image. The white contours are as in Fig. 2(i) for the background of (i) (with $\sigma_{\rm rms}$ = 3.8 mJy beam^{-1}). Red contours: TGSS image, in levels of $[\pm3, 6, 12, 24, 48] \times \sigma_{\rm rms}$ ($\sigma_{\rm rms}$ = 2.8 mJy beam^{-1}. Cyan contours: VAST +0.25 image, in levels of $[\pm3, 6, 12, 24, 48] \times \sigma_{\rm rms}$ ($\sigma_{\rm rms}$ = 0.14 mJy beam^{-1}). The dashed, magenta line on (iii) indicates the location of an XMM-*Newton* chip gap with lessened sensitivity. Other image features are as in Fig. 2.

radio is traced by an extension in the X-ray as well. The NE direction is ambiguous as the XMM-*Newton* exposure drops significantly due to a chip gap at that location. This is indicated on Fig. 12(iii) as a dashed, magenta line.

We see also an additional diffuse source resembling a remnant radio galaxy, D2; however, its SED shows significant curvature uncharacteristic of remnants (Fig. 26(xiii)).

3.1.4. FIELD6

Abell S0112. (Fig. 13). Abell S0112 is covered by the Australia Telescope Low Brightness Survey (ATLBS, region B; Subrahmanyan et al., 2010; Thorat et al., 2013) which reveals two extended radio galaxies (A and B) within the cluster. The MWA data reveal an additional emission component (D1) between the two bright radio galaxies, creating an asymmetric dumbbell shape. The emission is only detected across the MWA-2 band, from 88–185 MHz and in the 200-MHz GLEAM data. The extent of the emission between the two radio galaxies is ∼ 3 arcmin (LLS ≈ 230 kpc). We measure integrated flux density within the D1 region between A and B, finding a spectral index of $\alpha_{88}^{185} = -1.9 \pm 0.5$ Fig. 26(xiv)). In Fig. 13(ii) we show optical data which reveals a lack of obvious optical host for the emission, and Fig. 13(iii) shows the XMM-*Newton* image, highlighting the offset of the emission from the main component of the X-ray–emitting ICM. Source A is an active radio galaxy with a normal a radio spectrum ($\alpha \sim -0.8$), and D1 may be associated with an older episode of outflow. This could be true for B as well, with the extension of B to the north in the MWA-2 data also suggesting additional emission components not detected in higher-frequency/resolution images. We consider this emission fossil plasma associated with either A or B, with potential for some re-acceleration due to the dynamic nature of the cluster.

MCXC J0145.2−6033. (Fig. 14). We report the detection of a candidate mini-halo in MWA-2 and RACS data, shown in Fig. 14(i). The detection is marginal in the RACS data, and 2σ contours of the low resolution image are shown in Fig. 14(i) to highlight the extent of the emission. Fig. 14(ii) shows the robust +0.25 RACS data which stems from the BCG and extends northwards. We measure the flux densities across the available images and find $\alpha_{88}^{887} = -2.1 \pm 0.1$ (Fig. 26(xv), with the same value across only the MWA-2 band). The extent of the source is LAS = 1.9 arcmin; LLS = 350 kpc. The optical data is shown in Fig. 14(ii), with a BCG clear near the centre of the emission. RASS data shown in Fig. 14(iii) does not show any significant offset from the BCG, and we suggest the cluster is reasonably relaxed. With an LAS of 1.9 arcmin (LLS = 350 kpc), the source is only barely extended in the robust +2.0 MWA-2 images, and the robust 0.0 images show no significant extension. There is a ∼ 20 mJy difference between the 0.0 and +2.0 measurements at 154 MHz ($S_{\rm r0} = 110 \pm 10$ and $S_{\rm r2} = 130 \pm 10$) which may be allowable within uncertainties. Given the low SNR in the RACS data, it is difficult to confirm if this is an ultra-steep spectrum point source.

MCXC J0154.2−5937. (Fig. 15). We report peripherally located, elongated extended emission in the cluster, shown in Fig. 15(i). In Fig. 15(ii) a potential optical host is seen with matching emission in the RACS image (Source A, $S_{887} \sim 1$ mJy, WISEA J015436.21−593929.9, no redshift). The radio SED of the whole source is uncertain, but consistent with a radio galaxy ($\alpha_{88}^{887} = -0.65 \pm 0.13$; Fig. 26(xvi)). If in the cluster, the source is ∼ 1 Mpc in projected extent, classing it as a giant radio galaxy.

3.1.5. FIELD7

Abell 3186. (Fig. 16). From the data presented here we report Abell 3186 to be a double relic system, potentially with central

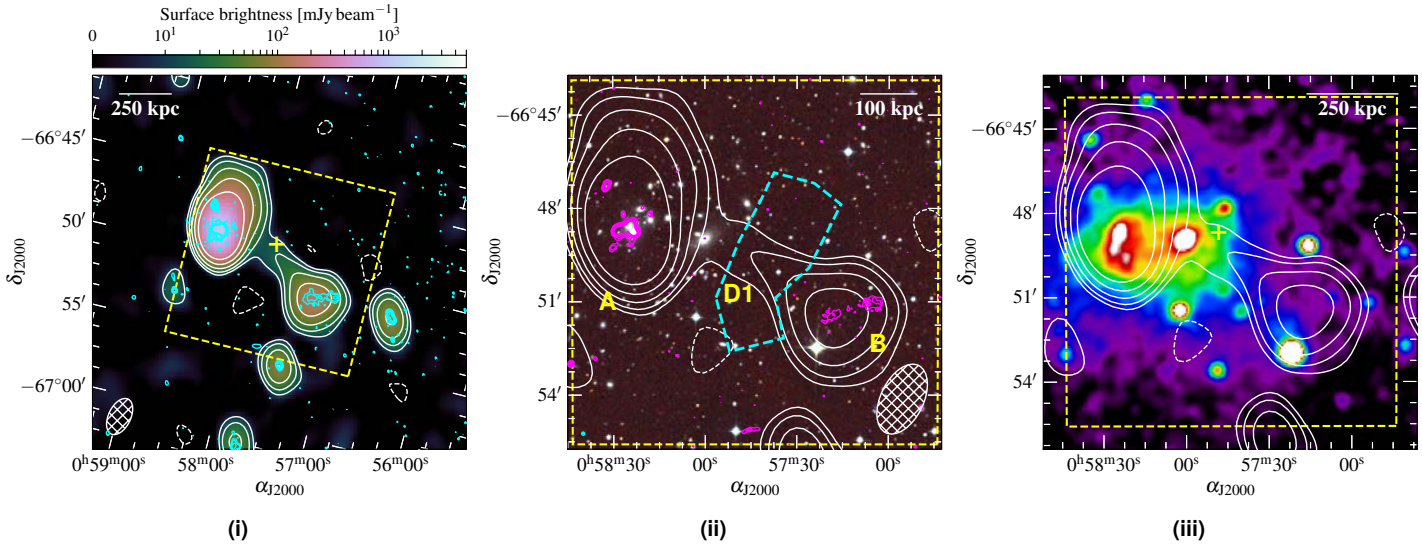

Figure 13. Abell S0112. (i) Background: MWA-2, 154-MHz, robust +2.0 image. (ii) Background: RGB SSS image (i, r, b). (iii). Background: smoothed XMM-*Newton* EPIC image. The white contours are as in Fig. 2(i) for the background of (i) (with $\sigma_{\rm rms}$ = 3.5 mJy beam^{-1}). Magenta contours: ATLBS high-resolution image, in levels of $[\pm3, 6, 12, 24, 48] \times \sigma_{\rm rms}$ ($\sigma_{\rm rms}$ = 0.08 mJy beam^{-1}. Cyan contours: RACS survey image, in levels of $[\pm3, 6, 12, 24, 48] \times \sigma_{\rm rms}$ ($\sigma_{\rm rms}$ = 0.29 mJy beam^{-1}). Other image features are as in Fig. 2.

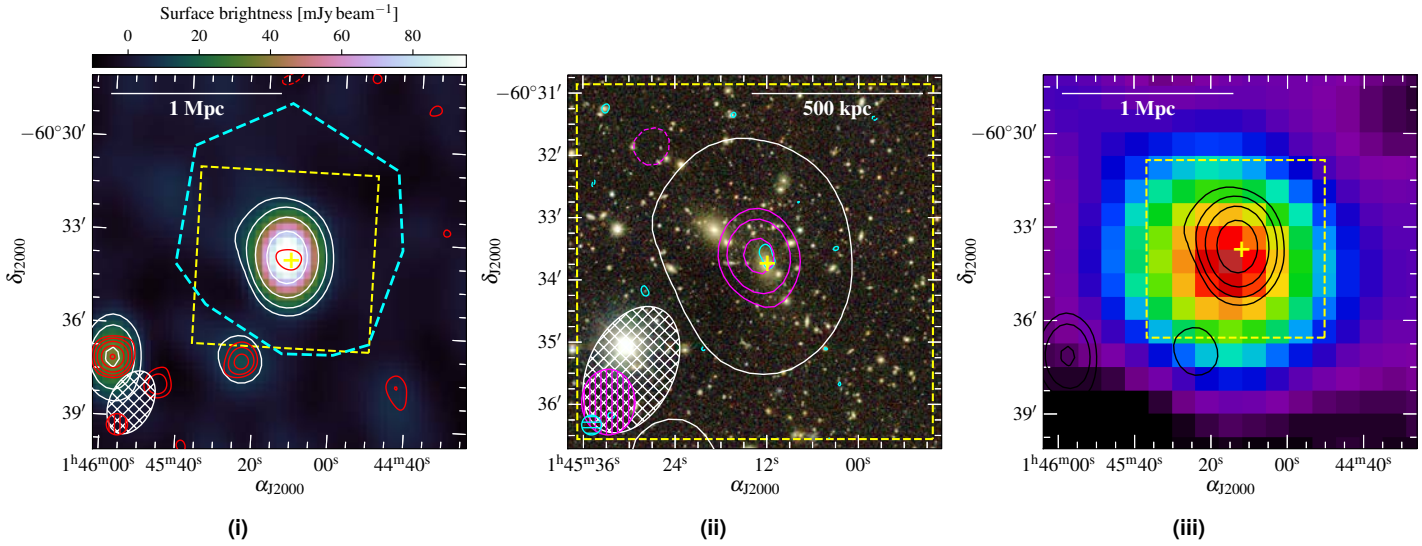

Figure 14. MCXC J0145.2−6033. (i) Background: MWA-2, 154-MHz, robust +2.0 image. (ii) Background: RGB DES image (i, r, g). (iii). Background: smoothed RASS image. The white (black) contours are as in Fig. 2(i) for the background of (i) (with $\sigma_{\rm rms}$ = 2.9 mJy beam^{-1}). Red contours: RACS low-resolution image, $[\pm3, 6, 12, 24, 48] \times \sigma_{\rm rms}$ ($\sigma_{\rm rms}$ = 0.34 mJy beam^{-1}). Cyan contours: RACS robust +0.25 image, $[\pm3, 6, 12, 24, 48] \times \sigma_{\rm rms}$ ($\sigma_{\rm rms}$ = 0.17 mJy beam^{-1}). Magenta contours: MWA-2, 216-MHz, robust 0.0 image, $[\pm3, 6, 12, 24, 48] \times \sigma_{\rm rms}$ ($\sigma_{\rm rms}$ = 3.4 mJy beam^{-1}). Other image features are as in Fig. 2.

diffuse emission possible from a radio halo. The cluster shows a similar morphology to older observations of the canonical double relic cluster Abell 3667 (Johnston-Hollitt, 2003; Hindson et al., 2014) with a larger, bright relic on one side and a smaller dimmer one on the other.

The larger relic, D1, is detected to the SW as an elongated structure on the periphery of Abell 3186 with the MWA and ASKAP, shown in Fig. 16(i). The angular extent of D1 is ∼ 12 arcmin, corresponding to ∼ 1650 kpc. The MWA-2 images in this region at 154-, 185-, and 216-MHz, which are generally less sensitive, suffered from significant noise from a nearby bright source and the large relic is poorly detected. A somewhat compact source is detected within the emission (Source A) which has a faint, blue optical counterpart, seen in Fig. 16(iii). After subtracting the contribution from A, we obtain a spectral index of $\alpha^{887}_{\rm D1,88} = -1.0 \pm 0.1$ (Fig. 26(xvii)), consistent with relic sources. We show the XMM-*Newton* image in Fig. 16(ii), and note that Lovisari et al. (2017) report the cluster has a 'mixed' morphology (i.e. semi-disturbed). Additionally, the cluster hosts a second relic to the NW seen as a patchy structure, with detections in all bands, though the full extent of the emission (∼ 14 arcmin, ∼ 1900 kpc), extending to the SW, is only seen at 88 and 118 MHz as with D1. After

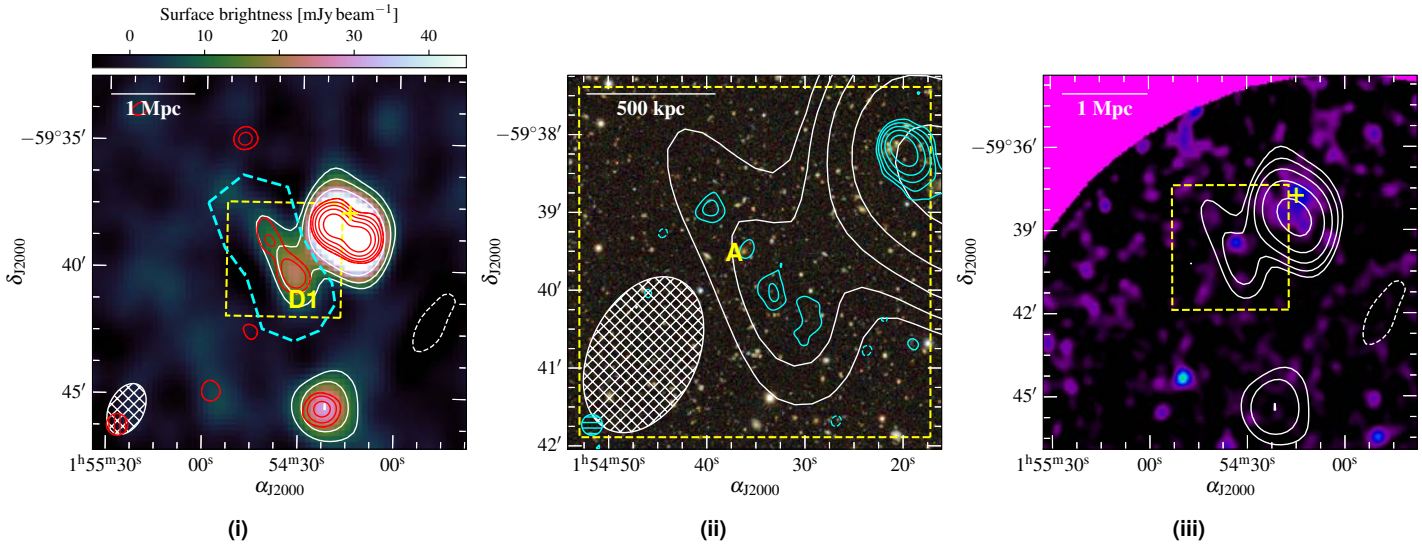

Figure 15. MCXC J0154.2−5937. (i) Background: MWA-2, 154-MHz, robust +2.0 image. (ii) Background: RGB DES image (i, r, g). (iii). Background: smoothed XMM-*Newton* EPIC image. The white contours are as in Fig. 2(i) for the background of (i) (with $\sigma_{\rm rms}$ = 2.5 mJy beam^{-1}). Red contours: RACS low-resolution image, $[\pm3, 6, 12, 24, 48]\times\sigma_{\rm rms}$ ($\sigma_{\rm rms}$ = 0.40 mJy beam^{-1}). Cyan contours: RACS robust +0.0 image, $[\pm3, 6, 12, 24, 48]\times\sigma_{\rm rms}$ ($\sigma_{\rm rms}$ = 0.20 mJy beam^{-1}). Other image features are as in Fig. 2.

subtraction of discrete source contributions (labelled B and C in Fig. 16(iv)), we derive a spectral index of $\alpha^{887}_{\rm D2,88} = -0.9 \pm 0.1$. The morphology and spectral properties of these relics are extremely reminiscent of Abell 3667 which as a bright, larger relic and a smaller more compact relic with average spectral indices of −0.9 for both across MWA bands (Hindson et al., 2014), though higher resolution, higher frequency spectral index measurements show α varies inside the relics from approximately −0.8 to −1 (Johnston-Hollitt, 2003). We consider this a classical double relic system. We note also the 88-MHz MWA-2 image (Fig. 16(i)) appears to show an excess of diffuse flux within the central cluster region which may indicate a radio halo, though the confusion from sources in the cluster make this impossible to confirm with the present data.

Abell S0405. (Fig. 17). We report a diffuse source in Abell S0405, with RACS data revealing a double-lobed radio galaxy structure (Fig. 17(i)) without a core or jets. No obvious optical host exists between the two lobes (Fig. 17(ii)) and we suggest this is a remnant radio galaxy. We find $\alpha^{887}_{88} = -1.99 \pm 0.08$ between the MWA and RACS data, after subtraction of Sources A and B from the MWA images (Fig. 26(xix)). The source is measured to be ∼ 185 kpc if at the redshift of the cluster (z = 0.0613; De Grandi et al. 1999), and sits within the X-ray–emitting ICM (Fig. 17(iii)).

PSZ1 G287.95−32.98. (Fig. 18). We report the detection of a diffuse source at the cluster centre with the MWA at 118 and 154 MHz as well as a partial detection at 887 MHz in RACS data. The projected size of the source is ∼ 320 kpc. Other MWA bands either suffer from lack of sensitivity or significant confusion with nearby Sources A and B (Fig. 18(i)). We obtain a spectral index of $\alpha^{887}_{118} = -1.5\pm0.2$ (Fig. 26(xx)). Fig. 18(iii) shows the XMM-*Newton* image, highlighting the central location of the candidate radio halo. Based on the XMM-*Newton* data, Rossetti et al. (2017) use the concentration parameter (see Santos et al., 2008) to determine the cluster is a non-CC cluster, and the emission is therefore unlikely to be a mini-halo. Additionally, no obvious BCG with core radio emission is seen in the optical data shown in Fig. 18(ii). We classify this source as a candidate radio halo.

Not to be confused with the double-relic system, PLCK G287.0+32.9 reported by Bagchi et al. (2011).

3.1.6. FIELD8

Abell 3399. (Fig. 19). We report the detection of a candidate radio relic on the periphery of Abell 3399 (D1 in Fig. 19(i)) with an angular extent of ∼ 3.6 arcmin (LLS ≈ 710 kpc) and a candidate radio halo at the centre of the cluster (D2 in Fig. 19(i)) with an angular extent of ∼ 2.8 arcmin (LLS ≈ 570 kpc). As is clear from the *Chandra* X-ray data shown in Fig. 19(iii), the cluster is undergoing a merger and Lovisari et al. (2017) consider the cluster 'disturbed' based on morphological analysis. Measuring flux densities of D1 at 88–154, and 887.5 MHz yields a spectral index of $\alpha^{887}_{\rm D1,88} = -1.6 \pm 0.3$ (Fig. 26(xxi)). For D2, the emission is is barely detected between 154–216 MHz and the 88-MHz image is too confused with D1 for a useful measurement. We instead calculate the two-point spectral index between 118 and 887 MHz, finding $\alpha^{887}_{\rm D2,118} = -1.5 \pm 0.2$ (Fig. 26(xxii), though note the line shown is derived from the two-point index and not a fitted power law model).

3.1.7. FIELD9

MCXC J1253.2−1522 (Abell 1631). (Fig. 20). We report a steep spectrum source projected onto MCXC J1253.2−1522 in MWA data, with no counterpart in RACS, and marginal detection in the TGSS image (Fig. 20(i)). Note the TGSS image has artefacts from the nearby complex radio galaxy that peak at the location of the diffuse source. Multiple cluster systems are reported along line of sight: MCXC J1253.2−1522 at z = 0.0462 (Piffaretti et al., 2011) and Abell 1631 at z = 0.01394 (Coziol et al., 2009). Additionally, Flin & Krywult (2006) report that the system has

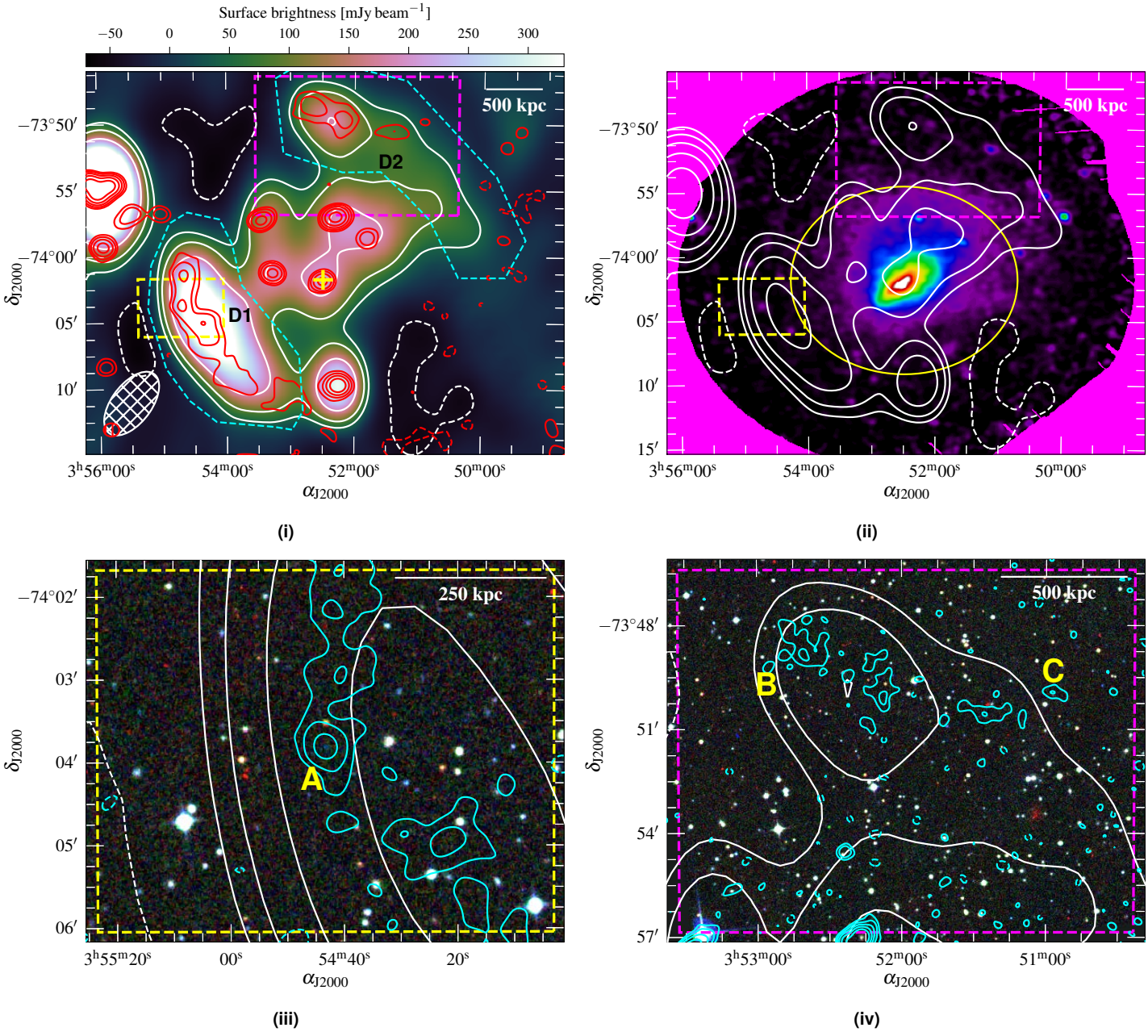

Figure 16. Abell 3186. (i) Background: MWA-2, 88-MHz, robust +2.0 image. (iii) and (iv) Background: RGB SSS image (*i*, *r*, *b*). (ii). Background: smoothed XMM-*Newton* EPIC image. The white contours are as in Fig. 2(i) for the background of (i) (with $\sigma_{\rm rms}$ = 15 mJy beam^{-1}). Red contours: deep ASKAP low-resolution image, $[\pm3, 6, 12, 24, 48]\times\sigma_{\rm rms}$ ($\sigma_{\rm rms}$ = 0.70 mJy beam^{-1}). Cyan contours: deep ASKAP robust +0.25, $[\pm3, 6, 12, 24, 48]\times\sigma_{\rm rms}$ ($\sigma_{\rm rms}$ = 0.32 mJy beam^{-1} and $\sigma_{\rm rms}$ = 0.25 mJy beam^{-1} for (iii) and (iv), respectively). Other image features are as in Fig. 2 and Fig. 3, with the magenta box indicating the location of (iv) on (i) and (ii).

complex substructure, which is clear in the smoothed RASS image shown in Fig. 20(iii). No obvious optical host is visible in PS1 data (Fig. 20(ii), and the projected linear extent is 200 kpc (or 70 kpc if at z = 0.01394). While just outside of the field-of-view (FoV) of archival XMM-*Newton* observations, RASS shows no significant X-ray emission at the location of the source, but the source sits between two X-ray clumps. We find the spectral index to be $\alpha_{88}^{200} = -1.8 \pm 0.4$ (Fig. 26(xxiii)), and suggest the source is fossil plasma or otherwise a remnant radio galaxy.

3.1.8. FIELD10

Abell 3164. (Fig. 21). MWA and the VAST data reveal a complex radio galaxy with at least three distinct remnant components (D1–3 in Fig. 21(i)) with LASs 3.5, 3.8, and 3.1 arcmin and LLSs of 240, 260, and 210 kpc for D1–3, respectively. The head-tail (HT) galaxy (hosted by FAIRALL 0757; Fairall 1984) in the cluster is clearly connected to D3 and is likely responsible for at least D2, however, it is not clear whether D1 has spawned from the same galaxy. The source-subtracted VAST data is shown in Fig. 21(i) and

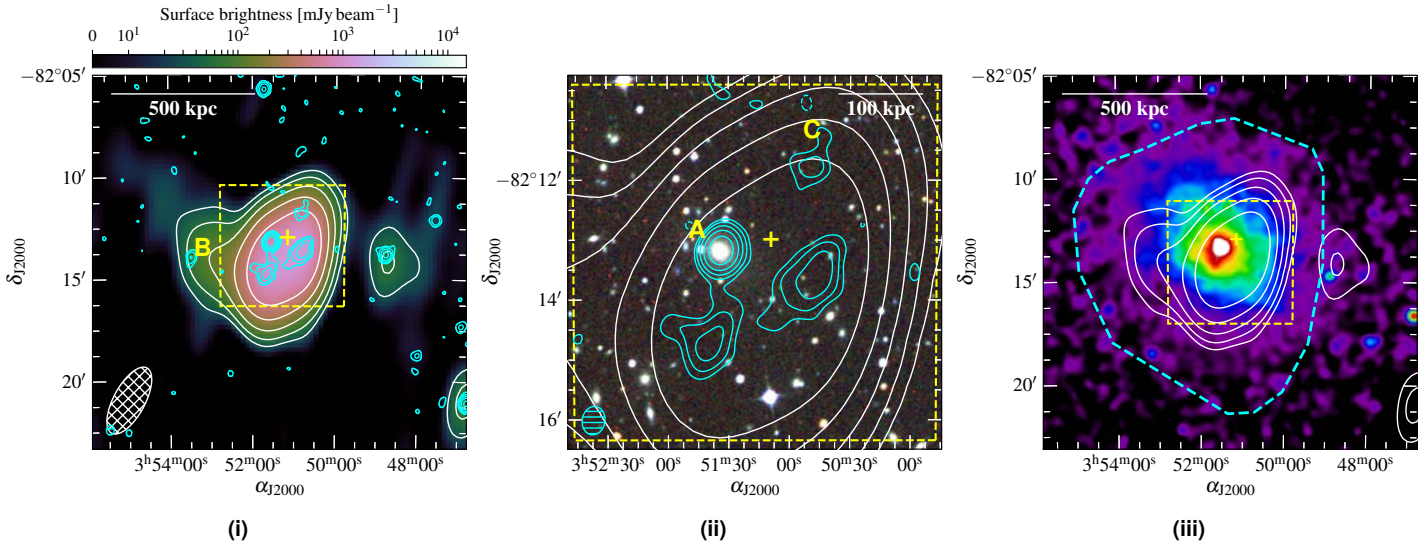

Figure 17. Abell S0405. (i) Background: MWA-2, 154-MHz, robust +2.0 image. (ii) Background: RGB SSS image (*i*, *r*, *b*). (iii). Background: smoothed *Chandra* image. The white contours are as in Fig. 2(i) for the background of (i) (with $\sigma_{\rm rms} = 10$ mJy beam^{-1}). Cyan contours: RACS survey image, $[\pm3, 6, 12, 24, 48] \times \sigma_{\rm rms}$ ($\sigma_{\rm rms} = 0.28$ mJy beam^{-1}). Other image features are as in Fig. 2.

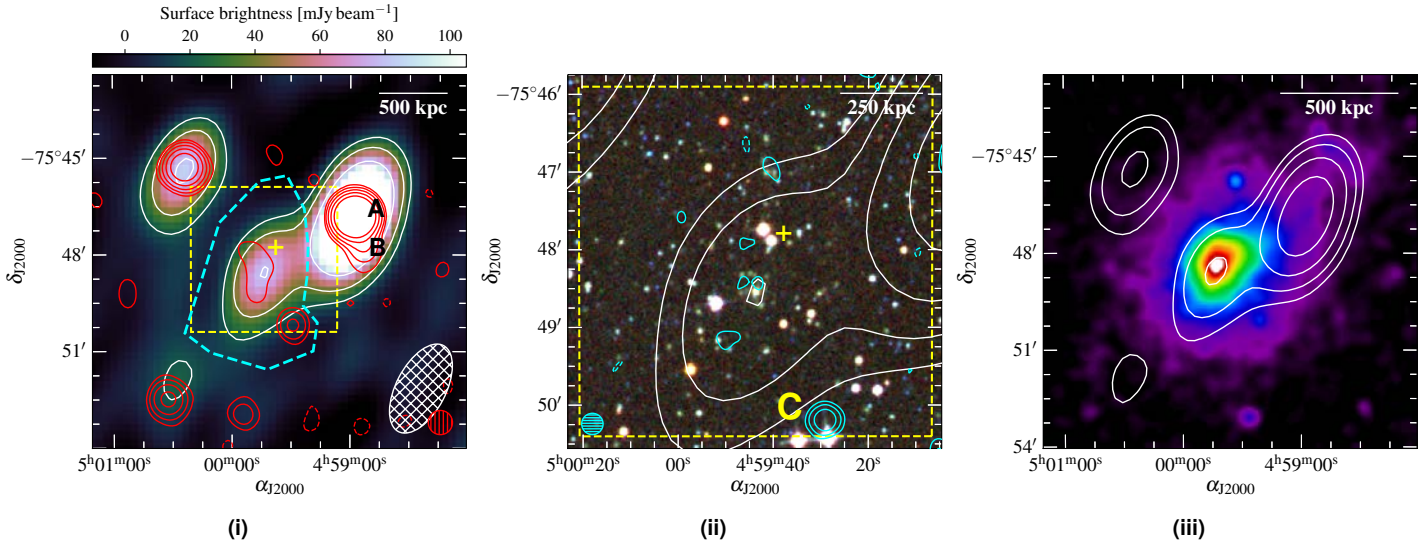

Figure 18. PSZ1 G287.95−32.98. (i) Background: MWA-2, 154-MHz, robust +2.0 image. (ii) Background: RGB SSS image (*i*, *r*, *b*). (iii). Background: smoothed XMM-*Newton* image. The white contours are as in Fig. 2(i) for the background of (i) (with $\sigma_{\rm rms} = 6.6$ mJy beam^{-1}). Red contours: RACS low resolution image $[\pm3, 6, 12, 24, 48] \times \sigma_{\rm rms}$ ($\sigma_{\rm rms} = 0.25$ mJy beam^{-1}). Cyan contours: RACS robust +0.25 image, $[\pm3, 6, 12, 24, 48] \times \sigma_{\rm rms}$ ($\sigma_{\rm rms} = 0.15$ mJy beam^{-1}). Other image features are as in Fig. 2.

highlights the steepness of D2. After subtraction of Sources A and B from the relevant measurements, we obtain spectral indices of D1: $\alpha_{88}^{887} = -1.48 \pm 0.08$ (Fig. 26(xxiv)), D2: $\alpha_{88}^{216} = -2.3 \pm 0.1$ (though Fig. 26(xxv) shows some curvature within the MWA band, and D2 is also fit with a generic curved model between 88–887.5 MHz), D3: $\alpha_{154}^{887} = -1.78 \pm 0.07$ (Fig. 26(xxvi)). We do not believe significant flux density is missing, since D1, which is comparative in angular scale, is recovered consistently alongside the MWA. We see steepening from D3–D2, but D1 is flatter, which suggests either (1) it may not be associated with past episode from the HT or (2) it has been re-accelerated/revived by ICM motion. Steepening of the spectrum of HT radio galaxies is observed to increase with distance from the host galaxy (e.g. the HT in Abell 1132; Wilber et al. 2018, or in Abell 1775; Botteon et al. 2021a).

The smoothed RASS image is shown in Fig. 21(iii) which highlights a faint X-ray structure detected as the cluster, elongated towards the SE. The X-ray emission does not elucidate the nature of the diffuse components based on location, however, the diffuse emission resides within the clearly elongated X-ray emission to the south of the cluster, thus is in a region where we can assume dynamical activity is occurring.

3.1.9. FIELD11

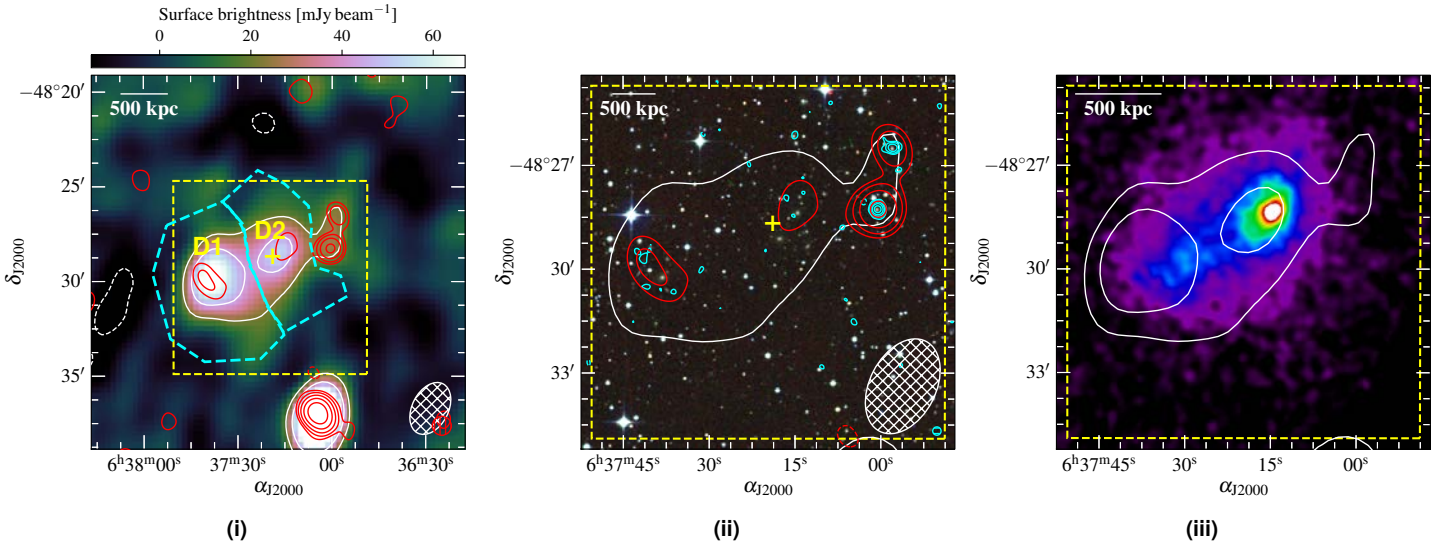

Figure 19. Abell 3399. (i) Background: MWA-2, 118-MHz, robust +2.0 image. (ii) Background: RGB SSS image (*i*, *r*, *b*). (iii). Background: smoothed *Chandra* image. The white contours are as in Fig. 2(i) for the background of (i) (with $\sigma_{\rm rms}$ = 7.3 mJy beam^{-1}). Red contours: RACS discrete source-subtracted image, $[\pm3, 6, 12, 24, 48] \times \sigma_{\rm rms}$ ($\sigma_{\rm rms}$ = 0.45 mJy beam^{-1}). Cyan contours: RACS survey image, $[\pm3, 6, 12, 24, 48] \times \sigma_{\rm rms}$ ($\sigma_{\rm rms}$ = 0.17 mJy beam^{-1}). Other image features are as in Fig. 2.

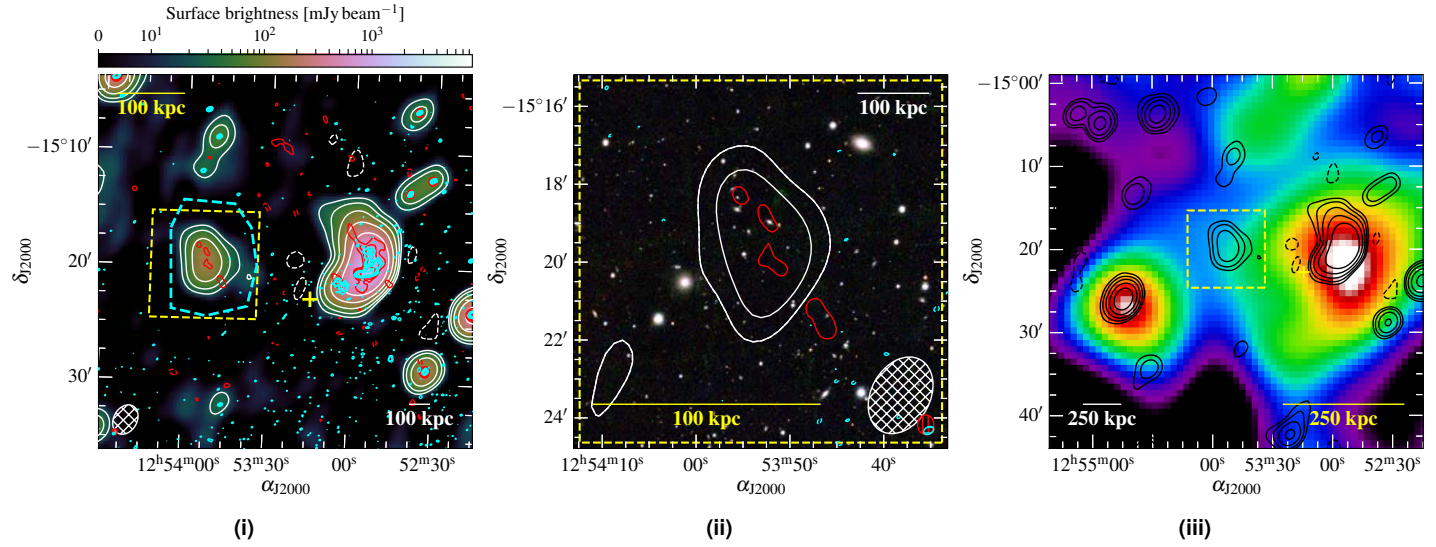

Figure 20. MCXC J1253.2−1522 (Abell 1631). (i) Background: MWA-2, 118-MHz, robust +2.0 image. (ii) Background: RGB PS1 image (*i*, *r*, *g*). (iii). Background: smoothed RASS image. The white (black) contours are as in Fig. 2(i) for the background of (i) (with $\sigma_{\rm rms}$ = 7.0 mJy beam^{-1}). Red contours: TGSS image, $[\pm3, 6, 12, 24, 48] \times \sigma_{\rm rms}$ ($\sigma_{\rm rms}$ = 3.5 mJy beam^{-1}). Cyan contours: RACS survey image, $[3, 6, 12, 24, 48] \times \sigma_{\rm rms}$ ($\sigma_{\rm rms}$ = 0.32 mJy beam^{-1}). Other image features are as in Fig. 2, with the addition of a separate, yellow linear scale at the redshift of Abell 1631.

Abell 3365. (Fig. 22). Abell 3365 (RXC J0548.8−2154) was reported to host a relic and candidate second relic by van Weeren et al. (2011)—at the time, spectral coverage was minimal. While not in our original survey scope, the cluster resides at the edge of a field that was opportunistically processed for other targets. We show the 154-MHz map in Fig. 22 with RACS contours overlaid. The NE relic is detected (D1), and the SW candidate relic source is also detected (D2). An additional extension, labelled D3, is also detected that has not been identified in other radio maps. We utilise the additional spectral coverage offered by the MWA-2 and find, after subtraction of Source A, a power law model for the NE relic, with $\alpha^{1420}_{\rm D1,88} = -0.85 \pm 0.03$ (Fig. 26(xxvii)). We note a curious feature of the flux density measurements wherein the lower MWA bands separate from the higher bands—we cannot explain this feature as either instrumental or physical. While the relic is detected in the RACS data, we note significant negative bowls around the source indicating a lack of flux recovery. A lower limit is provided but not used in fitting. The resultant spectral shape is reasonably shallow for a relic. The SW relic (D2) is detected in MWA-2 data as well, but is too confused in the 88-MHz band. The resultant SED provides $\alpha^{1420}_{\rm D2,118} = -0.76 \pm 0.08$ (Fig. 26(xxviii)), noting that the discrete Source A discussed by van Weeren et al. (2011) is not

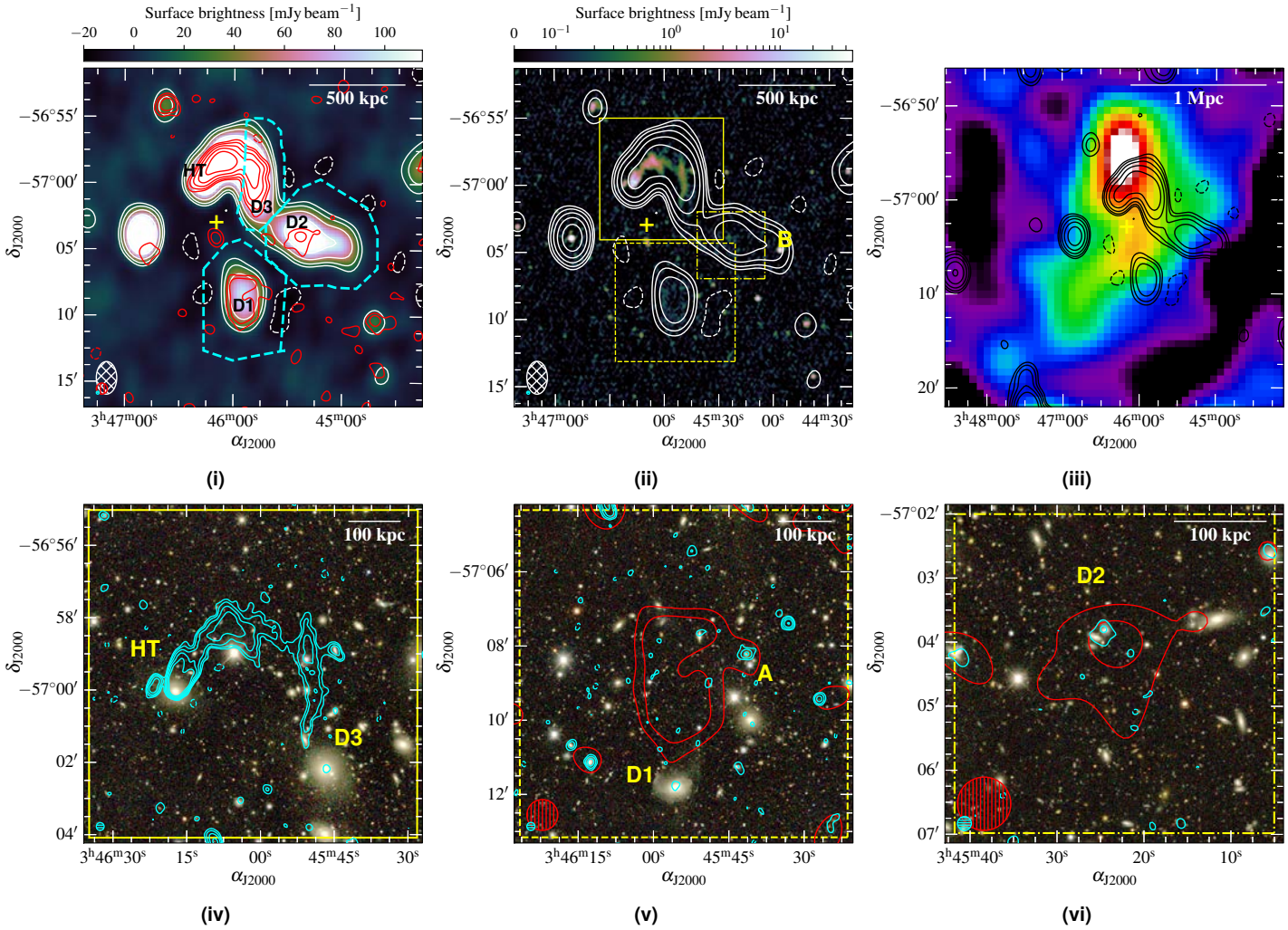

Figure 21. Abell 3164. Background: MWA-2, 154-MHz, robust +2.0 image. (ii) Background: VAST robust 0.0 image. (iii) Background: smoothed, RASS image. (iv)–(vi) Background: RGB DES image (i, r, g). The white contours are as in Fig. 2(i) for the background of (i) (with $\sigma_{\rm rms}$ = 4.3 mJy beam^{-1}). Red contours: VAST source-subtracted image, $[\pm3, 6, 12, 24, 48] \times \sigma_{\rm rms}$ ($\sigma_{\rm rms}$ = 0.17 mJy beam^{-1}). Cyan contours: VAST robust 0.0 image, $[\pm3, 6, 12, 24, 48] \times \sigma_{\rm rms}$ ($\sigma_{\rm rms}$ = 0.09 mJy beam^{-1}). Other image features are as in Fig. 2. Yellow boxes on (ii) indicate the locations of (iv)–(vi).

confused in these bands and is not required to be subtracted.

Golovich et al. (2019) present deep XMM-*Newton* observations of the cluster along with spectro-optical analysis (see their Fig. 25), highlighting the merger axis and location of the candidate SW relic with respect to three subclusters within the system. They note there is no distinct alignment of the subclusters with the W relic candidate (D2), and given the shallow spectrum we suggest this is not a relic source.

Despite this, Urdampilleta et al. (2021) find significant temperature jumps across both relics, finding evidence for shocks with Mach numbers $\mathcal{M}_{\rm west} = 3.9 \pm 0.8$ and $\mathcal{M}_{\rm east} = 3.5 \pm 0.6$, which for DSA may produce relics with flatter spectral indices as observed here. Assuming DSA for these relics, and assuming $\alpha_{\rm integrated} = \alpha_{\rm inj}$ as might be the case for a re-accelerated fossil electron population (e.g. van Weeren et al., 2016), we find radio Mach numbers of $\mathcal{M}_{\rm RW} = 4.2 \pm 0.4$ and $\mathcal{M}_{\rm RE} = 2.5 \pm 0.1$ for the western and eastern relics, respectively. If accelerated from the thermal pool, we would expect $\alpha_{\rm inj} = \alpha_{\rm integrated} + 0.5$, resulting in a non-physical Mach number under standard DSA. The nature of both sources (D1 and D2) is uncertain.

Abell 0550. (Fig. 23). We report the detection of a large-scale, elongated emission structure on the periphery of Abell 0550 (Fig. 23(i) with an LAS of $\sim$ 15 arcmin (LLS $\approx$ 1.6 Mpc). We detect the source between 88–154 MHz in the MWA-2 data. We note that there is a spiral galaxy (WISEA J055346.34−211119.6, no redshift) near the centre of the emission, shown in Fig. 23(ii), denoted with an 'S'. Spiral galaxies rarely host large-scale radio lobes, though a small number have been detected, sometimes with remnant lobes (e.g. Hota et al., 2011) and this may be such an example. With no compact emission detected in RACS from the spiral galaxy, we can rule out significant AGN contribution and suggest the emission seen in the NVSS and MWA-2 images is related to star-formation processes and that the galaxy, if the host, is not actively fuelling the lobes, consistent with a steep spectrum. The resultant spectrum (Fig. 26(xxix)), with the spiral and compact Source A subtracted flattens at 1.4 GHz, and is fit with a generic curved power law,

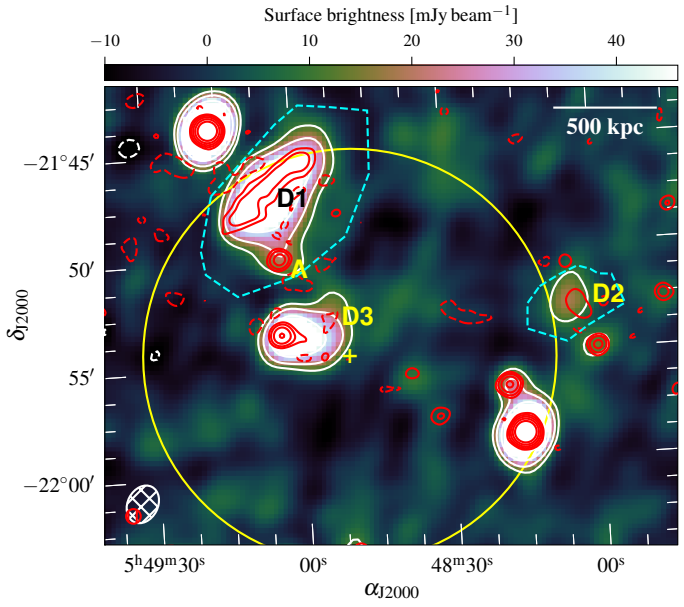

Figure 22. Abell 3365. Background: MWA-2, 154-MHz, robust +1.0 image. The white contours are as in Fig. 2(i) for the background image (with $\sigma_{\rm rms}$ = 3.5 mJy beam^{-1}). Red contours: RACS low-resolution, $[\pm3, 6, 12, 24, 48] \times \sigma_{\rm rms}$ ($\sigma_{\rm rms}$ = 0.47 mJy beam^{-1}). Other image features are as in Fig. 2 and Fig. 3. Note the white circle has a 1 Mpc radius, centered on the coordinates associated with RXC J0548.8−2154 (i.e. the X-ray component for the system).

though the physical interpretation of this is not clear. New kpc-scale jets from the spiral that are not subtracted may contribute to the spectral flattening, though this is unlikely to be so extreme and we suggest residual flux from the extended emission from the spiral is affecting the measurements. Across the MWA band we fit a power law model finding a spectral index of $\alpha_{88}^{154} = -2.4 \pm 0.3$. Fig. 23(iii) shows the emission with respect to the X-ray–emitting core of the cluster, though the source is at the edge of the X-ray data. Bernardi et al. (2016) observed the cluster with KAT-7, searching for a central radio halo. This elongated source is outside of their observed FoV but a halo was not detected, and the data here (MWA-2 and re-processed RACS) do not suggest the presence of a halo either.

4. Discussion

4.1. *Low frequency radio halos and relics*

Scaling relationships between diffuse source radio luminosity and cluster properties (e.g. M_{500}) have been established for halos, mini-halos, and relics. Recent works have shown that for radio halos these relationships are converging at 1.4 GHz and 150 MHz (Cuciti et al., 2021; van Weeren et al., 2021; Duchesne et al., 2021c). For relics this is less certain as confirmed radio relic numbers remain low, and scaling relations here typically utilise double relic detections (e.g. de Gasperin et al., 2014, 2015; Duchesne et al., 2021a). Similar relationships are found for mini-halos (e.g. Giacintucci et al., 2019; Richard-Laferrière et al., 2020), though the effect of the CC on cluster properties (e.g. mass) and contribution of the radio-loud BCG on the estimated mini-halo power may create additional uncertainty in the relations (e.g. Richard-Laferrière et al., 2020).

Despite scatter in these relations, sources in each class tend to stay near the currently determined fits. As a point of comparison, we plot a selection of our sources (namely, candidate halos, relics, and some of the miscellaneous fossil sources) on the P_ν–M_{500} planes to compare against the larger samples. Fig. 24 shows these relations for halos (Fig. 24(i) and Fig. 24(ii)) and relics (Fig. 24(iii) and Fig. 24(iv)) for $\nu \in \{150, 1400\}$ MHz. For each, we plot the best-fit relations from Duchesne et al. (2021c) and Duchesne et al. (2021a) for halos and relics, respectively. Additionally, the full literature samples used in those works are plotted, and the P_{150}–M_{500} relation for double relics is scaled from 1400 MHz following Equation 6 from Duchesne et al. (2021c), assuming a mean spectral index of $\alpha = -1.2$.

As expected, at 150 MHz the candidate USSRHs in Abell 2811 and PSZ1 G287.95−32.98 shift to be placed on the orthogonal regression line. This is largely consistent with the USSRH population (e.g. Cassano et al., 2013; Bruno et al., 2021; Duchesne et al., 2021c) which are normally found to be under-luminous with respect to the 1400 MHz scaling relations but shift towards the regression line when the relation is computed at 150 MHz. Conversely, the candidate halo (or point source) in Abell 2693 sits far above both relations, though the derived mass approaches the limits obtainable with RASS and carries significant uncertainty. Given how few halos are detected in low mass clusters ($\lesssim 5 \times 10^{14}$ M$_\odot$) and our lack of understanding in this low-mass regime it is difficult to rule out the radio halo classification, however, as discussed previously other characteristics (e.g. location) are less consistent with a halo interpretation. While we suggest the sources in Abell 3164 are fossil plasma sources, their nature is still somewhat uncertain and D1 and D2 are included on Fig. 24(iii) and Fig. 24(iv) as a reference.

4.2. *Clues from integrated spectra—seed electrons & palaeontology*

4.2.1. *Cluster diffuse sources samples*

We find that of the 31 sources reported in this survey [1], that 13 are likely fossil radio plasma sources: remnant radio galaxies or otherwise remnant outflows from AGN at unknown stages after cessation of an episode of nuclear activity. These sources are labelled 'F' and 'r' in Table 1. For classification purposes, in Table 1 remnant ('r') is used when the morphology still resembles a radio galaxy and when a possible host is identified. These sources are unlikely to be radio halos or relics based on largely morphological and other physical characteristics.

Having established this sample we wish to consider how fossil radio plasmas relate to other diffuse cluster emission. In particular, we wish to consider the question of whether these sources provide a link between the source of electrons in the ICM from which relics and halos may be generated. With the MWA (and ASKAP) we are able to obtain estimates of the spectral index in the MHz regime where most emission models retain power law shapes, and comparisons between different classes of sources (fossils, halos,

[1] Including candidate sources, and radio galaxies/point sources discussed in Section 3.1.

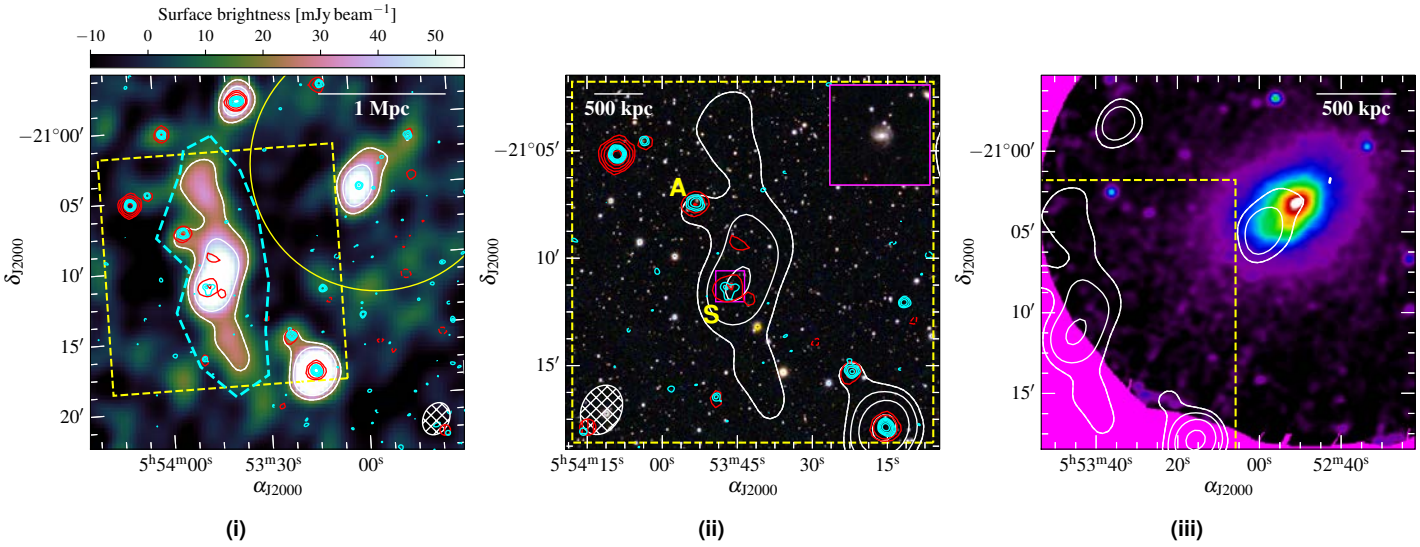

Figure 23. Abell 0550. Background: MWA-2, 118-MHz, robust +1.0 image. (ii) Background: RGB PS1 image (i, r, g). (iii). Background: smoothed XMM-*Newton* EPIC image. The white contours are as in Fig. 2(i) for the background of (i) (with $\sigma_{\rm rms}$ = 6.6 mJy beam^{-1}). Red contours: NVSS image, $[\pm3, 6, 12, 24, 48]\times\sigma_{\rm rms}$ ($\sigma_{\rm rms}$ = 0.57 mJy beam^{-1}). Cyan contours: RACS robust +0.25 image, $[\pm3, 6, 12, 24, 48]\times\sigma_{\rm rms}$ ($\sigma_{\rm rms}$ = 0.25 mJy beam^{-1}). Other image features are as in Fig. 2 and Fig. 3. Note (iii) clips at the location of relic as that is the FoV of the XMM-*Newton* observation.

relics, and remnant radio galaxies) will not be overly effected by spectral curvature.

Table 4 presents details of a literature sample of integrated spectral indices for populations of halos (H), relics (R), mini halos (mH), remnants (r), and cluster-based fossil sources (F), which we compare to our cluster remnant and fossil sample. Where available, we use spectral indices derived from low-frequency measurements (i.e. within the MWA band, ∼ 150 MHz up to ∼ 1 GHz).

Spectral indices have been derived from a variety of measurements/instruments and spectra may steepen (if a low-frequency observation is more sensitive; e.g. Macario et al., 2010) or flatten (if a high-frequency observation is more sensitive; e.g. Ogrean et al., 2015) artificially due to a mismatch of u, v sampling and general sensitivity between observations. This introduces further uncertainty to the spectral indices, but is not likely to bias the distributions significantly towards steeper or flatter spectra.

We show the histograms of reported α in Fig. 25 for our sample of cluster fossil plasma sources (r and F in Table 1) against three classes of objects from the samples described in Table 4: i) halos and mini halos, ii) relics (both single and double systems), and iii) cluster fossils sources and both field and cluster remnants.

Median α obtained for each distribution are reported in Table 4. We note the single relic population is unlikely to be fundamentally different to the double relic population, which are thought to form through the same shock-acceleration processes. This is evident in Fig. 25(ii) which shows the distribution of α is not significantly different between the two samples. Furthermore, the halo and relic median spectral indices are consistent, suggesting a common generation time if drawn from the same underlying electron population (though as discussed previously the generation mechanisms are thought to be different, but both associated with mergers). We note that the radio halo sample shown in Fig. 25(i) includes USSRHs as expected from turbulent (re-)acceleration processes which creates a significant tail in the distribution towards steeper spectra. Relics show a similar ultra-steep–spectrum tail but are much more densely peaked around their median value.

Table 4 Median spectral indices for the diffuse source populations.

Type	Number	med(α)	Ref.[a]
R	46	-1.2 ± 0.2	(a),(b)
H	35	-1.3 ± 0.3	(c)
mH	12	-1.2 ± 0.1	(d)
r (field)	35	-0.9 ± 0.2	(e),(f),(g)
r (cluster)	6	-1.8 ± 0.4	(h)
F	21	-1.7 ± 0.4	(b),(i),(j),(k),(l)
r/F	13	-1.7 ± 0.4	this work

[a] Samples drawn from: (a) Duchesne et al. (2021a); (b) van Weeren et al. (2019); (c) Duchesne et al. (2021c); (d) Richard-Laferrière et al. (2020); (e) Brienza et al. (2017); (f) Mahatma et al. (2018); (g) Quici et al. (2021); (h) Murgia et al. (2011); (i) Duchesne et al. (2020); (j) Mandal et al. (2020); (k) Giacintucci et al. (2020); (l) Hodgson et al. (2021).

4.2.2. *Remnants, fossils, and revived radio plasma: seed electron populations?*

Fig. 25 shows that, in general, fossil plasma sources tend towards steeper spectra than the relic and halo populations, and are significantly steeper than field remnant radio galaxies. The few remnants found in clusters (e.g. Murgia et al., 2011) typically have steeper spectra at equivalent frequencies than their field counterparts .

Note also Parma et al. (2007) reports a small number of remnants within cluster environments, though their sample was taken from sources with $\alpha < -1.3$ so by construction they are steeper than remnants found in recent searches.

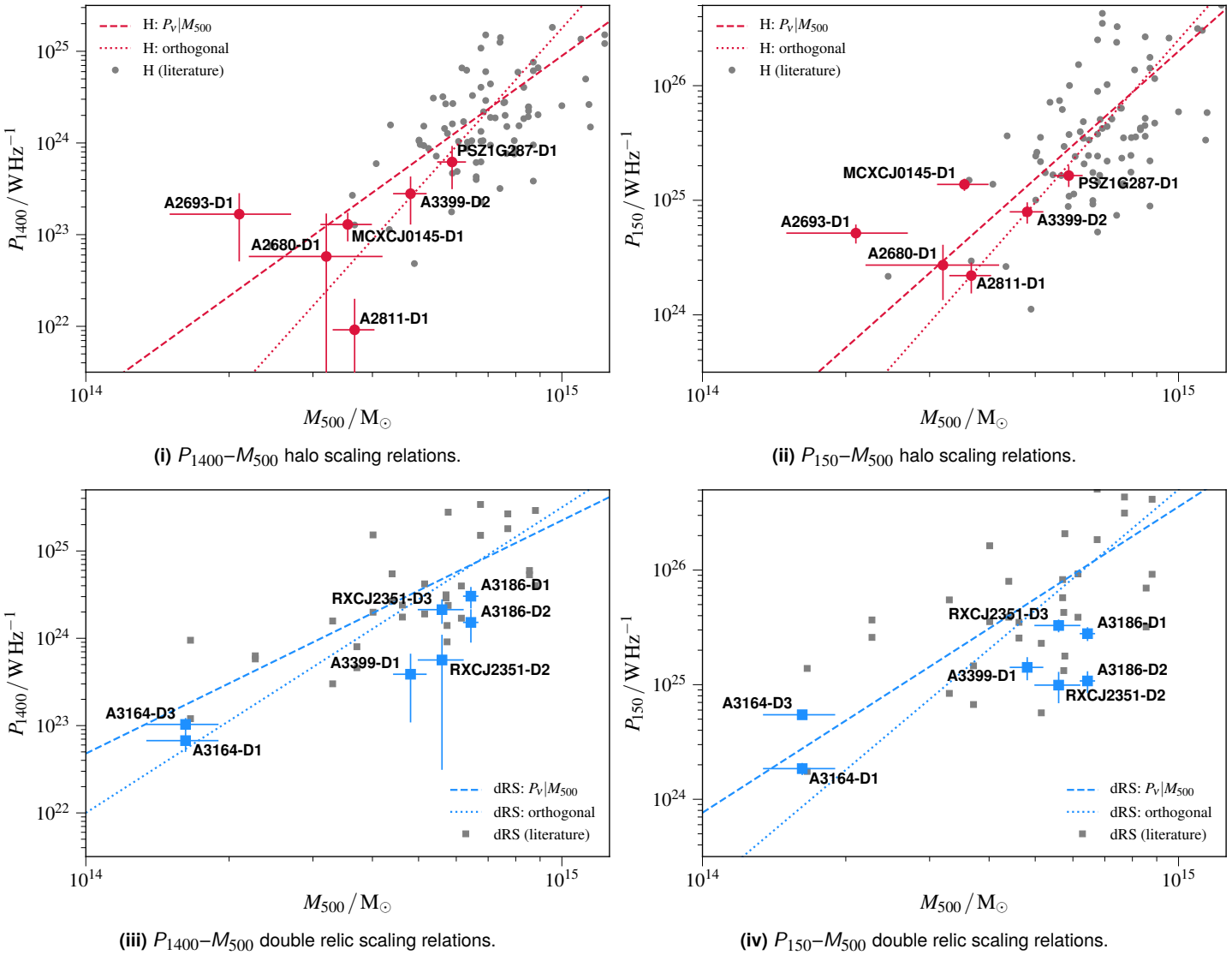

(i) P_{1400}–M_{500} halo scaling relations.

(ii) P_{150}–M_{500} halo scaling relations.

(iii) P_{1400}–M_{500} double relic scaling relations.

(iv) P_{150}–M_{500} double relic scaling relations.

Figure 24. Halo and double relic P_ν–M_{500} scaling relations with candidate sources from this work overlaid. Best-fit lines are also shown from Duchesne et al. (2021a) for relics, with scaling to 150 MHz, and Duchesne et al. (2021c) for halos. Literature data as discussed in Duchesne et al. (2021a) and Duchesne et al. (2021c) are also shown for reference. $P_\nu|M_{500}$ refers to fits determined assuming P_ν is the dependent variable and M_{500} the independent variable, and 'orthogonal' refers to an orthogonal regression using the Bivariate Correlated Errors and intrinsic Scatter method (BCES; Akritas & Bershady, 1996)—see Duchesne et al. (2021c) for further BCES fitting details.

Sources such as D1 in Abell S1099 may represent a younger cluster remnant, and with no evidence of morphological disturbance of the ICM we do not consider this a re-accelerated source. It is likely the cluster environment plays a role in allowing these sources to remain visible for longer (e.g. by constraining diffusion of the electrons into the surrounding ICM; Murgia et al. 2011). Studies (Brienza et al., 2017; Mahatma et al., 2018; Jurlin et al., 2020; Quici et al., 2021) suggest remnants have a short observable lifetime before surface brightness becomes prohibitively faint as the plasma both steepens in spectrum and expands. With low numbers of these remnant and fossil sources, it is difficult to draw firm conclusions about the role of the cluster environment.

Given the ubiquity of radio galaxies of complex morphologies in clusters (e.g. Hardcastle & Sakelliou, 2004; Clarke & Ensslin, 2006; Sakelliou et al., 2008; Botteon et al., 2020c; Brüggen et al., 2021) we expect a large population of these fossil plasma sources waiting to be re-accelerated by merger-based shocks and turbulence. By construction, we have steep-spectrum (and ultra-steep–spectrum) sources in either relaxed, or 'ambiguously dynamic' clusters that cannot be described as relics or halos—these are likely fossil radio plasma and highlight a population of sources in clusters that can provide seed electrons for relic and halo sources as well as smaller-scale revived fossil plasma like phoenices.

Examples exist in the literature of re-acceleration of fossil plasmas with some connection to AGN (e.g. Bonafede et al., 2014; van Weeren et al., 2017; de Gasperin, 2017; Wilber et al., 2019), and simulations have shown that fossil electrons from AGN outflows and long-dead radio galaxies can (1) exist diffusively within the ICM (Vazza et al., 2021) and (2) be re-accelerated by normal DSA-like processes (e.g. Kang, 2018). It is not clear that the accel-

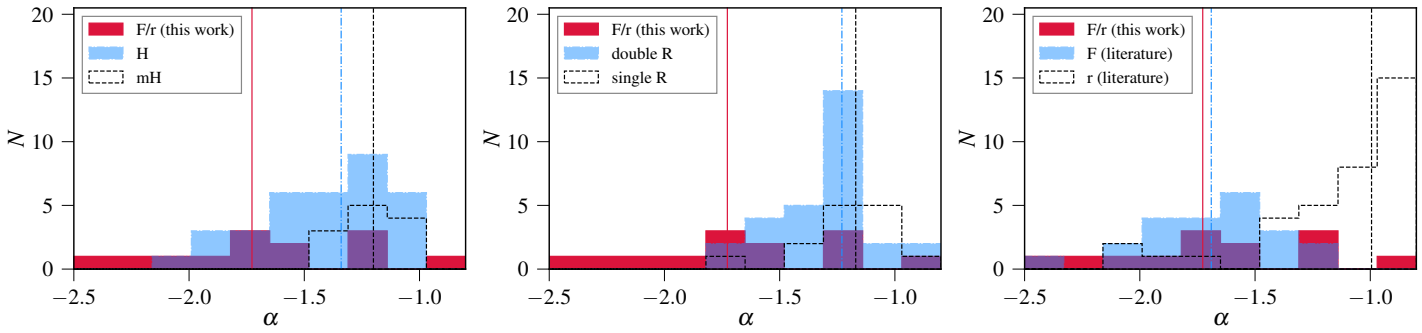

Figure 25. Spectral index distributions for (i) radio halos, (ii) relics (double and single), and (iii) remnant radio galaxies and fossil radio plasma sources, compared to the collection of fossils plasma sources reported in this work. See Section 4.2 and Table 4 for population details. Vertical lines indicate median population values. Note that bins are clipped at $-2.5 \geq \alpha \geq -0.8$, and our sample is generally clipped at ~ -0.9 by construction due to the original search criteria.

eration efficiency for electrons at shocks is sufficient to produce the observed relics unless there is a mildly-relativistic population (e.g. Botteon et al. 2020b), though many observed properties of relics do not require a population of fossil electrons (e.g. Rajpurohit et al., 2020, 2021b). The distribution of α for relics and halos extends into the ultra-steep–spectrum regime which would be consistent with a population of re-accelerated fossil electrons in low-energy events (e.g. from weak mergers triggering USSRH; Brunetti et al. 2008), though it is not clear whether the density of such a fossil electron population would be sufficient to produce the observed emission. In general, such weaker events should be more common and simulations suggest a large population of faint diffuse sources should exist (e.g. Nuza et al., 2012); however, these low surface brightness and ultra-steep spectrum sources are still challenging to detect and image. Surveys with e.g. LOFAR (especially combining HBA and LBA data for spectral information) should uncover a larger number of these ultra-steep–spectrum sources and indeed instruments like MWA, LOFAR, and the uGMRT are now starting to uncover them (e.g. Giacintucci et al., 2020; Mandal et al., 2020; Hodgson et al., 2021).

5. Summary

In this work we have reported an MWA-2 follow-up survey of candidate diffuse cluster radio sources originally detected in MWA Phase I data as part of the GLEAM survey and EoR0 field survey (D21). We have combined the MWA-2 data with recent ASKAP data at 887 MHz to (1) attempt to classify the sources based on their morphologies, host cluster properties, and SEDs and (2) simply ensure sources are not confused point sources—an ongoing problem with low-resolution interferometric observations. We report on 31 sources, with 6 candidate halos, 2 mini-halos (1 candidate), 3 relics (1 candidate and 1 double relic system), 13 remnant AGN or miscellaneous fossil plasmas. Some of the candidate sources are found to be point sources or radio galaxies, and we also follow-up the 'twin relic' in Abell 0168 reported by Dwarakanath et al. (2018) and the double-relic system in Abell 3365 reported by van Weeren et al. (2011). Specifically, we report the detection of a new double relic system associated with Abell 3186, a mini-halo associated with RXC J0137.2−0912 and that the candidate halo in Abell 2811 reported by D21 has a spectral index of $\alpha = -2.5 \pm 0.4$, though this will require follow-up high resolution, high-sensitivity observations to confirm its nature. We also observe an HT galaxy in Abell 3164 that exhibits episodic activity with a potentially re-accelerated component.

We find that generally the relics and halos presented here sit in reasonable locations on the established P_{1400}–M_{500} and P_{150}–M_{500} scaling relations, with the USSRHs shifting closer towards the P_{150}–M_{500} relation. We also compare the integrated spectra of our sample of cluster fossil and remnant sources against various samples of steep-spectrum, diffuse cluster sources as well as field remnant radio galaxies, finding that the general spectral properties are consistent with the literature fossil radio source population. This is in turn consistent with the integrated, low-frequency spectral indices of cluster-based remnant radio galaxies. We have discussed the putative link between these fossil sources and other diffuse cluster sources, noting that the distributions of spectral indices for diffuse clusters sources would be consistent with fossil radio plasmas as seed electrons for the emission.

In this work we have just gently brushed the dust off of a small collection of old fossils and large-scale, deep, and high-resolution surveys with the SKA pathfinders—particularly ASKAP and MeerKAT with $\sim$ 5–15 arcsec resolution over the Southern Sky—will enable high-fidelity follow-up of these types of sources placing constraints on the $\gtrsim$ 1 GHz spectrum. In the future SKA should dig deeper, revealing myriad new ultra-steep spectrum radio fossils, providing key observational evidence for any link between these sources and cluster halos and relics.

Acknowledgements. We would like to thank an anonymous referee for their useful feedback. The authors would like to thank Dr. Paula Tarrío Alonso for providing mass estimates for Abell 2680 and Abell 2693. SWD acknowledges an Australian Government Research Training Program scholarship administered through Curtin University. The Australian SKA Pathfinder is part of the Australia Telescope National Facility which is managed by CSIRO. Operation of ASKAP is funded by the Australian Government with support from the National Collaborative Research Infrastructure Strategy. ASKAP uses the resources of the Pawsey Supercomputing Centre. Establishment of ASKAP, the Murchison Radio-astronomy Ob-

servatory and the Pawsey Supercomputing Centre are initiatives of the Australian Government, with support from the Government of Western Australia and the Science and Industry Endowment Fund. We acknowledge the Wajarri Yamatji people as the traditional owners of the Observatory site. Support for the operation of the MWA is provided by the Australian Government (NCRIS), under a contract to Curtin University administered by Astronomy Australia Limited. This research has made use of data obtained from the *Chandra* Data Archive and the *Chandra* Source Catalog, and software provided by the *Chandra* X-ray Center (CXC) in the application package `CIAO`. This research has made use of the NASA/IPAC Extragalactic Database (NED), which is operated by the Jet Propulsion Laboratory, California Institute of Technology, under contract with the National Aeronautics and Space Administration. This research has made use of the VizieR catalogue access tool, CDS, Strasbourg, France. The original description of the VizieR service was described in Ochsenbein et al. (2000).

This research made use of a number of `python` packages not explicitly mentioned in the main text: `aplpy` (Robitaille & Bressert, 2012), `astropy` (Astropy Collaboration et al., 2013), `matplotlib` (Hunter, 2007), `numpy` (van der Walt et al., 2011) and `scipy` (Jones et al., 2001).

References

Abbott T. M. C., et al., 2018, ApJS, 239, 18
Abell G. O., 1958, ApJS, 3, 211
Abell G. O., Corwin Jr. H. G., Olowin R. P., 1989, ApJS, 70, 1
Akritas M. G., Bershady M. A., 1996, ApJ, 470, 706
Astropy Collaboration et al., 2013, A&A, 558, A33
Bagchi J., et al., 2011, ApJ, 736, L8
Bartalucci I., et al., 2017, A&A, 608, A88
Bernardi G., et al., 2016, MNRAS, 456, 1259
Bock D. C.-J., Large M. I., Sadler E. M., 1999, AJ, 117, 1578
Bogdán Á., et al., 2013, ApJ, 772, 97
Böhringer H., et al., 2004, A&A, 425, 367
Böhringer H., et al., 2010, A&A, 514, A32
Bonafede A., et al., 2012, MNRAS, 426, 40
Bonafede A., Intema H. T., Brüggen M., Girardi M., Nonino M., Kantharia N., van Weeren R. J., Röttgering H. J. A., 2014, ApJ, 785, 1
Botteon A., Gastaldello F., Brunetti G., Dallacasa D., 2016a, MNRAS, 460, L84
Botteon A., Gastaldello F., Brunetti G., Kale R., 2016b, MNRAS, 463, 1534
Botteon A., et al., 2018, MNRAS, 478, 885
Botteon A., et al., 2020a, MNRAS, 499, L11
Botteon A., Brunetti G., Ryu D., Roh S., 2020b, A&A, 634, A64
Botteon A., et al., 2020c, ApJ, 897, 93
Botteon A., et al., 2021a, A&A, 649, A37
Botteon A., et al., 2021b, ApJ, 914, L29
Bourdin H., Mazzotta P., 2008, A&A, 479, 307
Bourdin H., Mazzotta P., Markevitch M., Giacintucci S., Brunetti G., 2013, ApJ, 764, 82
Bravi L., Gitti M., Brunetti G., 2016, MNRAS, 455, L41
Brienza M., et al., 2017, A&A, 606, A98
Briggs D. S., 1995, PhD thesis, The New Mexico Institute of Mining and Technology, Socorro, New Mexico, `http://www.aoc.nrao.edu/dissertations/dbriggs/`
Brüggen M., et al., 2021, A&A, 647, A3
Brunetti G., Jones T. W., 2014, International Journal of Modern Physics D, 23, 1430007
Brunetti G., Vazza F., 2020, Phys. Rev. Lett., 124, 051101
Brunetti G., Setti G., Feretti L., Giovannini G., 2001, MNRAS, 320, 365
Brunetti G., et al., 2008, Nature, 455, 944
Brunetti G., Cassano R., Dolag K., Setti G., 2009, A&A, 507, 661
Bruno L., et al., 2021, A&A, 650, A44
Buote D. A., 2001, ApJ, 553, L15
Caretta C. A., Maia M. A. G., Kawasaki W., Willmer C. N. A., 2002, AJ, 123, 1200
Cassano R., Ettori S., Giacintucci S., Brunetti G., Markevitch M., Venturi T., Gitti M., 2010, ApJ, 721, L82
Cassano R., et al., 2013, ApJ, 777, 141
Cavagnolo K. W., Donahue M., Voit G. M., Sun M., 2008, ApJ, 682, 821
Cavaliere A., Fusco-Femiano R., 1976, A&A, 49, 137
Chambers K. C., et al., 2016, preprint, (`arXiv:1612.05560`)
Chapman J. M., Dempsey J., Miller D., Heywood I., Pritchard J., Sangster E., Whiting M., Dart M., 2017, CASDA: The CSIRO ASKAP Science Data Archive. p. 73
Chon G., Böhringer H., 2012, A&A, 538, A35
Clarke T. E., Ensslin T., 2006, Astronomische Nachrichten, 327, 553
Clarke T. E., Kronberg P. P., Böhringer H., 2001, ApJ, 547, L111
Cohen A. S., Clarke T. E., 2011, AJ, 141, 149
Condon J. J., Cotton W. D., Greisen E. W., Yin Q. F., Perley R. A., Taylor G. B., Broderick J. J., 1998, AJ, 115, 1693
Coziol R., Andernach H., Caretta C. A., Alamo-Martínez K. A., Tago E., 2009, AJ, 137, 4795
Cruddace R., et al., 2002, ApJS, 140, 239
Cuciti V., et al., 2021, A&A, 647, A51
De Grandi S., et al., 1999, ApJ, 514, 148
Di Gennaro G., et al., 2021, Nature Astronomy, 5, 268
Duchesne S., 2021, Data for an MWA-2 survey of diffuse radio emission in galaxy clusters, doi:10.26185/611f33b774e96, `https://dx.doi.org/10.26185/611f33b774e96`
Duchesne S. W., Johnston-Hollitt M., Zhu Z., Wayth R. B., Line J. L. B., 2020, PASA, 37, e037
Duchesne S. W., Johnston-Hollitt M., Bartalucci I., Hodgson T., Pratt G. W., 2021a, PASA, 38, e005
Duchesne S. W., Johnston-Hollitt M., Offringa A. R., Pratt G. W., Zheng Q., Dehghan S., 2021b, PASA, 38, e010
Duchesne S. W., Johnston-Hollitt M., Wilber A. G., 2021c, PASA, 38, e031
Duffy P., Blundell K. M., 2012, MNRAS, 421, 108
Dwarakanath K. S., Parekh V., Kale R., George L. T., 2018, MNRAS, 477, 957
Enßlin T. A., Brüggen M., 2002, MNRAS, 331, 1011
Enßlin T. A., Gopal-Krishna 2001, A&A, 366, 26
Enßlin T. A., Biermann P. L., Klein U., Kohle S., 1998, A&A, 332, 395
Fairall A. P., 1984, MNRAS, 210, 69
Finoguenov A., Sarazin C. L., Nakazawa K., Wik D. R., Clarke T. E., 2010, ApJ, 715, 1143
Flaugher B., et al., 2015, AJ, 150, 150
Fleenor M. C., Rose J. A., Christiansen W. A., Johnston-Hollitt M., Hunstead R. W., Drinkwater M. J., Saunders W., 2006, AJ, 131, 1280
Flin P., Krywult J., 2006, A&A, 450, 9
Fruscione A., et al., 2006, in Proc. SPIE. p. 62701V, doi:10.1117/12.671760
Garilli B., Maccagni D., Tarenghi M., 1993, A&AS, 100, 33
Garmire G. P., Bautz M. W., Ford P. G., Nousek J. A., Ricker George R. J., 2003, in Truemper J. E., Tananbaum H. D., eds, Society of Photo-Optical Instrumentation Engineers (SPIE) Conference Series Vol. 4851, X-Ray and Gamma-Ray Telescopes and Instruments for Astronomy.. pp 28–44, doi:10.1117/12.461599
Giacintucci S., Markevitch M., Cassano R., Venturi T., Clarke T. E., Kale R., Cuciti V., 2019, ApJ, 880, 70
Giacintucci S., Markevitch M., Johnston-Hollitt M., Wik D. R., Wang Q. H. S., Clarke T. E., 2020, ApJ, 891, 1
Gitti M., Brunetti G., Setti G., 2002, A&A, 386, 456
Golovich N., et al., 2019, ApJ, 882, 69
Govoni F., et al., 2019, Science, 364, 981
Hambly N. C., et al., 2001a, MNRAS, 326, 1279
Hambly N. C., Irwin M. J., MacGillivray H. T., 2001b, MNRAS, 326, 1295
Hambly N. C., Davenhall A. C., Irwin M. J., MacGillivray H. T., 2001c, MNRAS, 326, 1315
Hancock P. J., Trott C. M., Hurley-Walker N., 2018, PASA, 35, e011
Hardcastle M. J., Sakelliou I., 2004, MNRAS, 349, 560
Hindson L., et al., 2014, MNRAS, 445, 330
Hodgson T., Johnston-Hollitt M., McKinley B., Vernstrom T., Vacca V., 2020, PASA, 37, e032

Hodgson T., Bartalucci I., Johnston-Hollitt M., McKinley B., Vazza F., Wittor D., 2021, ApJ, 909, 198

Hoeft M., Brüggen M., 2007, MNRAS, 375, 77

Hota A., et al., 2011, MNRAS, 417, L36

Hotan A., McConnell D., Whiting M., Huynh M., 2020b, ASKAP Data Products for Project AS110 (The Rapid ASKAP Continuum Survey): images and visibilities. v1. CSIRO. Data Collection, http://hdl.handle.net/102.100.100/374841?index=1

Hotan A., Whiting M., Huynh M., Moss V., 2020a, ASKAP Data Products for Project AS113 (Other ASKAP pilot science including tests, TOOs or guest observations): images and visibilities. v1. CSIRO. Data Collection., http://hdl.handle.net/102.100.100/348894?index=1

Hotan A. W., et al., 2021, PASA, 38, e009

Hunter J. D., 2007, Computing in Science and Engineering, 9, 90

Hurley-Walker N., et al., 2017, MNRAS, 464, 1146

Huynh M., Dempsey J., Whiting M. T., Ophel M., 2020, in Ballester P., Ibsen J., Solar M., Shortridge K., eds, Astronomical Society of the Pacific Conference Series Vol. 522, Astronomical Data Analysis Software and Systems XXVII. p. 263

Intema H. T., Jagannathan P., Mooley K. P., Frail D. A., 2017, A&A, 598, A78

Jaffe W. J., 1977, ApJ, 212, 1

Johnston-Hollitt M., 2003, PhD thesis, University of Adelaide

Jonas J., MeerKAT Team 2016, in MeerKAT Science: On the Pathway to the SKA. p. 1

Jones E., Oliphant T., Peterson P., et al., 2001, SciPy: Open source scientific tools for Python, http://www.scipy.org/

Jones D. H., et al., 2009, MNRAS, 399, 683

Jurlin N., et al., 2020, A&A, 638, A34

Kang H., 2015, Journal of Korean Astronomical Society, 48, 155

Kang H., 2018, Journal of Korean Astronomical Society, 51, 185

Kang H., Ryu D., 2011, ApJ, 734, 18

Kang H., Ryu D., 2016, ApJ, 823, 13

Kempner J. C., Sarazin C. L., 2001, ApJ, 548, 639

Knowles K., et al., 2021, MNRAS, 504, 1749

Line J. L. B., Webster R. L., Pindor B., Mitchell D. A., Trott C. M., 2017, PASA, 34, e003

Loi F., et al., 2017, MNRAS, 472, 3605

Lovisari L., et al., 2017, ApJ, 846, 51

Macario G., Venturi T., Brunetti G., Dallacasa D., Giacintucci S., Cassano R., Bardelli S., Athreya R., 2010, A&A, 517, A43

Macario G., et al., 2013, A&A, 551, A141

Mahatma V. H., et al., 2018, MNRAS, 475, 4557

Mandal S., et al., 2020, A&A, 634, A4

Markevitch M., Govoni F., Brunetti G., Jerius D., 2005, ApJ, 627, 733

Mauch T., Murphy T., Buttery H. J., Curran J., Hunstead R. W., Piestrzynski B., Robertson J. G., Sadler E. M., 2003, MNRAS, 342, 1117

McConnell D., et al., 2020, PASA, 37, e048

Morganson E., et al., 2018, PASP, 130, 074501

Murgia M., Govoni F., Markevitch M., Feretti L., Giovannini G., Taylor G. B., Carretti E., 2009, A&A, 499, 679

Murgia M., et al., 2011, A&A, 526, A148

Murphy T., Mauch T., Green A., Hunstead R. W., Piestrzynska B., Kels A. P., Sztajer P., 2007, MNRAS, 382, 382

Murphy T., et al., 2013, PASA, 30, e006

Murphy T., Lenc E., Whiting M., Huynh M., Hotan A., 2019, ASKAP Data Products for Project AS111 (ASKAP Pilot Survey for Gravitational Wave Counterparts): images and visibilities. v1. CSIRO. Data Collection, http://hdl.handle.net/102.100.100/175570?index=1

Murphy T., et al., 2020, ASKAP Data Products for Project AS107 (ASKAP Pilot Survey for VAST): images and visibilities. v1. CSIRO. Data Collection, http://hdl.handle.net/102.100.100/340961?index=1

Nuza S. E., Hoeft M., van Weeren R. J., Gottlöber S., Yepes G., 2012, MNRAS, 420, 2006

Ochsenbein F., Bauer P., Marcout J., 2000, A&AS, 143, 23

Offringa A. R., Smirnov O., 2017, MNRAS, 471, 301

Offringa A. R., et al., 2014, MNRAS, 444, 606

Offringa A. R., et al., 2015, PASA, 32, e008

Offringa A. R., et al., 2016, MNRAS, 458, 1057

Ogrean G. A., et al., 2015, ApJ, 812, 153

Orrú E., Murgia M., Feretti L., Govoni F., Brunetti G., Giovannini G., Girardi M., Setti G., 2007, A&A, 467, 943

Parma P., Murgia M., de Ruiter H. R., Fanti R., Mack K. H., Govoni F., 2007, A&A, 470, 875

Pearce C. J. J., et al., 2017, ApJ, 845, 81

Piffaretti R., Arnaud M., Pratt G. W., Pointecouteau E., Melin J.-B., 2011, A&A, 534, A109

Planck Collaboration et al., 2014, A&A, 571, A29

Planck Collaboration et al., 2015, A&A, 581, A14

Planck Collaboration et al., 2016, A&A, 594, A27

Poole G. B., Fardal M. A., Babul A., McCarthy I. G., Quinn T., Wadsley J., 2006, MNRAS, 373, 881

Pratt G. W., Croston J. H., Arnaud M., Böhringer H., 2009, A&A, 498, 361

Quici B., et al., 2021, PASA, 38, e008

Rajpurohit K., et al., 2020, A&A, 642, L13

Rajpurohit K., et al., 2021a, arXiv e-prints, p. arXiv:2104.05690

Rajpurohit K., et al., 2021b, A&A, 646, A56

Rajpurohit K., et al., 2021c, A&A, 646, A135

Richard-Laferrière A., et al., 2020, MNRAS, 499, 2934

Robitaille T., Bressert E., 2012, APLpy: Astronomical Plotting Library in Python, Astrophysics Source Code Library (ascl:1208.017)

Rossetti M., Gastaldello F., Eckert D., Della Torre M., Pantiri G., Cazzoletti P., Molendi S., 2017, MNRAS, 468, 1917

Sakelliou I., Hardcastle M. J., Jetha N. N., 2008, MNRAS, 384, 87

Santos J. S., Rosati P., Tozzi P., Böhringer H., Ettori S., Bignamini A., 2008, A&A, 483, 35

Schwope A., et al., 2000, Astronomische Nachrichten, 321, 1

Slee O. B., Roy A. L., Murgia M., Andernach H., Ehle M., 2001, AJ, 122, 1172

Struble M. F., Rood H. J., 1999, ApJS, 125, 35

Strüder L., et al., 2001, A&A, 365, L18

Subrahmanyan R., Ekers R. D., Saripalli L., Sadler E. M., 2010, MNRAS, 402, 2792

Tarrío P., Melin J. B., Arnaud M., Pratt G. W., 2016, A&A, 591, A39

Tarrío P., Melin J. B., Arnaud M., 2018, A&A, 614, A82

Thierbach M., Klein U., Wielebinski R., 2003, A&A, 397, 53

Thorat K., Subrahmanyan R., Saripalli L., Ekers R. D., 2013, ApJ, 762, 16

Tingay S. J., et al., 2013, PASA, 30, 7

Tonry J. L., et al., 2012, ApJ, 750, 99

Trasatti M., Akamatsu H., Lovisari L., Klein U., Bonafede A., Brüggen M., Dallacasa D., Clarke T., 2015, A&A, 575, A45

Turner M. J. L., et al., 2001, A&A, 365, L27

Urdampilleta I., Simionescu A., Kaastra J. S., Zhang X., Di Gennaro G., Mernier F., de Plaa J., Brunetti G., 2021, A&A, 646, A95

Vazza F., Wittor D., Brunetti G., Brüggen M., 2021, arXiv e-prints, p. arXiv:2102.04193

Venturi T., Giacintucci S., Dallacasa D., Cassano R., Brunetti G., Bardelli S., Setti G., 2008, A&A, 484, 327

Vikhlinin A., McNamara B. R., Forman W., Jones C., Quintana H., Hornstrup A., 1998, ApJ, 502, 558

Voges W., et al., 1999, A&A, 349, 389

Wayth R. B., et al., 2015, PASA, 32, 25

Wayth R. B., et al., 2018, PASA, 35

Wen Z. L., Han J. L., 2015, ApJ, 807, 178

Wen Z. L., Han J. L., Liu F. S., 2012, ApJS, 199, 34

Wilber A., et al., 2018, MNRAS, 473, 3536

Wilber A., et al., 2019, A&A, 622, A25

Wilber A. G., Johnston-Hollitt M., Duchesne S. W., Tasse C., Akamatsu H., Intema H., Hodgson T., 2020, PASA, 37, e040

Xie C., et al., 2020, A&A, 636, A3

Zaritsky D., Gonzalez A. H., Zabludoff A. I., 2006, ApJ, 638, 725

de Gasperin F., 2017, MNRAS, 467, 2234

de Gasperin F., van Weeren R. J., Brüggen M., Vazza F., Bonafede A., Intema H. T., 2014, MNRAS, 444, 3130

de Gasperin F., Intema H. T., van Weeren R. J., Dawson W. A., Golovich N., Wittman D., Bonafede A., Brüggen M., 2015, MNRAS, 453, 3483
de Gasperin F., et al., 2017, Science Advances, 3, e1701634
van Haarlem M. P., et al., 2013, A&A, 556, A2
van Weeren R. J., Röttgering H. J. A., Brüggen M., Hoeft M., 2010, Science, 330, 347
van Weeren R. J., Brüggen M., Röttgering H. J. A., Hoeft M., Nuza S. E., Intema H. T., 2011, A&A, 533, A35
van Weeren R. J., Röttgering H. J. A., Intema H. T., Rudnick L., Brüggen M., Hoeft M., Oonk J. B. R., 2012, A&A, 546, A124
van Weeren R. J., et al., 2016, ApJ, 818, 204
van Weeren R. J., et al., 2017, Nature Astronomy, 1, 0005
van Weeren R. J., de Gasperin F., Akamatsu H., Brüggen M., Feretti L., Kang H., Stroe A., Zandanel F., 2019, Space Sci. Rev., 215, 16
van Weeren R. J., et al., 2021, A&A, 651, A115
van der Walt S., Colbert S. C., Varoquaux G., 2011, Computing in Science Engineering, 13, 22

A. Non-candidates

In this section we will record clusters previously reported as having candidate diffuse emission by D21 but are shown by the MWA-2 data to be discrete sources. Note that while `FIELD1` and `FIELD2` overlap with a majority image used by Duchesne et al. 2021b, for some clusters towards the edges of the fields we are unable to confirm the presence of either diffuse emission of discrete sources—these clusters are not mentioned here.

Abell 0022. Edge of image. Inconclusive.
Abell 0033. Edge of image. Inconclusive.
Abell 2798. Resolution still not sufficient. Inconclusive.
Abell S1136. To be discussed in Macgregor et al. (in prepatation).
Abell S1063. Halo reported by Xie et al. (2020).
Abell 2556. The MWA-2 216-MHz, robust +0.5 image breaks up into three discrete point sources. RACS data confirm the source is a number of point sources and a double-lobed radio galaxy, with a spectral index $\alpha \sim -0.8$. The steeper spectral index reported by D21 is a result of point sources contributing to the 168-MHz measurement but not the 1.4-GHz measurement.
Abell S0084. MWA-2 data breaks into two discrete components and RACS confirms this. We cannot confirm the candidate halo/mini-halo.
Abell S1121. Out of images.
PSZ G082.31−67.01. Out of images.

B. Measured source properties

A table of measured and derived source properties are provided for all frequencies (88, 118, 154, 169, 185, 200, 216, 887, 943, and 1400 MHz, though note not all sources are measured at every frequency) as supplementary online material available at the data store for the Publications of the Astronomical Society of Australia, hosted at `https://data-portal.hpc.swin.edu.au/institute/pasa` (Duchesne, 2021) . The following details the columns available for each source:

C0 `cluster_name`
Name of cluster as it appears in Table 1.

C1 `source_id`
ID of source as used in Section 3.1 and in figures.

C2 `flux_$nu` (mJy)
Final flux density of source at frequency `$nu` MHz.

C3 `err_flux_$nu` (mJy)
Uncertainty on the final flux density of source at frequency `$nu` MHz.

C4 `conf_$nu` (mJy)
Total confusing flux density subtracted from initial measurement at frequency `$nu` MHz.

C5 `err_conf_$nu` (mJy)
Uncertainty on total confusing flux density subtracted from initial measurement at frequency `$nu` MHz. This is added in quadrature to the initial measurement.

C6 `psf_a_$nu` (arcsec)
FWHM of PSF major axis in `$nu`-MHz image at the source location.

C7 `psf_b_$nu` (arcsec)
FWHM of PSF minor axis in `$nu`-MHz image at the source location.

⋮

C56 `alpha_mwa`
Spectral index across the MWA-2 images as shown in Fig. 26(i)–(xxix).

C57 `alpha`
Spectral index across all data for power law models as shown in Fig. 26(i)–(xxix).

C58 `q`
Curvature parameter for curved power law model fits (Eq. 6), as shown in Fig. 26(i)–(xxix).

C. Integrated spectra

Fig. 26(i)–(xxix) show the SEDs for all sources reported in Section 3.1. For each source with MWA-2 and additional data, we additionally provide a power law fit to the MWA-2 data only.

D. Flux recovery in MWA-2 data

Fig. 27(i)–(ix) show the ratios of dirty to CLEAN flux density for Gaussian models of varying FWHM. For each source the residual flux density is integrated and multiplied by the factor $S_{\rm CLEAN}/S_{\rm dirty}$ to account for this. Additional detail of this process is provided in Duchesne et al. (2021c).

`https://dx.doi.org/10.26185/611f33b774e96`

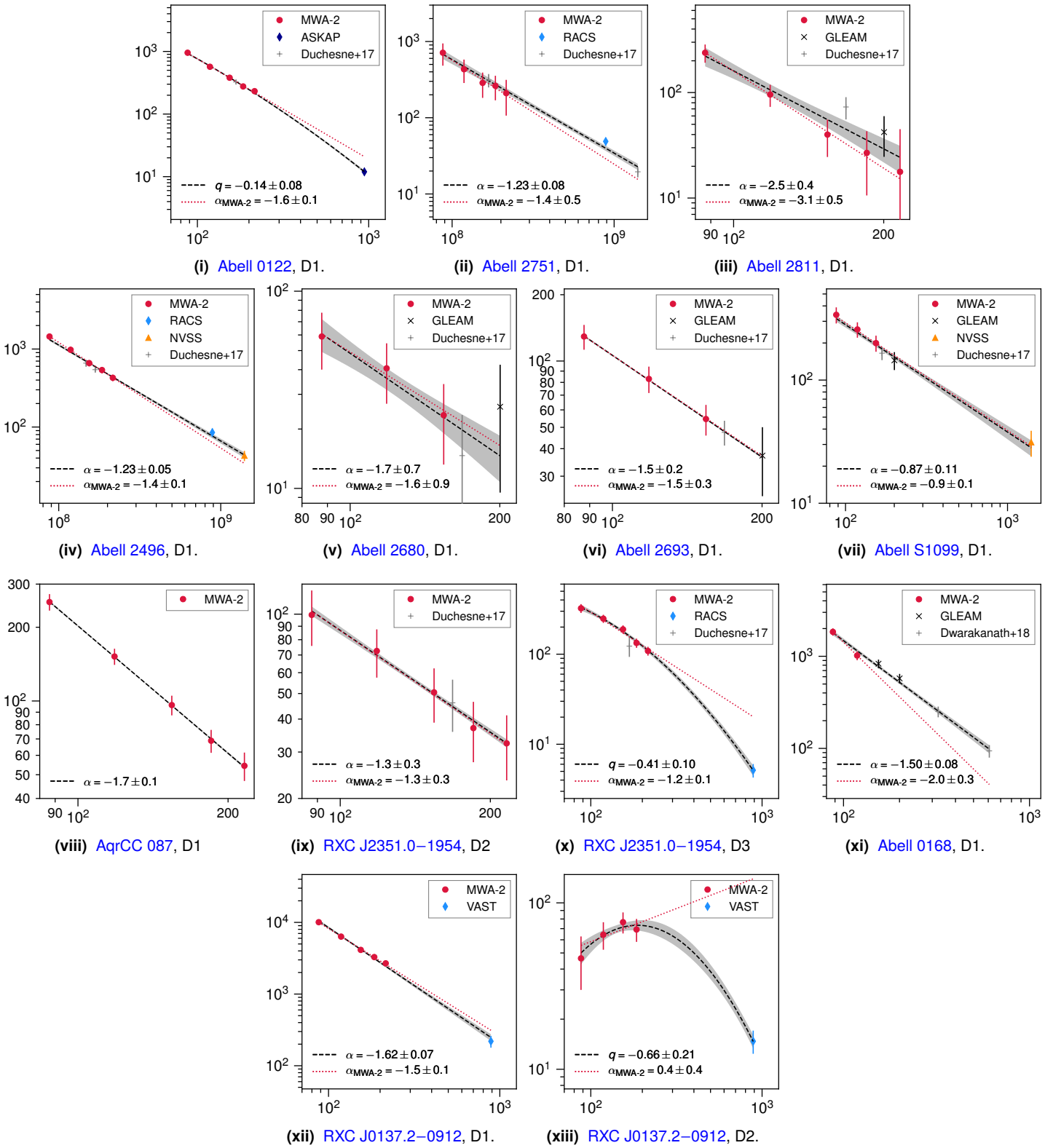

Figure 26. Integrated spectra of diffuse sources described in Section 3.1 in the order they are reported. The ordinate and abscissa are integrated flux density (mJy) and frequency (MHz), respectively. Individual measurements are reported in the online table described in Appendix B. The dashed, black lines are the fits for the full set of measurements (with grey, shaded regions corresponding to 95% confidence intervals) and the red, dotted lines are fits for only the MWA-2 data. Note black arrows represent limits. Note if only two data points are available, a two-point spectral index was calculated and the resultant line is drawn based on that spectral index. For curved power law spectra, we report the curvature, q, rather than the equivalent spectral index.

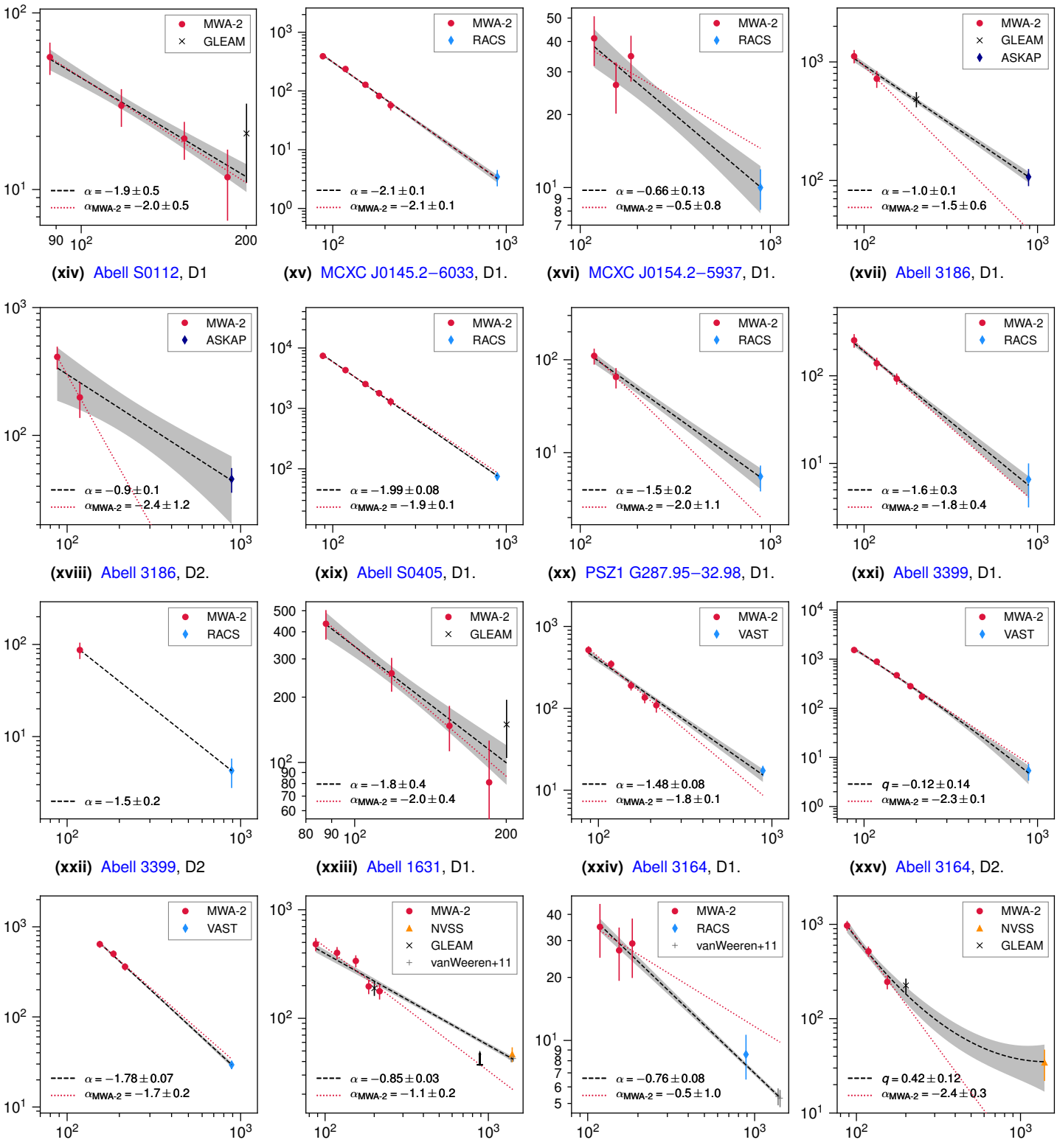

(xiv) Abell S0112, D1 **(xv)** MCXC J0145.2−6033, D1. **(xvi)** MCXC J0154.2−5937, D1. **(xvii)** Abell 3186, D1.

(xviii) Abell 3186, D2. **(xix)** Abell S0405, D1. **(xx)** PSZ1 G287.95−32.98, D1. **(xxi)** Abell 3399, D1.

(xxii) Abell 3399, D2 **(xxiii)** Abell 1631, D1. **(xxiv)** Abell 3164, D1. **(xxv)** Abell 3164, D2.

(xxvi) Abell 3164, D3. **(xxvii)** Abell 3365, D1. **(xxviii)** Abell 3365, D2. **(xxix)** Abell 0550, D1.

Figure 26. *continued.*

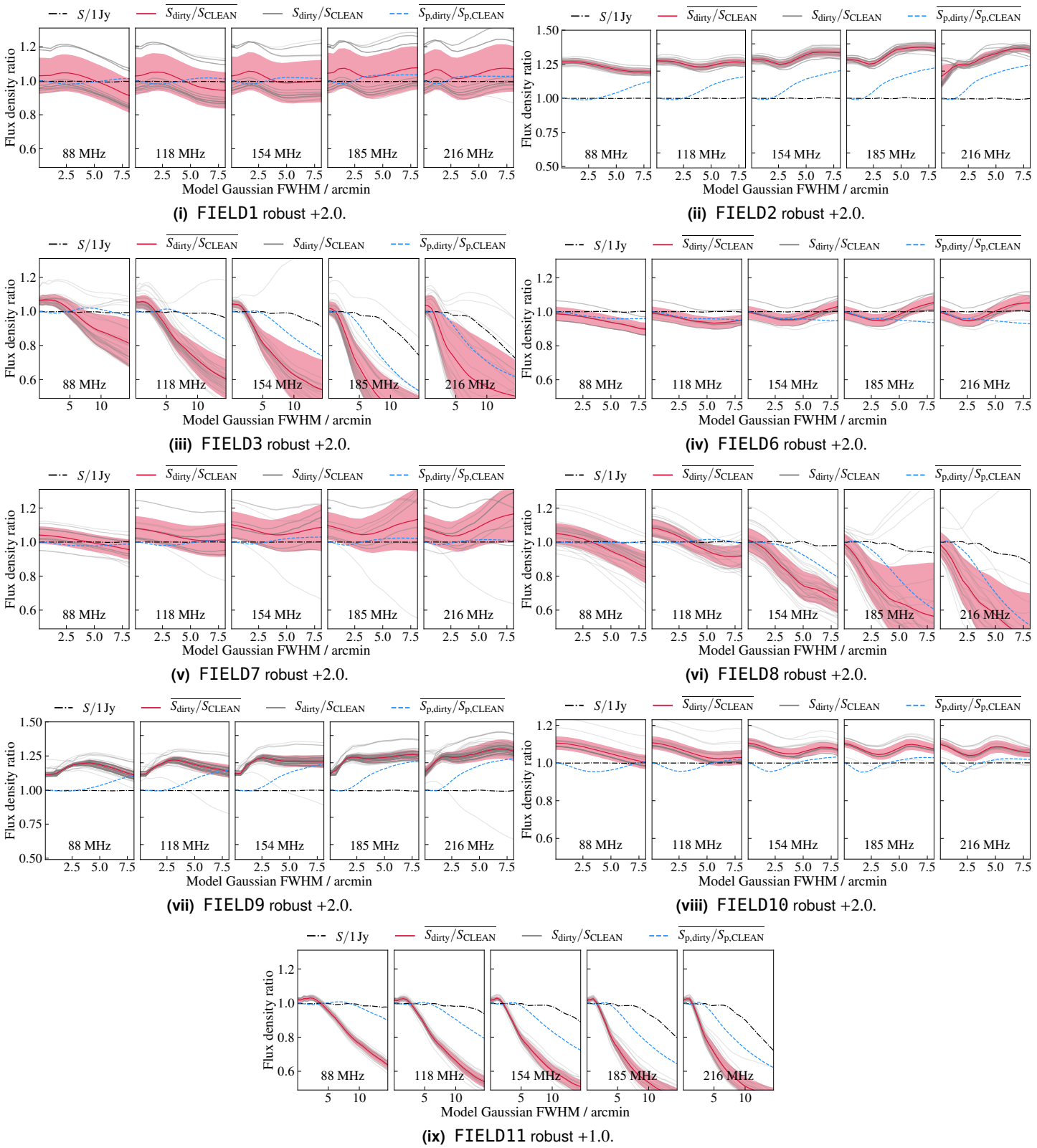

(i) FIELD1 robust +2.0.

(ii) FIELD2 robust +2.0.

(iii) FIELD3 robust +2.0.

(iv) FIELD6 robust +2.0.

(v) FIELD7 robust +2.0.

(vi) FIELD8 robust +2.0.

(vii) FIELD9 robust +2.0.

(viii) FIELD10 robust +2.0.

(ix) FIELD11 robust +1.0.

Figure 27. Flux recovery and ratio of deconvolved ('CLEAN') to un-deconvolved ('dirty') integrated flux density for individual snapshots (grey lines). The angular scale on the abscissa correspond to FWHM of the simulated Gaussian (sampled every 30 arcsec). The mean profile, $\overline{S_{\mathrm{dirty}}/S_{\mathrm{CLEAN}}}$, is plotted with the standard deviation plotted as a red shaded region. The mean peak flux profile, $\overline{S_{\mathrm{p,dirty}}/S_{\mathrm{p,CLEAN}}}$, is also shown. (i) and (vi) are re-produced from Duchesne et al. (2021c) for completeness.

Acronyms

ΛCDM Λ Cold Dark Matter.

AGN active galactic nucleus.

ASKAP Australian Square Kilometre Array Pathfinder.

ATCA Australia Telescope Compact Array.

BCG brightest cluster galaxy.

CC cool-core.

CI continuous injection.

$\mathbf{CI_{off}}$ CI with a switched 'off' component.

CMB Cosmic Microwave Background.

DES Dark Energy Survey.

DSA diffusive shock accceleration.

DSS2 Digitized Sky Survey.

EMU Evolutionary Map of the Universe.

eROSITA extended ROentgen Survey with an Imaging Telescope Array.

FOV field-of-view.

GLEAM GaLactic and Extra-galactic All-sky MWA.

GLEAM EGC GLEAM Extra-Galactic Catalogue.

GLEAM-X GLEAM eXtended.

GMRT Giant Metrewave Radio Telescope.

GRG giant radio galaxy.

ICM intra-cluster medium.

JVLA Karl G. Jansky Very Large Array.

LOFAR LOw Frequency ARray.

LoTSS LOFAR Two-metre Sky Survey.

MHD magneto-hydro dynamic.

MWA Murchison Widefield Array.

MWA-2 MWA phase II ‘extended’.

NED NASA/IPAC Extragalactic Database.

NVSS NRAO VLA Sky Survey.

PSF point-spread function.

RFI radio-frequency interference.

rms root mean square.

SED spectral energy distribution.

SKA Square Kilometre Array.

SNR signal-to-noise ratio.

SUMSS Sydney University Molonglo Sky Survey.

TGSS TIFR GMRT Sky Survey.

uGMRT upgraded GMRT.

USSRH ultra-steep–spectrum radio halo.

VLA Very Large Array.

Lilies and daisies.